Scientific Report 2008

Institut für Festkörperforschung
Institute of Solid State Research

JÜLICH
FORSCHUNGSZENTRUM

Aberration-corrected transmission electron microscopy image of a thin film of the relaxor ferroelectric $Ca_{0.28}Ba_{0.72}Nb_2O_6$ on a $SrTiO_3$ substrate (in false colours).

Both the amorphous area on the left (with predominant green colour), created by ion milling during processing, and the complex structure of the material viewed from the [001] crystallographic axis are clearly resolved. Image: Chun-lin Jia / Forschungszentrum Jülich, cover image of "nature materials insight", April 2008, Volume 8, No 4.
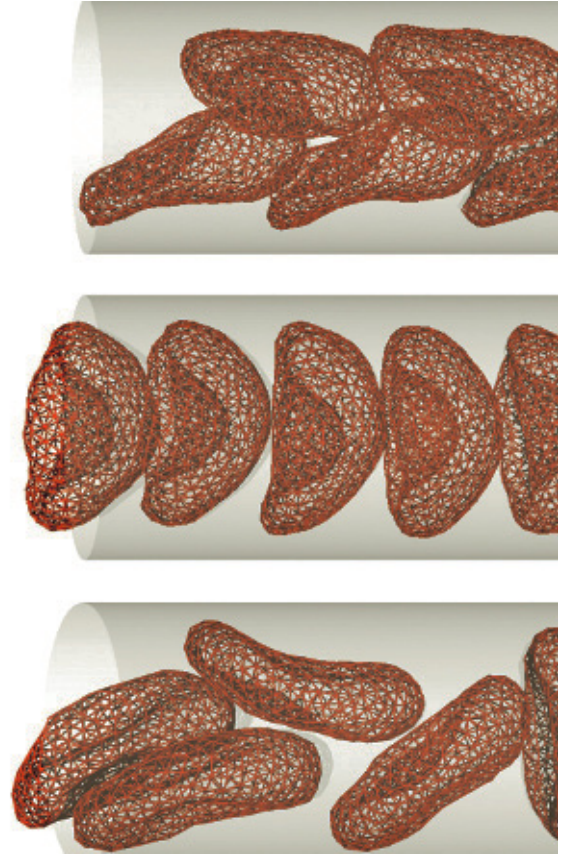
The flow behavior of red blood cells (RBCs) in microcapillaries and microfluidic devices is governed by the deformability of the cells, their hydrodynamic interactions, and thermally induced cell membrane undulations. These mechanisms can be studied in silico by using state-of-the-art simulation techniques. The simulations predict that, at physiological hematocrit values, 3 distinct phases exist: disordered biconcave-disk shapes (Top), parachute-shaped RBCs aligned in a single file (Middle), and slipper-shaped RBCs arranged as 2 parallel inter-digitated rows (Bottom). See the articles by J. Liam McWhirter et al. on pages NN and in PNAS 2009 106:6039-6043. Image: Hiroshi Noguchi / Forschungszentrum Jülich.

Scientific Report 2008

Institut für Festkörperforschung
Institute of Solid State Research

Directors of the Institute of Solid State Research (IFF) from left:

Prof. Dr. Jan K. G. Dhont (IFF-7: Soft Condensed Matter)
Prof. Dr. Knut Urban (IFF-8: Microstructure Research
Prof. Dr. Heiner Müller-Krumbhaar (IFF-3: Theory of Structure Formation)
Prof. Dr. Dieter Richter (IFF-5: Neutron Scattering)
Prof. Dr. Thomas Brückel (IFF-4: Scattering Methods)
Prof. Dr. Stefan Blügel (IFF-1: Quantum Theory of Materials)
Prof. Dr. Rainer Waser (IFF-6: Electronic Materials)
Prof. Dr. Claus M. Schneider (IFF-9: Electronic Properties)
Prof. Dr. Gerhard Gompper (IFF-2: Theoretical Soft-Matter and Biophysics)

Contents

5

HGF research programme
Information technology with nanoelectronic systems — page 156

Research reports

6

HGF research programme
Large-scale facilities for research with photons, neutrons and ions   page 192

7

Research reports

Appendix   page 216

Imprint   page 263

Foreword

The annual report 2008 is intended to inform the international scientific community, including our scientific advisory board and the Helmholtz Association (Helmholtz-Gemeinschaft, HGF) about the research activities of the IFF during the past year. We have attempted to present a typical cross section through the research conducted at the IFF, within the Helmholtz research programmes "Condensed Matter Physics", "Information Technology with Nanoelectronic Systems", and "Large-scale Facilities for Research with Photons, Neutrons, and Ions".

The IFF is engaged in investigating a multitude of condensed matter phenomena with special emphasis on studies of fundamental physical mechanisms, the development and improvement of experimental and theoretical concepts and methods, as well as the elucidation and exploitation of new material properties in complex systems. The Helmholtz research programmes follow this main aim in addition to exploit the full scale of analytical and numerical methods to disentangle interrelations between structural, electronic, magnetic, and dynamic properties of condensed matter together with describing underlying physical mechanisms on a microscopic and atomistic level.

In the area of nanoelectronics, the advancements today are driven by a unique interplay of scientific and technological issues. As a consequence, strong fundamental research in solid-state physics must be combined with leading edge fabrication and characterization techniques. Recognizing this situation, the Forschungszentrum Jülich and the RWTH Aachen University have joined forces and embarked on a long-term plan for the strategic development of the research environment in the field of nanoelectronics and information technology by founding the JARA section "Fundamentals of Future Information Technology" (JARA-FIT) in 2007.

As a further pivotal step within this concept, we initiated the formation of a central research infrastructure platform, which we named the Peter Grünberg Centre, honouring the Nobel Prize in Physics 2007. In its first stage, the Peter Grünberg Centre will comprise the planned Helmholtz Nano-electronics Facility as well as the Synchro-tron Radiation Laboratory. Future units in the fields of scanning probe spectroscopy, or ultrafast processes, as well as a centre for advanced technologies on the campus of the RWTH Aachen University are envisioned.

The Ernst Ruska-Centre for Microscopy and Spectroscopy with Electrons (ER-C) has been established as a national user facility housing several of the world's most advanced transmission electron microscopes (TEM) and tools fo nanocharacterization. It is operated conjointly by the IFF at the Forschungszentrum Jülich and the GfE at the RWTH Aachen University. During 2008, the PICO project was secured by funds of North-Rhine Westphalia, the RWTH Aachen, and the Deutsche Forschungsgemeinschaft (German Research Foundation). The PICO project aims at a new generation of an ultrahigh resolution TEM (PICO-UHT) equipped with a spectroscopy research tool (PICO-SRT) and features spherically and chromatically aberration corrected electron optics.

The Jülich Centre for Neutron Science (JCNS) operates instruments at some of the leading neutron sources worldwide: the Forschungs-reaktor München FRM II in Garching, Germany, the Institute Laue-Langevin ILL in Grenoble, France, and the Spallation Neutron Source SNS in Oak Ridge, USA. Under a common scientific objective and user programme, JCNS offers users state-of-the-art instruments at the neutron source best suited to the respective application. Beamtime at JCNS is allocated through an international peer-review panel on the basis of scientific merit only.

In the period 2007/2008, more than 200 external proposals for external beam time with a request for 1,288 beam days were received. 75 proposals by users were allocated 350 beam days at the instruments of JCNS at FRM II, corresponding to 63 % external use. At FRM II, four instruments were in full user operation in 2008: the spin-echo spectrometer NSE, the small angle camera KWS-2, the backscattering spectrometer SPHERES and the diffuse neutron scattering instrument DNS. Seven further instruments are in construction.

The Forschungszentrum Jülich hosts and operates one of the most powerful super-computers in the world. This opens new scientific opportunities for the three theory institutes. The development of the simulation sciences on such computers is one of the key challenges the Forschungszentrum addresses. This task is one of the missions of the newly inaugurated department Institute for Advanced Simulation (IAS). The foundation of this department is embedded in the JARA section "Simulation Sciences" (JARA-SIM) and is supplemented by the German Research School for Simulation Sciences (GRS). The theory institutes of the IFF have founded working groups in the IAS and contribute to the newly certified master's course in simulation sciences offered by GRS.

The quality of the research at the IFF is widely appreciated and respected by the scientific community as reflected by the numerous awards, for example, the Grand Cross with Star of the Order of Merit of the Federal Republic of Germany to our Nobel laureate, Prof. Dr. Peter Grünberg, in addition to honorary doctorates from the University in Cologne, the Tohoku University (Japan), and the Gebze Institute of Technology (Turkey). Together with Dr. Maxmilian Haider, Heidelberg, and Prof. Dr. Harald Rose, Darmstadt, Prof. Dr. Knut Urban (Institute of Microstructure Research) was awarded the Honda Prize 2008 for the development of aberration correction for transmission electron microscopes. Prof. Dr. Shigemasa Suga (Institute of Electronic Properties) received the Humboldt Research Prize from the Alexander von Humboldt Foundation. Dr. Martina Müller (Institute of Electronic Properties) won the Günter Leibfried Prize awarded by Forschungszentrum Jülich for communicating science successfully. The IFF was also particularly successful in establishing young investigator groups. Dr. M. Angst (Complex Ordering Phenomena in Multifunctional Oxides), Dr. M. Lezaic (Computational Nanoferronics Laboratory), and Dr. Y. Mokrousov (Topological Nanoelectronics) have started their activities in 2008. This success is complemented by appointments to young scientists who have been working at the IFF in recent years and now left to start scientific careers on their own. Dr. A. Rüdiger (Institute of Electronic Materials) accepted an appointment as a full professor for nanolelectronics/nanophotonics at the Institut National de la Recherche Scientifique of Québec University (Canada), Dr. H. Noguchi (Institute of Theory of Soft Matter and Biophysics) was appointed associate professor at the Institute for Solid State Physics (ISSP) by the University of Tokyo (Japan), and Dr. A. Schindlmayr (Institute of Quantum Theory of Materials) accepted an appointment as professor (W2) in Theoretical Physics at the University of Paderborn.

I hope you will enjoy reading the report and learning about our activities.

Prof. Dr. Rainer Waser
Managing Director of IFF in 2009
Director of IFF-6 "Electronic Materials"
May 2009

Snapshots 2008

*Peter Grünberg awarded order of Merit of the Federal Republic of Germany
by German President Köhler*

*8 April: The German President, Horst Köhler (right), awards the Nobel Laureate Prof. Dr. Peter
Grünberg (left) from the Jülich Institute of Solid State Research (IFF) with the Cross of the
Order of Merit of the Federal Republic of Germany. By presenting this award, the President
pays tribute to outstanding achievements in both basic and application-oriented cutting-edge
research. The physicist enabled and improved technological developments, without which our
every-day life would no longer be conceivable. The ceremony was held at the President's official
residence, Schloss Bellevue in Berlin.*

© Presse- und Informationsamt der Bundesregierung / REGIERUNGonline / Sandra Steins

19 February:
GMR exhibit on the road
in the "NanoTruck"

An exhibit on the GMR effect – the effect which earned the IFF physicist Prof. Dr. Peter Grünberg the Nobel Prize for Physics 2007 – is on display in a mobile nanotechnology exhibition supported by the German Federal Ministry of Education and Research (BMBF). The so-called "NanoTruck" visits events in schools, universities and research institutions among other things.

"The exhibition aims to explain the scientific, social and economic significance of nanotechnology and to stimulate the dialogue between the science community and the general public", said Grünberg. He is delighted that his work is contributing to this process. The Nobel Laureate was also involved in designing the exhibit.

A GMR exhibit tours Germany on board the "NanoTruck" .

Photo: Flad & Flad Communication GmbH

22 February:
Fastest civil supercomputer
in the world

An official ceremony in Jülich marked the inauguration of the fastest civil supercomputer in the world. The go-ahead was given by Prime Minister Jürgen Rüttgers together with State Secretary Thomas Rachel. The computer, known as JUGENE, performs around 167 trillion mathematical calculations per second and is Europe's fastest supercomputer. It held second place in the global TOP500 ranking list published in February 2008.

Computer simulations are a key technology for science and they have established themselves on an equal footing with theoretical and experimental research. The supercomputer has proven itself to be a flexible and powerful tool when complex problems have to be solved. Researchers from IFF, for example, use supercomputers to unravel the mysteries of high-temperature superconductivity.

At the time of its inauguration, the Jülich IBM Blue Gene supercomputer, known as JUGENE, was the fastest civil supercomputer in the world.

3 – 14 March:
39th IFF Spring School with 220 participants

220 students and young scientists from 25 countries attended the 39th international IFF spring school in Jülich. Under the motto "Soft Matter – From Synthetic to Biological Materials", they gained a comprehensive overview of the interdisciplinary research area of "soft matter" at the interface of physics, chemistry, biology and the life sciences.

The spring school covered a range of topics from the theoretical and experimental basis of soft matter to state-of-the-art investigation methods and examples of industrial application such as in cosmetics. Experts from For-schungszentrum Jülich and other European research institutions and industrial companies such as BASF SE or Unilever AG gave classes concerning topics such as computer simulations, research with the aid of light and particle scattering, and the synthesis of complex materials in theory and practice.

Participants and organisers of the IFF spring school 2008 "Soft Matter – From Synthetic to Biological Materials".

13 – 16 May:
Electronics on a millionth of a millimetre
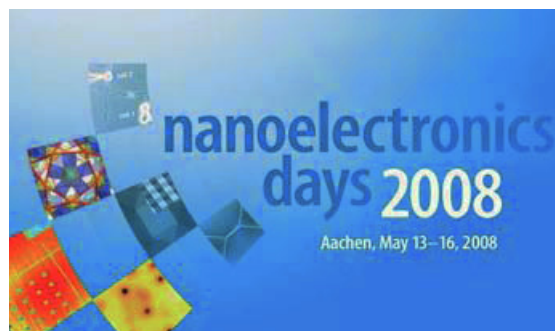
Recent research findings in nanoelectronics and new strategies for applications were the main topics addressed by a specialist meeting, which took place in Aachen. 160 researchers from science and industry registered for the "Nanoelectronics Days", which were organised by the JARA-FIT Section of the Jülich-Aachen Research Alliance (JARA). JARA is a cooperation between Forschungszentrum Jülich and RWTH Aachen University. The "Nanoelectronics Days" revolved around methods, techniques and new materials which can be used to advance the miniaturisation of electronic devices. The meeting focused, for example, on alternative ultra-small devices in the nanometre range, atomic structures, innovative architectures using proven semiconductor technology and exploiting the electron spin as a unit of information. It also looked at magnetic and resistive switching strategies and devices which may be of importance for the next generation of nonvolatile memories.

9 – 13 June:
Why do particles migrate in temperature gradients?

At the invitation of IFF, 80 international scientists met at the "8th International Meeting on Thermodiffusion" in Bonn. Thermodiffusion is a physical process that plays a major role in many technical fields. Two examples are the analysis of dispersions such as wall paint and the characterisation of oil deposits. Although this effect was observed for the first time 150 years ago, we still do not fully understand it. The aim of the scientists is to improve technical applications in the long run through an improved understanding of basic physical fluid properties
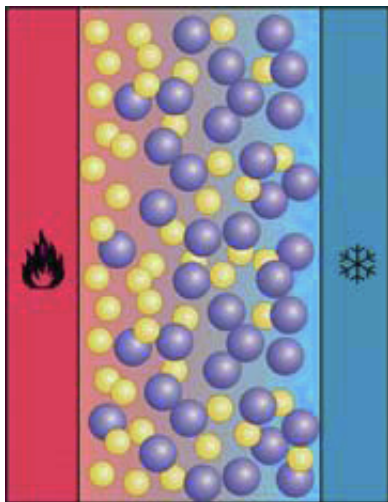
Thermal diffusion describes the movement of aerosol particles along a temperature gradient, typically from hot to cold in gases and liquids.

20 August:
Order of Merit of the federal state of North Rhine-Westphalia

Prof. Dr. Peter Grünberg and Prime Minister Jürgen Rüttgers.

Photo: State Chancellery of North Rhine-Westphalia; photographer: Ralph Sondermann.

The Jülich Nobel Laureate Prof. Dr. Peter Grünberg was awarded the Order of Merit of the federal state of North Rhine-Westphalia. The NRW Prime Minister, Jürgen Rüttgers, presented the award for outstanding service to North Rhine-Westphalia and its inhabitants to the Jülich solid-state physicist and another 14 celebrities, including the well-known former professional soccer player Rudi Völler, at a ceremony in the Ständehaus Art Museum in Düsseldorf. Grünberg received the award for his outstanding achievements as a researcher and for his efforts promoting basic research.

1 September:
Recipient of Helmholtz-Humboldt Research Award to work at IFF

IFF welcomed another distinguished Japanese visiting scientist. Prof. Dr. Shigemasa Suga from the University of Osaka, Japan, received a 2008 Helmholtz-Humboldt Research Award, which enabled him to spend twelve months conducting research in Germany. Together with colleagues from the Jülich Institute of Solid State Research (IFF) and several German universities, he studies magnetic structures in solids. Such systems are used, for example, as magnetic data storage systems in information technology. At IFF, Suga has access to special equipment enabling him to visualise tiny magnetic areas in materials known as domains. A scientific instrument operated by the Jülich Competence Centre for Synchrotron Science (JCCSS) at the Berlin storage ring "BESSY" is particularly important for Suga's research, as is a scanning tunnelling microscope, which permits spin analysis, and a photoelectron emission microscope in Jülich.
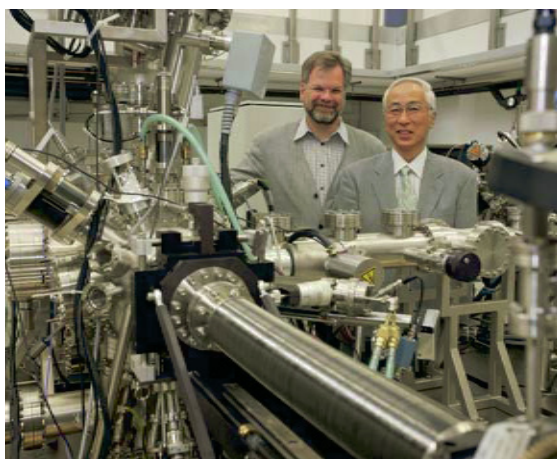
2 September:
New nanospintronics research laboratory at IFF

A new laboratory for investigating materials and concepts for tomorrow's information technology has been put into operation at IFF. The so-called nanospintronics cluster tool, which cost roughly € 3,000,000, combines a number of cutting edge research instruments, thus making it possible to perform new types of experiments. "The combination of instruments means that Forschungszentrum Jülich has a unique facility at its disposal capable of generating and characterising smallest structures in the nanometre range for nanoelectronics and spintronics without having to remove the samples from an ultrahigh vacuum environment," said Prof. Dr. Claus M. Schneider, director of IFF-9 "Electronic Properties". "An integrated focused ion beam source serves to cut out even the tiniest structures. This will allow minute components to be created, which can be switched by spin-polarised currents." The researchers are thus pursuing new strategies for the further miniaturisation of storage media and logic modules in information technology.

Guest scientist Prof. Dr. Shigemasa Suga (right) and his host Prof. Dr. Claus M. Schneider (left), head of IFF-9 "Electronic Properties", tour the IFF laboratories. The new nanospintronics cluster tool can also be seen here.

4 September:
Closer cooperation in electron microscopy

Forschungszentrum Jülich, RWTH Aachen University and the University of California, Berkeley, USA, signed a memorandum of understanding on cooperations between the Ernst Ruska-Centre for Microscopy and Spectroscopy with Electrons (ER-C) and the National Center for Electron Microscopy (NCEM). The long-standing good cooperation of the two internationally prominent centres for electron microscopy thus reached a new level. Joint studies on the development and improvement of state-of-the-art electron-optical methods were agreed upon which pave the way for materials research, a stronger exchange of know-how and personnel, and joint training for PhD students and postdocs.

From left to right, back: Member of the Board of Directors of Forschungszentrum Jülich Prof. Dr. Sebastian Schmidt, NRW Innovation Minister Andreas Pinkwart, Parliamentary State Secretary at the German Federal Ministry of Education and Research Thomas Rachel, the Directors of ER-C Prof. Dr. Knut Urban und Prof. Dr. Joachim Mayer, and, sitting: the Chairman of the Board of Directors of Forschungszentrum Jülich Prof. Dr. Achim Bachem, Director of NCEM Dr. Ulrich Dahmen, and Rector of RWTH Aachen University Prof. Dr. Ernst Schmachtenberg.

Picture: RWTH Aachen University

8 September:
PhD students communicate science successfully

Science fiction and sandwiches with a spin – these were some of the topics of this year's Günter Leibfried Prize. The first prize of € 3,000 went to the physicist Martina Müller, formerly IFF-9 (Electronic Properties). In a lively presentation, she described how the main memories in computers will be able to do with magnetism in the future. One of two second prizes, worth € 1,500 went to Samir Lounis from IFF-1 (Quantum Theory of Materials). In his lecture, the physicist referred to the science fiction movie "I, Robot" and showed that constructions previously believed to be impossible were indeed conceivable when nanoelectronics is combined with quantum mechanics. The Günter Leibfried Prize – named after the former IFF director who died in 1977 – is awarded annually to PhD students at Forschungszentrum Jülich who succeed in presenting the results of their PhD thesis in a lively and generally intelligible manner.

From left to right: Prof. Dr. Ulrich Samm, member of the jury, Anna Strózecka (2nd prize), Samir Lounis (2nd prize), Martina Müller (1st prize) and Prof. Dr. Achim Bachem, Chairman of the Board of Directors, Forschungszentrum Jülich.

2 October:
Japanese Honda Prize goes to Knut Urban

The Japanese Honda Foundation jointly awarded the Honda Prize 2008, being worth around € 70,000, to a group of three German researchers. Prof. Dr. Knut Urban, director of the Ernst Ruska-Centre for Microscopy and Spectroscopy with Electrons (ER-C) and head of IFF-8 "Microstructure Research", was among them. The Honda Foundation payed tribute to Dr. Maximilian Haider, Heidelberg, Prof. Dr. Harald Rose, Darmstadt and Prof. Dr. Knut Urban for the development of aberration correction for transmission electron microscopes, which made it possible to study materials with spatial resolution on a picometre level.
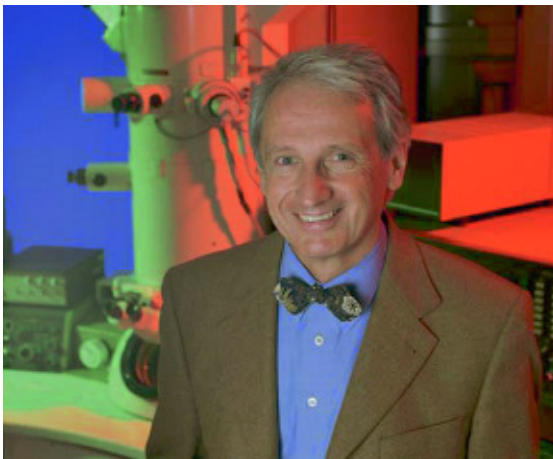
Prof. Dr. Knut Urban

22 October:
Rudolf Diesel Medal for Peter Grünberg

Nobel Laureate Prof. Dr. Peter Grünberg from IFF was awarded the Rudolf Diesel Medal by the German Institute for Inventions (Deutsches Institut für Erfindungswesen; DIE). The physicist received the award, which is named after the inventor of the diesel engine, for his discovery of giant magnetoresistance. The prize for pioneers and inventors in the field of technology and sciences was also awarded to the 2007 Nobel Laureate for Chemistry Prof. Dr. Gerhard Ertl and several successful entrepreneurs during an official event in the hall of honour of the German Museum (Deutsches Museum) in Munich.

Laureates and DIE board members at the Rudolf Diesel Medal ceremony (from left to right):

Dr. Aloys Wobben, Prof. Dr. Gerhard Ertl, Prof. Dr. Peter Grünberg, Dr. Klaus E. Tschira, DIE board member Prof. Dr. Viktor Dulger, Dipl.-Ing. Heinz Leiber, Gerhard Sturm, DIE board member Prof. Dr. Norbert Haugg, Dietmar Hopp, Dipl.-Ing. Hans A. Härle

Photo: obs/Deutsches Institut für Erfindungswesen

11 – 14 November:
Jülich Soft Matter Days 2008
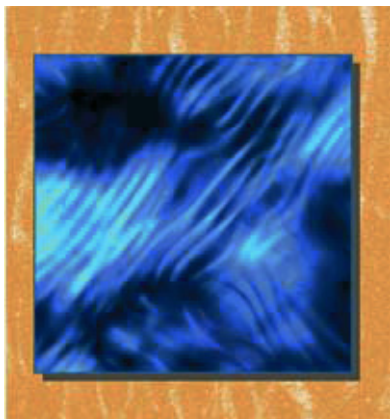
From 11 to 14 November, IFF held a conference on the topic of "soft matter" for the seventh time. More than 200 international researchers from the field at the interface of physics, chemistry, biology and the life sciences presented and discussed their research results at the Jülich Soft Matter Days 2008 in the Gustav Stresemann Institute in Bonn. The lectures dealt with questions such as how to explain internal motions in proteins using neutron scattering, how to improve the production of metal-gel composites with an application potential, for example, for catalysis, and why the set egg white of the famous century eggs from China is transparent instead of white.

12 December:
Most powerful microscope in the world comes to Jülich

An electron microscope with a record resolution of 50 picometres will be made available to a broad user community by RWTH Aachen University and Forschungszentrum Jülich in 2010. The instrument known as PICO will make details measuring only a fraction of an atomic diameter visible, going beyond the limits of current optical systems. This will enable atomic structures for materials in energy research and microelectronics to be investigated more precisely than has ever been possible before. The German Research Foundation, the Federal Government and the state of North Rhine-Westphalia approved around € 15 million for a new laboratory building and laboratory equipment. With this investment, the partners will keep their leading international position in ultrahigh resolution electron microscopy.

RWTH Aachen University and Forschungszentrum Jülich jointly operate the Ernst Ruska-Centre for Microscopy and Spectroscopy with Electrons (ER-C), which is at the same time a research platform and an international user centre in the area of this worldwide cutting-edge technology. With PICO, RWTH Aachen University will strengthen its contribution to the shared instruments and will provide the most powerful device of the ER-C.

Honours

Awards, honours, scholarships

• Dr. Bo Persson (Institute of Quantum Theory of Materials) received an award for one of the best publications of the year 2007 in the specialist journal "Journal of Physics: Condensed Matter".

• Sebastian Gliga (Institute of Electronic Properties) received a prize for the best presentation at the "Joint European Magnetics Symposia (JEMS) 2008" conference in Dublin, Ireland.

• Dr. Evgeny Gorelov (Institute of Theory of Structure Formation) received a prize together with an international team in a competition organised by the Russian Corporation of Nanotechnologies (RUSNANO) and the Intel Corporation for a project in the category of "Supercomputers for Nanotechnololgy and the Nano-industry".

• Prof. Dr. Peter Grünberg (Institute of Electronic Properties)
  o was awarded an honorary doctorate by the Mathematics and Science Faculty of the University in Cologne on 16 April. Afterwards he was awarded the university medal. Moreover, he was made an honorary member of the alumni network "Köln Alumni e.V.".
  o was awarded the Grand Cross with Star of the Order of Merit of the Federal Republic of Germany on 8 April 2008.
  o was elected regular member of the North Rhine-Westphalian Academy of Sciences on 10 April 2008.
  o was awarded an honorary doctorate on 24 April by the Faculty of Natural Sciences and Techno-

logy II (Physics and Mechatronics Engineering) at Saarland University.
  o was granted freedom of the city of Jülich on 25 April.
  o was awarded an honorary doctorate by the Tohoku University, Sendai, Japan.
  o was granted freedom of the city of Lauterbach on 18 August.
  o was awarded the Order of Merit of the federal state of North Rhine-Westphalia on 20 August for outstanding service to North Rhine-Westphalia and its people.
  o was awarded the Rudolf Diesel Medal by the German Institute for Inventions (Deutschen Instituts für Erfindungswesen) on 22 October.
  o was awarded an honorary doctorate from the Gebze Institute of Technology in Turkey in November.
  o was awarded the Minerva Prize of Jülich's Museum Association on 3 December.

• Dr. Samir Lounis (Institute of Quantum Theory of Materials)
  o was awarded the "ThyssenKrupp Electrical Steel PhD Dissertation Prize 2008 for the best PhD dissertation of 2006/07 in the field of magnetism" in Berlin.
  o ranked second in the Günter Leibfried Prize competition for communicating science successfully.
  o was awarded the Friedrich Wilhelm Prize 2008 by RWTH Aachen University for his excellent PhD in

physics and his PhD thesis "Theory of Magnetic Transition Metal Nanoclusters on Surfaces".

- Dr. Martina Müller (Institute of Electronic Properties) won the Günter Leibfried Prize awarded by Forschungszentrum Jülich for communicating science successfully.

- Dr. Ulrich Poppe (Institute of Microstructure Research) was awarded a prize for the best presentation at the conference: NANO-DDS 2007 (Nanoelectronic Devices for Security and Defense) in Crystal City, USA, in the category of "Device Concepts".

- Prof. Dr. Shigemasa Suga (Institute of Electronic Properties) received the Humboldt Research Prize from the Alexander von Foundation.

- Alexander Thiess (Institute of Quantum Theory of Materials) received a prize for his presentation at the European Conference on Surface Science ECOOSS 2008 in Liverpool.

- Together with Dr. Maxmilian Haider, Heidelberg, and Prof. Harald Rose, Darmstadt, Prof. Dr. Knut Urban (Institute of Microstructure Research) was awarded the Honda Prize 2008 for the development of aberration correction for transmission electron microscopes.

- Dr. Martin Weides (Institute of Electronic Materials) received a Feodor Lynen scholarship from the Alexander von Humboldt Foundation.

Appointments

- Prof. Dr. Thomas Brückel (Institute of Scattering Methods) was appointed

deputy chairman for 2008 of the "ILL Steering Committee" of the Institute Laue-Langevin in Grenoble, France.

- Dr. Hiroshi Noguchi (Institute of Theory of Soft Matter and Biophysics) was appointed associate professor at the Institute for Solid State Physics (ISSP) by the University of Tokyo (Japan) in January 2008.

- Dr. Andreas Rüdiger (Institute of Electronic Materials) accepted an appointment as professor for nanoelectronics/nanophotonics at the Institut National de la Recherche Scientifique of Québec University.

- Dr. Arno Schindlmayr (Institute of Quantum Theory of Materials) accepted an appointment as professor (W2) in Theoretical Physics at the University of Paderborn.

- Prof. Dr. Gunter M. Schütz (Institute of Theory of Soft Matter and Biophysics) received an invitation from the Weizmann Institute of Science (Israel) to come as a Weston Visiting Professor for three months.

New Helmholtz Young Investigators Groups

- Dr. Manuel Angst (Institute of Scattering Methods): Complex Ordering Phenomena in Multifunctional Oxides

- Dr. Yuryi Mokrousov (Institute of Quantum Theory of Materials/Institute for Advanced Simulation): Topological Nanoelectronics Group

Institute of Solid State Research (IFF)

IFF

spin transport

super-conductivity

magne-tism

conductivity

phenomena

crack propa-gation

structure formation

corrosion

phase transition

diffusion

alloys

semi-conductors

glasses

materials

polar crystals

polymers

nano-particles

membranes

thin films

colloids

numerical methods

neutron scattering

electron microscopy

methods

X-ray spectro-scopy

scanning tunnelling microscopy

electron spectro-scopy

light scattering

SQUID micro-scopy

Research topics at IFF

Founded in 1969, the scientific reputation of the Institute of Solid State Research (Institut für Festkörperforschung – IFF) still owes much to the conception of its founders that new discoveries are made at the boundaries of disciplines. This is as true today as it was forty years ago. In this spirit, the IFF has pioneered new research fields such as spintronics and set trends towards multi- and cross-disciplinary activities in both fundamental research as well as technological innovations.

Today, the IFF is engaged in investigating a multitude of condensed matter phenomena with special emphasis on three prime objectives:

• studies of fundamental physical mechanisms and phenomena of condensed matter,

• the development and improvement of experimental and theoretical analysis methods, as well as

• the elucidation and utilization of new material properties in complex systems.

The corresponding research programmes follow the main theme to exploit the full scale of analytical and numerical methods to elucidate interrelations between structural, electronic, and magnetic properties of the solid state together with describing underlying physical mechanisms. Research efforts are directed at obtaining a microscopic and atomistic understanding of phenomena based on fundamental interaction mechanisms.

Research at the IFF rests firmly on quantum mechanics and statistical physics. On a microscopic scale, they describe the interaction of electrons and atomic building blocks and determine how these entities respond to external influences. Particular strengths encompass the theory of electronic structures, clusters and polymer physics, biophysics, micromechanics of lattice imperfections, the dynamics of structure formation and phase transitions, materials and phenomena of magneto- and nanoelectronics, spintronics, spin dynamics, strongly correlated electron systems, as well as the instrumentation of electron, neutron, and synchrotron sources and their application to the study of condensed matter.

The experimental portfolio together with an acknowledged expertise enables the IFF to tackle complex problems in close cooperation with scientists and industry worldwide. Special state-of-the-art laboratories exist for thin film deposition and growth of bulk crystals as well as for the preparation of soft matter materials. In addition to standard methods for materials characterization, highly specialized techniques ranging from superconducting microscopy and spinpolarized microscopies to femtosecond laser spectroscopy are available at the IFF and are being constantly improved in performance.

With the Ernst Ruska-Centre for Microscopy and Spectroscopy with Electrons (ER-C) the IFF operates a national user facility housing several of the world's most advanced electron microscopes

and tools for nanocharacterization. In-house research programmes cover topical issues in condensed matter physics and – as a matter of course – future developments of subångström and sub-electronvolt microscopy.

Within the framework of the Jülich Synchrotron Radiation Laboratory (JSRL) a broad variety of spectroscopy, microscopy, and scattering experiments at various synchrotron radiation facilities are designed and realized. The SRL is part of the recently founded Peter Grünberg Centre and provides expertise for the development of new beamlines and experimental concepts and, thus, acts as a valuable partner for synchrotron radiation laboratories throughout the world.

The Jülich Centre for Neutron Science (JCNS) operates advanced neutron scattering instruments at the worldwide most modern and highest flux neutron sources. As a complement to local research opportunities, instruments are designed and operated at external national and international neutron sources, such as the FRM II in Munich or the neutron spallation source in Oak Ridge, USA.

The international networking of the IFF is a main pillar of its success; the institute initiated two EU Networks of Excellence (NoE), and co-founded the section "Fundamentals of Future Information Technology (FIT)" of the

Jülich-Aachen Research Alliance (JARA). JARA-FIT is the center of excellence for nanoelectronics research in the Jülich-Aachen region and is jointly operated by the Forschungszentrum Jülich and the RWTH Aachen University. It provides an excellent basis for future developments of nanoelectronics and information technology. To identify technology drivers the research areas cover quantum-electronics, magneto-electronics, ferro-electric and molecular nanostructures as well as Terahertz-electronics and bioelectronic signal processing.

The IFF is partner of more than one hundred universities and research institutions from all around the world. Last but not least, the IFF has a long tradition in the teaching and training of students, not only through the approximately 30 IFF staff scientists steadily giving lectures at universities, but in particular through the annual IFF Spring Schools, Neutron Laboratory Courses, and the Nanoelectronic Days.

Actually representing a department, the IFF currently comprises six experimental and three theoretical divisions as well as joint service facilities, which, however, cannot be regarded separately. The divisions present themselves on the following pages.

Being an institute of the Forschungs-
zentrum Jülich – itself belonging to
the Helmholtz Association of German
Research Centres (HGF) – the IFF pro-
vides key contributions to the strategic
mission of the Helmholtz Association
within three research programmes:

• Condensed Matter (pages 40 – 155),

• Large-Scale Facilities for Research
  with Photons, Neutrons, and Ions
  (pages 192 – 215),

• Information Technology with Nano
  electronic Systems (pages 198 – 219).

As a matter of fact, much of the success
of the IFF rests upon the inventiveness
and initiative of its more than 300 staff
members. The IFF supports independent
research by encouraging the responsi-
bility of individual scientists – a philo-
sophy that contributes greatly to the
stimulating atmosphere in the depart-
ment. In order to sustain this level on
the long run, special encouragement is
given to young scientists.

The casual observer may be struck by
the wide range of topics and extensive
networking at the IFF, whose strength
is to link complex issues together with
its scientific and industrial partners.
In the sixties, Germany seemed to be
about to miss the boat in solid-state
research. The success of the IFF demon-
strates, how a leading global position
may be achieved by a sound and clear-
sighted research strategy, which is able
to identify and address new develop-
ments and challenges at an early stage,
and pursue them on a long-term time
scale.

Read more:
Institute of Solid State Research:
www.fz-juelich.de/iff/e_iff/

Forschungszentrum Jülich:
www.fz-juelich.de

Ernst Ruska-Centre: www.er-c.org

Jülich Synchrotron Radiation Laboratory:
www.fz-juelich.de/iff/d_iee_jsrl/

Jülich Centre for Neutron Science:
www.jcns.info/

Jülich-Aachen Research Alliance:
www.jara-excellence.de

Helmholtz Association:
www.helmholtz.de/en/

23

Department IFF
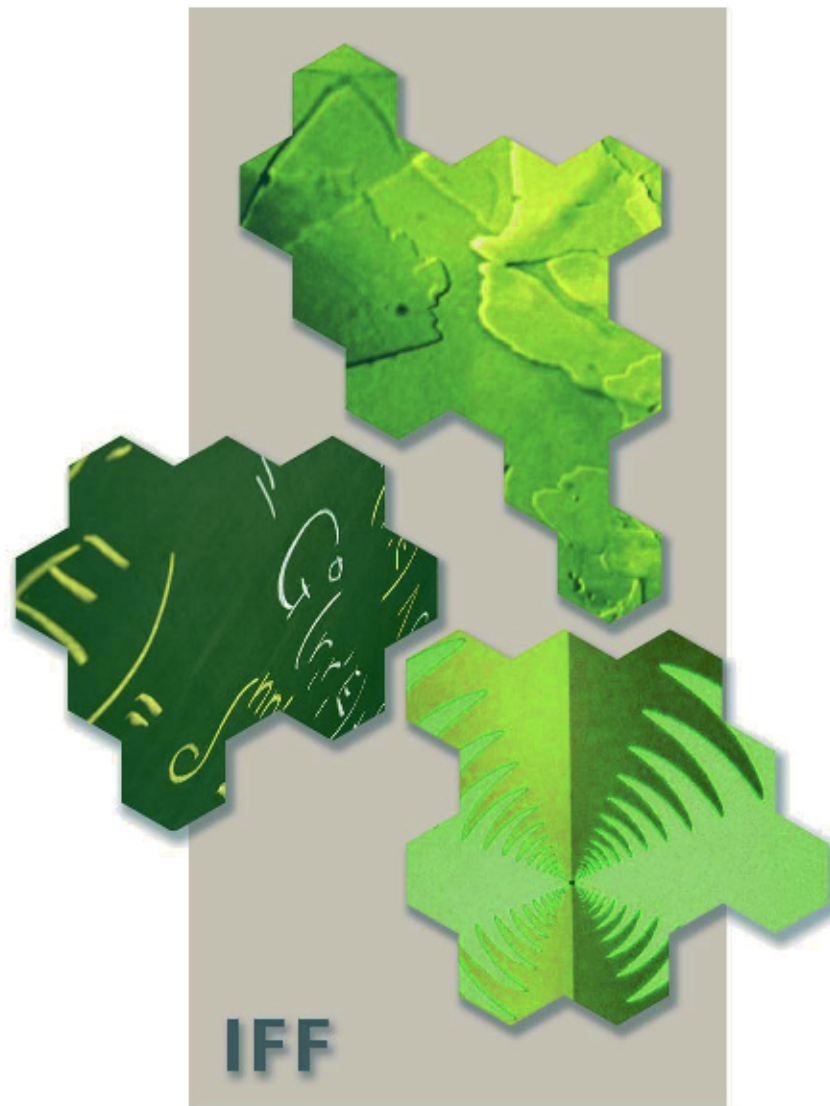
comprising the Institutes

IFF-1:	Quantum Theory of Materials	Prof. Dr. Stefan Blügel
IFF-2:	Theoretical Soft-Matter and Biophysics	Prof. Dr. Gerhard Gompper
IFF-3:	Theory of Structure Formation	Prof. Dr. Heiner Müller-Krumbhaar
IFF-4:	Scattering Methods	Prof. Dr. Thomas Brückel
IFF-5:	Neutron Scattering	Prof. Dr. Dieter Richter
IFF-6:	Electronic Materials	Prof. Dr. Rainer Waser
IFF-7:	Soft Condensed Matter	Prof. Dr. Jan K. G. Dhont
IFF-8:	Microstructure Research	Prof. Dr. Knut Urban
IFF-9:	Electronic Properties	Prof. Dr. Claus M. Schneider

IFF-1: Quantum Theory of Materials
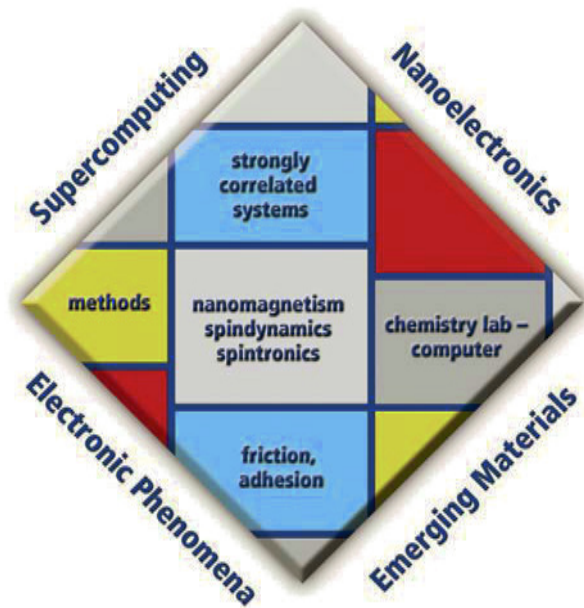
A major focus at "Quantum-Theory of Materials" is the analysis and computation of structural, electronic, magnetic, transport and chemical properties and processes in molecules and solids, in terms of both basic research and practical applications. The goal is to achieve a microscopic understanding of such complex phenomena.

Our research covers key areas of condensed matter theory, computational materials science, nanoelectronics and supercomputing. We explore the electronic and structural properties of systems from large organic (including biological) molecules, low-dimensional magnets, and magnetic multilayers, to complex solids. We consider transport properties across interfaces and molecules as relevant for spintronics and molecular electronics. We investigate the electronic excitations, and dynamical properties of atomic and molecular clusters, solids, and solid surfaces, as well as the quasiparticle behaviour of semiconductors, oxides and transition metals that results from electronic correlations. We analyze the physics of strongly correlated materials such

as transition-metal oxides and molecular crystals paying particular attention to complex ordering phenomena. Other areas include nanoscale tribology, including friction, plastic deformation, adhesion, and brittle fracture, as well as nonlinear processes in the atmosphere and agrosphere.

A major asset of our institute is the competence in developing conceptual and computational methods based on density functional theory, molecular dynamics simulations, and Quantum Monte Carlo methods.

IFF-2: Theoretical Soft-Matter and Biophysics
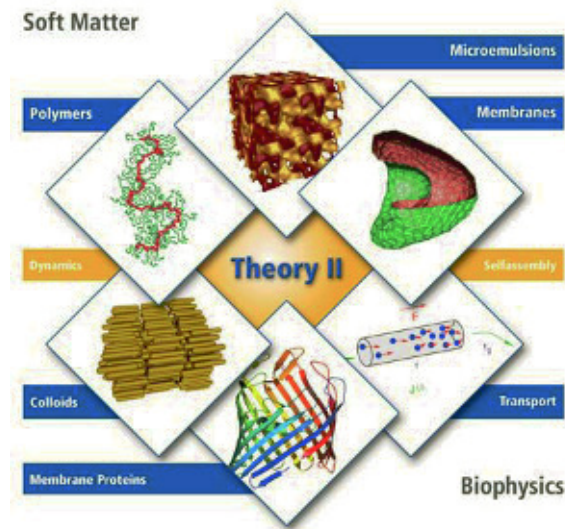
The main research topic of the Institute "Theoretical Soft Matter and Biophysics" is the theory of macromolecular systems. Soft matter physics and biophysics are interdisciplinary research areas encompassing statistical physics, materials science, chemistry, and biology. Our systems of interest include polymer solutions and melts, colloidal suspensions, membranes, vesicles and cells, but also composite systems ranging from colloids in polymer solutions to mixtures of surfactants and amphiphilic block copolymers. A major focus is the hydrodynamic behaviour of complex fluids and biological systems, both in equilibrium and under flow conditions.

At IFF-2, a large variety of methods are applied. In fact, a combination of analytical and numerical methods is often required to successfully characterize the properties of these complex systems. In particular, simulation methods (Monte Carlo, molecular dynamics), mesoscale hydrodynamic simulation techniques, field theory, perturbation theory, and exact solutions are employed. Since the building blocks of

soft matter systems often contain a large number of molecules, "simplified" mesoscale modelling is typically required, which is then linked to the molecular architecture.

A characteristic feature of soft-matter research is the fruitful interaction between theory and experiment. IFF-2 closely cooperates with the Institute for Neutron Scattering (Prof. Richter) and the Institute for Soft Condensed Matter (Prof. Dhont) to successfully tackle many of the essential aspects of the systems investigated.

IFF-3: Theory of Structure Formation
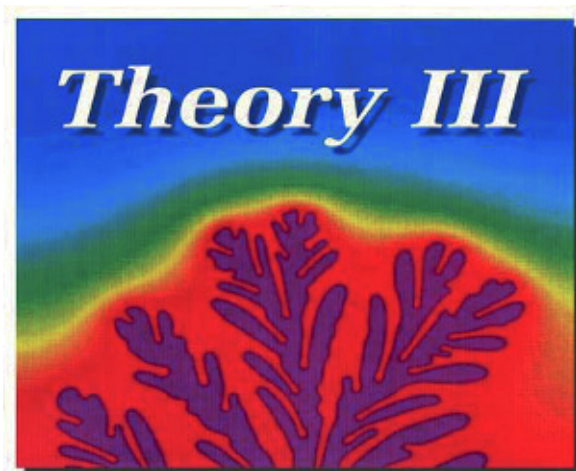
The research of the Institute "Theory of Structure Formation" is concerned with the mechanisms of the formation of structures and their consequences in condensed matter. The investigations start from electronic properties which define the shortest length and time scales, but they also encompass the macroscopic consequences. The analytical and numerical studies are in many ways closely connected to experimental research performed in other groups of the IFF, but also to activities in other Jülich institutes. The institute contributes mainly to the research programmes "Condensed Matter Physics" and "Information Technology with Nanoelectronic Systems" of the Research Centre.

Central points of interest for the research at IFF-3 are in the field of electronic structure of solids, in particular effects of strong electronic correlations. A specific interest concerns materials relevant for Information technology. A second mainstream is formed by cooperative phenomena in condensed matter. Questions here aim at the dynamics of structure and pattern formation and the statistical mechanics of order and disorder processes. Specific activities concern the effect of long-range interactions like elastic effects in solids, friction and fracture phenomena, or hydrodynamic interactions in solid-liquid systems.

The research of IFF-3 employs all analytical and numerical techniques applicable to many-body problems of equilibrium and non-equilibrium phenomena in condensed matter. In addition, the development of new methodological concepts and numerical procedures is part of our research interest. The development of parallel programme codes adapted to massively parallel computers has received special attention in recent years.

IFF-4: Scattering Methods
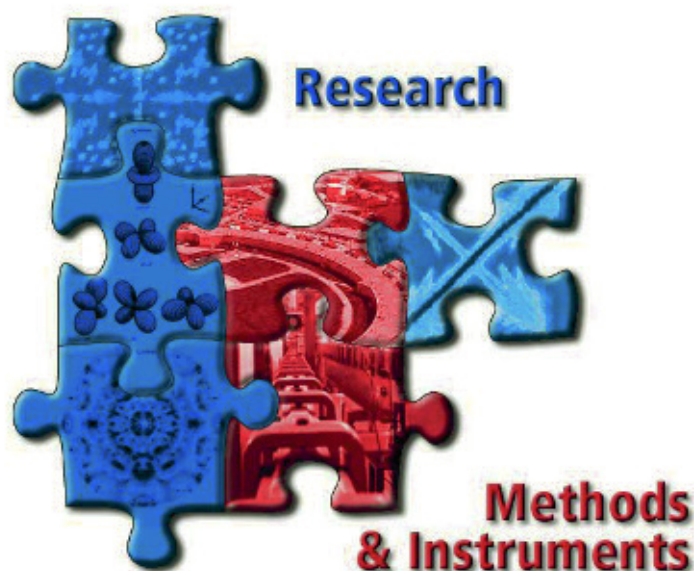
At the Institute for Scattering Methods, we focus on the investigation of structural and magnetic order, fluctuations and excitations in complex or nanostructured magnetic systems and highly correlated electron systems. Our research is directed at obtaining a microscopic atomic understanding based on fundamental interaction mechanisms and relating this microscopic information to macroscopic physical properties and functionalities.

The systems studied have a high potential for applications in future information technologies. In the field of nanomagnetism and Spintronics they range from magnetic molecules, via magnetic nanoparticles and magnetic thin film systems to laterally patterned superlattices. Among the correlated electron systems, we focus on transition metal oxides and -chalcogenides with unusual properties, such as colossal magnetoresistance or multiferroicity. Transition metal oxide superlattices, also laterally patterned, combine the aspects of correlated electron systems and nanomagnetism. Thermoelectric materials are being explored in the form of bulk and nanostructures.

Our emphasis lies in the application of most advanced synchrotron X-ray and neutron scattering methods. We place great emphasis on the complementary use of these two probes. Some of our efforts are devoted to dedicated sample preparation, from the synthesis of nanoparticles via physical thin film deposition techniques to single crystal growth. For sample characterisation, several ancillary techniques such as magnetometry, specific heat, conductivity etc. are being used to complement the scattering methods.

A significant part of our activity is devoted to the development of novel scattering techniques and the construction and continuous improvement of instruments at large scale neutron and synchrotron radiation facilities. Our strength lays in polarization analysis techniques. The Institute for Scattering Methods is partner in the Jülich Centre for Neutron Science JCNS, which operates instruments at some of the leading facilities: the research reactor FRM II in Garching, the Institute Laue-Langevin ILL in Grenoble, France and the Spallation Neutron Source SNS in Oak-Ridge, USA. Moreover, we contribute to the operation of a sector at the Advanced Photon Source APS (Argonne, USA).

IFF-5: Neutron Scattering
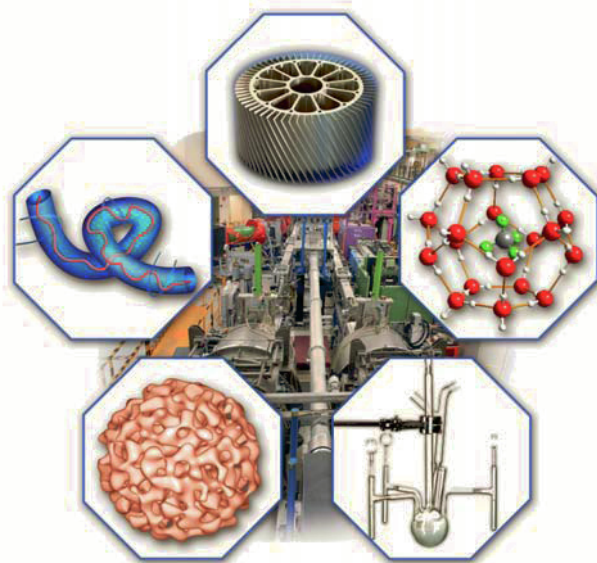
The Institute for Neutron Scattering is concerned with neutron research placing major emphasis on soft condensed matter, i.e. materials that react strongly to weak forces. Neutron scattering is a valuable tool for these systems because it reveals structure and dynamics of Soft Matter on the relevant length- and timescales.

A major part of the Soft Matter studies is done on polymers. Apart from their structure, we are interested in the dynamics of polymers in melts and solutions (e.g. gels, rubbery networks, aggregates). These polymers often have a complex architecture (copolymers, star-polymers etc.) to tailor them for industrial applications. Another field of interest are complex liquids such as microemulsions or colloid systems. Finally, biological materials (e.g. proteins) are studied concerning their structure and dynamics.

The institute has modern chemical laboratories for the synthesis, characterisation, and modification of Soft Matter. In order to complement neutron scattering experiments several ancillary techniques are used in the institute: rheology, light scattering, calorimetry, x-ray scattering, impedance spectroscopy, and computer simulation.

The Institute for Neutron Scattering is partner in the Jülich Centre for Neutron Science JCNS. In this position it operates several neutron scattering instruments at the research reactor FRM II in Munich, at the Institut Laue-Langevin in Grenoble, and at the Spallation Neutron Source in Oak Ridge, USA. These instruments are available to guest researchers on request. Another focus of research is the development of neutron instrumentation for research reactors and future spallation sources worldwide.

IFF-6: Electronic Materials
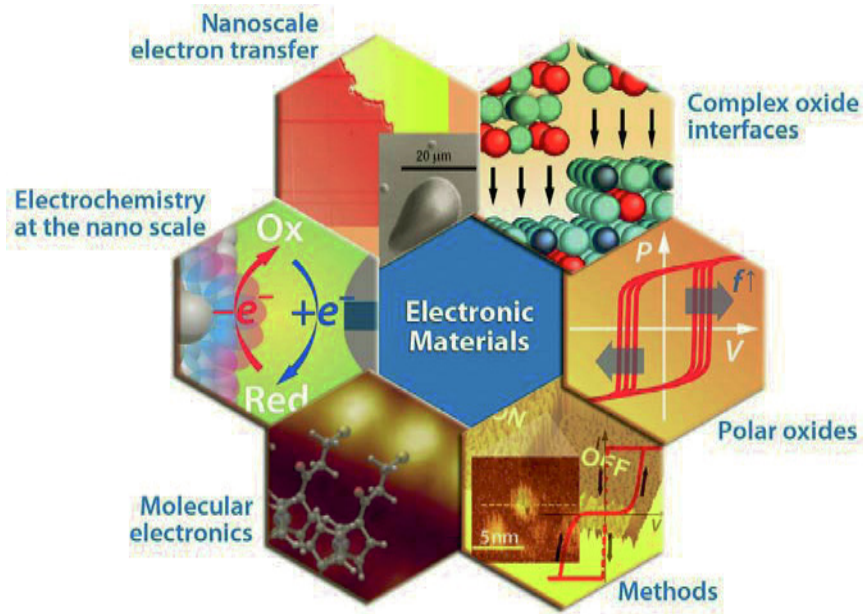
Progress in information technology and related fields such as energy storage and sensors originates to a large extent from novel electronic phenomena in functional materials as well as advances in the processing technology of these materials.

In this sense, at the Institute "Electronic Materials" we focus on the physics and chemistry of electronic oxides and electronically active organic molecules, which are promising for potential memory, logic, and sensor functions. Our research aims at the fundamental understanding of functional effects based on nano-scale electron transfer, electrochemical redox processes, space charge formation, electron/ion conduction in reduced dimensions, as well as ferro- and piezoelectricity, and at the elucidation of their potential for future device application. For this purpose, our institute provides a broad spectrum of facilities reaching from atomically controlled film deposition methods for heteroepitaxial oxide thin films, molecular self-assembly routes, and dedicated integration technologies. In addition, our institutes are equipped with tools for the characterisation of processes, structures, and electronic properties with atomic resolution. Circuit design is utilized for the development of hybrid and integrated circuits which comprise new electronic functions as well as advanced measurement systems. This is complemented by numerical simulation and modelling methods which aim at the theoretical explanation of the electronic phenomena and materials under study as well as the corresponding devices.

IFF-7: Soft Condensed Matter
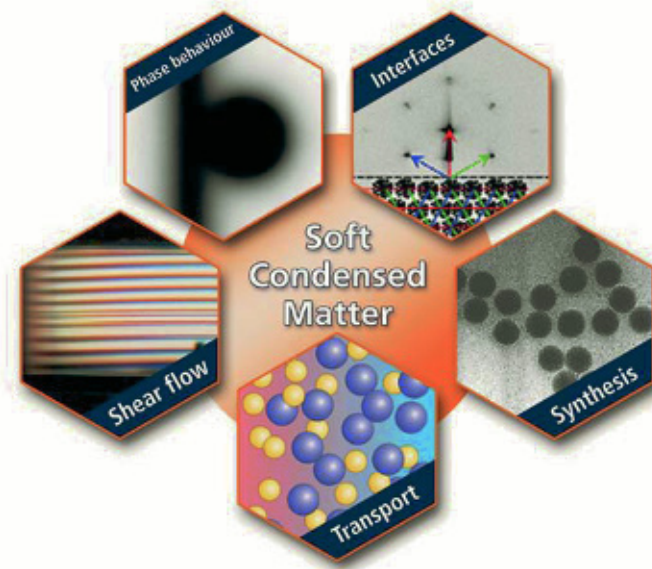
The Soft Condensed Matter group investigates the chemistry and physics of colloidal systems. Colloidal systems can be regarded as solutions of very large molecules which exhibit phase transitions and show non-equilibrium phenomena that are also found for simple molecular systems. Due to the slow dynamics of colloids and the tuneable interactions between the colloidal particles, however, there are many transitions and non-equilibrium phenomena that do not occur in simple molecular systems, like gellation and shear-band formation. The aim is to understand structure, dynamics and non-equilibrium phenomena on a microscopic basis with an open eye for possible technological applications.

The main topics that are studied include,
- the phase behaviour, pattern formation, phase separation kinetics and dynamics of suspensions of spherical and rod-like colloids under shear flow,
- mass transport induced by temperature gradients,
- dynamics and micro-structural properties of colloidal systems near walls and interfaces,
- the effects of pressure on interactions, the location of phase transition lines and gellation transitions and the dynamics of colloids and polymers,
- response of colloids to external electric fields,
- the equilibrium phase behaviour of mixtures of colloids and polymer-like systems,
- dynamics of various types of colloidal systems in equilibrium, and
- the synthesis of new colloidal model particles, with specific surface properties, interaction potentials and particle geometries.

IFF-8: Microstructure Research
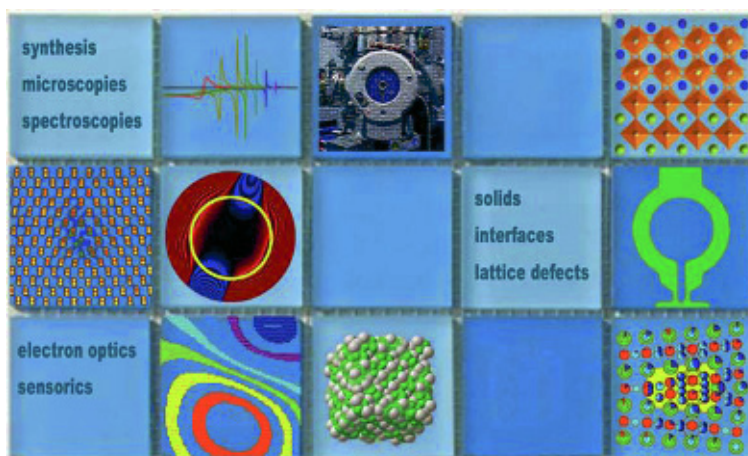
A major focus at "Microstructure Research" is the in-depth investigation of atomic-scale phenomena in crystalline solids with a special emphasis on electroceramics, complex metal alloys, and nanostructured semiconductors. Relevant issues cover the understanding of structural and electronic properties associated with heterointerfaces and lattice imperfections via a multidisciplinary research approach making use of a broad portfolio of microscopic and spectroscopic analysis techniques.

For the above purposes, IFF-8 continuously complements competence in the fields of single crystal growth, sputtering deposition technology, Josephson admittance and Hilbert spectroscopy as well as scanning tunnelling microscopy. In some of these fields, the competence covers the whole range from basic research via materials synthesis to the design and manufacturing of technical devices. In other fields, access to novel material classes and intricate problems are provided by qualified collaborations targeting on the application of ultra high-resolution transmission electron microscopy techniques accompanied by

the development of novel analysis methods.

Over and above general solid state and technology-related activities, IFF-8 operates the Ernst Ruska-Centre for Microscopy and Spectroscopy with Electrons (ER-C) on a pari passu base with the Central Facility for Electron Microscopy (GFE) of RWTH Aachen University. Representing one of the world's foremost establishments in the field of electron optics research, ER-C features several unique tools for nanocharacterisation complemented by a strong expertise in the development of advanced methods provided also to external researchers within the framework of ER-C user services. Pushing the limits in the field of fundamental electron optical research is, hence, accompanied by the application of advanced techniques to the investigation of a variety of solid state phenomena taking place on the atomic scale.

IFF-9: Electronic Properties
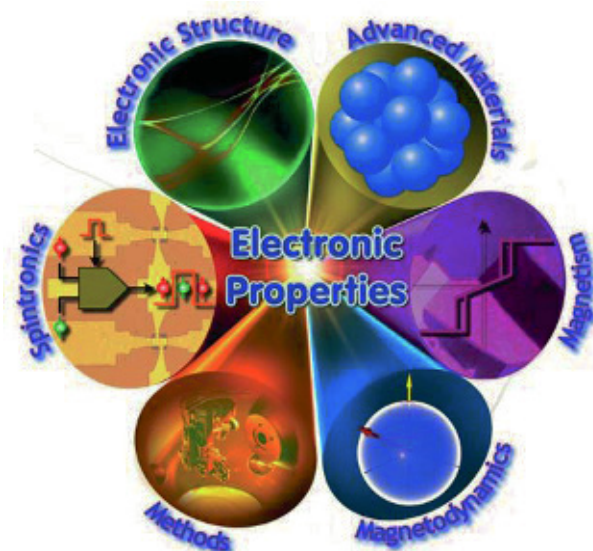
At the Institute "Electronic Properties" we explore the multifaceted interrelations between the electronic structure and the physical properties of matter. Our current research focus lies on magnetism, magnetic phenomena, and their exploitation in nanoscience and information technology. Systems of interest range from ultrathin films and thin film layer stacks through quantum wires and dots to clusters and molecules.

Magnetism displays a complicated interplay of competing interactions taking place on different length, energy, and time scales. We are particularly interested in the influence of the reduced dimensionality and the formation of quantum effects in nanoscale magnetic structures. The crosslinks between electronic structure and magnetism are addressed by a variety of spin-resolving spectroscopic techniques, such as spin-polarized photoemission and x-ray magnetooptics. These studies are carried out at dedicated beamlines at the synchrotron radiation facilities BESSY and DELTA.

The second line of research addresses the response of magnetic systems on short (magnetodynamics) and ultrashort timescales (spin dynamics). The magnetodynamics is experimentally accessed by pump-probe schemes and interpreted via micromagnetic simulations. Laser-based techniques provide high time-resolution, whereas time-resolved photoemission microscopy combines high lateral resolution with large magnetic sensitivity and element selectivity. In the realm of spin dynamics, we study energy and angular momentum transfer processes between the electron, spin, and lattice subsystems. Such experiments are performed by femtosecond pump-probe methods.

The third topic in the IFF-9 is Spintronics, i.e. the physics of spin-dependent transport processes. Resting on a long-standing experience with magnetoresistive phenomena, the current studies focus on the fundamental physics of spin transfer phenomena. This includes the development of new magnetic material systems and nanoscale devices. Particular emphasis lies on the exploration of smart magnetic switching alternatives involving spin-polarized electrical currents and photons.

Higher level education

With a reception at the Forschungszentrum's Faculty Club, the German Research School for Simulation Sciences welcomed its first doctoral researchers on 29 April, 2008. The eight successful candidates from Aachen and Jülich who hold diplomas in engineering, physics, or mathematics, have been chosen by a selection committee from a strong field of excellent nominees.

German Research School for Simulation Sciences (GRS)

The German Research School for Simulation Sciences (GRS) is a joint venture of RWTH Aachen University and Forschungszentrum Jülich. It combines, for the first time in Germany, the resources of a large federal research centre and a leading university in a research school which, formed as its own legal entity, may act autonomously in research and education. In its academic activity, GRS is closely connected with the RWTH; academic degrees are degrees of the RWTH. In its research activity, GRS takes advantage of the scientific environment, in particular the supercomputer facilities of the Forschungszentrum Jülich. There are close connections between GRS and all research groups in the field of simulation methods in Aachen and Jülich within the Jülich-Aachen Research Alliance JARA. The seat of the company is Jülich.

FUNDING: The funding is provided in equal parts by the BMBF (federal government), MIWFT (state government), HGF, RWTH and Forschungszentrum Jülich, initially for a period of five years.

BUILDINGS: In both Aachen and Jülich, separate buildings for the GRS including office space are under construction. The completion of the buildings is planned for summer 2009. The official inauguration of the buildings will take place on September 6 within the event *Tag der Neugier* in Jülich. Currently, interior furnishings of the building (furniture, information and media technology) are being prepared.

PERSONNEL: On 29 April 2008, the GRS welcomed its first eight doctoral candidates. A highly-competitive selection procedure involving experts from Aachen and Jülich ensures outstanding quality of the candidates, in accordance with the aim of GRS to strive for excellence. An international initiative by GRS to attract further postgraduates is in preparation. The process to fill the four planned W3 professorships at GRS is underway; their research areas are: Applied Supercomputing in Engineering, Parallel Programming, Computational Biophysics and Computational Materials Science.

MASTER PROGRAM: The GRS Master program *Simulation Sciences* started in the winter semester 2008/09 with special ministerial authorization. In parallel, the accreditation process with agency ASIIN was undertaken. A local auditing by the experts of the ASIIN took place on 19 November 2008 in Aachen and Jülich. After examination by the expert committees of ASIIN, the Master program has been formally accredited since end of March 2009.

COOPERATIONS: Future cooperations with foreign partners such as Ter@tec (France) are currently under consideration.

Read more: www.grs-sim.de

International Helmholtz Research School of Biophysics and Soft Matter

The International Helmholtz Research School of Biophysics and Soft Matter (IHRS BioSoft) provides intensive training in biophysics and soft matter. It also offers a comprehensive framework of experimental and theoretical techniques that will enable PhD students to gain a deeper understanding of the structure, dynamics, and function of complex systems.

In recent years, life science research has undergone a fundamental transition. It has become evident that even the simplest molecular machines display an astounding complexity, leaving alone networks of genes and proteins in a living cell. Thus, there is an urgent need for a more quantitative, theory-oriented approach. Soft matter research has, in parallel, made great progress in understanding the structure of complex multi-component macromolecular systems, their non-equilibrium behaviour and their response to external fields. A particular focus is laid upon unraveling the physics of biologically relevant systems. Thus, there is an urgent need for an interdisciplinary graduate education.

The IHRS BioSoft is located at Forschungszentrum Jülich, run in cooperation with the universities in Cologne and Düsseldorf and caesar Bonn, and funded by the Helmholtz Association. Its ultimate goal is to advance the integration and exchange between physics, chemistry, and biology in research and education. Students benefit not only from lectures, seminars, and lab courses given by experts in the field, but also from courses in transferable skills. Furthermore, they experience the environment provided by a large, multidisciplinary research centre.

The research school accepts fellows for three-year PhD projects and is open to highly qualified and motivated applicants from all countries. The fellow PhD students will be based in one of the groups that are part of the IHRS, but also participate in interdisciplinary courses. Other students are welcome to join most of these courses as long as there are free places. The lectures of the school usually attract a number of extra participants that choose the topics selectively according to their needs.

In 2007, two-semester introductory lecture courses, *'Introduction to Statistical Physics'* taught by Prof. Dhont and Prof. Gompper and *'Molecules of Life - Introduction to the Chemistry and Biology of Cells'* with various lecturers from within the IHRS BioSoft (Prof. Schurr, Prof. Merkel, Prof. Kaupp, Prof. Seidel, Prof. Richter, Prof. Büldt, Prof. Willbold, Dr. Enderlein, and Prof. Offenhäusser) were offered to the students. Both courses equip the students for their research projects with important basic knowledge: from a physics point of view, entropy and statistical physics have a large influence on the behaviour of the systems that are usually mesoscopic. The biological lectures covered systems from amino acids to the structure and dynamics of entire cells as well as methods such as X-ray crystallography, fluorescence spectroscopy, electrophysiology, and optical microscopy.

In 2007 and 2008, the students learned about the important tool of *'Computer Simulations in Physics and Biology'* by a two-semester advanced-seminar course that covered various, independent talks on different topics: Monte Carlo and Molecular Dynamics Simulations, Polyelectrolytes, Solid State NMR, Evolution of Bacterial Genomic Networks, Mesoscopic Hydrodynamics, Colloids, Proteins, Protein-Ligand Binding, Protein Structure Prediction, and Membrane Proteins. Most of the speakers were from Forschungszentrum Jülich and daily work with the methods and systems they presented: G. A. Vliegenthart, R. G. Winkler, H. Heise, M. Stoldt, M. Lercher, M. Ripoll, G. Naegele, A. Baumgärtner, M. Zacharias (IU Bremen), J. Granzin, and W. B. Fischer (NYMU, Taiwan).

Very recently, students were offered the one-semester introductory lecture course on *'Cell Biology'* by Prof. Müller and Prof. Baumann that included lab demonstrations, and the advanced lecture courses on *'Complex Fluids'* by Prof. Strey (Cologne) and *'Rheology'* by Prof. Vermant (Leuven).

Complementary laboratory courses provide the stu-

dents with practical experience and strengthen the interdisciplinary approach. Every year, the two-week *'Neutron Scattering'* course (organized by T. Brückel, G. Heger, D. Richter, and R. Zorn) is open for the participation of IHRS students. The course provides an extensive training by theoretical lectures and practical exercises. In a course on *'Optical Spectroscopy'*, G. Schuetz (Linz), J. Enderlein (Tübingen), J. Humplickova (Prague), M. Sauer (Bielefeld), J. Hofkens (Leuven), T. Gensch, and J. Heberle (Bielefeld) taught several optical techniques, such as fluorescence techniques, single-molecule spectroscopy, reaction-induced infrared difference spectroscopy, and Raman spectroscopy of biomolecules. The laboratory course *'Recording of Cell Activity'* — for example on Ca2+ imaging in living cells — was offered jointly by several institutes within the IHRS. In the last semester, a two-week course *'Fluorescence Spectroscopy'* by Prof. Seidel in Düsseldorf was open for IHRS fellows, a one-week course *'Cryo Transmission Electron Microscopy'* was organized exclusively for IHRS students by L. Belkoura and M. Baciu in Cologne and a one-day course on *'NMR Spectroscopy'* was offered by B. König in Jülich.

The PhD students regularly present their research in the Student's Seminar that is chaired by two IHRS BioSoft faculty members; every talk is followed by a long discussion. As the research in the participating groups, also the research topics of the PhD projects cover a wide range within biophysics and soft matter. Therefore a talk in the Student's Seminar is very challenging, because it needs to be prepared such that physicists, chemists, and biologists can benefit. Apart from questions and feedback about the research, the speakers usually receive also comments regarding the style of the presentation and whether it was suitable for the different parts of the audience. Topics of talks that were given include:

- Holographically induced nucleation (R. Hanes, Physics of Soft Matter, Düsseldorf)

- Regulation of HCN channels by phosphorylation (F. Winkhaus, Molecular Sensory Systems, Bonn)

- NMR as a tool to study protein structures (M. Schwarten, Structural Biochemistry)

- Non-genomic action of progesterone in human sperm (N. Goodwin, Molecular Sensory Systems, Bonn)

- Nanostructured gold electrodes for the functional coupling with neuronal cells (D. Brüggemann, Bioelectronics)

- Microinterferometry: a tool to study membrane fluctuations (C. Monzel, Biomechanics)

- Swarm behaviour of self-propelled particles (Y. Yang, Theory of Soft Matter and Biophysics)

- Photo-control of cell networks for extracellular recording systems (V. Maybeck, Bioelectronics)

- Self-assembly in a binary H2O-C12E4 system (I. Savic, Physical Chemistry, Cologne)

- Squeezing actin: a TIRF microscopy study (A. Tsigkri, Soft Condensed Matter)

- Microemulsions as delivery systems (Sabine Schetzberg, Physical Chemistry, Cologne)

- Polyelectrolyte electrophoresis (S. Frank, Theory of Soft Matter and Biophysics)

- Molecular Dynamics simulations of polyethylene oxide (PEO) and PEO/PMMA blends (M. Brodeck, Neutron Scattering)

- Combined single-molecule force and fluorescence spectroscopy (S. Grabowski, Molecular Physical Chemistry, Düsseldorf)

- How is shoot growth affected by low root temperature? (R. Poire, Phytosphere)

- HCN channels in the main olfactory bulb (A. Aho, Molecular Sensory Systems, Bonn)

- Morphologic and physiologic aspects of synaptic transmission in rat barrel cortex (G. Haack, Cellular Neurobiology)

Fellow PhD students already participated in two of the three seminars in transferable skills by Imperial College London that are organized by the Helmholtz Association. The seminars shall cover various aspects ranging from group work in the beginning of the thesis, presentation techniques up to writing of applications towards the end of the PhD project.

Currently, first students who have started their PhD projects within the IHRS BioSoft finish their thesis.

39th IFF Spring School: Soft Matter – From Synthetic to Biological Materials

The 39th international IFF Spring School took place from 3 March until 14 March 2008 at the Forschungszentrum Jülich. Leading scientists from research and industry gave 220 students and young scientists from 25 countries and five continents a comprehensive overview of the interdisciplinary research field "Soft Matter" at the interface between physics, chemistry, biology and the life sciences.

Soft matter is ubiquitous in a vast range of technological applications and is of fundamental relevance in such diverse fields as chemical, environmental, and food industry as well as life sciences. Over the past years, soft matter science has been largely extended in its scope from more traditional areas such as colloids and polymers to the study of biological systems, soft nanoscale materials, and the development of novel composites and microfluidic devices.
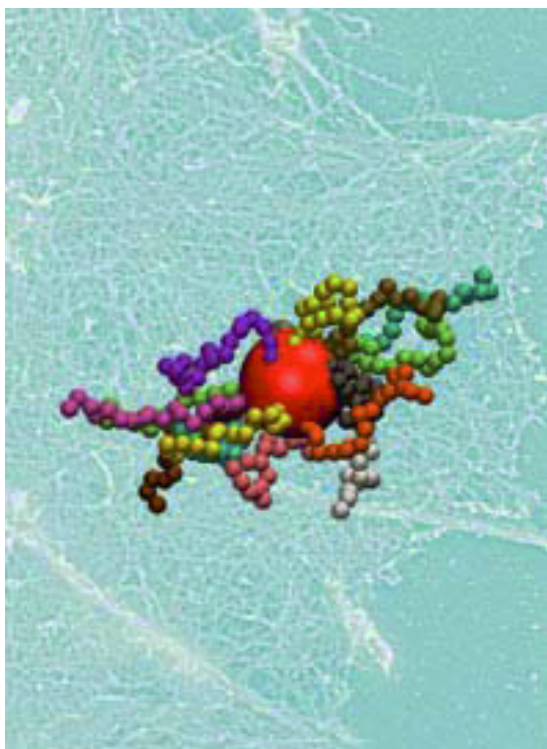
Soft and biological materials share fundamental structural and dynamical features including a rich variety of morphologies and non-equilibrium phenomena, self-organisation, an unusual friction-dominated flow dynamics, and a high sensitivity to external fields. These properties emerge from the cooperative interplay of many degrees of freedom, with spatio-temporal correlations that can span a huge range from nano- to millimetres and nanoseconds to days. The key requirements for the advancement in the field of these highly complex soft materials are:

- The development of novel experimental techniques to study properties of individual components in processes and the cooperative behavior of many interacting constituents. The synthesis of complex materials, self-organized and biomimetic systems with novel or unusual properties will broaden the spectrum of applications.

- The exploration of advanced theoretical and computer simulation methods that span the large range of time and length scales and allow to cope with an increasing complexity of molecular constituents. Existing methods need to be extended and new approaches are required to describe systems far from equilibrium, e.g., in life sciences and material processing.

- Structural and novel functional properties of soft and biological materials need to be studied invoking self-organization and hierarchical structure formation, entropic particle interactions and fluid-like aspects of biological materials such as vesicles and cells.

- The unusual dynamics of complex fluids requires special approaches to gain insight into diffusion transport properties, rheology and mesoscopic flow behavior, which are influenced by a delicate interplay of hydrodynamic interactions, thermal fluctuations, and external fields.

The IFF Spring School 2008 at the Forschungszentrum Jülich, Germany, addressed advanced experimental techniques and

applications, and theoretical and computer simulation methods on an undergraduate and graduate student level. Introductory lectures provided the basis of important experimental and theoretical tools. More advanced lectures explained practical aspects of various methods and lead the participants from basic methods to the frontiers of current research.

The lectures covered the following topics:

- Scattering Techniques
- Single Molecule Techniques
- Equilibrium- and Non-equilibrium Statistical Physics
- Microfluidics
- Computer Simulations
- Synthesis

- Self-Organisation
- Flow Properties and Rheology
- Biomechanics
- Macromolecules and Colloids
- Membranes and Interfaces
- Biomimetic Systems
- Glasses and Gels

The school offered about 50 hours of lectures plus discussions, as well as the opportunity to participate in practical courses and visits to the participating institutes at the Forschungszentrum Jülich.

The local media coverage included newspapers, radio and television.
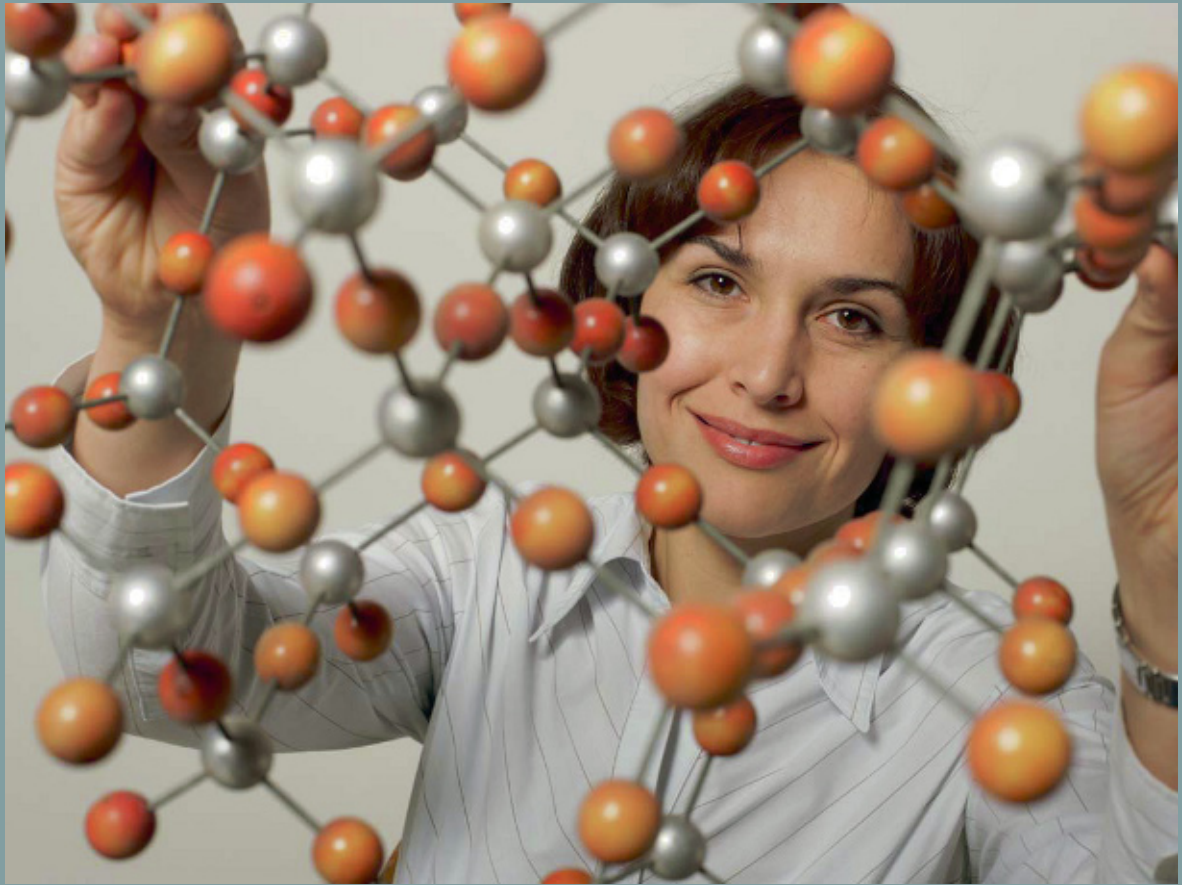
With its methods and models, physics forms the basis of the modern world – from industry and business to medicine and biology. Material samples are tested using neutron radiation, the mechanisms of the brain are investigated with the spin of a proton and individual cells are scrutinized using laser light. The main field of research is the physics of condensed matter, or the interaction between atoms in clusters, whether it be silicon in semiconductors or carbon in polymers and cell membranes or metallic alloys for high-temperature engineering. Well-devised microscopic models make the targeted search for innovative materials possible.

Condensed matter physics

Research in condensed matter is concerned with the complex interplay of the myriads of atoms in a solid or a liquid. Research in this field can thus be understood as the exploration of the „third infinity", being on equal footing with the exploration of the very small scales of elementary particle physics and the very large scales of astrophysics. The conceptual framework of quantum physics and statistical physics forms the basis for our understanding of condensed matter. The cooperation of the electrons and atoms within a many-body system is responsible for the different properties of the substances and determines why they are solid, fluid or gaseous, soft or hard, transparent or opaque, magnetic, metallic or even superconducting. Extreme length and time scales give rise to the characteristic complexity of condensed matter, ranging from subatomic sizes up to macroscopic measures, from electronic reaction times in the femtosecond range up to geological periods.

Our activities focus, in particular, on multi-scale phenomena in solid state and liquid phases and are organized in three topics:
- Electronic and Magnetic Phenomena,
- From Matter to Materials, and
- Soft Matter and Biophysics.

The studies in the first topic encompass electronic and magnetic quantum states and their properties. This includes problems in highly-correlated materials, superconductivity, magnetism in low dimensions and on short time scales. The second topic deals with phase transitions and transport processes, glass-like states, and complex metallic alloys, and finally structure formation and self-organization. In the third topic, structure formation and self-organization, mesoscopic dynamics and driven systems, as well as biology-inspired physics are addressed.

The spectrum of the materials investigated covers a wide range from metals, semiconductors and ceramics, through macromolecular systems up to biological systems and cells. For this purpose, a broad portfolio of theoretical and experimental techniques is utilized, which are constantly improved and progressed. The experimental emphasis lies on neutron scattering, synchrotron-radiation methods and ultrahigh resolution electron microscopy, whereas the theoretical treatments range from quantum theory to statistical physics and involve both analytical and numerical procedures.

41

Metalation/demetalation strategies for magnetic molecules

B. Botar[1], P. Kögerler[1,2]

[1] IFF-9: Electronic Properties
[2] Institute of Inorganic Chemistry, RWTH Aachen University

Chemical control of the magnetic properties of discrete (quasi-zerodimensional) and networked molecular magnets and networks implies the need for synthesis strategies that enable fine-tuning of the number and connectivity of spin centers in such molecules. Magnetically functionalized polyoxometalates are of particular interest in this context, as these systems combine structurally versatile and robust metal oxide-based fragments with a large variety and number of spin centers (3d and 4f ions). We developed a number of methods to control the number and connectivity of these spin centers for a family of polyoxotungstate clusters. The employed approach also allows the realization of unprecedented and highly anisotropic metal coordination geometries, in turn resulting in local magnetic anisotropy.

Polyoxometalates, i.e. the nanometer-sized condensation products of the early transition metal oxoanions in their high oxidation states, constitute a class of molecular metal oxide compounds that exhibit unmatched structural and chemical versatility. As these high-nuclearity cluster anions can be functionalized by a wide range of heterometal centers that can be integrated into the parental polyoxometalate (POM) structures, these systems represent ideal archetypes for highly tuneable molecular magnets.[1] Moreover, the high structural and redox stability common to polyoxometalates also allows depositing intact molecules onto surfaces as well as generating mixed-valent magnetic systems.

However, access to these systems is currently limited by a lack of understanding of the reaction mechanisms underlying the self-organized formation of such magnetically functionalized polyoxometalates. We target to systematically elucidate these mechanisms and focused on the solution chemistry of polyoxotungstate $\{\gamma$-M_2-$W_{12}E\}$ Keggin complexes (M = Mn(II), Cu(II), and Fe(III); E = Si(IV), Ge(IV),...). This choice is motivated by the solubility of these clusters not only in H_2O but also in organic solvents and by an interesting solvent-induced stereochemistry on the dinuclear M_2 unit in γ-Fe_2 complexes with implications for their electronic and magnetic properties: an "in-pocket" isomer (with the two Fe centers linked by two hydroxo bridges) observed in organic solvents and an "out-of-pocket" isomer (with the two Fe

centers linked by one hydroxo bridge and no longer bound to the central SiO_4 unit) present in aqueous solution, where these units oligomerize to e.g. form a trimer,

$$[(Fe_2(OH)_3(H_2O)_2)_3(\gamma-SiW_{10}O_{36})_3]^{15-} \quad \textbf{(1)}$$
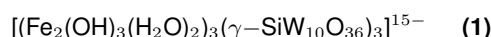
[2]. In the presence of acetate, an extensively used buffer component for aqueous solutions and also a versatile bridging ligand, a C_{2v}-symmetric acetate-bridged γ-di-iron(III) dimer,

$$[(Fe(OH)(OAc))_4(\gamma-SiW_{10}O_{36})_2]^{12-} \quad \textbf{(2)}$$

was found to form for a buffer concentration of 0.5 M CH_3COOH/CH_3COOK.[3] Probing the extent of ligand functionalization of γ-di-iron(III) complexes, we identified a higher buffer concentration (1 M), but otherwise identical synthetic conditions, to be crucial for the formation not of **(2)**, but of an unusual, open-shell diiron(III) derivative,

$$[(\beta-SiFe_2W_{10}O_{37}(OH))(\gamma-SiW_{10}O_{36})]^{13-} \quad \textbf{(3)}$$
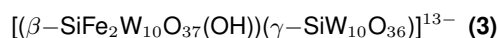
[4]. The structure of **(3)**(Fig. 1) reveals an asymmetric clam-shell-like arrangement of $\{\gamma$-$SiW_{10}\}$ and $\{\gamma$-$SiW_{10}Fe_2\}$ Keggin units connected by two Fe-O-W bridges acting as a 'hinge'. **(3)** also represents the first example of a polyoxometalate incorporating two different Baker-Figgis (rotational) isomers. The γ-Keggin unit in **(3)** incorporates two proximal ferric centers connected by a hydroxo ligand. As a result of the unusual connectivity of the two isomerically distinct units in **(3)**, the ferric centers have no terminal ligands and adopt distorted octahedral FeO_6 coordination environments with Fe-O bond lengths of 1.93–2.21 Å and *cis*-O-Fe-O bond angles of 77.6–99.2°. The structure of **(3)** is stabilized by an 8-coordinate K^+ cation located at the clam-shell opening created by the two polyanion subunits. The formation of **(3)** yielded several surprising findings:

- The facile incorporation of acetate ligands into the di-iron-POM framework observed in a 0.5 M CH_3COOH/CH_3COOK buffer is not observed at higher acetate concentrations.

- Instead of the expected structures based on "out-of-pocket" $\{\gamma$-$SiW_{10}Fe_2\}$ units, 1 M buffer solutions afford the formation of a lower-nuclearity Fe-POM.

One plausible explanation for this pronounced buffer
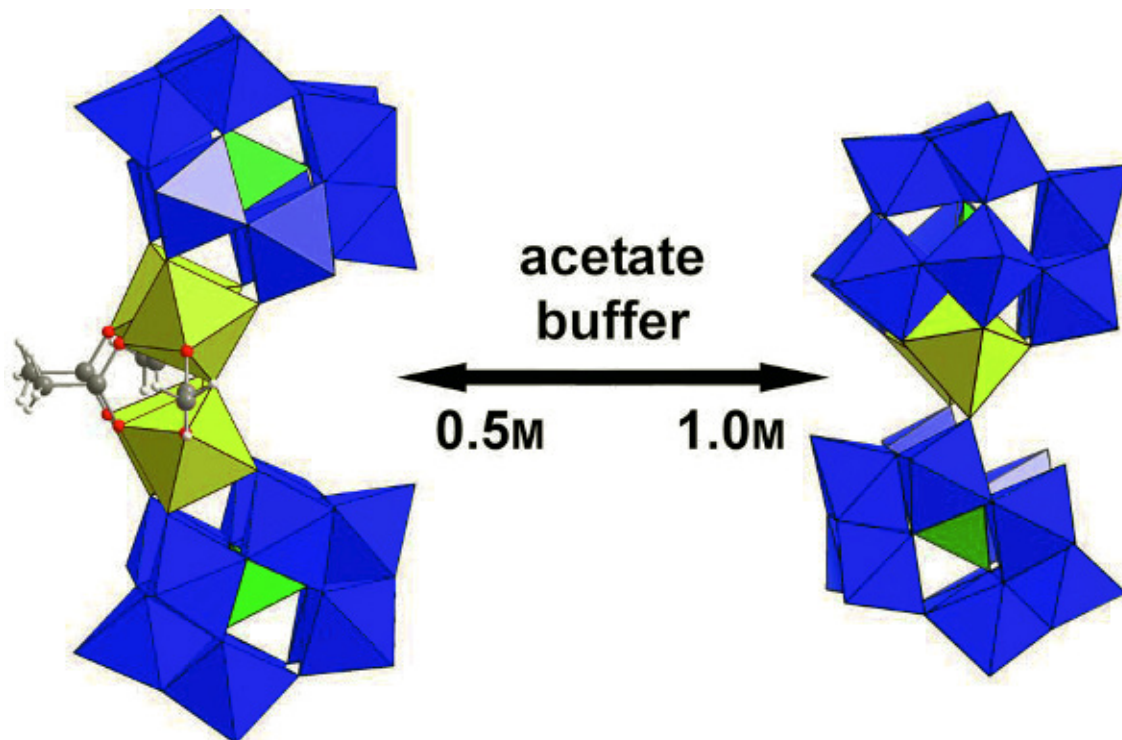
FIG. 1: *Schematic metalation/demetalation reactions in aqueous solution originating from {γ-$Fe_2W_{10}Si$} Keggin-based structures. The concentration of acetate surprisingly represents one critical reaction parameter. W: blue, Fe: yellow, Si: green polyhedra, acetate as ball-and-stick.*

concentration effect is that in stronger buffer solutions the acetate ligands bind stronger to the ferric centers, competing with the polytungstate ligands and thermodynamically removing the Fe cations from their polytungstate coordination environment (POM demetalation). Indeed, the reaction solution from which **(3)** was isolated produces red crystals after ca. 2 weeks which were crystallographically identified as the classical tri-ferric oxo/acetato complex,

$$[Fe_3(\mu-O)(H_2O)_3(CH_3COO)_6]^+ \qquad \textbf{(4)}$$
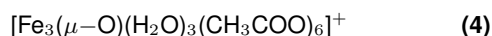
The effect of acetate on demetalation of diiron-POMs is also evidenced when the ratio of Fe(III) to [γ-$SiW_{10}O_{36}$]$^{8-}$ is increased (4:1 versus 2:1 used in the preparation of **(3)**). Under these conditions, **(4)** becomes the main reaction product, and no Fe-containing POMs can be obtained.

Compound **(3)** shows pronounced intramolecular antiferromagnetic exchange between the two $s = 5/2$ Fe(III) centers, mediated primarily by the single μ-hydroxo ligand and the O-Si-O pathway present in the γ-di-iron Keggin fragment and resulting in a singlet ground state. The low-field magnetic dc susceptibility data are very well reproduced by an isotropic spin-only Heisenberg model: employing a spin-only model for an s-5/2 dimer using a spin Hamiltonian of the type $\mathbf{H} = -JS_1 \cdot S_2$, we obtain a fit for J/k_B = –44.2 K and g_{iso} = 2.01. Given the Fe-O(H)-Fe angle of 139.6° of the dominant exchange pathway, this value of J is higher than comparable interactions in similar compounds (ca. –30 K in **(1)**)[2] and thus indicates a significant contribution of the O-Si-O bridge to the antiferromagnetic coupling.

In summary, the unexpected and critical effect of acetate concentration on the formation of {$SiW_{10}Fe_2$}-type derivatives, a finding so far unrecognized for any other class of magnetically functionalized polyoxometalates. While the extent of acetate-driven functionalization of {$SiW_{10}Fe_2$} derivatives is limited to dilute acetate solutions, higher acetate concentrations lead to partial de-metalation and subsequent formation of a di-iron tungstosilicate derivative. This synthetic control by carboxylate/polytungstate ligand competition constitutes a potentially attractive approach that is currently expanded to other multi-metal polyoxometalate systems.

[1] A. Müller, P. Kögerler, A.W.M. Dress, *Coord. Chem. Rev.* **2001**, 222, 193–218.

[2] B. Botar, Y. V. Geletii, P. Kögerler, D. G. Musaev, K. Morokuma, I. A. Weinstock, C. L. Hill, *J. Am. Chem. Soc.* **2006**, 128, 11268–11277.

[3] B. Botar, P. Kögerler, C. L. Hill, *Inorg. Chem.* **2007**, 46, 5398–5403.

[4] B. Botar, P. Kögerler, *Dalton Trans.* **2008**, 3150–3152.

Antiferroelectric charge order in $LuFe_2O_4$

M. Angst[1], R. P .Hermann[1,2], J. de Groot[1]

[1] IFF-4: Scattering Methods
[2] Department of Physics, Université de Liège, Belgium

"Multiferroic" materials in which magnetic order and ferroelectricity co-exist are highly sought for potential applications in future information technology. Of particular interest are multiferroics with a strong magnetoelectric coupling. For example, superior non-volatile memory devices based on multiferroics have been conceptualized. However, suitable materials are still lacking: multiferroic materials are rare because the traditional mechanisms of ferroelectricity and magnetism are incompatible. Potential ways out of this dilemma involve new mechanisms of ferroelectricity. A promising alternative mechanism, which allows both large polarizations and strong magnetoelectric couplings, is ferroelectricity arising from specific charge configurations in charge ordering materials. Only few example compounds have been proposed so far, with the best case having been made for $LuFe_2O_4$, which has charge ordering and magnetic transitions both near room temperature. We have elucidated the full three-dimensional charge ordering and shown that it corresponds to an antiferroelectric ground state. The ferroelectric state has only slightly higher energy, and might be stabilized in related structures.

For many applications, for example in information technology, it would be advantageous to be able to manipulate a magnetization with electric fields or electric polarization with magnetic fields. This can be achieved with materials that are both ferroelectric and magnetic, with a coupling in between. Such "multiferroics" are rare because the usual mechanism of ferroelectricity is incompatible with magnetic order. A potential alternative mechanism, which is compatible with magnetism and could sustain large polarizations is ferroelectricity arising from charge order, the ordered arrangement of valence states on a constituent element. This mechanism had been proposed to be active in $LuFe_2O_4$ [1].

The structure of $LuFe_2O_4$ (Fig. 1) contains triangular double-layers of Fe/O. With two Fe ions sharing a formal charge of 5+, at sufficiently low temperatures a charge-separated state with Fe^{2+} and Fe^{3+} ions is expected. In case of an ordered arrangement of the two valence states of Fe, superstructure reflections should appear. Superstructure reflections had indeed been observed below $\sim$320 K, at $(\frac{1}{3}\frac{1}{3}\ell)$ type

positions. From these positions, a charge configuration within an individual double-layer as sketched in the left panel of Fig. 1 was inferred. Because of a surplus of Fe^{2+} in one of the two layers and a surplus of Fe^{3+} in the other layer, the double-layer with this charge configuration becomes intrinsically polar. Together with pyroelectric current measurements indicating a remanent polarization, this was taken as proof of ferroelectricity originating from charge order and, as the material is also magnetic below 240 K, of a novel type of multiferroicity [1].
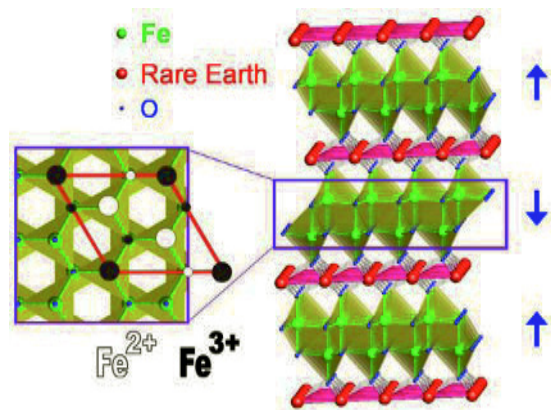
FIG. 1: *$LuFe_2O_4$ crystal structure containing Fe/O double-layers. $Fe^{2+/3+}$ ordering in these double-layers, sketched schematically, involves a charge imbalance between upper and lower layers, resulting in an electric polarization.*

However, the full three-dimensional charge configuration has not been established, nor has any coupling between charge and magnetic orders as a basis for magnetoelectric coupling been observed. We used synchrotron x-ray scattering and other techniques to unambiguously determine the full charge configuration of $LuFe_2O_4$ crystals whose quality has been fine-tuned by magnetization measurements, and which had allowed the first refinement of a three-dimensional magnetic structure [2].

Superstructure reflections were observed below 320 K (Fig. 2 top panel). The main superstructure reflections (much weaker reflections are attributed to higher harmonics, likely due to a small incommensuration) could be consistently indexed with three domains of charge order, symmetry related by 120° rotation of the propagation vectors. Each domain has

strong reflections for two propagations, e.g., in commensurate approximation, $(\frac{1}{3}\frac{1}{3}\frac{3n}{2})$ and $(00\frac{3n}{2})$. We performed an analysis of the irreducible representations for these propagations [3]. With the physical boundary condition that each individual double-layer be overall charge-neutral and a bimodal charge distribution as implied by Mössbauer spectroscopy [4] the full charge configuration is uniquely determined. For an individual double-layer, this configuration is as previously surmised [1] and sketched in Fig. 1, confirming the polar nature of the charge ordered double-layers.
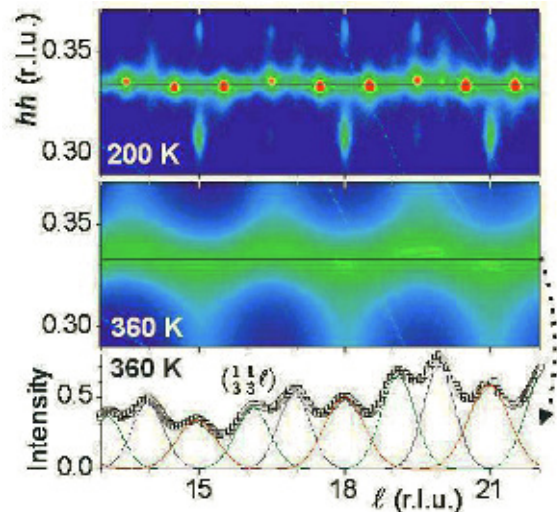
FIG. 2: Intensity of x-rays scattered off $LuFe_2O_4$. Below 320 K charge order leads to superstructure reflections, from which we inferred a charge configuration with antiferroelectric stacking of the polarization of the individual double-layers [3], see text. In contrast, short-range charge correlations at higher T lead to specific diffuse scattering suggesting dominantly ferroelectric correlations [3].

However, the stacking of the polarization of the individual double-layers, indicated by blue arrows in Fig. 1, is antiferroelectric rather than ferroelectric, with no net polarization within the supercell containing six double-layers, an experimental result subsequently corroborated by electronic structure calculations [3]. This finding raises the question how the remanent polarization indicated by pyroelectric current measurements [1] could be explained. Sample differences are an unlikely explanation because the superstructure reflections reported in [1] are inconsistent with a charge symmetry-allowed polar charge configuration.

An *Ansatz* to a possible reconciliation is found in the diffuse scattering we observed above the charge order transition (Fig. 2 bottom panels). A careful analysis of the diffuse scattering reveals broad and strongly overlapping peaks corresponding to propagation $(\frac{1}{3}, \frac{1}{3}, 0)$ and symmetry-equivalent. These suggest strong short-range correlations, and with representation analysis ferroelectric correlations between neighboring double-layers. This contrast between dominant correlations in the charge-disordered state

and the actual charge order established at lower temperatures indicate, as do the electronic structure calculations, that ferro- and antiferroelectric charge configurations are almost degenerate. It is thus conceivable that a ferroelectric charge order is established when cooling the sample in an electric field of sufficient strength, which would explain the pyroelectric current measurements [1], which were done after cooling in an electric field. Scattering measurements with applied electric fields carried out in order to test this hypothesis have so far not been conclusive.
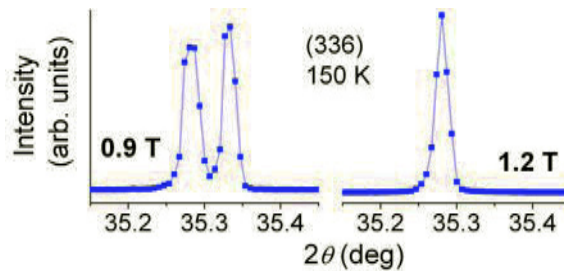
FIG. 3: Detector scans over the (336) structural reflection. The split peak (left) indicates a monoclinic distortion of the structure. Applying a sufficiently high magnetic field removes the peak splitting (right), indicating that the structure can be switched with a magnetic field [4].

We also obtained several indications of coupling between charge order and magnetism, such as a minimum in the temperature-dependence of the slight incommensuration of the charge order at the magnetic transition. The clearest indication is given by a monoclinic distortion allowed due to the removal of crystallographic symmetries by the charge order. A distortion sufficiently large to be observable appear at low temperatures, and can subsequently be removed by application of a sufficiently large (14.5 T at 4 K) magnetic field (Fig. 3)[4]. With the significant coupling to magnetism, $LuFe_2O_4$ based materials appear promising candidates for multiferroic devices. If the correlation between double-layers can be tuned from anti- to ferroelectric, which might be achieved e.g. by intercalation.

[1] N. Ikeda, H. Ohsumi, K. Ohwada, K. Ishi, T. Inami, K. Kakurai, Y. Murakami, K. Yoshii, S. Mori, Y. Horibe, and H. Kito, Nature 436, 1136 (2005).

[2] A.D. Christianson, M.D. Lumsden, M. Angst, Z. Yamani, W. Tian, R. Jin, E.A. Payzant, S.E. Nagler, B.C. Sales, and D. Mandrus, Phys. Rev. Lett. 100, 107601 (2008).

[3] M. Angst, R.P. Hermann, A.D. Christianson, M.D. Lumsden, C. Lee, M.-H. Whangbo, J.-W. Kim, P.J. Ryan, S.E. Nagler, W. Tian, R. Jin, B.C. Sales, and D. Mandrus, Phys. Rev. Lett. 101, 227601 (2008).

[4] X.S. Xu, M. Angst, T.V. Brinzari, R.P. Hermann, J.L. Musfeldt, A.D. Christianson, D. Mandrus, B.C. Sales, S. McGill, J.-W. Kim, and Z. Islam, Phys. Rev. Lett. 101, 227602 (2008).

45

Volume dependence of T_{Curie} in diluted magnetic semiconductors

L. Bergqvist[1,2], B. Belhadji[1], S. Picozzi[3], P. H. Dederichs[1]

[1] IFF-3: Theory of Structure Formation
[2] Dept. of Physics and Material Science, Uppsala University, Sweeden
[3] Consiglio Nazionale delle Ricerche-Instituto Nazionale Fisica della Materia, L'Aquila, Italy

Since the discovery of dilute magnetic semconductors (DMS) about 10 years ago [1, 2], these systems are hopeful materials for an all semiconductor spintronics. Here we study, using electronic structure calculations and statistical methods, the volume dependence of the exchange interactions and Curie temperatures in such diluted magnetic semiconductors. In both Mn-doped GaAs and Mn-doped InAs, the Curie temperatures obtained by numerical exact Monte Carlo simulations are more or less constant for a large volume interval. We have compared the exchange mechanisms in Mn-doped GaAs using both the local density approximation (LDA) and the LDA+U method. It is demonstrated that within LDA+U the magnetic properties can be understood by Zener's p-d exchange model, while in LDA they reflect a mixture between double and p-d exchange mechanisms.

We have used density functional theory to calculate the electronic structure of 5% Mn impurities in GaAs for different lattice constants by using the local density approximation (LDA) and LDA+U [3]. Figure 1 shows the calculated density of states of the Mn imputities for three different lattice constants ($\Delta a/a_{exp}$ = +3%, 0% and -4%) in LDA and LDA+U. For all lattice constants, a Mn impurity peak is present at the top of the valence band, being much weaker than the peak toward the bottom of the valence band. With increasing volume, the Mn density of states (DOS) narrows. This aries because of the hybridization with the valence p band, which strongly narrows since the p states become more localized. In parallel to this, the minority d peak moves to higher energies, from about 0.45 to 0.90 eV above E_F, which is directly related to an increase of the local moments. There is a strong tendency toward antiferromagnetic coupling upon compression arising from super exchange, which basically varies as

$$\Delta E_{super} \sim c \frac{|t_{dd}|^2}{\Delta_{xs}} \tag{1}$$

where c denotes the Mn-concentration, t_{dd} is the hopping matrix element between majority d states and minority d states of the neighboring impurities, and Δ_{xs} is the exchange splitting, being in LDA proportional to the local moment. Upon compression, t_{dd}
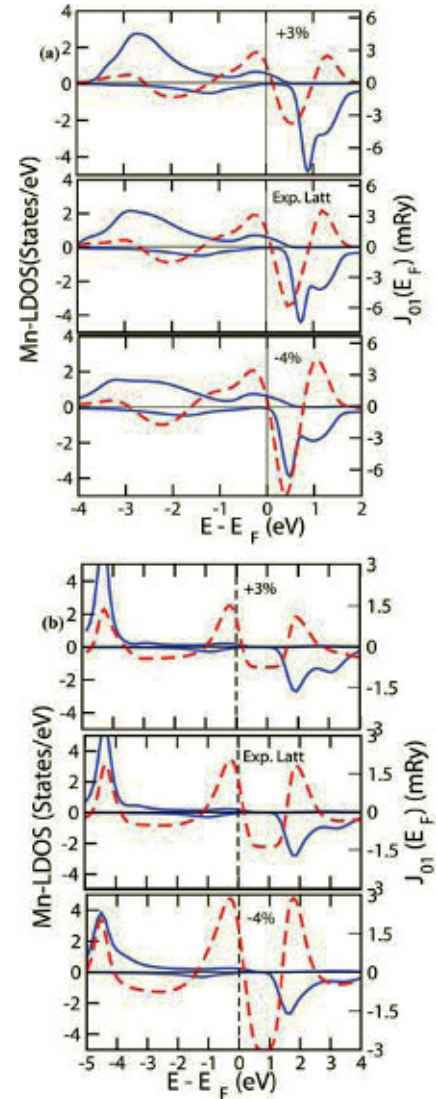
FIG. 1: Local density of states (LDOS)(blue full line, left scale) of $Ga_{0.95}Mn_{0.05}As$ in (a) LDA approximation and in (b) LDA+U approximation. For each figure, the topmost panel corresponds to an expanded lattice (+3% of a_{exp}), the middle panel the experimental lattice, and the lowest panel a compressed lattice (-4% of a_{exp}). Here, a_{exp} denotes the experimental lattice constant. The dashed line (red, right scale) shows the exchange coupling constant J_{01} for nearest neighbor Mn impurity as a function of fictive values of E_F.

increases, while at the same time Δ_{xs} decreases due to the reduction of the local moment. Usually, super exchange is very short ranged, affecting mostly the nearest neighbor couplings.

A clearer picture of the behavior of the different coupling mechanisms with compression can be obtained from Fig.1, which shows in addition to the local DOS curve versus the energy $E\text{-}E_F$, also the exchange coupling constants $J_{01}(E_F^*)$ to the nearest neighbors as a function of an artificially changed Fermi level E_F^*, away from the self-consistent value of E_F. These curves show three peaks close to E_F: First, a peak at around -0.3 eV arises due to $p-d$ exchange and double exchange from the resonance at E_F. Second, the strongly negative value above E_F arises from the super exchange. Third, the positive peak at around 1 eV above E_F arises from double exchange due to minority d state in this energy. The most important difference between the LDA and LDA+U is the much larger exchange splitting U, which shifts the majority peak down below -4 eV and at the same time, the minority peak up by about 1.5 eV. Due to this, the exchange splitting in Eq. (1) is strongly increased, significantly reducing the super exchange in the energy gap region by as much as a factor of 2 since in LDA+U the exchange Δ_{xs} in Eq. (1) is given by the U value. As a consequence, in LDA+U the super exchange is not important for the self-consistent J_{01} values in GaMnAs, whereas in LDA the J_{01} values strongly decrease with compression due to super exchange. Thus, in LDA the behavior of (Ga,Mn)As is determined by a complex superposition of double exchange, $p-d$ exchange, and super exchange, while in LDA+U approach, $p-d$ exchange alone dominates.

In Fig. 2, the calculated critical temperatures in $Ga_{0.95}Mn_{0.05}As$ using exchange intearctions from LDA and LDA+U approximations, are displayed. In the mean field approximation (MFA), all exchange interactions have the same weight, and due to the dominating nearest neighbor exchange interaction the values are very high. However, as have been demonstrated in many studies, the MFA is oversimplified and cannot be applied to DMS systems. Instead, one has to rely on a numerical solution of the Heisenberg model. We employ the Monte Carlo method, which, in principle, solves the spin fluctuations and disorder in the Heisenberg model exactly. One of the reasons that the MFA description does not work for diluted systems is that the average separation between magnetic impurities is much larger than the nearest neighbor distance. In LDA, the Curie temperatures from MC are basically constant around 100 K for the whole volume interval in $Ga_{0.95}Mn_{0.05}As$ (Although a flat maximum is obtained around the experimental lattice constant), while the results from MFA show a distinct maximum of J_1 at this volume. In LDA+U, the mean field Curie temperatures increase strongly with pressure and have a maximum at a much smaller lattice constants. The more correct Monte Carlo results increase slightly upon pressure, but overall the values are lower than the LDA results, in agreement with previous calculations.

The pressure dependence of the critical tempera-
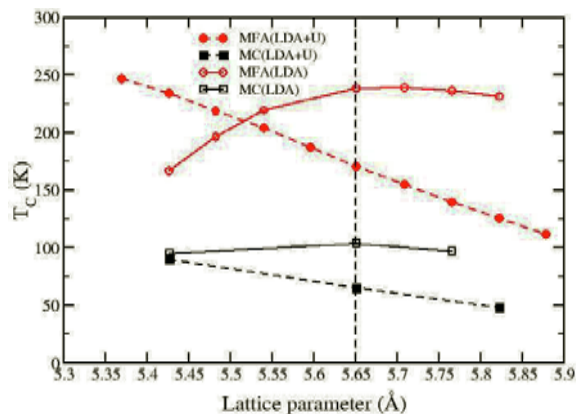
FIG. 2: Calculated critical temperatures of $Ga_{0.95}Mn_{0.05}As$ in LDA and LDA+U approximations. MFA denotes the mean field approximation, and MC the numerically exact Monte Carlo results.

tures calculated for the case of $In_{0.95}Mn_{0.05}As$ using LDA shows a different behavior from $Ga_{0.95}Mn_{0.05}As$ (LDA). Due to the much larger lattice constant of InAs, the critical temperatures increase with pressure, although the effect is rather weak. A similar kind of behavior has been observed in Mn-doped InSb [4], which goes from a nonmagnetic material to a magnetic material (although with very low T_C) under pressure. However, in rare-earth systems with localized $4f$ states, the opposite is true; i.e., they typically have an increasing T_C under pressure.

In conclusion, the exchange mechanisms in Mn-doped GaAs using LDA is a mixture between double and $p-d$ exchange, while in LDA+U the dominating exchange mechanism is Zener's $p-d$ exchange mechanism and the super exchange is strongly suppressed. The critical temperatures calculated employing a classical Heisenberg model and numerically exact Monte Carlo simulations stay rather constant in a large volume interval in both Mn-doped GaAs and InAs systems.

[1] H. Ohno *et al.*, Science **281**, 951 (1998).

[2] K. W. Edmonds *et al.*, Appl. Phys. Lett., **81**, 3010 (2002).

[3] L. Bergqvist *et al.*, Phys. Rev. B. **77**, 014418 (2008).

[4] M. Csontos *et al.*, Nature Materials **4**, 447 (2005)

47

Magnetic domain structure of Heusler/MgO/Heusler trilayer systems

A. Kaiser, C. Wiemann, S. Cramm, C.M. Schneider

IFF-9: Electronic Properties

We have investigated the magnetic domain structure of magnetic trilayers consisting of the two Heusler compounds Co$_2$FeSi (CFS) and Co$_2$MnSi (CMS) and a thin MgO barrier by X-Ray Photoemission Electron Microscopy (XPEEM). The measurements revealed a parallel coupling of the two magnetic films and different micromagnetic properties depending on the layer sequence. The results are discussed in terms of the material properties and growth conditions.

Heusler alloys [1] are considered as interesting ferromagnetic electrode materials for magnetic tunnel junctions (MTJ). Due to their high spin polarization at the Fermi level they are expected to show extremely high tunnelling magnetoresistance (TMR) values. MgO as a tunneling barrier material has a comparable lattice constant and thus provides the possibility of epitaxial growth of trilayer systems. Due to the reduction of defects and the onset of resonant tunnelling mechanisms an increase of the TMR effect can be expected.

Co$_2$FeSi (CFS) and Co$_2$MnSi (CMS) are two protagonists of the class of half-metallic Heusler compounds. They have similar lattice constants providing structural compatibility to MgO. Both materials have high Curie temperatures around 1000 K and magnetic moments per formula unit of 5.07 μ_B (CMS) and 6 μ_B, respectively. Hysteresis measurements reveal clearly distinguishable coercive fields of 2.8 mT (CMS) and 6.5 mT (CFS). Single films and trilayer structures with asymmetric electrode configurations have been prepared by magnetron sputtering. The films have been subsequently microstructured by optical lithography and argon ion beam milling into squares with areas ranging from 2×2 to $100 \times 100 \ \mu m^2$. A more detailed description of the growth conditions and the experimental results can be found elsewhere [2].

The micromagnetic structure of the films has been studied by XPEEM exploiting the XMCD effect for the element-selective study of magnetic domain configurations [3]. The measurements have been carried out using an Elmitec PEEM III at the beamline UE56/1-SGM at BESSY-II. All measurements shown in this report have been generated by tuning the photon energy to the appropriate L$_3$ absorption edge and calculating the XMCD asymmetry value for each pixel.

(a) CMS 10x10 μm^2

(b) Sketch of domain pattern in CMS 10x10 μm^2

(c) CMS 20x20 μm^2

(d) CFS 20x20 μm^2
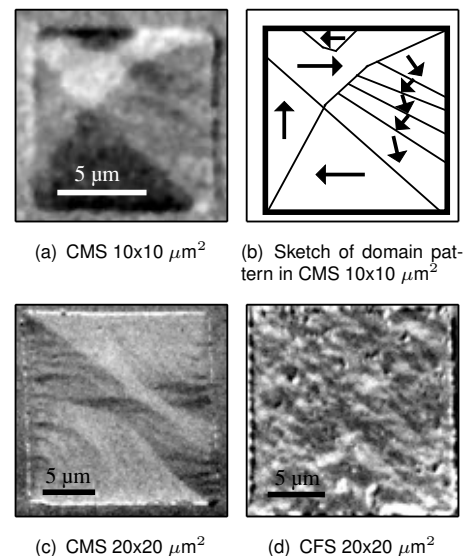
FIG. 1: Magnetic domain structures in patterned CMS and CFS elements. The magnetic contrast has been obtained at the Co L$_3$ edge.

Fig. 1 shows the magnetic domain patterns from single CMS and CFS films. Under the influence of the shape-induced demagnetizing field, the magnetization configuration of elements of comparable size is distinctly different. The CMS film develops a so-called concertina or buckling pattern (fig. 1(c)). It is formed by alternating low-angle walls with the local magnetization direction varying around the average magnetization [4]. With decreasing element size the effect of the demagnetizing field becomes stronger and successively simpler flux-closure patterns reminiscent of Landau states start to form (Fig. 1(a) and 1(b)), which are still accompanied by buckling structures. The latter disappear for elements in the micrometer regime. However, the occurrence of the buckling state is not necessarily the magnetic ground state configuration, but may arise due to a local energetic minimum caused by neighbouring domains blocking each other. A completely different response is observed in the CFS films. Even under the influence of the demagnetizing field in small $10 \times 10 \ \mu m^2$ elements (Fig. 1(d)), the polycrystalline nature of the film is dominating the magnetization pattern and the fine-grained domain structure remains essentially un-

48

(a) Fe-L$_3$ (b) Mn-L$_3$
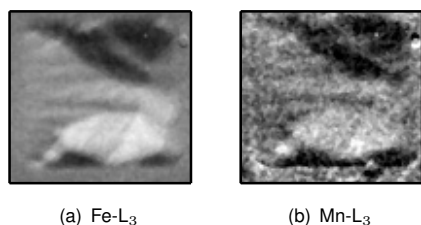
FIG. 2: Element-selective domain imaging in the layer system CMS/MgO/CFS, revealing a parallel magnetic coupling of the CFS and CMS films.

(a) CMS (20 nm)/ MgO (3 nm)/ CFS (2 nm)

FIG. 3: Comparison of magnetic domain patterns acquired at the Co L$_3$ edge of $20 \times 20 \ \mu m^2$ square elements of both trilayers.

changed from that observed in the extended film (not shown). This result shows that the intrinsic anisotropy of the CFS-film is much stronger than the demagnetizing field of the square element.

In a second step the single Heusler films have been combined into trilayer structures with a MgO interlayer of 3 nm thickness. In order to separate the magnetic response of the individual layers in this stack, the full versatility of XPEEM is needed. By tuning the photon energy to the L$_3$-absorption edges of Fe and Mn the magnetization of both ferromagnetic layers can be investigated independently. Resulting domain images for a square element of CMS(20 nm)/MgO(3 nm)/CFS(2 nm) with 10 μm edge length are compiled in fig. 2. Due to the limited escape depth of the photoelectrons, the Mn signal is rather weak and had to be upscaled by a factor of five. Comparing the domain patterns of the Fe and Mn data reveals identical structures consisting of Landau flux-closure pattern superposed by concertina features in both films. The reasons for this coupling can be a roughness-induced Néel/orange-peel mechanism [5] or pinholes in the MgO layers, which favour a ferromagnetic contact between the CFS and CMS layer through a direct exchange interaction. The domain patterns of the trilayer film resemble the situation of the single CMS film (fig. 1a). Due to the difference in thickness in both films the micromagnetic structure is strongly dominated by the CMS bottom layer. For larger $20 \times 20 \ \mu m^2$ elements (fig. 3a) the magnetic structure is no longer determined by the flux-closure but by local anisotropy fluctuations leading to a magnetization ripple due to the polycrystalline structure of the films is formed

In the inverse trilayer system the magnetic microstructures changes drastically. Instead of the ripple pattern we find a higher average domain size and the formation of a low-remanence magnetization pattern consisting of two antiparallel Landau domains (fig. 3b). Some of the 90°-walls have been replaced by an additional domain with two low-angle walls (known as "Tulip" state). The 180°-walls between neighbouring antiparallel domains are modified by a high density of cross-ties replacing 180°-walls by energetically more favorable 90°-walls.

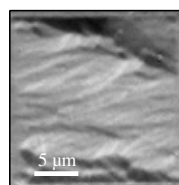In this trilayer structure we do not find a magnetic contrast at the Mn edge. This fact is surprising since the CMS film is the top layer and is expected to yield a higher intensity than in the reversed stack.

Thus we must conclude that the CMS film is nonmagnetic at room temperature. This behaviour may be attributed to a strong thickness dependence of the CMS magnetic moment that has been reported by other groups. The strongly reduced Curie temperature in the 2 nm CMS film may be explained by interdiffusion at the interface leading to a higher atomic disorder. Furthermore, this result seems to indicate that the MgO barrier in this layer has only a negligible density of pinholes, because a direct exchange coupling to the bottom CFS layer should also result in a common Curie temperature for both layers.

In conclusion our element-selective domain imaging experiments reveal the complexity of the magnetic microstructure in Heusler-based thin film systems. The results also show that the micromagnetic structure depends on fine details of the formation process of the Heusler phases. Analysis of the domain configurations shows that the ferromagnetic coupling observed in the dual-Heusler trilayers can be attributed to roughness-induced Néel coupling. This can be overcome by an improvement of the preparation conditions. The surprising difference of the magnetic behaviour between the CMS/MgO/CFS and CFS/MgO/CMS trilayer structures is due to a strong thickness dependence of the magnetic ordering in CMS and must be taken into account for the construction of magnetic tunnelling junctions.

[1] Heusler, F. *Verh. Dtsch. Phys. Ges.* **12**, 219 (1903).

[2] Kaiser, A., *et al.*, *J. Magn. Magn. Mater.* (2008). doi:10.1016/j.jmmm.2008.10.037.

[3] Schönhense, G. *J. Phys.: Cond. Matt.* **11**, 9517 (1999).

[4] Hubert, A., Schäfer, R. *Magnetic domains - The analysis of magnetic microstructures* (Springer, 1998).

[5] Neel, L. *C. R. Acad. Sci.* **255**, 1676 (1962).

49

Anisotropy and exchange interactions in a gradient nanocrystalline multilayer

E. Kentzinger[1], U. Rücker[1], Th. Brückel[1,2]

[1] IFF-4: Scattering Methods
[2] JCNS: Jülich Centre for Neutron Science

50

The magnetization reversal in a gradient nanocrystalline multilayer proceeds sequentially from the bottom-most and thinnest ferromagnetic layers to the top-most and thickest ones. This is quantitatively explained by a correlation between grain size and layer thickness within the random anisotropy model including dominant uniform uniaxial anisotropy. The magnetic microstructure of the layers consists of regions laterally spin-misaligned one with respect to the other. Two types of lateral spin misalignment were deduced, random and not random, the former one in all layers due to the random orientation of the grains, the latter one in the layers with non-reversed magnetizations only and due to the applied field acting against the uniaxial anisotropy.

Over the past 20 years, the ability to build magnetic materials nanostructured along one dimension has led to the exciting possibility of utilizing electron spin for information processing [1]. In samples nanostructured along several dimensions, such as "nanostripes" or "nanodots", novel properties can be expected if the size of the structures becomes comparable to or smaller than certain characteristic length scales, such as the spin diffusion length. From the point of view of applications, magnetic nanostructures are the critical building blocks of important magnetoelectronics devices, such as the magnetic random access memory or patterned recording media. Due to the necessary miniaturization of such devices and the proximity of the superparamagnetic limit, the magnetic interaction between the neighboring cells is becoming a more and more important parameter that has to be understood and, hitherto, controlled.

The system investigated here is a ferromagnetic/non magnetic multi-bilayer with a gradient in the bilayer thicknesses (Fig. 1). It can be considered as laterally nanostructured due to the nanocrystallinity of the ferromagnetic layers with randomly oriented grains and random orientations of their uniaxial magnetic anisotropy axis. The grains are exchange coupled with their neighbors and have sizes smaller than the ferromagnetic exchange length, leading to reduced coercivity of the ferromagnetic layers. Superimposed to the random anisotropy, a macroscopic uniform uniaxial magnetic anisotropy is induced. In the following, we quantitatively correlate the coercive field of each layer to the grain size within the random anisotropy

model. We also obtain detailed information on the in-plane magnetic microstructure and on the correlations between the spin fluctuations within each layer.
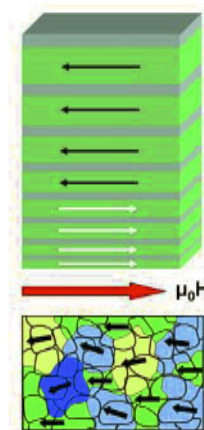
FIG. 1: The sample consists of 100 $Fe_{50}Co_{48}V_2$ layers separated by 100 TiN_x layers. The $Fe_{50}Co_{48}V_2/TiN_x$ bilayer thickness increases continuously from the bottom to the top of the structure. The bottom-most ferromagnetic layers have lower coercivities than the top-most. Below a certain grain size, exchange coupling leads to the formation of regions larger than the grains in which the magnetization is approximately uniform.

The remagnetization process was investigated by neutron reflectometry and off-specular scattering with polarization analysis. The data, together with their analysis within the distorted wave Born approximation (DWBA), are thoroughly presented in [2]. The magnetization reversal proceeds sequentially from the bottom-most thinnest to the top-most thickest layers. In Fig.2.a the number of reversed layer magnetizations, as deduced from the fit of the specular reflectivity data, is depicted as a function of the applied field $\mu_0\mathbf{H}$.

Lateral correlations of the spin misalignment are present inside the magnetic layers, with an average correlation length ξ_l^M equal to 0.2 ± 0.05 μm (see Fig. 3). The off-specular scattering with polarization analysis allowed us to separate the fluctuations into transverse and longitudinal ones, i.e. into fluctuations of the component of the magnetization perpendicular and parallel to the applied field direction, respectively. Those two types of fluctuations are interpreted in the

following way: from one laterally correlated region to the other, two types of spin misalignment coexist in the non-reversed layers, i.e. a non-random one (given by the parameter Φ_l) onto which a Gaussian random fluctuation of the misalignment is superimposed with RMS width ω_l. In the reversed layers only the random fluctuations are present.
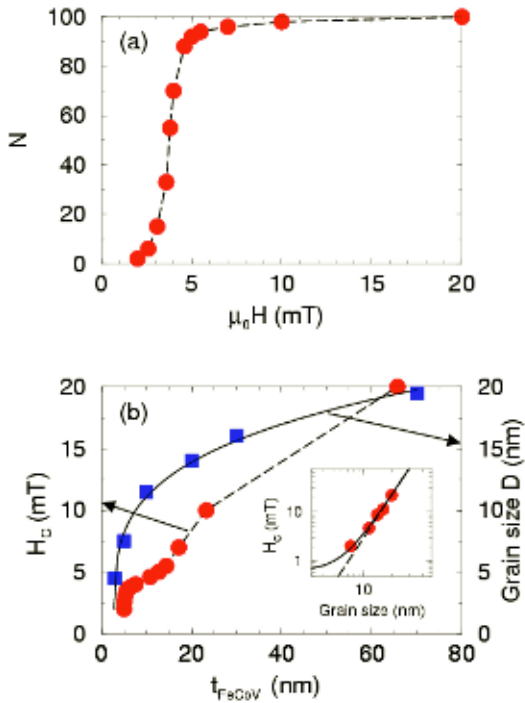
FIG. 2: (a) Number N of reversed FeCoV layer magnetizations as a function of the applied field. (b) Circles: Coercive field H_C of FeCoV layer magnetizations deduced from (a) as a function of the layer thickness. Squares: Grain size D as a function of layer thickness. Insert: Points: Coercive field as a function of grain size deduced from the two other curves. Solid line: Fit to the data leading to $H_C = 0.6 + 7.1 \times D^3$. Dashed line: Simulation $H_C = 7.1 \times D^3$.

The magnetization reversal model as described above, i.e. an increase of the coercive field as a function of the FeCoV layer thickness, can be understood from the nanocrystalline nature of the layers. The dependence of the grain size D on FeCoV thickness t_{FeCoV} has been deduced from X-ray diffraction [3] and is reported in Fig. 2.b: D increases with t_{FeCoV}. In the same plot, we present the variation of the coercive field H_C as a function of t_{FeCoV} deduced from Fig. 2.a. From those two plots, it is possible to deduce the variation of H_C as a function of grain size (insert of Fig. 2.b). The coercive field H_C increases steeply with grain size D.

A steep increase of the coercive field as a function of grain size is a general feature of soft magnetic nanocrystalline alloys [4] and can be explained in the framework of the random anisotropy model. The low coercive field in nanocrystalline alloys is the result of the competition between uniaxial anisotropy of strength K_1 varying randomly from grain to grain and exchange coupling A that tends to align the magnetization of neighboring grains along a common direc-

tion. When the grains are big enough, domain walls of thickness of the order of $l_W = \sqrt{A/K_1}$ can form at the interface between grains and the magnetizations tend to follow the random anisotropy. Below a grain size D of the order of l_W, D is so small that the idea of a magnetization transition region at the grain boundaries loses significance. When $D \ll l_W$, exchange coupling leads to the formation of regions of size $D_{eff} \gg D$ inside which the magnetization is approximately uniform (see bottom part of Fig. 1).
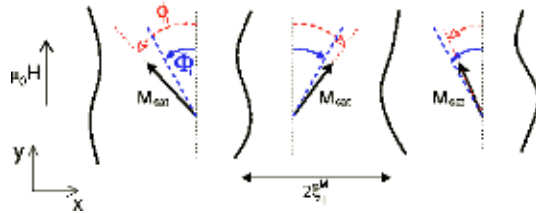
FIG. 3: Model of lateral magnetic correlations within layer l. ϕ_l varies randomly from one correlated region (of size $2\xi_l^M$) to the other around the mean value Φ_l and follows a Gaussian distribution of RMS width ω_l. $\Phi_l = 150^o$ in the non-flipped layers and $\Phi_l = 0$ in the flipped ones. $\omega_l \neq 0$ in all the layers. ξ_l^M can very well be associated to D_{eff} of the random anisotropy model.

In our system, a uniform uniaxial anisotropy K_u superimposes to the random anisotropy. In the limiting case of dominating uniform anisotropy, the effective anisotropy is given by $K_{eff} \propto K_u + \beta D^3$ where β is a constant [4]. Neglecting the magnetostatic interactions, the coercive field H_C should also follow such a law. Fitting the variation of the coercive field as a function of grain size to a law deduced from the random anisotropy model with uniform uniaxial anisotropy reproduces perfectly the data! See solid line in the insert of Fig.2.b.

Two types of spin misalignment are deduced, random and non-random. We attribute the non-random spin misalignment to the applied field that acts against the uniform anisotropy creating an energy barrier for the spins to flip along $\mu_0\mathbf{H}$. Due to exchange interactions, the system reacts by creating neighboring regions of constant magnetizations that make sequentially angles Φ_l and $-\Phi_l$ with respect to $\mu_0\mathbf{H}$. On top of that, the nanostructure of the layers with random orientation of the grains introduces randomness in φ_l characterized by the RMS amplitude ω_l.

To conclude, neutron scattering under grazing incidence with polarization analysis, coupled with state-of-the-art data treatment [2], has allowed us to deduce detailed information on the balance between anisotropy and exchange interactions in a gradient nanocrystalline multilayer.

[1] P. Grünberg, JPCM **13**, 7691 (2001)

[2] E. Kentzinger, U. Rücker, B. Toperverg, F. Ott, Th. Brückel, PRB **77**, 104435 (2008)

[3] M. Senthil Kumar and P. Böni, JAP **91**, 3750 (2002)

[4] G. Herzer, JMMM **294**, 99 (2005)

Magnetic coupling across highly oriented oxidic interfaces: Fe_3O_4/NiO

I. P. Krug[1], M. W. Haverkort[2], H. Gomonaj[3], L. H. Tjeng[4], C. M. Schneider[1]

[1] IFF-9: Electronic Properties
[2] Max-Planck-Institut für Festkörperforschung, 70569 Stuttgart, Germany
[3] Bogolyubov Institute for Theoretical Physics, 14-b Metrologichna Street, 03680, Kiev, Ukraine
[4] Physikalisches Institut II, Universität zu Köln, 50937 Köln, Germany

NiO thin films on Fe_3O_4 represent a fully oxidic model system for proximity effects at an antiferromagnet/ferromagnet interface. Our microspectroscopy studies reveal a strong influence of the crystallographic interface orientation on the magnetic coupling. Both the {110} and the {111} interfaces produce collinear coupling, while at the {001} interface a spin-flop coupling is observed. These differences are caused by the specific interfacial bonding and strain situation.

Two distinct magnetic materials in direct contact will experience a strong coupling across the interface mediated through short-ranged exchange interactions. This magnetic coupling causes a change in the magnetic properties of the individual constituents – a complex situation, which is sometimes termed "proximity effect". The latter can have different facets reflected in a change of the magnetic anisotropy, the magnetic moments, the local spin configuration, or the magnetic ordering temperature. The interaction between a ferromagnet (FM) and an antiferromagnet (AF) gives rise to a particular proximity effect, which is known as *exchange bias* and exhibits all of the features mentioned above. Discovered in the 1950s by Meiklejohn and Bean [1], it has in the meantime become a key ingredient for the fabrication of high-density hard disks, magnetic-field sensors, and more sophisticated spintronic devices [2, 3].

A central aspect of the magnetic proximity effect is the crystallographic structure of the boundary region between the two materials, which may influence the interfacial coupling in two ways:

i) Breaking of translational symmetry causes electronic effects, for example, an anisotropic exchange interaction, altered crystal-field symmetry, and electronic hybridization across the interface. Those effects will be generally confined to the interface region.

ii) Epitaxial lattice mismatch causes magnetoelastic effects, which depend on the orientation of the planar epitaxial strain with respect to the crystal lattice. The strain-induced effects will extend farther into the sample.

In our work we addressed the question of how the crystallographic orientation influences the FM/AF magnetic proximity effect via exchange coupling and magnetoelastic effects in the specific system NiO on Fe_3O_4. We can distinguish two basic coupling ge-

ometries in FM/AF systems, namely, collinear and spin-flop coupling. In the latter configuration, the AF spin axis orients by $90°$ with respect to the FM.

The spectromicroscopy studies were carried out by means of a photoemission microscope, using x-ray magnetic circular (XMCD) and linear dichroism (XMLD) for the imaging of the domain structures in the FM and AF, respectively. The analysis of the spectroscopic data must take into account the delicate anisotropy of the XMLD signal in single-crystalline systems [4]. In spite of these complications it is possible to analytically calculate the absorption spectra for arbitrary orientations of the AF spin
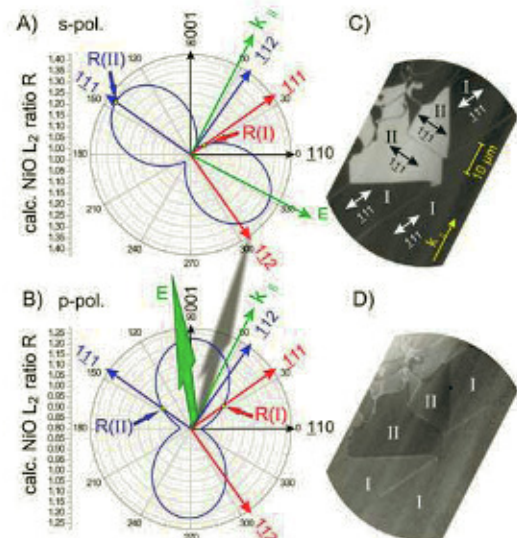
FIG. 1: 35 monolayers of NiO on Fe_3O_4 (110). Polar plots in (A) and (B): calculated L_2 intensity ratio for every possible in-plane direction of the spin quantization axis, for the polarization in s- (A) and p-geometry (B). The plots include crystallographic directions for collinear and spin-flop coupling, as well as the surface projection of light incidence k and light polarization E. The calculated magnetic contrast for a given spin orientation in the sample plane is defined by its intersection with the L_2-ratio curve. (C) and (D): PEEM images. For collinear coupling we assign the axis [111] to set I and [1$\bar{1}$1] to set II. Conversely for spin-flop coupling, the assignment is [11$\bar{2}$] for set I and [1$\bar{1}$2] for set II. Only the collinear case matches the theoretical prediction, with set II being brighter in s and slightly darker in p geometry [points R(I) and R(II) in (A) and (B)].

52

quantization axis and for s- and p-polarized light, using only few fundamental spectra gained from atomic multiplet calculations (symmetry-adapted basis set). This allows a convenient comparison to the experiment, minimizing the computational effort.

A result of this procedure is shown in Fig. 1 for the example of the {011} interface. For clarity, we anticipate that the XMCD in the Fe_3O_4 substrat yielded two different $\langle 111 \rangle$-type in-plane easy-axes for the domains, and that the exchange coupling limits the NiO spin axis alignment to the sample plane as well. Furthermore we classify the coupling angle in term of collinear (near $0°$) or spin-flop (near $90°$). The blue dumbell-shaped curves in panels (A) and (B) depict the angular dependence of the XMLD signal with respect to the crystalline axes. For the comparison with the experiment we define two sets of domains (I and II) with different contrast levels in the panels (C) and (D), each type correlated with an easy-axis in the substrate. As apparent in the PEEM images, this domain contrast inverts, when going from s- to p-polarized light, but the relative contrast between type I and type II domains is smaller than in the s-polarized case. The expected contrast level for an arbitrary spin quantization axis in the film plane is given by its intersection with the blue contrast curve. From inspection of (A) it becomes clear that a spin-flop coupling should yield a bright contrast for set I and a dark contrast for set II, quite opposite to the experimental observation. A similar contradiction is encountered for p-polarized light. The experimental data can be explained consistently only if a *collinear* coupling between FM and AF is assumed [4, 5].

At first glance, this result contradicts Koon's theory [6] which predicts spin-flop or collinear coupling, if the AF surface termination is compensated or uncompensated, respectively. In our case, we thus would expect spin-flop coupling for a ferromagnet in contact with the compensated {110} and {001} NiO surfaces. In our experiments we find spin-flop coupling only for the {001} interface and collinear coupling for {110} and {111}. In order to understand this discrepancy, we have to consider that the interface has two sides, i.e., a NiO and an Fe_3O_4 side. We must take into account the full crystalline and magnetic structure of the transition Fe_3O_4 (ferrimagnetic, spinel) $\rightarrow$ NiO (two sublattices, rocksalt). In all three crystalline orientations investigated, one can find a configuration where the magnetic unit cells of NiO and Fe_3O_4 match. This implies that the two magnetic sublattices (spin up and spin down) of NiO will experience different magnetic environments at the interface. Consequently, in a more realistic picture the interface cannot be compensated anymore and a tendency for collinear coupling should result. In fact, the microspectroscopy studies of the Ni L_3 XMCD signal reveal different amounts of uncompensated magnetic moments in NiO at each interface orientation (Fig.2). We note that these uncompensated moments may also result from a reconstruction of the interface, leading to the formation of an interfacial $NiFe_2O_4$ (NFO) phase.

The extreme case is the {111} interface, where locally only one type of AF sublattice meets the interface
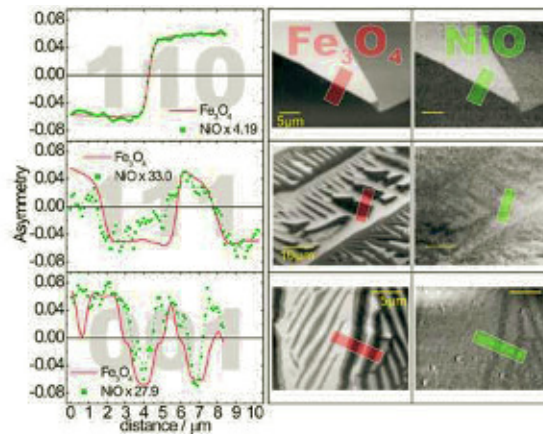
FIG. 2: Comparison of the amount of uncompensated magnetization at the interface for the three orientations {110}, {111}, and {001}. For comparison, the NiO XMCD has always been scaled to match the size of the Fe_3O_4 XMCD.

(locally uncompensated). In principle, partial compensation is realized for all interface orientations investigated in this study, rendering spin-flop coupling unlikely. Experimentally, however, we find perpendicular coupling for the {001} interface, contradicting the structural argument given above.

This indicates that a further mechanism must be at play, favoring a perpendicular over a collinear spin arrangement, thereby overcoming the influence of exchange interactions and the particular interface structure. Our analysis shows that magnetoelastic effects can indeed lead to spin-flop coupling at the {001} interface if the magnetoelastic energy gain dominates over interfacial exchange coupling. It is interesting to note that for $NiFe_2O_4$ coupled to magnetite, the situation would be the same as for NiO – so spin-flop coupling could result even for a NFO-type reconstructed zone at the interface.

Further details may be found in Refs. [4, 5].

[1] W. Meiklejohn and C. Bean, Phys. Rev. **102**, 1413 (1956).

[2] J. Nogues and I. K. Schuller, J. Magn. Magn. Mater. **192**, 203 (1999).

[3] R. Coehoorn, in *Handbook of Magnetic Materials*, edited by K. Buschow (Elsevier Science, Amsterdam, 2003), Vol. 15, p. 4.

[4] I. P. Krug, F. U. Hillebrecht, M. W. Haverkort, et. al., Europhys. Lett. **81**, 17005 (2008).

[5] I. P. Krug, F. U. Hillebrecht, M. W. Haverkort, et al., Phys. Rev. B **78**, 064427 (2008).

[6] N. C. Koon, Phys. Rev. Lett. **78**, 4865 (1997).

53

Domino behavior in nanowires

S. Lounis[1,2], P. H. Dederichs[2,3], S. Blügel[1,2]

[1] IFF-1: Quantum Theory of Materials
[2] IAS: Institute for Advanced Simulation
[3] IFF-3: Theory of Structure Formation

54

Resting on first-principles, the parity of the number of atoms in finite antiferromagnetic nanowires deposited on ferromagnets is shown to be crucial in determinig their magnetic ground state. One additional adatom changes the magnetic structure dramatically across the entire nanowire. Even-numbered nanochains exhibit always non-collinear magnetic order, while odd-numbered wires lead under given conditions to a collinear ferrimagnetic ground state.

Controlling the flow of charge and spin information to and from increasingly smaller structures hinges on the meticulous control of the coupling between spins[1, 2, 3, 4, 5, 6, 7]. Frequently at the nanoscale, when antiferromagnetic interactions prevail, a phenomenon called magnetic frustration occurs that describes the inability to satisfy competing exchange interactions between neighboring atoms. It is partially removed by creating non-collinear structures with lower energies [8, 9, 10, 11, 12].
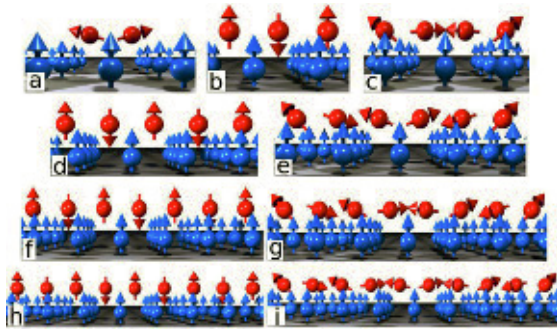
FIG. 1: *Different magnetic ground configurations of the Mn nanowires on Ni(001). The nanochains with even number of Mn atoms (2, 4, 6, 8, 10) prefer a non-collinear ground state, the odd ones a collinear one[13].*

The most evident examples of frustration is the so-called geometric frustration arising from the antiferromagnetic interaction between adatoms forming *e.g.* a trimer with a shape of an equilateral triangle. In this contribution we present a novel frustration phenomenon due to the coupling with the ferromagnetic substrate: Below a particular size, nanowires exhibit totally different magnetic structures depending on the parity of the number of adatoms[13]. The differences between the magnetic structures of the even and odd

atom wires are predicted to be sufficiently large to be observed experimentally. Throughout the paper, results are shown primarily for Mn chains on Ni(001), but they are general and hold also for antiferromagnetic chains on different substrates.

The ground-state spin structure of nanowires with up to 11 adatoms is investigated with the full-potential screened Korringa-Kohn-Rostoker Green function method (KKR) [14, 8] based on density functional theory (DFT) employing the Local Spin Density Approximation (LSDA). A Heisenberg model is used to interpret the results of the aforementioned density-functional calculations, to extend the results to larger chains and provide so an overall picture. We assume a simple classical spin-Hamiltonian in which magnetic exchange interactions between first-neighbor atoms are taken into account

$$H = -J_1 \sum_{i=1}^{N-1} \cos(\theta_i - \theta_{i+1}) - J_2 \sum_{i=1}^{N} \cos(\theta_i). \quad (1)$$

N is the number of atoms in the chain and θ is the rotation angle of the wire atom moment with respect to the magnetization of the surface. The magnetic exchange interactions (J_1 and J_2) are extracted from our *ab initio* calculations [15] and inserted into the present model: $J_1(< 0)$ stands for an (antiferromagnetic) exchange interaction between two neighboring wire atoms at sites i and $i \pm 1$ in the chain, while J_2 is the total magnetic exchange interaction between a given wire atom and its neighboring surface atoms.

Mn-dimer atoms as well as Cr-dimer atoms couple strongly AF to each other ($J_1 < 0$), which is in competition with the ferromagnetic (FM) interaction of Mn (Cr) with the substrate atoms ($J_2 > 0$) favoring a parallel alignment of the dimer moments[13]. Thus, frustration in the interactions occurs and a non-collinear (NC) structure (see Fig. 1(a)) is obtained as ground state. Here the Mn moments are aligned antiparallel to each other and roughly perpendicular to the substrate moments. Moreover, the weak FM interaction with the substrate causes a slight tilting of the moments leading to an angle θ of 73° instead of 90°. Out of the six nn Ni(001) substrate moments, the four outer ones show a small tilting of $7.4°$, while the two inner ones do not tilt due to symmetry reasons.

For our preliminary discussion, we use the Heisenberg model (Eq. 1). For the dimer-case, a potential ferrimagnetic (FI) solution depends only on J_1

($E_{\mathrm{FI}} = J_1$), because the contributions J_2 of both adatoms cancel out due to their antiparallel alignment. On the other hand, the NC solution depends also on the magnetic interaction with the substrate in terms of J_2 ($E_{\mathrm{NC}} = -J_1 \cos(2\theta) - 2J_2 \cos(\theta)$) being clearly the cause of the non-collinearity of the system as energy is gained by the upward tilting (Fig. 1(a)) of the moments from $90°$ to $73°$. For three Mn adatoms (Fig. 1(b)), we find the FI solution to be the ground state. Contrary to the dimer, the energy of the collinear solution of the trimer depends on J_2 ($E_{\mathrm{FI}} = 2J_1 - J_2$) due to the additional third adatom, which in fact allows the FI solution to be the ground state.

One sees here the premise of an odd-even effect on the nature of the magnetic ground state. Indeed, the longer chains with even number of atoms have a NC ground state (see Fig. 1(c)-(e)-(g)-(i)) that keeps, in first approximation, the magnetic picture seen for the dimer almost unchanged because an additional interaction energy with the substrate proportional to J_2 can only be gained in the NC state by the small tiltings off the 90° angle. The odd-numbered nanochains, however, are characterized by a FI ground state (see Fig. 1(c)-(e)-(g)-(i)), similar to the trimer, in which the majority of atoms are coupled FM to the surface. In this case, the wires can always gain energy in the collinear state due to one J_2 interaction term which does not cancel out. This gain decays as N^{-1} till the transition to a non-collinear ground state for a length of 9 atoms, as predicted from the Heisenberg model, while DFT results exhibit a longer critical length (~ 16 atoms).

Fig. 2 is interesting since it shows a phase diagram that can be used to predict the general behavior of AF chains on FM substrates. The curve also decays roughly as N^{-1} from the very long transition lengths obtained with small exchange interaction ratios while very small transition lengths are obtained for $J_2 >> J_1$. This model predicts for example a transition length of 5 atoms for Mn/Fe(001) while Mn/Ni(111) is characterized by a value of 17 atoms. Certainly, this transition length is subject to modifications depending on the accuracy of the exchange interactions, spin-orbit coupling and geometrical relaxations.

To conclude, using DFT calculations, a strong novel phenomenon was found for finite antiferromagnetic nanowires on ferromagnetic substrates by which the parity of the number of atoms in a wire is an essential quantity determining the magnetic structure. Even-numbered nanochains exhibit a NC ground state, nano-sized odd-numbered chains below a particular length have a collinear ground state. Adding one atom to the chain can lead to complete change of the magnetic structure across the entire chain elucidating the extreme non-locality of the effect. Finally, we predict the infinite chains to be of non-collinear magnetic nature. We encourage experimental efforts to investigate this intriguing parity effect.
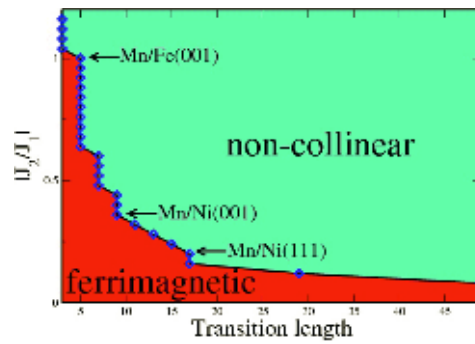
FIG. 2: Magnetic phase diagram of the odd chains showing the effect of the ratio J_2/J_1 on the transition lengths. If the length of the chains is smaller than the transition length, the FI configuration is the ground state.

[1] I. Zutic, J. Fabian, S. Das Sarma, Rev. Mod. Phys. **76**, 323 (2004).

[2] Y. Yayon, V. W. Brar, L. Senapati, *et al.* Phys. Rev. Lett. **99**, 67202 (2007).

[3] T. Mirkovic, M. L. Foo, A. C. Arsenault, *et al.* Nature Nanotechnology 2, 565 - 569 (2007).

[4] S. Rusponi, T. Cren, N. Weiss, *et al.* Nature Materials **2**, 546 (2003); W. Kuch, *ibid.* **2**, 505 (2003).

[5] J. A. Stroscio and R. J. Celotta, Science **306**, 242 (2004).

[6] J. T. Lau, A. Föhlisch, R. Nietubyć, *et al.* Phys. Rev. Lett. **89**, 57201 (2002).

[7] C. F. Hirjibehendin, C. P. Lutz, J. Heinrich, Science **312**, 1021 (2006); A. J. Heinrich, *et al.* Science **306**, 466 (2004).

[8] S. Lounis, Ph. Mavropoulos, P. H. Dederichs, and S. Blügel, Phys. Rev. B **72**, 224437 (2005); S. Lounis, *et al. ibid.* **75**, 174436 (2007); S. Lounis, M. Reif, Ph. Mavropoulos, *et al.* Eur. Phys. Lett. **81**, 47004 (2008).

[9] A. Bergman, L. Nordström, A. B. Klautau, *et al.* Phys. Rev. B **73**, 174434 (2006).

[10] R. Robles and L. Nordström, Phys. Rev. B **74** 094403 (2006).

[11] S. Uzdin, V. Uzdin, C. Demangeat, Europhys. Lett. **47**, 556 (1999).

[12] A. T. Costa, R. B. Muniz, and D. L. Mills, Phys. Rev. Lett. **94**, 137203 (2005).

[13] S. Lounis, P. H. Dederichs, S. Blügel, Phys. Rev. Lett. **101**, 107204 (2008).

[14] K. Wildberger, R. Zeller, and P. H. Dederichs, Phys. Rev. B **55** 10074 (1997) and references therein.

[15] A. I. Liechtenstein, M. I. Katsnelson, V. P. Antropov and V. A. Gubanov, J. Magn. Magn. Mat **67**, 65–74 (1987).

55

Deep view into the twisted magnetization state in a Fe/Si multilayer

A. Paul[1,3], U. Rücker[1], M. Buchmeier[2,4]

[1] IFF-4: Scattering Methods
[2] IFF-9: Electronic Properties
[3] Hahn-Meitner-Institut Berlin
[4] Institut für Angewandte Physik, Westfälische Wilhelms-Universität Münster

In Fe/Si multilayers one can find the antiferromagnetic coupling strength to be in the order of the exchange energy inside the Fe layer. At some intermediate field strength the competition between Zeeman energy, AF coupling energy and exchange energy results in a twisted magnetization state inside every Fe layer.

The depth sensitive investigation with polarized neutron scattering under grazing incidence gives a good agreement with the twisted state model in the intermediate field range and shows the presence of buried magnetic domains depending on the magnetic field history.

Interlayer exchange coupling between two ferromagnetic layers across a non-magnetic spacer has been one of the remarkable discoveries in thin film magnetism. In this context, the behaviour of the Fe/Si system is very peculiar and far from being completely understood. Under some growth conditions of the Si interlayer [1], epitaxial Fe/Si/Fe trilayers exhibit a very strong antiferromagnetic (AF) interlayer exchange coupling strength up to $-6mJ/m^2$.

With this unusually high coupling strength, the AF coupling can compete with the exchange energy inside the Fe layer, so that at some intermediate field strenght the competition between Zeeman energy, AF coupling energy and exchange energy results in a twisted magnetization state inside every Fe layer. Typically, the magnetization of a ferromagnetic layer in an exchange coupled system can be described by a single vector. Here, we find one of the rare exceptions, where the direction of the magnetization in the Fe layer varies along the surface normal on a length scale much smaller than the width of a typical domain wall. This state has been discovered by magnetometry and inelastic Brillouin light scattering (BLS) of the spinwave excitations of the twisted magnetization state together with micromagnetic calculations that model the depth dependent magnetization inside the Fe layer [1].

In this work [2], we intended to attack this effect with a depth sensitive probe, which is polarized neutron scattering under grazing incidence. Specular reflectivity of polarized neutrons is sensitive to the depth dependence of the direction of the magnetization vector, so it is a good tool for testing the twisted state model derived by micromagnetic calculations.
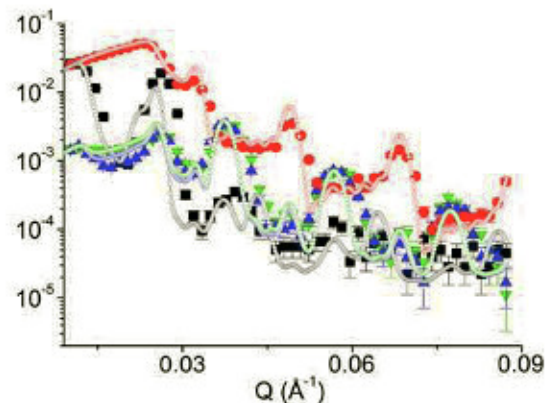
FIG. 1: Specular reflectivity patterns for the non-spinflip [R_{++} (red) and R_{--} (black)] and spinflip [R_{-+} (green) and R_{+-} (blue)] channels at the applied magnetic field of $mue_0 H_a = 0.25$ T. Solid symbols are experimental data and open circles are fits to the twisted state model.

Offspecular scattering yields additional information about the magnetic domain formation.

The typical approach for the fitting of experimental specular reflectivity data as in Fig. 1 is the rigid state approximation. This means that the magnetization of every ferromagnetic layer is taken as a single vector that can be varied in direction but not in modulus. During the fitting procedure, all angles of the magnetization of the different ferromagnetic layers are varied to receive the best agreement with the experimental data.

In the case of the Fe/Si multilayer, this approach works reasonably good except the intermediate field region around 0.25 T. At small fields, the magnetization is mainly determined by the interlayer exchange coupling and the crystalline anisotropy, which favour 180° between the magnetization directions of neighboring layers, all magnetized along one of the easy axis. At high fields, the Zeeman energy forces all magnetization directions along the applied field. Only in the intermediate field region where Zeeman energy and interlayer exchange coupling have comparable strength, a deviation from the rigid magnetization can occur.

Due to the failure of the rigid state approximation, we introduced the twisted state model, which was inferred earlier from the BLS experiments on similar
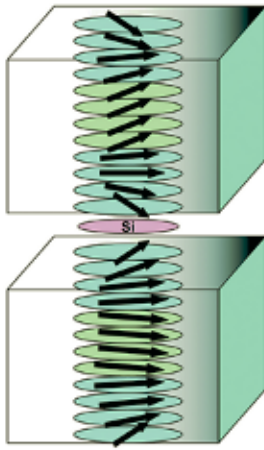
FIG. 2: Schematic representation of the magnetization profile of two adjacent Fe layers corresponding to the experimental data obtained at $H_a = 0.25$ T.

systems [1]. The spatial variation of the magnetization vector was extracted from micromagnetic simulations, which allow vertical variations only. The orientation relative to the applied field was obtained by minimizing the energy equation, taking into account the interlayer exchange coupling, the exchange energy inside the Fe layers, the crystalline anisotropy and the Zeeman energy. The deviation from the applied field direction increases from the middle of the layer towards the interfaces, where the AF coupling acts strongest. Fig. 2 illustrates the chiral spin arrangement resulting from this calculation.

This result is then used as an input for the fitting of the specular reflectivity. As fitting parameter we now use the interlayer coupling strength, which is an input parameter for the micromagnetic calculation. We receive the best agreement using a total interlayer coupling of $J_1 + J_2 = -2.34 mJ/m^2$. The simulation of the polarized neutron reflectivity using this twisted state model is shown in Fig. 1.
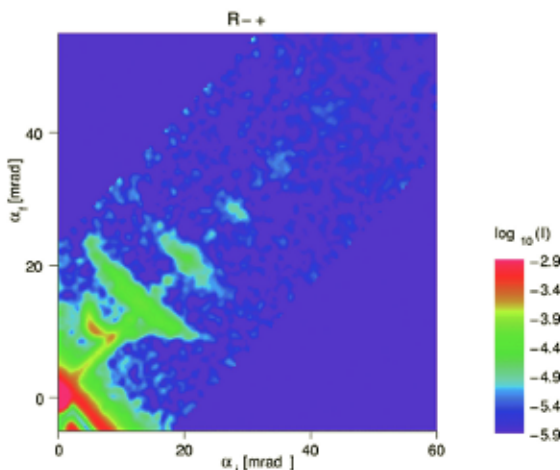
Offspecular scattering gives additional information about the formation of lateral magnetic domains in the buried ferromagnetic layers. The integral measurements by SQUID magnetometry and BLS did not indicate a dependence of the magnetic state of the sample in the intermediate field region on the magnetic history. To our surprise, we found a strong dependence on the magnetic history. The offspecular spinflip scattering seen in Fig. 3 appears only when the sample has been saturated in negative field before applying $H_a = 0.25$ T. When reducing the field from positive saturation to 0.25 T, the spinflip signal is purely specular, no offspecular contribution can be observed. When coming from negative saturation over the remanence to the twisted state, we observe a multi-domain state with vertically correlated domains and a typical lateral correlation length of 0.5 μm . In contrast to that, we observe a single domain state on the length scale of the correlation length of our instrument when we come from positive saturation. Here, we observe a coherent rotation from the saturated state into the twisted state when reducing the field strength.

In conclusion, we have shown that the magnetization profile of a strongly AF coupled Fe/Si multilayer significantly deviates from the simplistic rigid state model. It can be described by a twisted ground state, which is particularly pronounced around an intermediate applied magnetic field. Micromagnetic simulations provide a physically realistic energy-minimized configuration for the rotating moments. They have been proven an essential tool for the data analysis of the polarized neutron reflectometry experiments.

[1] M. Buchmeier, B.K. Kuanr, R.R. Gareev, D.E. Bürgler, and P. Grünberg, Phys. Rev. B **67**, 184404 (2003)

[2] A. Paul, M. Buchmeier, D.E. Bürgler, U. Rücker, and C.M. Schneider, Phys. Rev. B **77**, 184409 (2008)

FIG. 3: Spinflip intensity map (R_{+-}) of a Fe/Si multilayer measured at $H_a = 0.25$ T after negative saturation. The color bar encodes the scattered intensity on a logarithmic scale as a function of incident angle α_i and scattered angle α_f.

Magnetization dynamics induced by ultra-short optical pulses

A. A. Rzhevsky[1,2], B. B. Krichevtsov[2], D. E. Bürgler[1], C. M. Schneider[1]

[1] IFF-9: Electronic Properties
[2] Ioffe Physical Technical Institute, Russian Academy of Sciences, St. Petersburg, Russia

The interplay of interface and bulk magnetization dynamics of Cr-capped Fe(001) thin films have been studied by the time-resolved Kerr effect (TR-MOKE) and time-resolved magnetization-induced second harmonic generation (TR-MSHG) using an all-optical pump-probe technique. Long-lived ($\approx$1 ns) MOKE and MSHG oscillations are excited by ultra-short ($\approx$0.15 ps) optical pulses and reveal a similar behavior of the interface and bulk magnetization dynamics. The in-plane amplitude of the optically excited magnetization precession is determined and gives evidence that the observed dynamics reaches beyond the usually considered linear range. These results are of importance for the application of ultra-fast optical switching schemes in opto-magnetic devices.

The magnetization dynamics is currently intensively studied both in thin magnetic films and bulk crystals with emphasis on the dynamic response induced by ultra-short optical pulses [1]. The practical interest in this type of excitation mechanism is driven by the possibility of ultra-fast optical switching of local magnetic areas, which might be employed in new types of opto-magnetic devices for information and data processing technology. From a more fundamental point of view this optical approach enables the investigation of the microscopic mechanisms governing the excitation of magnetization dynamics on a very short time scale and allows testing the applicability, the limits, and validity of the classical Landau-Lifshitz-Gilbert (LLG) formalism.

The magnetization dynamics probed by the TR-MOKE reflects the properties of the bulk magnetization, because the Kerr signal stems from the entire thickness of the film, provided it is less than the information depth of light. The dynamic behavior of the interfacial magnetization, however, can selectively be probed by means of TR-MSHG. In this method a pump beam (frequency ω) excites magnetization precession and a probe beam is used to generate a MSHG signal $I_{2\omega}$, the amplitude of which depends on the transient magnetic state at a time delay Δt after the excitation. (M)SHG in centrosymmetric structures originates from a very narrow region of one or two monolayers at the surface or interface, where the inversion symmetry is broken. Previous TR-MOKE and TR-MSHG studies [2, 3] of epitaxial Fe/AlGaAs

films surprisingly revealed different dynamic behavior of bulk and interfacial magnetization. This finding was interpreted as an indication that the interfacial and bulk magnetization contributions in Fe/AlGaAs are to some extent decoupled. However, the microscopic origin has not been addressed, and the general validity of this observation remained unclear. Here, we employed both TR-MOKE and TR-MSHG to study interfacial and bulk magnetization dynamics induced by ultra-short laser pulses in epitaxial GaAs(100)/Ag/Fe/Cr structures [4].

The Fe films were grown by molecular beam epitaxy onto GaAs(001) substrates with an Ag(150 nm)/Fe(1 nm) buffer layer and are covered by a Cr(2 nm) protective cap layer. Fe and Cr layers crystallize in the bcc structure, which for Fe gives rise to cubic magnetocrystalline anisotropy. The strong demagnetizing field of the thin film geometry confines the static magnetization predominantly in the film plane. Therefore, the overall magnetic anisotropy can be described by an effective in-plane, four-fold anisotropy energy. The dynamic response of the magnetization $\mathbf{M}$ resulting in TR-MSHG and TR-MOKE signals was induced by 150 fs optical pump pulses at $\lambda = 800$ nm generated by a regenerative amplifier with 1 kHz repetition rate. For TR-MSHG a photon counting technique was used to record the SHG intensity of the probe beam at the
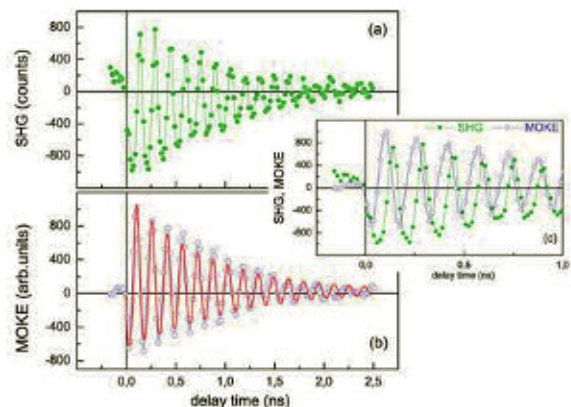

FIG. 1: (a) MSHG and (b) MOKE time profiles in pp polarization combination for a Fe(26 nm)/Cr(2 nm) bilayer. An offset of 2500 counts is subtracted in (a). The red line is a calculated trace (see text). Inset: TR-MOKE and TR-MSHG signals are shifted by a 90°.
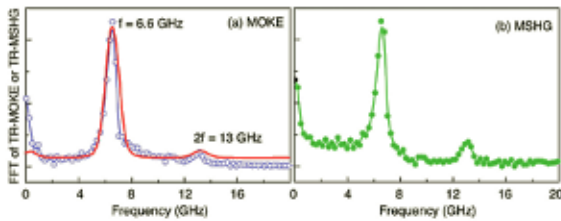
FIG. 2: *Fourier transforms (FFT) of (a) TR-MOKE and (b) TR-MSHG signals for a Fe(26 nm)/Cr(2 nm) bilayer measured under the same conditions as in Fig. 1.*

FIG. 3: *Magnetic field dependence of the MSHG intensity for a Fe(26 nm)/Cr(2 nm) bilayer in the longitudinal geometry. The red line shows a fit from which the coefficients a, b, and c in Eq. (1) are determined.*

double frequency ($\lambda = 400$ nm). The fundamental light at $\lambda=800$ nm was rejected by a blue filter in the reflected beam. In the case of TR-MOKE, we employed lock-in technique and a differential photodetector. In both approaches the probe beam incidence angle was $\theta \approx 10°$. The diameter of the illuminated area was about 1 and 0.3 mm with an average power of 10 and 3 mW for the pump and probe beam, respectively. The measurements of TR-MSHG and TR-MOKE were carried out at a magnetic field of 0.5 kOe oriented close to an in-plane hard-axis direction.

Figure 1 shows MOKE and MSHG time profiles of an Fe(26 nm)/Cr(2 nm) film for the pp polarization combination. The main oscillations in both TR-MOKE and TR-MSHG occur at the same frequency, but their phase is shifted by $\approx 90°$. The Fourier transforms of the time profiles in Fig. 2 yield a main frequency $f = 6.6$ GHz, which corresponds to the frequency of the uniform precession mode. In addition, we observe weak intensities at the double frequency $2f$. For the analysis of the experimental results we use expressions linking the MSHG intensity to components of the interfacial magnetization **M**, which are based on effective nonlinear susceptibilities [5]. The MSHG intensity for the pp polarization combination is given by the interfacial magnetization component M_y and contains both linear and quadratic contributions

$$I_{2\omega} = a + bM_y + cM_y^2. \qquad (1)$$

The coefficients a, b, and c are related to the effective nonlinear susceptibilities and can be determined from the field dependencies of the static MSHG in pp configuration (Fig. 3). For this procedure the M_x and M_y components as a function of the applied are described within a Stoner-Wolfarth model taking into account the Zeeman and four-fold in-plane magnetic anisotropy energies. The calculated MSHG field dependence is superimposed in Fig. 3 as a red line. Since the static field dependence and optically induced time-dependent variations of the MSHG response were measured at the same experimental conditions the coefficients a, b, and c from Fig. 3 may also be used to calculate the time traces and Fourier spectra of the TR-MSHG and TR-MOKE oscillations. For these calculations we assume that the magnetization follows an exponentially damped precession. The results of the calculations are shown as red lines in Figs. 1 and 2. The best agreement between the experimental and calculated data is obtained at a max-

imum oscillation amplitude of $13°$. This large amplitude value means that at the given excitation power the system may be already at the threshold of the applicability of the LLG equations. As it is known, these equations are linearized and only valid for small deflections of the magnetization vector from the equilibrium value. The Fourier spectrum of the calculated MSHG oscillations shown in Fig. 2(a) displays a strong first harmonic and a much weaker $2f$ second harmonic contribution due to the nonlinearity of the $I_{2\omega}(M_y)$ function in Eq. (1). The phase shift observed between MOKE and MSHG oscillations (Fig. 1) is a clear evidence that the linear response relates to the polar Kerr effect and is caused by time variations of the magnetization component M_z normal to the film plane. On the other hand, the nonlinear MSHG response is related to the M_y component [Eq. (1)].
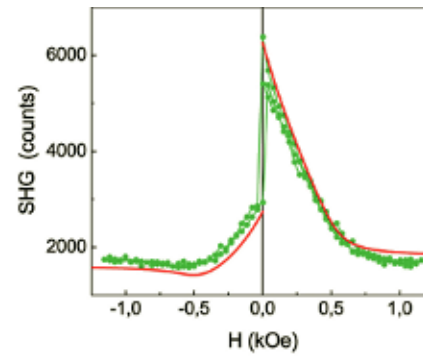
Our investigations show that in GaAs(001)/Ag/Fe/Cr –in contrast to AlGaAs/Fe films [2, 3]– the oscillations of the interfacial and bulk magnetizations appear at the same frequency corresponding to the uniform mode frequency and, thus, reveal a similar magnetization dynamics. A possible source for this discrepancy may be related to the different nature of the samples, i.e. the properties of the interfaces between a metal and semiconductor (Fe/AlGaAs) and between two metals (Ag/Fe and Fe/Cr). The semiconductor/metal interface has a stronger tendency for intermixing, which can have a significant influence on the magnetic properties in the entire interface-near region. The large amplitude of the oscillations of up to $13°$ gives evidence that the dynamical behavior of the system is at the limit of the linearized LLG equation's applicability and that next order effects should be considered when developing novel opto-magnetic switching schemes.

[1] A. Kimel *et al.*, Proc. SPIE **6892**, 68920P (2008).

[2] H. B. Zhao *et al.*, Appl. Phys. Lett. **91**, 052111 (2007).

[3] H. B. Zhao *et al.*, Phys. Rev. Lett. **95**, 137202 (2005).

[4] A. A. Rzhevsky *et al.*, J. Appl. Phys. **104**, 083918 (2008).

[5] A. A. Rzhevsky *et al.*, Phys. Rev. B **75**, 144416 (2007).

Ultrafast dynamics of a magnetic antivortex

S. Gliga[1], M. Yan[1], R. Hertel[1], C.M. Schneider[1]

[1] IFF-9: Electronic Properties

Within the past years, research on nanoscale magnetization dynamics has made great progress in isolating fundamental magnetization structures and investigating their individual properties. In particular, the study of magnetic vortices has recently emerged as one of the most important topics in nanomagnetism, especially following the discovery that the vortex core can easily be switched by means of short field pulses [1, 2]. The investigation of this micromagnetic reversal process has shown that it is in part mediated by the formation of an *anti*vortex – the topological counterpart of the vortex. However, not much is known to date about the dynamics of antivortices. Using micromagnetic finite-element simulations we have studied the ultrafast magnetization dynamics of an individual antivortex, which was stabilized in a specially tailored soft-magnetic thin-film element. We find that a short perturbation induced by a single in-plane field pulse can cause the reversal of the antivortex core, following a process which is perfectly complementary to the case of a vortex [3]. These findings show that the complementarity between vortices and antivortices does not only apply to their static structure, but also to their ultrafast dynamics. The new antivortex core switching process could be used for the effective generation of spin waves to drive novel logical circuits [4].

Antivortices spontaneously form alongside vortices in thin ferromagnetic films above a critical size. Both structures possess a tiny core at their center in which the magnetization points perpendicular to the plane and which has been found to decisively affect their dynamics. Only few studies exist however on antivortex dynamics and these have focussed on the antivortex response to small perturbations from equilibrium, such as in a recent experiment by Kuepper *et al.* [5]. Using fully three-dimensional micromagnetic simulations we have investigated the ultrafast dynamic response of a single magnetic antivortex to an external field pulse a few tens of ps long. This triggers a highly non-linear behavior leading to irreversible changes in the antivortex structure. In particular, we find that suitably shaped field pulses can induce a rapid series of vortex-antivortex creation and annihilation processes, complementary to the ones observed in a vortex [2], and which ultimately lead to the reversal of the antivortex core.

In contrast to vortices, it is rather difficult to isolate an antivortex, *i.e.*, to prepare a nanostructure that contains only a single antivortex. This is due to divergences in the in-plane magnetization distribution of the antivortex which tend to destabilize the structure, in contrast to the vortex which is divergence-free. The different in-plane structures of vortices and antivortices are schematically illustrated in Fig. 1a. We have successfully isolated an antivortex in a Permalloy sample constructed from four circular segments, shown in Fig 1b. The in-plane shape anisotropy of this particular geometry can sustain an antivortex due to the tendency of the magnetization to align with the sample boundaries.

The dynamic simulations have been performed with our micromagnetic finite-element code which has also been used in Ref. [2]. The magnetic volume was discretized into about 200,000 tetrahedral elements and the magnetization dynamics was calculated using the Landau-Lifshitz-Gilbert equation with damping parameter $\alpha = 0.01$. The magnetization dynamics in response to a short 60 mT in-plane Gaussian-shaped pulse of a duration of 80 ps is shown in Fig. 1c-j. Figs. c-f show the in-plane magnetic structure at the indicated times while in Figs. g-j the colors represent the out-of-plane component of the magnetization (m_z). The isosurface representation introduced in Ref. [6] has been used to highlight the precise location of the antivortex core, that is, the region where the magnetization is exaclty perpendicular to the sample plane $(m_z = \pm 1)$. This situation occurs where the $m_x = 0$ and $m_y = 0$ isosurfaces intersect, as shown in Fig. 1. Following the application of the field pulse, the antivortex is displaced from its equilibrium position and the in-plane magnetization of the sample is distorted (Fig. 1d). In a region close to the core, this distortion leads to the formation of a "dip" in which the magnetization rotates out of the plane in the direction opposite to the antivortex core (Fig. 1h). Approximately 80 ps after the pulse maximum, a new antivortex is emitted from the original antivortex (Fig. 1e). However, the formation of a single antivortex would violate the conservation of a topological invariant (the winding number). A new vortex is thus also produced, which is located between the two antivortex structures. The newly formed antivortex-vortex pair is made clearly visible
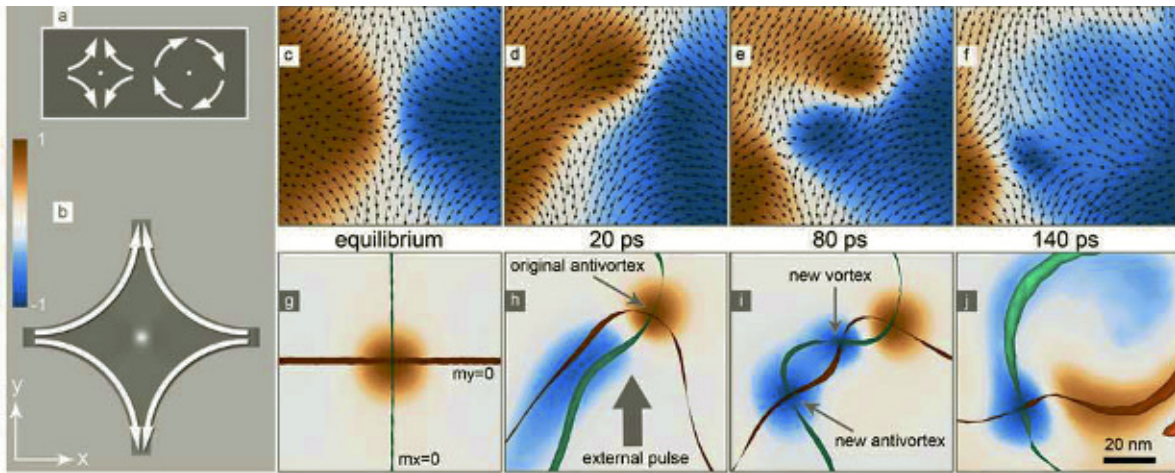
FIG. 1: Ultrafast dynamic response of an isolated magnetic antivortex. **a**, Schematic respresentation of the in-plane structure of an antivortex as compared to a vortex. The two structures are related by underlying topological properties: In both cases, the local magnetization rotates by 360° on a closed loop around the core. **b**, Modeled sample: the circular segments have a 200 nm radius and are 20 nm thick. The arrows indicate the direction of the magnetization, which aligns with the sample boundary. The frames **c-j** show the distortion of the antivortex structure induced by an in-plane field pulse. The frames are snapshots of the magnetic structure around the core at different times relative to the maximum of the applied pulse. The arrows in the top row (**c-f**) represent the in-plane magnetization while the colors represent the x component of the magnetization. In the bottom row (**g-j**) the colors represent m_z while the green and red "ribbons" are the $m_x = 0$ and $m_y = 0$ isosurfaces, respectively.

by the two additional isosurface crossings in Fig. 1i. This strongly inhomogeneous structure is eventually resolved through the annihilation of the initial antivortex with the newly created vortex, whose cores have opposite orientations [6]. This results in a sudden reduction of the local exchange energy density and leaves behind the newly formed antivortex with oppositely magnetized core as shown in Fig. 1f,j.
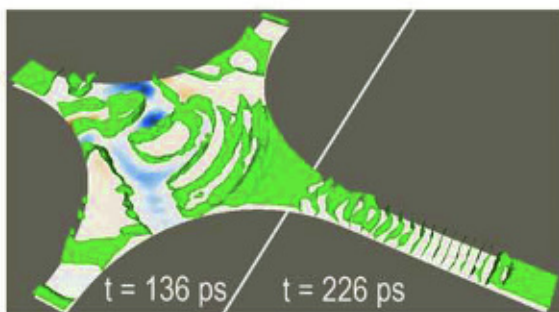
FIG. 2: Spin wave propagation in an extended branch of the sample at two different times following the field pulse maximum. The $m_z = 0$ isosurfaces shown in green allow to visualize the wave fronts. The blue spot represents the switched core.

The annihilation of a vortex-antivortex pairs with opposite core magnetization has been shown to be connected with the emission of spin-wave bursts in the GHz range [6, 7]. The core reversal of the antivortex structure could therefore be used for the generation of spin-waves. By extending the branches of the sample, the spin waves produced in the antivortex can smoothly be injected into a strip acting as a waveguide as simulated in Fig. 2. Such spin waves would then be processed in logical circuits where their phase can be manipulated to perform logical op-

erations [4].

We have presented a new fundamental process in magnetism on the nanoscale which consists in the reversal of the antivortex core. This is the result of complex and ultrafast modifications which can be triggered by applying a short field pulse. It is remarkable that, in spite of the very different magnetic in-plane structure of vortices and antivortices, their ultrafast dynamics are analogous, involving the creation of new magnetic structures followed by a destruction process.

[1] B. Van Waeyenberge, A. Puzic, H. Stoll, K. W. Chou, T. Tyliszczak, R. Hertel, et al., Nature 444, 461 (2006)

[2] R. Hertel, S. Gliga, M. Fähnle and C. M. Schneider, Phys. Rev. Lett. 98, 117201 (2007)

[3] S.Gliga, M. Yan, R. Hertel and C. M. Schneider, Phys. Rev. B 77, 060404(R) (2008)

[4] R. Hertel, W. Wulfhekel and J. Kirschner, Phys. Rev. Lett. 93, 257202 (2004)

[5] K. Kuepper and M. Buess and J. Raabe and C. Quittmann and J. Fassbender, Phys. Rev. Lett. 99, 167202 (2007)

[6] R. Hertel and C. M. Schneider, Phys. Rev. Lett. 97, 177202 (2006)

[7] K.-S. Lee, S. Choi and S.-K. Kim, Appl. Phys. Lett. 87, 192502 (2005)

61

Magnetic ordering in FeAs-based superconducting compounds

Y. Su[1], Y. Xiao[2], R. Mittal[1], T. Chatterji[1], C.M.N. Kumar[2], Th. Brückel[1,2]

[1] JCNS: Jülich Centre for Neutron Science
[2] IFF-4: Scattering Methods

Recently discovered iron pnictide superconductors represent another remarkable example in which superconductivity is in proximity to magnetism. It is thus essential to establish the nature of magnetism in order to understand the mechanism of superconductivity in this new class of materials. We have determined the magnetic structures of two representative parent compounds, $BaFe_2As_2$ and CaFeAsF via comprehensive neutron scattering experiments. A peculiar coexistence of superconductivity and spin-density wave ordering in the underdoped regime of CaFeAsF has also been observed.

Recent discoveries of iron pnictide superconductors such as $LaFeAsO_{1-x}F_x$ [1] ("1111"-family) and $Ba_{1-x}K_xFe_2As_2$ [2] ("122"-family) have attracted tremendous amount of attention in the quest to understand the mechanism of high transition temperature superconductivity. Neutron scattering has been playing a decisive role in the understanding of structural and magnetic properties of iron pnictides, as demonstrated from the first observation of antiferromagnetic ordering (AFM) of the iron moment in LaFeAsO via neutron powder diffraction [3]. Spin-density-wave (SDW) ordering from itinerant Fe spins is believed to be responsible for AFM. It has also been established that magnetic ordering in iron pnictides is strongly coupled to lattice instabilities. Superconductivity emerges upon electron- or hole-doping via chemical substitution. The highest T_C of iron pnictide superconductors currently stands at about 56 K, far beyond the limits ($\sim$ 40 K) set by the BCS theory, it is therefore generally accepted that superconductivity is unlikely mediated by electron-phonon coupling. Experimental evidence on the unconventional nature of superconductivity in iron pnictides has been recently obtained from the observation of resonant spin excitation in polycrystalline $Ba_{0.6}K_{0.4}Fe_2As_2$ via inelastic neutron scattering [4]. Due to an apparent proximity between magnetic ordering and superconductivity in iron pnictides, it is essential to establish the nature of magnetism in the parent compounds. We have carried out comprehensive neutron scattering experiments to investigate magnetic ordering and the coupling between magnetic and lattice instabilities in two representative iron pnictides compounds, $BaFe_2As_2$ [5] and CaFeAsF [6].

A three dimensional long-range antiferromagnetic ordering of the iron magnetic moment, with a unique magnetic propagation wavevector $\mathbf{k} = (1, 0, 1)$, has been found to take place at 90 K in Sn-flux grown $BaFe_2As_2$ single-crystalline samples [5]. The magnetic ordering is accompanied by a simultaneous tetragonal (*I4/mmm*) to orthorhombic (*Fmmm* with b<a<c) structural phase transition. The experiments have been performed at PANDA and HEIDI, FRM II. The ordered magnetic moment of iron has been determined to be aligned along the longer a axis of the low temperature orthorhombic phase. The magnetic moments of iron are arranged in such a way that they are anti-parallel to the neighboring ones along orthorhombic a- and c-axis, while they are parallel along b-axis (in Fig. 1(d)). The saturation moment has been determined to be 0.99(6) μB. Our results thus demonstrate that the magnetic structure of $BaFe_2As_2$ single crystal is the same as in the polycrystalline samples and in other "122" iron pnictides compounds. 5 percent of Sn are expected to be incorporated in the lattice from the flux growth process. We argue that the Sn incorporation is responsible for a smaller orthorhombic splitting and lower Néel temperature T_N observed in the experiments.

A neutron powder-diffraction experiment has been performed to investigate the structural phase transition and magnetic ordering in $CaFe_{1-x}Co_xAsF$ superconducting compounds (x=0.00, 0.06, 0.12) at D20, ILL [6]. The parent compound CaFeAsF undergoes a tetragonal to orthorhombic phase transition at 134 K, while the AFM in the form of a SDW sets in at $\sim$ 114 K (in Fig. 2). The magnetic structure of the parent compound has been determined with a unique propagation vector $\mathbf{k} = (1, 0, 1)$ and the Fe saturation moment of 0.49(5) μB, aligned along the long a axis, same as in $BaFe_2As_2$. With increasing Co doping, the long-range AFM has been observed to coexist with superconductivity in the orthorhombic phase of the underdoped $CaFe_{0.94}Co_{0.06}AsF$ with a reduced Fe moment 0.15(5) μB. AFM is completely suppressed in optimally doped $CaFe_{0.88}Co_{0.12}AsF$. We argue that the coexistence of SDW and superconductivity might be related to mesoscopic phase separation.
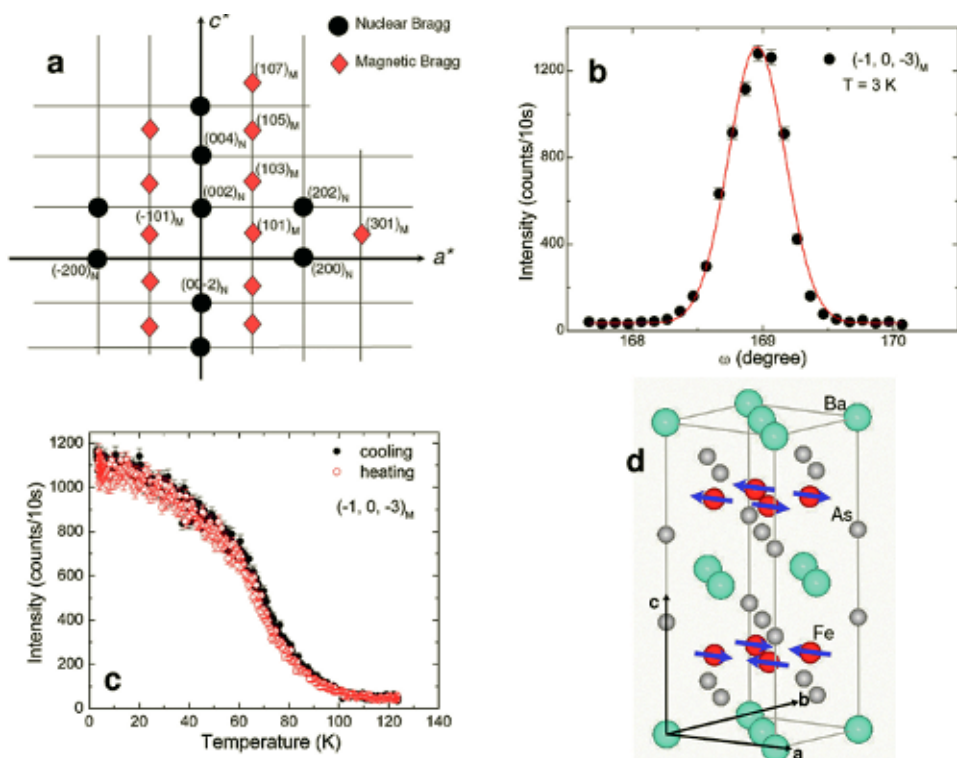
FIG. 1: (a) A schematic drawing of the (h, 0, l) plane in the reciprocal space, where the positions of the nuclear and magnetic Bragg reflections are marked by different symbols. (b) Rocking curves of the $(-1,0,-3)_M$ magnetic reflection measured at 3 K, indicating the occurrence of the antiferromagnetic ordering. The solid lines are the Gaussian fittings. (c) The temperature dependence of the intensity of $(-1,0,-3)_M$, upon cooling (black) and heating (red). (d) The magnetic structure of $BaFe_2As_2$.
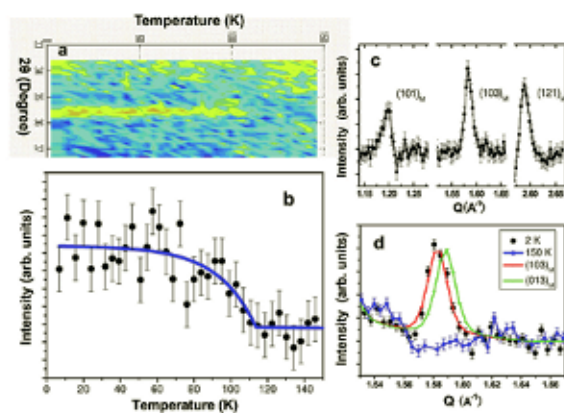
FIG. 2: (a) Temperature evolution of the reflection at $Q=1.583$ Å^{-1} indicating the onset of long-range magnetic ordering in CaFeAsF. (b) Temperature dependence of the integrated intensity of magnetic Bragg reflection. (c) The magnetic reflections obtained by subtracting the NPD pattern measured at 150 K from the pattern measured at 2 K. (d) Comparison of NPD patterns for CaFeAsF measured at 2 K (black) and 150 K (blue), respectively. The red and green curves are the calculated patterns of $(1,0,3)_M$ and $(0,1,3)_M$ reflections, respectively. The magnetic peak at $Q=1.583$ Å^{-1} can be indexed as the $(1,0,3)_M$ properly within the magnetic unit cell.

The successful determination of the magnetic structures of these two compounds paves a way for a more thorough understanding of magnetism of iron pnic-

tides in the future. In particular, this is essential to our ongoing research on magnetic excitations in both parent and superconducting single-crystalline samples via inelastic neutron scattering.

[1] Kamihara Y. et al., J. Am. Chem. Soc. **130** (2008) 3296.

[2] Rotter M. et al., Phys. Rev. Lett. **101** (2008) 107006.

[3] de la Cruz C. et al., Nature **453** (2008) 899.

[4] Christianson A.D. et al., Nature **456** (2008) 930.

[5] Su, Y. et al., Phys. Rev. B **79** (2009) 064504.

[6] Xiao, Y.. et al., Phys. Rev. B **79** (2009) 060504(R).

63

Phonon dynamics in parent and superconducting FeAs compounds

R. Mittal[1], Y. Su[1], S. Rols[2], H. Schober[2], S. L. Chaplot[3], T. Chatterji[1], M. Tegel[4], M. Rotter[4], D. Johrendt[4], Th. Brückel[1,5]

[1] JCNS: Jülich Centre for Neutron Science
[2] ILL, Grenoble, France
[3] BARC, Trombay, India
[4] LMU, Munich, Germany
[5] IFF-4: Scattering Methods

We have measured phonon density-of-states in the parent $BaFe_2As_2$ and superconducting $Sr_{0.6}K_{0.4}Fe_2As_2$ (T_c=32 K) and $Ca_{0.6}Na_{0.4}Fe_2As_2$ (T_c=21 K) compounds using inelastic neutron scattering and carried out lattice dynamics calculations. Compared with the parent compound $BaFe_2As_2$ doping affects mainly the lower and intermediate frequency part of the vibrations in the superconducting samples. Mass effects and lattice contraction cannot solely explain these changes. Softening of phonon modes below 10 meV has been observed in the superconducting samples on cooling from 300 K to 140 K. There is no appreciable change in the phonon density of states when crossing T_c.

The discovery [1,2] of high transition temperature (T_c) superconductivity in fluorine-doped RFeAsO (R = rare earth) and K-doped $BaFe_2As_2$ has attracted immense attention. It is important to note that these compounds have high superconducting transition temperatures without requiring the presence of copper oxide layers. The role of lattice dynamics in the mechanism of superconductivity in these newly discovered doped materials that superconduct with relatively high T_c is still to be settled. The parent MFe_2As_2 (where M=Ba, Sr, Eu, Ca) compounds also show pressure-induced superconductivity. Therefore it is very important to study the phonons in these compounds carefully as a function of pressure and temperature.

We are exploring [3,4] these compounds using the techniques of inelastic neutron scattering and lattice dynamics. We have measured (Fig. 1,2) temperature dependence of phonon density-of-states in the parent $BaFe_2As_2$ [3] and superconducting $Sr_{0.6}K_{0.4}Fe_2As_2$ (T_c=32 K) and $Ca_{0.6}Na_{0.4}Fe_2As_2$ (T_c=21 K) compounds [4] using IN4C and IN6 spectrometers at ILL on polycrystalline samples. By comparing the experimental phonon spectra with the calculated neutron-weighted density of states obtained from a lattice-dynamical model, the dynamical contribution to frequency distribution from various atoms has been identified.
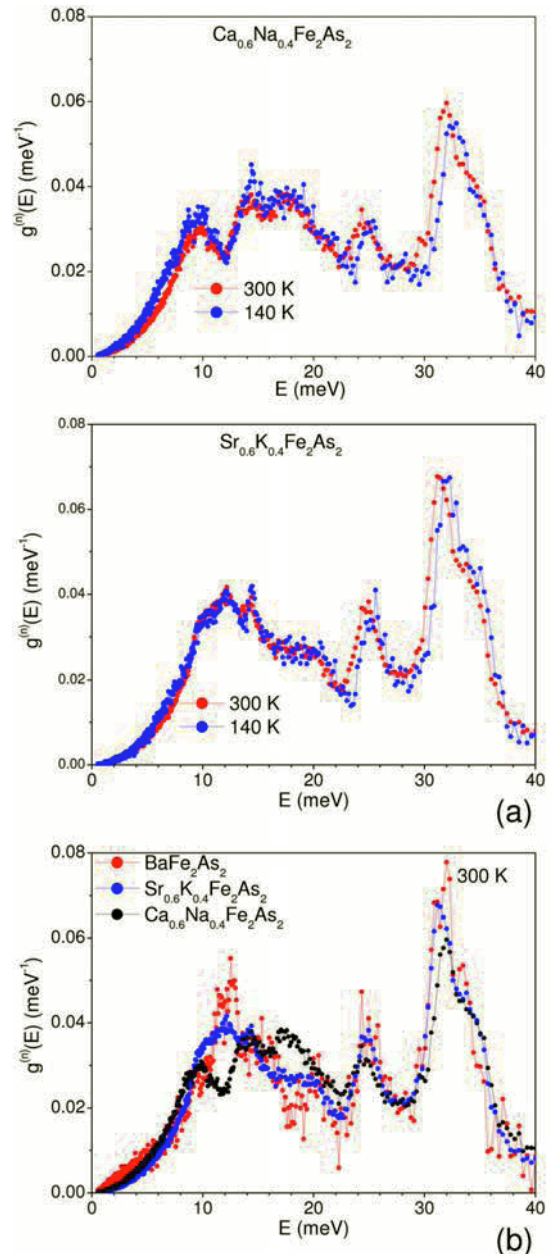
FIG. 1: (a)The experimental phonon spectra of $Sr_{0.6}K_{0.4}Fe_2As_2$ and $Ca_{0.6}Na_{0.4}Fe_2As_2$ measured with incident neutron wavelength of 5.1 Å (3.12 meV) using IN6 spectrometer at ILL. (b) Comparison of the experimental phonon spectra of $BaFe_2As_2$, $Ca_{0.6}Na_{0.4}Fe_2As_2$ and $Sr_{0.6}K_{0.4}Fe_2As_2$.
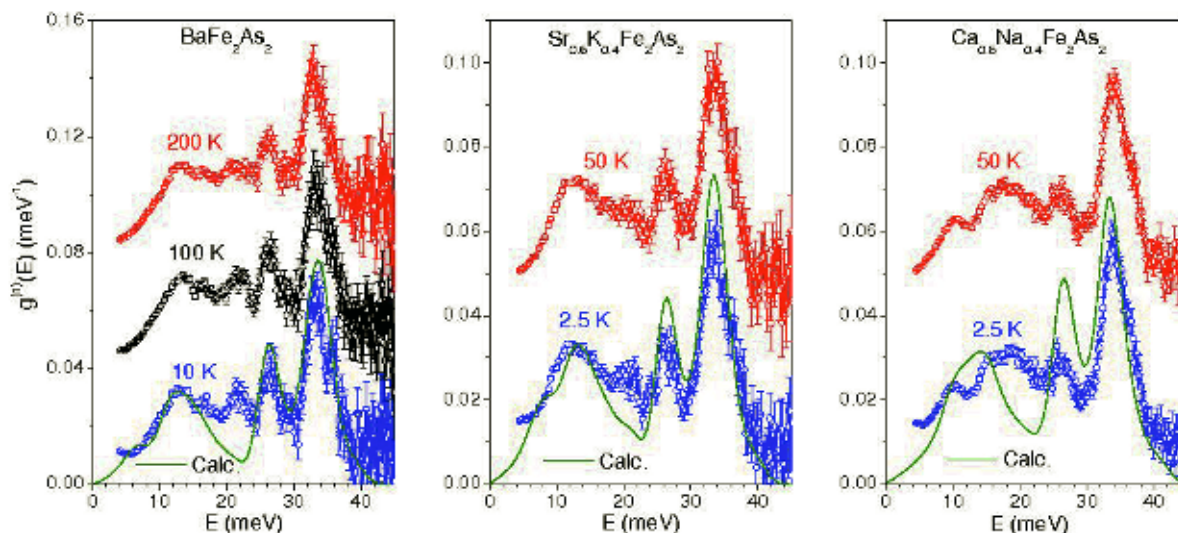
FIG. 2: *Comparison between the calculated and experimental phonon spectra of parent BaFe$_2$As$_2$ and superconducting Sr$_{0.6}$K$_{0.4}$Fe$_2$As$_2$ and Ca$_{0.6}$Na$_{0.4}$Fe$_2$As$_2$ compounds. The measurements are carried out with incident neutron wavelength of 1.18 Å (58.8 meV) using IN4C spectrometer at ILL. For better visibility the experimental phonon spectra at various temperatures are shifted along the y-axis by 0.04 meV^{-1}. The calculated spectra have been convoluted with a Gaussian of FWHM of 3 meV in order to describe the effect of energy resolution in the experiment.*

In comparison of the parent compound BaFe$_2$As$_2$, the phonon spectra of Sr$_{0.6}$K$_{0.4}$Fe$_2$As$_2$ and Ca$_{0.6}$Na$_{0.4}$Fe$_2$As$_2$ show (Fig. 1(b)) a very strong renormalization in the lower and intermediate frequency part of the vibrations. The high-frequency band reacts moderately to the doping. Mass effects and lattice contraction in the CaNa compound solely cannot explain these changes. Therefore, the type of buffer ion influences the bonding in the Fe-As layers.

The buffers thus cannot be considered a mere charge reservoir. The high resolution data collected using the IN6 spectrometer show softening of phonon modes (Fig. 1(a)) below 10 meV as we decrease the temperature from 300 K to 140 K. Softening of low energy phonons is larger for Ca compound (about 1 meV) in comparison to that in the Sr compound (about 0.5 meV). These phonon modes below 10 meV arise from the atomic vibrations of Ca/Na or Sr/K atoms. No anomalous effects are observed in the phonon spectra when passing the superconducting transition temperature. All this indicates that while electron-phonon coupling is present it cannot be solely responsible for the electron pairing.

[1] Y. Kamihara, T. Watanabe, M. Hirano and H. Hosono, J. Am. Chem. Soc. **130** (2008) 3296.

[2] M. Rotter, M. Tegel and D. Johrendt, Phys. Rev. Lett. **101** (2008) 107006.

[3] R. Mittal, Y. Su, S. Rols, T. Chatterji, S. L. Chaplot, H. Schober, M. Rotter, D. Johrendt and Th. Brueckel, Phys. Rev. B **78** (2008) 104514.

[4] R. Mittal, Y. Su, S. Rols, M. Tegel, S. L. Chaplot, H. Schober, T. Chatterji, D. Johrendt and Th. Brueckel, Phys. Rev. B **78** (2008) 224518.

65

Low energy nuclear spin excitations in Nd-based compounds

T. Chatterji[1], G. J. Schneider[2], J. Persson[3]

[1] JCNS, Forschungszentrum Jülich Outstation at Institut Laue-Langevin, B.P. 156, 38042 Grenoble Cedex, France
[2] JCNS: Jülich Centre for Neutron Science
[3] IFF-4: Scattering Methods

We investigated the low energy excitations in several Nd-based compounds in the μeV range by a back scattering neutron spectrometer. The energy spectra of these compounds revealed inelastic peaks at a few μeV at low temperatures on both energy gain and energy loss sides. The inelastic peaks move gradually towards lower energy with increasing temperature and finally merge with the elastic peak at the electronic magnetic ordering temperature T_N/T_C. We interpret the inelastic peaks to be due to the transition between hyperfine-split nuclear level of the ^{143}Nd and ^{145}Nd isotopes with spin $I = 7/2$.

The inelastic spin-flip scattering of neutrons from the nuclear spins can yield information about the hyperfine field at the nucleus of a magnetic ion [1]. The hyperfine field causes splitting of the nuclear levels by energies that are typically in the range of a few μeV. In order to investigate the nuclear excitations the neutron spectrometer therefore must have resolution at least of about $1\mu eV$ and also the incoherent scattering of the nucleus should be strong enough. Heidemann [1] worked out the double differential cross section of this scattering process. The process can be summarized as follows: If neutrons with spin $\mathbf{s}$ are scattered from nuclei with spins $\mathbf{I}$, the probability that their spins will be flipped is $2/3$. The nucleus at which the neutron is scattered with a spin-flip, changes its magnetic quantum number M to $M \pm 1$ due to the conservation of the angular momentum. If the nuclear ground state is split up into different energy levels E_M due to the hyperfine magnetic field or an electric quadrupole interaction, then the neutron spin-flip produces a change of the ground state energy $\Delta E = E_M - E_{M\pm1}$. This energy change is transferred to the scattered neutron.

The Nd has the natural abundances of 12.18% and 8.29% of ^{143}Nd and ^{145}Nd isotopes, respectively. Both of these isotopes have nuclear spin of $I = 7/2$ and their incoherent scattering cross sections [2] are relatively large, 55 ± 7 and 5 ± 5 barn for ^{143}Nd and ^{145}Nd , respectively. Therefore Nd based compounds are very much suitable for the studies of nuclear spin excitations. We did such studies on several Nd-based compounds [3, 4, 5] and found that the energy of the excitations in these compounds are approximately proportional to the ordered 4f electronic magnetic moment that is usually much reduced from

the free ion value of $3.27\mu_B$ due to the crystal-field effects.
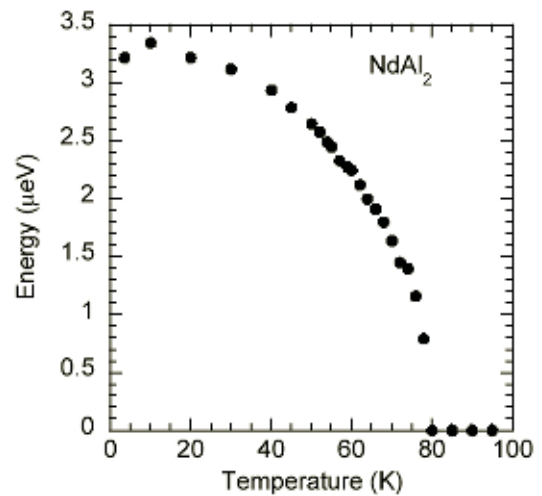
FIG. 1: Temperature variation of the energy of the inelastic peak of NdAl$_2$.

Here we describe our recent investigation of the Nd-based compound NdAl$_2$ that orders with a ferromagnetic structure at low temperatures. NdAl$_2$ belongs to the family of RAl$_2$ compounds that crystallizes with the fcc Laves phase crystal structure with the $Fd3m$ space group. The lattice constant of NdAl$_2$ at room temperature is 7.987 Å. Neutron diffraction investigations [6, 7] have established that NdAl$_2$ undergoes a ferromagnetic transition at $T_C \approx 79$ K. The ordered electronic moment of NdAl$_2$ at low temperature has been determined by neutron diffraction [6] to be $2.5 \pm 0.1\mu_B$. We performed inelastic neutron scattering experiments on a NdAl$_2$ single crystal by using the high resolution back-scattering neutron spectrometer SPHERES of the Jülich Centre for Neutron Science located at the FRMII reactor in Munich. We observed inelastic signals in NdAl$_2$ at energies $E = 3.3 \pm 0.1\mu$eV on both energy gain and loss sides at $T = 2$ K. The energy of the inelastic signal decreases continuously as the temperature is increased and finally merges with central elastic peak at $T_C \approx 79$ K.

Figure 1 shows temperature variation of the energy of inelastic signals. Figure 2 shows typical energy spectra of NdAl$_2$ at several temperatures. Figure 3
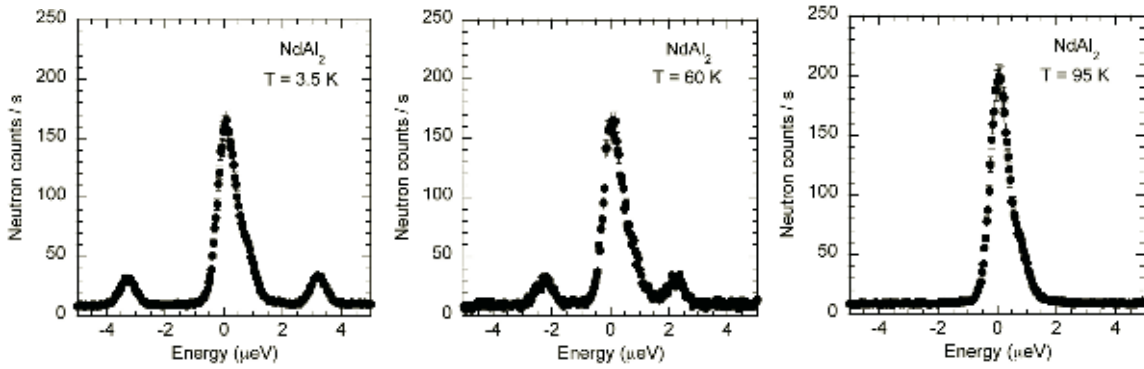
FIG. 2: Typical energy spectra of NdAl$_2$ at several temperatures.

shows a plot of energy of inelastic peaks vs. the corresponding electronic magnetic moment of Nd in several Nd-based compounds determined by the refinement of the magnetic structure using magnetic neutron diffraction intensities. The data lie approximately on a straight line showing that the hyperfine field at the nucleus is approximately proportional to the electronic magnetic moment. The slope of the linear fit of the data gives a value of $1.27\pm0.03\mu eV/\mu_B$. It is to be noted that the data for the hyperfine splitting is rather accurate whereas the magnetic moment determined by neutron diffraction have large standard deviation and are dependent on the magnetic structure model. The magnetic structures are seldom determined unambiguously and the magnetic moment determined from the refinement of a magnetic structure model is relatively uncertain. In such cases the investigation of the low energy excitations described here can be of additional help. This is specially true for the complex magnetic structures with two magnetic sublattices of which one sublattice contains Nd.
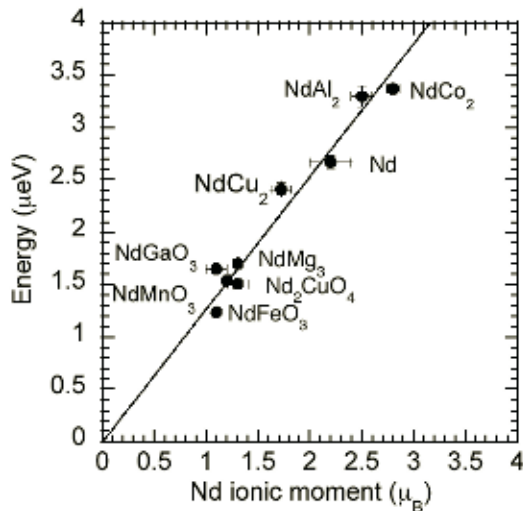
FIG. 3: Plot of energy of the inelastic signals vs. the corresponding electronic magnetic moment of Nd in several Nd-based compounds.

We interpret the inelastic signal observed in NdAl$_2$ due to the excitations of the Nd nuclear spins $I = \frac{7}{2}$ of the ^{143}Nd and also ^{145}Nd isotopes. In a first approximation one can consider these inelastic peaks to arise due to the transitions between the hyperfine-field-split nuclear levels. This is the single-nucleus effect. However the nuclear spins are coupled through Shul-Nakamura interaction [8, 9]. So one expects nuclear spin wave excitations (co-operative lattice effect) discussed by de Gennes et al. [10] according to which the nuclear spin waves should have dispersions at a very small q. Word et al. [11] discussed the possibility of measuring nuclear spin waves by inelastic neutron scattering. Also they have developed the differential scattering cross section and scattered state polarisation for the scattering of neutrons from systems described by Suhl-Nakamura Hamiltonian in the formalism of van Hove correlation function. In our experiment, due to the insufficient Q resolution of the back-scattering spectrometer, we could not measure the expected dispersion of the nuclear spin waves. The dispersion of the nuclear spin waves can perhaps be measured on single crystals at very low temperatures by a neutron spin echo (NSE) spectrometer.

[1] A. Heidemann, Z. Phys. **238**, 208 (1970).

[2] V.F. Sears in International Tables for Crystallography, Second Edition, vol. C, p. 445, ed. A.J.C. Wilson and E. Prince, Kluwer Academic Publishers (1999)

[3] T. Chatterji and B. Frick, Solid State Comm. **131**, 453 (2004).

[4] T. Chatterji, G.J. Schneider and R.M. Galera, Phys. Rev. B **78**, 012411 (2008).

[5] T. Chatterji, G.J. Schneider, L. van Eijk, B. Frick and D. Bhattacharya, J. Phys: Condens. Matter (2008).

[6] N. Nereson, C. Olsen and G. Arnold, J. Appl. Phys. **37**, 4575 (1968).

[7] J.X. Boucherle and J. Schweizer, J. Magn. Magn. Mater. **24**, 308 (1981).

[8] H. Shul, Phys. Rev. **109**, 606 (1958)

[9] T. Nakamura, Progr. Theotet.Phys. (Kyoto) **20**, 542 (1958)

[10] P.G. de Gennes et al., Phys. Rev. **129**, 1105 (1963)

[11] R. Word, A. Heidemann and D. Richter, Z. Phys. **B 28**, 23 (1977)

67

Tuning the frustration of Li_2VOSiO_4 exchange couplings with high pressure

E. Pavarini[1], M. Zema[2,3], S.C. Tarantino[3], T. Boffa Ballaran[4], P. Ghigna[3], P. Carretta[5]

[1] IFF-3: Theory of Structure Formation
[2] Dipartimento di Chimica Fisica, Università di Pavia, I-27100 Pavia, Italy
[3] Dipartimento di Scienze della Terra and CNR-IGG Sezione di Pavia, I-27100 Pavia, Italy
[4] Bayerisches Geoinstitut, Universität Bayreuth, 95440 Bayreuth, Germany
[5] Dipartimento di Fisica "A. Volta", Università di Pavia, I-27100 Pavia, Italy

We study the evolution of the electronic structure of Li_2VOSiO_4 under pressure. We obtain the crystal structure up to 7.6 GPa from x-ray diffraction measurements. We study the effects of pressure by means of first-principles calculations. We found a decrease of about 40% in the ratio J_2/J_1 between the next-nearest neighbor and nearest neighbor magnetic coupling. This suggests that one could tune the ground state of this frustrated two-dimensional antiferromagnet from collinear to disordered by applying high pressures.

68

Frustration of the exchange couplings is known to enhance the quantum fluctuations and to lead to the onset of novel disordered ground states [1]. Accordingly an intense research activity on frustrated magnets has emerged and prototype compounds have been synthesized. Particular attention has been addressed to the two-dimensional $S = 1/2$ systems, frustrated either by the spin lattice geometry, as the Kagomé lattice compounds, or by the geometry of the interactions, as the $J_1 - J_2$ model on a square lattice. The latter model has received much attention after the discovery of Li_2VOSiO_4, which is characterized by a square-lattice arrangement of $S = 1/2$ V^{4+} ions, interacting either through nearest neighbor J_1 or next-nearest neighbor J_2 antiferromagnetic exchange couplings. Li_2VOSiO_4 is characterized by $J_2/J_1 > 1$, namely, it is deeply in the part of the phase diagram characterized by a collinear ground state. Recently, other prototypes of the $J_1 - J_2$ model have been synthesized, either with positive or negative values of J_2/J_1. Despite the efforts in the chemical synthesis of novel materials none of the compounds grown so far lies in the most debated region of the phase diagran with $J_2/J_1 > 0$, the one with $J_2/J_1 \sim 0.5$, where a disordered ground state is expected. In fact, although it seems well established that for $J_2/J_1 = 0.5$ long range order should be suppressed, there is no general consensus on which should be the ground state in this region and up to which values of J_2/J_1 the disordered ground state should exist.

In order to tune the ratio between the exchange couplings one could think of adopting an approach which is alternative to the chemical one, as the application of a high pressure P. In view of the possi-

FIG. 1: Structure (top: ambient P; bottom: P=7.6 GPa) of Li_2SiOVO_4, composed of VO_5 pyramids in a tetragonal Li cage with a Si at the center. V is red, O blue, Si and Li (small) gray. A primitive cell contains two formula units, and thus two pyramids (the ridges are shown as black lines); the pyramid around the V in $(1/4, 1/4, z_V)$ (site 1, at the center) points upward and that around the V in $(-1/4, -1/4, 1 - z_V)$ (a site 2) downward. The xy Wannier function is superimposed to site 1; red (blue) is positive (negative). Increasing P, the lattice contracts and the xy orbital becomes more extended in the xy plane.

bility to apply P of several GPa by means of diamond anvil cells (DAC) one could envisage to modify the structure and tune the overlap among the atomic orbitals involved in the superexchange couplings with high P. Accordingly, in order to affect
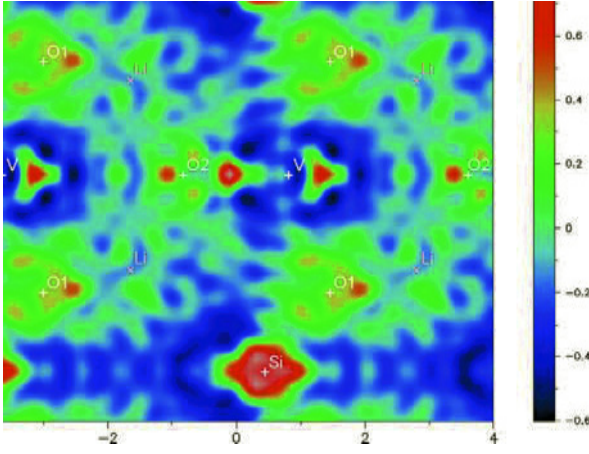
FIG. 2: *Electron density distribution for Li$_2$VOSiO$_4$ in the ac plane at $y/b = 0.25$ level, derived from the high P experiments. Relative distances in Å are reported on the axes. Li x, z coordinates are also indicated.*

P/lmn	$\frac{1}{2}\frac{1}{2}0$	100	
	t_1	t_2	J_2/J_1
0	10.0	37.0	13.7
2.4	11.2	38.4	11.9
5.8	14.0	42.2	9.1
7.6	15.0	42.5	8.0

TAB. 1: *Hopping integrals t^{lmn} (in meV) from site i to site j distant $l\mathbf{a} + m\mathbf{b} + n\mathbf{c}$ and for different applied pressures (in GPa). The ratio J_2/J_1 between the exchange couplings is given in the last column.*

the J_2/J_1 ratio and possibly approach the 0.5 region, we have applied pressures up to 7.6 GPa on Li$_2$VOSiO$_4$ single crystals and investigated the structure modifications with x-ray diffraction (XRD) measurements. Then, using density functional theory in the local-density approximation (LDA) we have calculated ab initio the corresponding variation in the hopping integrals of the partially filled V xy band. Finally, by using superexchange theory, we have estimated the pressure-induced modifications of the competing magnetic exchange couplings. This procedure has already been successfully used to estimate the exchange couplings of other prototypes of the $J_1 - J_2$ model [3].

Li$_2$VOSiO$_4$ structure (tetragonal, with space group $P4/nmm$) is formed by piling up parallel [VOSiO$_4$]$_n^{2-}$ layers containing VO$_5$ square pyramids, enclosed in a Li tetragonal cage, sharing corners with SiO$_4$ tetrahedra. Each pyramid is made of four equivalent basal oxygens (O1) and an apical oxygen (O2), and has a V at about the center ~ 1.6 Å below O2, and distant ~ 1.9 Å from the basal O1 atoms. In each layer two nearest neighbor VO$_5$ pyramids point alternatively downward (sites 1 in Fig. 1) or upward (sites 2 in Fig. 1). The V atoms in a layer form pseudo square lattices with axes $(\mathbf{a+b})/2$ and $(\mathbf{a-b})/2$, with two near neighbor V atoms (the V at site 1 and the V at site 2 in Fig. 1) displaced along $\mathbf{c}$ by $z_V\mathbf{c}$ and $1 - z_V\mathbf{c}$, respectively.

In order to analyze the effect of the structural modifications on J_2/J_1, we have determined the nearest-neighbors and next-nearest-neighbors hopping integrals from band-structure calculations. First we have obtained the LDA bands for the different structures (ambient P, $P = 2.4$, 5.8 and 7.6 GPa). As a method we have adopted the Nth-order muffin-tin orbital method. The oxygen p bands are completely filled and divided by a gap of about 1.5 eV from the narrow bandwidth $W \sim 0.4$ eV half-filled xy bands, while the remaining d states are empty. Next we downfold all degrees of freedom but the xy and construct a basis of localized xy Wannier functions which

span these bands [2]. The band-energy dispersions can be written as follows:

$$
\begin{aligned}
\varepsilon_\pm(\mathbf{k}) = & +2t_2(\cos k_a + \cos k_b) \\
& \pm 4t_1 \cos\frac{k_a}{2}\cos\frac{k_b}{2} - 2t_z \cos k_c \\
& +4t_{2z}(\cos k_a + \cos k_b)\cos k_c + \ldots
\end{aligned}
$$

where $t_1 = t^{\frac{1}{2}\frac{1}{2}0}$, $t_2 = t^{100}$, $t_z = t^{001}$, $t_{2z} = t^{101}$ and $t^{lmn} = |t_{ij}|$, where t_{ij} are the hopping integrals from site i to a site j distant $l\mathbf{a} + m\mathbf{b} + n\mathbf{c}$. The values of t_1 and t_2 are reported in Table 1 for the different structures. Both Table 1 and the Wannier function in Fig. 1 show that the basic effect of pressure is to increase the extension of the xy Wannier function in the ab plane, with a more sizeable increase of t_1, the hopping between nearest neighbors.

From our calculations $J_2/J_1 \sim 14$ at ambient P, which indicates that Li$_2$VOSiO$_4$ lies in the part of $J_1 - J_2$ model phase diagram characterized by a collinear ground state. This ground state has been confirmed by several experiments. The ratio J_2/J_1 decreases with pressure, but remains large (~ 8.0) up to 7.6 GPa.

Our XRD data indicate that the exchange couplings in Li$_2$VOSiO$_4$ are basically two-dimensional at ambient pressure. The absence of any significant orbital overlap along the $\mathbf{c}$ axis is shown by the electron density distribution in the ac plane, which we derived from the Fourier transform of the XRD pattern (Fig. 2). Up to 7.6 GPa, despite of the sizeable contraction of $\mathbf{c}$ axes, the effect on J_z seems to be minor.

In conclusion, from the analysis of the effect of the structural modifications on Li$_2$4VOSiO$_4$ exchange couplings, we show that upon increasing pressure J_2/J_1 decreases, possibly approaching the part of the phase diagram of the $J_2 - J_1$ model characterized by a disordered ground state and which is subject of an intense scientific debate [4].

[1] see H.T. Diep in *Frustrated Spin Systems* (World Scientific, Singapore, 2004).

[2] E. Pavarini, A. Yamasaki, J. Nuss and O. K. Andersen, New J. Phys. **7** 188 (2005).

[3] P. Carretta, N. Papinutto, C. B. Azzoni, M. C. Mozzati, E. Pavarini, S. Gonthier, P. Millet, Phys. Rev. B **66**, 094420 (2002).

[4] E. Pavarini, S. C. Tarantino, T. Boffa Ballaran, M. Zema, P. Ghigna, and P. Carretta, Phys. Rev. B **77**, 014425 (2008).

Kondo proximity effect: How does a metal penetrate into a mott insulator?

R. W. Helmes[1], T. A. Costi[2], A. Rosch[1]

[1] Institute for Theoretical Physics, University of Cologne, 50937 Cologne, Germany
[2] IFF-3: Theory of Structure Formation

We consider a heterostructure of a metal and a paramagnetic Mott insulator using an adaptation of dynamical mean-field theory to describe inhomogeneous systems. The metal can penetrate into the insulator via the Kondo effect. We investigate the scaling properties of the metal-insulator interface close to the critical point of the Mott insulator. At criticality, the quasiparticle weight decays as $1/x^2$ with distance x from the metal within our mean-field theory.

In the last few years, an enormous amount of interest has arisen in heterostructures fabricated out of strongly correlated materials. Driven by the prospect of new effects and devices based on correlated electron compounds, a wide range of systems has been studied experimentally and theoretically [1, 2, 3, 4, 5].

Here, we investigate the interface of a metal and a Mott insulator [6]. How does a metal penetrate into a Mott insulator? The main difference between a Mott insulator and an ordinary band insulator is the presence of magnetic degrees of freedom arising from the localized spins. While the large charge gap, of the order of the local Coulomb repulsion U, prohibits tunneling of electrons into a Mott insulator, the resonant spin flip scattering opens a new channel for tunneling via the well-known Kondo effect and allows metallic behavior to be induced within the Mott insulator. Due to this 'Kondo proximity effect' an insulating layer adjacent to the metal will also become metallic. In this manner the metal 'eats' itself layer by layer into the Mott insulator.

We study the above physics within the Hubbard model where the local interaction U jumps across the interface from $U = U_{left} \ll U_c$ to a value $U = U_{right}$ close to the critical coupling U_c of the Mott transition. The method of choice to study the Mott transition is the dynamical mean-field theory (DMFT) [7, 8]. Within DMFT, the only approximation is to neglect non-local contributions to the self-energy. This approximation can be used both for homogeneous [7, 8] and inhomogeneous [9, 10] problems.

A main challenge of DMFT is the need for reliable and efficient quantum impurity solvers. Recently [11, 12], the numerical renormalization group (NRG) method [13] was implemented as an efficient impurity solver to study the Mott transition of trapped atoms in an optical lattice. We use this approach here as the

NRG appears to be the only method presently available which can quantitatively resolve quasiparticle weights as small as 10^{-3} which are needed to describe the physics close to the Mott transition.

To investigate the junction of the metal and the Mott insulator, we consider the half-filled Hubbard model

$$\mathcal{H} = -t \sum_{\langle ij \rangle, \sigma} c_{i\sigma}^{\dagger} c_{j\sigma} + \sum_{i} U_i (n_{i\uparrow} - \tfrac{1}{2})(n_{i\downarrow} - \tfrac{1}{2}) \tag{1}$$

on a three-dimensional cubic lattice with the half band width $D = 6t$. We choose $U_i = U_{left} = D$ for $x \leq 0$ describing a metal with a sizable quasiparticle weight $Z_{metal} = 0.62$. For sites with $x \geq 1$, we use an interaction $U_i = U_{right} \sim U_c$ close to the the the critical value, $U_c \approx (2.79 \pm 0.01)D$ which separates the metallic from the insulating phase in the bulk.

The DMFT algorithm for this heterostructure is almost identical to the standard one [8]. An effective Anderson impurity problem is solved using NRG for each yz layer to obtain an x dependent self energy $\Sigma_x(\omega)$. From this one obtains the lattice Greens function

$$\hat{G}^{lat}(\epsilon_{\vec{k}_\perp}, \omega) = \left(\omega - \epsilon_{\vec{k}_\perp} - t_{xx'} - \delta_{xx'} \Sigma_x(\omega) \right)^{-1} \tag{2}$$

written as a matrix in the x coordinates where $t_{xx'} = t$ for $x' = x \pm 1$ and 0 otherwise and $\epsilon_{\vec{k}_\perp}$ is the dispersion within each layer. From $\hat{G}^{lat}$ one determines the *local* Greens function which is used [8] to derive a new effective Anderson impurity model with the Greens function $G_{imp}(x)$ for each layer using the self-consistency equation

$$G_x^{imp}(\omega) = \int d\epsilon_{\vec{k}_\perp} N_{2d}(\epsilon_{\vec{k}_\perp}) \hat{G}^{lat}(\epsilon_{\vec{k}_\perp}, \omega) \Big|_{xx}, \tag{3}$$

where $N_{2d}(\epsilon) = \sum_{\vec{k}_\perp} \delta(\epsilon - \epsilon_{\vec{k}_\perp})$ is the two-dimensional density of states of the yz layers. We use 20 metallic layers with $U = D$ and 40 layers with $U \sim U_c$ which is sufficiently large to avoid any finite size effects.

Fig. 1 shows the layer dependence of the spectral function for $U_{right} = U_c$ for $x \geq 0$ and for a low temperature $T = 1.14 \times 10^{-5} D$. All layers with $U = U_c$ show pronounced Hubbard bands. The width of the sharp quasiparticle peak, which describes the penetration
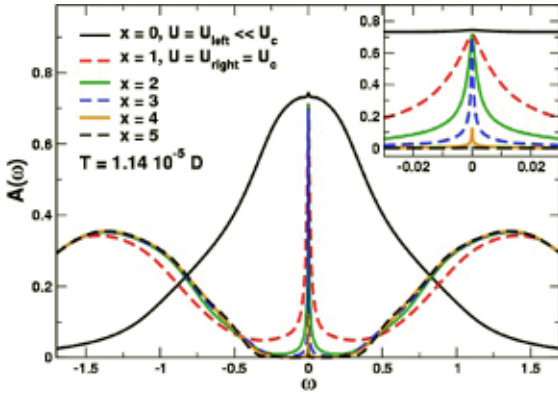
FIG. 1: Layer dependence of local spectral function close to the interface $x = 0$ for $U_{right} = U_c$ and $T = 1.14 \times 10^{-5} D$. Inset: $A(\omega)$ near $\omega = 0$.

FIG. 2: Quasiparticle weight Z for an inhomogeneous layered system describing a 'good' metal ($U = U_{left} = D$ for $x < 1$) in contact with a 'bad' metal ($U_{right} \lesssim U_c = (2.79 \pm 0.01)D$ for $x \geq 1$). Inset: Quasiparticle weight for a heterostructure of a good metal and a Mott insulator ($U_{right} \gtrsim U_c$). In both cases, Z drops as $1/x^2$ for $x < \xi$.

of the metal into the quantum critical Mott state, decays rapidly. The quasiparticle peak collapses completely from the 5th layer on, when the Kondo temperature of the corresponding impurity model becomes much smaller than T.

For a quantitative analysis of how the metal penetrates into the Mott insulator we investigate a heterostructure consisting of a 'good metal', $U_{left} = D$ and a 'bad metal', $U_{right} \lesssim U_c$ at $T = 0$. For $T = 0$ the quasiparticle weight Z_x of layer x can be obtained from $Z_x = (1 - \partial_\omega \mathrm{Re}\Sigma_x(\omega))^{-1}$. Fig. 2 shows Z_x as a function of the distance x from the interface. Close to the critical point one finds the scaling behavior

$$Z_x \approx \frac{0.008 \pm 0.002}{x^{1/\nu}} f\left[x \left(\frac{U_c - U_{right}}{U_c} \right)^\nu \right] \quad (4)$$

with $\nu = 1/2$ where $f[u]$ is an universal scaling function with $f[0] = 1$ and $f[u \to \infty] \approx (0.150 \pm 0.005)u^2$ for $U_{right} \lesssim U_c$. The observation that DMFT is characterized by the usual mean-field exponent $\nu = 1/2$ and the $1/x^2$ decay of the correlation function in the quantum critical regime is one of the main results of this paper. Defining the correlation length ξ by $f[u] = 2$, we obtain

$$\xi \approx 0.3 \left(\frac{U_c}{U_c - U_{right}} \right)^{1/2}. \quad (5)$$

In the Mott insulating phase at $T = 0$, $U_{right} \gtrsim U_c$, the quasiparticle weight drops rapidly, see inset of Fig. 2. In the quantum-critical regime, i.e. for $x < \xi$, the quasiparticle weight decays as $1/x^2$ with the same prefactor as in Eq. (4). For $x > \xi$, however, Z drops exponentially but remains always finite.

In summary, we have studied how a metallic state penetrates into a paramagnetic Mott insulator (or a bad metal) [6]. Using a scaling analysis close to the quantum critical point we have determined within DMFT the critical exponents and the asymptotic behavior of the quasiparticle weight close to and far away from the interface.

The main physical mechanism governing the interface of a metal and a Mott insulator is the Kondo effect: the localized spins of the Mott insulator are

screened when they are brought into contact with the metal and become therefore part of the metal. Our numerical results show that this mechanism is *not* very effective: Even for $U_{right} = U_c$, the quasiparticle weight is only of size $0.008/x^2$. Also the correlation length is extremely short: to obtain a correlation length of 10 lattice spacings, one has to approach the critical point with a precision of 10^{-4}. Our results imply that the Mott insulator is de facto impenetrable to the metal: nevertheless metallization by the 'Kondo proximity effect' may be relevant for controlling conductivity of very thin films of Mott insulators sandwiched between metals.

[1] A. Ohtomo *et al.*, Nature **419**, 378 (2002).

[2] S. Thiel, et al., Science **313**, 1942 (2006).

[3] S. Okamoto and A. J. Millis, Nature **428**, 630 (2004).

[4] W.-C. Lee and A. H. MacDonald, Phys. Rev. B **74**, 075106 (2006).

[5] S. S. Kancharla and E. Dagotto, Phys. Rev. B **74**, 195427 (2006).

[6] R. W. Helmes, T. A. Costi, and A. Rosch, Phys. Rev. Lett. **101**, 066802 (2008).

[7] W. Metzner and D. Vollhardt, Phys. Rev. Lett. **62**, 324 (1989).

[8] A. Georges, et al. Rev. Mod. Phys. **68**, 13 (1996).

[9] V. Dobrosavljević and G. Kotliar, Phys. Rev. Lett. **78**, 3943 (1997).

[10] M. Potthoff and W. Nolting, Phys. Rev. B **59**, 2549 (1999).

[11] R. W. Helmes, T. A. Costi, and A. Rosch, Phys. Rev. Lett. **100**, 056403 (2008).

[12] M. Snoek *et al.*, New J. Phys. **10**, 093008 (2008).

[13] R. Bulla, T. A. Costi, and D. Vollhardt, Phys. Rev. B **64**, 045103 (2001); R. Bulla, T. A. Costi, and T. Pruschke, Rev. Mod. Phys. **80**, 395 (2008).

On the mechanism for orbital-ordering in KCuF$_3$

E. Koch[1,3], E. Pavarini[2,3], A.I. Lichtenstein[4]

[1] IFF-1: Quantum Theory of Materials
[2] IFF-3: Theory of Structure Formation
[3] IAS: Institute for Advanced Simulation
[4] Institute of Theoretical Physics, University of Hamburg

The Mott insulating perovskite KCuF$_3$ is considered the archetype of an orbitally-ordered system. By using the LDA+dynamical mean-field theory (DMFT) method, we investigate the mechanism for orbital-ordering (OO) in this material. We show that the purely electronic Kugel-Khomskii super-exchange mechanism (KK) alone leads to a remarkably large transition temperature of $T_{KK} \sim 350$ K. However, orbital-order is experimentally believed to persist to at least 800 K. Thus Jahn-Teller distortions are essential for stabilizing orbital-order at such high temperatures [1].

72

In a seminal work [2] Kugel and Khomskii showed that in strongly correlated systems with orbital degrees of freedom many-body effects could give rise to orbital-order (OO) via a purely electronic super-exchange mechanism. Orbital-ordering phenomena are now believed to play a crucial role in determining the electronic and magnetic properties of many transition-metal oxide Mott insulators. While it is clear that Coulomb repulsion is a key ingredient, it remains uncertain whether it just enhances the effects of lattice distortions [3] or really drives orbital-order via superexchange.

We analyze these two scenarios for the archetype of an orbitally-ordered material, KCuF$_3$. In this $3d^9$ perovskite the Cu d-levels are split into completely filled three-fold degenerate t_{2g}-levels and two-fold degenerate e_g-levels, occupied by one hole. In the first scenario Jahn-Teller elongations of some Cu-F bonds split the partially occupied e_g-levels further into two non-degenerate crystal-field orbitals. The Coulomb repulsion, U, then suppresses quantum orbital fluctuations favoring the occupation of the lower energy state, as it happens in some t_{2g}-perovskites [4]. In this picture the ordering is caused by electron-phonon coupling; Coulomb repulsion just enhances the orbital polarization due to the crystal-field splitting. In the second scenario the purely electronic super-exchange mechanism, arising from the e_g-degeneracy, drives orbital-ordering, and Jahn-Teller distortions are merely a secondary effect. In this picture electron-phonon coupling is of minor importance.

The key role of Coulomb repulsion is evident from static mean-field LDA+U calculations, which show
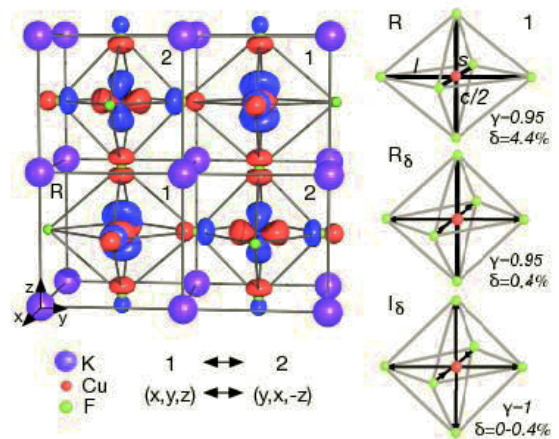
FIG. 1: (Color online) Left: Crystal structure and orbital-order in a-type KCuF$_3$. Cu is at the center of F octhaedra enclosed in a K cage. The conventional cell is tetragonal with axes $\mathbf{a}$, $\mathbf{b}$, $\mathbf{c}$, where $a = b$, $c = 0.95\, a\sqrt{2}$. The pseudo-cubic axes are defined as $\mathbf{x} = (\mathbf{a} + \mathbf{b})/2$, $\mathbf{y} = (-\mathbf{a} + \mathbf{b})/2$, and $\mathbf{z} = \mathbf{c}/2$. All Cu sites are equivalent. For sites 1 the long (short) bond l (s) is along $\mathbf{y}$ ($\mathbf{x}$). Vice versa for sites 2. Orbital $|2\rangle$, occupied by one hole, is shown for each site. Right: Jahn-Teller distortions at sites 1, measured by $\delta = (l - s)/(l + s)/2$ and $\gamma = c/a\sqrt{2}$. R is the experimental structure, R_δ and I_δ two ideal structures with reduced distortions, and I_0 is cubic.

that in KCuF$_3$ the distortions of the octahedra are stable with a energy gain $\Delta E \sim 150\text{-}200$ meV per formula unit, at least an order of magnitude larger than in LDA and GGA; recent GGA+DMFT calculations yield very similar results, suggesting in addition that dynamical fluctuations play a small role in determining the stable crystal structure of this system. However, these results might merely indicate that the electron-phonon coupling is underestimated in LDA or GGA, probably due to self-interaction, rather than identifying Kugel-Khomskii super-exchange as the driving mechanism for orbital-order. This is supported by ab-initio Hartree-Fock (HF) calculations which give results akin to LDA+U. Moreover, in the superexchange scenario it remains to be explained why $T_{OO} \sim 800$ K, more than twenty times the 3D antiferromagnetic (AFM) critical temperature, $T_N \sim 38$ K, a surprising fact if magnetic- and orbital-order were driven by the same super-

exchange mechanism.

In this Letter we study the Kugel-Khomskii mechanism at finite temperature and identify the origin of orbital-ordering in KCuF$_3$. We will show that super-exchange alone leads to orbital-order with $T_{KK} \sim 350$ K, less than half the experimental value. Thus Jahn-Teller distortions are essential for driving orbital-order above 350 K.

KCuF$_3$ is a tetragonal perovskite made of Jahn-Teller distorted CuF$_6$ octahedra enclosed in an almost cubic K cage. The Jahn-Teller distortion amounts to a 3.1% elongation/shortening of the CuF distances in the xy-plane. The tetragonal distortion reduces the CuF bond along $\mathbf{z}$ by 2.5%, leaving it of intermediate length. The long (l) and short (s) bond alternate between $\mathbf{x}$ and $\mathbf{y}$ along all three cubic axes (a-type pattern). At each site one hole occupies the highest e_g-orbital, $\sim |s^2 - z^2\rangle$, i.e., the occupied orbitals ($\sim |x^2 - z^2\rangle$ or $\sim |y^2 - z^2\rangle$) alternate in all directions. This ordering and the crystal structure are shown in Fig. 1. As a method for studying the electronic structure of KCuF$_3$ and the super-exchange mechanism we adopt the LDA+DMFT approach.

In the paramagnetic phase, single-site DMFT calculations yield a Mott gap of about 2.5 eV for $U = 7$ eV, and 4.5 eV for $U = 9$ eV. The system is orbitally ordered, and the OO is a-type as the distortion pattern; static mean-field (LDA+U, HF) calculation give similar orbital-order, however also antiferromagnetism. We define the orbital polarization p as the difference in occupation between the most and least occupied natural orbital (diagonalizing the e_g density-matrix). It turns out that to a good approximation p is given by the difference in occupation between the highest ($|2\rangle$) and the the lowest ($|1\rangle$) energy crystal-field orbital. In Fig. 2 we show p as a function of temperature. We find that the polarization is saturated ($p \sim 1$) even for temperatures as high as 1500 K. We obtain very similar results in two-site CDMFT calculations.

To understand whether this orbital-order is driven by the exchange coupling or merely is a consequence of the crystal-field splitting, we consider hypothetical lattices with reduced deformations, measured by $\gamma = c/\sqrt{2}a$ (tetragonal distortion) and $\delta = (l-s)/(l+s)/2$ (Jahn-Teller deformation). To keep the volume of the unit cell at the experimental value, we renormalize all lattice vectors by $(\gamma/0.95)^{-1/3}$. We calculate the Hamiltonian for a number of structures reducing the distortion of the real crystal with $\gamma = 0.95$ and $\delta = 4.4\%$ to the ideal cubic structure $\gamma = 1$ and $\delta = 0$. We use the notation R_δ for structures with the real tetragonal distortion $\gamma = 0.95$ and I_δ for ideal ($\gamma = 1$) structures. The distortions affect the hopping integrals, both along (001) and in the xy-plane. The main effect is, however, the crystal-field splitting $\Delta_{2,1}$ which decreases almost linearly with decreasing distortion, as expected for a Jahn-Teller system. For each structure we obtain the Hamiltonian H^{LDA} for the e_g-bands and perform LDA+DMFT calculations for decreasing temperatures. At the lowest temperatures we find a-type OO with full orbital polarization for all structures (see Fig. 2). At 800 K, the situa-
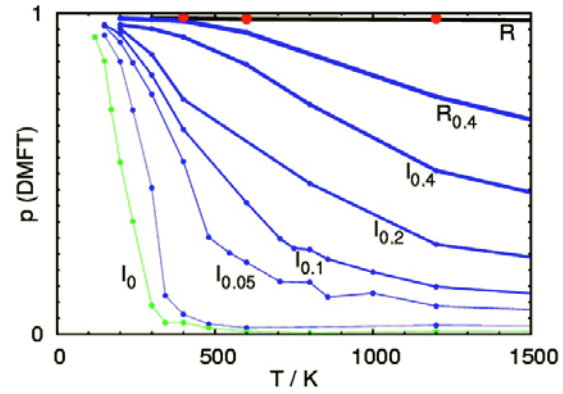
FIG. 2: (Color online) Orbital polarization p as a function of temperature calculated with LDA+DMFT (black, blue, green). Black: $U = 7$ eV, experimental structure. Blue: $U = 7$ eV, idealized structures R_δ and I_δ (see Fig. 1) with decreasing crystal-field. Green: $U = 9$ eV, I_0 only. Red: cluster DMFT for the experimental structure and $U = 7$ eV.

tion is qualitatively different. Orbital polarization remains saturated when reducing δ from 4.4% to 1%. For smaller distortions, however, p rapidly goes to zero: For $\delta = 0.2\%$ and $\gamma = 1$, p is already reduced to ~ 0.5, and becomes negligible in the cubic limit. Thus super-exchange alone is not sufficiently strong to drive orbital-ordering at $T \gtrsim 800$ K.

From the temperature dependence of the orbital polarization we can determine the transition temperature T_{KK} at which the Kugel-Khomskii superexchange mechanism would drive orbital-ordering, and thus disentangle the superexchange from the electron-phonon coupling. For this we study the ideal cubic structure, introducing a negligible (1 meV) crystal-field splitting as an external-field to break the symmetry. We find a phase transition to an orbitally-ordered state at $T_{KK} \sim 350$ K. The hole orbitals at two neighboring sites are $\sim |y^2 - z^2\rangle$ and $\sim |x^2 - z^2\rangle$, in agreement with the original prediction of Kugel and Khomskii. This critical temperature is sizable, but significantly smaller than $T_{OO} \sim 800$ K.

This indicates that in KCuF$_3$ the driving mechanism for orbital-ordering is not pure superexchange.

[1] E. Pavarini, E. Koch, and A.I. Lichtenstein, Phys. Rev. Lett. **101**, 266405 (2008).

[2] K. I. Kugel and D. I. Khomskii, Sov. Phys.-JETP **37**, 725 (1973).

[3] B. Halperin and R. Englman, Phys. Rev. B **3**, 1698 (1971).

[4] E. Pavarini et al., Phys. Rev. Lett. **92**, 176403 (2004); E. Pavarini, A. Yamasaki, J. Nuss and O.K. Andersen, New J. Phys. **7** 188 (2005).

73

Mott phase of repulsively interacting fermions in a 3D optical lattice

U. Schneider[1], L. Hackermüller[1], S. Will[1], Th. Best[1], I. Bloch[1], T. A. Costi[2], R. W. Helmes[3], D. Rasch[3], A. Rosch[3]

[1] Institute of Physics, Johannes Gutenberg-University, 55099 Mainz, Germany
[2] IFF-3: Theory of Structure Formation
[3] Institute for Theoretical Physics, University of Cologne, 50937 Cologne, Germany

The fermionic Hubbard model plays a fundamental role in the description of strongly correlated materials. We have realized this Hamiltonian using a repulsively interacting spin mixture of ultracold ^{40}K atoms in a 3D optical lattice. Direct measurement of the compressibility of the quantum gas in the optical lattice and comparison with ab initio dynamical mean field theory calculations demonstrates the emergence of an incompressible Mott insulating phase for strong interactions.

Interacting fermions in periodic potentials lie at the heart of modern condensed matter physics, presenting some of the most challenging problems to quantum many-body theory. A prominent example is high-T_c superconductivity in cuprate compounds [1] and the recently discovered iron-arsenic alloys [2]. In order to capture the essential physics of such systems, the fermionic Hubbard Hamiltonian [3] has been introduced as a fundamental model describing interacting electrons in a periodic potential [1]. In a real solid, however, the effects of interest are typically complicated by e.g. multiple bands and orbital degrees of freedom, impurities and the long-range nature of Coulomb interactions which becomes especially relevant close to a metal to insulator transition. It is therefore crucial to probe this fundamental model Hamiltonian in a controllable and clean experimental setting. Ultracold atoms in optical lattices provide such a defect-free system [4, 5], in which the relevant parameters can be independently controlled, allowing quantitative comparisons of the experiment with modern quantum many-body theories.

In this work [6], we directly probe the compressibility of the many-body system by monitoring the in-trap density distribution of the fermionic atoms for increasing harmonic confinements. This allows us to distinguish compressible metallic phases from globally incompressible states and reveals the strong influence of interactions on the density distribution. For repulsive interactions, we find the cloud size to be significantly larger than in the non-interacting case, indicating the resistance of the system to compression. For strong repulsion, the system evolves from a metallic state into a Mott insulating state and eventually a band insulator as the compression increases.

The experimentally results are compared to numerical calculations using Dynamical Mean Field Theory (DMFT) [7, 8, 9, 10]. DMFT is a central method of solid state theory and is widely used to obtain ab-initio descriptions of strongly correlated materials [8]. This comparison of DMFT predictions with experiments on ultracold fermions in optical lattices constitutes the first parameter-free experimental test of the validity of DMFT in a three-dimensional system.

Restricting to the lowest energy band of a simple cubic 3D optical lattice, the fermionic quantum gas mixture can be modeled via the Hubbard-Hamiltonian [3] together with an additional term describing the potential energy due to the underlying harmonic potential:

$$\hat{H} = -J \sum_{\langle i,j \rangle, \sigma} \hat{c}_{i,\sigma}^{\dagger} \hat{c}_{j,\sigma} + U \sum_i \hat{n}_{i,\downarrow} \hat{n}_{i,\uparrow}$$
$$+ V_t \sum_i (i_x^2 + i_y^2 + \gamma^2 i_z^2)(\hat{n}_{i,\downarrow} + \hat{n}_{i,\uparrow}).$$

Here, $i = (i_x, i_y, i_z)$, denote lattice sites, $\sigma \in \{\downarrow, \uparrow\}$ the two different spin states, J the tunneling matrix element and U the effective on-site interaction. The strength of the harmonic confinement V_t is conveniently parameterized by $E_t = V_t (\gamma N_\sigma / (4\pi/3))^{2/3}$ with N_σ the number of atoms of spin σ and γ the aspect ratio of the trap.

The experiments used an equal mixture of fermionic ^{40}K atoms in the two hyperfine states $|F, m_F\rangle = |\frac{9}{2}, -\frac{9}{2}\rangle \equiv \downarrow$ and $|\frac{9}{2}, -\frac{7}{2}\rangle \equiv \uparrow$. Using evaporative cooling, we reach temperatures of $T/T_F = 0.15(3)$ with $1.5 - 2.5 \times 10^5$ potassium atoms. A Feshbach resonance located at 202.1 G [11] is used to tune the scattering length between the two spin states and thereby control the on-site interaction U.

An in-situ image of the cloud is subsequently taken along the short axis of the trap using phase-contrast imaging [12]. As the latter is non-destructive, it allows us to also measure the quasi-momentum distribution of the atoms in the same experimental run using a band-mapping technique [13, 14, 15].

All experimental data are compared to numerical calculations, in which the DMFT equations are solved for a wide range of temperatures and chemical potentials using a numerical renormalization group approach [16, 17]. As shown in [18, 9], the trapped system can be approximated to very high accuracy by the uniform system through a local density approximation (LDA) even close to the boundary between metal and insulator.
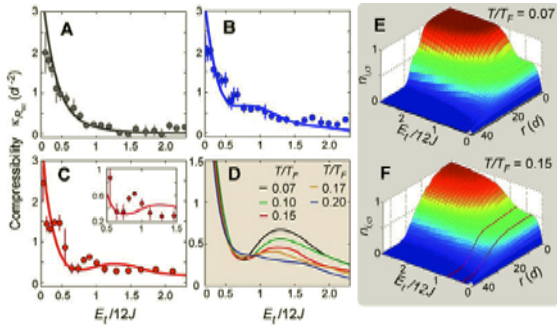
FIG. 1: *Compressibility and in-trap density distribution. (**A-C**) Global compressibility $\kappa_{R_{sc}}$ of the atom cloud for various interactions. Dots denote the result of linear fits on the measured data with the error bars being the fit uncertainty for three interaction strengths ((**A**) $U/12J = 0$, (**B**) $U/12J = 1$, (**C**) $U/12J = 1.5$) Solid lines display the theoretically expected results for an initial temperature of $T/T_F = 0.15$. The influence of the initial temperature on the calculated compressibility is shown in **D** for $U/12J = 1.5$. The corresponding density distributions are plotted in **E, F** with r denoting the distance to the trap center. The red lines mark the region where a Mott-insulating core has formed in the center of the trap and the global compressibility is reduced.*

The global compressibility $\kappa_{R_{sc}} = -\frac{1}{R_{sc}^3}\frac{\partial R_{sc}}{\partial(E_t/12J)}$ (see Fig. 1) of the system is extracted from the measurements by using linear fits to four consecutive data points to determine the derivative. For stronger confinements the compressibility approaches zero (Fig. 1A), as almost all atoms are in the band insulating regime while the surrounding metallic shell becomes negligible.

The green, blue and red dots in Fig. 1 represent the compressibility of repulsively interacting clouds with $U/12J = 0.5, 1$ and 1.5 in comparison with the DMFT calculations (lines). For strong repulsive interactions ($U/12J = 1.5$) we find the onset of a region ($0.5 < E_t/12J < 0.7$), denoting a very small compressibility, whereas for stronger confinements the compressibility increases again. This is consistent with the formation of an incompressible Mott-insulating core with half filling in the center of the trap, surrounded by a compressible metallic shell, as can be seen in the corresponding in-trap density profiles (see Fig. 1E, F). For higher confinements an additional metallic core ($1/2 < n_{i,\sigma} < 1$) starts to form in the center of the trap. A local minimum in the global compressibility is in fact a genuine characteristic of a Mott-insulator and for large U and low temperature, we expect the global compressibility in the middle of the Mott region to vanish as $1/U^2$. The experimental data, indeed, show an indication of this behavior (see Fig. 1 C) for increasing interactions. For $E_t/12J \simeq 0.5$ a minimum in the compressibility is observed, followed by an increase of the compressibility around $E_t/12J \simeq 0.8$, slightly earlier than predicted by theory.

In conclusion, we have investigated a spin mixture of repulsively interacting fermionic atoms in a 3D optical lattice[6]. Using a novel measurement technique,

we have been able to directly determine the global compressibility of the many-body quantum system and have explored the different regimes of the interacting mixture from a Fermi liquid to a Mott and band insulating state upon increasing harmonic confinements and increasing interactions. Our measurements are in good agreement with the results predicted by DMFT for interaction strengths up to $U/12J = 1.5$ and initial temperatures of the mixture of $T/T_F = 0.15$.

Our measurements are an important first step in the direction of analyzing fermionic many-body systems with repulsive interactions in a lattice. For initial entropies lower than $S/N \lesssim k_B \ln 2$, one expects the system to enter an antiferromagnetically ordered phase. This would open the path to the investigation of quantum magnetism with ultracold atoms, being an encouraging starting point to ultimately determine the low-temperature phase diagram of the Hubbard model, including the search for a d-wave superconducting phase that is believed to emerge from within the two-dimensional Hubbard model.

[1] P. Lee, N. Nagaosa, X.-G. Wen, Rev. Mod. Phys. **78**, 17 (2006).

[2] Y. Kamihara, et al., J. Am. Chem. Soc. **130**, 3296 (2008).

[3] J. Hubbard, Proc. R. Soc. Lond. A **276**, 238 (1963).

[4] D. Jaksch, P. Zoller, Ann. Phys. (N.Y.) **315**, 52 (2005).

[5] I. Bloch, J. Dalibard, W. Zwerger, Rev. Mod. Phys. **80**, 885 (2008).

[6] U. Schneider, L. Hackermüller, S. Will, Th. Best, I. Bloch, T. A. Costi, R. W. Helmes, D. Rasch, A. Rosch, Science **322**, 1520 (2008).

[7] A. Georges, et al., Rev. Mod. Phys. **68**, 13 (1996).

[8] G. Kotliar, D. Vollhardt, Phys. Today **57**, 53 (2004).

[9] R. W. Helmes, T. A. Costi, A. Rosch, Phys. Rev. Lett. **100**, 056403 (2008).

[10] L. DeLeo, et al., Phys. Rev. Lett. **101**, 210403 (2008).

[11] C. A. Regal, et al., Nature **424**, 47 (2003).

[12] M. R. Andrews, et al., Science **273**, 84 (1996).

[13] A. Kastberg, et al., Phys. Rev. Lett. **74**, 1542 (1995).

[14] M. Greiner, et al., Phys. Rev. Lett. **87**, 160405 (2001).

[15] M. Köhl, et al., Phys. Rev. Lett. **94**, 080403 (2005).

[16] R. Bulla, T. A. Costi, D. Vollhardt, Phys. Rev. B **64**, 045103 (2001).

[17] R. Bulla, T. A. Costi, T. Pruschke, Rev. Mod. Phys. **80**, 395 (2008).

[18] R. W. Helmes, T. A. Costi, A. Rosch, Phys. Rev. Lett. **101**, 066802 (2008).

[19] F. Werner, et al., Phys. Rev. Lett. **95**, 056401 (2005).

[20] K. Winkler, et al., Nature **441**, 853 (2006).

[21] F. Gerbier, Phys. Rev. Lett. **99**, 120405 (2007).

Nanoscale phase transitions in phase change materials: What's new?

R. O. Jones[1], J. Akola[1,2]

[1] IFF-1: Quantum Theory of Materials
[2] Nanoscience Center, University of Jyväskylä, Finland

Phase change (PC) materials are the leading candidates for the next generation of computer random access memory (RAM) and rewritable storage devices. The past year has emphasized this, when the Blu-ray Disc (BD) became the de facto standard as the successor to the digital versatile disk (DVD). The recording medium of all BD products comprise PC materials. A write/erase cycle involves the switching between amorphous and ordered states when an electric current or laser pulse is applied, and the state can be determined by monitoring the optical or electrical properties. It is astonishing that materials based on *structural* phase changes now support a mature industry, while at the same time only sketchy information is available about the *structures* involved. We have used the BlueGene/L and BlueGene/P supercomputers to extend our simulations of the amorphous and ordered states of a range of alloys used in PC memory and storage materials. There have been some unexpected and exciting results.

The demands placed by computers and other electronic devices on the density, speed, and stability increase without any sign of saturation. Phase change (PC) materials are familiar to us all as rewritable media (CD-RW, DVD-RW, DVD-RAM), but 2008 brought the announcement that Blu-ray Disc (BD) was the only survivor of the battle to succeed the DVD. The BD standard focuses mainly on the aperture and wavelength (405 nm) of the laser, but the recording materials in use are all of the PC variety and often alloys of Ge, Sb, and Te. The basis of their function is the rapid and reversible transition between the crystalline and amorphous forms of nanoscale bits ($\lesssim$ 100 nm), which arise from quenching after a localized and short ($\sim$ 1 ns) laser annealing to a temperature above the melting point. Longer laser heating ($\sim$ 50 ns) to a temperature above the glass transition temperature but below the melting point leads to a metastable crystalline form. The diameters of the amorphous marks ("bits") currently possible yield storage densities far in excess of those found in current magnetic memory devices.

Many of the materials of choice for PC storage and memory materials [1] can be seen in Fig. 1. GeTe was the first system to show (1986) real promise as a PC material, and alloys along the tie-line between GeTe and Sb_2Te_3 are in widespread use today. $Ge_2Sb_2Te_5$ (GST), in particular, is used in DVD-RAM and is viewed as the prototype PC memory material. Prominent alloys used in BD applications also belong to this family, an example being $Ge_8Sb_2Te_{11}$.
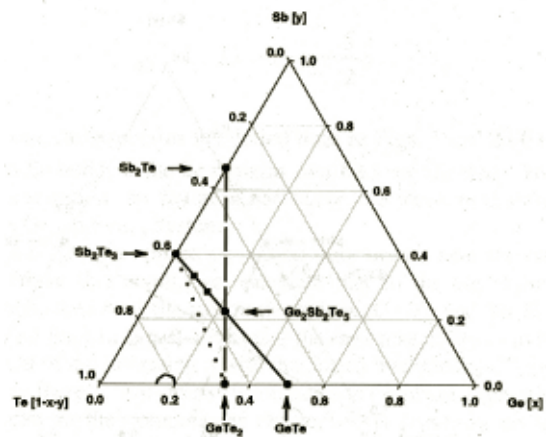
FIG. 1: *Alloy diagram for $Ge_xSb_yTe_{1-x-y}$.*

To understand the properties of these materials it is essential to know the atomic arrangement ("structure") in the phases involved, but these are difficult to measure or calculate in ternary alloys with a significant number of vacancies. The analysis of experiments often requires wide-ranging assumptions about the atomic arrangements, an example being the widespread use of reverse Monte Carlo methods to find structural information from measured x-ray and neutron scattering experiments. Several calculations have been performed in recent years, but the unit cells (with $\sim$ 60 atoms) are usually too small to describe structural details, and the simulation times (typically a few picoseconds) are too short to describe vibrational and other thermodynamic properties reliably. There are also several "models" of the structural phase changes that have survived stubbornly in the literature regardless of new developments. As we mentioned last year, we have used the Blue Gene supercomputers in Jülich to extend greatly

the range of density functional (DF) calculations on these and related materials. We have performed simulations with hundreds of atoms in the unit cell over several hundred picoseconds, beginning with a high temperature liquid in order to avoid bias towards particular structural types. In addition to the liquid and amorphous materials (at 900 K and 300 K, respectively), we have simulated rock-salt (ordered) structures of GST and states of the prototype PC material $Ge_{0.50}Te_{50}$. Full details are provided in Ref. [2].

These simulations allow us to follow the motion of all atoms throughout. Amorphous GST shows long-range ordering (at least to 10 Å) of Te atoms and a high degree of AB alternation (A: Ge, Sb; B: Te). This is also true in the case of GeTe [2], which is much less attractive than GST for these purposes. More recently we have studied the eutectic alloy $Ge_{0.15}Te_{0.85}$, i.e. the binary Ge/Te alloy with the lowest melting point (650 K) [3]. There is no Te segregation at the eutectic composition, where the material resembles neither GeTe nor Te.

The alloy $Ge_8Sb_2Te_{11}$ is used by some manufacturers as the recording medium in Blu-ray Disc applications. The choice of alloys on the pseudobinary line GeTe-Sb_2Te_3 requires compromise: near the GeTe end there is good contrast between the optical properties of the amorphous and ordered phases, but the crystallization process is too slow. At the other (Sb_2Te_3) end the reverse is true: short crystallization times, but poor optical contrast. $Ge_2Sb_2Te_5$ was viewed as a satisfactory compromise, but alloys nearer to GeTe appear to be even better. We have performed a simulation of $Ge_8Sb_2Te_{11}$ (the ratio of GeTe to Sb_2Te_3 is 8:1) with 630 atoms in the unit cell over 400 picoseconds. [4] A comparison of the results (structure, valence density of states, ...) with those for GeTe and $Ge_2Sb_2Te_5$ showed remarkable similarities to the latter, although GeTe is much closer on the plot of Fig. 1. It appears that GeTe is a singular case (this is also evident in the structures of the crystalline phases), and that *other* members of this pseudobinary family have much more in common.

Optical storage media are not limited to these pseudobinary alloys. Alloys of Sb and Te with compositions near the eutectic ($Sb_{70}Te_{30}$) are used for CD-RW and DVD-RW applications, usually with small amounts of Ag and In present. The crystallization of amorphous marks in a thin film proceeds by growth from the edge (rather than nucleation, as in the GST alloys), and this leads to some advantages. We have simulated a common composition of this alloy as well [5], and we shall present the results in next year's Report. These are among the most extensive such simulations that we have performed to date (640 atoms in the unit cell, more than 200 ps).
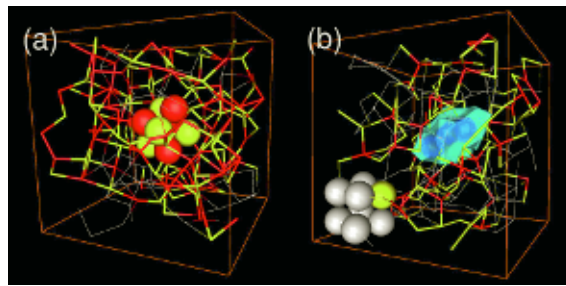
FIG. 2: (a) Simulation box of a-GeTe (18.6 Å, 216 atoms) with $ABAB$ squares highlighted. An $ABAB$ cube is also shown. Red: Ge, yellow: Te. (b) Simulation box of $Ge_{0.15}Te_{0.85}$ (19.7 Å, 216 atoms) with Ge and Ge-coordinating Te atoms highlighted. A multivacancy and a cubic Te subunit are shown.

This continues to be an exciting area in which to work. Do look at the references for more details, and we expect you to return again next year for the latest developments! Better still, why not contact us for more information in person or by e-mail?

[1] M. Wuttig and N. Yamada, Nature Mater. **6**, 824 (2007) provide a review of the history of these materials.

[2] J. Akola and R. O. Jones, Phys. Rev. B **76**, 235201 (2007); J. Phys.: Condens. Matter **20**, 465103 (2008).

[3] J. Akola and R. O. Jones, Phys. Rev. Lett. **100**, 205502 (2008).

[4] J. Akola and R. O. Jones, submitted.

[5] J. Akola and R. O. Jones, submitted.

77

Multisite Coulomb correlations: cluster dynamical mean field theory

A. Liebsch[1], H. Ishida[2], J. Merino[3]

[1] IFF-1: Quantum Theory of Materials
[2] College of Humanities and Sciences, Nihon University, Tokyo,Japan
[3] Departamento de Física Teórica de la Materia Condensada, Universidad Autónoma, Madrid, Spain

The influence of short-range Coulomb correlations on the Mott transition in the single-band Hubbard model is studied within cluster dynamical mean field theory and finite-temperature exact diagonalization. Both square and triangular two-dimensional lattices are considered. Transforming the non-local self-energy from a site basis to a diagonal molecular orbital basis, we study the inter-orbital charge transfer between cluster molecular orbitals in the vicinity of the Mott transition. The charge transfer is found to be small, indicating that all cluster molecular orbitals take part in the Mott transition. Thus, the insulating gap opens simultaneously across the entire Fermi surface. Nevertheless, the approach towards the transition differs greatly between cluster orbitals, giving rise to a pronounced momentum variation along the Fermi surface.

Considerable progress has recently been achieved in the understanding of the Mott transition in a variety of transition metal oxides. Whereas density functional theory in the local density approximation (LDA) predicts many of these materials to be metallic, the explicit treatment of local Coulomb interactions via dynamical mean field theory (DMFT) [1] correctly yields insulating behavior for realistic values of the on-site Coulomb energy U. In the single-site or local version of DMFT, the complex self-energy is purely frequency dependent, i.e., its momentum variation is neglected. To investigate the role of short-range Coulomb correlations on the quasi-particle bands it is necessary to go beyond the single-site approximation. For instance, the existence of the so-called hot spots and cold spots in the Brillouin Zone is intimately related to the momentum dependence of the self-energy. This topic has recently become of great interest in the field of strongly correlated materials.

In Ref. [2] we use a multi-site 'cluster' generalization of DMFT [3] in combination with finite temperature exact diagonalization (ED) [4] in order to investigate the two-dimensional single band Hubbard model for square and triangular lattices, with unit cells consisting of 2, 3, and 4 sites. The formalism is similar to the multi-orbital ED/DMFT scheme [5] which has recently been employed to discuss the nature of the Mott transition in several transition metal oxides [6]. Within cluster DMFT the interacting lattice Green's function
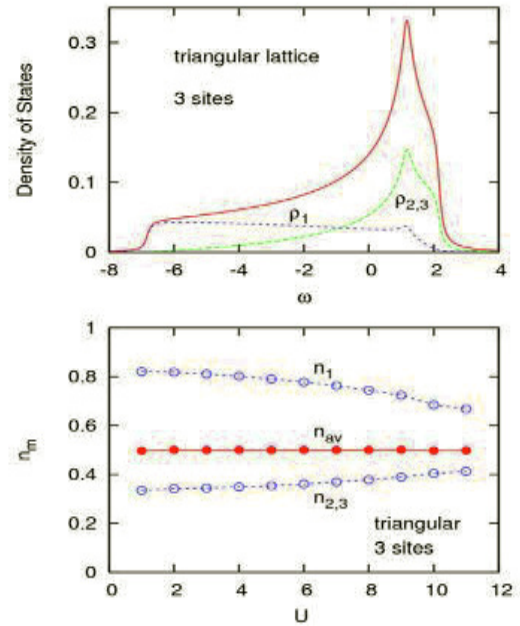
FIG. 1: Top: Density of states $\rho(\omega)$ and molecular orbital components $\rho_m(\omega)$ for three-site cluster of triangular lattice. Bottom: Occupancies of cluster molecular orbitals as functions of Coulomb energy U ($T = 0.02$). The Mott transition occurs near $U_c \approx 9.5$.

in the site basis is given by

$$G_{ij}(i\omega_n) = \sum_{\mathbf{k}} (i\omega_n + \mu - t(\mathbf{k}) - \Sigma(i\omega_n))_{ij}^{-1} \quad (1)$$

where the $\mathbf{k}$ sum extends over the reduced Brillouin Zone, $\omega_n = (2n + 1)\pi T$ are Matsubara frequencies and μ is the chemical potential. $t(\mathbf{k})$ denotes the hopping matrix for the superlattice and $\Sigma(i\omega_n)$ represents the cluster self-energy matrix. We consider here the paramagnetic metal insulator transition.

From the self-energy matrix in the site basis the approximate momentum variation of the self-energy may be obtained via

$$\Sigma(\mathbf{k}, i\omega_n) \approx \frac{1}{n_c} \sum_{ij} e^{i\mathbf{k}\cdot(\mathbf{R}_i - \mathbf{R}_j)} \Sigma_{ij}(i\omega_n) \quad (2)$$

where n_c is the number of sites in the unit cell and $\mathbf{R}_i$ are lattice vectors. To analyze this momentum varia-
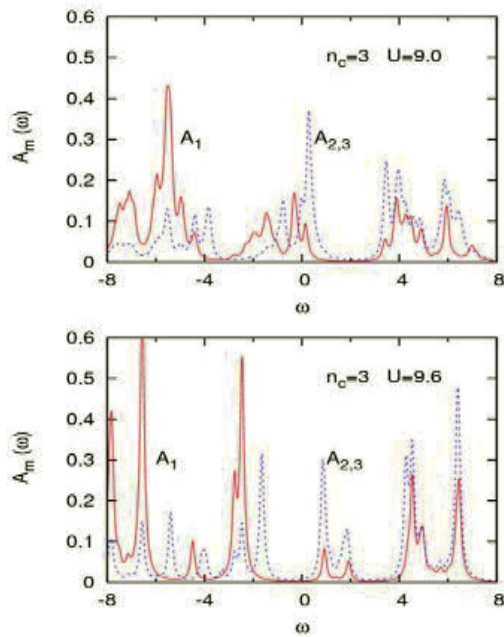
FIG. 2: *Spectral distributions of cluster molecular orbitals below and above the Mott transition ($U_c \approx 9.5$) for triangular lattice ($T = 0.02$, $E_F = 0$).*

tion, it is convenient to carry out a transformation from sites to molecular orbitals since the cluster Green's function and self-energy then become diagonal. For the triangular lattice, the molecular orbital decomposition of the non-interacting density of states is shown in Fig. 1. The question arises whether these cluster molecular orbitals undergo a similar correlation induced enhancement of orbital polarization as found within local DMFT for a variety of multi-orbital systems. In striking contrast to these materials, the occupancies of the cluster molecular orbitals show very little variation if U is increased from the metallic to the insulating phase, as shown in the lower panel of Fig. 1. The analysis carried out in [2] reveals that the strong coupling between cluster orbitals via the highly non-diagonal single-electron hopping matrix $t(\mathbf{k})$ is the origin of this qualitatively different behavior. Thus, within the cluster extension of DMFT the Mott transition involves all orbitals, i.e., there is no evidence for orbital-selective transitions, nor for a partial Mott transition within some subbands, combined with filling or emptying of the remaining subbands.

The fact that all cluster orbitals remain partially occupied across the transition implies that the Mott gap opens simultaneously in all orbitals. This can be seen most clearly in the spectral distributions which are shown in Fig. 2. Plotted are the distributions $A_1 = A_{11} + 2A_{12}$ and $A_{2,3} = A_{11} - A_{12}$, where $A_{ij}(\omega) = -(1/\pi) \operatorname{Im} G_{ij}(\omega + i\delta)$. Evidently, all orbitals contribute to the spectral weight at E_F in the metallic phase, as well as to the lower and upper Hubbard bands in the insulating phase.

As indicated in Eq. 2, the cluster molecular orbital components of the self-energy may be used to derive an approximate expression for the momentum variation of the lattice self-energy. An anologous relation holds for the lattice Green's function. Although the molecular orbitals share a common critical U_c, the momentum variation of the self-energy and Green's function demonstrates that certain regions of the Brillouin Zone exhibit stronger correlation effects than others. This is particularly evident in the case of the square lattice where the self-energy along the Fermi surface is essentially driven by the singular behavior at the hot spot $X = (\pi, 0)$, with weak additional non-singular contributions associated with the cold spot $M/2 = (\pi/2, \pi/2)$ [2].

The first-order nature of the Mott transition at finite temperature has been verified by analyzing the spectral weights of the cluster molecular orbitals at the Fermi level, $A_m(\omega = 0)$, and the double occupancy $d_{\mathrm{occ}} = \sum_m \langle n_{m\uparrow} n_{m\downarrow} \rangle / 3$. Both quantities exhibit hysteresis for increasing and decreasing U, indicating the coexistence of metallic and insulating solutions.

The work discussed above has recently been extended to obtain the complete T/U phase diagram of the triangular lattice [7]. For the isotropic case with $t_{12} = t_{13} = t_{23} = t$ the metal insulator phase boundaries have the same overall shape as the ones found within single-site DMFT, as expected for a fully frustrated system. The main difference is the considerably lower critical Coulomb energy U_c. The non-isotropic lattice, on the other hand, with $t_{13} = t_{23} = t$ and $t_{12} < t$, exhibits qualitatively different phase boundaries as a result of incomplete magnetic frustration. These results are consistent with experimentally observed T/P phase diagrams of strongly correlated organic salts, where the single-particle band width can be tuned with hydrostatic pressure P. Thus, increasing P is approximately equivalent to decreasing U in the DMFT calculation. Organic compounds with isotropic versus anisotropic lattices reveal qualitatively different metal insulator phase boundaries, in agreement with the results obtained via cluster DMFT.

[1] A. Georges, G. Kotliar, W. Krauth and M.J. Rozenberg, Rev. Mod. Phys. **68**, 13 (1996).

[2] A. Liebsch, H. Ishida, and J. Merino, Phys. Rev. B **78**, 165123 (2008).

[3] G. Kotliar, S. Y. Savrasov, G. Palsson, and G. Biroli, Phys. Rev. Lett. **87**, 186401 (2001).

[4] M. Caffarel and W. Krauth, Phys. Rev. Lett. **72**, 1545 (1994).

[5] C.A. Perroni, H. Ishida, and A. Liebsch, Phys. Rev. B **75**, 045125 (2007). See also: A. Liebsch, Phys. Rev. Lett. **95**, 116402 (2005); A. Liebsch and T.A. Costi, Eur. Phys. J. **51**, 523 (2006).

[6] A. Liebsch and H. Ishida, Phys. Rev. Lett. **98**, 216404 (2007), A. Liebsch, Phys. Rev. B **77**, 115115 (2008), H. Ishida, and A. Liebsch, Phys. Rev. B **77**, 115350 (2008), A. Liebsch and H. Ishida, Eur. Phys. J. **61**, 405 (2008).

[7] A. Liebsch, H. Ishida, and J. Merino, to be published.

79

Transport through quantum dots – a new electron-pair tunneling resonance

M. R. Wegewijs[1], M. Leijnse[2], M. H. Hettler[3]

[1] IFF-3: Theory of Structure Formation
[2] Institute for theoretical Physics A, RWTH Aachen, 52056 Aachen, Germany
[3] Forschungszentrum Karlsruhe, Institute for Nanotechnology, 76021 Karlsruhe, Germany

We predict a new electron pair-tunneling (PT) resonance in transport through quantum dots due to the Coulomb charging energy. This resonance shows up in the non-linear *single-electron* transport (SET) regime, midway between the electrochemical potentials of two subsequent single-electron additions. The PT resonance may easily be mistaken for a weak SET resonance, and we calculate its anomalous shape, temperature- and magnetic field dependence which allow for its identification.
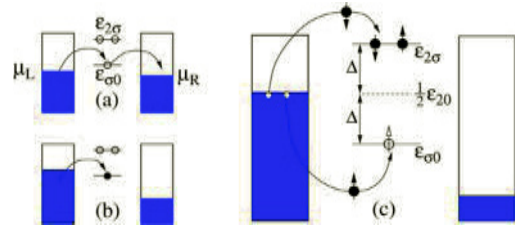
Three-terminal electron tunneling spectroscopy has nowadays become a standard tool for investigating the in situ properties of quantum dots in semiconductor hetero-structures and nanowires, carbon nanotubes and even single molecules. The basic spectroscopy rules derive from the simple conditions for energy conservation of single-electron tunneling (SET) onto the nanoscopic system. As a result, bias positions of differential conductance (dI/dV) resonances depend linearly on the gate voltage due to capacitive effects. Weaker resonances due to inelastic cotunneling (COT) processes. can often also be distinguished as steps or even peaks in dI/dV. Since these electron-hole charge-transfer resonances involve only a *virtual* charging of the dot, they appear at a bias threshold $V = \Delta\epsilon$, independent of the gate voltage. Here an electron is transferred from the high- to low-bias electrode, while using the excess bias-energy to excite the dot by an energy $\Delta\epsilon$. This process arises only in second order perturbation theory in the tunnel rate Γ. Here we report that, in the same order, electron-pair tunneling (PT) processes occur giving rise to distinct, measurable transport effects which have been overlooked so far.

Recently [1] we have developed a numerical program which calculates the transport current through an arbitrary interacting quantum dot system coupled by a standard tunnel Hamiltonian to metallic electrodes (non-interacting electron gas) in the framework of the real-time transport theory [2]. This allows the study of complex transport models for molecular transistors, which involve spin- and vibrational-excitations in addition to electronic charge excitations [3]. Importantly, Coulomb interaction effects are accounted for *non-perturbatively*. Especially relevant for this report is that *all* coherent one and two electron tunnel processes are summed up, which in-

FIG. 1: *Energy differences $\epsilon_{ij} = \epsilon_i - \epsilon_j$ between many-body eigenstates $i, j = 0, \sigma, 2$. (a) cotunneling process (b) single-electron tunneling (SET) process (c) pair-tunneling (PT) process, giving rise to a resonance at $\Delta = U/2$ above the threshold for SET. Filled (unfilled) circles and arrows indicate real (virtual) occupation.*

cludes pair-tunneling. Pair tunneling refers to a single coherent process, in which a pair of electrons is transferred between one electrode and the quantum dot, changing the charge of the dot by $\pm 2e$. We show that this process can be observed experimentally as a specific pair-tunneling transport resonance. This can be demonstrated for the generic model for a quantum dot, the non-equilibrium Anderson model, described by the Hamiltonian $H = \sum_\sigma \epsilon_\sigma d_\sigma^\dagger d_\sigma + U\hat{n}_\uparrow \hat{n}_\downarrow$. It consists of a single orbital with number operator $\hat{n}_\sigma = d_\sigma^\dagger d_\sigma$ with a finite positive charging energy U. The *many-body* eigenstates are $|0\rangle$, $|\sigma\rangle$ and $|2\rangle$ with energies $\epsilon_0 = 0$, ϵ_σ and $\epsilon_2 = \sum_\sigma \epsilon_\sigma + U$. The dot is coupled by a tunneling Hamiltonian, $H_T = \sum_{r=L,R} \sum_{k,\sigma} T_r d_\sigma^\dagger c_{rk\sigma} + h.c.$, to macroscopically large reservoirs, described by $H_R = \sum_{r=L,R} \sum_{k,\sigma} \epsilon_k c_{rk\sigma}^\dagger c_{rk\sigma}$. The electrons in the reservoirs are assumed to be non-interacting, with operators $c_{rk\sigma}^\dagger, c_{rk\sigma}$ for state k and spin σ in electrode $r = L, R$. The tunneling amplitudes can be expressed in the tunneling rates Γ_r through $T_r = \sqrt{\Gamma_r/2\pi}$. Throughout the paper we use natural units where $\hbar = k_B = |e| = 1$ where $-|e|$ is the electron charge. Our real-time approach allows us to access the interesting limit of strong, finite Coulomb charging energy and moderate tunnel rates: $U \gg T > \Gamma$

Fig. 1 presents the basic physics of different types of tunneling processes when the orbital energy $\epsilon_\uparrow = \epsilon_\downarrow$ exceeds the average chemical potential $(\mu_L + \mu_R)/2$ of the reservoirs, which we can define as zero. The quantum dot orbital is then empty at zero bias voltage V. At low bias, $\mu_L = V/2$, $\mu_R = -V/2$, transport is then dominated by cotunneling involving *virtual* oc-

cupation of state $|\sigma\rangle$. For larger bias, when the singly occupied state lies between the chemical potential of the reservoirs, i.e. $|V/2| > \epsilon_\sigma$, electrons can sequentially tunnel into and out of the dot, involving *real* occupation of state $|\sigma\rangle$. In this regime real double occupation of the dot through two consecutive SET processes only becomes energetically allowed when additionally the energy difference $\epsilon_{2\sigma} = \epsilon_2 - \epsilon_{\bar{\sigma}}$ is below the chemical potential of one lead, i.e. when $|V/2| > \epsilon_{\bar{\sigma}} + U$, where $\bar{\sigma}$ denotes the opposite of σ. However, midway between these resonances at ϵ_σ and $\epsilon_{\bar{\sigma}} + U$ the coherent tunneling of a *pair* of electrons from the same reservoir becomes possible, as shown in Fig. 1(c), i.e. at the resonance position

$$|V/2| > \tfrac{1}{2}\sum_\sigma \epsilon_\sigma + \tfrac{1}{2}U. \qquad (1)$$

Naively, one can think of this as one electron from just below the Fermi edge of the left reservoir tunneling onto state $|\sigma\rangle$, leaving an excess energy $\Delta = U/2$, which can be used to assist the second electron in reaching state $|2\rangle$. Thus, the *total* PT process is energy-conserving. However, since there are no internal degrees of freedom on the dot to store the energy Δ, these two processes have to take place coherently in the short time set by the time-energy uncertainty relation. This process leads to a small real occupation of the doubly charged state.

Experimentally, the dot energies ϵ_σ can be controlled linearly by the gate voltage V_g. This produces the characteristic "Coulomb diamond" shaped stability plots i.e. the differential conductance color-map as function of gate- and bias voltage. Fig. 2 (a) shows such a calculated stability diagram. SET processes give rise to the conductance peaks i.e. the strong yellow lines which cross at zero bias at the charge degeneracy points. The PT resonance associated with an electron pair tunneling onto (off) the dot, appears between these lines, i.e. deep inside the SET regime where a finite current is flowing. This is indicated by the red solid (green dotted) arrow in Fig. 2(a). Since the average orbital energy $\frac{1}{2}\sum_\sigma \epsilon_\sigma$ appears in Eq. (1) the PT and SET resonances have the same gate-voltage dependence. Therefore, one might confuse them and thereby extract an erroneous level-structure from the transport spectroscopy data. However, the resonance shape provides one crucial clue to the identification: the PT causes a peak in d^2I/dV^2, rather than in dI/dV as for SET, as a trace in Fig. 2(c) along the red vertical line indicated in Fig 2(a) shows. The analytical expression for the peak shape function, $F(x) = d^2\left(xb(x)\right)/dx^2$, shows that dI^2/dV^2 basically maps out the Bose distribution function $b(x) = 1/\left(e^x - 1\right)$ for electron *pairs*.

Another characteristic of the PT resonance is that it exhibits no Zeeman splitting since it involves a transition between two spin-less states of the quantum dot ($N = 0, 2$) as Fig. 2(b) illustrates, where the spin-degeneracy is lifted by an applied magnetic field. In contrast, in this figure the SET dI/dV peaks clearly split up and connect to additional gate-independent dI/dV steps in the Coulomb blockade regime associated with inelastic spin-flip cotunneling. This figure
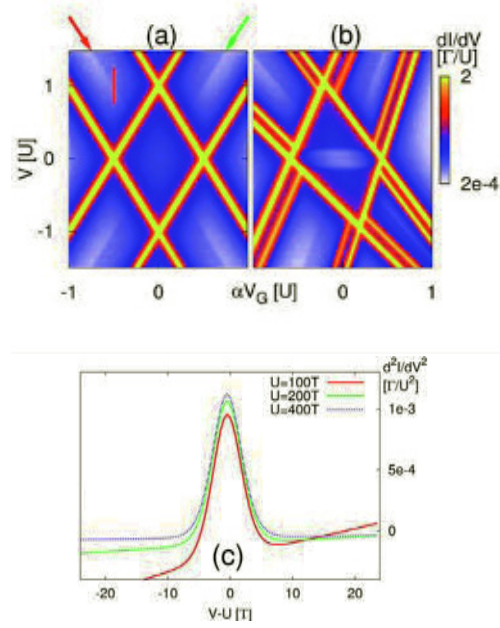
FIG. 2: dI/dV vs V, V_g plotted on logarithmic color scale for $U = 100T = 500\Gamma$, where $\Gamma_L = \Gamma_R = \Gamma/4$. (a) zero field case (b) non-zero magnetic field with Zeeman splitting $h = \epsilon_\downarrow - \epsilon_\uparrow = 15T$ (T = temperature). Also, the capacitances now depend on the quantum dot state and on the tunnel junction (left/right). Here the doubly occupied state couples better to the gate. (c): d^2I/dV^2 vs V for $U = 100T, 200T, 400T$, taken along the line $V_g = 0$, indicated in (a) by the red line.

also illustrates that in cases which deviate from the simplest capacitive model, the PT resonance can be identified by taking the average bias voltage positions of the SET resonance lines (yellow lines), as Eq. (1) predicts. Clearly, Fig. 2(b) also shows that the pair-tunneling signal is comparable in magnitude with the horizontal inelastic cotunneling feature, which is experimentally measurable.

Finally, we mention that the PT also shows up in the current shot noise, which is sensitive to the effective charge transferred in a tunnel processes. Since PT involves transfer of twice the electron charge, it is associated with a resonant increase in the Fano factor.

Current state of the art low-temperature measurements can access all the predicted signatures, e.g. fine details in the first three derivatives of the current with respect to voltage without dropping below the noise level [3].

[1] M. Leijnse and M. R. Wegewijs, Phys. Rev. B 78, 235424 (2008)

[2] J. König, H. Schoeller, and G. Schön, Phys. Rev. Lett.78, 4482 (1997)

[3] E. A. Osorio, K. O'Neill, M. R. Wegewijs, N. Stuhr-Hansen, J. Paaske, T. Bjørnholm, and H. S. van der Zant, Nanolett. 7, 3336 (2007)

Band mapping in higher-energy X-ray photoemission

L. Plucinski[1,2], J. Minár[3], B. C. Sell[2,4], J. Braun[3,5], H. Ebert[3], C. M. Schneider[1], C. S. Fadley[1,2,4]

[1] IFF-9: Electronic Properties
[2] Materials Sciences Division, Lawrence Berkeley National Laboratory, Berkeley, California 04720, USA
[3] Department of Chemistry and Biochemistry, Physical Chemistry Institute, Ludwig Maximillian University, Munich, D-81377 Munich, Germany
[4] Department of Physics, University of California Davis, Davis, California 95616, USA
[5] Hildesheim University, D-31141 Hildesheim, Germany

We have studied the temperature dependence of W(110) soft x-ray angle-resolved photoemission spectra between 300K and 780K. The temperature dependence of the data can be analyzed qualitatively in terms of a direct-transition band-dispersion regime ("UPS" limit) versus a non-direct-transition density-of-states regime ("XPS" limit). We also discuss the implications of this work for future experiments on other materials and at even higher photon energies up to 10 keV.

There is growing interest in extending valence electronic studies with angle-resolved photoemission (often referred to as "band mapping", but more correctly viewed as quasiparticle spectra) into the soft x-ray, and even hard x-ray, regimes. Such measurements take advantage of the greater photoelectron information depths at higher kinetic energies, thus probing more accurately bulk, rather than surface, electronic structure. Furthermore, three-dimensional, rather than two-dimensional, band structure and Fermi surfaces may be studied by going to higher photon energies. In comparison to low-energy band mapping, however, additional effects must be taken into account in both carrying out such measurements and in interpreting data. These include the increased angular resolution required to probe a small enough region in the Brillouin zone (BZ), the need to allow for the photon momentum in wave-vector conservation, and thermal effects due to phonon creation and annihilation during photoexcitation that smear out the specification of the initial wave vector. It is useful in this discussion to think in terms of two limiting regimes: very low energies and/or temperatures in which band mapping is possible via direct or k-conserving transition (DTs)–the so-called UPS limit, and high energies and/or temperatures in which emission is fully averaged over the BZ to yield density-of-states (DOS) sensitivity–the XPS limit.

Our measurements (see [1] for details) were carried out on a (110)-oriented tungsten crystal at beamline 4.0.2 of the Advanced Light Source in Berkeley, using the Multi-Technique Spectrometer/Diffractometer located there. The exciting synchrotron radiation was p-polarized and the angle between photon incidence and electron exit was fixed at $70°$. The sample orientation was adjusted after allowing for photon momen-
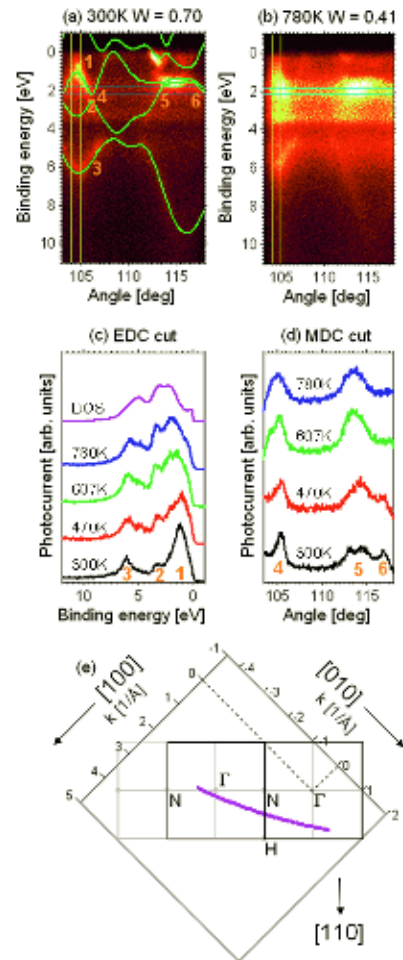
FIG. 1: (a)-(b) Plots of intensity versus angle of emission for $h\nu$ = 870 eV. In (a) also the transitions allowed with free-electron final states are shown. (c) The temperature dependence of energy distribution curves integrated over 20 channels in angle as indicated in (a) and (b). A comparison to the W density of states (DOS), as broadened by experimental resolution of 150 meV is also shown in the topmost curve. (d) The temperature dependence of momentum distribution curves at one selected energy, again as indicated in (a) and (b). (e) The average locus of points in the BZ sampled in this data, assuming direct transitions and free-electron final states.

tum so as to as nearly as possible sample points along the Γ-to-N line in the BZ. A Scienta electron spectrometer with SES2002 performance was used

to accumulate angle-resolved spectra with a standard 2D detection scheme, the average angular resolution was approximately 0.5°.
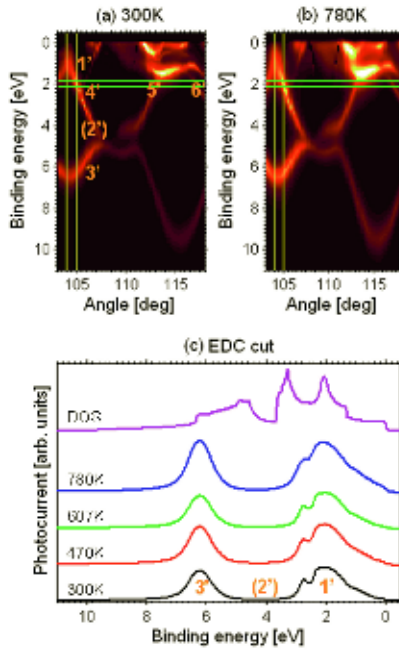
FIG. 2: As Fig. 1, but for one-step photoemission calculations including temperature effects via complex phase shifts. See text for details.

We have analyzed the data in first approximation by requiring wave-vector conservation according to $\vec{k}_f = \vec{k}_i + \vec{g}_{hkl} + \vec{k}_{h\nu}$ where the $\vec{k}$-conservation condition has been modified to allow for the non-negligible photon momentum at higher excitation energies, by assuming free-electron final states for which the energy inside the solid is $E_f(\vec{k}_f) = \hbar^2 k_f^2 / 2m_e = E_{kin} - V_0$, where m_e is the mass of the electron, E_{kin} is the kinetic energy outside the surface, V_0 is the inner potential of 15 eV, and by using initial state energies from a band structure calculated using the WIEN2k code [4].

The novel aspects of this work are in measuring detailed two-dimensional plots of binding energy vs. wave vector as a function of temperature, with prior work on tungsten only considering selected single directions of emission and lower energy and angular resolution [2]. Furthermore, we compare the experimental data with state-of-the-art one-step photoemission theory [3] which includes a precise evaluation of matrix element effects and an attempt to include phonon effects, while prior work used only simple direct-transition theory together with free-electron final states and a qualitative/semi-quantitative estimate of the fraction of DTs via suitable Debye-Waller (DW) factors [2] with these being calculated from: $W(T) = \exp[-\frac{1}{3}g_{hkl}^2\langle U^2(T)\rangle]$ where g_{hkl} is the magnitude of the bulk reciprocal lattice vector involved in the direct transitions at a given photon energy and $\langle U^2(T)\rangle$ is the three-dimensional mean-squared vibrational displacement.
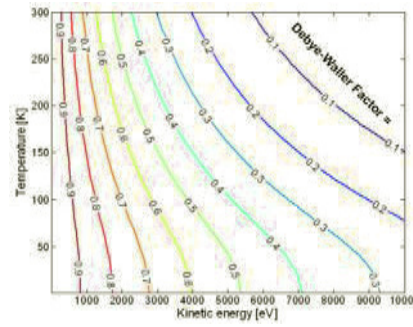
FIG. 3: Debye-Waller factors for valence-band photoemission from W at various temperatures over 0-300K and electron kinetic energies over 0-10 keV. These permit a rough estimate of the fraction of transitions yielding simple band mapping features.

Figures 1 and 2 show experimental and theoretical photoemission data presented both as two-dimensional maps and energy distribution curve (EDC) and momentum distribution curve (MDC) cuts. From Fig. 1(a) the agreement between the experiment and free-electron theory is very good, which proves that band mapping is indeed possible at 870 eV, an energy higher than used in most prior ARPES work. Similarly comparison between Figs. 1(a) and 2(a) is favorable. However, by comparing Figs. 1(c) and 2(c), it is clear that theory in which phonon effects are incorporated only via complex phase shifts is not found to reproduce the smearing of the spectral features at the higher temperature, and this indicates that a more accurate approach in which phonon creation and annihilation are taken into account in the photoemission process is needed to adequately describe such data.

Finally, we consider what might be expected if the photon energy is taken to much higher values up to 10 keV, again for the example case of tungsten. At this point, we can only make use of the DW factors to estimate the fraction of transitions that are direct, and a family of curves for different temperatures over 0-300K and electron kinetic energies over 0-10 keV are shown in Fig. 3. From these curves, it is clear that, if we use the rough criterion of at least 50% direct transitions, then at least for W, one can work at 300K with photon energies up to about 1.7 keV, and with cooling to 4 K, with photon energies up to about 5.4 keV.

[1] L. Plucinski, J. Minár, B. C. Sell, J. Braun, H. Ebert, C. M. Schneider, and C. S. Fadley, Phys. Rev. B **78**, 035108 (2008).

[2] R. C. White, C.S. Fadley, M. Sagurton, and Z. Hussain, Phys. Rev. B 34, 5226 (1986).

[3] F. Venturini, J. Minar, J. Braun, H. Ebert and N. B. Brookes, Phys. Rev. B 77, 045126 (2008).

[4] P. Blaha, K. Schwarz, G. K. H. Madsen, D. Kvasnicka, and J. Luitz, http://www.wien2k.at/.

83

A linear scaling algorithm for density functional calculations

R. Zeller[1,2]

[1] IFF-3: Theory of Structure Formation
[2] IAS: Institute for Advanced Simulation

The work in standard density functional calculations increases cubically with the number of atoms in the system. Several linear scaling techniques, which trade accuracy for speed, have appeared in recent years, but their applicability and accuracy for metallic systems remains rather unclear. In the last two years we have developed a new algorithm with linear scaling behaviour and investigated its suitability in model calculations for large metallic supercells with up to 131072 atoms. Our algorithm is based on the tight-binding Korringa-Kohn-Rostoker Green function method and utilizes an exponential decay of the Green function matrix elements, iterative solution techniques and a spatial truncation of the Green function in the sense of Kohn's principle of nearsightedness of electronic matter.

In the last decades density functional theory has emerged as a powerful tool for the quantum mechanical description of chemical and physical properties of materials. Density functional theory treats the many-electron problem by single-particle equations using the electron density instead of the many-electron wavefunction as the basic quantity. Although this represents an obvious simplification, calculations for systems with many atoms still represent a serious computational challenge. The main bottleneck is that the computing time increases with the third power of the number of atoms in the system. Systems with a few hundred atoms can be treated routinely today, but larger systems with thousands of atoms require enormous computer resources. In recent years considerable effort has been spent to reduce the computational work by exploiting the short range of the density matrix which decays exponentially in semiconducting and insulating materials and several linear scaling techniques have been developed which treat large systems with satisfactory accuracy.

The problem for metallic systems is that the density matrix decays only algebraically. In principle, this does not exclude to apply the concept of nearsightedness of electronic matter, a term phrased by Nobel Prize winner Walter Kohn. Nearsightedness means that in systems without long range electric fields (and for fixed chemical potential) the density change at a point in space is negligibly affected, if the electronic potential is changed sufficiently far away from this point. For metallic systems this property is used in locally self-consistent approaches based on the Korringa-Kohn-Rostoker (KKR) and local muffin-tin orbital (LMTO) methods. Each atomic cell and its local surrounding are treated as independent subsystems with naturally linear scaling effort. The densities of the subsystems are then patched together. A disadvantage of these approaches is that it is difficult to assess and expensive to improve the accuracy since the work scales with third power of the number of atoms in the local interaction zone. This disadvantage is avoided in our new KKR algorithm, which exploits not only the nearsightedness, but also the use of sparse matrices and iterative solution techniques as it is done in most other linear scaling techniques.

In the last two years we have implemented the combined use of sparse matrices, iterative solutions and nearsightedness into our existing KKR Green function programs which we have developed over the years at the IFF to study defects, surfaces and bulk systems. In the KKR Green function method [1] space is divided into nonoverlapping cells around the atomic sites. For each cell a single-site problem is solved using an angular momentum expansion of density, potential and wavefunctions. From the site dependent quantities the Green function of the system is then obtained by multiple scattering theory, which computationally requires to invert the KKR matrix $M(E)$ at a set of energy mesh points E_i used to obtain the electron density by energy integration. The computational effort is determined by the matrix dimension $N(l_{max} + 1)^2$ where N is the number of atoms in the system and l_{max} the highest angular momentum used, usually $l_{max} = 3$ is sufficient. The standard KKR matrix with its free space Green function matrix elements is a dense matrix which requires $O(N^3)$ computing effort for inversion. Here the tight-binding (TB) KKR method [1] which is based on a repulsive reference system with exponentially decaying Green function matrix elements is much better suited. Setting exponentially small elements to zero makes the TB-KKR matrix sparse and reduces the computational effort from $O(N^3)$ to $O(N^2)$.

One difficulty for the iterative determination of $M^{-1}(E)$ is that iterations cannot converge at or near energies E, where the Green function has singularities. Such singularities appear on the real energy

axis as poles (bound states) resembling the atomic core states and branch cuts (continuous eigenstates) resembling the valence and conduction bands. The singularities are avoided by calculating the density with complex energy contour integration for which a suitable set of mesh points is found by using a finite temperature T in density functional theory [1].

Another difficulty for the iterative determination of $M^{-1}(E)$ is that straightforward iterations, which correspond to Born iterations in scattering theory, usually diverge. Thus more sophisticated schemes must be used. For our algorithm with a complex non-Hermitian matrix $M(E)$ we found that the quasi-minimal-residual (QMR) method in its transpose free version is suitable to achieve convergent iterations.

An important feature of the iterative solution is that each atom can be treated almost independently so that our algorithm is ideally suited for massively parallel computing. High parallel efficiency and small memory requirements per processor have been found in our test calculations for large supercells with up to $N = 2048$ atoms using up to 8192 processors on 2048 nodes of the IBM Blue Gene/P JUGENE.

In order to arrive at an $O(N)$ algorithm we use the nearsightedness of electronic matter by neglecting potential differences between system and reference system outside of a truncation region around each atom. Then the inversion of the KKR matrix is only required within the truncation region and the overall computational effort is reduced from quadratic $O(N^2)$ to linear $O(N)$ scaling.
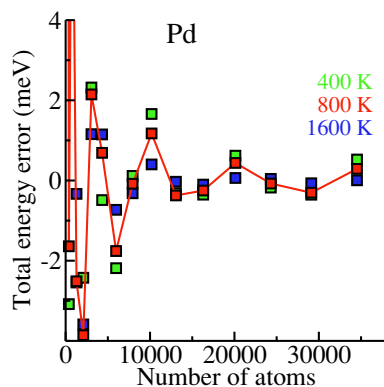
FIG. 1: *Total energy error per atom as function of the number of atoms in the truncation region for different temperatures. The line connecting the results for* $T = 800$ *K serves as a guide for the eye.*

Since the truncation necessarily introduces errors, it is important, for instance, to determine the total energy accuracy which can be achieved. We investigated this question in a model study for large Cu, Ni and Pd supercells with $4 \times 32^3 = 131072$ atoms. The supercells were obtained by repeating a simple cubic unit cell with four atoms 32 times in all three space directions. The truncation regions were constructed by using more and more neighbour shells around the central atom so that always one more shell in the close-packed (110) direction

was included. For the Brillouin zone integration a single point $(1/4, 1/4, 1/4) \times 2\pi/a$ was used in the irreducible Brillouin zone. Since all atoms in the supercell are equivalent, the iterative solution was needed for only one atom and the calculations could be performed on one processor of a desktop computer. The equivalent atoms also enabled to determine the self-consistent potential and the total energy for the supercell with no truncation of the Green function from calculations for the small simple cubic unit cell with an appropriate mesh of 5984 points in its irreducible Brillouin zone.

The total energy error for the Pd supercell (results for Cu and Ni are similar) is shown in FIG. 1. The figure illustrates that the error can be made smaller than 2 meV if truncation regions with a few thousand atoms are used.
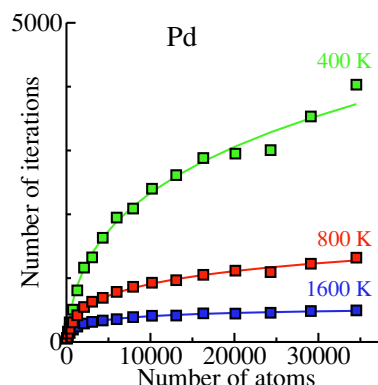
FIG. 2: *Number of matrix vector multiplication required to obtain a residual norm smaller than* 10^{-6} *in the QMR method.*

An important issue for our algorithm is how many iterations or equivalently how many matrix vector multiplications are required. The highest number of matrix vector multiplications is needed for the energy mesh point with smallest imaginary part (which decreases with temperature). For this point FIG. 2 shows the typical behaviour that the number of matrix vector multiplications increases with the number of atoms in the truncation region and with decreasing temperature. The curves in FIG. 2 are fits to exponential functions which approach constant values for large truncation regions indicating that the work per atom becomes independent of system size for large systems.

From the results obtained so far [2, 3], we conclude that our linear scaling algorithm can be used in accurate density functional calculations for large metallic systems on massively parallel computers.

[1] N. Papanikolaou, R. Zeller and P.H. Dederichs, J. Phys.: Condens. Matter **14**, 2799 (2002)

[2] R. Zeller, J. Phys.: Condens. Matter **20**, 294215 (2008)

[3] R. Zeller, Phil. Mag. **88**, 2807 (2008)

Optimized tomographic reconstruction applied to electric currents in fuel cells

H. Lustfeld[1], J. Hirschfeld[1], M. Reißel[2], B. Steffen[3]

[1] IFF-1: Quantum Theory of Materials
[2] FH-Aachen, Abteilung Jülich
[3] JSC: Jülich Supercomputing Centre

86

We suggest two novel tomographic diagnostic methods for analyzing the electric currents in a fuel cell and a fuel cell stack. The first method is quite general and can be used for any tomographic procedure. It leads to an essential reduction of measuring points and at the same time to an increase of the precision. Applied to a single fuel cell the reduction amounts to 90% while the precision is increased by a factor of 3. The second method exploits the high electrical conductivity of slitted metallic (e.g. aluminum) plates to induce surface currents whenever the electric current density in the stack becomes inhomogeneous. These currents can be measured either directly or by measuring their magnetic field thus leading to a basic information about the state of every fuel cell in the stack.

The characteristic of fuel cells and fuel cell stacks is their large internal current densities (typical values are $250\,mA\,cm^{-2}$) generated by catalytic reactions in the Membrane Electrode Assembly (MEA) of each cell. This suggests a noninvasive diagnostics, the so called magnetotomography, by measuring the external magnetic fields and then, applying tomographic methods, to determine the internal currents [1]. Of course the question arises where to place the measuring points. An intuitive and - from the experimental point of view - easy method would be to distribute as many as possible measuring points *homogeneously* on a cuboid around the fuel cell.

We have shown that a homogeneous distribution is in general not at all a very good procedure since every measuring point provides information *and* an error. There are measuring points delivering extremely important information and small errors, but others that contribute nearly nothing of information but large errors. The latter points have to be excluded. We have found a ζ function evaluating each measuring point and discarding the latter ones [2]. This procedure can be applied to any given set of measuring points. Furthermore it can be systematically optimized and various constraints can be taken into account (e.g. measurements at certain locations may be more difficult or more expensive) [3]. The procedure turned out to be very successful. In the case of the fuel cells only $\approx 10\%$ of the original set were relevant measuring points and restriction to this subset increased the precision typically by a factor of 3, cf Fig.1. It
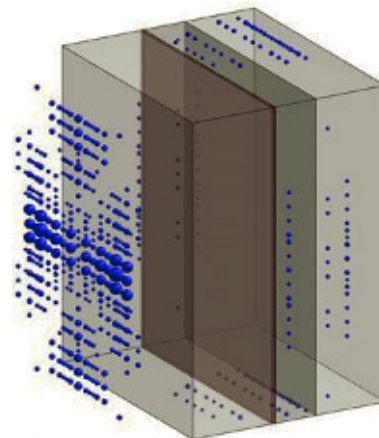
FIG. 1: *Reduced measuring point distribution for the magnetotomography of a single fuel cell with a cross section of $138mm \times 178mm$. The size of the spheres denotes the importance of the measuring points. Their number, originally 6702, is reduced to 498. It is obvious, that the most important ones are located on the front side of the fuel cell.*

should be pointed out that the optimized selection of the relevant measuring points could be applied to any tomographic problem (e.g. computer tomography in medicine).

The evaluation of the measuring points show also that for magnetotomography of a fuel cell the relevant measuring points are located close to the front-side and back side of the fuel cell. This makes it awkward to diagnose a fuel cell in a stack consisting of about 100 fuel cells connected in series.

Therefore we suggest a modified procedure: Place a thin ($\approx 1\,[mm]$), slitted metal (e.g. copper or aluminum) plate between each of the fuel cells[4], cf Fig.2. This leads to detectable surface currents whenever there is an inhomogenuity of electric current generation in the MEA of an individual fuel cell.

An example may clarify the phenomenon further: Consider one plate m of perfect conductivity between two fuel cells $M1$ and $M2$ both having an effective MEA area A. Assuming a damaged area a with zero conductivity in the first fuel cell $M1$, the lacking current through this area

$$i = I\frac{a}{A},\ \text{I is the total electric current}$$

has to be compensated. Assuming the resistance of
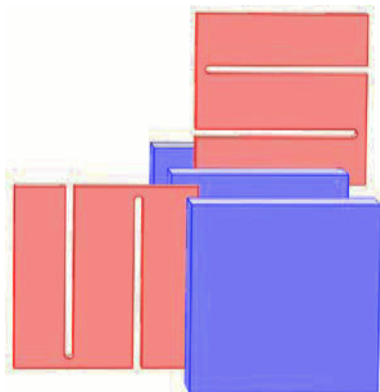
FIG. 2: *Exploded view of the diagnostic scheme. The blue plates represent individual fuel cells, while the red ones represent the slitted metal plates.*

plate m to be negligible the normal component of the current density must be the same everywhere in the remaining fuel cell
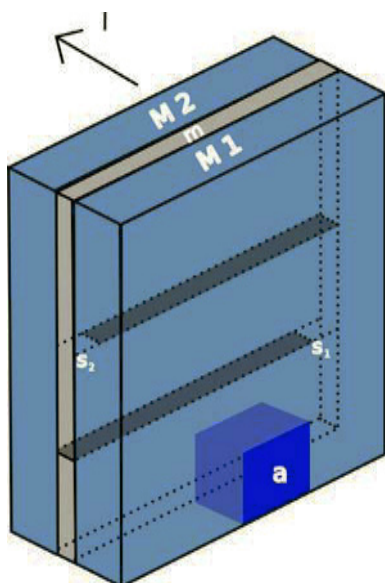
FIG. 3: *Schematic view showing a plate m of a material (e.g. aluminum) with very high conductivity. The plate is located between the fuel cells $M1$ and $M2$ and split into stripes (slits indicated by shaded areas). The main direction of the current is indicated by an arrow. It is assumed that the MEA of $M1$ has a damaged area a acting as an insulator. Because of the very high conductivity in m, the current density in each of the cells is practically constant - except in the area a where it is zero. Due to current conservation, transverse currents will rise in m flowing through the connections between the stripes at locations s_1 and s_2.*

area of $M1$. This requires a transverse compensation current and because of the slits, part of this current has to pass the locations s_i. If there are two slits in the plate m as shown in Fig.2 and Fig.3, two different currents are detected, one at s_1 the other at s_2. If the damaged area is e.g. in the lower part of the MEA (cf Fig.3) the currents are

$$i_{s_1} = \frac{2}{3} \frac{Ia}{A-a}$$

and

$$i_{s_2} = \frac{1}{2} i_{s_1}$$

These currents have to pass the bridges connecting the slits where they can be detected either by measuring the current directly or by measuring the magnetic field generated by these surface currents. It turns out that the information obtained by this scheme is sufficient to determine the state of a fuel cell located between two metal plates[4].

The thin metallic plates have another favorable effect: They smoothe inhomogenuities in the electric current generation of a fuel cell preventing a disturbance from penetrating to a previous or next fuel cell as it will happen without metallic plates between the MEAs. Thus the metallic places lead to a better diagnostics *and* to a stabilization of the fuel cell stack.

[1] K.-H. Hauer, R. Potthast, T. Wüster, D. Stolten: J. Power Sources **143**, 67 (2005)

[2] H. Lustfeld, M. Reißel, U. Schmidt, B. Steffen: Patent application PT 1.2354 and J. Fuel Cell Sci. Technol., in press and
U. Schmidt, Diploma Thesis and
R. Telschow, Diploma Thesis

[3] J. Hirschfeld, H. Lustfeld, M. Reißel, B. Steffen: Patent application PT 0.2656-1.2354 PCT

[4] H. Lustfeld, M. Reißel, B. Steffen: Patent application PT 1.2373 and
J. Hirschfeld, H. Lustfeld, M. Reißel, B. Steffen: paper submitted to J. Fuel Cell Sci. Technol. and
J. Hirschfeld: Diploma Thesis

87

Nuclear inelastic scattering by ^{121}Sb and ^{125}Te in thermoelectric materials

R. P. Hermann[1,2], T. Claudio[1], A. Möchel[1], J. Perßon[1], H.-C. Wille[3], I. Sergueev[3]

[1] IFF-4: Scattering Methods
[2] Dept. Physics, University of Liege, Belgium
[3] ESRF, Grenoble, France

Thermoelectric materials might provide a significant contribution to sustainable energy development, by improving waste heat recovery, and in information technology, by improving the local thermal management. We have contributed to the development of the nuclear inelastic scatering technique for new elements, antimony and tellurium, and have studied the lattice dynamics of several thermoelectric materials with low thermal conductivity, one of the key features in improving the efficiency of thermolectric energy conversion. Our studies have revealed a specific coupling mechanism related to the observed low thermal conductivity.

In order to enhance the efficiency of materials for thermoelectric energy conversion, simultaneous tuning of electronic properties, such as the Seebeck coefficient S, the electric conductivity σ, and the electronic thermal conductivity κ_{el}, and of the lattice thermal conductivity κ_{lat} is necessary. The figure of merit of a thermoelectric material is given by $ZT = \sigma S^2/(\kappa_{lat} + \kappa_{el})$. Our research aims to gain insight into the lattice dynamics of model systems for thermoelectric materials and to use this insight for reducing the lattice thermal conducting, which, in bulk materials, is the only parameter that is tuneable somewhat indepently from the other parameters.

Experimentally, access to lattice dynamics is obtained on the macroscopic scale by thermal transport, specific heat, or elastic constants measurements. Microscopically, scattering methods are the method of choice for accessing the underlying phonon scattering mechanisms that are related to limiting the thermal conductivity. In order to complement insight gained by inelastic neutron scattering techniques[1, 2], we have in the recent years used nuclear inelastic scattering by Mössbauer active nuclides, such as ^{57}Fe and ^{151}Eu [3], a technique which gives access to the element specific phonon density of states of the studied nuclide.

In order to achieve a resolution of a few meV that is necessary for determining the phonon DOS, high resolution monochromators with $\Delta E/E \leq 10^{-7}$ are required, as the Mössbauer resonances have an energy in the range of a few tens of keV. Because of the rapid loss in reflectivity for silicon based

monochromators for energies above 30 keV, a single bounce sapphire backscattering monochromator was developed at the ESRF, a monochromator for which the energy tuning is carried out at the fixed ~90° backscattering angle by tuning the lattice parameters through a control of the temperature of the sapphire crystal [4]. The large number of Bragg reflections in sapphire combined with the temperature control gives access to the Mössbauer resonances of several nuclides of interest, such as ^{121}Sb and ^{125}Te.
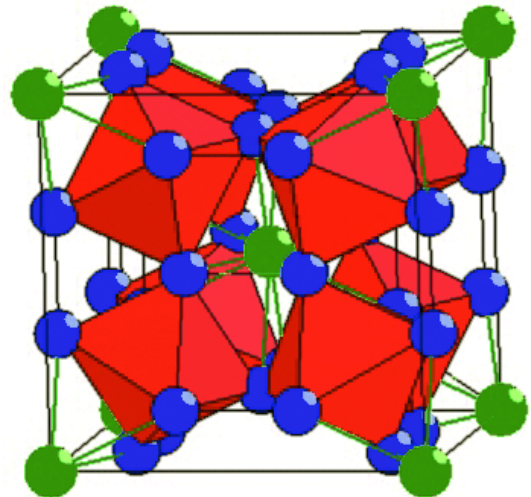
FIG. 1: *The skutterudite structure. Transition metal atoms are located in the center of the red octahedra that have pnictogen atoms, in blue, at the vertices. The structure can be empty, for example Co_4Sb_{12}, or filled by an electropositive element, such as Eu, in $EuFe_4Sb_{12}$.*

In our first measurements that have demonstrated the feasibility of a single crystal sapphire backscattering monochromator for inelastic scattering by high energy nuclear resonances, we have concluded our study of the partial phonon density of states in the filled $EuFe_4Sb_{12}$ skutterudite, see Fig. 1, a model system for so-called rattler based thermoelectric materials, by determining the antimony partial density of states using the 37.1 keV ^{121}Sb nuclear resonance [5]. In complement with our earlier ^{57}Fe and ^{151}Eu measurements, these measurement have yielded the first complete and direct determination of the element specific density of states in a complex ternary material, see Fig. 2. In comparing the anti-

mony density of states in $EuFe_4Sb_{12}$ with its counterpart in unfilled parent compound Co_4Sb_{12}, we were able to reveal the weak coupling of the mostly localized,"rattler" like, vibrational modes of the Eu guests with the Sb-cage vibrational modes. Such coupling is required if the presence of the low lying "rattler" modes is to have an impact on the thermal conducitivity, as is observed [5]. The scenario of the coupling of the guest and host vibrational modes in skutterudites was recently also demonstrated by an inelastic neutron scattering study [2].
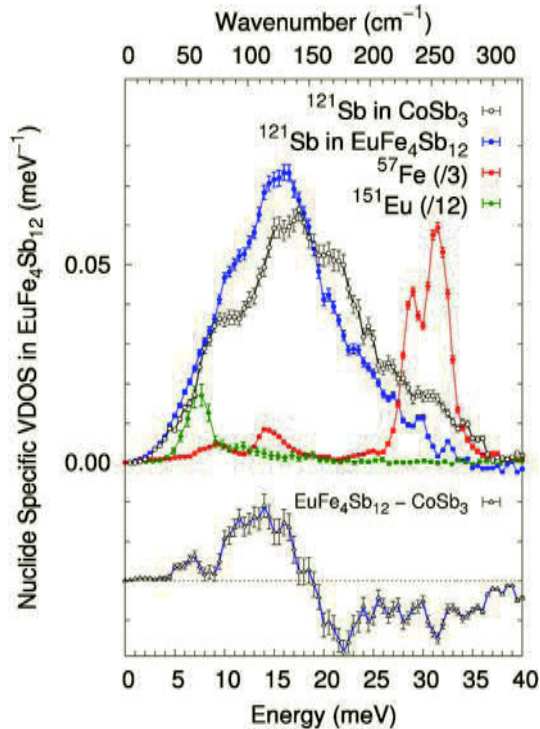
FIG. 2: *The elements specific density of states for Sb, Eu, and Fe in $EuFe_4Sb_{12}$ and Co_4Sb_{12}, weighted by the elemental content per formula unit. The difference in the Sb density of states in $EuFe_4Sb_{12}$ and Co_4Sb_{12} reveals a specific contribution at the energy of the 7 meV Eu vibrational mode that indicates guest-host coupling, in addition to a general softening upon filling.*

In pursuit of our investigation of the lattice dynamics of interesting thermoelectric compounds, such as Sb_2Te_3, we also have very recently demonstrated [6] the usability of the sapphire monochromator to the ^{125}Te nuclear resonance at 35.5 keV, see Fig. 3, with a resolution of 2.7 meV, an extension that was possible owing to the development of fast avalanche photodiode detectors by the ESRF nuclear resonance scattering group. These fast detectors allow to discriminate the prompt electronic x-ray scattering from the delayed nuclear fluorescence with a time of resolution of ∼2 ns. Such fast response is absolutely required for ^{125}Te with a half-life of 1.48 ns, *i.e.* a natural linewidth $\Gamma_0 = 0.313$ μeV, one of the shortest lived transitions studied by nuclear inelastic scattering so far.
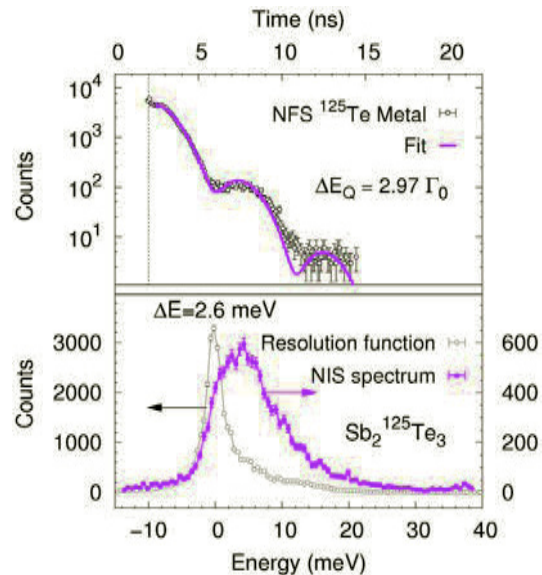
FIG. 3: *The nuclear forward scattering in Te metal (where ΔE_Q is the quadrupole interaction), at the top, and the nuclear inelastic scattering by ^{125}Te in Sb_2Te_3 with the associated resolution function.*

The combined access to element specific phonon density of states measurements of antimony and tellurium bearing compounds is invaluable not only for thermoelectric materials, materials in which Sb and Te are often the major constituents, but also for a large number of other materials of timely interest, such as phase change materials for information technology, or the Sb and Te bearing compounds in the family of the newly developed iron based superconductors.

[1] R. P. Hermann, R. Jin, W. Schweika, F. Grandjean, D. Mandrus, B. C. Sales, and G. J. Long, Phys. Rev. Lett. 90, 135505 (2003).

[2] M. M. Koza, M. R. Johnson, R. Viennois, H. Mutka, L. Girard, and D. Ravot, Nature Materials 7, 805 - 810 (2008).

[3] Long G. J., Hermann R. P., Grandjean F., Alp E. E., Sturhahn W., Johnson C. E., Brown D. E., Leupold O., and Rüffer R., Phys. Rev. B 71, 140302(R) (2005).

[4] H.-C. Wille, Yu. V. Shvyd'ko, E. E. Alp, H. D. Rüter, O. Leupold, I. Sergueev, R. Rüffer, A. Barla, and J. P. Sanchez, Europhys. Lett. 74, 170 (2006).

[5] Wille H.-C., Hermann R. P., Sergueev I., Leupold O., van der Linden P., Sales B. C., Grandjean F., Long Gary J., Rüffer R., and Shvyd'ko Yu. V., Phys. Rev. B 76, 140301(R) (2007).

[6] See also ESRF Highlights (2008), pp. 20-21; manuscript in preparation.

A stable molecular water oxidation catalyst for artificial photosynthesis

B. Botar[1], P. Kögerler[1,2]

[1] IFF-9: Electronic Properties
[2] Institute of Inorganic Chemistry, RWTH Aachen University

The oxidation of water represents a key reaction in many proposed artificial photosynthesis systems that aim to convert sunlight energy into the splitting and formation of chemical bonds. However, catalysts are required to eliminate kinetic obstacles inherent to this elementary reaction. While numerous relevant molecular catalysts were tested in the past decades, all systems suffer from oxidative degradation of their organic constituents during the course of the catalyzed reaction. We now identified an all-inorganic that retains its high efficiency at ambient temperature under turnover conditions.

The design of viable and well-defined molecular catalysts for water oxidation, in part inspired by the Mn_4Ca-centered water oxidation-oxygen evolving center (OEC) in photosystem II, is being pursued for three decades and centers on transition metal coordination complexes such as the classic $[(bpy)_2(H_2O)RuORu(H_2O)(bpy)_2]^{4+}$ system.[1] Despite ongoing research, however, stable and rapid molecular and homogeneous catalysts for the elementary reaction ($2 H_2O \rightarrow O_2 + 4 H^+ + 4 e^-$) that exhibit long-term stability have yet to be achieved: Homogenous catalytic oxidation studies suggest that likely intermediates in H_2O oxidation would degrade all organic ligands, a point consistent with the findings in the molecular H_2O oxidation catalysts reported to date.[2] Thus, the need to develop highly active and stable H_2O oxidation catalysts remains of considerable importance. Based on the reported Ru_2 catalysts for H_2O oxidation, documented polyoxometalate complexes with multinuclear d-electron-containing centers capable of accepting several electrons needed for H_2O oxidation, and the report of electrocatalytic O_2 evolution by the complex $[WZnRu_2(OH)(H_2O)(ZnW_9O_{34})_2]^{11-}$,[3] we developed a tetraruthenium(IV) polyoxotungstate complex, isolated as

$$Rb_8K_2[\{Ru_4O_4(OH)_2(H_2O)_4\} (\gamma-Si\,W_{10}O_{36})_2] \cdot 25\,H_2O \ , \quad \textbf{(1)}$$
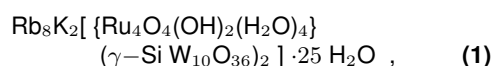
an oxidatively and hydrolytically stable complex that addresses some of the core challenges – it catalyzes the rapid oxidation of H_2O to O_2, does so in aqueous solution, and is quite stable under turnover conditions.[4]

The X-ray crystal structure of **(1)** reveals the same "out-of-pocket" d-metal coordination polyhedra observed in water-soluble γ-di-iron(III) derivatives; namely, the Ru centers are corner-sharing and not ligated to the central SiO_4 unit. The two "out-of-pocket" $\{\gamma$-$SiW_{10}Ru_2\}$ monomeric units are rotated by 90° around the vertical C_2 axis relative to one another defining overall D_{2d} symmetry for the polyanion (Fig. 1). The staggered structure facilitates incorporation of a $[Ru_4(\mu$-$O)_4(\mu$-$OH)_2(H_2O)_4]^{4+}$ core in which the four Ru centers span a slightly distorted tetrahedron with Ru-Ru distances of 3.47-3.66 Å. The adjacent Ru centers within each $\{\gamma$-$SiW_{10}Ru_2\}$ unit are bridged by hydroxo ligands, while oxo ligands bridge the Ru centers of different monomeric units. The presence of μ-oxo Ru-O-Ru bridges is consistent with other structural reports on dimeric Ru-containing polyoxometalates. Several lines of evidence – magnetic properties, bond valence sums, electrochemical properties – indicate that during the synthesis of **(1)**, the Ru(III) reactant is oxidized by O_2 to give a $Ru(IV)_4$ complex.

In preparation for catalytic studies, several techniques were used to further characterize oxidation states and potentials of the ruthenium centers and the protonation states of the $[Ru_4(\mu$-$O)_4(\mu$-$OH)_2(H_2O)_4]^{4+}$ core. Repeated acid-base titration in both directions monitored both by pH and the UV-visible spectra indicate that **(1)** has 2 pK_a values in the pH range 3.5-4.5 and these titrations are reversible. Cyclic voltammograms (CVs) of aqueous solutions of **(1)** are pH dependent. At pH 1.0, two oxidation peaks at ca. 940 and at 1050 mV are observed in a scan from the rest potential (800 mV) to positive potentials and corresponding reduction peaks at ca. 750 and 965 mV are observed on the reverse scan. The currents at 950-1050 mV are several-fold higher in the presence of less than 1 mM of **(1)**, consistent with electrocatalytic H_2O oxidation at these unusually low potentials, which motivated us to evaluate **(1)** as a catalyst for homogeneous H_2O oxidation in aqueous solution.

The test reaction for H_2O oxidation was the well-studied model reaction: $4 [Ru(bipy)_3]^{3+} + 2 H_2O \rightarrow 4 [Ru(bipy)_3]^{2+} + O_2 + 4 H^+$ (employing the Ru(III) bipyridine complex as a chemical oxidation agent). A CV of $[Ru(bipy)_3]^{2+}$ at pH 7.0 shows reversible behavior ($E_a = 1100$, $E_c = 940$ mV, and $I_a/I_c \sim 1$), and this potential is higher than both the most pos-
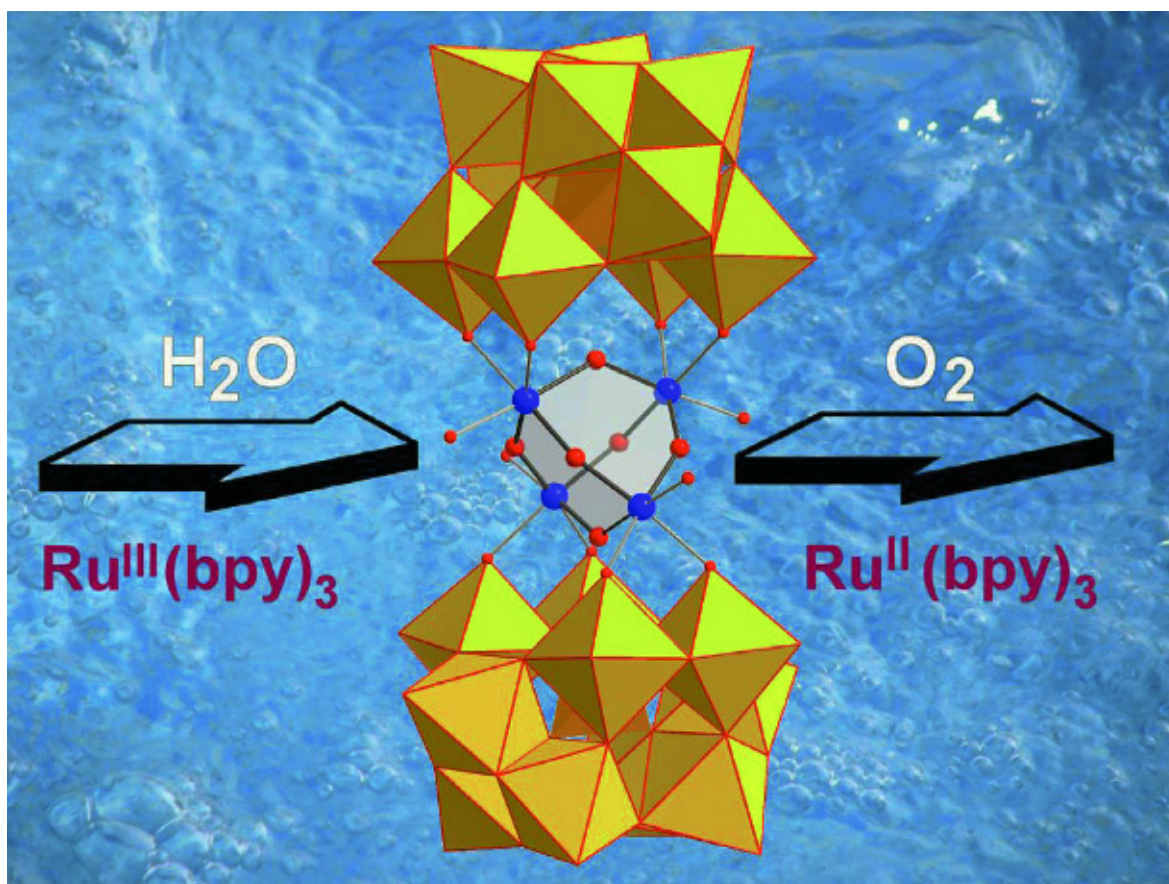
FIG. 1: Scheme of the water oxidation catalyst $\left[\{Ru_4O_4(OH)_2(H_2O)_4\}(\gamma-SiW_{10}O_{36})_2\}\right]^{10-}$. Ru: blue spheres, O: red spheres, tungstate units: yellow polyhedra.

itive peak observed for **(1)** (at pH 1.0) and the standard potential for the 4-electron oxidation of H_2O to O_2 (E^0 = 0.82 V at pH 7). At a very low concentrations of **(1)** (several μM), catalytic currents are observed at potentials corresponding to the oxidation of $[Ru(bipy)_3]^{2+}$ to $[Ru(bipy)_3]^{3+}$, where the peak current increases almost linearly with the concentration of **(1)**. An increase in the anodic peak is accompanied by a complete disappearance of a cathodic peak.

These electrochemical findings led us to investigate catalysis of the model reaction by **(1)**, monitored spectrophotometrically (determining the accumulated $[Ru(bpy)_3]^{2+}$) and chromatographically (detecting formed O_2). In the absence of **(1)** the typical reaction time, $\tau_{1/2}$ is > 30 min. Addition of very small amounts of **(1)** (0.5 to 1.5 μM) considerably shortens the reaction time. Furthermore, experiments performed in ^{18}O-labelled water prove that H_2O is not only the solvent but also the source of oxygen atoms in the produced O_2. Although the kinetics of H_2O oxidation catalyzed by **(1)** are complicated, possibly indicating multiple intermediates, several observations (fully reversible acid-base titrations, reproducible CVs, catalytic turnover numbers) suggest that **(1)** remains intact in many oxidation states in neutral aqueous solutions.

In summary, we document an all-inorganic catalyst with long-term stability for rapid H_2O oxidation to O_2 that is operational in H_2O under ambient conditions. Work is ongoing to integrate this system into photochemical cells.

[1] S. W. Gersten, G. J. Samuels, T. J. Meyer, *J. Am. Chem. Soc.* **1982**, 104, 4029–4030.

[2] J. K. Hurst, *Coord. Chem. Rev.* **2005**, 249, 313–328.

[3] A. R. Howells, A. Sankarraj, C. Shannon, *J. Am. Chem. Soc.* **2004**, 126, 12258–12259.

[4] Y.V. Geletii, B. Botar, P. Kögerler, D.A. Hillesheim, D.G. Musaev, C.L. Hill, *Angew. Chem. Int. Ed.* **2008**, 47, 3896–3899.

Magnetic memory effect in the complex metallic alloy T-Al-Mn-Pd

M. Feuerbacher[1], M. Heggen[1], J. Dolinsek[2], J. Slanovec[3], Z. Jaglicic[3]

[1] IFF-8: Microstructure Research
[2] J. Stefan Institute, University of Ljubljana, Jamova 39, SI-1000 Ljubljana, Slovenia
[3] University of Ljubljana, Jadranska 19, SI-1000 Ljubljana, Slovenia

The Taylor-phase T-Al$_3$Mn, T-Al$_3$(Mn,Pd) and T-Al$_3$(Mn,Fe) series of complex intermetallic compounds, belong to the class of magnetically frustrated spin systems that exhibit rich out-of-equilibrium spin dynamics in the nonergodic phase below the spin–freezing temperature T_f. We observe a memory effect in these materials: the spin structure of the material stores information on isothermal aging steps carried out during zero-field cooling, which is detected by measuring the magnetization of the sample.

The most prominent example of magnetically frustrated systems are spin glasses (SGs). A SG is a site-disordered spin system that is frustrated and spatially disordered in the sense that the spins are positioned randomly in the sample. These two properties lead to highly degenerate free-energy landscapes with a distribution of barriers between different metastable states, resulting in broken ergodicity. Typical SGs are dilute magnetic alloys of noble metal hosts (Cu, Ag, Au) with magnetic impurities (Fe, Mn), the so-called canonical spin glasses. In this paper we show that pronounced broken-ergodicity phenomena are present also in a class of ordered complex intermetallic Taylor phases [1] T-Al$_3$Mn, T-Al$_3$(Mn,Pd) and T-Al$_3$(Mn,Fe).

We have investigated samples grown by means of the Bridgman technique. Compositions were Al$_{73}$Mn$_{27}$ for the binary basic phase and ternary extensions with Pd and Fe substituting 2, 4 and 6 at.% Mn. Magnetic measurements were conducted in a Quantum Design SQUID magnetometer equipped with a 50 kOe magnet, operating in the temperature range 2 – 300 K.

Fig. 1 shows low-temperature measurements of the magnetic susceptibility χ for samples with Pd contents between 2 and 6 at.% at constant field of 8 Oe. The curves show a pronounced maximum, the freezing temperature T_f, which represents the transition from the non-ergodic to the ergodic regime. Above T_f, the curves show regular Curie-Weiss behaviour typical for a paramagnetic state. Below T_f, the curves show splitting between the field cooled (fc) and zero-field cooled (zfc) susceptibility, which is a fingerprint behaviour of a SG. Similar curves are found for the binary T-phase and that containing Fe. The labels fc and zfc refer to the conditions under

which the sample was cooled down to the lowest temperature of the experiment, before the actual susceptibility measurement is taken. Under fc conditions, the sample is cooled down in a constant field, while under zfc conditions no field is present.
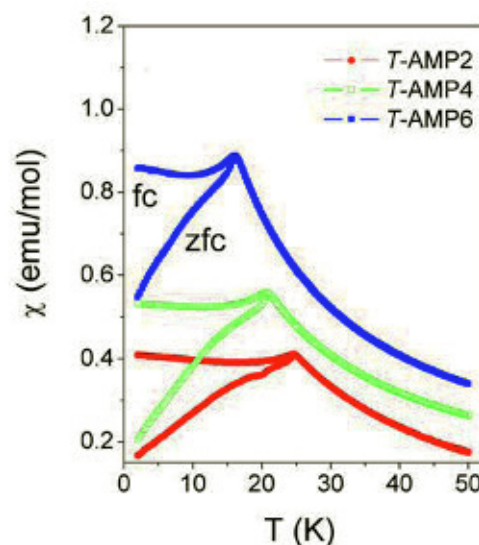
FIG. 1: Low-temperature susceptibility χ for samples with Pd contents of 2 (T-AMP2), 4 (T-AMP4), and 6 at.% Pd (T-AMP6) at constant field H = 8 Oe. Below the freezing temperature the shows clear splitting between the fc and zfc susceptibility, which is typical for a spin glass.

We have then carried out the following measuring procedure: The samples are zero-field-cooled continuously from the starting temperature of 100 K into the nonergodic regime with a cooling rate of 2 K/min. At a temperature T_a, cooling is temporarily stopped and the spin system is let to age isothermally for a certain time t_w, after which continuous cooling is resumed down to 2 K. At this temperature, a small magnetic field of 2 Oe is applied and the magnetization M is measured in a subsequent heating run to a temperature above T_f.

Fig. 2a shows corresponding magnetization measurements for the binary T-Al$_3$Mn sample [2]. Here the isothermal aging stop was carried out at T_1 = 12 K for t_w =10 min, 1 h, and 4 h. A reference run with no stop (t_w = 0) at T_1 was also performed. For nonzero aging times we find a dip in the magnetization, which
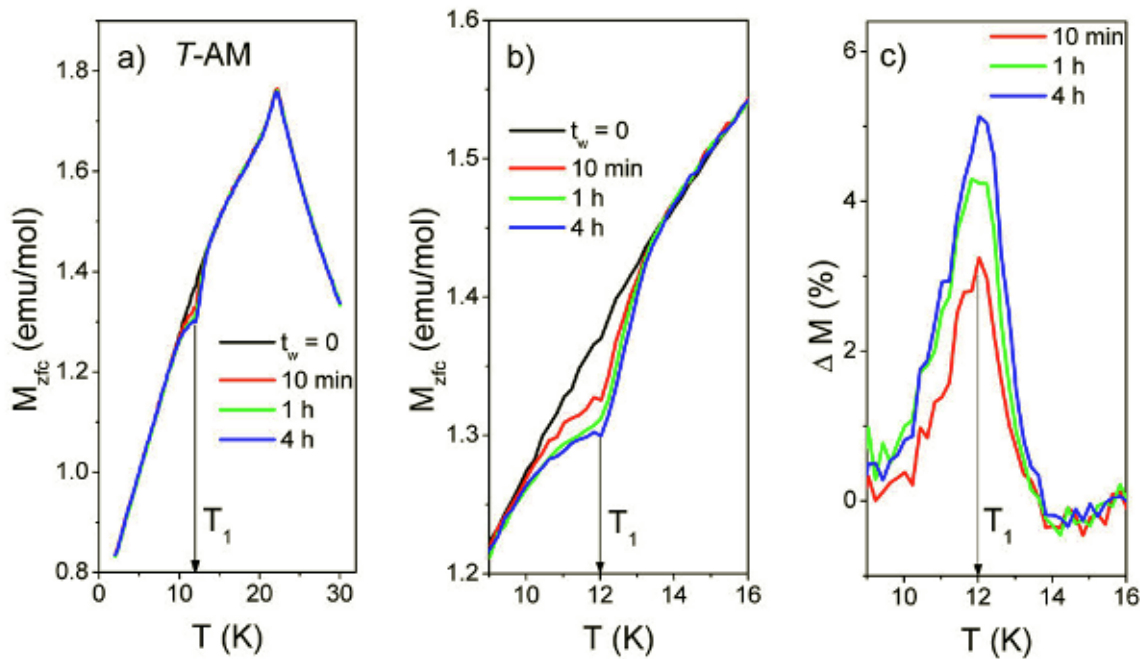
FIG. 2: The memory effect: if an isothermal aging step is carried out during zfc cooling, the magnetization shows a dip at the aging temperature, which increases in depth with annealing time.

is located at the aging temperature, and the depth of which increases with aging duration. The material is thus able to store information on the aging temperature and duration, which we refer to as memory effect (ME). Fig. 2b shows an expanded portion of the curves in the vicinity of T_1. In Fig. 2c, the normalized difference ΔM between the reference curve and the curves with aging is displayed. ΔM resembles a resonant curve, peaked at the aging temperature and smeared over a finite temperature interval of about ± 2 K.

Similar experiments were carried out on the T-phases containing Fe and Pd. In all cases we consistently find the signatures of the ME effect regardless of the differences in the samples composition and structure. The aging temperature T_a can be varied within the nonergodic regime, i.e. between 2 and 24 K for the present material. Aging at any temperature in this interval leads to a clear dip in the magnetization curve.

The memory imprint can be erased by a positive temperature cycle within the nonergodic regime. If the temperature is increased to about T_a+2 K the memory is erased, i.e. the spin system is rejuvenated. In a zfc experiment after a positive temperature cycle, the magnetization is again that of the unaged system with no memory imprint, corresponding to the reference curve with $t_w = 0$. Memory is erased thermally, regardless of the presence or absence of a small magnetic field. Any heating above T_f into the ergodic phase erases the memory as well. The spin system is ready to memorize isothermal aging again just after the memory has been erased by a positive temperature cycle within the nonergodic phase. Memory erase has no effect on the subsequent memory imprint.

The effects observed can be discussed in terms of a "spin-droplet model". During aging at T_a, the mobile spins at that temperature try to equilibrate in an energetically favourable configuration among themselves and with those spins already frozen. The degree of quasi-equilibration depends on the aging time the spin system is subjected to a given temperature under constant external conditions. In this way, quasi-equilibrated "spin droplets" are formed. Due to the predominant antiferromagnetic type coupling, the magnetization of the droplets tends to zero. Magnetically quasi-ordered spin droplets are in a more stable configuration than the rest of the spin-glass matrix, so that higher thermal energy is needed to reverse a spin within a droplet. Resuming continuous zero-field-cooling after the isothermal aging, magnetic order within the droplets is partially frozen, whereas weaker-coupled spins gradually freeze in a spin-glass configuration at lower temperature. At the lowest temperature of the zfc run, all spins with re-orientational energies differing from $k_b T_a$ are in a spin-glass configuration, whereas those with energies of about $k_b T_a$ form regions with more stable quasi-equilibrated configurations. In a subsequent heating run, the magnetization linearly builds up except in the vicinity of T_a, where higher thermal energy is needed to reorient the spins in the more stable quasi-ordered droplets, and consequently a diminution at T_a relative to the no-aging case is found.

[1] M. A. Taylor, Acta Cryst.. 14,1961, 84

[2] J. Dolinsek, J. Slanovek, Z. Jaglicic, M. Heggen, S. Balanetskyy, M. Feuerbacher, and K. Urban. Phys. Rev. B 77, 2008, 064430.

Al-Cr and ternary alloy systems of Al and Cr with Mn, Fe, Ni and Cu

B. Grushko[1], W. Kowalski[2], B. Przepiórzyński[1,2], D. Pavlyuchkov[1,3], S. Balanetskyy[1,3], M. Surowiec[2]

[1] IFF-8: Microstructure Research
[2] Institute of Materials Science, University of Silesia, Katowice, Poland
[3] I.N. Frantsevich Institute for Problems of Materials Science, Kiev, Ukraine

The Al-Cr constitutional diagram and those of Al-Cr with Mn, Fe, Ni and Cu were revised and completed. The study was carried out by a combination of powder XRD, DTA, SEM/EDX and TEM and concentrated on the Al-rich compositional regions in the temperature range up to 1100°C.

Apart from commercial importance of Al-based alloys containing Cr and other transition metals, they have a scientific interest because of formation their structurally complex intermetallics. Because of controversies in the literature, the Al-Cr phase diagram was reinvestigated in the range up to 50 at.% Cr. Apart from the earlier reported $Al_{45}Cr_7$ (θ), $Al_{11}Cr_2$ (η) and Al_4Cr (μ) phases a new ν-phase structurally similar to triclinic $Al_{11}Mn_4$ was revealed at about Al_3Cr composition. Only one high-temperature (γ_1) and one low-temperature (γ_2) phase were revealed in the compositional range between about 30 and 42 at.% Cr. The γ_2-phase has a rhombohedrally distorted γ-brass structure with α $<90°$ continuously varying with the composition. It exhibited twin-oriented domains which, in turn, consisted of the second-order twins. At 36 at.% Cr and below very fine and periodically arranged stripes were revealed in γ_2, which resulted in additional reflections in the corresponding electron diffraction patterns. The compositional and temperature ranges of stability of the above mentioned phases were specified (see Fig. 1 [1, 2]). No stable orthorhombic structure with $a\approx3.46$, $b\approx2.00$ and $c\approx1.24$ nm related in the literature to either $Al_{45}Cr_7$ or $Al_{11}Cr_2$ or Al_4Cr was confirmed in Al-Cr, but this so-called ε-phase was revealed close to Al_4Cr in ternary alloys containing a few at.% of Fe or Ni (see below) or Pd.

The Al-Cr-Mn phase diagram was investigated between 60 to 100 at.% Al and 560 to 1010°C [3]. Continuous ternary solid solutions were confirmed between the isostructural binary μ-Al_4Cr and μ-Al_4Mn phases, between the low-temperature $Al_{11}Mn_4$ and Al_3Cr ν-phases, between the high-temperature γ_1-phases and between the low-temperature γ_2-phases. The range of the Al-Cr θ-phase was found to extend up to 7.3 at.% Mn and that of the Al-Cr η-phase up to 15 at.% Mn. The dissolution of Mn decreases the melting temperatures of the θ-phase and η-phases. Of the Al-Mn phases, the high-temperature Al_3Mn phase (T-phase) dissolves up to 12.5 at.% Cr, λ-Al_4Mn up to 3 at.% Cr, Al_6Mn less than 1 at.% Cr, while $Al_{12}Mn$ (G-phase) up to 4.7 at.% Cr. The dissolution of Cr increases the melting temperatures of the λ-phase and G-phase. The compositional ranges of the phases apart from G and ν completely forming in the solid state are shown in the projection of the solidus surface of Al-Cr-Mn in Fig. 2.
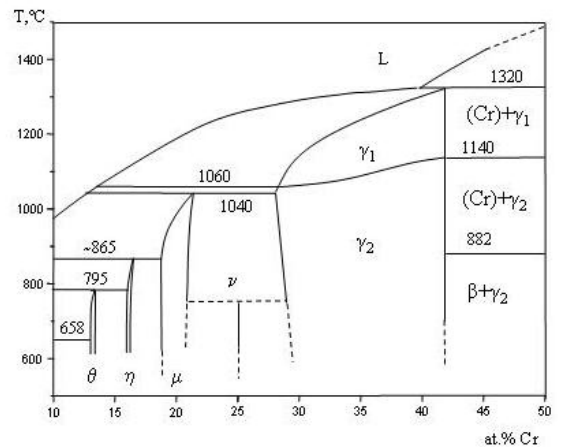
FIG. 1: Updated Al-rich part of the Al-Cr phase diagram.

In contrast to Al-Cr-Mn exhibiting extended solid solutions of binary intermetallics, in the other title systems the solubility of the third elements in the binary phases was quite limited. Instead, several ternary phases were observed in these alloy systems.

The Al–Cr–Fe alloy system was investigated at 700 to 1100°C in the compositional range above 60 at.% Al. Binary $Al_{13}Fe_4$, Al_5Fe_2 were found to extend up to 7 at.% Cr and Al_2Fe up to 4 at.% Cr. The dissolution of Cr in these binaries only slightly influences their Al concentrations. The high-temperature Al-Fe ε-phase and Al-Cr γ_1 probably form a continuous range of solid solutions. The Al–Cr η-phase dissolves up to 5 at.% Fe, which results in a sharp decrease of its Al concentration and increase of the melting temperature. A stable quasicrystalline decagonal phase was found around $Al_{72}Fe_{12}Cr_{16}$ [4]. It exhibits periodicity of ~1.2 nm along the 10-fold symmetry axis (D_3 structure). The decagonal phase was only produced after prolonged thermal annealing at subsolidus temperatures (max. 1090°C). Three ternary periodic phases: O_1, H and ε were also observed (see Table 1).
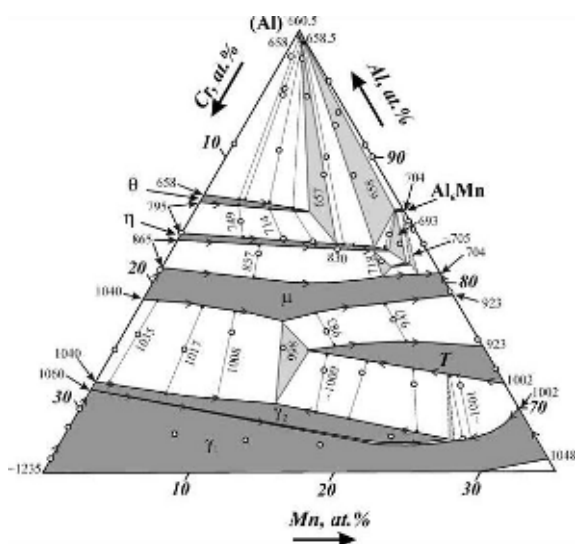
FIG. 2: Projection of the solidus surface of Al–Cr–Mn between 60 and 100 at.% Al.
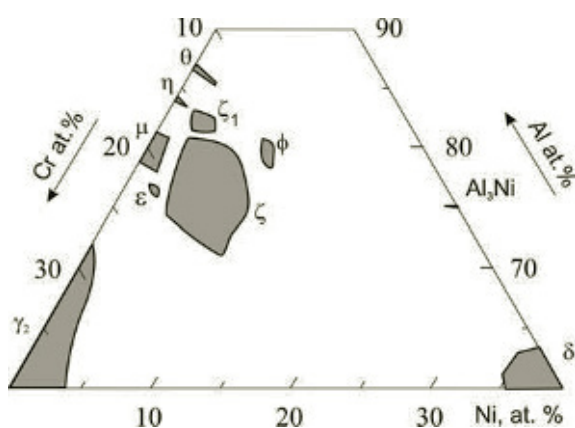
FIG. 3: Overall compositions of the Al-rich Al-Ni-Cr phases.

TAB. 1: Crystallographic data of the ternary phases in Al-Cr-TM (TM=Fe,Ni,Cu).

	S.G. or symmet.	Lattice parameters			
		a, nm	b, nm	c, nm	β, °
ε	$Cmcm$	1.27	3.46	2.04	-
H	hexag.	1.74	-	4.14	-
O_1	orthor.	3.27	1.24	2.34	-
ζ	$P6_3/m$	1.765	-	1.257	-
ϕ	$P2_1$	1.34	1.255	1.255	100
ζ_1	$R3$	1.77	-	8.04	-
κ	$F\bar{4}3m$	1.811	-	-	-
β	$Pm\bar{3}m$	0.298	-	-	-
φ	?	?	?	?	?
ψ	cubic	1.261	-	-	-
Λ	fcc	0.582	-	-	-

low 3 at.% of the third element. Four ternary periodic phases were revealed: the high-temperature ε-phase (as with Fe), ζ (as with Cu), ζ_1 and ϕ (see Table 1). Their compositional ranges are shown in Fig. 3.

[1] B. Grushko, B. Przepiórzyński, D. Pavlyuchkov, S. Mi, E. Kowalska-Strzeciwilk and M. Surowiec, J. Alloys Comp. **442**, 114-116 (2007).

[2] B. Grushko, B. Przepiórzyński and D. Pavlyuchkov, J. Alloys Comp. **454**, 214-220 (2008).

[3] B. Grushko, W. Kowalski, D. Pavlyuchkov, S. Balanetskyy and M. Surowiec, J. Alloys Comp. **468**, 87-95 (2009).

[4] D. Pavlyuchkov, S. Balanetskyy, W. Kowalski, M. Surowiec and B. Grushko, J. Alloys Comp. in press.

[5] B. Grushko, W. Kowalski, D. Pavlyuchkov, B. Przepiórzyński and M. Surowiec, J. Alloys Comp. **460**, 299-304 (2008).

95

The Al-Cu-Cr system was reinvestigated at 600 to 1000°C [1]. The total Al-Cr γ-range was found to extend up to 18 at.% Cu in its high-Cr limit. The $\gamma_2 \leftrightarrow \gamma_1$ transition temperatures decrease with the increase of the Cu concentration, together with a significant decrease of the melting temperatures. At 700°C the binary θ_{Cr}-phase exhibits visible solubility of Cu. The other Al-Cr phases dissolve only a little of the Cu. A ternary ζ-phase (see Table 1) is formed in a compositional range between $Al_{82}Cu_2Cr_{16}$, $Al_{75}Cu_4Cr_{21}$ and $Al_{71}Cu_{11}Cr_{18}$. The high-temperature β-phase exists around $Al_{46}Cu_{36}Cr_{18}$ between $\sim$906°C and $\sim$815°C. Below 842°C a κ-phase was observed between about $Al_{65}Cu_{15}Cr_{20}$ to $Al_{58}Cu_{26}Cr_{16}$. The φ-phase is formed around $Al_{70.5}Cu_{18}Cr_{11.5}$ and ψ-phase around $Al_{65}Cu_{25}Cr_{10}$. Below 638°C the Λ-phase was revealed around $Al_{61}Cu_{35.5}Cr_{3.5}$.

The region of Al-Ni-Cr above 60 at.% Al was specified at 900 to 1150°C [5] and more recently at 700 to 900°C. In total, the ternary extensions of the binary Al-Cr and Al-Ni phases were found to be be-

Complex intermetallic phases in the Al-Pd-Ru and Al-Pd-Ir alloy systems

B. Grushko[1], D. Pavlyuchkov[1,2], T. Ya. Velikanova[2]

[1] IFF-8: Microstructure Research
[2] I.N. Frantsevich Institute for Problems of Materials Science, Kiev, Ukraine

Basing on the updates of the Al-Ru and Al-Ir constitutional diagrams the Al-rich parts of the Al-Pd-Ru and Al-Pd-Ir constitutional diagrams were determined in the temperature range up to 1100°C. The study was carried out using powder XRD, DTA, SEM/EDX and TEM. Both alloy systems exhibit formation of complex intermetallic phases.

Known to date binary and ternary alloy systems of aluminum with platinum metals (Ru, Rh, Pd, Os, Ir and Pt) usually contain structurally complex intermetallics, including stable ternary quasicrystals (see [1] for references). The title ternary alloy systems, studied for the first time, are linked to either Al-Pd-Fe (Ru and Fe belong to the same column in the periodic table) or Al-Pd-Co and Al-Pd-Rh (Co, Rh and Ir belong to the same column in the periodic table) previously also studied in FZJ [1].

Basing on the updated Al-Ru constitutional diagram (see in [1]), the partial isothermal sections of Al-Pd-Ru were determined at 1000, 1050 and 1100°C in [2] and completed with the partial isothermal sections at 790 and 900°C. The latter is presented in Fig. 1.
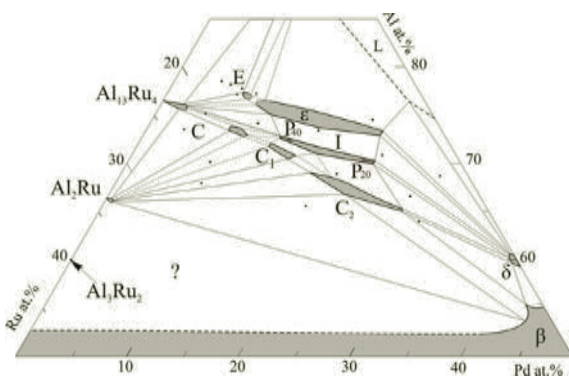
FIG. 1: Partial isothermal section of Al-Pd-Ru at 900°.

The isostructural binary AlPd and AlRu phases form a continuous β-range of the CsCl-type solid solutions. A number of ternary phases were revealed. Between 66 and 75 at.% Al, three structurally related cubic phases: C (primitive, a=0.7757 nm), C_1 (bcc, a=1.5532 nm) and C_2 (fcc, a=1.5566 nm) are formed. The same structures are also typical of the Al-Pd-Fe alloy system [1]. Although their compositional regions were somewhat different from those in Al-Pd-Fe, the "chain" arrangement of these regions and their sequence were the same in both these systems.
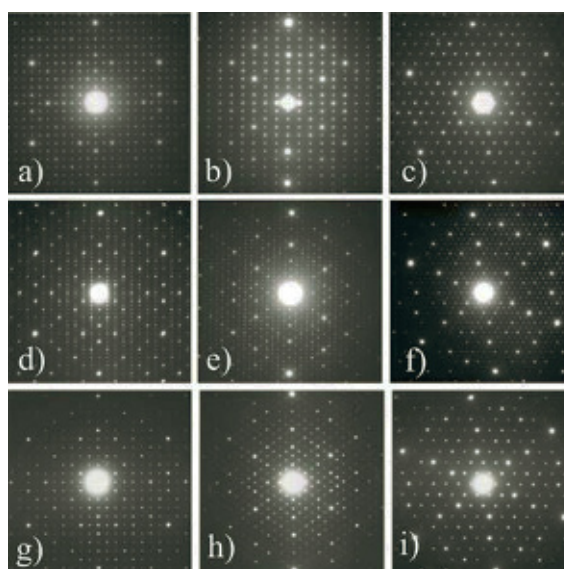
FIG. 2: Electron diffraction patterns of the: (a-c) P_{20}-phase, (d-f) P_{40}-phase and (g-i) F_{40}-phase [1] along the [1 0 0], [1 1 0], and [1 1 1] zone axes.

A stable icosahedral quasicrystalline I-phase is formed below 1080°C around the $Al_{71.5}Pd_{17}Ru_{12.5}$ composition. Similarly to that concluded for other Al-TM alloy systems [1], the stable ternary Al-Pd-Ru I-phase is actually a ternary extension of a metastable Al-Ru icosahedral phase stabilized by Pd. At nearby compositions complex cubic phases were observed (see Fig. 2): primitive P_{20} with the lattice parameter $a{\approx}2.0$ nm, P_{40} with $a{\approx}4.0$ nm and fcc F_{40} also with $a{\approx}4.0$ nm. Despite their definite periodicity, these phases exhibit powder X-ray diffraction patterns very similar to that of the quasiperiodic I-phase, and the phase boundaries between these periodic phases and the I-phase are not clearly detectable.

The complex ε-phases, also structurally related to quasicrystals, widely extend from "Al_3Pd" to ternary compositions. Similarly to that in Al-Pd-Fe or Al-Pd-Mn (see [1] for references), the orthorhombic ε_6, ε_{16}, ε_{22} and ε_{28} phases were observed. Their lattice parameters $a{\approx}2.34$ and $b{\approx}1.62$ nm are essentially the same, while the c parameters are ${\sim}1.23$, 3.24, 4.49 and 5.70 nm, respectively. Apart from these regu-

FIG. 3: Overall compositions of the Al-Pd-Co (a), Al-Pd-Rh (b) and Al-Pd-Ir (c) phases.

sicrystalline structure were revealed. These structures are formed in a small compositional region designated E in Fig. 1.

The Al-Ir phase diagram was specified in the range from 65 to 90 at.% Al [3]. At $\sim$1600°C the congruent $Al_{2.7}Ir$ phase forms a eutectic with the congruent AlIr phase. At higher Al concentrations four intermediate phases were found to be formed by a cascade of peritectic reactions: Al_3Ir at 1466°C, $Al_{28}Ir_9(\chi)$ at 1446°, $Al_{45}Ir_{13}$ (ϕ) at 993°C and Al_9Ir_2 at 877°C.

Basing on the updated Al-Ir constitutional diagram, the partial isothermal sections of Al-Pd-Ir were determined at 1100, 1000, 900 and 790°C [4]. As in Al-Pd-Ru, Al-Pd-Co and Al-Pd-Rh, the isostructural binary AlPd and AlIr phases (probably) form a continuous β-range of the CsCl-type solid solutions (see Fig. 3). The above-mentioned complex ε-phases extend from "Al_3Pd" up to 22 at.% Ir, i.e. almost up to the Al-Ir terminal. Also the Al_4Pd phase (λ-phase) dissolves up to 15.5 at.% Ir, which significantly increases its higher existence temperature limit. As a result, this phase only forming in Al-Pd in the solid state, can be in equilibrium with the liquid at its high-Ir concentrations. The C-phase, similar to that observed in Al-Pd-Ru at ternary compositions, is already forms in the binary Al-Ir alloy system (above-mentioned $Al_{2.7}Ir$) and it can dissolve up to 15 at.% Pd. The C_2-phase is also formed in Al-Pd-Ir at ternary compositions, while the C_1-phase was not observed in this alloy system. Instead, a hexagonal C_3-phase (a=1.09135, c=1.3418 nm), structurally related to the cubic C, C_1 and C_2 phases, was revealed. The ternary C_2 phase is also formed in Al-Pd-Co, while both C_2 and C_3 phases are formed in Al-Pd-Rh.

The overall compositions of the phases in the Al-rich parts of the Al-Pd-Co, Al-Pd-Rh and Al-Pd-Ir alloy systems are compared in Fig. 3. In contrast to Al-Pd-Ru, neither of these alloy systems contain stable quasicrystals. In Al-Pd-Rh the isostructural ε-phases form a continuous range of solid solutions between the binary terminals. Since in Al-Pd-Ir the Al-Pd ε-phases extend almost up to the Al-Ir terminal, this is plausible to suggest that the ε-phases are also typical of this binary alloy system. In contrast to Al-Pd and Al-Rh, in Al-Ir the ε-phases are metastable but are stabilized by only a few at.% Pd. In Al-Pd-Co the ε-phases "only" extend up to $\sim$16 at.% Co.

[1] B. Grushko and T. Velikanova, CALPHAD, **31**, 217-232 (2007).

[2] D. Pavlyuchkov, B. Grushko and T. Ya. Velikanova, J. Alloys Comp. **464**, 101-106 (2008).

[3] D. Pavlyuchkov, B. Grushko and T. Ya. Velikanova, Intermetallics. **16**, 801-806 (2008).

[4] D. Pavlyuchkov, B. Grushko and T. Ya. Velikanova, J. Alloys Comp. **453**, 191-196 (2008).

lar structures, also structures aperiodic along the c-direction were revealed at intermediate compositions. Thus, inside the wide ε-phase range only slight continuous variation of the orthorhombic a and b cell parameters are accompanied by complicated modulations of the c cell parameter.

The ε-range in Al-Pd-Ru broadens up to 15 at.% Ru. In Fig. 1 only its high-temperature part is shown: at lower temperatures it links to the Al-Pd terminal. At compositions close to the high-Ru limit of the ε-range the electron diffraction patterns of complex orthorhombic structures and one-dimensional qua-

97

Atomic structure of the interfaces in the SrTiO$_3$/Si(001) system

S. B. Mi[1,2], C. L. Jia[1,2], V. Vaithyanathan[3], L. Houben[1,2], J. Schubert[4,5], D. G. Schlom[3], K. Urban[1,2]

[1] IFF-8: Microstructure Research
[2] ER-C: Ernst Ruska-Centre for Microscopy and Spectroscopy with Electrons
[3] Department of Materials Science and Engineering, Cornell University, Ithaca, USA
[4] CNI: Center of Nanoelectronic Systems for Information Technology
[5] IBN-1: Semiconductor Nanoelectronics

The structure of the SrTiO$_3$/Si(001) interface is determined by means of aberration-corrected ultrahigh-resolution transmission electron microscopy. At the interface, a monolayer of SrO faces a terminating plane of silicon. In this monolayer, the strontium atoms lie above the face-center of four silicon atoms in the terminating plane, and the oxygen atoms are located directly above the terminating silicon atoms. This structure, which is the dominant type of interface structure observed in this system, agrees with one of the interface structures predicted by first principles calculations [1].

The search for suitable alternative gate dielectric materials to replace SiO$_2$ in microelectronic devices and to allow miniaturization to continue to follow Moore's law is an active research topic in the materials science community and the silicon-based semiconductor industry [2, 3]. SrTiO$_3$ has been touted as a promising candidate for this purpose due to its high dielectric constant (k=300) at room temperature and a relatively small lattice mismatch ($\sim$1.7%) with the silicon lattice if the SrTiO$_3$ unit cell is rotated by an in-plane rotation of 45° with respect to silicon [3]. This good lattice match also makes SrTiO$_3$ an excellent candidate for use as a buffer layer which could enable various functional oxide thin films, such as ferro-electrics and high-Tc superconductor thin films, to be integrated in epitaxial form into silicon substrates for various device applications. Establishing the electrical properties and stability of the SrTiO$_3$/Si interface is the key to these applications.

Several interface structure have been proposed after McKee and coworkers demonstrated that this SrO layer could be made as thin as a single monolayer [2]. The significant differences in band offsets among these proposed interfaces arise due to a multiplicity of interfacial structures proposed in theoretical studies. In contrast to the theoretical studies on the interface structure of SrTiO$_3$/Si, the experimental data on the interface structure is far from sufficient for clarifying the atomic structure. In particular, the atomic configuration that includes oxygen at the interfaces is unknown. Although efforts have been made to determine the structure of the interfaces,[2, 3, 4] the goal of directly imaging the interface on an atomic level (with respect to all of the atoms including oxygen at the interface) was still unrealised.

In this work, we investigate the interface structure of SrTiO$_3$/Si using aberration-corrected high-resolution transmission electron microscopy (HRTEM) and high-resolution scanning transmission electron microscopy (HRSTEM). The recently developed negative C_S imaging (NCSI) technique[5], in particular, allows us to image all types of atoms including chemical elements with a low atomic number such as oxygen. The NCSI technique thus has the potential of determining the full structural arrangement at the SrTiO$_3$/Si interface.
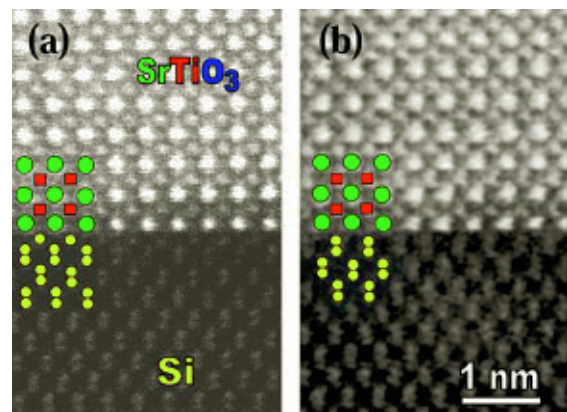
FIG. 1: AADF images of SrTiO$_3$/Si interfaces along $<110>_{Si}$. The atomic arrangement is denoted by colors: green: Sr; red: Ti; yellow: Si. (a) A plane of Sr(O) facing a silicon plane with a half dumbbell configuration. (b) A plane of Sr(O) facing a silicon plane with a full dumbbell configuration.

Figures 1a and 1b show STEM high-angle annular dark field (HAADF) images of the SrTiO$_3$/Si interfaces. The bright dots are strontium atoms, the less bright dots represent titanium, and the least bright ones are silicon. The starting atomic plane of SrTiO$_3$ on a silicon surface is the plane containing strontium in both Figs. 1a and 1b. The terminating plane of silicon, however, looks different. In Fig. 1a, the terminating plane shows a half-dumbbell character while in Fig. 1b, it exhibits a full-dumbbell character. In addition, the atom columns of silicon in the terminating plane are located in the middle below two columns of strontium in the starting plane of the SrTiO$_3$ in Fig. 1a and Fig. 1b. These two interface variants were frequently observed in the samples. In some cases, the two variants appeared across a surface step with a

height of one quarter of the silicon unit cell. Based on the HAADF image, it can be concluded that SrTiO$_3$ starts with the Sr(O) atomic plane.
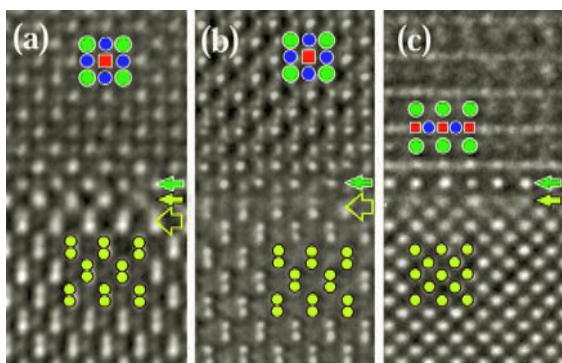
FIG. 2: *Phase contrast images showing the interfacial structure including oxygen. The atom columns are denoted by color symbols: green: Sr; red: Ti; blue: O: yellow: Si. (a) A <110>$_{Si}$ image of the interface showing an SrO plane (green arrow) facing a silicon plane with a half dumbbell configuration (thin yellow arrow). (b) A <110>$_{Si}$ image of the interface showing a SrO plane (green arrow) facing a silicon plane with a full dumbbell configuration (thick yellow arrow). (c) A <100>$_{Si}$ image of the interface.*

In order to solve the oxygen configuration at the interface, HRTEM performed on the SrTiO$_3$/Si interface using the NCSI technique. Under our experimental conditions, all atom columns along the viewing direction appear bright in the experimental image. Fig. 2a shows an interface where the lattice plane directly above the uppermost dumbbell is separated by about 0.138 nm, which matches the (004) plane spacing of silicon very well. Therefore, the atomic plane directly above the uppermost dumbbell can be concluded to be the terminating plane of silicon. The lattice spacing between the SrTiO$_3$ starting layer and the uppermost silicon is about 0.194 nm. The value of the spacing was calibrated using the lattice parameter of Si. We note that in the interface area the contrast for oxygen is visible in the plane (green arrow) directly above the silicon terminating plane (thin yellow arrow). Fig. 2b shows an interface where SrO is the starting plane of the SrTiO$_3$ film directly above the uppermost dumbbell (thick yellow arrows). The lattice spacing between the starting layer and the uppermost silicon in this interface is also about 0.194 nm, which agrees well with the image in Fig. 2a. It should be noted that the interface structure in Fig. 2a is identical to that in Fig. 1a, and that Fig. 2b shows the same structure as Fig. 1b.

This interfacial structure was further investigated along the [100] direction of silicon. Fig. 2c shows an image of the interface recorded along the [100] direction of silicon (the [110] direction of SrTiO$_3$). The stacking of the atomic planes across the interface was determined by checking the atomic arrangement from both the top and bottom of the image of the interface. In Fig. 2c, the lattice planes down to the Sr-O plane marked by a green arrow are in the SrTiO$_3$ film and the planes up to the one marked by a yellow arrow belong to the silicon lattice. A spacing

of 0.196 nm was again obtained between the starting SrO plane and the terminating plane of silicon. This result is in excellent agreement with the images viewed along the <110> directions.

Based on the atom arrangement at the interface, the structures of the interfaces shown in Fig. 1 and Fig. 2, can be considered identical. The difference in interface structure observed in the images along the Si <110> was due to the different viewing directions: rotating of the sample imaged in Figs. 1a and 2a by 90° around the film normal results in the images in Figs. 1b and 2b. This interfacial structure was confirmed by the image in Fig. 2c which is a consequence of rotating the sample from <110> to <100> by 45° around the film normal. It can be concluded that in our SrTiO$_3$/Si system, the interface consists of a Sr-O plane connecting to the silicon plane. The strontium atoms are located above the face-center formed by four silicon atoms in the terminating plane. The oxygen atoms are located directly above the terminating silicon atoms. It is worth to mention that another interfacial structure was also observed but less frequently [1], which will not discuss in the present contribution.

By combining HAADF imaging with the NCSI technique, the interfacial structure of SrTiO$_3$/Si is determined, which agrees with the interface model with a full monolayer of SrO proposed by calculations based on density functional theory in ref. 4. This type of interfacial structure was shown to have lower energy in comparison to the structure with a half monolayer of SrO. The observed interfacial structure shows that the SrTiO$_3$ film wets the surface of the silicon substrate better, which results in improved epitaxy. This result agrees with our HRTEM study of the samples, in which atomically sharp interfaces were observed. Calculations indicated that the conduction band offset between SrTiO$_3$ and silicon at the dominant interface determined by our study is small[4] which means that this interface is not suitable for conventional transistors. Nonetheless, it could be interesting for other applications where a negligible band offset is desired, e.g. spin injection structures.

[1] S. B. Mi, C. L. Jia, et al., Appl. Phys. Lett. 93, 101913 (2008).

[2] R. A. McKee, F. J. Walker, and M. F. Chisholm, Phys. Rev. Lett. 81, 3014 (1998).

[3] K. J. Hubbard, and D. G. Schlom, J. Mater. Res. 11, 2757 (1996). C. J. Först, et al., Nature 427, 53 (2004).

[4] X. Zhang, A. A. Demkov, et al., Phys. Rev. B 68, 125323 (2003).

[5] C. L. Jia, M. Lentzen, and K. Urban, Science 299, 870 (2003).

High-resolution TEM studies of inorganic nanotubes and fullerenes

L. Houben[1,2], M. Bar Sadan[1,2], A. Enyashin[3], R. Tenne[4], G. Seifert[3]

[1] IFF-8: Microstructure Research
[2] ER-C: Ernst Ruska-Centre for Microscopy and Spectroscopy with Electrons
[3] Physikalische Chemie, Technische Universität Dresden, 01062 Dresden, Germany
[4] Materials and Interfaces Department, Weizmann Institute of Science, Rehovot 76100, Israel

Iterative refinement of aberration-corrected transmission electron microscopy images with advanced modelling and image calculation was used to study the atomic structure of inorganic nanotubes and inorganic fullerene-like particles. The atomic arrangement in the nanostructures gives new insights regarding their growth mechanism and physical properties of these nanomaterials, for which imminent commercial applications are unfolding.

The characterization of nanostructures down to the atomic scale becomes essential since physical properties are strongly related with it. Properties, like electrical conductivity, depend closely upon the interface between different phases or compounds inside the particle, or correlate sensitively with the atomic configuration of the nanoparticle. The characterization of individual nanostructures is possible today in direct imaging methods like aberration-corrected high resolution transmission electron microscopy (HRTEM).

The case of inorganic fullerene-like nanoparticles (IF) and inorganic nanotubes (INT) [1] makes a special case in this context for a number of reasons. First, these unique phases are truly stable only in the nanoregime, i.e. between a few to 100 nm. Second, the IF are ubiquitous among layered compounds so their discovery led to the birth of a new field in inorganic chemistry. Moreover, these structures already hold perspectives for current and future applications e.g. as solid lubricants, as additives in high strength and toughness nanocomposites as well as catalysts.

Here, advanced slectron microscopy was used combined with ab-initio calculations to reveal new details on inorganic nanostructures [2]. Regarding the smallest stable symmetric closed-cage structure in the inorganic system, a MoS_2 *nanooctahedron*, aberration-corrected microscopy allowed validating suggested ab-intio models. Structures diverging from the energetically most stable ones were found and correspond with the high energy synthetic route. The study of WS_2 *nanotubes* combined with modelling brings about new information regarding the chirality of each shells within a multishell tube and allows a refining of their previously unknown growth mechanism.

Sub-ångström resolution and direct atomic imaging in aberration-corrected HRTEM allowed validating the suggested atomic structure and stability range of the nanooctahedra. Due to their large sizes, the nanoparticle structure could not be calculated by full DFT code. Nevertheless, using an approximate model based on density functional based tight binding (DFTB) calculations [3] and MD annealing, striking correspondence between the experimental images and suggested models was established. An example is given in Fig. 1 which presents a comparison between suggested structures calculated by the DFTB method and experimental images taken under negative spherical abberration imaging (NCSI) conditions. Fig. 1b demonstrates the excellent fit with the apex structure of a calculated model with octahedral coordination of the light sulfur atoms, characteristic of one of the most energetically stable structures calculated by the DFTB method. The DFTB calculations have shown that small octahedral fullerenes of MoS_2 have metallic-like character of electronic density of states despite the semiconducting nature of the bulk and the nanotubular material [4]. The calculations suggest that octahedral MoS_2 and related WS_2 nanoparticles may demonstrate catalytic properties, similar to the respective nanosized bulk material or monolayered nanoplatelets deposited on a metal surface.
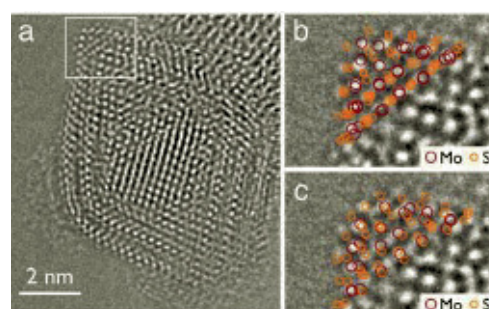
FIG. 1: (a) Atomic resolution image of a hollow multishell MoS_2 nanooctahedron taken in an image-side aberration-corrected FEI Titan 80-300 under NCSI conditions. (b), (c) Magnified part of the tip of the octahedron revealing the sulfur atoms at the surfaces with a superposition of two out of 15 hypothetical structures proposed in [4]. One of the most stable models with octahedral Mo-S coordination coincides (b) while the less stable structure fails to match (c). Taken from [2].
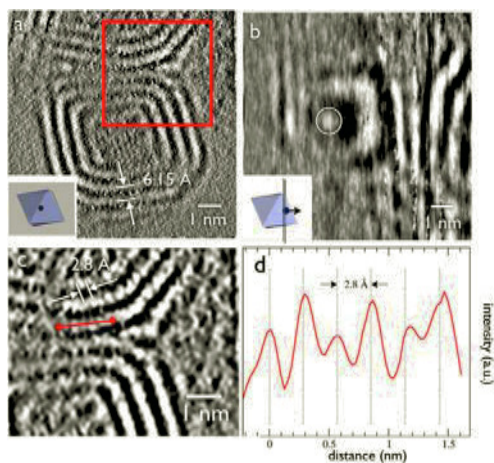
FIG. 2: Experimental tomogram of a MoS_2 nanooctahedron: (a) A slice in the xy plane containing the tilt-axis (b) A slice in the xz plane orthogonal to the tilt-axis. (c) A magnified part of (a), showing the resolved Mo-Mo distances, also presented in the line profile (d) along the marked arrow in c. Taken from [5].

High-resolution tomography techniques were developed further in order to study the symmetry of the nanostructures at high resolution [5]. The basis of the approach to atomic-resolution tomography is delocalisation-reduced phase contrast in an aberration-corrected TEM in combination with low voltage operation. Tilt series were taken at an acceleration voltage of 80 kV where the rate for knock-on radiation damage is significantly reduced compared to highe voltages, while a resolution of 2 Å can be maintained in a single image. The tomogram in Fig. 2 was reconstructed from a set of 22 experimental images with an angular step of $3°$. The nested shells with their smallest separation of 6.15 Å are reproduced in all of the slices, proving outstanding resolution in electron tomography.

The tomogram data showed that non-symmetric structures of less stability, unfavourable by calculation, are present in the experiment. Therefore it is evident that kinetics plays a major role in the synthetic process, supported by the presence of several other nanostructures in the soot as well. The reaction mechanism is still unknown, however it might be speculated that one of the building blocks of the nanooctahedra are the MoS_2 triangular monolayer.

The folding of sheets of WS_2 into single or multi-walled *nanotubes* may result in a multitude of hypothetical atomic coordinations, similar to their carbon counterparts. A basic question, which was raised in the past but could not have been answered, concerns the chirality of different shells in a single nanotube: Do the nanotubes consist of a single chirality (all the shells possess a single chiral angle) or could there be a situation where each shell acquires a different chiral angle than its adjacent ones. Here, advanced high-resolution TEM and STEM provide additional insight into the real space
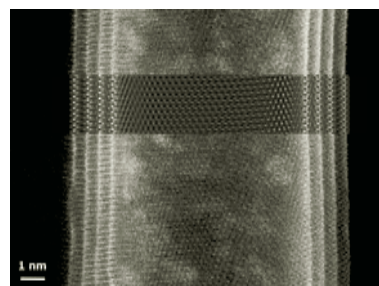
FIG. 3: HAADF-STEM image of a WS_2 nanotube taken in a probe-side corrected FEI Titan 80-300 microscope operated at 300 kV. Overlaid is the projected potential of a matching model of a 4-shell tube. Roll-up vectors and chiral angles: (4,92, 2.1°) (6,103, 2.8°) (5,115, 2.1°) (7,123, 2.7°). Taken from [2].

structure of individual nanotubes, complimentary to diffraction data and Moiré-based techniques. In particular, the real-space analyses of the chirality and the registry of the shells is aided.

Fig. 3 displays exemplarily a HAADF image of a four-shell WS_2-nanotube and for comparison the projected potential of a matching model structure. The roll-up vectors of all shells can be determined by refining the match between model and experiment.

In general, it was found that most of the tubes had a majority of non-chiral shells. In particular, the outer shells are of zig-zag or armchair type. This suggest that, although the growth front of the nanotubes is probably dictated by the chiral shell, it is embedded within armchair or zigzag shells. The reason would be the need to lower the energy and maintain the vdW distance of 0.62 nm between shells. The armchair or zigzag tubes are more easily adjusted to the required diameter since their roll up vector lies along the lattice base vectors. A refined growth mechanism for the nanotubes would include the growth of a chiral shell on which rings of WS_2 are threaded, producing concentring shells that form the multiwall nanotubes. The observation that the outermost shells are more likely of the trivial zig-zag or armchair type corroborates such computer models, refined by MD, for a simulation of a tensile stress-strain test on individual nanotubes [6]. The good correspondence between the model and the experimental work originates probably from the fact that the tensile force is applied on the outermost shell, which is in most cases a non-chiral one, therefore matching closely with the calculated models.

[1] R. Tenne, Nature Nanotechnology 1 (2006) 103.

[2] M. Bar Sadan et al., PNAS 105 (2008) 15643.

[3] G. Seifert, J. Phys. Chem. A, 111, 5609 2007.

[4] A. Enyashin et al., Angew. Chem.-Int. Ed. 46 (2007) 623.

[5] M. Bar Sadan et al., Nano Lett. 8 (2008) 891.

[6] I. Kaplan-Ashiri et al., PNAS 103 (2006) 523-528.

101

Reconstruction of the projected crystal potential in high-resolution TEM

M. Lentzen[1,2], K. Urban[1,2]

[1] IFF-8: Microstructure Research
[2] ER-C: Ernst Ruska-Centre for Microscopy and Spectroscopy with Electrons

The projected electrostatic crystal potential is reconstructed from a high-resolution exit wave function, which can be measured using wave function reconstruction techniques in transmission electron microscopy. Projected-potential reconstruction is achieved by maximum likelihood refinement from a model potential within the framework of electron chanelling. This work extends the maximum likelihood refinement to the case of electron scattering including phenomenological absorption, which is important in high-resolution transmission electron microscopy already for crystal thicknesses of a few nanometres. A simulation study assuming a YBCO crystal of several nanometres in thickness demonstrates a successful refinement for all atom columns, comprising a wide range of scattering power.

In high-resolution transmission electron microscopy information on the object under investigation can be derived from recorded image intensities or, by means of wave function reconstruction [1, 2, 3], from exit wave functions. Two processes, however, severely hamper the direct interpretation of image intensities or exit wave functions with respect to the object structure: 1. Dynamical electron scattering along atomic columns of a crystalline material leads in general to a non-linear relation between the atomic scattering power and the local modulation of the exit wave function. 2. Lens aberrations of the electron microscope impose phase changes on the wave function passing from the object plane to image plane and induce an unwanted contrast delocalisation [4].

The interpretation of reconstructed exit wave functions with respect to the object structure can be strongly improved by simulating the effects of dynamical electron diffraction using test object structures [5]. The simulation of microscopic imaging [5] can help in a similar way in the interpretation of experimentally recorded image intensities by injecting knowledge of imaging parameters, in particular lens aberration parameters. It is, however, highly desirable to find ways for the structure interpretation in high-resolution electron microscopy which do not rely on simulations of dynamical electron scattering and microscopic imaging with a possibly excessive number of test object structures.

The reconstruction of the projected crystal potential from an exit wave function is one of the ways to avoid tedious simulations, and it is the logical extension of already successfully implemented exit wave function reconstruction methods. The two reconstruction steps combined would lead from the recorded image intensities over the reconstructed exit wave function to the reconstructed projected crystal potential, and this measurement of the potential would allow a direct structure interpretation.

In the past decades few attempts have been made to solve the potential reconstruction problem for the case of thick objects including the effects of dynamical diffraction. In a first attempt by Gribelyuk [6] an estimate at the projected potential $U(\vec{r})$ was iteratively refined using forward multislice iterations [7] and evaluations of the difference between the simulated and the reconstructed exit plane wave functions, $\psi_{\mathrm{sim}}(\vec{r})$ and $\psi_{\mathrm{exp}}(\vec{r})$. In the second attempt by Beeching and Spargo [8] the same scheme was applied using reverse multislice iterations and comparing the respective entrance plane wave functions. Both attempts fail already at small specimen thickness, mostly due to improper use of the weak phase object approximation for the first estimate and for the correction steps.

The attempt by Lentzen and Urban [9] successfully solved the potential refinement problem within the least-squares formalism by implementing a search for the projected potential along the gradient of the figure of merit, $S^2 = \int |\psi_{\mathrm{sim}}(\vec{r}) - \psi_{\mathrm{exp}}(\vec{r})|^2 \, \mathrm{d}\vec{r}$, with respect to the potential. Together with use of the channelling model of electron diffraction [10, 11] a successful reconstruction of the crystal potential was achieved for non-periodic objects over a wide thickness range.

In this work the former treatment of Lentzen and Urban [9] has been extended to include phenomenological absorption, which turned out to be important already for thin objects of few nanometres in thickness. Accuracy and stability of the refinement algorithm are greatly improved by a new formulation for the gradient of S^2 with respect to the potential. If $\psi_{\mathrm{e}}(\vec{r}, t')$ denotes the difference of $\psi_{\mathrm{exp}}(\vec{r})$ and $\psi_{\mathrm{sim}}(\vec{r})$ being back-propagated through the object from the exit plane t to a plane t' inside the crystal, and if $\psi_{\mathrm{s}}(\vec{r}, t')$ denotes the entrance plane wave being propagated through the object from the entrance plane 0 to the

same plane t' inside the crystal, then

$$\delta U(\vec{r}) = \frac{1}{\pi \lambda t^2} \text{Im} \left\{ (1 - i\kappa) \int_0^t \psi_s^*(\vec{r}, t') \, \psi_e(\vec{r}, t') \, dt' \right\}$$

denotes the correction of the projected potential for each iteration step, with t the object thickness, λ the electron wavelength, and κ the phenomenological absorption parameter ranging from 0 to around 0.2.

Simulation studies assuming an $YBa_2Cu_3O_7$ crystal of several nanometres in thickness show that the use of the new gradient formulation improves the convergence of the refinement algorithm considerably in comparison to the use of the gradient presented in [9] for the case of absorption being present. The reconstruction algorithm is successful even at larger object thickness, where the exit wave function exhibits strongly differing modulations in amplitude and phase at the Y and Ba atom columns of strong scattering power, the Cu-O atom columns of medium scattering power, and the O atom columns of weak scattering power.

[1] H. Lichte, Ultramicroscopy 20 (1986) 293

[2] W. Coene, G. Janssen, M. Op de Beeck and D. Van Dyck, Phys. Rev. Lett. 69 (1992) 3743

[3] A. Thust, W.M.J. Coene, M. Op de Beeck and D. Van Dyck, Ultramicroscopy 64 (1996) 211

[4] W. Coene and A.J.E.M. Jansen, Scan. Microsc. Suppl. 6 (1992) 379

[5] P.A. Stadelmann, Ultramicroscopy 21 (1987) 131

[6] M.A. Gribelyuk, Acta Cryst. A47 (1991) 715

[7] J.M. Cowley and A.F. Moodie, Acta Cryst. 10 (1957) 609

[8] M.J. Beeching and A.E.C. Spargo, Ultramicroscopy 52 (1993) 243

[9] M. Lentzen and K. Urban, Acta Cryst. A56 (2000) 235

[10] K. Kambe, G. Lehmpfuhl and F. Fujimoto, Z. Naturforsch. A29 (1974) 1034

[11] F. Fujimoto, Phys. Status Solidi A45 (1978) 99

Quantification of the information limit of transmission electron microscopes

J. Barthel[1,2], A. Thust[1,2]

[1] IFF-8: Microstructure Research
[2] ER-C: Ernst Ruska-Centre for Microscopy and Spectroscopy with Electrons

The resolving power of high-resolution transmission electron microscopes is characterized by the information limit, which reflects the size of the smallest object detail observable with a particular instrument. We introduce a highly accurate measurement method for the information limit, which is suitable for modern aberration corrected electron microscopes. An experimental comparison with the traditionally applied Young's-fringe method yields severe discrepancies and confirms theoretical considerations according to which the Young's-fringe method does not reveal the information limit.

The resolving power of a high-resolution transmission electron microscope is ultimately limited by the degree of temporal coherence available for the imaging process. A fundamental benchmark parameter, which reflects the effect of the partial temporal coherence, and which is commonly used to characterize the performance of a high-resolution electron microscope, is the information limit. The information limit d_{info} corresponds to the size of the smallest object detail that can be imaged by the electron microscope in a linear way, and is defined by the spatial frequency $g_{info} = 1/d_{info}$ where the partial temporal coherence causes a contrast damping of $1/\mathrm{e}^2 \approx 13.5\%$ compared to the coherent contrast.

Since a long time the Young's-fringe test is used as a standard method to determine the information limit [1]. The Young's-fringe resolution test is based on the assessment of the Fourier power spectrum of an image taken from an amorphous object, which is often called a *diffractogram*, where one tries to identify the highest image frequency that can be undoubtedly discerned from detection noise. In order to distinguish the signal content from the detection noise, two separate images from the same object area are superimposed with a slight real-space displacement, either directly in experiment by a double exposure, or a-posteriori by digital methods. Due to the mutual real-space displacement, a sinusoidal Young's-fringe pattern appears in the diffractogram of the superimposed images, which helps to distinguish between transferred signal and detection noise (Fig. 1a).

A pragmatic approach to assess the information limit, which is often used due to the lack of a feasible alternative, is to equate simply g_{info} with g_{max}, where
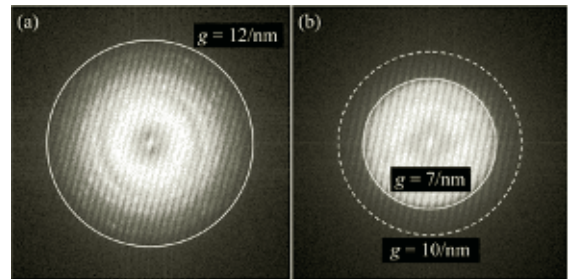
FIG. 1: (a) Young's fringe pattern recorded from thin amorphous tantalum using a FEI Titan 80-300 electron microscope operated at 300 kV accelearting voltage. The resulting Young's fringes extend up to a spatial frequency of 12/nm corresponding to a 0.8 Å spacing in the images. (b) Failure of the Young's fringe method. Despite the intentional limitation of the input object spectrum to 7/nm by an objective aperture, the resulting Young's fringes are observed up to 10/nm.

the latter frequency is the highest detectable signal frequency in a Young's-fringe pattern. However, this approach is flawed due to a multitude of reasons. Apart from the unjustified neglect of non-linear contrast contributions, which can potentially double the frequency spectrum, this method reveals only a net resolution restriction due to the cumulation of very different effects, such as the coherence properties, the object scattering-function, mechanical vibrations, and the modulation-transfer-function of the detector.

We present a new quantitative method, which allows one to measure directly and seperately the information limit of transmission electron microscopes from diffractograms of high-resolution micrographs [2]. The micrographs are recorded from thin amorphous objects under tilted illumination. Our measurement principle is based on the fact that large beam tilts cause an anisotropic deformation of the diffractogram damping envelope and the appearance of an additional "holographic" background contribution (Fig. 2). These two effects are primarily caused by the partial temporal coherence of the electron beam. The information limit is determined by fitting a model function based on a Gaussian focal distribution to the envelope and the background extracted from experimental diffractograms (Fig. 3).

We applied the present method to measure the information limit of two high-resolution transmission elec-
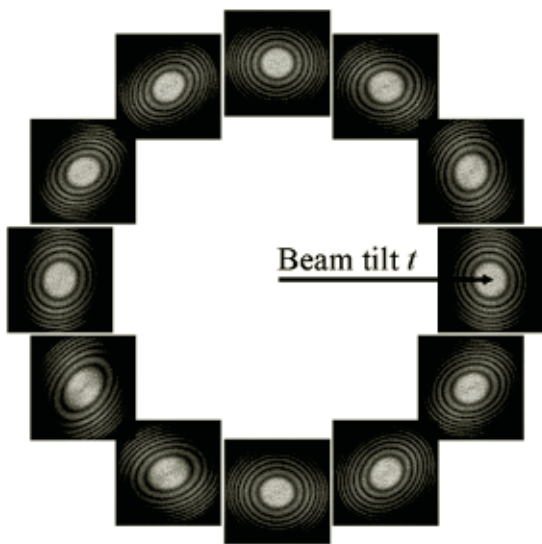
FIG. 2: *Series of diffractograms arranged according to the azimuth of the beam-tilt. The large-scale intensity anisotropy of the diffractograms due to the partial temporal coherence, rotating with the beam-tilt azimuth, is clearly visible.*
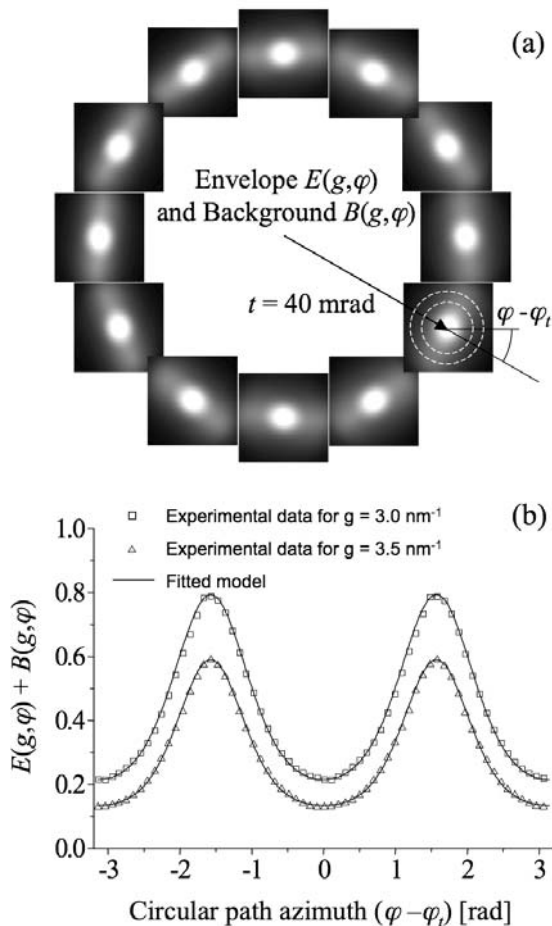
FIG. 3: *(a) Large-scale intensity variation extracted from the diffractogram series of Fig. 2. (b) Intensity profiles along the two selected circular paths marked in (a).*

tron microscopes installed at the Jülich Ernst Ruska Centre. These microscopes are a Philips CM200 operated at 200 kV accelerating voltage, and a FEI Titan 80-300 operated at 80 kV, 200 kV, and 300 kV. The respective measurement results are listed in Table 1 in comparison to the outcome of additionally performed Young's-fringe tests. In general, the information limit determined quantitatively by our new method differs significantly from the results of the traditional Young's-fringe method. The most prominent discrepancy is observed at 80 kV accelerating voltage: Whereas the traditional (and incorrect) interpretation of the Young's-fringe test leads to a seemingly good information limit near 1.1 Å, the value determined by the present method is 1.89 Å. We explain this drastic discrepancy by the fact that the nonlinear frequency-doubling effect is almost completely observable because the damping effects competing with the nonlinear frequency-doubling effect play a less significant role at the resolution achievable with 80 kV. The situation is different for 200 and 300 kV accelerating voltage. Here, only moderate to no differences occur between the two methods, which indicates that the above-mentioned competing effects are balanced by chance, hiding the principal weakness of the Young's-fringe method. With future improvements of the information limit towards 0.5 Å again a massive discrepancy can be expected between the two methods. In contrast to the method proposed here, the Young's-fringe method is then likely to yield a worse information limit than actually available because the attenuation effects not related to the coherence of the electron beam may hide a further improvement of the coherence properties.

In conclusion, complementary information about the resolution limitation of transmission electron microscopes is obtained by the traditional Young's-fringe method and the new approach presented here. The Young's-fringe method reveals qualitatively a kind of net resolution limit as a result of a mixing of several accumulating effects related to the object, to the microscope's optical transfer properties, to the camera, and to environmental influences. In contrast, our new approach allows us to isolate the resolution limiting effect caused by the partial temporal coherence and thereby to quantify precisely the information limit according to its theoretical definition.

Instrument	Info-limit	Young's fr.
FEI Titan (80 kV)	1.89($\pm$0.09) Å	≈ 1.1 Å
FEI Titan (200 kV)	1.11($\pm$0.01) Å	≈ 1.0 Å
FEI Titan (300 kV)	0.83($\pm$0.02) Å	≈ 0.8 Å
Philips CM200 (200 kV)	1.10($\pm$0.02) Å	≈ 1.3 Å

TAB. 1: *Information limit measured by the present method in comparison to results of Young's-fringe tests for two microscopes installed at the Ernst Ruska-Centre in Jülich.*

[1] J. Frank, Optik 44 (1976) 379.

[2] J. Barthel and A. Thust, Phys. Rev. Lett. 101 (2008) 200801.

Leak-rate of seals: comparison of theory with experiment

B. Lorenz, B. N. J. Persson

IFF-1: Quantum Theory of Materials

Seals are extremely useful devices to prevent fluid leakage. We present experimental results for the leak-rate of rubber seals, and compare the results to a novel theory, which is based on percolation theory and a recently developed contact mechanics theory. We find good agreement between theory and experiment.

A seal is a device for closing a gap or making a joint fluid tight. Seals play a crucial role in many modern engineering devices, and the failure of seals may result in catastrophic events, such as the Challenger disaster. In spite of its apparent simplicity, it is not easy to predict the leak-rate and (for dynamic seals) the friction forces for seals. The main problem is the influence of surface roughness on the contact mechanics at the seal-substrate interface. Most surfaces of engineering interest have surface roughness on a wide range of length scales[1], e.g, from cm to nm, which will influence the leak rate and friction of seals, and accounting for the whole range of surface roughness is impossible using standard numerical methods, such as the Finite Element Method.

In this paper we present experimental results for the leak-rate of rubber seals, and compare the results to a novel theory[2], which is based on percolation theory and a recently developed contact mechanics theory[3], which accurately takes into account the elastic coupling between the contact regions in the nominal rubber-substrate contact area. We assume that purely elastic deformation occurs in the solids, which is the case for rubber seals.

Consider the fluid leakage through a rubber seal, from a high fluid pressure P_a region, to a low fluid pressure P_b region. Assume that the nominal contact region between the rubber and the hard countersurface is rectangular with area $L \times L$. Now, let us study the contact between the two solids as we change the magnification ζ. We define $\zeta = L/\lambda$, where λ is the resolution. We study how the apparent contact area (projected on the xy-plane), $A(\zeta)$, between the two solids depends on the magnification ζ. At the lowest magnification we cannot observe any surface roughness, and the contact between the solids appears to be complete i.e., $A(1) = A_0$. As we increase the magnification we will observe some interfacial rough-
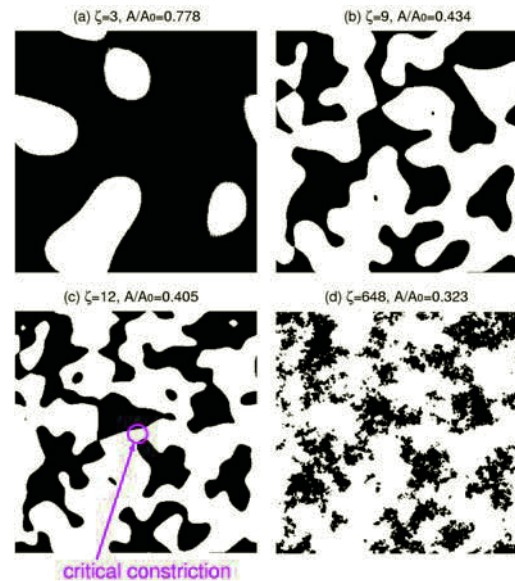
FIG. 1: *The contact region at different magnifications $\zeta = 3$, 9, 12 and 648, are shown in (a)-(d) respectively. When the magnification increases from 9 to 12 the non-contact region percolate. The figure is the result of Molecular Dynamics simulations of the contact between elastic solids with randomly rough surfaces, see Ref. [2].*

ness, and the (apparent) contact area will decrease. At high enough magnification, say $\zeta = \zeta_c$, a percolating path of non-contact area will be observed for the first time, see Fig. 1. The most narrow constriction along the percolation path, which we denote as the *critical constriction*, will have the lateral size $\lambda_c = L/\zeta_c$ and the surface separation at this point is denoted by $u_c = u_1(\zeta_c)$, and is given by a recently developed contact mechanics theory. As we continue to increase the magnification we will find more percolating channels between the surfaces, but these will have more narrow constrictions than the first channel which appears at $\zeta = \zeta_c$, and as a first approximation we will neglect the contribution to the leak-rate from these channels[2].

A first rough estimate of the leak-rate is obtained by assuming that all the leakage occurs through the critical percolation channel, and that the whole pressure drop $\Delta P = P_a - P_b$ occurs over the critical constriction [of width and length $\lambda_c \approx L/\zeta_c$ and height $u_c = u_1(\zeta_c)$]. Thus for an incompressible Newtonian
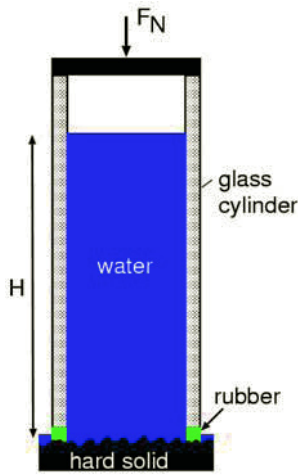
FIG. 2: *Experimental set-up for measuring the leak-rate of seals. A glass (or PMMA) cylinder with a rubber ring attached to one end is squeezed against a hard substrate with well-defined surface roughness. The cylinder is filled with water, and the leak-rate of the water at the rubber-countersurface is detected by the change in the height of the water in the cylinder.*

fluid, the volume-flow per unit time through the critical constriction will be

$$\dot{Q} = \alpha \frac{u_1^3(\zeta_c)}{12\eta} \Delta P, \qquad (1)$$

where η is the fluid viscosity. In deriving (1) we have assumed laminar flow and that $u_c << \lambda_c$, which is always satisfied in practice. In (1) we have introduced a factor α which depends on the exact shape of the critical constriction, but which is expected to be of order unity.

To complete the theory we must calculate the separation $u_c = u_1(\zeta_c)$ of the surfaces at the critical constriction. We first determine the critical magnification ζ_c by assuming that the apparent relative contact area at this point is given by site percolation theory. Thus, the relative contact area $A(\zeta)/A_0 \approx 1 - p_c$, where p_c is the so called site percolation threshold[?]. For an infinite-sized systems $p_c \approx 0.696$ for a hexagonal lattice and 0.593 for a square lattice[?]. For finite sized systems the percolation will, on the average, occur for (slightly) smaller values of p, and fluctuations in the percolation threshold will occur between different realization of the same physical system. We take $p_c \approx 0.6$ so that $A(\zeta_c)/A_0 \approx 0.4$ will determine the critical magnification $\zeta = \zeta_c$.

The (apparent) relative contact area $A(\zeta)/A_0$ and the separation $u_1(\zeta)$ at the magnification ζ can be obtained using the contact mechanics formalism developed elsewhere[3], where the system is studied at different magnifications ζ.

We have performed a very simple experiment to test the theory presented above. In Fig. 2 we show our set-up for measuring the leak-rate of seals. A glass (or PMMA) cylinder with a rubber ring (with rectangular cross-section) attached to one end is squeezed against a hard substrate with well-defined surface
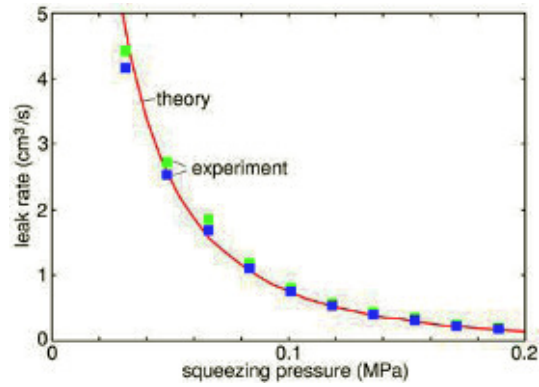
FIG. 3: *Square symbols: the measured leak rate for ten different squeezing pressures. Solid line: the calculated leak rate using the measured surface topography and the measured rubber elastic modulus.*

roughness. The cylinder is filled with water, and the leak-rate of the fluid at the rubber-countersurface is detected by the change in the height of the fluid in the cylinder. In this case the pressure difference $\Delta P = P_a - P_b = \rho g H$, where g is the gravitation constant, ρ the fluid density and H the height of the fluid column. With $H \approx 1$ m we get typically $\Delta P \approx 0.01$ MPa. With the diameter of the glass cylinder of order a few cm, the condition $P_0 >> \Delta P$ (which is necessary in order to be able to neglect the influence on the contact mechanics from the fluid pressure at the rubber-countersurface) is satisfied already for loads (at the upper surface of the cylinder) of order kg. In our study we use a silicon rubber ring with the Young's elastic modulus $E = 2.3$ MPa, and with the inner and outer diameter 3 cm and 4 cm, respectively, and the height 1 cm.

In Fig. 3 we show the measured leak rate for ten different squeezing pressures and for two differently prepared (but nominally identical) silicon rubber seals (square symbols). The solid line is the calculated leak rate using the measured rubber elastic modulus $E = 2.3$ MPa and the surface power spectrum $C(q)$ obtained from the measured surface roughness topography.

[1] See, e.g., B.N.J. Persson, O. Albohr, U. Tartaglino, A.I. Volokitin and E. Tosatti, J. Phys. Condens. Matter **17**, R1 (2005).

[2] B.N.J. Persson and C. Yang, J. Phys.: Condens. Matter **20**, 315011 (2008).

[3] C. Yang and B.N.J. Persson, J. Phys.: Condens. Matter **20**, 215214 (2008).

107

Theory of dendritic growth in the presence of lattice strain

D. Pilipenko, E. Brener, C. Hüter

IFF-3: Theory of Structure Formation

The elastic effects due to lattice strain are a new key ingredient in the theory of dendritic growth for solid-solid transformations. Both, the thermal and the elastic fields are eliminated by the Green's function techniques and a closed nonlinear integro-differential equation for the evolution of the interface is derived. We find dendritic patterns even without anisotropy of the surface energy required by classical dendritic growth theory. In this sense, the elastic effects serve as a new selection mechanism.

Solvability theory has been very successful in predicting certain properties of dendritic growth and a number of related phenomena. The solution of the two-dimensional steady state growth is described by a needle crystal, which is assumed to be close in shape to the parabolic Ivantsov solution [1]. If anisotropic capillary effects are included, a single dynamically stable solution is found for any external growth condition. The capillarity is a singular perturbation and the anisotropy of the surface energy is a prerequisite for the existence of the solution. In the case of isotropic surface energy, dendritic solution does not exist and instead the so-called doublon structure is the solution of the problem. Usually, the structural phase transitions in solids are accompanied by small lattice distortions leading to elastic deformations.

We discuss here the influence of elastic strain on dendritic growth in solids controlled by heat diffusion. Significant progress in the description of dendritic growth was made by the elimination of the thermal field using the Green's function technique. The crucial point of the present analysis is that the elastic field can also be eliminated by the corresponding Green's function technique. By these means, we derive here, as in the classical dendritic growth theory, a single integro-differential equation for the shape of the interface which takes into account elastic effects.

Thermodynamics of the model. Let us consider the growth of a new β-phase inside of an unbounded mother α-phase. We denote the characteristic lattice strain (also known as the stress-free strain tensor), associated with the phase transition, by ϵ_{ik}^0. The free energy density in the initial α-phase is

$$F_\alpha = F_\alpha^0(T) + \frac{\lambda}{2}\epsilon_{ii}^2 + \mu\epsilon_{ik}^2, \qquad (1)$$

where $F_\alpha^0(T)$ is the free energy density without elastic effects, which depends only on the temperature T, ϵ_{ik} are the components of the strain tensor, and λ and μ are the elastic moduli of isotropic linear elasticity. The free energy density of the growing β-phase is given by:

$$F_\beta = F_\beta^0(T) + \frac{\lambda}{2}\left(\epsilon_{ii} - \epsilon_{ii}^0\right)^2 + \mu\left(\epsilon_{ik} - \epsilon_{ik}^0\right)^2. \qquad (2)$$

Here, we neglect the difference between the elastic coefficients in the two phases. We also assume that the elastic effects are small i.e., $\epsilon_{ik}^0 \ll 1$. Since in our description the reference state for both phases is the undeformed initial phase, the coherency condition at the interface reads $u_i^{(\alpha)} = u_i^{(\beta)}$, where u_i is the displacement vector. Mechanical equilibrium at the interface demands $\sigma_{nn}^{(\alpha)} = \sigma_{nn}^{(\beta)}$ and $\sigma_{n\tau}^{(\alpha)} = \sigma_{n\tau}^{(\beta)}$, $\sigma_{ns}^{(\alpha)} = \sigma_{ns}^{(\beta)}$. Here indices n and (τ, s) denote the normal and tangential directions with respect to the interface. In the general case of curved interfaces, the surface energy γ has also to be incorporated, and the phase equilibrium condition for each interface point in the case of isotropic surface energy reads

$$\tilde{F}_\alpha - \tilde{F}_\beta - \gamma\kappa = 0, \qquad (3)$$

where κ is the local curvature of the interface. Because the forces act only at the interface, the strain field can be written as an integral over the interface surface.

Diffusional growth. For simplicity, we consider transitions in pure materials and assume that the heat diffusion constants are equal in both phases. We assume that the β phase is the low temperature phase. We introduce the dimensionless temperature field $w = c_p(T - T_\infty)/L$, where L is the latent heat, c_p is heat capacity, and T_∞ is the temperature in the α phase far away from the interface. The temperature field w obeys the following heat diffusion equation and boundary conditions

$$D\nabla^2 w = \partial w/\partial t, \qquad (4)$$

$$v_n = D\mathbf{n}(\nabla w_\beta|_{int} - \nabla w_\alpha|_{int}), \qquad (5)$$

$$w|_{int} = \Delta - d_0\kappa + T_{eq}c_p\delta\tilde{F}^{el}/L^2, \qquad (6)$$

where $d_0 = \gamma T_{eq} c_p / L^2$ is the capillarity length, κ is the curvature of the interface, which assumed to be positive for convex interfaces, D is the thermal diffusion constant, and T_{eq} is the equilibrium temperature for the flat interface without elastic effects i.e, it is determined by the condition $F_\alpha^0(T_{eq}) = F_\beta^0(T_{eq})$. We also introduce the dimensionless undercooling $\Delta = c_p(T_{eq} - T_\infty)/L$. The thermal field can be eliminated by using the Green's function techniques (see for example [3]), and consequently together with a proper Green's tensor $G_{ik}(\mathbf{r}, \mathbf{r}')$ for the elastic field, one can write a single integro-differential equation for the shape of the solid-solid interface [2].

Shear transition. Let us consider now a simple type of transition in hexagonal crystals involving the shear strain. For the transitions lowering the symmetry from C_6 to C_2 the shear strain in the basic plane appears. Let the principal axis C_6 be orientated in the z direction. Although the general approach presented above is valid in the three dimensional case, we assume from now on that the system obeys translational invariance in this direction, and thus, it is effectively two-dimensional. By proper choice of the crystal orientation around the main axis in the initial phase, we obtain the new phase in three possible states, having the following nonvanishing components of the strain tensor ϵ_{ik}^0:

$$\epsilon_{xx}^0 = -\epsilon_{yy}^0 = \varepsilon/2 \quad \epsilon_{xy}^0 = -\varepsilon\sqrt{3}/2, \tag{7}$$

Because the elasticity of hexagonal crystals is axisymmetric in the harmonic approximation and $\epsilon_{iz}^0 = \epsilon_{iz} = 0$, we can use the isotropic theory of elasticity i.e., expressions for free energy (1,2). The moduli of the effective isotropic elasticity, λ and μ, can be expressed in terms of the elastic constants of the original hexagonal crystal. Eliminating the thermal field, we obtain the steady state equation for the shape of the solid-solid interface [2] In the co-moving frame of reference, this equation reads:

$$\Delta - \frac{d_0 \kappa}{R} + \frac{T_{eq} c_p \delta \tilde{F}^{el}}{L^2} = \tag{8}$$

$$= \frac{p}{\pi} \int dx' \exp[-p(y(x) - y(x'))] K_0(p\eta),$$

where $\eta = [(x - x')^2 + (y(x) - y(x'))^2]^{\frac{1}{2}}$, and K_0 is the modified Bessel function of third kind in zeroth order, and $p = \upsilon R/2D$ is the Peclet number.

Let us introduce the shifted, due to the elastic hysteresis, undercooling:

$$\tilde{\Delta} = \Delta - \Delta_{el}, \quad \Delta_{el} = T_{eq} c_p E \varepsilon^2 / 8(1 - \nu^2) L^2.$$

The dimensionless parameter Δ_{el} describes the strength of the elastic effects. The relation between this shifted undercooling $\tilde{\Delta}$ and the Peclet number is given by the two-dimensional Ivantsov formula [1]: $\tilde{\Delta} = \sqrt{p\pi} \exp(p) \, \mathrm{erfc}(\sqrt{p})$.

Note that without elastic effects, this problem is equivalent to the classical dendritic growth problem with isotropic surface tension. The latter does not have a solution with angles $\phi \geq 0$ [5]. This statement

can be expressed in the following form. For any given positive values of the Peclet number p and the so-called stability parameter $\sigma = d_0/pR$, the symmetric solution which is close to the Ivantsov parabola in the tail region has an angle at the tip $\phi = f(\sigma, p) < 0$. The limit $\sigma = 0$ and $\phi = 0$ is a singular limit for that problem. For example, Meiron [4] calculated the angle ϕ as a function of σ for several values of the Peclet number with isotropic surface tension numerically and found that the angle $\phi < 0$ for any positive σ. Now, we discuss the numerical results obtained by the solution of Eq. (8) in the spirit of Ref. [4]. In the important regime of small Peclet numbers, the eigenvalue $\sigma = \sigma^*(\phi, \Delta_{el}, p)$ depends only on the ratio Δ_{el}/p for a fixed angle ϕ. While the strength of the elastic effects is assumed to be small, $\Delta_{el} \ll 1$, the control parameter Δ_{el}/p can be varied in a wide region in the limit of small p. The eigenvalue σ^* as a function of Δ_{el}/p for two values of the angle, $\phi = 0$ and $\phi = \pi/6$, is shown in Fig. 1. The situation with $\phi \approx 0$ is realized if $\gamma_b \ll \gamma$, while $\phi \approx \pi/6$ corresponds to $\gamma_b \approx \gamma$. The Poisson ratio was fixed to $\nu = 1/3$. The most remarkable feature of these results is that we do find dendritic solutions for the isotropic surface tension in the presence of the elastic effects. In this sense, the elastic effects serve as a new selection mechanism. We note that σ^* becomes large for large values of Δ_{el}/p, while in the classical dendritic growth σ^* is always small, being controlled by tiny anisotropy effects. Thus, the growth velocity, $\upsilon = 2D\sigma^* p^2/d_0$, can be much larger due to elastic effects, compared to the classical dendritic growth.
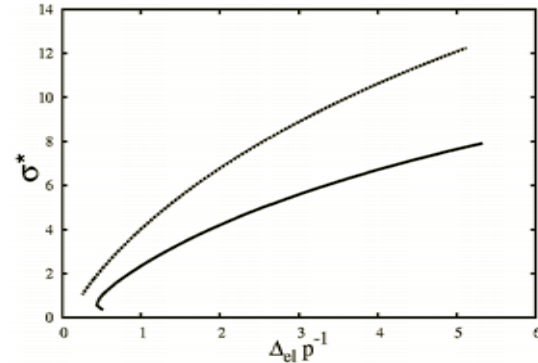
FIG. 1: Stability parameter σ^* versus Δ_{el}/p for two values of ϕ: the dashed line corresponds to $\phi = 0$, and the solid line corresponds to $\phi = \pi/6$.

[1] G. P. Ivantsov, Dokl. Akad. Nauk USSR **58**, 567 (1947)

[2] D. Pilipenko, E. Brener, C. Hüter, Phys. Rev. E **78**, 060603 (2008)

[3] J. S. Langer, Rev. Mod. Phys. **52**, 1 (1980)

[4] D. I. Meiron, Phys. Rev. A **33**, 2704 (1986)

[5] E. A. Brener, and V. I. Mel'nikov, Adv. Phys. **40** 53 (1991)

Crack growth by surface diffusion in viscoelastic media

R. Spatschek, E. Brener, D. Pilipenko

IFF-3: Theory of Structure Formation

We discuss steady state crack growth in viscoelastic media in the spirit of a free boundary problem. It turns out that mode I and mode III situations are very different from each other: In particular, mode III exhibits a pronounced transition towards unstable crack growth at higher driving forces, and the behavior close to the Griffith point is determined entirely through crack surface dissipation, whereas in mode I the fracture energy is renormalized due to a remaining finite viscous dissipation.

One of the central questions for any crack model is the role of dissipation, which is directly connected to the quest for selection mechanisms for a tip scale. The elastic loading, which is applied far away from the crack tip, is usually only partially used to create the (macroscopically visible) crack surfaces; especially for higher propagation speeds a microbranching instability can significantly increase the fracture energy [1]. This already indicates that the aspect of dimensionality is important for a full understanding of crack propagation, and we therefore investigate here different modes of loading. Although we have demonstrated that even pure dynamical linear elasticity can regularize the singular crack tip [2, 3], it is natural to assume that deviations from a pure elastic behavior can play a crucial role, which can also contribute to dissipation.

To address these important questions, we propose a description of crack propagation in the spirit of interfacial pattern formation processes by inclusion of viscoelastic effects. This picture goes beyond the usual small scale yielding that is frequently used in the modeling of brittle fracture and includes two dissipative mechanisms: First, there is dissipation directly at the crack surface; the incoming flow of elastic energy is partially converted to surface energy in order to advance the crack, and the remaining part is converted to heat. Second, an extended zone of viscous dissipation is formed around the crack. We note that this problem is quite complicated as the shape of the crack, its velocity and the distribution between viscous and interfacial dissipation have to be determined self-consistently.

For simplicity we assume that the system obeys a translational invariance in one direction, thus it is ef-fectively two-dimensional. We assume an isotropic linear viscoelastic medium, u_i and ϵ_{ik} are displacement and strain respectively. The total stress, $\sigma_{ik} = \sigma_{ik}^{(el)} + \sigma_{ik}^{(vis)}$, is decomposed into the elastic stress, which is given by Hooke's law (with elastic modulus E, Poisson ratio ν),

$$\sigma_{ik}^{(el)} = \frac{E}{1+\nu}\left[\epsilon_{ik} + \frac{\nu}{1-2\nu}\delta_{ik}\epsilon_{ll}\right], \qquad (1)$$

and the viscoelastic stress

$$\sigma_{ik}^{(vis)} = 2\eta\left[\dot{\epsilon}_{ik} - \delta_{ik}\dot{\epsilon}_{ll}/3\right] + \zeta\dot{\epsilon}_{ll}\delta_{ik}, \qquad (2)$$

which is related to the displacement rate through the viscosities η and ζ. Since we concentrate here on slow fracture with velocities far below the Rayleigh speed, the assumption of static viscoelasticity is legitimate, thus $\partial\sigma_{ik}/\partial x_k = 0$. On the crack contour, the total normal and shear stresses have to vanish, $\sigma_{nn} = \sigma_{ns} = 0$, with the interface normal and tangential directions n and s. The driving force for crack propagation is given by the chemical potential

$$\mu_s = \Omega(\sigma_{ij}^{(el)}\epsilon_{ij}/2 - \gamma\kappa), \qquad (3)$$

with γ being the interfacial energy per unit area and Ω the atomic volume; the interface curvature κ is positive for a convex crack shape. Surface diffusion leads to the following expression for the normal velocity at each interface point

$$v_n = -\frac{D}{\gamma\Omega}\frac{\partial^2\mu_s}{\partial s^2}, \qquad (4)$$

with the surface diffusion constant D (dimension m^4/s). Notice that $\tau_0 = 2\eta(1+\nu)/E$ defines a timescale, thus $(D\tau_0)^{1/4}$ defines a lengthscale parameter which ultimately leads to selection of the tip scale. We note that for steady state growth with velocity v, the last equation can be integrated once, and we obtain

$$vy = \frac{D}{\gamma\Omega}\frac{\partial\mu_s}{\partial s}. \qquad (5)$$

The strategy of solution is therefore as follows: First, for known crack shape, the total stress problem is solved by multipole expansion technique [3, 4]. Then, in the next step, the chemical potential (3) can be computed using Hooke's law. Finally, the steady state equation (5) is a nonlocal and nonlinear relation

which is used to determine a new guess for the crack shape and velocity. With them, the whole procedure is iterated until a self-consistent solution is found. We define a dimensionless driving force $\Delta = \Delta_I + \Delta_{III}$ where we already included the possibility of mixed-mode loading, and $\Delta = 1$ is the Griffith point. From now on, we set $\nu = 1/3$.
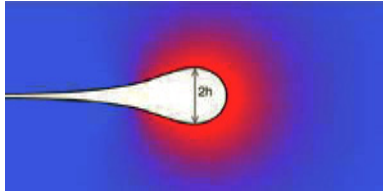

FIG. 1: Shape of a mode III crack for $\Delta = 2.5$ in the steady state regime. The total incoming elastic energy flux is converted into surface energy, surface dissipation and viscous bulk dissipation, which is localized to the scale $v\tau_0$ around the crack tip (visualized by the color coding)

Fig. 1 shows a typical steady state crack shape for mode III loading in the reference frame (Lagrangian coordinates), i.e. the elastic displacement is not included. First, we clearly see that the crack tip scale is selected self-consistently, and the finite time cusp singularity of the ATG instability does not occur. Therefore, the presence of viscous bulk dissipation is a way to cure this well-known problem. Second, it is important that far behind the crack tip the opening decays to zero, which is a consequence of mass conservation, as expressed by the equation of motion for surface diffusion (4). Diffusive transport is therefore restricted to the tip region, and no long-range transport is required. Qualitatively, the crack shapes for mode I look very similar.
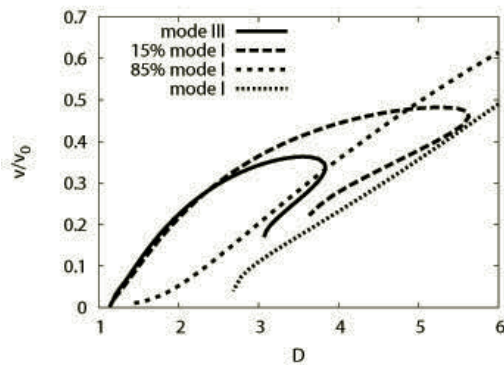
FIG. 2: Steady state propagation velocity as function of the driving force for pure mode III and mode I fracture. Additionally, mixed mode situations with $\Delta_I/\Delta = 0.15$ and $\Delta_I/\Delta = 0.85$ are displayed. The velocity scale is $v_0 = (D\tau_0^{-3})^{1/4}$.

The propagation velocity differs quite significantly for mode I and mode III fracture, as shown in Fig. 2: For mode III, the crack speed increases with the driving force, until it reaches a maximum at $\Delta \approx 3.5$, then it decreases, and obviously steady state solutions do not exist beyond the point $\Delta \approx 3.8$. There, the stable branch merges with another (unstable) solution

on which the tip curvature becomes negative. Beyond the bifurcation point we expect crack branching, in analogy to our findings for fast brittle fracture [2]. We note, however, that the scale of the critical crack speed is here not related to the Rayleigh speed.

Starting from a pure mode III crack, we can now include additional mode I loadings. Fig. 2 shows that this shifts the bifurcation point towards higher values and therefore extends the range of steady state solutions towards higher driving forces. Again, the crack blunts close to the 'nominal' Griffith point $\Delta = 1$. Simultaneously, the propagation velocity is significantly reduced in the regime of small Δ, as can be clearly seen in the comparison between the cases with 15% and 85% mode I contribution. Effectively, this establishes an interval of driving forces, where the crack speed is very low, and only after this plateau it sharply increases; this effect becomes more pronounced as the crack loading is more mode I dominated.

For the case of mode I, finally, steady state solutions do not exist below $\Delta = 2.6$; this result has to be interpreted as a limiting case with very slow creep with velocities and tip radii significantly lower than above the point $\Delta = 2.6$. Literally, of course, growth starts at $\Delta = 1$ due to energy conservation. The presence of this plateau is quite remarkable, as this effectively renormalizes the 'apparent' Griffith point – the driving force where the velocity starts to increase sharply – to a substantially higher value than $\Delta = 1$, although the viscous dissipation remains finite on the 'creep branch'. Again, the crack speed increases monotonically with the driving force, and the bifurcation to unstable growth occurs only at very high driving forces.

The obtained results lead to the striking conclusion, that the apparent Griffith point may depend quite substantially on the mode of loading. Although most models in the literature are discussed either in the mode I or mode III case only, we clearly see here that the behavior can be significantly different in these cases, as soon as bulk dissipation is taken into account. For the specific case of crack propagation in viscoelastic media we obtain that the onset of steady state growth is shifted towards higher values in mode I. It is therefore possible that local rotations or deformations of the crack front could lead to faster crack growth and a lower apparent Griffith point. We will leave this point, also in the context of the principle of local symmetry, open for future fully time-dependent three-dimensional investigations.

[1] J. Fineberg and M. Marder, Phys. Rep. **313**, 1 (1999).

[2] R. Spatschek, M. Hartmann, E. Brener, H. Müller-Krumbhaar, and K. Kassner, Phys. Rev. Lett. **96**, 015502 (2006)

[3] D. Pilipenko, R. Spatschek, E. A. Brener, and H. Müller-Krumbhaar, Phys. Rev. Lett. **98**, 015503 (2007)

[4] R. Spatschek, E. A. Brener, D. Pilipenko, Phys. Rev. Lett. **101**, 205501 (2008)

Polymerization study of 1-octene by a pyridylamidohafnium catalyst

A. Niu[1], J. Stellbrink[1], J. Allgaier[1], D. Richter[1], R. Hartmann[2], G. J. Domski[3], G. W. Coates[3], L. J. Fetters[4]

[1] IFF-5: Neutron Scattering
[2] ISB-3: Structural Biochemistry
[3] Department of Chemistry and Chemical Biology, Cornell University, USA
[4] School of Chemical and Biomolecular Engineering, Cornell University, USA

We assayed the polymerization of 1-octene in d_8-toluene polymerized by a pyridylamido-hafnium catalyst precursor activated by the co-catalyst tris(pentafluorophenyl)boron [1]. In-situ small angle neutron scattering (SANS) and ^{1}H-NMR spectroscopy were used together with time resolved size exclusion chromatography (SEC) to investigate the polymerization process. The catalyst system contains several polymerization active species. About 98% of the active catalyst is of uniform activity. The resulting polymers show relatively narrow molecular weight distributions. The residual catalyst exhibits an increased activity, leading to the formation of notably higher molecular weights than is generated by the majority of available active centers. With the help of NMR and SEC results the SANS data could be interpreted quantitatively on an absolute scale. Good agreement was found between the expected scattering profile for non-aggregated chains and their measured counterparts. At no stage during the polymerization process could more than single polymer chains be detected.

A facet of certain ionic metallocene catalysts is the capacity in olefin polymerizations to undergo self-assembly in hydrocarbons of the resulting propagating head groups. Mainly dynamic NMR techniques were used to study the aggregation behavior. In solvents like nonpolar aromatic hydrocarbons or moderately polar chlorinated hydrocarbons the ion aggregates take the generic form of $[LMR^+\text{- - -}X^-]_n$. M denotes Hf, Ti or Zr, n the average association state (2 or higher), L the ancillary ligand set and X the weakly coordinating anion. In the catalyst R represents an alkyl group while in the polymerizing state it is the growing polymer chain. It should be pointed out that in all previous cases catalysts, but not polymerizing systems, were investigated. Therefore it is not known to which extent the knowledge gained with the examination of the catalysts can be transferred to polymerization processes. The study of aggregation phenomena is not only interesting from the structural aspect since the aggregation state can significantly influence catalyst activity and polymerization behavior.

In our investigation 1-octene was chosen as the monomer since poly(1-octene) is soluble in toluene in the temperature range under investigation (-10°C and 20°C) irrespective of tacticity. The polymerization reactions carried out in the NMR and SANS instruments were performed in flame sealed cells since the catalyst system is highly sensitive to contamination with oxygen or water and the catalyst quantities for the experiments ranged from only 3 to 10 micromols. Fig. 1 shows the type of glass reactor used for the NMR sample preparation.

FIG. 1: Reactor fort the preparation of NMR samples.

In addition to the in-situ NMR and SANS studies, polymerization reactions were carried out in conventional glass reactors under the same conditions. Samples were taken at different reaction times and analyzed by SEC. Fig. 2 shows SEC chromatograms of some samples. All traces show two peaks, P1 and P2, which move to lower elution times or higher molecular weights with the ongoing polymerization. All signals for P1 show a low molecular weight tailing. The tailing event is not due to terminated polymer chains since the peak moves to higher molecular weights with reaction time. We assume that the tailing results from a retarded initiation process.

The molecular weight in the final sample of the polymer fraction represented by P1 corresponds to about 22,000 g/mol. This is approximately the value expected from the amounts of monomer and initiator for a termination free polymerization process. A quantitative analysis showed that 98% of the active catalyst initiates the chains represented by P1.

Accompanying the P1 component additional small signals of higher molecular weight P2 are visible. Their molecular weights are 6 – 7 times higher than those of P1. The trace of the final sample taken at 100 min shows a third peak at an elution time of about 12.5 min. This signal is hardly visible in the earlier chromatograms. In order to analyze the high molecular weight regions LS detection was used. This study revealed a small fraction of polymer having molecular weights up to more than 10^6 g/mol. Only about 2% of the active catalyst produces the material belonging to P2 or the high molecular weight product.

Time dependent monomer consumption was monitored by ^{1}H-NMR. The decrease of the vinyl proton signals between 5 and 6 ppm was used as a measure for the monomer concentration. In order to compare different spectra, intensities were normalized to the aromatic toluene signals at 7.2 ppm. For all measurements the logarithm of the normalized monomer concentrations $[M]_t/[M]_0$ drop linearly with time, showing the expected first order reaction kinetics. SANS experiments were performed at FRJ-
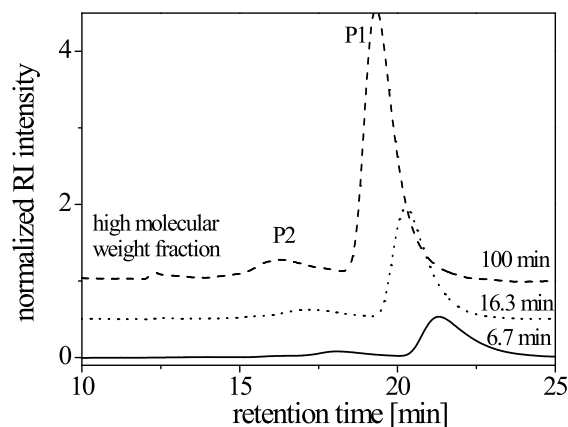
FIG. 2: SEC results using RI detection of samples taken at different reaction times.

2 research reactor, Forschungszentrum Jülich, Germany, using the instrument KWS-1. SANS is an ideal tool to investigate possible aggregation processes of the ionic head groups taking place during the polymerization event. In such a study it is necessary to compare the expected scattering profile of nonaggregating chains with the real SANS data of the growing chains. This requires the knowledge of polymer chain concentration and molecular weight as a function of time. This information can be extracted from in situ NMR data, by comparing signal intensities of the growing polymer and the initiating unit [2]. Additionally, a living process is required: In other words the number of growing chains is constant and no termi-

nation processes occur. In our present work two major polymerization processes with different rate constants take place simultaneously and the initiating units cannot be detected in NMR. Therefore time-resolved SEC was used as an additional method to measure molecular weights and relative amounts of each polymer fraction. If the NMR and SEC results
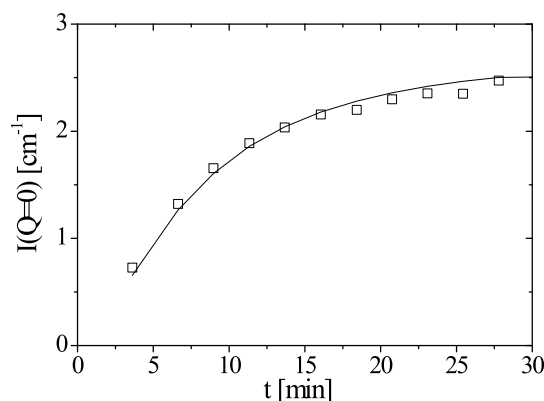
FIG. 3: SANS intensity I(Q=0) vs. reaction time. Solid line: Expected total SANS intensity from time-resolved SEC.

are used as an input for the SANS study there is a good agreement between expected scattering profile for non-aggregated chains and measured profiles, see Fig. 3. At all stages during the polymerization process isolated growing polymer chains were detected. Additionally, our work shows that less than perfectly living systems are useful for structural in situ studies. Also more complex polymerization processes, leading to more complex product mixtures, can be analyzed quantitatively. In the case of the 1-octene polymerization, we examined in this work, most of the monomer is converted into the main polymer product, having a relatively narrow molecular weight distribution. The overall mass fraction of higher molecular weight product is only about 11%. However, in terms of scattering intensity the products of higher molecular weights dominate, which complicates the SANS analysis. High molecular weight by-products are of relevance not only in scattering experiments. They can alter for example rheological properties dramatically and so have a crucial influence of the processing behaviour of polymers. But it should be pointed out that the SANS analysis can be carried out only with the additional information from NMR and SEC about molecular weights and distributions of the single polymerizing species. Such a time-resolved "multitechniques" approach will certainly help in the search for more efficient catalysts, optimization of reaction conditions and even clarification of reaction kinetics and mechanism in any polymerization process.

[1] A. Niu, J. Stellbrink, J. Allgaier, D. Richter, R. Hartmann, G. J. Domski, G. W. Coates, L. J. Fetters Macromolecules, accepted for publication.

[2] A. Niu, J. Stellbrink, J. Allgaier, L. Willner, A. Radulescu, D. Richter, B. W. Koenig, R. May, L. J. Fetters J. Chem. Phys. 2005, 122, Art. No. 134906.

Comparing MD-simulations and neutron scattering experiments of polymer melts

M. Brodeck [1], R. Zorn [1], F. Alvarez [2,3], A. Arbe [2], J. Colmenero [2,3,4], D. Richter [1]

[1] IFF-5: Neutron Scattering
[2] Centro de Física de Materiales, CSIC-UPV/EHU, San Sebastián
[3] Departamento de Física de Materiales, UPV/EHU, San Sebastián
[4] Donostia International Physics Center, San Sebastián

Due to its biocompatibility Poly(ethylene oxide) (PEO) is an important polymer in many applications such as cosmetics or polymer electrolyte in lithium-ion batteries. In order to learn in detail about the structure and dynamics we have performed fully atomistic molecular dynamics simulations. A comparison with neutron scattering experiments has allowed us to verify these simulations regarding structure, self-motion and collective motion of the atoms. After this validation an in-depth study of the simulated system was performed with a focus on its dynamic behavior in context of the Rouse model.

114

PEO is found ubiquitously in a variety of applications. One of the most important is its use as polymer electrolyte, but it can also be employed for many other very different purposes, like e. g. in the fields of cosmetics and pharmaceutics. Recently, this homopolymer has also drawn attention for its dynamic behavior in miscible blends with polymers of much higher glass transition temperatures T_g, like poly(methyl methacrylate) (PMMA) and poly(vinyl acetate) (PVAc). PEO has also been a focus of interest for studying confinement effects under different conditions, for example in nanocomposites. The proper characterization of the deviations from the bulk behavior of PEO under different confinement situations demands the detailed knowledge of the structural and dynamical properties of the neat polymer at a molecular scale. This can be provided by the combination of neutron scattering experiments and molecular dynamics (MD) simulations. The complementary use of these techniques has proven to be an extremely successful route to address a number of similar problems in the field of soft matter [1]. After the thorough validation of the MD-simulations by direct comparison with neutron diffraction data and results on the coherent and incoherent structure factors, we have addressed the question of the single chain dynamics of this flexible polymer and investigated the limits of applicability of the widely accepted Rouse model.

The simulations have been carried out using Materials Studio 4.1 and the Discover-3 module (version 2005.1) from *Accelrys* with the COMPASS forcefield. A cubic cell containing five polymer chains of 43 monomer units of ethylene oxide was constructed at 400 K under periodic boundary conditions, with a density fixed to be 1.0440 g/cm^3 (experimental value). Three temperatures (350 K, 375 K and 400 K) have been simulated (with the corresponding densities) for 200 ns each.

FIG. 1: The simulated system contains 5 PEO-chains with 43 monomers each. Periodic boundary conditions are applied during the simulation, the size of the cell is fixed.

The static structure factor of deuterated PEO as measured by neutron scattering has been compared with the simulation results and shows good agreement. A comparison of the protonated system has yielded similar agreements. With these results we have shown that the short-range order in PEO is well reproduced by our simulated cell. The dynamic properties of the simulated system have been compared in two different ways: the self-motion of hydrogen atoms is experimentally accessed by incoherent scattering functions, collective dynamics of the whole system are measured by the dynamic coherent structure factor.

The self-motion of the hydrogen atoms in the sample is seen in the experiment on hydrogenated PEO due to the high incoherent scattering cross section of hydrogen atoms. The comparison between neutron scattering and simulation results is accomplished through the intermediate scattering function $S_{inc}^H(Q,t)$. It can be computed from the simulations via a Fourier transformation of the corresponding radial probability distribution function into the Q-space:

$$S_{inc}(Q,t) = \left\langle \int_{-\infty}^{\infty} d^3 r e^{i\vec{Q}\vec{r}} G_{self}(\vec{r},t) \right\rangle_{\Omega} \quad (1)$$

A stretched exponential function with $\beta = 0.5$ can be used to describe both the simulated as well as the experimental data.

$$\phi_{KWW}(t) = A \exp\left[-\left(\frac{t}{\tau_W(Q,T)}\right)^\beta\right] \quad (2)$$

Experiments on hPEO have been performed at the instrument FOCUS (PSI, Time-of-Flight spectrometer), BSS (Jülich, High Resolution Backscattering Spectrometer) [2] and IN16 (ILL, Cold Neutron Backscattering Spectrometer). Figure 2 shows the almost perfect agreement between the timescales deduced from such a parametrization for all three temperatures.
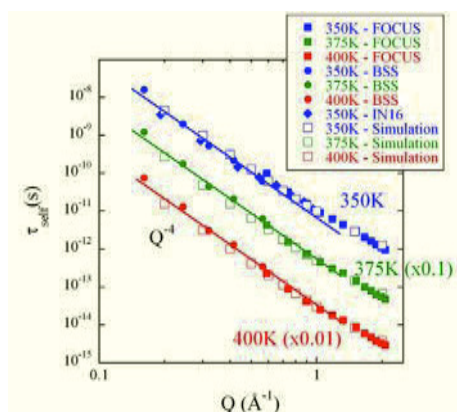
FIG. 2: Parameters of fits of stretched exponential functions to $S_{inc}^H(Q,t)$ for the simulated system (hollow symbols) and results from experiments (full symbols). For clarity the points for T=375 K and T=400 K have been scaled. The solid lines show Q^{-4} laws.

As mentioned above we have also checked the collective dynamics. For this analysis (deuterated PEO samples) we have used the neutron scattering instruments J-NSE (JCNS, Neutron Spin Echo) and TOFTOF (FRM-II, High Resolution Time-of-Flight Spectrometer). We can state that the collective dynamics of PEO are also well reproduced by the simulated cell.

After these critical checks of the reliability of the simulations we can calculate quantities which are not accessible experimentally. The Rouse model, which describes the behavior of polymer chains in a melt, starts from a Gaussian chain representing a coarse grained polymer model where springs stand for the entropic forces between hypothetic beads [3]. Important predictions are expressed in the behavior of so-called Rouse correlators that are defined within the model. Orthogonality and exponentiality of these Rouse modes are two main predictions and are the basis for the derivation of the correlators probing chain relaxation. These magnitudes can now be calculated directly using the simulations. We have chosen one monomer to represent one bead and found that the condition $|\langle \vec{X}_p(0)\vec{X}_q(0)\rangle| \ll 1$ for $p \neq q$ (orthogonality) is nearly always fulfilled. The Rouse correlators have been fitted with stretched exponential functions, results are shown in Figure 3.
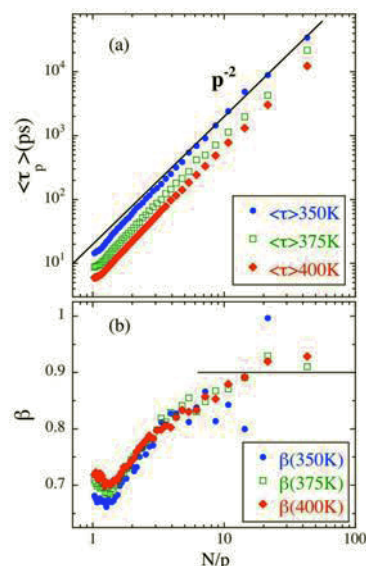
FIG. 3: Mode-wavelength dependence of the fitting parameters obtained for the KWW descriptions of the Rouse-mode correlators at the different temperatures investigated.

The upper figure displays the average relaxation time $\langle\tau\rangle = \tau_W \Gamma(1/\beta)/\beta$. Below this the stretching parameter β is shown in dependence of N/p and T. For smaller p the relaxation times show the expected $\propto 1/p^2$ behavior (solid lines display predictions of the Rouse model). For p-values above ≈ 20 the obtained mode relaxation tends to be faster than Rouse indicating that at wavelengths corresponding to about two to three beads the validity of the model is limited (due to local potentials). For small p the stretching parameters have values of $\beta \approx 0.9$ confirming an almost exponential behavior. Using the simulations it was also possible to independently extract the mode amplitudes. It was shown that the deviations occurring at larger mode numbers cannot be explained by a local stiffness alone but require a significant increase of the mode friction for higher mode numbers.

In summary, the MD simulation based on the COMPASS force field yield a quantitative agreement with quasielastic neutron scattering results establishing a quantitatively valid computer model for this important polymer.

[1] A.-C. Genix, A. Arbe, F. Alvarez, J. Colmenero, B. Farago, A. Wischnewski, and D. Richter, Macromolecules **39**, 6260 (2006).

[2] A.-C. Genix, A. Arbe, F. Alvarez, J. Colmenero, L. Willner, and D. Richter, Phys. Rev. E **72**, 031808 (2005).

[3] P. E. Rouse, A theory of the linear viscoelastic properties of dilute solutions of coiling polymers, Journal of Chemical Physics **21(7)**, 1272-1280, (1953).

115

Chain dynamics and viscoelastic properties of poly(ethylene oxide)

K. Niedzwiedz, A. Wischnewski, W. Pyckhout-Hintzen, D. Richter

IFF-5: Neutron Scattering

The chain dynamics and viscoelastic properties of poly(ethylene oxide) were studied covering a wide range of molecular weights and temperatures. Two experimental techniques were combined: rheology to study the large scale viscoelastic properties and neutron spin echo spectroscopy to investigate the chain dynamics on the microscopic level. The common parameter between the methods is the monomeric friction coefficient. We show that for all molecular weights and accounting for the molecular weight dependent glass transition temperature it can be consistently described by the Vogel-Tamman-Fulcher (VFT) temperature dependence.

Poly(ethylene oxide) (PEO) is a commodity product which finds applications in cosmetical, plastics and industrial sectors. Also, favourable interactions with clays or generally with nanocomposites makes PEO a model polymer for investigation. An interesting fundamental property is its ability to mix with other chemically different polymers. The most prominent example is PEO/PMMA where the wide separation in the glass transition temperature of the pure components leads to a dynamical heterogeneity although it is perfectly miscible. Here, we present a comprehensive and consistent study on the segmental dynamics and rheological properties for molecular weights between 1 and 930 kg/mol. The basic concepts, i.e. Rouse dynamics for the short un-entangled system and the reptation model for the long chain system apply both in the limiting cases for both techniques whereas again a systematic discrepancy in the size of the confinement is confirmed.

Measurements of the complex dynamic modulus were obtained from isothermal oscillatory shear over the full range of the rheometer and the time-temperature-superposition principle applied to the different temperatures in order to obtain a master-curve at the reference temperature $T_0 = 348K$. The shift factors follow the Williams-Landel-Ferry (WLF) equation with which the dynamic properties at any temperature T can be predicted. Neutron Spin echo (NSE) measurements were performed on blends of protonated and deuterated PEO and the single chain dynamic structure factor $S(q,t)/S(q,0)$ obtained. Experiments on the low molecular weight sample were done at the NSE spectrometer at FZJ, Jülich whereas the entangled species was investigated at the NSE instrument at NIST, USA.

The storage $G'(\omega)$ and loss modulus $G''(\omega)$ for the higher molecular weights were fitted using a phenomenological ansatz for the relaxation time spectrum. A plateau modulus, $G_N^0 = 1.28$ MPa emerged. This corresponds to an entanglement molecular weight of about 2.1 kg/mol, in good agreement with literature. From the loss peak maximum, the reptation time was extracted. Since contour-length fluctuations are in-effective at higher molecular weights, well-known microscopic relations between elementary times τ_e and τ_d can be applied in order to be used for the comparison with the short-time NSE results.
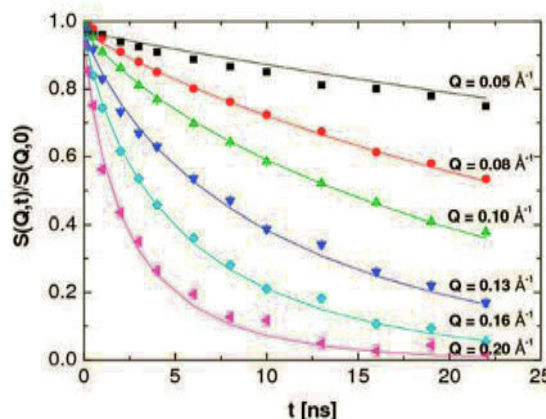
FIG. 1: NSE data for PEO with Mw=2.1 kg/mol at T=413K. Solid lines show the fit with the Rouse model.

From Fig 1 a very good fit to the Rouse model for un-entangled polymers to a low M_w is shown. For the higher M_w 80 kg/mol sample the Rouse model fails already from t=10 ns. The topological confinement due to entanglements leads to the much slower reptation motion. This can be identified clearly from Fig 2. For longer times the further relaxation is impeded and the structure factor displays plateaus. From their Q-dependence the size of the tube confinement of $d_t \sim 50A$ may be directly inferred.

An appropriate way to compare the dynamics is to focus on the monomeric friction coefficient which is a central quantity in both techniques as well as on the tube diameter and the plateau modulus. The

monomeric friction coefficient on the molecular level can be extracted directly from the Rouse regime in NSE for the unentangled polymer. For entangled polymers the situation is more complex and random walk statistics for the tube as well corrections for Rouse motion of the tube itself for the description of constraint-release have to be estimated if they are to be estimated from large scale viscoelastic properties. Fig. 3 clearly shows that the temperature dependence follows a single mastercurve and covers a wide range of temperatures and molecular weights. This can be theoretically described by the Vogel-Tamman-Fulcher (VFT) law using reasonable parameters.
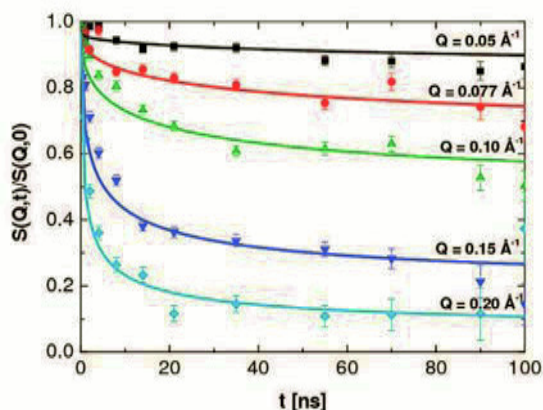
FIG. 2: NSE results for the 81 kg/mol sample, obtained at T=400K. The solid lines which correspond to the reptation model fit simultaneously for all Q and yield a tube diameter of roughly 50A.
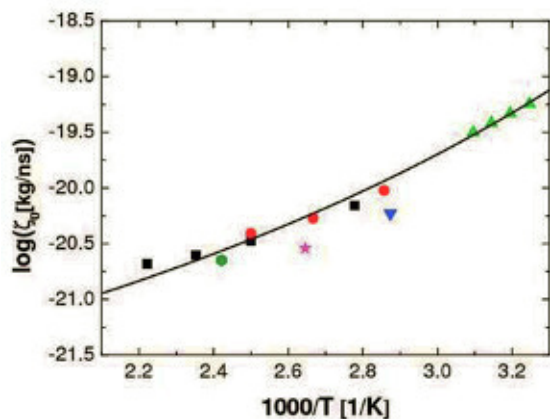
FIG. 3: Monomeric friction coefficients obtained experimentally by the combination of NSE and rheology for the different molecular weights. The data are compared at a temperature with the same distance to the glass transition temperature. The mastercurve covers 2 orders of magnitude. The 2 outliers are due to clear polydispersity effects in commercially obtained high M_w polymers.

The second item of comparison between rheology and NSE relates to the tube diameter and plateau modulus. As for PI, PEP and PE, the PEO polymer in this investigation is the next polymer in row for which the tube diameter from the macroscopically determined plateau modulus is about 1.5 times smaller than from the direct microscopic observations in NSE. The discrepancy may have partly to do with the rubbery nature of the rheological interpretation of the modulus which is compared simply to the lateral confinement but this topic needs further investigation for model systems.

We conclude that a synergy of linear rheology and neutron spin echo methods leads to consistent and unique results concerning the polymeric dynamics as a function of molecular weight. Quantitative comparison could be clearly achieved and the difference in the tube diameter as in other polymers was confirmed independently again.

[1] Reference oneK. Niedzwiedz, A. Wischnewski, W. Pyckhout-Hintzen, J. Allgaier, D. Richter, A. Faraone, Macromolecules, **41**,4866-4872(2008).

[2] Reference oneK. Niedzwiedz, A. Wischnewski, M. Monkenbusch, D. Richter, A. Genix, J. Colmenero, M. Strauch, E. Straube, Phys. Rev. Lett, **98(16)**,168301(2007).

117

Unexpected power-law stress relaxation of entangled ring polymers

W. Pyckhout-Hintzen[1], D. Richter[1], D. Vlassopoulos[2], M. Rubinstein[3]

[1] IFF-5: Neutron Scattering
[2] FORTH, Institute of Electronic Structure and Laser, Heraklion, Crete,Greece
[3] University of North Carolina, Department of Chemistry, Chapel Hill,USA

Linear and long-chain branched polymers relax by reptation processes out of the confining tube or via arm retraction respectively. Both mechanisms are intimately related to the presence of chain end material. It is of major interest how entangled ring polymers which lack this basic ingredient of chain ends proceed to relax stress. Self-similar dynamics yielding a power-law stress relaxation is reported on model ring polymers. Here, the importance of some linear impurities becomes evident. The combination of neutron scattering and rheology for rings is a promising tool therefore to unravel details of their dynamics and their difference with linear chains.

The investigation of polymer dynamics is always closely related to the particular structure or even the architecture that the polymers adopt. Fig 1a represent a reptational-like motion through an obstacle field of chains, which is clearly different from star fluctuations in Fig 1b where only arm retraction modes can relax the stress. Rings in Fig 1c and 1d may occur in double-fold shape or even behave like lattice-animals respectively. Latter has a very strong similarity with a random cayley tree (Fig 1e) for which the relaxation time spectrum corresponds to long logarithmically-spaced time scales for each of the different chain sections. These follow a hierarchical scheme and relax as is well known from former works from the outside-inwards in a sequential way, leading to typical patterns in the complex relaxation modulus. For model-branched architectures, the number of generations is coupled to the number of loss peaks. It is, however, not obvious how a ring-like polymer will perform. Fig f depicts e.g. self-interpenetration and blockage of the rings.

In the former considerations the influence of linear contaminants which are the product of non-perfect linking chemistry or degradation of closed cycles to open linear chains, was not yet included. To verify theories which focus on the special structure-dynamics associated with the odd architecture, it is a prerequisite to purify the rings. Recently, developments of liquid chromatography at the critical condition have shown to efficiently separate rings and linear chains via the compensation of entropic size exclusion and enthalpic interactions with the pores. The polymers so obtained were analyzed by rheology and SANS in order to assure their unchanged,

original closed structure.

The linear rheology for the purified rings is very compatible to the model of self-similar lattice animals of Fig 1(d,e). The associated exponentially decreasing relaxation modulus G(t) is then given as

$$G(t) = G_{N0} \left(\frac{t}{\tau_e} \right)^{-\frac{2}{5}} \exp\left(-\frac{t}{\tau_{ring}} \right)$$
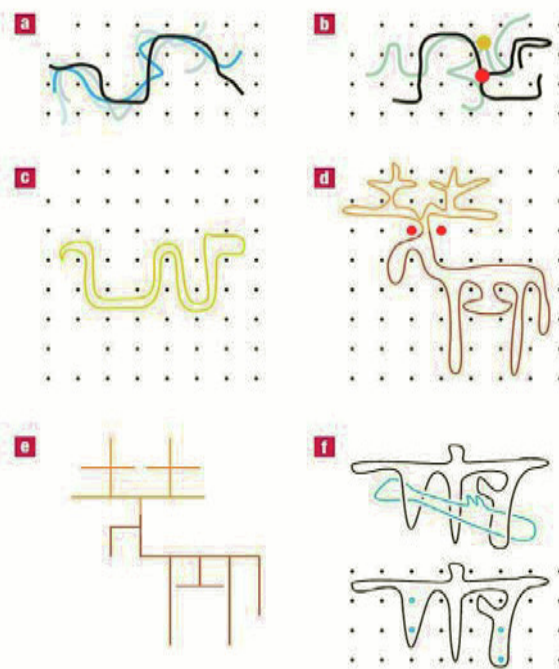
FIG. 1: *Different correlations of structure with assumed dynamics are summarized and explained in the text. The comparison of ring with branched polymers is made clear.*

This is distinctly different in linear or branched polymers which show an extended entanglement plateau. This expression for the relaxation modulus already includes constraint-release effects for loop rearrangement as well as dynamic dilution and contains no further adjustable parameters.

SANS measurements are shown in Fig 2. From dilute solution and in a melt of linear chains (not shown), unperturbed chain dimensions as well as the swelling of the ring by excluded-volume statistics could be

confirmed. The experimental slopes in Fig 2 are typical. Very good agreement in both size as well as the scattering amplitudes was obtained. The ring in good solvent is swollen by a factor of 1.5 which is in accordance with estimates of about 1.4 in literature. No traces of impurities of linear chain could be spotted from SANS.
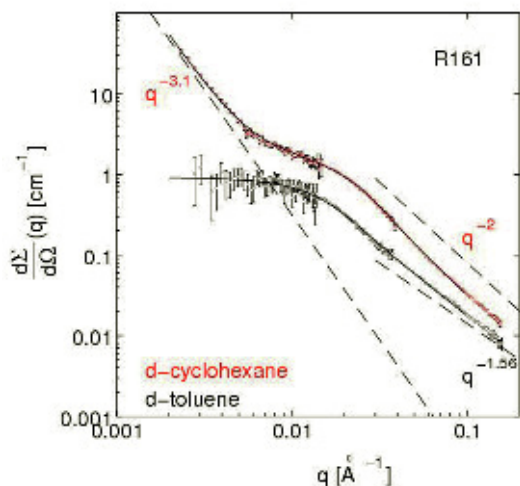
FIG. 2: *SANS experiments on dilute solutions under θ and good solvent conditions show the characteristic scattering vector dependences. q^{-2} is random-walk statistics on intermediate length scales whereas the $q^{-1.6}$ is prominent for excluded-volume interactions in swollen rings. The strong parasitic forward scattering at low q for the cyclohexane sample following $q^{-3.1}$ is due to density fluctuations in the theta-state.*

FIG. 3: *Linear chains are percolating through bridging by the rings at low concentrations.*

The effect of the linear chain on the dynamics of a ring could be quantified by deliberately mixing in the sample again known amounts of linear chains and remeasure the relaxation modulus. It shows that even at concentrations of 1/50th of the overlap concentration of the rings, the relaxation time spectrum gets a new long-lived component which grows substantially with concentration. The viscosity rises and a plateau shows up again. The understanding of this is important to relate former experiments in literature on rings which were not purified so extensively as here and therefore always showed a plateau modulus value.

We have forwarded in Fig 3 the molecular picture that linear chains must be bridged at this extremely low concentration by the rings to be so effective and therefore provide considerable increase in the melt viscosity. The entropically driven penetration of rings by linears leads then to a transient network.

As both natural and synthetic polymers can be found in this severe cyclic architecture the present results are of both fundamental and practical significance. Optimized microprocessing as well as rheology modifications are thus within reach. Rings will be investigated further using adequately isotope-labeled systems to study differences in segmental dynamics and chain fluctuations compared to their linear analogs. Also the question whether a plateau modulus shows up or power law relaxation persists if the rings get considerably larger will be investigated. Additionally blends with linear homopolymers will be addressed as well to be compared with recent advances in blends of linear with dendritic polymers. The techniques of interest are neutron spin echo (NSE) and small angle scattering (SANS) in quenched state which focus on the short times i.e. high-temperature motion and long times i.e. large-scale dynamics respectively. The present work was carried out in the framework of the Joint Programme of Activities of the SoftComp Network of Excellence (contract number NMP3-VT-2004-502235) granted under the FP6 by the European Commission.

[1] M. Kapnistos, M. Lang, D. Vlassopoulos, W. Pyckhout-Hintzen, D. Richter, D. Cho, T. Chang, M. Rubinstein, Nature Materials, **7,** 997-1002(2008)

[2] M. Rubinstein, R. Colby, Polymer Physics, (Oxford University Press, 2003)

[3] M. Rubinstein, Phys. Rev. Lett., **24**, 3023-3026(1986)

119

A neutron scattering study of asphaltene aggregates in crude oil

T. F. Headen[1,2], E. S. Boek [1], J. Stellbrink [3], U. M. Scheven [1]

[1] Schlumberger Cambridge Research, High Cross, Madingley Road, Cambridge, CB3 0EL, UK
[2] Dept. Physics and Astronomy, University College London, Gower Street,London WC1E 6BT, UK
[3] IFF-5: Neutron Scattering

We report temperature dependent neutron scattering experiments on crude oils. We observed two different types of asphaltene aggregates with largely different characteristic length scales. Analysis of the high Q region as observed by Small Angle Neutron Scattering (SANS) has probed the asphaltene aggregates on the nanometer length scale. We find that their radius of gyration decreases with increasing temperature. We show that SANS measurements on crude oils give similar nano-aggregate sizes to those found for asphaltene nano-aggregates redispersed in deuterated toluene. The combined use of SANS and Very Small Angle Neutron Scattering (V-SANS) on crude oil samples has allowed the determination of the radius of gyration of large scale asphaltene aggregates of approximately 0.45μm. Analysis at very low Q has shown that the large scale aggregates are not simply made by aggregation of all the smaller nano-aggregates. Instead, they are two different aggregates coexisting.

In crude oils, frequently colloidal structures are observed, which are thought to arise from aggregation of molecules mainly in the asphaltene solubility class [1]. Colloidal asphaltenes may deposit in reservoir rock or oil pipe lines, thus giving rise to severe problems with respect to hydrocarbon recovery. Asphaltenes are defined as the fraction of crude oil insoluble in n-alkanes and soluble in aromatics. There is intense debate about the size and structure of these molecules. In this paper [2], we report results on the temperature dependence of the size of asphaltene aggregates in their natural crude oil environment investigated by Small Angle Neutron Scattering (SANS). In addition we provide Very Small Angle Neutron Scattering (V-SANS) results for one of the crude oils. This allows a complete analysis of the data over many length scales. SANS and V-SANS measurements were performed at FRJ-2 research reactor, Forschungszentrum Jülich, Germany, using the instrument KWS-1 (SANS) and the focusing mirror instrument KWS-3 (V-SANS).

Fig.1 shows the combined V-SANS and SANS data, which in total cover nearly three orders of magnitude in scattering vector Q. Clearly two different Guinier regimes are visible resulting from two different types of aggregates with largely different charac-

teristic length scales. The extension in Q-range by V-SANS allows a determination of the characteristic size of the large scale aggregates, since we are also probing their Guinier regime. Strikingly, at 20°C the analysis of the larger aggregates gives a radius of gyration, Rg≈0.45μm, only slightly decreasing with increasing temperature. This is lower than sizes reported from dynamic light scattering experiments and confocal microscopy which show an aggregate radius of greater than 4 μm. However these are sizes of flocs/aggregates initiated by n-heptane addition. In the SANS experiments outlined here no flocculation was visible. The larger aggregates observed by SANS exist in equilibrium with all the aggregates.
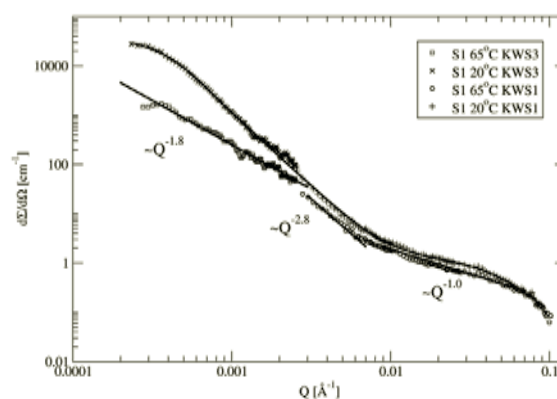
FIG. 1: Intensity vs. scattering vector Q for sample S1 at 20° C (x and+) and 65° C (circle and square); Solid lines: Fit to a sum of two Beaucage mass fractal form factors [2].

The 20°C data show a continuous power law decay, I∼Q^{-3}, over more than one order of magnitude in Q covering both V-SANS and standard SANS data. For the 65°C data, on the other hand, a more complicated Q-dependence is visible. At least three power law regions are observed indicating a more complex hierarchy of structural levels in the large scale aggregates. This structure prohibits the use of the Beaucage equation for analyzing the 65°C data [2, 3], so that only a qualitative description of the temperature dependence can be given: The radius of gyration of the large scale aggregates seems to be temperature-independent, but their amplitude cru-

cially diminishes with increasing temperature. This clearly indicates a decreasing fraction of large scale aggregates at higher temperatures.
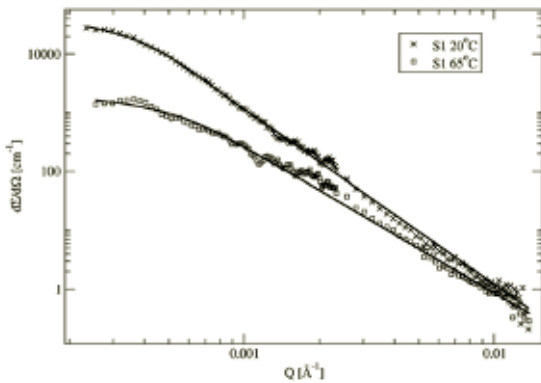
FIG. 2: *V-SANS and SANS data for S1 crude at 20°C and 65°C with corresponding nanoaggregates Beaucage function subtracted.*

Also in the low-Q regime, Q $\leq 2 \times 10^{-3}$Å^{-1}, their fractal dimension d$_f$ seems to decrease from 3 (space-filling) to 1.8, indicating a substantially less dense structure. On the other hand, in the intermediate-Q regime, 2×10^{-3}Å$^{-1} \leq$ Q $\leq 6 \times 10^{-3}$Å^{-1}, the observed power law is nearly temperature independent indicating the same internal structure. Probably the large scale aggregates are "melting from the rim" with increasing temperature.

The characteristic features of the large scale aggregates become even more visible if we subtract the scattering contribution from the asphaltene nanoaggregates. From previous SANS analysis in the high Q region [1] it is reasonable to represent smaller nanometer scale aggregates using a single length-scale Beaucage function [3],

$$\frac{d\Sigma}{d\Omega}(Q) = G \exp(-Q^2 R_{g_i}^2/3) + B\{[erf(QkR_{g_i}/6^{1/2})]^3/Q\}^{d_{f_i}}$$

which we may subtract from total scattering. The remaining intensity in the low Q-region (KWS3 and KWS1 data) is shown in Figure 2. For T=20°C the power law decay with slope d$_f \approx 3$ is clearly visible for more than one order of magnitude. The amplitude factors G can now be determined much more precisely. G describes the forward scattering I(Q→0), which in its turn is the product of contrast factor $\Delta\rho^2$/N$_a$, concentration Φ and volume of the scattering particles. Since we know neither the exact contrast factor, nor the amount of asphaltenes in the crude oils, we cannot derive the volume of the large scale asphaltene aggregates. Nevertheless we can make the following estimations about the general underlying physical picture of asphaltene aggregation. We assume that the contrast factor is the same for the large scale asphaltene aggregates and the asphaltene nanoaggregates, which is certainly reasonable. If there is only one species of scattering particles present in the crude oil, i.e. assuming a

general structure, where the large scale aggregates are built from nanoaggregates, we can make the following calculation. For such a scenario the relation $V_{large}/V_{nano} \sim (R_{large}/R_{nano})^{d_j}$ should hold with a prefactor of the order of unity. Inserting the results from the fit we obtain the following number: $\frac{G_{large}}{G_{nano}} = \frac{V_{large}}{V_{nano}} = \frac{4.4 \times 10^4}{1.38} \approx 3.2 \times 10^4$ but,

$$\left(\frac{R_{large}}{R_{nano}}\right)^{d_j} = \left(\frac{4690}{36.9}\right)^{2.98} \approx 1.8 \times 10^6$$

So obviously the scenario that all scattering results from a single species is wrong. That means there is a coexistence of large scale asphaltene aggregates and asphaltene nanoaggregates. The relative amount of asphaltene molecules participating in the large scale aggregates can be estimated by:

$$\frac{V_{large}}{V_{nano}} / \left(\frac{R_{large}}{R_{nano}}\right)^{d_j} = \frac{\Phi_{large}}{(\Phi - \Phi_{large})}$$

Inserting our numbers, we find that only approximately 2% of the asphaltene molecules are forming the large scale aggregates. This finding, combined with results from filtration experiments, is very strong evidence that the very low Q scattering is not due to density fluctuations of the smaller aggregates, but larger aggregates coexisting with smaller ones.

In conclusion, SANS and V-SANS have been successfully used as a technique to characterize asphaltene aggregates on the nanometer and micrometer length scale. We found that asphaltene aggregates in crude oil show a broadly similar size, and temperature dependence of size, as asphaltene aggregates in aromatic solvents usually interpreted as model systems for crude oil.

[1] Asphaltenes, Heavy Oils, and Petroleomics, O.C. Mullins, E.Y. Sheu, A. Hammami and A. G. Marshall, Eds., Springer New York, 2007.

[2] T. F. Headen, E. S. Boek, J. Stellbrink, U. M. Scheven, Langmuir, **25**, 422, 2009

[3] G. J. Beaucage, Appl. Cryst., **29**, 134-146, 1996.

121

A-B diblock copolymer in a three component A/B/A-B polymer blend

V. Pipich[2], L. Willner[1], D. Schwahn[1]

[1] IFF-5: Neutron Scattering
[2] JCNS: Jülich Centre for Neutron Science

Thermal copolymer fluctuations were explored in a three component blend consisting of a critical (A/B) homopolymer blend and a symmetric A-B diblock copolymer using the technique of neutron small angle scattering. The copolymer has the function of an external non-ordering field and thereby determines phase behavior as well as the regimes of 3d-Ising, isotropic Lifshitz, and Brasovskiî critical universality. A weak coupling of copolymer and homopolymer was confirmed in consistence with predictions from RPA. Self-assembly of the copolymers was observed prior to the ordering of the "total" blend, e.g. inclusive of the homopolymers, into bicontinuous and lamellar ordered phases.

Three component A/B/A-B polymer mixtures are described by three order parameters which can be defined as deviations from the average of (i) the total A or B monomers, (ii) the copolymer, and (iii) the difference of the A and B homopolymer concentrations. We are particularly interested in the ordering behavior of the diblock copolymer as it is considered as an external field determining the complex phase behavior in those systems. SANS technique can distinguish between the above mentioned order parameters by properly adjusting the scattering contrast of the polymer components. This is possible for polymers by the exchange of hydrogen and deuterium which for neutrons deliver a sufficiently different coherent scattering length. So, in order to explore the ordering behavior of the copolymer one needs one block protonated and the other components deuterated or vice versa.

Most chemically distinct homopolymers such as the presently explored polystyrene (PS) and polybutadiene (PB) are immiscible because of their low entropy of mixing which is inversely proportional to their molar volumes V [1, 2, 3]. Compatibilization of chemically distinct homopolymers is an important issue of research as polymer blends are of great practical interest. Special additives might exist with similar properties such as those of amphiphilic molecules in water/oil mixtures. In the case of our study the A-B diblock copolymer is an efficient compatibilizer as the molar volume of the (PB/PS) blend was properly chosen according to the Flory-Huggins parameter at the critical temperature, e.g. $\chi_{AB} \cong 2/V$. So, there was only a weak tendency of segregation.

Aside of their practical relevance A/B/A-B polymer systems are interesting objects for basic research in statistical mechanics. They belong to a broad class of systems characterized by competing interactions such as in magnetic materials, ferroelectric crystals, and liquid crystals [4, 5].
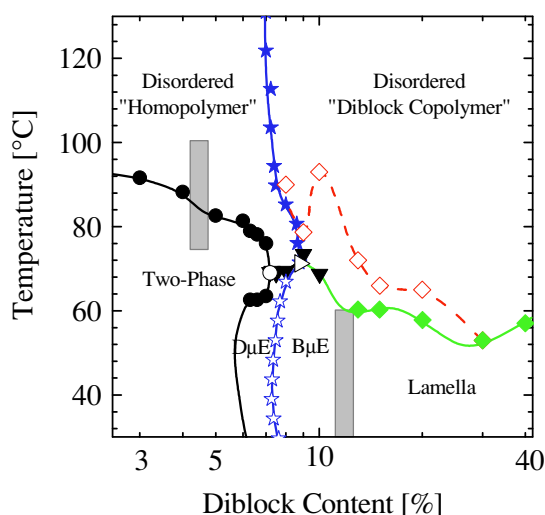
FIG. 1: *Phase diagram of the PB/PS/PB-PS polymer system achieved from bulk and block contrast SANS experiments, respectively. The filled symbols (♦) represent the bulk whereas the opened symbols (◊) represent the ordering transition of the copolymers. Beyond the Lifshitz line the same ordering transition temperatures are observed in block and bulk contrast as indicated from the temperature dependence of Q*. In addition preordering of the diblock copolymer is visible in block contrast. Such a preordering could be interpreted also from the temperature dependence of Q* in the bulk contrast samples. This means that the copolymers order some degrees before all polymers show ordering.*

The phase diagram of the present blend is depicted in figure 1. It shows a disordered phase at high temperatures and two ordered phases at low temperatures, one spatially uniform and the other one spatially modulated at low and large copolymer concentrations, respectively. Both ordered phases are separated by a Lifshitz line (blue symbols). The order-disorder phase transition occurs when passing the λ line (black symbols) representing a line of second-order phase transition. The point of the λ line where all three phases meet is the Lifshitz point (LP) representing a multiple critical point.
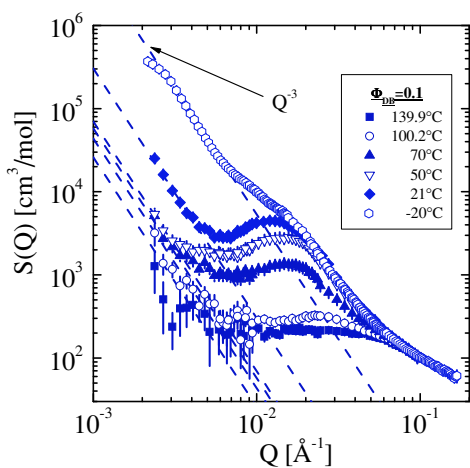
FIG. 2: Structure factor S(Q) of a sample with Φ_{DB}=10% diblock content which is beyond the Lifshitz Line. S(Q) shows strong temperature dependence as well for the interference peak as well for the Q^{-3} power law at low Q.
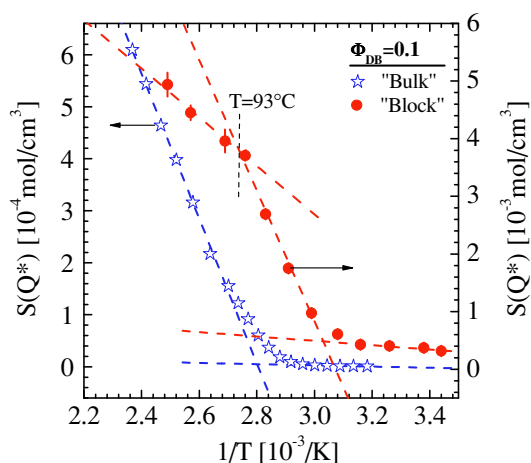
FIG. 3: Susceptibility for bulk (blue) and block (red) contrast is depicted. Below 93° C much stronger change is observed for the "copolymer" susceptibility.

The LP is characterized by three parameters, namely the order parameter and space dimensions as well as the wave length of the modulated phase. The Lifshitz point of A/B/A-B blends is characterized by an isotropic Lifshitz critical point and a scalar order parameter. In particular isotropic Lifshitz critical points do not exist in 3 dimensions [4]. Strong thermal fluctuations are observed in particular near the expected Lifshitz point (LP) and lead to a destruction of the ordered phases. Instead a channel of micro emulsion phases is observed between the ordered phases. Such a droplet and bicontinuous microemulsion channel is separated by the Lifshitz line depicted as blue symbols (line) in figure 1. The main focus of the present study was the ordering behavior of the copolymer. Figure 2 shows the structure function S(Q) of a 10% copolymer blend plotted as function of temperature. Lowering the temperature leads to an increase of the scattering signal due to an increase of thermal fluctuations and due to the transition to a bicontinuous phase as characterized by the interference peak at Q of the order of 10^{-2}Å^{-1}. In parallel
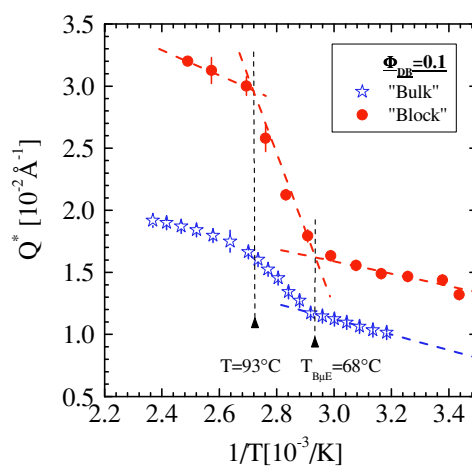
FIG. 4: Peak positions are qualitatively the same for bulk and block contrast.

we observe a Q^{-3} power law at small Q indicating copolymer aggregation [3]. Figure 3 shows the susceptibility and compares block and bulk contrast samples. The strong enhancement of the "block" susceptibility below 93°C indicates strong copolymer self-assembly. Similarly, the peak positions Q^* of bulk and block contrast decrease much stronger below the same temperature (figure 4). A comparison of "block" and "bulk" contrast shows similar shape but a larger Q^* in the "block" sample. The two kinks at 93°C and 68°C for the two samples are caused by copolymer self-assembly and a transition to a bicontinuous microemulsion phase, respectively (see figure 1). These observations give evidence of a preordering (self-assembly) of the copolymers below 93°C which is far above T=68°C when all components including the homopolymers start ordering. Preordering is observed above the microemulsion and lamellar phases between 8 and 30% copolymer concentration as depicted in figure 1 by the red dots.

In summary: The exploration of a A/B/A-B polymer blend with small angle neutron scattering showed enhanced copolymer self-assembly prior to the "bulk" ordering transition within the Lifshitz critical regime. These observation were consistently determined from susceptibility, interference peak Q^*, and Q^{-3} power law at small Q. Such copolymer self-assembly was not visible in the regimes of 3d-Ising and lamellar ordering at low and large copolymer concentration, respectively. The copolymer self-assembly must play a relevant role for the crossover from Ising to isotropic Lifshitz classes of critical universality.

[1] V. Pipich, L. Willner, and D. Schwahn, J. Phys. Chem. B **112**, 16170 (2008).

[2] D. Schwahn, Adv. Polym. Sci **183**, 1-61(2005).

[3] D. Schwahn et al., J. Chem. Phys. **112**, 5454 (2000); V. Pipich, D. Schwahn, L. Willner, J. Chem. Phys. **123**, 124904 (2005)

[4] H. W. Diehl, Acta Physica Slovaca, **52**, 271 (2002).

[5] R. Holyst and M. J. Schick, J. Chem. Phys. **96**, 7728 (1992).

123

Twist grain boundaries in cubic surfactant phases

M. Belushkin, G. Gompper

IFF-2: Theoretical Soft-Matter and Biophysics

Cubic surfactant phases are mesoscale liquid-crystalline structures in which the surfactant monolayer separating the oil-rich and water-rich domains often has a triply-periodic minimal-surface geometry where the mean curvature H vanishes on the whole surface. The lattice constant which corresponds to the dimensions of the fundamental building block - the unit cell - is large, of the order of 10 nm. During the nucleation of a cubic phase, many classes of defects arise. We have investigated twist grain boundaries in the lamellar, gyroid, diamond and Schwarz P phases. The structure of the monolayer in the grain boundaries is found to be very close to a minimal-surface geometry. The interfacial free energy per unit area is found to be very small, therefore the density of grain boundaries should be high in these surfactant phases.

Amphiphilic molecules added to an immiscible oil-water system self-assemble into a large variety of structures. Phases with cubic symmetry often feature a triply-periodic minimal surface (TPMS) configuration of the surfactant monolayer. Examples of such phases include the gyroid G, diamond D, Schwarz P, Schoen $I - WP$, $F - RD$, Neovius $C(P)$ and others, which are encountered in physical systems. Properties of cubic surfactant phases have been a subject of extensive theoretical and experimental interest, with applications in biological systems, as templates for mesoporous systems and for the crystallization of membrane proteins.

In amphiphilic systems many kinds of interfaces occur: between two ordered phases, between ordered and disordered phases, and between two grains of the same ordered phase which differ by their spatial orientation. Experiments on block copolymer systems have revealed the structure of many interfaces. For example, twist grain boundaries in the lamellar phase are well described by Scherk's minimal surfaces at large twist angles and are helicoid-shaped at small twist angles [1, 2], whilst tilt grain boundaries in the lamellar phase have been shown to be omega-shaped at large tilt angles and chevron-shaped at small tilt angles [3].

We report here on the investigation of twist grain boundaries in cubic surfactant phases. The calculations are based on a Ginzburg-Landau theory of ternary amphiphilic systems [4, 5] with a single scalar order parameter $\phi(\vec{r})$ which describes the local oil-water concentration difference. The geometrical properties of the grain boundaries are evaluated on the isosurface $\phi(\vec{r}) \equiv 0$ which defines the position of the surfactant monolayer. The interfacial free energy per unit area of a grain boundary depends on the angles with respect to the crystalline axes. It is determined using the Ginzburg-Landau theory and a complementary geometrical approach based on the Canham-Helfrich curvature Hamiltonian.

The calculations are performed on a discrete three-dimensional real-space lattice ϕ_{ijk}. Initially, half of each calculation box is filled with a phase rotated by an angle $-\alpha/2$ and the other half with a phase rotated by an angle $+\alpha/2$. The free energy is minimized using a method based on the gradient descent algorithm [6].
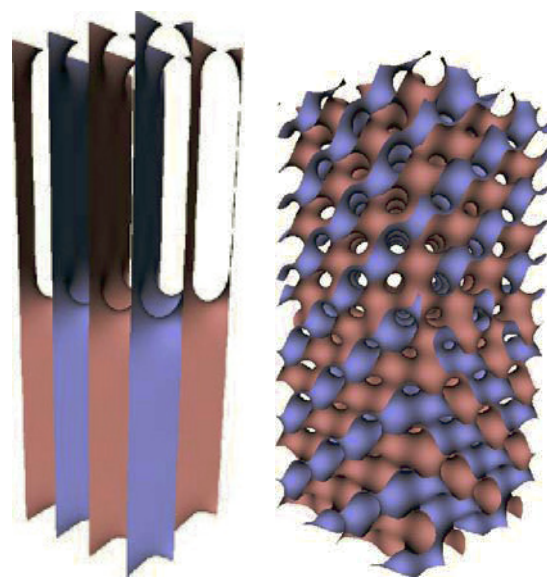
FIG. 1: *Configuration of the surfactant monolayer for the lamellar phase at a twist angle of $53°$ (left) and the gyroid phase at a twist angle of $90°$ (right). The grain boundaries are located in the middle and at the top/bottom of each box.*

Configurations of the surfactant monolayer in the full simulation boxes of the lamellar phase at a twist angle of $53°$ and the gyroid phase at a twist angle of $90°$ are shown on Fig. 1.

The locations of the grain boundaries are determined quantitatively by relating the inital and final simulation boxes [6]. In the lamellar, gyroid and diamond phases the thickness of the grain-boundary regions is about one unit cell of the bulk-phase regions, thus grain boundaries preserve the typical length scales of the bulk phases. The bulk-phase regions of the Schwarz P phase are greatly affected by the presence of grain boundaries. The surfactant monolayers in grain-boundary regions of the lamellar (top), gyroid (middle) and diamond (bottom) phases are shown on Fig. 2 for twist angles of $53°$ (left) and $90°$ (right).
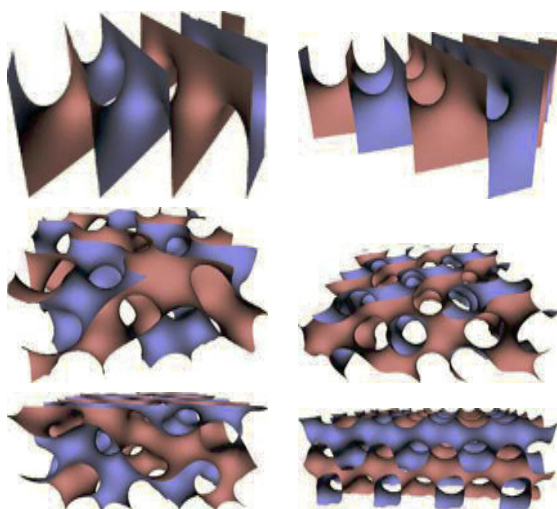
FIG. 2: Twist grain boundary geometries for the lamellar (top), gyroid (middle) and diamond (bottom) phases for twist angles of $53°$ (left) and $90°$ (right).

Squared-mean and Gaussian curvature distributions are calculated for each phase and twist angle. Squared-mean-curvature distributions show that the mean curvature of the surfactant monolayer essentially vanishes both in the bulk-phase and grain-boundary regions, therefore the configurations of the surfactant monolayer are good approximations of minimal surfaces [6].
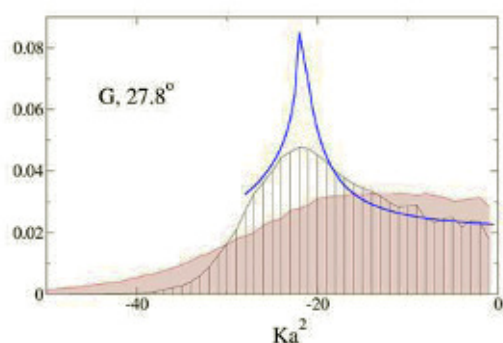
FIG. 3: Gaussian-curvature distribution for the G phase at a twist angle $\alpha = 27.8°$. The blue solid line corresponds to the exact result obtained from the Weierstrass representation. The black vertically-shaded and red slant-shaded histograms correspond to bulk and grain-boundary regions, respectively.

Gaussian-curvature distributions (Fig. 3) show that [6]

- the Gaussian curvature distributions in the bulk-phase regions are consistent with the exact results obtained from the Weierstrass representation

- in the L_α, G and D phases the geometry of the grain boundaries is significantly different from the geometry of the bulk phases

Excess free energy per unit area of the grain boundaries determined from Ginzburg-Landau theory as a function of the twist angle α is shown on Fig. 4. Geometrical approaches based on the Canham-Helfrich curvature energy Hamiltonian yield similar results [6]. The excess free energy of the grain boundaries exhibits a non-monotonous dependence on the twist angle α, and the negative values for the P phase show it to be unstable with respect to the nucleation of grain boundaries at the investigated point in the phase diagram.
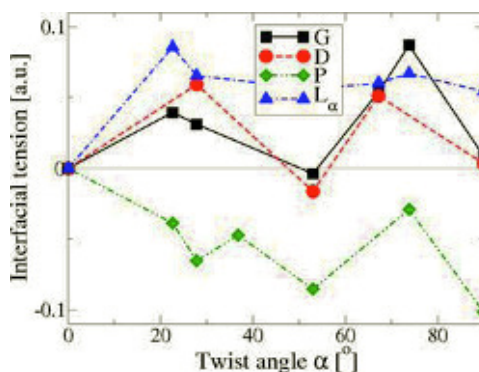
FIG. 4: Grain-boundary excess free energy per unit area as a function of the twist angle α for the lamellar, gyroid G, diamond D and Schwarz P surfactant phases as extracted from Ginzburg-Landau theory.

The free energy of the grain boundaries is very small. The difference in the grain-boundary free energy and the free energy of bulk-phase regions of equal volume is of the order of 1% at the maxima of Fig. 4. Therefore, the density of grain boundaries should be high in these surfactant phases.

[1] S. Gido *et al.*, Macromolecules **26**, 4506 (1993)

[2] H. Jinnai *et al.*, Macromolecules **39**, 5815 (2006)

[3] Y. Cohen *et al.*, Macromolecules **33**, 6502 (2000)

[4] G. Gompper, M. Schick, Phys. Rev. Lett. **65**, 1116 (1990)

[5] U. S. Schwarz, G. Gompper, Phys. Rev. E **59**, 5528 (1999)

[6] M. Belushkin, G. Gompper, J. Chem. Phys. **130**, 134712 (2009)

125

Synthesis of silica rods, wires and bundles using filamentous fd virus as template

J. Buitenhuis, Z. Zhang

IFF-7: Soft Condensed Matter

We explored fd as a template to direct the formation of silica nanomaterials with different morphologies through simple sol-gel chemistry[1]. Depending on the conditions silica nanowires can be formed, which seem to accurately transcript the bending conformation and the length of the fd viruses in solution. But also surprisingly straight silica rods may be formed, and under other conditions bow-tie-shaped bundles of rods are formed, which have a remarkably well defined shape and dimension.

126

One dimensional anisotropic inorganic nanostructures such as tubes, rods, wires, fibers, etc. are in the focus of research interests due to their potential applications, for example in optical, electronic and mechanical devices, sensors and catalysis[2, 3]. The synthesis of these anisotropic nanostructures is a big challenge, because most inorganic materials do not form the desired structure by themselves. In contrast to inorganic systems, biological and organic materials, especially supramolecular systems, usually have a well defined structure down to the nanoscale. Using (bio)organic materials as a template to build up anisotropic inorganic nanostructures has therefore emerged as a highly attractive method in recent years. The results described in the present paper may serve as a basis for the further development of the synthesis of inorganic materials using biopolymers as a template.

In this paper, the filamentous fd virus is used as a template to regulate the formation of silica nanomaterials with well-defined morphologies. Fd viruses have a length of 880 nm and a diameter of 6.6 nm. M13, a virus which is almost identical to fd, differing only in one amino acid per coating protein, has been intensively explored by Belcher, Hammond and co-worker as a template in the synthesis of metallic and other magnetic and semiconducting nanowires[4]. Their strategy is to modify the coat protein of M13 via genetic engineering specifically for each metal or oxide, so that the coat protein can selectively induce precipitation or assembly of that specific metal or oxide on the surface of the virus. However, as far as we know, there is no report concerning the application of fd or M13 as a template for silica precipitation.

In contrast to the complicated genetic engineering
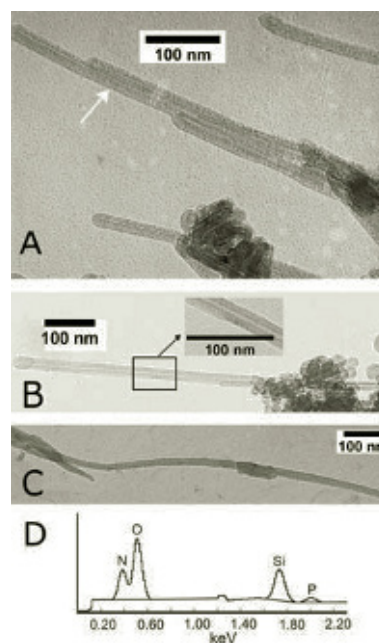
FIG. 1: TEM images of typical rods. (A) rods with a uniform silica layer and semi-spherical ends, an assembly of three rods is indicated by the arrow; (B) a rod with a clear core-shell structure; (C) a slightly curved rod where no core-shell structure is visible; (D) EDAX analysis of the rod shown in C.

route used with the M13 virus, we show here that wild-type fd virus can also be used as a template in the synthesis of inorganic materials using simple sol-gel chemistry. Under different conditions, using acid-catalyzed hydrolyzation and condensation of tetraethoxysilane as silica precursor, three kinds of morphologies are observed: 1) silica nanorods with a diameter of 20 nm and a homogeneous silica layer, 2) nanowires with a curved shape and 3) bow-tie-shaped bundles with well-defined shape and hierarchy. As far as we know, we are the first to use fd as a template for material synthesis and have observed several interesting structures.

Single silica rods with high uniformity, aggregated silica-virus hybrid nanorods as well as pronounced granular silica are observed for sample type 1, see fig. 1. Along the axis of the rods, the diameter is constant and the silica layer is homogeneous. The surface of these rods is smooth under the maximum

FIG. 2: TEM of nanowires. A broken wire can be seen in the inset as indicated by the arrow.

FIG. 3: TEM image of bow-tie-shaped bundles dispersed in the background of granular silica. A possible subunit of the bundles, a silica fan is indicated by the arrow. Inset: schematic drawings of possible structures of the bundles.

resolution of the TEM we used and the shape of the ends of the rods is semi-spherical. Some of the rods show a clear core-shell structure with a low contrast part along the center of the whole rod (fig. 1b). The low contrast part might be fd. However, some rods do not show such low contrast part and look like pure silica rods (fig. 1c). The "pure" silica rod shown in fig. 1c was subjected to EDAX analysis. Apart from silicon and oxygen, nitrogen and phosphorus are detected (fig. 1d). The nitrogen and phosphorus can only be attributed to fd, given that no agents containing nitrogen or phosphorus were used during the synthesis. Although fd is semi-flexible and somewhat curved in dispersion, most of the rods are straight and only a few slightly curved rods are seen (fig. 1c). From a single rod point of view, the silica coating is highly uniform. Also the diameters of different rods are all close to the average value of about 20 nm. However, large differences in length are seen for different rods. Long rods with a length comparable to the length of intact fd are observed along with short rods, which might form from the silica coating of the fragments of decomposed fd.

At somewhat different reaction conditions, long, curved wires are observed entangled with each other (sample type 2, fig. 2). The surface of these wires is less smooth than that of the straight rods described before, and the diameter of these wires shows a less sharp distribution with an average diameter of about 23 nm. The contour length of these wires is in the range of that of intact fd, while long wires with a length twice that of fd are also observed. The longer wires seem to consist of two viruses sticking together by partial parallel overlap. These results imply that most fd remains intact during wire formation (an exception is the broken wire shown in the inset of fig. 2 by the white arrow), in contrast to the case of the straight rods described above, where many rods much shorter than fd are observed. The curved shape of these wires probably originates from the bending configurations of the semi-flexible fd virus in aqueous media. Therefore, these hybrid silica wires show an example of a quite precise transcription of the template, here, semi-flexible fd. Whether or not
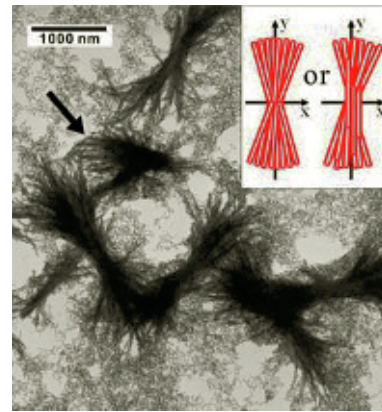
the silica coating solidifies the fd virus completely so that the flexibility is lost is not clear.

Bow-tie-shaped bundles of silica rods are formed (fig. 3) if the aqueous straight rod sample of type 1 is mixed with a methanol/ammonia mixture. This morphology is remarkable because as far as we know, no similar morphology has been reported for any other virus or organic template in the past. The bundles all have similar dimensions. The maximum length along the y axis of the well-defined bundles is ab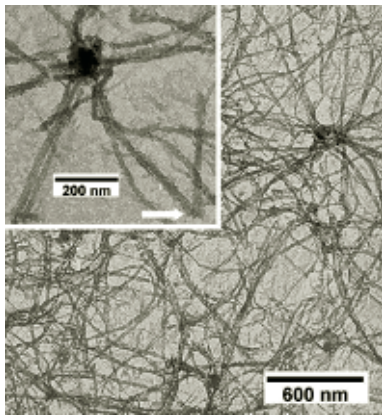out 2000 nm, comparable to the total length of two intact fd viruses joined with each other head-to-tail (see the cartoon in fig. 3). The formation of the bow-tie-shaped bundles seems to originate from an aggregation of (silica coated) fd viruses (and granular silica) after addition of the methanol/ammonia mixture, but the exact reason for the shape and size of the bundles remains unclear.

We demonstrated the capability of fd viruses to be used as a template for the formation of 1D silica nanomaterials. Three nanostructures with distinct morphologies have been observed under different sol-gel conditions using TEOS as silica precursor: silica rods, wires and bow-tie-shaped bundles. Silica wires seem to transcript the bending conformation and length of intact semi-flexible fd, but under somewhat different reaction conditions also remarkably straight silica rods are formed that have a high uniformity in terms of the thickness and homogeneity of the silica layer. Work devoted to further understanding the results obtained in this paper and exploring the above problems is ongoing.

[1] Z. Zhang, J. Buitenhuis, Small **2007**, 3, 424.

[2] Y. N. Xia, P. D. Yang, Y. G. Sun, Y. Y. Wu, B. Mayers, B. Gates, Y. D. Yin, F. Kim, Y. Q. Yan, in Advanced Materials, **2003**, 15, 353.

[3] G. R. Patzke, F. Krumeich, R. Nesper, Angew. Chem.-Int. Edit. **2002**, 41, 2446.

[4] C. B. Mao, D. J. Solis, B. D. Reiss, S. T. Kottmann, R. Y. Sweeney, A. Hayhurst, G. Georgiou, B. Iverson, A. M. Belcher, Science **2004**, 303, 213.

127

Phase behaviour and kinetics of rod-like viruses under shear

P. Holmqvist, M. P. Lettinga

IFF-7: Soft Condensed Matter

Dispersions of colloidal rods are very susceptible to external fields like, for example, shear flow and a magnetic field. It is therefore interesting to investigate the phase behaviour of a dispersion of rods affected by a shear flow. Here we investigate the non-equilibrium phase behaviour for the isotropic to nematic transition as a function of shear rate and rod concentration, using an improved time resolved Small Angle Light Scattering set-up combined with a couette shear cell. In earlier studies under shear we were limited to the *binodal* line, which gives the shear rate and concentration where the dispersions become metastable [1]. We now access the full phase diagram, including the *spinodal* line, which gives the shear rate and concentration where the dispersions become unstable. We perform these experiments at varying rod concentration and rod-attraction and show that the phase diagrams for all attraction investigated can be collapsed on a single master curve with a simple scaling.

To carry out this investigation long thin monodisperse colloidal rod are needed. A very good model system for this is fd-virus (880 nm long, aspect ratio 120, persistence length 2.2 μm). The fd-virus suspensions were used in a 20 mM Tris buffer with 100 mM NaCl at a pH of 8.2. Attractions between the rods were varied through depletion by addition of dextran (480 kd, Pharmacosmos). Three different dextran concentration were used in this study A=6 mg/ml, B=13 mg/ml and C=20 mg/ml dextran at 21.1 mg/ml fd virus. The two phases, isotropic and nematic, were then separated into two different vials and the dextran and fd-virus concentrations were determined spectroscopically. By combining different volumes of the isotropic, V_{iso}, and the nematic, V_{nem}, phase from the initially phase separated sample we can prepare any concentration with the same osmotic pressure and chemical potential. In the investigated two phase region it is many time convenient to express the concentration relative to the phase boundaries, $\phi_{nem} = V_{nem}/(V_{nem} + V_{iso})$. The non-equilibrium phase diagrams and the kinetic of the phase separation of attractive colloidal rods in shear flow were investigated by small-angle light-scattering (SALS) experiments in an optical transparent couette shear cell.[2] The fd-virus solution was always pre sheared at 100 s^{-1} in order to homogenise the sample. At

this shear rate a shear stabilised fully nematic phase is induced. After a quench of the shear rate to zero or a finite rate at time zero the scattering pattern is recorded at a rate of about two frames per second with a CCD camera. A typical scattering pattern of the formed structures are shown in the inset of figure 1. The time evolution of several parameters can be deduced from these pictures: the position of the structure peak, the intensity change of this peak, the anisotropy of the structure for example. In figure 1 the time evolution of the max intensity of the peak is shown for $\phi_{nem} = 0.30$ and a dextran concentration of 20 mg/ml (sample C) for a quench to zero shear rate. From this plots induction times can be deter-
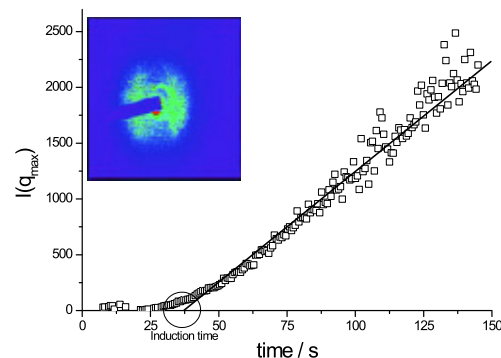
FIG. 1: *The intensity at the peak, $I(q_{max})$, as a function of time after a quench to zero shear rate for $\phi_{nem} = 0.30$. The line indicates the extrapolation to determine the induction time. The inset: Snapshot of the 2D-scattering pattern sample C.*

mined as indicated in the figure. The induction time is a convenient tool to determine if the phase separation takes place via nucleation and growth or spinodal decomposition. When approaching the unstable point (the spinodal) in the meta stable region, nucleation and growth, the induction time goes to zero. In figure 2a the induction time is plotted against the ϕ_{nem}. By extrapolating to zero induction time the spinodal point is determined to $\phi_{nem} = 0.25$. In figure 2b the growth rate of the formed structure is shown as a function of for both the flow and vorticity direction. It is notable that the growth rate is fastest around the spinodal point, for both the flow and vorticity direc-

tion, and then naturally goes to zero at the two phase boundaries.
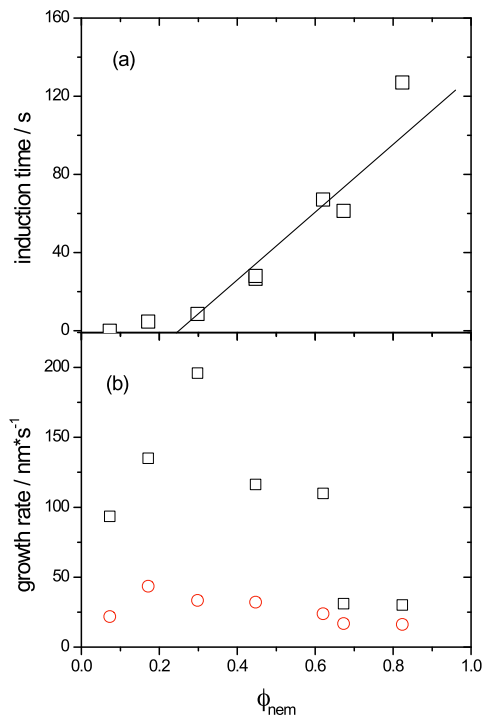
FIG. 2: *a) induction time vs. ϕ_{nem} for a dextran concentration of g 20 g/l. b) Time development of the structure size at a dextran concentration of g 20 g/l for the flow (□) and vorticity (○) direction after a quench to zero shear rate.*

This type of analysis is then done for different shear rates and rod attraction. Now a steady state non-equilibrium phase diagram can be constructed. From the induction time the spinodal is determined and from the inverse induction time the high concentration binodal, the nematic phase boundary, was found. This together with manual analysing of the scattering patterns gives us the full binodal and spinodal line. The phase diagram for the three attractions can be found in the inset of figure 3. As expected the phase coexistence is getting broader at zero shear rates with increasing attraction and a higher shear is needed to homogenize the sample.

If the concentration is normalized against the phase boundaries, ϕ_{nem}, and the shear rate with the maximum shear rate where the sample still can be found to phase separate, all the phase diagrams falls on the same master curve as seen in figure 3. Interestingly, the same master curve was found from simulations performed in IFF-2 (Theoretical Soft-Matter and Biophysics). The combination of the simulations and the experiments show that the non-equilibrium phase behaviour is dominated by the different dynamic behaviour of the isotropic and nematic phase [3].

These results also have implications on the equilibrium phase behaviour for attractive rods. Since for all three investigated dextran concentrations (attrac-
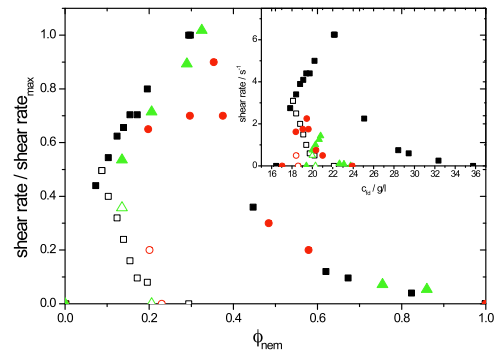
FIG. 3: *Steady state non-equilibrium phase diagram for three attraction A(green), B(red) and C(black). The shear rate is normalized against the max shear rate. The inset shows the same phase diagram but not normalized. The lines are guide for the eye.*

tions) the spinodal point at zero shear rate was found at $\phi_{nem} = 0.25$, we conclude that the spinodal point is not sensitive to attraction but only to the fraction of the nematic phase. This results are presently compared to theory [4].

[1] Lettinga, M. P. , Dhont J. K. G., J. Phys.: Condens. Matter 2004, 16, S3929.

[2] Holmqvist P, Lettinga MP, Buitenhuis J, Dhont JKG, LANGMUIR, 2005, 21, 10976

[3] Ripoll, M., Holmqvist P., Winkler, R. G., Gompper, G., Dhont, J. K. G., Lettinga, M. P., Phys. Rev. Lett., 2008, 101, 168302

[4] Holmqvist P., Ratajczyk M., Meier G., Wensink H. H., Lettinga, M. P., *In preparation*

129

Attractive colloidal rods in shear flow

M. Ripoll, R. G. Winkler, G. Gompper

IFF-2: Theoretical Soft-Matter and Biophysics

Suspensions of rod-like colloids show in equilibrium an isotropic-nematic coexistence region, which depends on the strength of an attractive interaction between the rods. By means of hydrodynamic simulations, we study the behavior of this system in shear flow for various interaction strengths. The shear flow induces alignment in the initially isotropic phase which generates additional free volume around each rod and causes the densification of the isotropic phase at the expense of an erosion of the initially nematic phase. Furthermore, the nematic phase exhibits a collective rotational motion. The density difference between these two regions at different shear rates, allows us to determine the binodal line of the phase diagram. The results are in good agreement with experimental observations.

Phase transitions occurring in soft matter systems are significantly affected by flow. Both the nature and location of the phase transition lines are changed due to the applied flow. The challenge is to find the parameters that determine the non-equilibrium steady states under flow conditions. Colloidal-rod suspensions constitute a particularly interesting system to study the effect of flow on their phase behavior, since rod orientation is strongly coupled to the shear field. Rods in the isotropic (I) phase align with the flow and become paranematic (P). This suggests that the transition to the nematic (N) phase, where rods have orientational order, is facilitated by shear. On the other hand, rods in the nematic phase undergo a collective tumbling motion in the presence of shear flow. The question that then arises is how these two effects will affect I-N detailed understanding of the flow behavior of a model system of attractive colloidal rods is useful for industrial applications where shear alignment of elongated objects, such as carbon nanotubes, worm-like micelles, and polymers, play a role.

The non-equilibrium phase diagrams of attractive colloidal rods in shear flow have been investigated by mesoscale hydrodynamic simulations and compared to small-angle light-scattering (SALS) and rheology experiments [1, 2]. Earlier rheology experiments [3] have studied the non-equilibrium binodal of fd-virus dispersions under shear flow conditions for a single,
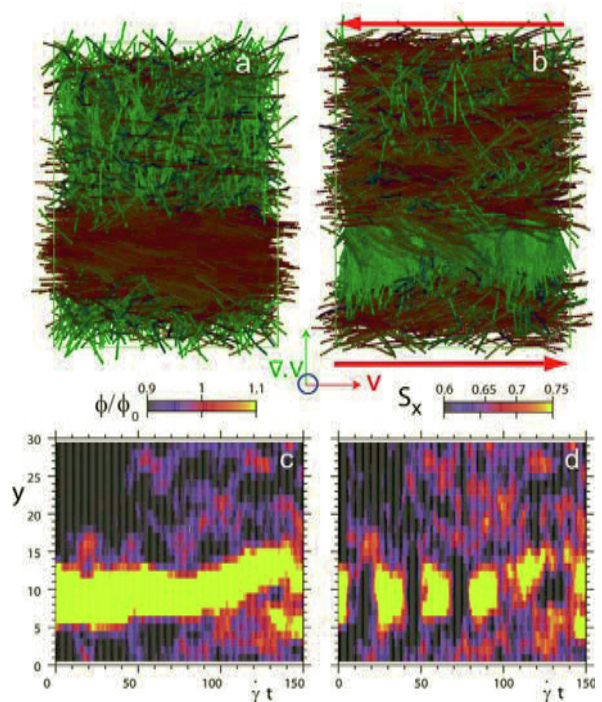
FIG. 1: Snapshots of the simulation box with $\epsilon = 3.5$, (a) at equilibrium, and (b) in a tumbling event at $\dot{\gamma} = 0.003$. Colors in (a) and (b) are coding the rod orientation: horizontal is red, vertical is green and perpendicular to plane of view is blue. Red arrows in (b) denote flow direction. (c) Time evolution of the normalized density ϕ/ϕ_0, and (d) of the orientational order parameter S_x, along the gradient direction.

fixed strength of attraction. This study showed that the P-N transition changes on applying flow. The simulations allow for a microscopic understanding of the behavior of coexisting phases and their interface under shear, including the possible role of collective tumbling motion of rods. The attractive rod-rod interactions are systematically varied, which affects the phase behavior, interfacial properties of coexisting phases as well as the tumbling behavior.

Molecular dynamic simulations of rod-like colloids of aspect ratio 20 with attractive interactions (Lennard-Jones potential with a minimum of ϵ, in units of the thermal energy $k_B T$), are combined with a mesoscopic description of the solvent known as multiparticle-collision dynamics (MPC). This hybrid approach has been shown to account for long-range
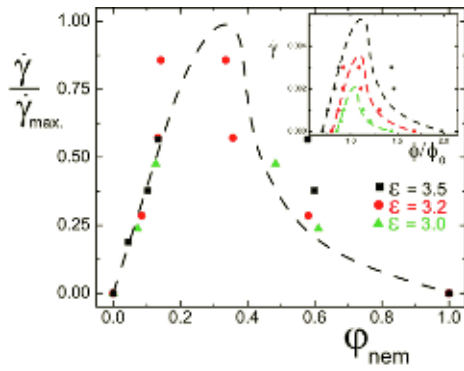
FIG. 2: Non-equilibrium phase diagram obtained from simulations for various values of the strength of attraction interaction, with shear rates normalized by the maximum shear versus the fraction of equilibrium nematic phase. The inset presents the unscaled data. The dashed lines are the conjectured master curve, which are identical in the actual study and in the experimental one [1].

hydrodynamic interactions between rods [4]. The simulated system is prepared in equilibrium with co-existing isotropic and nematic phases, where the director of the nematic phase is aligned parallel to the interface. A snapshot of I-N coexistence is shown in Fig. 1a. We determine the equilibrium phase diagram as a function of the strength of an attractive interaction between the colloidal particles. We find a widening of the two-phase coexistence region, which is small for weak interactions strengths, and becomes very pronounced for stronger interactions. This result very nicely agrees with recent experimental results in equilibrium [5] in which attraction is induced by a variable amount of depleting polymer.

Shear is then applied with the imposed flow direction parallel to the interface, $(v_x, v_y, v_z) = (\dot{\gamma}y, 0, 0)$, with $\dot{\gamma}$ the applied shear rate. Shear flow orients the particles in the initially isotropic phase. This generates free space around each rod and facilitates the transfer of rods from the nematic into the paranematic layer. This mechanism is responsible for the reduction of the density difference between the two phases. Shear flow also induces a rotational motion of individual rods. More interestingly, it leads to a collective rotation motion of large groups of rods in the nematic phase, as indicated in Fig. 1b. This behavior is characterized by both the local concentration and the local orientational order parameter $S_x(y) \equiv \left[3\,\overline{\hat{u}_x\,\hat{u}_x} - 1\right]/2$, where $\hat{u}_x$ is the component of the unit vector connecting the end-points of a rod along the flow direction, and the overline indicates averaging over the vorticity and flow directions. The time dependence of the density ϕ and orientational order parameter S_x of rods as a function of the position y along the gradient direction is plotted in Fig. 1c,d. As can be seen from Fig. 1c, the nematic phase has a higher concentration than the isotropic phase, as expected. More importantly, Fig. 1d demonstrates the periodic tumbling motion of rods in the nematic phase. This is seen for all nematic domains in coexistence with paranematic regions and for all strengths of attractions studied.

Binodals are determined at times where the density of the paranematic state has reached a stationary value and are plotted in Fig. 2 for different attractions. The inset in Fig. 2 shows that an increasing attraction between rods broadens the coexistence region and leads to an increase of $\dot{\gamma}_{max}$. The the coexistence region widening is the same effect as observed in equilibrium. The factor $\dot{\gamma}_{max}$ can be identified with the maximum of the binodal. Simulations for shear rates just above $\dot{\gamma}_{max}$ indicate in fact that the system evolves into an homogeneous state. In Fig. 2, the concentration is expressed in terms of φ_{nem}, i. e. the proportion of the nematic phase in the equilibrium state. The shear rate is scaled by $\dot{\gamma}_{max}$. With this normalization, all data points fall onto a master curve. Precisely the same master curve was also extracted from experimental results. From this striking result we conclude that the effect of attractive interactions on the non-equilibrium phase diagram is reduced to two parameters, $\dot{\gamma}_{max}$ and the difference in packing fractions between the isotropic and nematic phase in equilibrium.

The collective rotational motion induced by shear has been observed only in the coexisting nematic phase. This is in contrast to the paranematic phase that remains flow-aligned without any collective motion. The interface between the coexisting tumbling and flow aligned states is therefore highly dynamic. The periodic motion of the nematic director during tumbling and kayaking is characterized by a time τ between subsequent flow-aligned states. Although this time is not uniquely defined, a clear trend can be observed. We find that τ decreases linearly with the inverse shear rate, as observed previously well inside the nematic region. Furthermore, we observe that the tumbling time increases with increasing interaction strength. We believe that this is due to the higher packing fraction of rods in the nematic phase. This implies that the distance between rods is smaller, and therefore the hydrodynamic friction for their motion parallel to each other is larger.

We want to emphasize that no nematic tumbling states have been found in the homogeneously nematic phase obtained for rates above the maximum of the binodal. This agrees with the experimentally determined tumbling-to-aligning phase separation line that appears at high concentrations and high shear rates and ends at the maximum of the binodal.

[1] M. Ripoll, P. Holmqvist, R. G. Winkler, G. Gompper, J. K. G. Dhont, and M. P. Lettinga. Phys. Rev. Lett. **101**, 168302 (2008).

[2] M. Ripoll, R. G. Winkler, K. Mussawisade, and G. Gompper, J. Phys.: Cond. Matt. **20**, 404208 (2008).

[3] M. P. Lettinga and J. K. G. Dhont. J. Phys.: Cond. Matt. **16**, S3929 (2004).

[4] R. G. Winkler, K. Mussawisade, M. Ripoll, and G. Gompper, J. Phys.: Cond. Matt. **16**, S3941 (2004).

[5] Z. Dogic, K. R. Purdy, E. Grelet, M. Adams, and S. Fraden, Phys. Rev. E **69**, 051702 (2004).

131

Dynamic response of block copolymer wormlike micelles to shear flow

M. P. Lettinga[1], B. Lonetti[2], L. Willner[2], J. Kohlbrecher[3]

[1] IFF-7: Soft Condensed Matter
[2] IFF-5: Neutron Scattering
[3] Laboratory for Neutron Scattering, ETH Zürich and Paul Scherrer Institut, Villigen PSI, Switzerland

The flow behavior of giant wormlike micelles consisting of Pb-Peo block copolymers in the vicinity of the isotropic-nematic phase transition concentration is studied. We explain the appearance of shear banding close to this transition by critical slowing down of the rotational diffusion. This is evidenced by a combination of Fourier transform rheology, time-resolved Small Angle Neutron Scattering (SANS), using a microscopic theory for stiff rods to interpret the dynamic response of the system.

Dispersions of surfactant wormlike micelles form a class of systems that has been intensively studied during the past two decades. Wormlike micellar systems sometimes exhibit extreme shear-thinning behaviour, resulting in shear-induced structure formation like shear banding. Strong shear thinning is of practical interest, since often systems are required in practical applications that exhibit extreme differences in viscosity between the sheared and quiescent state. The reason for the popularity of wormlike micelles for physicists lies in their complex rheological behavior like shear banding and chaotic response, which are connected to the thinning behaviour of these systems. It is therefore important to understand the microscopic mechanism underlying the very strong shear-thinning behaviour of wormlike micelles. It is thought that one mechanisms for the occurrence of strong shear thinning is related to the breaking and/or merging of worms. Another possible mechanism for strong shear thinning is connected to the fact that wormlike systems can undergo an isotropic-nematic (I-N) phase transition. Close to the spinodal point, where the isotropic sample becomes unstable against fluctuations in the orientation, the collective rotational diffusion is critically slowing down, which is quantified by

$$D_r^{eff} = D_r \left\{ 1 - \frac{1}{4} \frac{L}{d} \phi \right\}. \tag{1}$$

Here D_r is the rotational diffusion at infinite dilution, L is the length of the particle, d its thickness and ϕ the volume fraction. The system will show strong shear thinning since the susceptibility of the system to shear depends on the ratio of the applied shear rate to this rotational diffusion coefficient, given by the

effective 'dressed' Peclet number $Pe_{eff} = \dot{\gamma}/D_r^{eff}$. Similarly, the dynamic response of the system to oscillatory flow is expected to be non-linear, which depends on Pe and on the scaled frequency, i.e. the effective 'dressed' Deborah number $\Omega_{eff} = f/D_r^{eff}$, with f is the applied frequency.

Here we study the flow behavior of poly(butadiene)-poly(ethylene oxide) (Pb-Peo) diblock copolymer with a $50 - 50$ block composition in aqueous solution, which are produced by living anionic polymerization in a two-step procedure[1]. This system exhibits many of the properties of surfactant wormlike micellar systems that are responsible for their interesting rheological behaviour. However, in contrast to surfactant systems, the I-N transition can be accessed at a modest concentration of about 5 %[2]. This is due to its stiffness, with a persistence length of around 500 nm and a diameter of 14 nm. The contour length of the Pb-Peo worms is around 1 μm. However, so far the I-N binodal and spinodal I-N transition points have not been determined. A feature of this diblock copolymer system that is probably not shared with micellar systems is that the polymers do not easily break and merge under flow. We thus focus on the microscopic mechanism mentioned above, related to critical slowing down of rotational diffusion close to the I-N transition.
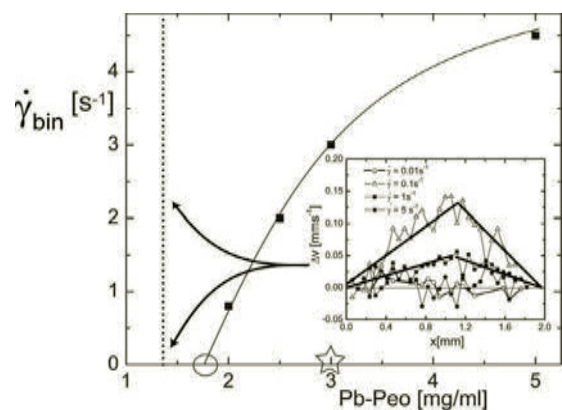

FIG. 1: The binodal points obtained from shear rate quenches. The circle indicates the equilibrium I-N binodal, that is, the binodal point in the absence of flow. The line is a guide to the eye representing the non-equilibrium binodal. The open star indicates the location of the spinodal at zero shear rate. The insert shows banded flow curves.

We determined the equilibrium and non-equilibrium I-N binodal point by performing shear rate quenches and measuring the rheological response using a ARES, TA instruments, with couette geometry. As in earlier work on rod like viruses[3], we define the binodal by the shear rate at which no increase of the viscosity can be detected after the shear rate is quenched from a high shear rate, where the nematic phase is stabilized, to some lower finite shear rate. This is a good measure since the isotropic phase is more viscous than the nematic phase. The resulting points are plotted in Fig. 1. Extrapolation to zero shear also yields the quiescent binodal point with a high precision. Having located the I-N transition and keeping in mind the strong shear thinning in this part of the phase diagram (data not shown) we also determined the flow profile in a couette shear cell in this part of the phase diagram, using spatially resolved Heterodyne dynamic light scattering. A few typical velocity profiles relative to the applied shear rate within the gap of the couette cell are plotted in the inset of Fig. 1. Shear banding is only observed between $0.1\ s^{-1}$ and $0.75\ s^{-1}$. As such this is the first system that shows shear banding as a result of the critical slowing down at the I-N transition.
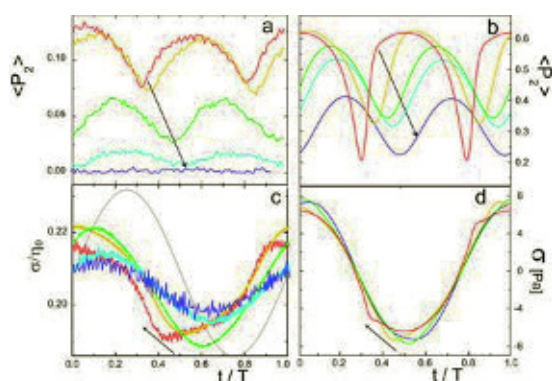
FIG. 2: Time-dependent response of the orientational order parameter $\langle P_2 \rangle$ (a,b) and the stress σ (c,d) to an oscillatory shear flow for experiments ($\dot{\gamma}_{max} = 1.0\ s^{-1}$, a concentration of $2\ \%Pb\text{-}Peo$, frequency between 0.025 and $1.0\ Hz$) (a,c) and theory ($Pe_{eff} = 75$, concentration is $\frac{L}{d}\varphi = 3.3$, frequency varying between $\Omega_{eff} = 3$ and 60). The thin dotted curves indicate the applied shear rate. The arrows indicates increasing frequency. The time t is scaled with the period T of oscillation.

Having evidenced the appearance of shear bands close to the binodal, we still need to prove that the system actually shows critical slowing down. Theoretical calculations for hard rods show how rheological as well as structural signatures can be obtained performing perform dynamic, i.e. oscillatory, experiments[4]. These experiments we perform using a combination of *in situ* time-resolved SANS (SINQ spallation source at the PSI in Villigen, Switzerland) in combination with Fourier Transform Rheology. In the SANS experiments we obtain the orientational distribution of the Kuhn segments of the worm-like micelles due to the observed q-range. This distribution is characterized by the order parameter

$\langle P_2 \rangle$, which can be obtained with a time resolution of up to $5\ ms$. Such curves are plotted in Fig.2a for increasing frequency, while similar theoretical curves are plotted in Fig. 2b. Since the stress is directly related to the order parameter also the stress response is monitored. Thus we make the link between the microscopic order parameter, which is in general difficult to obtain, and the standard macroscopic stress, see Fig. 2c and d.
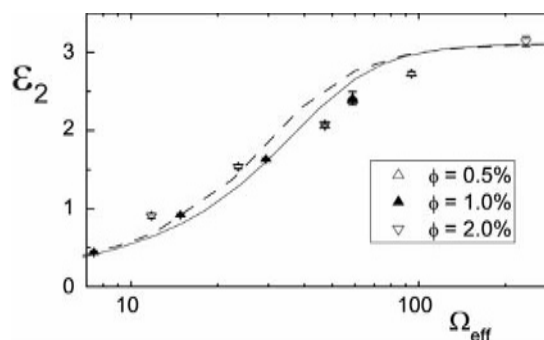
FIG. 3: The phase shift of the orientational response as a function of the effective Deborah number for different scaled concentrations.

The first feature to note is that the order parameter oscillates with twice the frequency of the applied shear rate, even for low shear rates where the stress response is linear in the shear rate. The reason for this is that the scattering experiments probe the flow-vorticity plane, so that the measured order parameter characterizes the orientational order within that plane for which the leading response is quadratic in the shear rate. Second, and more interestingly, we see both with theory and experiments that with increasing frequency the response becomes more linear, i.e. more sinusoidal, but also more phase-shifted. In order to predict the phase shift, one has to relate the frequency with the collective rotational diffusion coefficient, which is given in Eq. 1. This means that the experiments can be scaled with the concentration, using the spinodal point, i.e. $\frac{1}{4}\frac{L}{d}\phi$ as a fit parameter. Performing this scaling, as shown in Fig. 3, and calculating the actual volume fraction of the wormlike micelles from the average length and thickness leads to two separate determinations of the spinodal point that are not further apart than about $30\ \%$. In view of the poly-dispersity and flexibility of the system, this is a surprisingly good comparison. This equilibrium spinodal point is plotted as a star in Fig. 1. More information can be found in reference [5].

[1] J. Allgaier et al., Macromolecules, **1997**, 30, 1582.

[2] Y.-Y. Won et al., Science, **1999**, 283, 960.

[3] M. P. Lettinga and J. K. G. Dhont, J. Phys.: Condens. Matter, **2004**, 16, S3929.

[4] J. K. G. Dhont, W. J. Briels, Colloid Surface A **2003**, 213, 131.

[5] B. Lonetti et al., J. Phys.: Condens. Matter, **2008**, 20, 404207.

Dynamics in colloidal suspensions: from neutral to charged particles

G. Nägele[1], A.J. Banchio[2]

[1] IFF-7: Soft Condensed Matter
[2] Universidad Nacional de Córdoba, Argentina

We have made a comprehensive study on the dynamics of suspensions of charge-stabilized and neutral colloidal spheres. Numerous short-time dynamic properties including diffusion functions, translational and rotational self-diffusion coefficients and the high-frequency viscosity have been computed by means of a powerful accelerated Stokesian Dynamics simulation method. The results of this study were used, in particular, to explore the validity of generalized Stokes-Einstein relations, and the possibility of measuring self-diffusion in a scattering experiment at an experimentally accessible wavenumber.

The dynamics of suspensions of charged colloidal particles is of fundamental interest in soft matter science, surface chemistry and food science. The scope for these systems has been broadened even further through the increasing importance of biophysical research dealing with charged biomolecules such as proteins and DNA [1]. Many of the theoretical and computer simulation methods developed in colloid physics are applicable as well to biological molecules and cells. In addition, suitably modified methods from colloidal physics can also be applied to dispersions of very small, i.e., nanosized particles not much bigger than the solvent molecules. Charged colloidal particles interact with each other directly by means of a screened electrosteric repulsion, and through solvent-mediated hydrodynamic interactions (HIs). These interactions cause challenging problems in the theory and computer simulation of the colloid dynamics.

In this communication, we report on extensive Stokesian Dynamics (SD) simulations where the influence of electrosteric and hydrodynamic interactions has been studied for numerous short-time properties including the high-frequency viscosity η_∞, the wavenumber-dependent diffusion function $D(q)$ determined in a scattering experiment, the so-called hydrodynamic function $H(q)$, and the rotational and translational short-time self-diffusion coefficients D_r and D_s, respectively. The simulations have been performed, with a full account of the many-body HIs, in the framework of the model of dressed spherical macroions interacting by an effective pair potential of screened Coulomb type [2, 3]. A large variety of sys-

FIG. 1: Simulation test of short-time GSE relations relating the rotational and translational self-diffusion coefficients D_s and D_r, and the cage diffusion coefficient, $D(q_m)$, respectively, to the high-frequency shear viscosity η_∞. All depicted quantities are normalized by their zero concentration values marked by the subindex 0. Symbols: SD simulation data. Lines: theoretical results. (a) Charged particles in salt-free solvent (water). (b) Suspension of neutral colloidal spheres. From [2].

tems with differing particle concentrations, charges and added salt concentrations have been considered, spanning the range from hard-sphere systems to low-salinity suspensions where the charged particles repel each other over long distances. Through comparison with the simulation data, the applicability and the level of accuracy of analytical methods

and ad-hoc concepts has been tested, which are frequently applied in the description of the colloid dynamics.
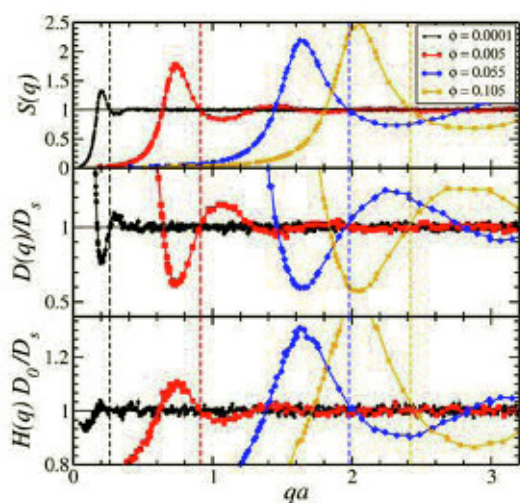
FIG. 2: SD results for the static structure factor, $S(q)$, normalized short-time diffusion function, $D(q)$, and hydrodynamic function $H(q) = S(q) \times D(q)/D_0$ of a salt-free suspension of charged particles, as a function of the wavenumber q times the particle radius a. The dynamic quantities $D(q)$ and $H(q)$ are scaled by the respective short-time self-diffusion coefficient D_s. The dashed vertical lines mark the wavenumber q_s where $S(q_s) = 1$. From [3].

As an important application, the SD simulation scheme has been used to scrutinize the validity of short-time generalized Stokes-Einstein (GSE) relations that provide an approximate link between diffusion coefficients and the high-frequency viscosity. GSE relations are fundamental to a growing number of microrheological experiments. The assessment of the quality of these relations is a necessary prerequisite for the experimentalist interested in deducing rheological information from dynamic scattering experiments. Our simulation results show that the accuracy of a GSE relation is strongly dependent on the range of the interaction potential, and the particle concentration. See Fig. 1 for an illustration of this important point where simulation results for the static structure factor $S(q)$ at various volume fractions are compared to corresponding results for $D(q)$ and $H(q)$. The function $H(q)$ is a direct measure of the HIs. Without HI, $H(q)$ would be a constant equal to one, independent of the scattering wavenumber.

A strictly valid GSE relation would be represented in Fig. 1 by a horizontal line of height equal to one, independent of the colloid volume fraction ϕ. As shown in this figure, the GSE relation for the cage diffusion coefficient, $D(q_m)$, related to the position, q_m, of the static structure factor peak, applies reasonably well to neutral hard spheres and to high-salinity systems (see Fig. 1b). However, it is strongly violated in the case of salt-free suspensions of charged particles (see Fig. 1a). Our simulations show further that rotational self-diffusion, and to a lesser extent also translational self-diffusion, are faster than predicted by the

corresponding GSE relations. The general trends in the concentration and salt-dependence of the transport coefficients predicted in our SD simulations are in agreement with experimental findings on charge-stabilized suspensions and neutral particle systems.

It has been suggested that the (short-time) self-diffusion coefficient can be probed in a dynamic light scattering (DLS) experiment at a specific wavenumber q_s located to the right of the principal peak in $S(q)$, where $S(q_s) = 1$. The assumption made here is that the dynamic scattering function at such a wavenumber is essentially determined by self-diffusion, without noticeable collective diffusion contributions. Indeed, if this assumption is valid at least on an approximate level, $D_s \approx D(q_s)$, where $D(q_s)$ is the diffusion function measured at q_s. Fig. 2 includes SD simulation results for $S(q)$, $D(q)$ and the hydrodynamic function $H(q)$ for a salt-free suspension of charged particles. All dynamic quantities are normalized by the self-diffusion coefficient D_s. As can be noticed, $D_s \approx D(q_s)$ is obeyed indeed within reasonable accuracy. For all systems examined in our SD study, we find the difference between $D(q_s)$ to be less than ten percent, both for charged and neutral particles. Thus, DLS at the specific point q_s can be used to obtain a decent estimate for the value of D_s. This finding is of relevance in numerous scattering experiments on colloidal systems where the large wavenumber regime is not accessible experimentally, and where alternative techniques to measure D_s directly are not applicable or unavailable.

Colloidal hard spheres have a common static and hydrodynamic length scale set by the particle radius a. This leads to the occurrence of an isobestic wavenumber $qa \approx 4.02$ where both $S(q)$ and $D(q)/D_s$ are equal to one, independent of the volume fraction. In low-salinity suspensions, the geometric mean particle distance becomes another length scale of physical relevance. Consequently, in these systems there is no isobestic point for $S(q)$ and $H(q)$. The non-existence of a ϕ-independent isobestic point in salt-free suspensions is exemplified in Fig. 2.

In summary, our comprehensive SD simulation study of short-time transport properties forms a useful database for researchers interested in information on the suspension dynamics of globular colloidal particles, from systems of large, micron-sized colloids down to proteins in the nanometer range such as lysozyme and apoferritin. A simulation analysis of the long-time dynamics of charged colloidal spheres with a full account of the HIs remains as a major challenge which we plan to address in future work.

[1] M.G. McPhie and G. Nägele, Phys. Rev. E **78**, 78, 060401(R) (2008).

[2] A.J. Banchio and G. Nägele, J. Chem. Phys. **128**, 104903 (2008).

[3] A.J. Banchio, M.G. McPhie and G. Nägele, J. Phys.: Condens. Matter **20**, 404213 (2008).

135

Diffusion in a fluid membrane with a flexible cortical cytoskeleton

T. Auth[1], N. S. Gov[2]

[1] IFF-2: Theoretical Soft-Matter and Biophysics
[2] The Weizmann Institute of Science, Department of Chemical Physics, P.O. Box 26, Rehovot 76100, Israel

The cytoskeleton hinders protein diffusion in the lipid bilayer of the cell's plasma membrane. We calculate the influence of a flexible network of long-chain protein filaments, which is sparsely anchored to the bilayer, on protein diffusion. We define a potential landscape for the diffusion based on the steric repulsion between the cytosolic part of the protein and the cytoskeletal filaments, using the pressure field that the cytoskeleton exerts on the bilayer. We predict the changes of the diffusion coefficient upon removal of anchor proteins and for a stretched cytoskeleton.

Diffusion within the fluid membrane plays an important role for cellular processes, because the cell communicates with its surrounding via its lipid bilayer [1]. For example, diffusion of activated receptor molecules leads to signal amplification and diffusion of adhesion molecules to the contact area is important for cell adhesion.

The cytoskeleton, which is in close proximity to the membrane, has been identified to act as a strong regulator of the diffusion within the cellular membrane. For the red blood cell (RBC), several experiments show that the spectrin cytoskeleton slows down translational diffusion. Using single-molecule tracking techniques, small compartments have been found for the diffusion in the cell membrane [2] that may be explained by the cytoskeletal network below the bilayer.

Our work focusses on the diffusion in the membrane of cells that have a cortical, two-dimensional cytoskeleton, which is composed of flexible long-chain proteins [3]. A prominent example of such cells are RBCs, where the long-chain proteins are spectrin tetramers. However, a similar cortical cytoskeleton is found on the plasma membrane of other mammalian cells, and spectrin has been identified in neurons and on membranes of intracellular organelles.

A pressure field on the bilayer is generated by the conformational fluctuations of the cytoskeletal filaments to which they are anchored at their ends via anchor complexes [4] . We calculate the pressure field using a linear, flexible polymer with bulk radius of gyration R_g that is attached to a hard wall at $\boldsymbol{\rho}_1 = (x_1, y_1)$ and $\boldsymbol{\rho}_2 = (x_2, y_2)$. The pressure diverges close to the anchor points and decreases
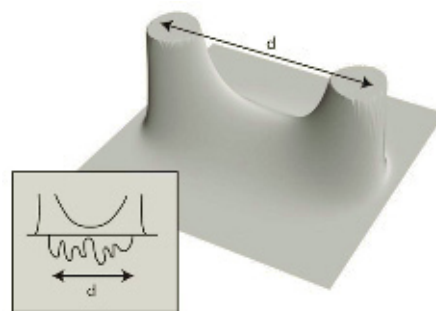
FIG. 1: *Entropic pressure that a flexible, cytoskeletal protein that is anchored to a lipid bilayer with its ends exerts on the cell membrane.*

exponentially for large distances from the anchors, $|\boldsymbol{\rho}| \gg |\boldsymbol{\rho}_i|$ $(i = 1, 2)$, see Fig. 1.

The calculation of the pressure is based on the diffusion equation to calculate the polymer conformations. This implies an infinite contour length of the polymer, which is certainly a bad approximation if the distance d between the anchor points is comparable with the contour length. This situation is addressed in Ref. [5], where a Gaussian polymer model is combined with the condition of a finite contour length. Force-extension relations and end-to-end distribution functions have been calculated and the analytic theory describes experimental and simulation data very well.

We use a simple argument to illustrate how a finite contour length affects the fluctuation pressure: we subtract from the contour length $L = 6R_{g,0}^2/\ell$ (where $\ell = L/N$ is the Kuhn length of the polymer, N the number of repeat units in the chain, and $R_{g,0}$ the radius of gyration of the free chain) the anchor distance d, because this length of the chain is 'needed to connect the anchor points' and is therefore not available for conformation fluctuations.

To calculate the pressure field of the stretched chain, we simply replace R_g in the expression for the pressure by the new, effective R_g, which we obtain using the effective Kuhn length, $\ell' = (L - d)/N$: $R_g^2 = \ell'^2 N/6 = (\ell/6)(L - d)^2/L$. The pressure along the connection line of the anchor points is large either for very small anchor distances because of the high pressure at the anchor points or for very large anchor distances that are comparable with the countour

FIG. 2: Pressure field for an unstretched RBC cytoskeleton.

FIG. 3: Anisotropic diffusion for a cytoskeleton that is stretched by a factor 1.5 and accordingly compressed in the perpendicular direction (for two different orientations of the hexagonal network).

length when the polymer conformation is stretched and therefore everywhere close to the lipid bilayer.

Fig. 2 shows a superposition of the single-filament pressure fields for an idealized arrangement of spectrin bonds on a hexagonal lattice, as in the RBC cytoskeleton. We use a random walk and Metropolis Monte Carlo to simulate the diffusion process in the lipid bilayer. The step length is $a = 1\,\mathrm{nm}$, which is the typical size of the lipid molecules. The influence of the cytoskeleton is taken into account by the potential landscape that is determined for the pressure field of the cytoskeleton multiplied with the effective interaction volume for the protein under consideration. The interaction volume is determined by the size of the cytosolic part of the protein that sterically interacts with the cytoskeleton. It can be obtained either from electron microscopy data for the spectrin and the diffusing protein or phenomenologically as a fit parameter using measurements of the effective diffusion coefficient.

Once the effective interaction volume is determined, we can predict several aspects of the protein diffusion [3]. For short times, the protein shows normal, fast diffusion within a single corral that is formed by the cytoskeletal bonds. Also for long times normal diffusion is observed, but with a smaller, effective diffusion constant. Long-time diffusion is hindered because the protein needs to hop across the potential barriers. The crossover between both regimes can also be observed in single-particle tracking experiments.
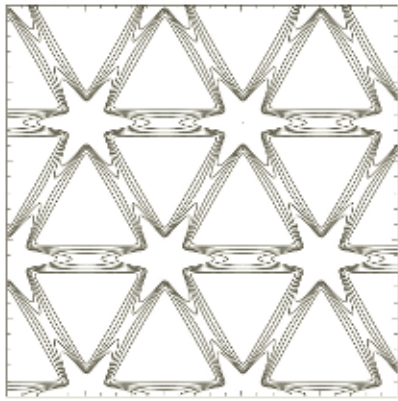
In healthy red blood cells, the cytoskeletal filaments are usually attached at their ends but also — with a different protein complex — in their middle. In disease, the middle anchor complex can be missing. We predict that the diffusion coefficient in the disease case is by a factor 25 larger than for healthy RBCs.

Furthermore, we can predict the influence of compression or stretching of the cytoskeleton on protein diffusion. For isotropic stretching, we find a decrease of the effective diffusion constant because of the increased height of the cytoskeletal barriers. For the normal RBC, the simulation results are well described by a rescaled analytic expression: the height of the potential barrier is given by the value in the middle of the bond where the cytoskeletal pressure is lowest. For anisotropic stretching, which constantly occurs in vivo when the RBC is deformed in blood flow, we predict increased diffusion along the direction of the stretch and decreased diffusion perpendicular to the stretching.
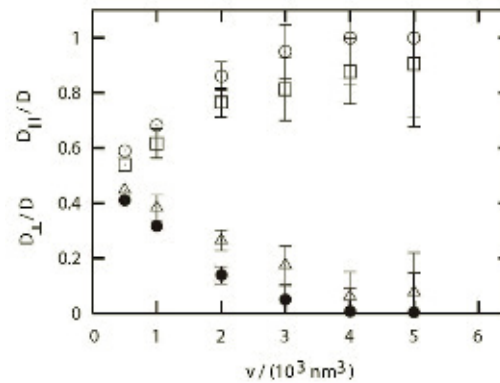
In Fig. 3, we plot the relative diffusion for an anisotropically stretched network parallel and perpendicular to the direction of the stretch for different values of the effective interaction volume. For the effective interaction volume $v = 6000\,nm^3$ that applies for the band-3 protein in RBCs, we find that the diffusion is almost completely asymmetric if the RBC cytoskeleton is stretched by a factor 1.5 and accordingly compressed in the perpendicular direction (to preserve the total area, which is fixed by the lipid bilayer).

Our results quantify the interaction between the cytosolic part of a transmembrane protein and a cytoskeleton that consists of a two-dimensional network of flexible polymers, as for example found in RBCs. We predict the changes in the diffusion due to lack of anchor proteins, such as a missing middle anchor complex in forms of hereditary spherocytosis. We also predict changes of the diffusion caused by a stretched cytoskeleton.

[1] M. J. Saxton, Curr. Top. Membr. **48**, 229 (1999).

[2] M. Tomishige, Y. Sako, and A. Kusumi, J. Cell Biol. **142**, 989 (1998).

[3] T. Auth and N. S. Gov, Biophys. J. **96**, 818 (2009).

[4] T. Auth, S. A. Safran, and N. S. Gov, New J. Phys. **9**, 430 (2007).

[5] R. G. Winkler and P. Reinecker, Macromolecules **25**, 6891 (1992).

137

Membrane fluctuations determine the short-time movements of cells

A. Baumgaertner[1], S. L. Narasimhan[2]

[1] IFF-2: Theoretical Soft-Matter and Biophysics
[2] Solid State Physics Division, Bhabha Atomic Research Centre, Mumbai, India

It is shown that a fluctuating surface with non-zero surface tension, driven by a second surface, moves subdiffusively at intermediate times before drifting asymptotically. This is demonstrated for a one dimensional solid-on-solid model of a surface interacting repulsively with a randomly fluctuating one dimensional substrate surface. Such a model of interacting surfaces provides a better alternative to the commonly used Brownian ratchet model for describing the protrusions of a cell membrane caused by the polymerizing front of the cell's actin network.

138

Propagating or driven surfaces such as shock waves, reaction fronts in reaction-diffusion systems and field-driven domain walls in ferromagnetic nanowires are frequently encountered in many physico-chemical processes. A study of a driven surface is also a challenging 'moving boundary problem' that can shed light on ubiquitous far-from equilibrium phenomena. Even in biological processes such as wound healing, embryogenesis, immunology and metastasis, driven surfaces are fundamental to the mechanism underlying the movements of biological cells.

FIG. 1: Crossover scaling, Eq.(3), for various values of t_F = 0.001, 0.002, 0.004, 0.008, 0.032; the $a\ priori$ probabilities are $p_F = 1/2$ and $q_F = 1/4$. respectively, for the case $M = 512$, $\mu = 1$, $h_0 = 1$. INSET: Log-log plot of subdiffusion time τ_f versus ϕ_a.

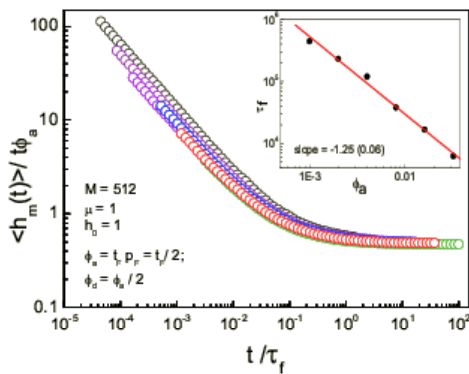For example, the motion of a cell starts with a protrusion of the cell membrane caused by the actin-based extensions of the cell's leading edge [1]. The protrusive structure at the leading edge are called lamellipodia and filopodia. A lamellipodium is a thin (≈ 0.1 μm) sheet-like structure that is filled with actin filaments. The fast growing ends of the filaments, with association and dissociation constants $k_a > k_d$, respectively, are oriented towards the membrane; their elongation pushes the leading edge forward, thereby promoting cell movements [1, 2].

Surface model: Since the thickness of the lamellipodium (0.1 μm) is very small as compared to the lamellipodial margin along the membrane (10 - 100 μm), this lamellipodial section of the cell membrane can be modeled as a flexible one dimensional surface without loops or overhangs. Such a surface can be conveniently generated by a $(1 + 1)$-dimensional Solid-on-Solid (SOS) model (for reviews see e.g. [3]). The SOS interface is a reasonable model to decribe the collective protrusion modes of membranes. The Hamiltonian of the 1d SOS model is [4],

$$H = \mu \sum_{<ij>} \mid h_i - h_j \mid \qquad (1)$$

where the summation is over nearest neighbors, and μ is a microscopic surface energy ('surface tension'), in units of $k_B T/\ell$, which has the dimension of a line tension. A surface thus generated by the diffusion-less SOS model of particle deposition and evaporation may be called a 'membrane' configuration. The mean square fluctuation in the surface heights, for a given realization of the surface, is given by $\sigma^2(t) = \sum_{j=1}^{M}[h_j(t) - \bar{h}(t)]^2/M$ where M is the projection of the surface, and $\bar{h}(t)$ denotes the mean height of the surface. It can be shown that for $\mu > 0$ and for M large enough, the surface belongs to the Edwards-Wilkinson (EW) class [5, 6], exhibiting the finite size crossover scaling $\langle \sigma_m(t) \rangle = M^\alpha\ f(tM^{-z})$ with $f(x) \sim x = const$ for $x \gg 1$ and $f(x) \sim x^{\alpha/z}$ for $x \ll 1$, and the limiting cases

$$\langle \sigma^2(t) \rangle^{1/2} \sim \begin{cases} t^\beta & : t \ll M^z \\ M^\alpha & : t \gg M^z. \end{cases} \qquad (2)$$

where the dynamical and roughness exponents are $z = 2$ and $\alpha = 1/2$, respectively, and $\beta = \alpha/z = 1/4$. Such a free surface performs symmetric random motions, $\langle h(t) \rangle \rightarrow 0$, which is different in the presence of a repelling second surface. The consequences are dicussed as follows [7].

Filament model: The ensemble of filaments, whose ends are assumed to be densely packed and directed towards the membrane, is modeled by a second $(1 + 1)$-dimensional surface, which evolves randomly (uncorrelated). The interaction between the two surfaces is taken to be purely repulsive. The parameter, $0 \leq t_F \leq 1$ denotes the probability that the 'filament' surface is updated, and p_F and q_F denote the probability that a filament-column is incremented and decremented, respectively. Then, the polymerization rates for association and dissociation are given by $\phi_a \equiv t_F p_F$ and $\phi_d \equiv t_F q_F$.

Interacting surfaces: Fig. 1 shows the crossover scaling of the average time-dependent center of mass displacement of the membrane, $\langle h_m(t) \rangle$, for various values of the association rate ϕ_a and for $M = 512$. It is observed that $\langle h_m(t) \rangle$ exhibits a crossover scaling from subdiffusive movements at times $t < \tau_f$, to filament-induced drift at $t > \tau_f$ (independent of M) given by

$$\langle h_m(t) \rangle = v \, t \, f(t/\tau_f), \qquad (3)$$

where $f(x) = const$ for $x \gg 1$ and $f(x) \sim x^{\beta-1}$ for $x \ll 1$; the anomalous exponent is $\beta = 1/4$, v is the asymptotic velocity of the membrane.

The 'subdiffusion' time τ_f characterizing the crossover from subdiffusion to drift has been estimated by the best data collapse as function of ϕ_a and μ. It is found that τ_f exhibits a power law of ϕ_a (inset of Fig.1) and decays exponentially with μ,

$$\tau_f \sim \phi_a^{-\omega} \, e^{-c\mu}, \qquad \phi_a > 0, \qquad (4)$$

where $c \approx 1/3$ is a constant. The exponent ω can be understood by considering the two different time evolutions, the advancement of the filament surface, $\sim \phi_a t$, and the growth of the membrane $\sim t^\beta$. As long as $t^\beta/\phi_a t > 1$ the growth of fluctuations is not suppressed, which changes when both are comparable at $t \approx \tau_f$. This leads to $\omega = 1/(1-\beta) = 4/3$. Our numerical estimate of $\omega \approx 1.25 \pm 0.06$ is close to this theoretical value.

From estimates of $v = h(t)/t$ in the limit $t \to \infty$ one can show that approximately

$$v \approx \ell \, \phi_a \, e^{-b\mu}, \qquad \phi_a > 0 \qquad (5)$$

where b depends on the polymerization rate constants. It should be noted that this formula, valid in the general case of association and dissociation, is at variance with the classical formula, Eq.(6); however, the comparison identifies the load force with the surface tension, $f\delta \sim \mu$.

The crossover can be understood by considering the growth of fluctuations of the membrane, $\sigma_m(t)$. In particular, the M-$independence$ of $\langle h_m(t) \rangle$ and the M-$dependence$ of $\langle \sigma_m(t) \rangle$, as expected from Eq.(2), can be reconciled. Similar to the case of a free surface, Eq.(2), the time of saturation, τ_s, for the growth of fluctuations in the presence of a reflecting boundary and in the case of 'weakly suppressed' fluctuations ($\phi_a \ll 1$) can be expected to be $\tau_s \sim M^z$.

Discussions: Our current physical understanding of cell protrusion is based on the concept of the 'Brow-

nian ratchet' (BR) model [8, 9]. The ratchet mechanism [8] is the intercalation of an actin monomer of size δ between the membrane and the filament tip, when a sufficiently large fluctuation of either the tip of the filament or the membrane occurs. The force-velocity relationship can be worked out by using thermodynamic arguments [8]. For a single filament growing against a load force, $-f$, at rate much slower than the diffusion rate D of the membrane (i.e., $k_a \delta^2/D \ll 1$), the growth velocity is given by [8, 9]

$$v = \delta[k_a \, \rho \, e^{-f\delta/k_B T} - k_d], \qquad (6)$$

where ρ is the concentration of actin monomers. This force-velocity relation is valid if the thermal fluctuations of the barrier (membrane) are uncorrelated and characterized by a single parameter, the diffusion constant. If, however, the fluctuations are correlated, as in the case of membranes [4], then the force-velocity relation is qualitative different from Eq.(6) and the ratchet concept of less importance.

In summary, the present study shows that correlated membrane fluctuations must be expected to govern the protrusive dynamics of a lamellipodium leading to subdiffusive behavior which is at variance to solely drifting movements caused by a Brownian ratchet mechanism. This is a general result, irrespective of the membrane model used. The present model of a driven surface will be of general interest as it belongs to a class of 'moving boundary' problems.

[1] D. Bray, Cell Movements : from molecules to motility, Garland Publ., New York, 2001

[2] S.V.M.Satyanarayana and A.Baumgaertner, J.Chem.Phys. 121, 4255 (2004)

[3] A. L. Barabasi and H. E. Stanley, Fractal concepts in surface growth, Cambridge University Press, 1995

[4] D. Nelson, in Statistical mechanics of membranes and surfaces, World Scientific, Singapore, ed. by D. Nelson, T. Piran, S. Weinberg, 2004

[5] S. F. Edwards and D. R. Wilkinson, Proc. R. Soc. Lond. A 381, 17 (1982)

[6] M. Kardar, G. Parisi and Y. C. Zhang, Phys. Rev. Lett. 56, 889 (1986)

[7] S.L Narasimha and A.Baumgaertner (submitted)

[8] C. Peskin, G. Odell and G. Oster, Biophys. J. 65, 316 (1993)

[9] A. Mogilner and G. Oster, Biophys. J. 71, 3030 (1996)

Clustering and alignment of red blood cells in microcapillaries

J. L. McWhirter, H. Noguchi, G. Gompper

IFF-2: Theoretical Soft-Matter and Biophysics

The shapes, aggregation, and alignment of red blood cells (RBCs) in cylindrical capillary flow is investigated by mesoscopic hydrodynamic simulations. We study the collective flow behavior of many RBCs, where the capillary diameter is comparable to the diameter of the RBCs. Two essential control parameters in our study are the volume fraction of RBCs (the tube hematocrit, H_T), and the flow velocity of the RBC suspension. At very high flow velocities and very low H_T, the parachute-shaped RBCs can be found in clusters that are stabilized by the hydrodynamic solvent flows. At high H_T, the RBCs can exhibit one disordered phase and two distinct ordered phases depending on H_T and the flow velocity. Thermal fluctuations, included in the simulation method, coupled to hydrodynamic flows are important contributors to the RBC morphology.

FIG. 1: *Sequential simulation snapshots of six RBCs in a dilute blood suspension ($L_{\text{ves}}^* = 3.3$ or $H_{\text{T}} = 0.084 = n_{\text{ves}}V_{\text{ves}}/\pi L_z R_{\text{cap}}^2 = 0.28/L_{\text{ves}}^*$) at $v_0^* = 7.7$ and $n_{\text{ves}} = 6$. The full length of the cylindrical simulation tube is L_z. The critical flow velocity associated with the shape transition from a discocyte at low velocities to a parachute at higher velocities is $v_c^* \sim 5$. Top panel shows a 6 RBC cluster while the bottom two show the break-up of this cluster at a later time.*

In the absence of flow, human RBCs have a biconcave-disc (discocyte) shape whose maximum diameter and thickness are 7.6 μm and 2 μm with constant area and volume, V_{ves}. The RBC membrane consists of a lipid bilayer supported by an attached spectrin network, which acts as a cytoskeleton and is responsible for the shear elasticity of the membrane. The bilayer's resistance to a bend is controlled by a curvature energy with a bending rigidity, κ, and the spectrin's resistance to a shear strain is characterized by a shear modulus, μ. At thermal equilibrium, the discocyte shape of a RBC can be predicted theoretically by minimizing the membrane's bending and stretching energy subject to a fixed surface area and volume. However, under flowing, nonequilibrium conditions, the shape adopted by the RBCs is determined by the competition between these mechanical properties and the external hydrodynamic flow forces arising from the blood plasma (the solvent) suspending the RBCs.

The spectrin network enables an RBC to remain intact while changing its shape in blood flow through narrow capillaries with diameters of 0.2 μm to 10 μm. At high dilution in fast blood flows through narrow capillaries, optical microscopy of micro vessels [1] have shown that individual RBCs can adopt a parachute shape; the faster flow in the center of the capillary and the slower flow near the walls in-

duces this shape change. The RBC deformability is reduced in blood related diseases, such as diabetes mellitus and sickle cell anemia; with these diseases the resistance to flow is relatively high and the heart must work harder to produce the higher pumping pressures needed to ensure normal blood flow. Therefore, the deformability of a RBC is important for the regulation of oxygen delivery.

We have already studied the shape changes of a single, isolated RBC in a blood flow at high dilution [2] using a mesoscopic simulation technique which combines two methods. The solvent hydrodynamics is described by an explicit, particle-based dynamics called Multi-particle Collision Dynamics (MPC). The RBC membrane is treated by a discretized mechanical model of a two-dimensional elastic membrane parametrized by κ and μ, that is, a dynamically triangulated surface model [3]. Our studies showed that the shape change of an RBC from a discocyte to a parachute occurs at a critical flow velocity which depends on the material parameters κ and μ [2]. As the RBC became more rigid, a faster the blood flow was needed to achieve this shape transition. This transition was accompanied by a sudden drop in the pressure needed to drive the flow at a given velocity.

The main focus of the present work is to study the collective flow behavior of many interacting RBCs at very low and high H_T [4, 5]. We consider a number n_{ves} of vesicles in capillary tube segments of length L_z and radius R_{cap} with periodic boundary conditions in the flow direction, Z. Here $L_{\text{ves}}^* = L_z/n_{\text{ves}}R_{\text{cap}}$
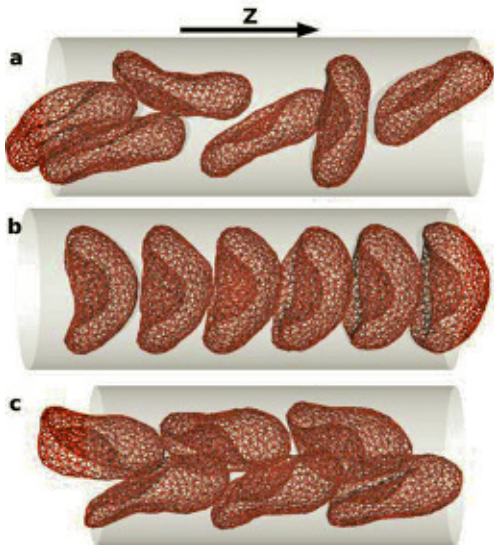
FIG. 2: Simulation snapshots of $n_{\mathrm{ves}} = 6$ RBCs: (a) Disordered-discocyte phase for $L^*_{\mathrm{ves}} = 0.875$ and $v^*_0 = 2.5$; (b) Aligned-parachute phase for $L^*_{\mathrm{ves}} = 0.875$ and $v^*_0 = 10$; and (c) Zigzag-slipper phase for $L^*_{\mathrm{ves}} = 0.75$ and $v^*_0 = 10$.

FIG. 3: (a) Phase behavior as a function of average vesicle distance L^*_{ves} and mean flow velocity v^*_0, for $n_{\mathrm{ves}} = 6$. The hematocrit varies between $H_{\mathrm{T}} = 0.22$ and $H_{\mathrm{T}} = 0.45$, since $H_{\mathrm{T}} = 0.28/L^*_{\mathrm{ves}}$. Symbols represent the disordered-discocyte ($\star$), aligned-parachute ($\blacksquare$), and zigzag-slipper ($\bullet$) phases, respectively. (b) Pressure drop $\Delta P^*_{\mathrm{drp}}$ per vesicle for the aligned-parachute phase (simulations with $n_{\mathrm{ves}} = 1$) and the zigzag-slipper phase (simulations with $n_{\mathrm{ves}} = 6$) at the same volume fraction ($L^*_{\mathrm{ves}} = 0.75$, corresponding to $H_{\mathrm{T}} = 0.37$).

and $v^*_0 \equiv v_0 \tau / R_{\mathrm{cap}}$, where the characteristic shape relaxation time is $\tau = \eta_0 R^3_{\mathrm{cap}} / \kappa$. A gravitation force mg is used to generate flow along the Z axis where $v_0 = m n_s g R^2_{\mathrm{cap}} / 8 \eta_0$ and η_0 is the viscosity of the suspending solvent.

At very low H_T, parachute shaped RBCs form stable clusters at flow velocities v^*_0 much higher than the critical flow velocity, v^*_c, associated with the discocyte to parachute transition. There are two reasons for the cluster formation. First, a single RBC separated from a neighbouring cluster of RBCs is more deformed by the flow than its neighbours, bending closer to the capillary axis or center where the flow is fastest; therefore, this single RBC approaches the cluster, forming a larger cluster. Second, the effective hydrodynamic flow mediated attractions between the RBCs in a cluster stabilize the cluster, increasing its lifetime. As v^*_0 approaches v^*_c, fluctuations in the RBC shape increase, leading to cluster break-up events as shown in Fig. 1.

At high H_T, three distinct RBC 'phases' exist (Fig. 2); one is disordered, the disordered-discocyte (D) phase, while the remaining two are ordered, the aligned-parachute (P) and zig-zag slipper (S) phases (Fig. 3). In the D phase at $L^*_{\mathrm{ves}} \gtrsim 0.85$ and low v^*_0, the RBCs appear as discocytes with random orientations and no significant long-range spatial correlations. The P phase was expected at higher v^*_0 based on the simulations examining the shape transition to a parachute of a single, isolated RBC under flow [2]. However, given these earlier simulations, the S phase occurred unexpectedly at smaller L^*_{ves}. Here, slipper-shaped RBCs form two regular, interdigitated parallel rows. Curiously, the S phase produces a larger pressure drop $\Delta P^*_{\mathrm{drp}}$, or resistance to flow, than the periodic P phase under equivalent conditions, as shown in Fig. 3(b). An aligned-parachute conformation at $L^*_{\mathrm{ves}} \lesssim 0.85$ is destabi-

lized by the thermal fluctuations that are incorporated into the mesoscopic simulation method; these fluctuations have the effect of moving an RBC off the capillary axis to regions of slower flow. In other theoretical approaches, thermal fluctuations are not incorporated, or their incorporation is not as simple as in MPC.

In summary, we have shown that at very low RBC volume fractions the RBC deformability implies a flow-induced cluster formation at high blood flow velocities. In addition, at high volume fractions, the collective behavior of several RBCs determines their flow-induced morphology and resistance to flow. Future studies will examine the dependence of flow properties on channel geometry, polydispersity of the RBC suspension, and the introduction of more rigid, spherical white blood cells.

[1] Y. Suzuki, N. Tateishi, M. Soutani, and N. Maeda, Microcirculation **3**, 49 (1996).

[2] H. Noguchi and G. Gompper, Proc. Natl. Acad. Sci. **102**, 14159 (2005).

[3] H. Noguchi and G. Gompper, Phys. Rev. E **72**, 011901 (2005).

[4] J.L. McWhirter, H. Noguchi, and G. Gompper, Proc. Natl. Acad. Sci. **106**, 6039 (2009).

[5] P. Gaehtgens, C. Dührssen, K.H. Albrecht, Blood Cells **6**, 799 (1980).

141

Cooperation of sperm in two dimensions: synchronization and aggregation through hydrodynamic interactions

Y. Yang, E. Elgeti, G. Gompper

IFF-2: Theoretical Soft-Matter and Biophysics

Sperm swimming at low Reynolds number have strong hydrodynamic interactions when their concentration is high in vivo or near substrates in vitro. The beating tails not only propel the sperm through a fluid, but also create flow fields through which sperm interact with each other. We study the hydrodynamic interaction and cooperation of sperm embedded in a two-dimensional fluid. Two effects of hydrodynamic interaction are found, synchronization and attraction. With these hydrodynamic effects, a multi-sperm system shows swarm behavior with a power-law dependence of the average cluster size on the width of the distribution of beating frequencies.

Sperm motility is important for the reproduction of animals. Before they find the ova, sperm have to overcome many obstacles in their way. A healthy mature sperm of a higher animal species usually has a flagellar tail, which beats in a roughly sinusoidal pattern and generates forces that drive fluid motion. The snake-like motion of the tail propels the sperm through a fluid medium very efficiently. In nature, the local density of sperm is sometimes extremely high. For example, in mammalian reproduction, the average number of sperm per ejaculate is tens to hundreds of millions, so that the average distance between sperm is on the scale of ten micrometers, comparable to the length of their flagellum. On this scale, the hydrodynamic interaction and volume exclusion are not negligible. In experiments with rodent sperm at high densities [1], motile clusters consisting of hundreds of cells have been found, which show much stronger thrust forces than a single sperm. The sperm seem to take advantage of strong interactions with neighbor cells of the same species to win the fertilization competition.

The higher animal sperm typically have tails with a length of several tens of micrometers. At this length scale, viscous forces dominate over inertial forces. Thus, the swimming motion of a sperm corresponds to the regime of low Reynolds number. We describe the motion of the surrounding fluid by using a particle-based mesoscopic simulation method called multi-particle collision dynamics (MPC) [2, 3]. This simulation method has been shown to capture the hydrodynamics and flow behavior of complex fluids over a wide range of Reynolds numbers very well [3]. In

particular, it describes the helical motion of swimming sperm in three dimensions [4].

Here, we construct a coarse-grained sperm model in two dimensions. The sperm model consists of particles connected by stiff springs, which form a circular head and a filament-like tail, see Fig. 1. The beating motion is determined by a time-dependent, spontaneous curvature

$$c_{s,tail}(x,t) = c_{0,tail} + A\sin\left[-2\pi f_s t + qx + \varphi_s\right],$$

which generates a propagating, sinusoidal wave along the tail. The wave number $q = 4\pi/L_0$ is chosen to mimic the tail shape of sea-urchin sperm, and L_0 is the tail length. f_s is the beating frequency of the s-th sperm. The constant $c_{0,tail}$ determines the average spontaneous curvature of the tail. φ_s is the initial phase of the s-th sperm, and A is a constant related to the beating amplitude.

We analyzed the hydrodynamic interaction between two sperm and the aggregation behavior of multi-sperm system. In our simulations, sperm clusters are always seen after the system has reached a stationary state. We concluded that hydrodynamic interaction and volume exclusion play important roles in the cluster formation of healthy and motile sperm. We also found that the average cluster size has a power-law dependance on the width of beat frequency distribution [5].
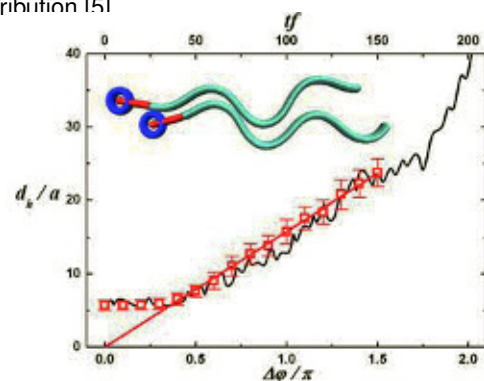

FIG. 1: Head-head distance d_h of two cooperating sperm. Simulation data are shown for fixed phase difference (red, □). The interpolating (red) line is a linear fit for $0.4\pi < \Delta\varphi < 1.5\pi$. The distance d_h is also shown as a function of time t (top axis) in a simulation with a 0.5% difference in the beat frequencies of the two sperm (solid line).

In two-sperm simulations, we found two effects of the hydrodynamic interaction, synchronization and attraction. When two sperm are close in space and swimming parallel, they synchronize their tail beats by adjusting their relative position. This "synchronization" process is accomplished in a very short time. Then, the synchronized sperm have a tendency to get close and form a tight pair. This "attraction" process takes much longer time then synchronization. Two sperm stay locked in phase and swim together until their phase difference becomes too large. This coordinating behavior decreases the total energy consumption of two sperm. Fig. 1 shows the linear relation between phase difference and head-head distance of a sperm pair. The cooperation of our sperm model fails when the phase difference $\Delta\varphi > 1.5\pi$.

With the knowledge of hydrodynamic interaction between two sperm, we study multi-sperm systems. Synchronization and attraction effects help the sperm to form large, motile clusters. We give each sperm random initial position and orientation. Considering that in real biological systems the beat frequency is not necessary the same for all sperm, we perform simulations with Gaussian-distributed beating frequencies. $\delta_f = \langle(\Delta f)^2\rangle^{1/2}/\langle f\rangle$ denotes the width of the Gaussian frequency distribution. Here, $\langle(\Delta f)^2\rangle$ is the mean square deviation of the frequency distribution, and $\langle f\rangle = 1/120$ is the average frequency.
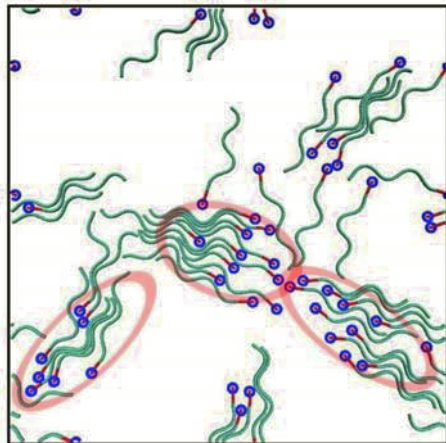
FIG. 2: *A snapshot from simulation of 50 sperm with widths* $\delta_f = 0.9\%$ *of a Gaussian distribution of beating frequencies. The red ellipses indicate large sperm clusters. The black frames show the simulation boxes. Note that we employ periodic boundary conditions.*

The motile sperm embedded in a two-dimensional fluid aggregate through hydrodynamic interactions and volume exclusion. Fig. 2 shows a snapshot of a 50-sperm system with $\delta_f = 0.9\%$. Large clusters of synchronized and tightly packed sperm are formed. If $\delta_f = 0$, once a cluster has formed, it does not disintegrate without a strong external force. A possible way of break-up is by bumping head-on into another cluster. As the cluster size increases, the possibility to bump into another cluster decreases, thus the rate of break-up decreases. The average cluster
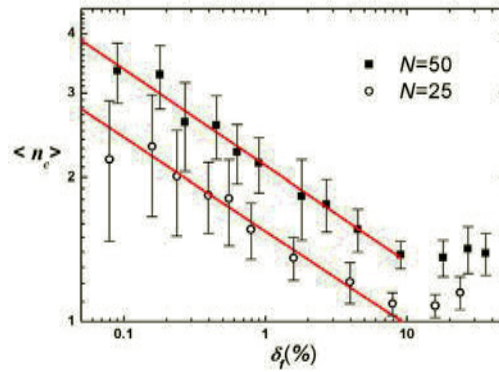
FIG. 3: *Dependence of the average stationary cluster size,* $<n_c>$, *on the width of the frequency distribution* δ_f. *Data are shown for a 50-sperm system (■) and a 25-sperm system (○). The lines indicate the power-law decays* $<n_c> = 2.12\,\delta_f^{-0.201}$ *(upper) and* $<n_c> = 1.55\,\delta_f^{-0.196}$ *(lower).*

size always increases for $\delta_f = 0$. For $\delta_f > 0$, however, sperm cells can leave a cluster after sufficiently long time, since the phase difference to other cells in the cluster increases in time due to the different beat frequencies. At the same time, the cluster size can grow by collecting nearby free sperm or by merging with other clusters. Thus, there is a balance between cluster formation and break-up when $\delta_f > 0$.

Once a system reaches a stationary state, the cluster-size distribution function obeys a power law. Similar power-law behaviors have been found in simulation studies of swarm behavior of self-propelled particles [6].

The average cluster size $<n_c>$ is plotted in Fig. 3 as a function of the width δ_f of the frequency distribution. Generally, it decreases with decreasing sperm density or increasing δ_f. Figure 3 also shows a power law decay,

$$<n_c> \sim \delta_f^{-\gamma} \qquad (1)$$

with $\gamma = 0.20 \pm 0.01$. The negative exponent indicates that the cluster size diverges when $\delta_f \to 0$.

[1] S. Immler, H. D. M. Moore, W. G. Breed and T. R. Birkhead, PLos One **2**, e170 (2007).

[2] A. Malevanets and R. Kapral, J. Chem. Phys. **110**, 8605 (1999).

[3] G. Gompper, T. Ihle, D. M. Kroll, and R. G. Winkler, Adv. Polym. Sci. **221**, 1 (2009).

[4] J. Elgeti and G. Gompper, NIC proceedings, Vol. 39 of NIC series, edited by G. Münster, D. Wolf, and M. Kremer, pp. 53-61 (2008).

[5] Y. Yang, J. Elgeti, and G. Gompper, Phys. Rev. E **78**, 061903 (2008).

[6] C. Huepe and M. Aldana, Phys. Rev. Lett. **92**, 168701 (2004).

Protein domain motions observed in space and time by NSE

R. Biehl[1], M. Monkenbusch[1], B. Hoffmann[2], P. Falus[3], S. Prévost[4], R. Merkel[2], D. Richter[1]

[1] IFF-5: Neutron Scattering
[2] IBN-4: Biomechanics
[3] Institut Laue Langevin, Grenoble, France
[4] Hahn Meitner Institut, Berlin, Germany

To bind a cofactor to the active center of a protein often a structural change is mandatory. This "induced fit" includes small changes of single bonds but also large domain motions to prepare the active atomic configuration. Neutron spin echo spectroscopy is used to directly observe the domain dynamics of the protein alcohol dehydrogenase [1]. The collective motion of domains as revealed by their coherent formfactor relates to the cleft opening dynamics between the binding and the catalytic domains enabling binding and release of the cofactor to the active center.

Proteins are the molecular machinery of life. As nanomachines of metabolism, they are in every cell of our body tirelessly active, transport, synthesize, divide and transform substances. Many transformation processes are underway in characteristic shaped bags, in which only certain substances fit, as a key fits to the lock. The shape of these pockets is determined by the sequence and three-dimensional arrangement of amino acids. Sometimes the binding of the cofactor or substrate is responsible for the formation of the right shape of the pocket. Through this "induced fit" the lock for a certain key is arranged to fit. There must be movements of atoms, amino acids or entire domains to bring the atoms in the right configuration to get active.

This effect is so far mainly known from structural studies of crystallized proteins, which represent snapshots of different configurations. Internal movements could also be observed by fluorescent labelling of two points on a protein with molecular biological methods to track distance changes [2]. Further information is attainable only by computer simulations.

One of the most studied proteins and one of the key enzymes is Alcohol Dehydrogenase (ADH, Figure 1). It produces ethanol in yeast or converts it back to acetaldehyde in the human liver. A functional important molecule (cofactor) Nicotinamide Adenine Dinucleotide (NAD) and a substrate molecule (ethanol or acetaldehyde) bind to the binding domain in a cleft between active and binding domain. The active domain, with a catalytic Zinc atom in the active centre, opens and closes the cleft by thermal movements. The closing places the active centre in the right position for the transfer of a hydrogen atom between the substrate and cofactor molecule, and another hydrogen atom is released. Again opened, the cofactor and the product of the reaction will be released.
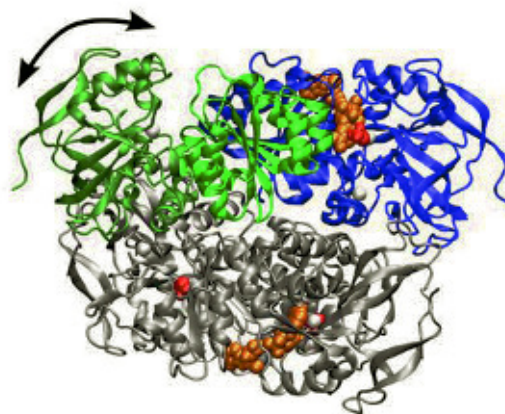
FIG. 1: *Tetrameric Alcohol Dehydrogenase of yeast is build up from two dimers (green-blue and gray). The blue monomer is in the closed conformation with a NAD cofactor (orange) and an ethanol (red) in the cleft between binding domain and the active domain. In the cleft between both domains of the open configuration (green monomer) the catalytic Zinc atom at the catalytic centre is visible. The second dimer (gray) is bound at the backside of the first dimer. The arrow indicates schematically the movement of the active domain here without a bound cofactor.*

Neutron scattering provides the possibility to investigate the timescale of these large scale movements in biomolecules. It provides information on the location and movement of atoms, without destroying the sample. The measurements were done in dilute D_2O buffer solutions, close to the natural environment of the protein, but with the possibility to focus on the protein scattering.

Scattering at the atomic nuclei of the protein will produce a characteristic interference pattern. Movements of the atoms during the scattering process change the speed of the neutrons in the scattered beam. The change in speed for the scattered neutrons is very small. In order to detect it, NSE spectroscopy uses the Larmor precession of the neutron spins in a magnetic field as a stopwatch. The result is a length scale dependent flexibility, which differs from the expected motion of a rigid protein, only showing translation and rotation movements of diffu-

sion. These length scale variations reflect the pattern of the movements due to the underlying dynamics.

FIG. 2: a, Single tetramer diffusion coefficient D_{0eff} after corrections with and without bound cofactor. The black solid line represents the calculated effective diffusion coefficients for the ADH crystal structure, including translational and rotational diffusion of the stiff protein. b, Difference of the corrected diffusion coefficients and the calculated translational/rotational diffusion coefficient, reflecting the internal dynamics.

Neutron scattering provides the possibility to investigate the timescale of these large scale movements in biomolecules. It provides information on the location and movement of atoms, without destroying the sample. The measurements were done in dilute D_2O buffer solutions, close to the natural environment of the protein, but with the possibility to focus on the protein scattering..

Scattering at the atomic nuclei of the protein will produce a characteristic interference pattern. Movements of the atoms during the scattering process change the speed of the neutrons in the scattered beam. The change in speed for the scattered neutrons is very small. In order to detect it, NSE spectroscopy uses the Larmor precession of the neutron spins in a magnetic field as a stopwatch. The result is a length scale dependent flexibility, which differs from the expected motion of a rigid protein, only showing translation and rotation movements of diffusion. These length scale variations reflect the pattern of the movements due to the underlying dynamics.

The NSE spectroscopy always measures the collective movement of all protein atoms, so in the evaluation the contribution of diffusion to the observed scattering has to be separated from the internal dynamics.

We found in our studies that the patterns of the movements observed are mainly due to the movement of the active domain relative to the binding domain at a timescale of 30 ns. Figure 1 illustrates schematically the movement of the active domain, leading to

the opening of the gap. If the cofactor binds, it stiffens the protein, and the domain movement is significantly reduced. In ADH, we find an average amplitude of about 0.8 nm for the extent of the spatial movements between the two domains. Also we determined a spring constant of about 5 pN/nm for the stiffness of the cleft opening.

[1] Ralf Biehl, Bernd Hoffmann, Michael Monkenbusch, Peter Falus, Sylvain Prévost, Rudolf Merkel and Dieter Richter Phys. Rev. Lett. 101 (2008) 138102

[2] D. W. Pistona, G.-J. Kremers Trends in Biochemical Sciences, 32 (2007) 407

145

Electrostatics of DNA and DNA-protein interactions

A. G. Cherstvy

IFF-2: Theoretical Soft-Matter and Biophysics

We present below a short description of some problems of DNA electrostatics. The biological systems considered include DNA cholesteric phases, DNA-DNA friction in tight DNA plies, target search on DNA by DNA-sliding proteins, and structure of DNA protein complexes. We discuss in particular the electrostatic mechanism of DNA-protein recognition and analyze the details of charge distribution on DNA-protein complexes from the Protein Data Bank structures.

DNA cholesteric phases: Many chiral bio-macromolecules are highly charged and form a variety of dense liquid-crystalline phases *in vivo* and *in vitro*. The list includes DNA, f-actin, some polysaccharides and polypeptides, filamentous viruses (*fd*, M13). Nature uses the ability of DNA to form chiral phases for packaging the genomes of bacteria and viruses and for DNA compactification in sperm of some vertebrates. However, how the DNA molecular chirality manifests itself through intermolecular interactions in macroscopic cholesteric properties is still not fully understood. For instance, for the DNA twisted phases *in vitro*, the cholesteric pitch is extremely large, 2-4 μm, being dependent however on temperature, the surrounding electrolyte, and density of DNA lattice.

We considered DNA-DNA chiral electrostatic interactions in dense liquid crystalline DNA phases [1]. In particular, we have treated theoretically the conditions for existence of DNA cholesterics, the relevant densities of DNA lattices, the influence of added salts (mono- *vs.* multivalent), the strength of azimuthal DNA correlations, and calculated the value of DNA cholesteric pitch. Some comparison with recent experiments on response of DNA cholesterics to external osmotic stresses as well as on boundaries of DNA cholesteric-isotropic and cholesteric-hexagonal phase transition was presented. The dependence of the cholesteric pitch on the density of DNA lattice obtained was shown be to in agreement with experiments. The twist direction of cholesteric phases in the theory was however right-handed, opposite to typically left-handed phases observed for dense DNA assemblies.

DNA-DNA electrostatic friction: Recent single molecule experiments on superhelical DNA plies have revealed that in the presence of DNA-binding proteins the forces required to shear two DNAs along each other in the ply are several pN. Without proteins, DNA-DNA friction was detected to be very small, independent on the valence of cations added and number of DNA turns in the ply.

We have estimated theoretically the DNA-DNA electrostatic frictional forces emerging upon dragging one DNA over another in a close parallel juxtaposition [2]. For ideally helical DNA duplexes, the electrostatic DNA-DNA friction occurs due to correlations in electrostatic potential variations near the DNA surface. The latter originate from intrinsic helicity of DNA negative phosphate charges and of positive cations adsorbed in DNA grooves. The length scale of the charge periodicity along DNA is its pitch of 3.4 nm. These potential barriers produce positive-negative charge interlocking along the contact of two DNAs.

Realistic DNAs are however non-ideal helices. DNA base pair parameters strongly depend on DNA sequence, producing quite corrugated quasi-helical DNA structures. In this case, electrostatic potential barriers become decorrelated after some DNA-DNA interaction length due to accumulation of mismatches in the DNA structure. This strongly impedes DNA-DNA frictional forces. We calculated the magnitude of frictional forces in tight DNA plies that are strongly stretched by the end forces. We discussed the possibilities of probing DNA-DNA interactions in confined DNA superhelical plies as obtained in single molecule experiments.

Facilitated diffusion of proteins on DNA and DNA-protein electrostatic interactions: Several types of interactions occur between DNA and its binding proteins: hydrogen bonding, electrostatic, van der Waals. Protein structures and domains of DNA recognition are extremely diverse. Many DNA-binding and DNA-sliding proteins are known to find their target sites on DNA with the rates that are much faster than allowed by thermal diffusion in 3D solution (e.g., the *lac* repressor). Being capable to scan the DNA very fast, proteins often recognize DNA base pair sequences with high specificity tolerating only little mismatch. All this complicates the construction of general theory of DNA-protein interactions. The mechanisms of protein diffusion in DNA coil (3D *vs.* 1D diffusion) and the peculiarities of DNA-protein recognition are also not completely understood.

For some protein-DNA complexes, like non-specifically bound *lac*, electrostatic interactions of protein

146

and DNA charges give the dominant contribution to the energy of binding. DNA-binding domains of many proteins contain positively charged patches that ensure net attractive DNA-protein electrostatic interactions, both for small and large proteins. Upon protein binding to DNA, positively charged protein residues replace the counterions condensed previously on DNA. The cations are displaced in front of the protein and bind back to DNA behind it. Electrostatic DNA-protein interactions are however believed to possess *little* specificity to the DNA base pair sequence. They keep proteins close to DNA allowing other sequence-specific forces, e.g. hydrogen bonding interactions, recognize the actual sequence of DNA bases.

We have tried to check this assumption and suggested a model [3] to study quantitatively the specificity of electrostatic protein-DNA interactions (with A. A. Kornyshev and A. B. Kolomeisky). The specificity comes into the model from base pair dependent phosphate positioning on DNA, but also probably from some typical charge patterns in DNA-binding domains of proteins.

First, we have constructed a kinetic model of facilitated protein diffusion on DNA that combines 3D protein diffusion in solution and 1D protein sliding along the DNA. The model contains a non-equilibrium protein adsorption onto DNA upon the target search process. We have shown that for an intermediate strength of protein-DNA binding the mean first passage time of proteins to the target on DNA is 1-2 orders of magnitude shorter than for the Smoluchovskii 3D diffusion suggesting plausible explanation for facilitated protein diffusion on DNA.
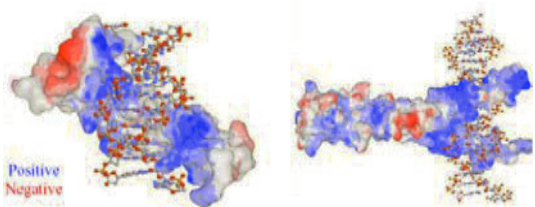

FIG. 1: *The distribution of electrostatic potential on zinc finger 1aay.pdb (left) and leucine zipper 1ysa.pdb (right) DNA-protein complexes, as calculated by visualization programs MDL Chime and Protein Explorer using the Protein Data Bank crystal data.*

Secondly, we constructed a mechanism of DNA-protein recognition based on complementarity of their charge patterns. We considered linear DNA and protein charge arrays that are fully complementary for the DNA recognition sequence, while for other DNA sequences the charge patterns are quasi-random. The parameters of the potential well near the recognizable DNA sequence were determined. The well is typically 3-10 $k_B T$ in depth and several nm in width. The well slows down the diffusion of proteins along DNA, the proteins are trapped inside it for μs-ms. This time is long enough to trigger some conformational changes in the protein structure that can result in stronger (chemical) binding to DNA. Calcu-

lating the potential distribution around some protein-DNA complexes, we observed that positively charged protein residues are indeed situated within several Å from DNA phosphates, "embracing" the DNA duplex very efficiently, Fig. 1.

DNA sequence recognition by proteins: Recently, we studied the details of distribution of positive protein charges on many DNA-protein complexes. In particular, we have considered structural complexes like nucleosome core particles of eukaryotes and architectural proteins of prokaryotes, both involving extensive wrapping of DNA around protein cores. We have written the code for extracting the atomic coordinates of DNA phosphates and protein charges from the Protein Data Bank pdb files of DNA-protein complexes [4]. We have shown that for the nucleosomes the histone positive charges are mainly located in the outer histone "ring" close to the wrapped DNA. On the opposite, the negative charges on Aspartic and Glutamic acids are positioned inside the core of the particles, far away from DNA. Not only positive charges are close to DNA, the N^+ atoms on Lysine and Arginine protein residues actually track the positions of *individual* DNA phosphates in these large complexes. As the phosphate positions on DNA are sequence specific, this charge tracking contributes to a non-zero specificity of electrostatic DNA-protein interactions for these complexes. This supports our previous hypothesis about commensurate charge lattices on DNA and proteins and the mechanism suggested for DNA-protein charge-charge recognition.

On the contrary, for small DNA-protein complexes involving simple motifs of DNA-protein recognition (helix-turn-helix, zinc finger, leucine zipper) we did *not* detect any statistical preference in distribution of protein positive charges in close proximity to DNA. We suggest that for large complexes involving several tens up to a hundred of charge-charge contacts with DNA, the energetic preference of having positive protein charges as close as possible to the nearest phosphates is quite large. For small complexes, with much weaker binding energies and probably other types of interactions more pronounced, DNA charge tracking appears to be not so important for protein-DNA recognition.

[1] A. G. Cherstvy, J. Phys. Chem. B, 112 12585 (2008).

[2] A. G. Cherstvy, J. Phys. Chem. B, 113 jp810473m (2009).

[3] A. G. Cherstvy, A. B. Kolomeisky, and A. A. Kornyshev, J. Phys. Chem. B, 112 4741 (2008).

[4] A. G. Cherstvy, J. Phys. Chem. B, 113 jp810009s (2009).

Hydrodynamic interactions in polyelectrolyte electrophoresis

R. G. Winkler[1], S. Frank[2]

[1] IFF-2: Theoretical Soft-Matter and Biophysics
[2] Institut für Theoretische Physik, Universität Göttingen, 37077 Göttingen

The dynamical and conformational properties of short polyelectrolytes are studied in salt free solution exposed to an external electric field taking hydrodynamic interactions into account by a mesoscale simulation technique. As a function of polymer length, we find a non-monotonic electrophoretic mobility, in agreement with experiments, and diffusion coefficients, which are well described by the expression of rodlike objects. Both aspects reflect the importance of hydrodynamic interactions in free polyelectrolyte electrophoresis.

The structural and dynamical properties of polyelectrolyte solutions in an external electric field are governed by the interplay of various interactions. The Coulomb interaction among the various charges (monomers, counterions, coions) generates conformations which strongly deviate from those of neutral polymers and gives rise to particular phenomena such as counterion condensation. The applied electric field itself causes a flux of polyions, charges, and part of the solvent and induces a charge asymmetry, which in turn influences the polyelectrolyte structure and mobility. In addition, hydrodynamic interactions are present despite the common assumption that hydrodynamic interactions are screened as deduced from the molecular weight independent polyelectrolyte mobility [1].

Recent experiments on strong polyelectrolytes, e.g., polystyrenesulfante (PSS), at low or no salt content suggest that the mobility of short polyelectrolytes (oligomers) increases initially with increasing molecular weight, passes through a maximum and reaches a plateau for long and flexible polymers [1]. Similar results are reported for single-stranded DNA, although with a less pronounced maximum [2]. This non-monotonic behavior explicitly reflects the linkage of the various interactions mentioned above.

Full insight into the interplay of the various interactions present in free flow electrophoresis is difficult to achieve by analytical theory, particularly due to the non-equilibrium and non-linear character of the problem. Computer simulations, specifically mesoscale simulations which take hydrodynamic interactions adequately into account, provide the opportunity to tackle the challenging problem.

By hybrid mesoscale simulations, which combine molecular dynamics simulations and the multiparticle collision dynamics (MPC) algorithm, we determined the mobilities and conformational properties of strong polyelectrolytes in dilute solution at zero salt concentration.

The calculation of the conformational properties of the considered polyelectrolytes yields a rodlike scaling relation for the mean square end-to-end distance, i.e., it is proportional to N_m^2, for parameters comparable to PSS. This is related to the fact that the amount of condensed counterions (N_c) is very small for short oligomers and the ratio N_c/N_m increases monotonically with increasing polymer length. This implies that the effective charge of the polymer increases slower than its length.

Figure 1 displays the polymer length dependence of the electrophoretic mobility. We measure μ in units of the bare mobility μ_0 which we determined from a simulation of a single monomer in the presence of the solvent. The interaction strength is comparable to that of PSS. The initial increase of the mobility is caused by hydrodynamic interactions of a rodlike object. For such short chains with $N_m \lesssim 5$, counterions only very weakly influence the polymer dynamics and the radius of gyration R_G obeys $R_G \ll \lambda_D$, where λ_D is the Debye screening length. Thus, μ increases logarithmically with the polymer length ($\mu \sim \ln N_m$) due to hydrodynamic interactions. The maximum and the following decrease is induced by counterion condensation, which reduces the charge of the polymer and hence the mobility. For even longer chains with $R_G \gg \lambda_D$, electrostatic screening of the Coulomb interaction appears and the mobility approaches a constant value [1]. As shown in Fig. 1, the simulation data quantitatively agree with experimental results obtained by capillary electrophoresis [1] and NMR [3]. Interestingly, there is no adjustable parameter and the course-grained model captures the essential physical aspects of the polyelectrolyte dynamics.

The red bullets in Fig. 1 present simulation results without hydrodynamic interactions. As expected, the lack of hydrodynamic interactions leads to a decrease of the mobility at short polymers and μ approaches a constant value at large molecular weights. Since the Nernst-Einstein relation $\mu = DQ/k_BT$ applies in this situation, we can successfully describe the chain length dependence by $\mu \sim (N_m - N_c)/(N_m + N_c)$, where we use the relation
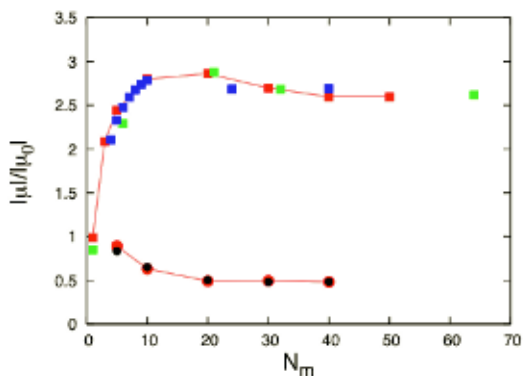
FIG. 1: Electrophoretic mobilities μ/μ_0 of polyelectrolyte chains as function of the monomer number N_m with (■) and without (●) hydrodynamic interactions. (Lines are guides for the eye only.) The black bullets are obtained by a fit of the dependence $\mu \sim (N_m - N_c)/(N_m + N_c)$. The squares indicate experimental results on PSS obtained by capillary electrophoresis (blue) and NMR (green), respectively [1, 3].

FIG. 2: Polyelectrolyte diffusion coefficients for various polymer lengths with (squares) and without (bullets) hydrodynamic interactions. The solid lines are calculated according to Eq. (1). The green squares indicate experimental results for PSS obtained by NMR [3].

$Q \sim (N_m - N_c)$ for the effective charge, and assume that the local friction term $\zeta \sim (N_m + N_c) \sim 1/D$, with D the diffusion coefficient, comprises contributions from monomers as well as counterions, because the condensed counterions are dragged along with the polymer [2].

Since the considered polyelectrolytes exhibit rodlike scaling behavior, we expect that the chain length dependence of the diffusion coefficient can be described by the expression for rodlike objects in the presence of hydrodynamic interactions. Figure 2 displays diffusion coefficients for polymers of various lengths with and without hydrodynamic interactions, which are determined via the center-of-mass mean square displacements without external field. The solid lines are calculated using the expression

$$\hat{D} = \frac{a}{3\pi\hat{\nu}\rho l}\left(\frac{\delta_1}{N_m + N_c}\right.$$
$$\left. + \frac{\delta_2}{N_m - 1}\left[\ln(N_m - 1) - 0.185\right]\right), \quad (1)$$

where the local friction as well as hydrodynamic interactions are taken into account. Here, $\hat{D} = \tau D/a^2$ and the kinematic viscosity is $\hat{\nu} = \tau\nu/a^2 = 2.75$, with the simulation units τ and a for time and length, respectively [2]. As a result of counterion condensation, the slope of the diffusion coefficient with the friction term only ($\delta_2 = 0$) is smaller than -1. The fit of the simulation data by expression (1) without hydrodynamic interactions yields $\delta_1 = 1.37$. The fit of the full expression gives $\delta_2 = 0.79$, which is smaller than unity due to the fact that the polymers are no real rods, but behave in a rodlike manner only. Obviously, the simulation data are very well described by the theoretical expressions, both, with and without hydrodynamic interactions. We would like to point out that the diffusion coefficient cannot be described by the relation $D \sim R_G^{-1}$, which would apply in the Zimm regime.

The length dependence of D agrees well with the experimental data of Ref. [3]. For higher molecu-

lar weights, the conformations change and the Zimm description is more adequate. We cannot expect a power-law dependence to apply for all monomer numbers $N_m > 1$, because the scaling properties of, e.g., the radius of gyration change considerably with molecular weight.
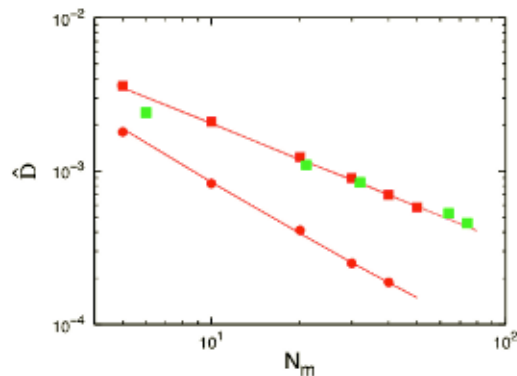
The Nernst-Einstein relation $\mu \sim QD$ does not apply in general, because of the multicomponent nature of the solution and the screening of the charges by counterions. The latter is responsible for the constant mobility at large molecular weights, since the flow field, which is created by the motion of a monomer and its counterion cloud in an electric field vanishes at large distances.

Together with the chain length dependence of the radius of gyration, it is evident that the considered polyelectrolytes behave as rodlike (blobs) objects and that hydrodynamic interactions are relevant for the whole investigated length range. The crossover to a molecular weight independent mobility appears at even longer polymers, namely for polyelectrolytes with $R_G \gg \lambda_D$.

The theoretical concept of the *electrophoretic effect* [2] assumes that counterions flow in the opposite direction to the polyelectrolyte dragging solvent molecules along when an electric field is applied. Thus, we might speculate that hydrodynamic interactions lead to a modification of the diffusion coefficient transverse to the electric field. However, our simulations show that the diffusion coefficients perpendicular to the electric field are identical to those in the absence of the field, in agreement with experimental measurements in free flow electrophoresis of single-stranded DNA.

[1] H. Cottet, P. Gareil, O. Theodoly, and C. E. Williams, Electrophoresis **21**, 3529 (2000)

[2] S. Frank and R. G. Winkler, EPL **83**, 38004 (2008)

[3] U. Böhme and U. Scheler, Macromol. Chem. Phys. **208**, 2254 (2007)

149

Condensation in the zero-range process with random interaction

S. Grosskinsky[1], P. Chleboun[1], G. M. Schütz[2]

[1] Mathematics Institute, University of Warwick, Coventry CV4 7AL, UK
[2] IFF-2: Theoretical Soft-Matter and Biophysics

The zero-range process is a stochastic interacting particle system that is known to exhibit a condensation transition. We present a detailed analysis of this transition in the presence of quenched disorder in the particle interactions. Using rigorous probabilistic arguments we show that disorder changes the critical exponent in the interaction strength below which a condensation transition may occur.

The zero-range process is a stochastic lattice gas where the particles hop randomly with an on-site interaction that makes the jump rate dependent only on the local particle number. It was originally introduced nearly 40 years ago as a mathematical model for interacting diffusing particles, and since then has been applied in a large variety of contexts, often under different names, see e.g. [1] and references therein. The model is simple enough for the steady state to factorize, on the other hand it exhibits an interesting condensation transition under certain conditions. Viz. when the particle density exceeds a critical value ρ_c the system phase separates into a homogeneous background with density ρ_c and all the excess mass concentrates on a single lattice site. This has been observed and studied in some detail in experiments on shaken granular media and there is a well-established analogy to Bose-Einstein condensation. It is also relevant as a generic mechanism for phase separation in single-file diffusion and condensation phenomena in many complex systems such as network rewiring or traffic flow.

The transition can be caused by site-dependent jump rates g_x due to the slowest site acting as a trap [2]. It also appears in a more subtle fashion in homogeneous systems where condensation may result from the growth of large clusters on the expense of small clusters, if the jump rates $g(n)$ as a function of the number n of particles on the starting site have a decreasing tail. A well-studied model with a generic power law decay is defined by

$$g(n) = 1 + b/n^\sigma \qquad (1)$$

with positive interaction parameters b, σ. Condensation occurs if $0 < \sigma < 1$ and $b > 0$ or if $\sigma = 1$ and $b > 2$.

All previous studies of zero-range processes assume that the on-site interaction between particles is spa-
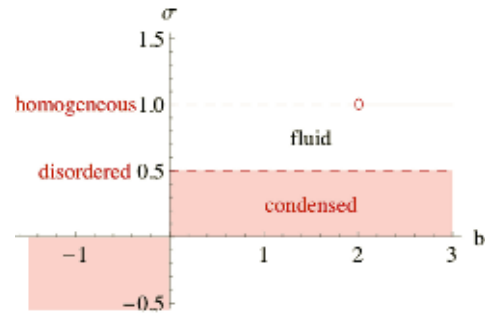
FIG. 1: *Change of the phase diagram under random perturbations of the jump rates (1). Disorder changes the critical interaction exponent from 1 to 1/2 and leads to a critical density that increases with system size. Inside the red-shaded region condensation occurs above a non-zero critical density for $b > 0$, and for $b < 0$ (2) and negative σ the critical density is zero.*

tially strictly homogeneous. Here we study the effect of disorder on this interaction and show that even a small random perturbation of the n-dependence of the jump rates $g(n)$ leads to a drastic change in the critical behaviour [3]. Namely, for positive b condensation only occurs for $0 < \sigma < 1/2$ (see Figure 1), excluding in particular the frequently studied case $\sigma = 1$. Due to the wide applicability of the zero-range process, the change of the critical interaction exponent σ is particularly relevant for applications in complex systems which often involve heterogeneous and disordered structures.

We consider a lattice Λ_L, which we take to be periodic and of finite size $|\Lambda_L| = L$. A configuration is denoted by $(\eta_x)_{x \in \Lambda}$ where $\eta_x \in \{0, 1, \dots\}$ is the occupation number at site x. The dynamics is defined in continuous time, such that with rate $g_x(\eta_x)$ site $x \in \Lambda_L$ loses a particle, which moves to a randomly chosen nearest neighbour site.

A generic perturbation of the jump rates (1) can be written in a convenient general way

$$g_x(n) = e^{E_x(n)} \quad \text{for } n \geq 1, \quad g(0) = 0, \qquad (2)$$

where the exponents are given by

$$E_x(n) = e_x(n) + b/n^\sigma, \quad b, \sigma \in \mathbb{R} \qquad (3)$$

with $e_x(n)$ being iid random variables with respect to x and n and spatially uniform mean $\mathbb{E}(e_x(n)) = 0$

and variance $\delta^2 > 0$. The physically interesting case is $b, \sigma > 0$.

It is well known that the process has a grand-canonical factorized steady state ν_μ^L with single-site marginal

$$\nu_{x,\mu}(n) = \frac{1}{z_x(\mu)} \exp\left(n\,\mu - \sum_{k=1}^{n} E_x(k)\right) \quad (4)$$

where the chemical potential $\mu \in \mathbb{R}$ fixes the particle density. The single-site normalization is given by the partition function

$$z_x(\mu) = \sum_{n=0}^{\infty} \exp\left(n\,\mu - \sum_{k=1}^{n} E_x(k)\right) \quad (5)$$

which is strictly increasing and convex in μ. The local density can be calculated as usual as a derivative of the free energy with respect to μ.

With (3) we have to leading order as $n \to \infty$

$$\sum_{k=1}^{n} E_x(k) \simeq \delta\sqrt{n}\,\xi_x(n) + \begin{cases} \frac{b}{1-\sigma} n^{1-\sigma} & , \sigma \neq 1 \\ b\ln n & , \sigma = 1 \end{cases} , \quad (6)$$

where by the central limit theorem

$$\xi_x(n) := \frac{1}{\delta\sqrt{n}} \sum_{k=1}^{n} e_x(k) \overset{n\to\infty}{\longrightarrow} N(0,1) \quad (7)$$

converges to a standard Gaussian. Moreover, the process $\left(\sqrt{n}\,\xi_x(n) : n \in \mathbb{N}\right)$ is a random walk with increments of mean zero and variance 1. Since the fluctuations of such a process are of order $\sqrt{n}$ we have for all $C \in \mathbb{R}$

$$\mathbb{P}\left(\xi_x(n) \lessgtr C \text{ for infinitely many } n\right) = 1 , \quad (8)$$

and for all $\gamma > 0$, $C > 0$

$$\mathbb{P}\left(|\xi_x(n)| > C n^\gamma \text{ for infinitely many } n\right) = 0 . \quad (9)$$

This is a direct consequence of the law of the iterated logarithm (see e.g. [4], Cor 14.8). Together with (5) and (6) this implies that $z_x(\mu) < \infty$ for all $\mu < 0$ with probability one. So for almost all (in a probabilistic sense) realizations of the $e_x(k)$ the critical chemical potential is $\mu_c = 0$ and we find

$b \leq 0$: In this case (6) and (8) imply that there are infinitely many terms in (4) which are bounded below by 1. Since all terms of the sum are non-negative it diverges and $z_x(\mu_c) = \infty$ with probability one.

$b > 0$: In this case the asymptotic behaviour of the terms in the sum (4) depends on the value of $\sigma > 0$, since the sign of the exponent can change.

- For $\sigma > 1/2$, $n^{1-\sigma} \ll \sqrt{n}$ and (6) is dominated by $\delta\sqrt{n}\,\xi_x(n)$. Applying (8) with $C = 0$ we get $z_x(\mu_c) = \infty$ with probability one.

- For $\sigma = 1/2$ both terms in (6) are of the same order since $n^{1-\sigma} \sim \sqrt{n}$ and

$$-\sum_{k=1}^{n}\left(e_x(k) + \frac{b}{k^\sigma}\right) \simeq -\delta\sqrt{n}\left(\xi_x(n) + \frac{2b}{\delta}\right) . \quad (10)$$

Again, (8) this time with $C = 2b/\delta$ implies $z_x(\mu_c) = \infty$ with probability one.
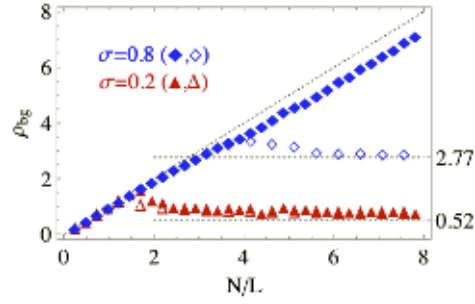
FIG. 2: *Background density ρ_{bg} as a function of N/L for $b = 1.2$. Data for fixed uniform disorder with $\delta^2 = 1/12$ and $L = 1024$ show condensation for $\sigma = 0.2$ and no condensation for $\sigma = 0.8$. Data for $\delta^2 = 0$ are shown by unfilled symbols, dotted lines indicate the critical densities. Data points are averages over 100 MC samples with errors of the size of the symbols.*

- For $0 < \sigma < 1/2$ we have $n^{1-\sigma} \gg \sqrt{n}$ and (6) is dominated by $\frac{b}{1-\sigma} n^{1-\sigma}$. We apply (9) for $\gamma = 1 - \sigma - 1/2 > 0$ to see that the random quantity $\xi_x(n)$ can change the sign of the exponent in (4) only for finitely many terms in the sum. Therefore $z_x(\mu_c) < \infty$ with probability one since $\frac{b}{1-\sigma} n^{1-\sigma}$ has a fixed negative sign in (4).

Whenever $z_x(\mu_c) = \infty$ the local critical density

$$\rho_c^x := \rho^x(\mu_c) = \infty \quad (11)$$

also diverges and there is no condensation transition. However, for $b > 0$ and $0 < \sigma < 1/2$ we have $z_x(\mu_c) < \infty$ and by the same argument as above it follows that

$$\rho_c^x = \frac{1}{z_x(\mu_c)} \sum_{n=0}^{\infty} n\, e^{-\sum_{k=1}^{n}\left(e_x(k) + \frac{b}{k^\sigma}\right)} < \infty \quad (12)$$

with probability one, since the factor n in the sum only gives a logarithmic correction in the exponent. Therefore there is condensation.

We support this conclusion by MC simulations, some of which are shown in Figure 2. For fixed L we plot the stationary background density as a function of the total density $\rho = N/L$. For $\sigma = 0.2$, ρ_{bg} converges to a critical density $\rho_c(L)$ which is slightly higher than for the unperturbed model. For $\sigma = 0.8$, ρ_{bg} increases approximately linearly with ρ, which is clearly different from the unperturbed model condensing with critical density 2.77.

---

[1] M.R. Evans, T. Hanney, J. Phys. A **38**, R195 (2005).

[2] J. Krug, P.A. Ferrari, J. Phys. A **29**, L465 (1996); M.R. Evans, Europhys. Lett. **36**, 13 (1996).

[3] S. Grosskinsky, P. Chleboun, G.M. Schütz, Phys. Rev. E **78** 030101(R) (2008).

[4] O. Kallenberg, *Foundations of Modern Probability* (Springer, New York, 2002).

Soret effect: experiments and simulations

P. Polyakov[1], F. Müller-Plathe[2], S. Wiegand[1]

[1] IFF-7: Soft Condensed Matter
[2] Eduard-Zintl-Institut für Anorganische und Physikalische Chemie, Technische Universität Darmstadt, Petersenstrasse 20 D-64287 Darmstadt, Germany

The Soret effect describes the build up of a concentration gradient caused by a temperature gradient. The origin of this effect is one of the unsolved puzzles in physical chemistry. In order to get to the bottom of this effect we performed experimental studies in combination with reverse nonequilibrium molecular dynamic simulations. For n-heptane/benzene mixtures we investigated the concentration dependence of the Soret coefficient. Additionally we investigated equimolar mixtures of three heptane isomers in benzene. The simulation and experimental result show the same trend in dependence of the mole fraction and degree of branching.

Thermal diffusion in a liquid mixture describes the movement of molecules due to the inhomogeneity of the temperature distribution. In the stationary state, the mass fluxes induced by the temperature gradient and the concentration gradient cancel. The ratio of the concentration gradient ∇c and temperature gradient ∇T that comply with such a stationary state is characterized by the Soret coefficient S_T, which is defined as, $S_T = D_T/D$, where D_T is the thermal diffusion coefficient and D is the mass-diffusion coefficient.

Thermal diffusion is of interest because of its potential to be applied for polymer characterization, crude oil exploration, combustion and alternative energies such as solar ponds. Additionally the effect contributes also to the understanding of some fundamental aspects related to life science.

We follow two general strategies to get to the bottom of this unsolved problem. One is to study colloidal model systems and to compare with analytical theories such as in the case of charged colloidal particles [1]. Another possibility is the study of low molecular weight mixtures, which are also easy accessible by molecular dynamic simulations. We perform reverse non-equilibrium molecular dynamic (RNEMD) simulations in order to gain a deeper microscopic understanding of the physical process underlying the thermal diffusion effect.

For ideal solutions of spherical molecules, for which the enthalpy of mixing and the mixing volume are close to zero, we found that the heavier molecule moves to the cold [2]. In associated and highly polar mixtures the mass of the components is irrelevant [3]. Those mixtures are affected by strong interactions and structural changes lead of to sign changes of the Soret coefficient with concentration. But not only for polar mixtures but also for mixtures of a linear alkane in benzene [4] the simple rule of the thumb with the mass fails. The heavier linear alkane always moves to the warm side, as illustrated in figure 1.
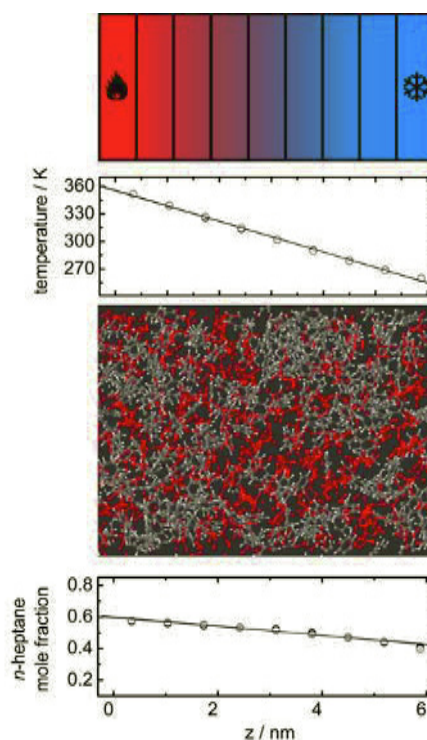
FIG. 1: *Simulation shot of the binary mixture of* n-*heptane (red) and benzene (grey) with the corresponding temperature and concentration profile.*

We investigated the thermal diffusion behavior of binary mixtures of linear alkanes (heptane, nonane, undecane, tridecane, pentadecane, heptadecane) in benzene by thermal diffusion forced Rayleigh scattering (TDFRS) for a range of concentrations and temperatures [4]. For the compositions investigated, the magnitude of the Soret coefficient decreases with increasing chain length and increasing alkane content of the mixtures. The temperature dependence

of the Soret coefficient depends on mixture composition and alkane chain length; the slope of S_T versus temperature changes from positive to negative with increasing chain length at intermediate compositions. For the linear chains, we were able to reproduce the experimental trends by a simple lattice model [4].

To study the influence of molecular architecture on the Soret effect, mixtures of branched alkanes (2-methylhexane, 3-methylhexane, 2,3-dimethylpentane, 2,4-dimethylpentane, 2,2,3-trimethylbutane and 2,2,4-trimethylpentane) in benzene were also investigated. Fig. 2 shows the experimental Soret coefficient S_T for equimolar mixtures of benzene and isomers of heptane as a function of temperature. As in the case of the linear alkanes, the Soret coefficients are negative, except for the strongly branched 2,2,3-trimethylbutane, which has a positive Soret coefficient. With increasing degree of branching the tendency of the alkane to move to the warm side becomes weaker. This observation holds for all investigated temperatures. We were not able to explain this effect within a simple lattice model [4], therefore we performed RNEMD simulations.

FIG. 2: Soret coefficient S_T heptane (■), 2-methylheptane (●), 3-methylheptane (▼), 2,3-dimethylpentane (◆), 2,4-dimethylpentane (▶), and 2,2,3-trimethylbutane (▲) in benzene at a mole fraction of 0.5 as a function of the temperature. The lines connect the data points.

For comparison we calculated the Soret coefficient for equimolar mixtures of the three heptane isomers 3-methylhexane, 2,3-dimethylpentane and 2,4-dimethylpentane in benzene by RNEMD [5]. Fig. 3 shows the calculated Soret coefficient in comparison with experimen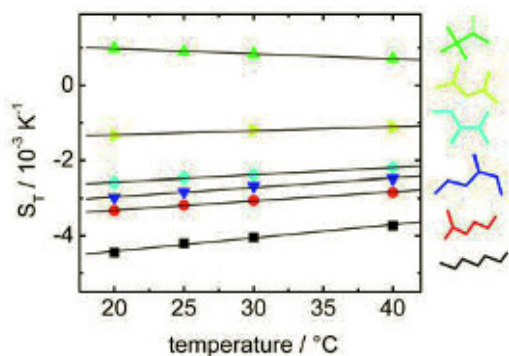tal data[4] at a temperature of $T = 30°$ C. Compared to the experimental data, the simulation results show the same trend in dependence of the mole fraction and degree of branching, however the simulated values are systematically $\approx 3 \times 10^{-3} \text{K}^{-1}$ ($\approx 25\%$) lower than in experiment. For 2,3-dimethylpentane/benzene system with the smallest Soret coefficient we performed a second, independent RNEMD simulation with a simulation time of 4.5 ns. The magnitude of the obtained Soret coefficient $S_T = 3.2 \times 10^{-3} \text{K}^{-1}$ agrees within the error bars with the value $S_T = (3.04 \pm 0.2) \times 10^{-3} \text{K}^{-1}$ obtained after 10.5 ns.
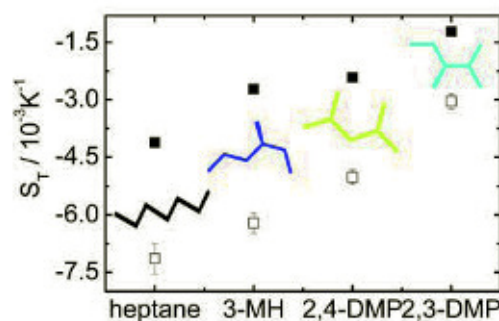
FIG. 3: Comparison of the simulated Soret coefficients (□) with the experimental values (■) [4] for equimolar mixtures of n-heptane and the isomers 3-methylheptane (3-MH), 2,4-dimethylpentane (2,4-DMP) and 2,3-dimethylpentane (2,3-DMP) in benzene at $T = 30°$ C.

The observed decreasing of the magnitude of S_T for equimolar alkane/benzene mixtures with branching of the alkane can not be explained by mass and size effects. Nevertheless we observe a linear increase of S_T with increasing moment of inertia, which could be purely to kinetic but also due to static contributions due to simultaneous change of the anisotropy of the molecules. The effect of the molecular shape, which affects the liquid structure, as well as kinetic properties of the mixture, needs to be considered additionally. We have, however, not found a simple relation to take branching or, more generally, molecular shape, into account.

Presently, we are analyzing the orientation of the two components and try to make a correlation with the observed Soret coefficient. We consider the planarity of the components and look at the radial distribution functions in order to determine the spatial coordination of the molecules. This will give us an estimate for the strength of the interaction, which is related with the Soret coefficient.

[1] Ning, H., Dhont, J. K. G., and Wiegand, S. *Langmuir* **24**, 2426–2432 (2008).

[2] Polyakov, P., Zhang, M., Müller-Plathe, F., and Wiegand, S. *J. Chem. Phys.* **127**, 014502 (2007).

[3] Polyakov, P. and Wiegand, S. *J. Chem. Phys.* **128**, 034505 (2008).

[4] Polyakov, P., Luettmer-Strathmann, J., and Wiegand, S. *J. Phys. Chem. B* **110**, 26215–26224 (2006).

[5] Polyakov, P., Müller-Plathe, F., and Wiegand, S. *J. Phys. Chem. B* **112**, 14999–15004 (2008).

153

Orientational ordering in solid C_{60} fullerene-cubane

B. Verberck[1,3], G.A. Vliegenthart[2], G. Gompper[3]

[1] Departement Fysica, Universiteit Antwerpen, Antwerpen, Belgium
[2] IAS: Institute for Advanced Simulation
[3] IFF-2: Theoretical Soft-Matter and Biophysics

We study the structure and phase behavior of fullerene-cubane $C_{60}.C_8H_8$ by Monte Carlo simulation. Using a simple potential model capturing the icosahedral and cubic symmetries of its molecular constituents, we reproduce the experimentally observed phase transition from a cubic to an orthorhombic crystal lattice and the accompanying rotational freezing of the C_{60} molecules. We elaborate a scheme to indentify the low-temperature orientations of individual molecules and detect a pattern of orientational ordering similar to the arrangement of C_{60} molecules in solid C_{60}. Our configuration of orientations supports a doubled periodicity along one of the crystal axes.
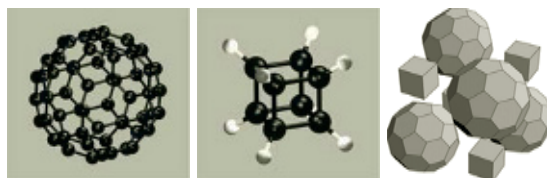
The recent synthesis of fullerene-cubane, $C_{60}.C_8H_8$, by Pekker et al. [1] has marked the beginning of experimental and theoretical research on a new class of fullerene-containing crystals.

While C_{60} fullerite, the solid built from C_{60} fullerene molecules only was successfully doped with alkali atoms soon after its macroscopic production, it took a decade and a half to come up with a crystal combining fullerenes with other molecules. Cubane, C_8H_8, the partner molecule, has eight carbon atoms arranged on the corners of a cube to each of which a hydrogen atom is bound. Each of the two molecules has a remarkably high symmetry: icosahedral and cubic for C_{60} and C_8H_8, respectively. In fact, the very existence of fullerene-cubane in stoichiometry 1:1 and its stability has been attributed by Pekker et al. [1] to the perfect matching of the two molecular geometries: at room temperature, the almost spherical C_{60} molecules leave voids at the octahedral interstices of a face-centered cubic (fcc) lattice into which a cubane molecule, having concave faces, fits perfectly.

The room temperature phase of fullerene-cubane is well understood [1]: a binary fcc cubic structure of freely rotating C_{60} molecules and non-rotating C_8H_8 molecules. Below $T \approx 140$ K, the crystal structure is orthorhombic, the C_{60} molecules do not rotate, and the cubane molecules maintain their fixed orientations. The room temperature phase has been termed "rotor-stator phase" and the role of the cubane molecules as "molecular bearings" for the rotating fullerene molecules. The phase transition

FIG. 1: A C_{60} molecule (a) and a C_8H_8 molecule (b), the fcc unit cell of fullerene-cubane (c).

in $C_{60}.C_8H_8$ is similar to the structural transition in solid C_{60}: at room temperature, the C_{60} molecules in C_{60} fullerite are arranged on a fcc lattice and rotate nearly freely while below $T \approx 249$ K the molecules adopt well-defined orientations in a sublattice structure. This structure has been interpreted as an optimal ordering scheme where pentagons (the centres of which are electron-poor) face electron-rich bonds fusing hexagons. Comparing the transition temperatures of C_{60} fullerite and C_{60} fullerene-cubane shows that in the latter, the concavely shaped C_8H_8 molecules can indeed be seen as bearings facilitating the rotation of the C_{60} molecules.

We performed a Monte Carlo simulation study of binary fullerene-cubane crystals [2, 3] focussing on the low-temperature phase behaviour, rotational dynamics and orientational ordering of the molecules. From all possible force fields we chose a very simple one based on Lennard Jones interactions between the C_{60} carbon atoms and modeling the cubane molecule as a cube with four equivalent interaction centers. The potential model was tuned such that the room temperature structure as well as the low temperature structure have the same symmetry as the experimentally observed ones.

The phase diagram and the total interaction energy of this system is shown in Fig 2. At room temperature, we find that the system adopts cubic symmetry. Upon cooling down, we observe a jump in the energy and a transition to a secondary cubic phase with larger density at $T_1 = 100$ K. This cubic phase transforms to an orthorhombic phase at $T_2 = 85$ K. The lattice constants of the orthorhombic phase lie very close together ($A = 14.48$ Å, $B = 14.50$ Å, $C = 14.54$ Å at 50 K). We note that none of the other parameter sets we tried resulted in values closer to the experimentally reported ones ($A = 14.1$ Å, $B = 14.6$ Å,
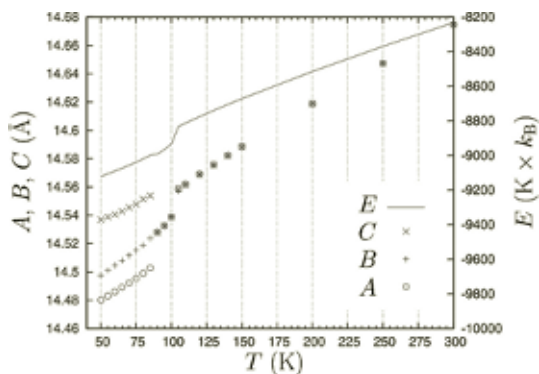
FIG. 2: Evolution of lattice constants (left abscissa, symbols) and energy (right abscissa, full line) as a function of temperature.

FIG. 3: OMSD values I and II for the C_{60} molecules as a function of temperature. The free-rotation values $2z_a^2 = 24.22$ Å^2 and $z_a^2 = 12.11$ Å^2 are shown as horizontal lines.

$C = 15.3$ Å) at $T = 105$ K.

During the MC simulation, a sequence of orientations is generated for every C_{60} and cubane molecule. As a molecule adopts various orientations, any point $\vec{r}_i$ of the molecule, e.g. an atom or the center of a bond results in a set of locations $\{\vec{r}_i(p), p = 1, \ldots, N_{MC}\}$, where i labels the molecule, p labels subsequent MC steps and N_{MC} is the total number of MC steps. The coordinates $\vec{r}_i = (x_i, y_i, z_i)$ of this "monitored" point are defined with respect to a local coordinate system. For a freely rotating molecule, the set $\{\vec{r}_i(p)\}$ covers a sphere with radius $R_i = |\vec{r}_i|$ whereas $\vec{r}_i$ remains constant if the molecule is fixed. Apart from the monitored point $\vec{r}_i$ we select a reference point $\vec{r}_i^0$ and define the orientational mean squared displacement (OMSD),

$$\langle u_i^2 \rangle = \langle |\vec{r}_i(p) - \vec{r}_i^0|^2 \rangle \qquad (1)$$

The value of $\langle u_i^2 \rangle$ depends on the particular choice of monitored *and* reference point and on the dynamical state of the molecule. For freely rotating molecules the average in Eq. (1) can be calculated exactly. In Fig. 3 we show the OMSD as a function of temperature for two choices of the reference point $\vec{r}_i^0$. The first choice of the reference point corresponds to the center of the double bond when a C_{60} molecule is in its standard orientation $\vec{r}_i^0 = \vec{r}_a = (0, 0, z_a = 3.48\text{Å})$ while the second choice corresponds to $\vec{r}_i^0 = \langle \vec{r}_i \rangle$. For freely rotating molecules we expect $\langle u_i^2 \rangle^I = 2z_a^2$ and $\langle u_i^2 \rangle^{II} = z_a^2$ (superscripts indicating reference point I and II) whereas for non-rotating molecules we have $\langle u_i^2 \rangle^I = \hat{u}_i^2$ and $\langle u_i^2 \rangle^{II} = 0$. Clearly, at room temperature, the C_{60} molecules are rotating freely. At about 100 K, the OMSD values start to decrease as orientational freezing sets in. At 50 K, the value of $\langle u_i^2 \rangle^{II}$ is close to zero ($\langle u_i^2 \rangle^{II} = 0.035$ Å^2). This value can be interpreted as resulting from small rotational fluctuations around a fixed orientation. The value of $\langle u_i^2 \rangle^I = 0.706$ Å^2 is different from zero, however, implying that the molecules are *not* in the standard orientation.

In order to elucidate the orientational ordering in the crystal we investigated the value of $\langle u_i^2 \rangle^I$ per molecule and by doing so we detected two values
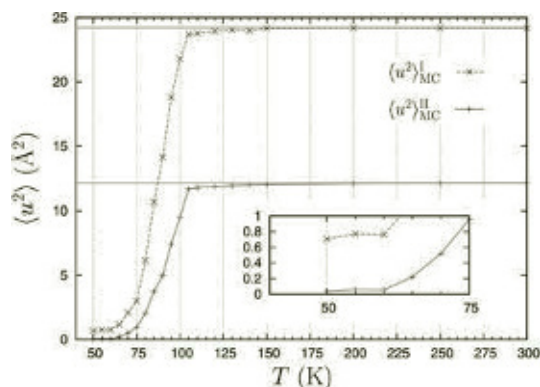
of $\langle u_i^2 \rangle^I$ corresponding to two different classes of orientations. Further analysis shows that within in each class of orientations (read: value of $\langle u_i^2 \rangle^I$) four subgroups can be distinguished. This leads to the final result that the orthorombic crystal consists of of a 5x1x1 super cel that is repeated 5 times along the B direction and 5 times along the C direction of the crystal. The orientations that we find here bear a striking resemblance to the orientations of the C_{60} molecules in fullerite, in fact, both families are small deviations from the low-T fcc arrangement of C_{60} molecules in fullerite. It is interesting to note that we recover one of the low-T C_{60} fullerite orientations as the lowest-energy orientation of a C_{60} molecule in our orthorhombic phase when considering the interaction with its 6 nearest cubane neighbors only. Because the optimal structure without cubane molecules (fullerite) preserves this orientation, i.e. results from C_{60}-C_{60} interactions in a *cubic* lattice, the deviations seen in the actual orientations of fullerene-cubane's orthorhombic phase seem to be the result of the symmetry lowering of the crystal lattice (cubic-to-orthorhombic) induced by the cubane molecules. The occurrence of two slightly differing families of molecular orientations can be interpreted as orientational frustration; no single set of 4 orientations minimises the free energy, but two sets of 4 orientations do.

[1] S. Pekker, É. Kováts, G. Oszlányi, G. Bényei, G. Klupp, G. Bortel, I. Jalsovszky, E. Jakab, F. Borondics, K. Kamarás, M. Bokor, G. Kriza, K. Tompa, and G. Faigel, Nature Mater. **4**, 764 (2005).

[2] B. Verberck, V. Heresanu, S. Rouzière, J. Cambedouzou, P. Launois, É. Kováts, S. Pekker, G.A. Vliegenthart, K.H. Michel, and G. Gompper, Full. Carb. Nano. **16**, 293 (2008).

[3] B. Verberck, G. A. Vliegenthart, and G. Gompper, submitted (2008).

155
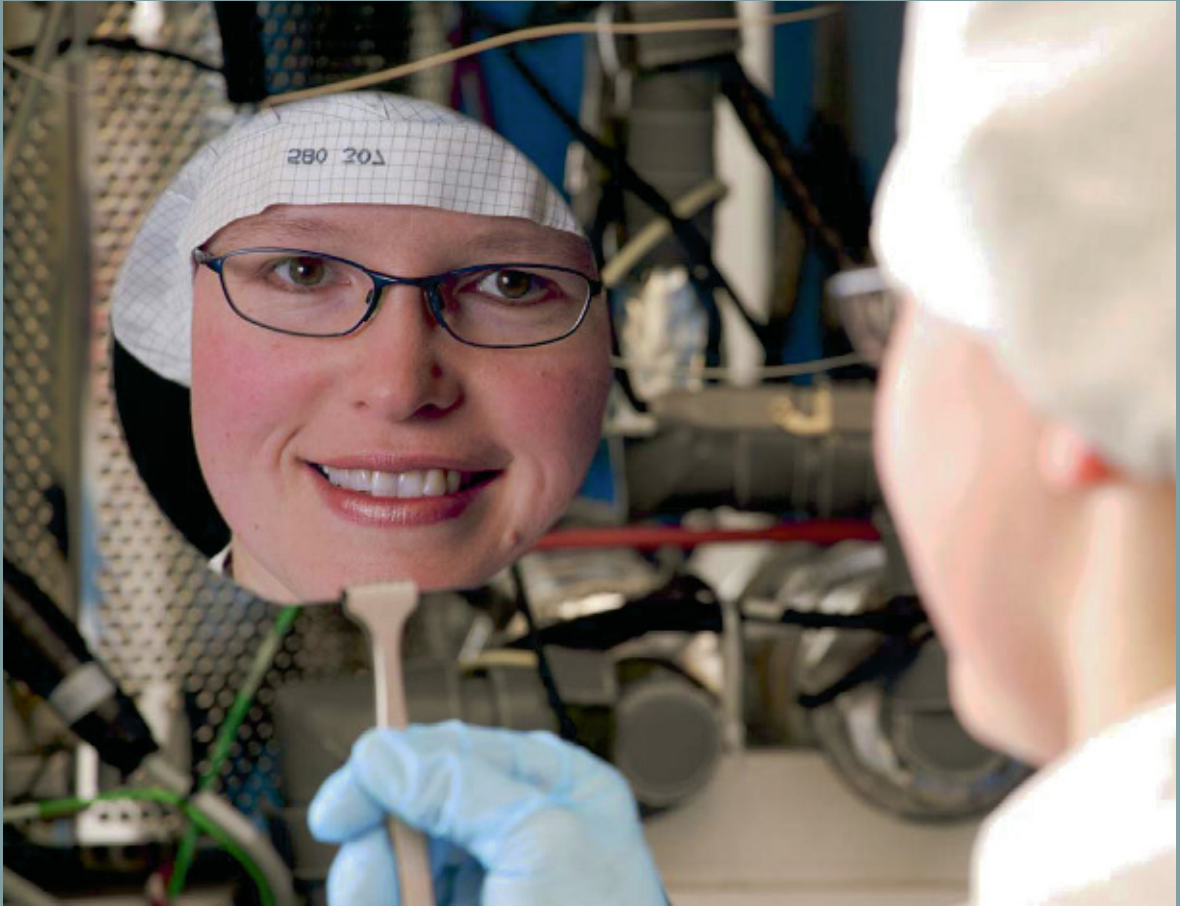
Progress in the rapidly developing field of information and communication technologies depends decisively on the use we make of the materials and methods of semiconductor technology. Miniaturization is still the order of the day, but it does have its physical limits. We will therefore need completely new concepts in the next 20 years in order to come to terms with the burgeoning volumes of information and thereby keep the innovation engine in motion. With our research on future information technologies, scientists at the IFF are pursuing divers concepts.

Information technology with nanoelectronic systems

This research programme focuses on medium-term and long-term tasks in nanoelectronics, on emerging far-reaching concepts, and on issues of physics and technology well ahead of the mainstream development. On the eve of the transition from microelectronics to nanoelectronics, the traditional routes of down-scaling along the roadmap will no longer guarantee a long-term success. Exploratory research in the field of information technology is entering a new era and is unfolding into new degrees of freedom. This applies to all three major fields, information processing, information storage, and information transmission. The major routes of exploratory research in nanoelectronic systems to be followed are:

- scalability of device concepts,
- exploration of new material classes and phenomena,
- new concepts beyond conventional CMOS technology, and
- alternative architectures.

Our research towards these general goals utilizes three approaches, irrespective of the specific programme topics. One approach is dedicated to new electronic materials such as ferromagnetic and ferroelectric layer structures, group III nitrides, and electronically active organic molecules. These material classes are studied because of their potential for introducing improved or completely new functions onto Si chips and new emerging substrates. Another approach is devoted to process technologies for minimum feature sizes well below 100 nm. Apart from using conventional top-down approaches, which are limited to lithographically defined resolutions, we are investigating cost-effective bottom-up approaches, which aim at the generation and assembly of functions from self-organized inorganic nanostructures as well as tailored organic molecules at surfaces. Yet another approach explores novel electronic functions as the basis for new device concepts. These may aim at, for instance, bioelectronic applications, ultra-dense and non-volatile resistive memories, spin-controlled devices, Terahertz imaging systems, and self-organized semiconductor nanostructures.

157

A crossbar memory with resistively switching Pt/MSQ/Ag nanocells

M. Meier[1], R. Rosezin[1], S. Gilles[2], D. Mayer[2], C. Kügeler[1], R. Waser[1,3]

[1] IFF-6: Electronic Materials
[2] IBN-2: Bioelectronics
[3] Institute of Electronic Materials II, RWTH Aachen University

Crossbar structures with integrated methyl-silsesquioxane (MSQ) were fabricated by UV nanoimprint lithography. The sandwiched MSQ film was used for the planarization of the bottom electrodes' interface as well as for the realization of functional, resistively switching crosspoint junctions. With our process future non-volatile crossbar memories with stacking and thus high integration density potential can be realized. Using MSQ as functional material additionally indicates an attractive opportunity because it is highly CMOS compatible. By programming word registers with different bit patterns we demonstrate the potential of this crossbar architecture for future memory applications.

Crossbar architectures are of increasing interest because they provide the potential for next generation memory devices due to their simple device structure and the possibility of a high integration density [1]. By integrating resistively switching materials a single crosspoint in such architecture defines a passive memory cell.

Resistively switching materials are under investigation for the use in the field of novel memory concepts [2]. These materials can be switched between a high-ohmic and a low-ohmic state by applying appropriate voltages to a two terminal device.

The aim of this work is to introduce an attractive technology aspect for crossbar architectures by using SiO_x-based spin-on glass (methyl-silsesquioxane; MSQ) as resistively switching material [3].

Fabrication Process: Single crosspoint devices as well as word structures were fabricated by UV nanoimprint lithography (UV NIL) using a Nanonex-2000 system. A four inch $Si/SiO_2/Pt$ wafer was the substrate for the realization of bottom electrodes. UV-curable resist (NXR-2010) was spun on the wafer. In a UV NIL process the low-viscosity resist was patterned with electrode structures and crosslinked by UV light while pressing a glass mold against the substrate. After separating mold and substrate, the residual layer of UV resist was removed in a CF_4 reactive ion beam process (with an Ionfab300plus – Oxford Instruments). The patterns were transferred into the Pt layer by Ar^+ sputtering.

The bottom electrodes were embedded with spin-on glass to realize a planar surface for the following process steps and a planar top electrode. Therefore, Accuglass T-111 from Honeywell (MSQ) was spun on the wafer and dried under N_2 atmosphere at 425˚C. Using an Ar^+ sputtering technique the MSQ film thickness was reduced to 20 nm - 30 nm on top of the bottom electrodes.

50 nm Ag and 15 nm Pt were deposited on the thin MSQ layer for the realization of the top electrodes. The imprint process as well as the etching was done in the same way as for the bottom electrodes.

Single crosspoint structures as well as 8 bit word structures with a line width of approximately 100 nm were realized (Figure 1).
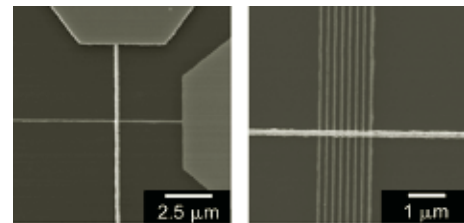
FIG. 1: Single crosspoint structure (left) and 8 bit word structure (right).

Measurements: Electrical measurements were done on an Agilent B1500A semiconductor device analyzer in combination with a semi automatic probe station from Süss Microtec.

I(V)-measurements on 100 nm x 100 nm single cross structures showed resistive switching of the Pt/MSQ/Ag/Pt cells. A typical I(V)-curve for one cycle can be found in Figure 2. The direction of the cycling is indicated by arrows. By applying a positive voltage to the Ag/Pt top electrode the resistance of the material stack changed from the initial high ohmic OFF-state to a low ohmic ON-state at around 1.7 V. To prevent cell destruction the maximum current limit was set to 50 μA. By reversing the voltage polarity the resistance jumped back to the high ohmic OFF-state at around -150 mV.

Regarding the switching speed fast pulse experiments with pulse widths of 10 ns were performed (Figure 3). Voltage pulses of +/- 3.5 V were applied with a pulse generator (Agilent 81110A) to switch the cell ON and OFF (Figure 3 a, b, c). After every switching pulse the state of the cell was measured with 100 mV using the B1500A analyzer (Figure 3 d). In
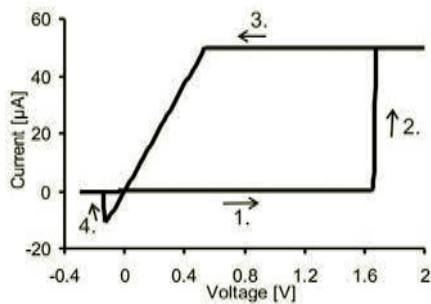
FIG. 2: I(V)-curve of a 100 nm x 100 nm single cross junction.

FIG. 4: Bit patterns, which were programmed to a 100 nm word structure. The low resistance state in the range of kΩ defines "1". The high resistance state which is minimum 1 MΩ defines "0".

crossbar architecture with integrated MSQ indicate the potential for next generation non-volatile memory and logic devices due to the possibility to program crossbar word structures with a defined bit pattern. Additionally a switching speed of 10 ns has been achieved. The fabrication process is very attractive because it combines the planarization of the bottom electrodes' interface and the deposition of resistively switching material in one step.

[1] W. Wu, G.-Y. Jung, D. L. Olynick, J. Straznicky, Z. Li, X. Li, D. A. A. Ohlberg, Y. Chen, S.-Y. Wang, J. A. Liddle, W. M. Tong, R. Stanley Williams, Appl. Phys. A, vol. 80, pp. 1173-1178, Mar. 2005.

[2] R. Waser and M. Aono, Nature Materials, vol. 6, pp. 833-839, Nov. 2007.

[3] M. Meier, C. Schindler, S. Gilles, R. Rosezin, A. Rüdiger, C. Kügeler, R. Waser, IEEE Electron Devices Lett., vol. 30, no. 1, pp. 8-10, Jan. 2009.

159

FIG. 3: Fast pulse measurements on single 100 nm x 100 nm Pt/MSQ/Ag/Pt cells. The +/- 3.5 V pulses are as short as 10 ns (upper part). The ON-resistance is defined to be < 1kΩ. The OFF-resistance is defined to be ≥ 100 kΩ.

general the ON state resistance was measured to be < 1 kΩ and the OFF state resistance was measured to be ≥ 100 kΩ after each corresponding switching event, which demonstrated the fast switching potential of the Pt/MSQ/Ag/Pt cells.

Next, an 8 bit crossbar word structure was programmed. Therefore, the top electrode was contacted with a manual probe needle and the corresponding bottom electrode was contacted with a second, automatic probe needle. Four patterns were written to and subsequently read from the word register: 11111111, 00000000, 10101010 and 01010101. A "1" was defined by the low resistive state in the range of kΩ and was programmed under positive potential on the top electrode and grounded bottom electrode. A "0" was defined by the high resistive state which was at least 1 MΩ and could be realized by reversing the polarity on the top electrode. Figure 4 shows a representative result of a programming cycle of an 8 bit word memory.

Summary and Outlook: The presented results on a

Surface states and origin of the Fermi level pinning on non-polar GaN $(1\bar{1}00)$ surfaces

Ph. Ebert[1], L. Ivanova[2], S. Borisova[1], H. Eisele[2], M. Dähne[2]

[1] IFF-8: Microstructure Research
[2] Institut für Festkörperphysik, Technische Universität Berlin
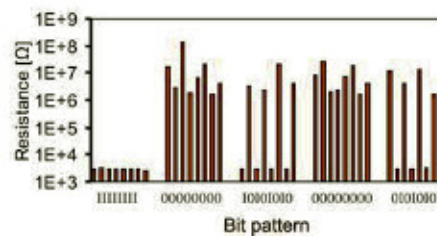
GaN $(1\bar{1}00)$ cleavage surfaces were investigated by cross-sectional scanning tunneling microscopy and spectroscopy. It is found that both the N and Ga derived intrinsic dangling bond surface states are outside of the fundamental band gap. Their band edges are both located at the $\bar{\Gamma}$ point of the surface Brillouin zone. The observed Fermi level pinning 1.0 eV below the conduction band edge is attributed to the high step density but not to intrinsic surface states.

Group-III nitrides raised considerable attraction for green, blue, and ultraviolet laser and light emitting devices. Therefore, intensive efforts have been invested to improve the quality of the epitaxial growth. One particular challenge is the position of the Fermi level at the growth surface. For the presently used polar GaN(0001) growth surface, surface states were identified as origin of the Fermi level pinning. In contrast, for the non-polar GaN surfaces only little is known about the positions of the surface states and thus their possible influence on the Fermi energy. This is due to the lack of experimental data and disagreements between the existing theoretical calculations. This lack of understanding is particularly embarrassing in the light that the growth along non-polar GaN directions is very appealing, due to the absence of electric fields caused by piezoelectricity and spontaneous polarization. Therefore, we investigated non-polar n-type GaN$(1\bar{1}00)$ cleavage surfaces by scanning tunneling microscopy (STM) and spectroscopy (STS) [1]. We identify that no filled N or empty Ga derived dangling bond surface states are present within the fundamental band gap. The only spectroscopic feature within the band gap arises from electrons accumulated in defect states, pinning the Fermi energy at about 1 eV below the conduction band minimum.

Figure 1a illustrates the typical morphology of the GaN$(1\bar{1}00)$ cleavage surface, which consists of atomically flat terraces separated by monoatomic steps. On terraces we measured the current-voltage spectra at different tip-sample separations (Fig. 1b). In order to identify the origins of the tunnel current and thus the positions of the band edges relative to the Fermi energy E_F, we turn to the logarithmic display of the current I and the normalized differential conductiv-ity $(\mathrm{d}I/\mathrm{d}V)/(\overline{I/V})$ as a function of the sample voltage (Fig. 2). The logarithmically displayed current curve in Fig. 2a exhibits (i) a clear onset at +1.0 V of the tunnel current into the empty conduction band states of the surface (I_C) and (ii) two different current contributions at negative voltages, i.e. I_{acc} at voltages between 0 and −2.5 V and $I_V + I_{acc}$ at voltages V < -2.5 V. The current contribution I_{acc} is located at energies within the band gap of GaN.
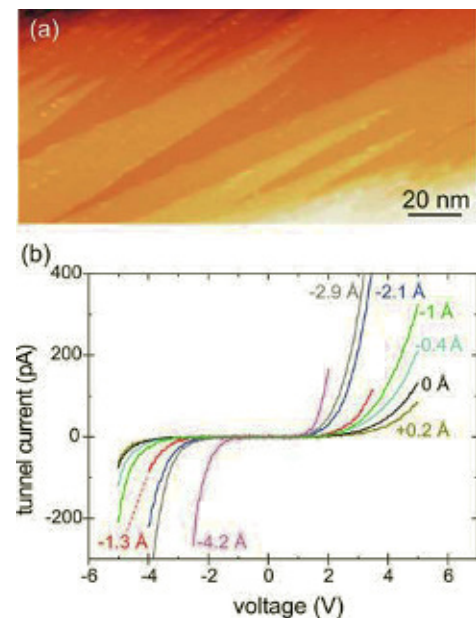
FIG. 1: (a) Constant-current empty state STM image of a cleaved GaN$(1\bar{1}00)$ surface. (b) Current-voltage spectra measured on the flat terraces. The different curves correspond to different tip-sample separations $z = z_0 + \Delta z$ (Δz given at each curve and z_0 defined by a set voltage and current).

The different observed current contributions can be explained as follows [1]: (i) I_C arises from a direct tunneling into empty conduction band states. Thus, the onset voltage at +1.0 V corresponds to the position of the conduction band edge at the surface (E_C). This indicates a Fermi level pinning 1.0 eV below E_C. (ii) the currents (I_{acc}) arises from an accumulation of electrons in the empty defect band, which induces the observed pinning of the Fermi energy as illustrated in detail in Ref. [1]. Finally, (iii), if the magni-

tude of negative voltage is increased above the corresponding energy of the valence band edge E_V, also filled valence band states face empty tip states and additional electrons can tunnel yielding the I_V current contribution. This effect leads to a second onset of the tunnel current close to –2.5 V in Fig. 2a, which thus corresponds to the valence band edge of the GaN surface (E_V).
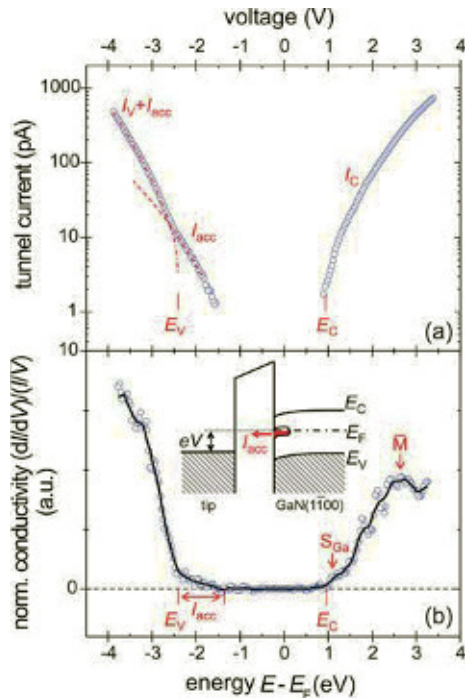
FIG. 2: (a) Logarithmic display of the tunnel current as a function of voltage. The conduction band (I_C), accumulation (I_{acc}), and valence band (I_V) currents are indicated. The positions of the valence and conduction band edges (E_V and E_C) are marked. (b) Normalized differential conductivity (dI/dV)/($\overline{I/V}$). S_{Ga} marks the energetic minimum and $\overline{\mathrm{M}}$ the maximum DOS of the empty Ga dangling bond surface state. The band onsets E_V and E_C and the effect of the accumulation current I_{acc} are clearly visible. Inset: Schematic of the origin of the accumulation current. Note, only the effect of the tip-induced band bending is shown.

The energetic positions of E_V and E_C can be seen even better in the normalized differential conductivity (dI/dV)/($\overline{I/V}$) (Fig. 2b), which corresponds to the density of states (DOS). At E_F– 2.4 eV and at E_F + 1.0 eV clear onsets of the valence and conduction band DOS are visible, respectively. Thus, the band gap at the surface is (3.4±0.2) eV wide, matching well the bulk band gap of GaN, supporting our identification of the band edges. The minimum of the empty Ga dangling bond surface state (S_{Ga}) can be attributed to the shoulder 0.1-0.2 eV above E_C. The large peak at about E_F+2.5 eV ($\overline{\mathrm{M}}$ in Fig. 2b) can also be related to the flat part of the empty dangling bond's band dispersion around the $\overline{\mathrm{M}}$ point of the surface Brillouin zone, where the DOS is largest.

This can be further supported by an estimation of the momentum of the tunneling electrons through an analysis of the exponential decay of the tunnel cur-

rent $I \sim \mathrm{e}^{-2\kappa \cdot z}$ with increasing tip-sample separation z. Figure 3 shows the measured decay constant 2κ as a function of the voltage obtained for the largest tip-sample separations, where the effect of tip-sample interactions are negligible. The decay constant 2κ is approximately given by:

$$2\kappa = 2 \cdot \sqrt{\frac{2m_e}{\hbar^2}\left(B - \frac{|eV|}{2}\right) + |k_{||}|^2}$$

with m_e the electron mass and $k_{||}$ the parallel wave vector of the tunneling electrons. This approximation is shown as solid line in Fig. 3 for $k_{||}$ =0 and an estimated effective tunneling barrier B= 4.3 eV. At negative voltages and at small positive voltages (around 2 to 3 V) the measured values lie close to the calculated curve, indicating tunneling of electrons with $k_{||}$ =0. Thus, the N and Ga derived dangling bond surface states form a direct band gap at the $\overline{\Gamma}$ point. At larger positive voltages the decay constant is larger than expected for tunneling with $k_{||}$ =0. This indicates tunneling from the edge of the Brillouin zone, in agreement with the predicted dispersion of the empty surface state and the above interpretation of the peaks in the conduction band.
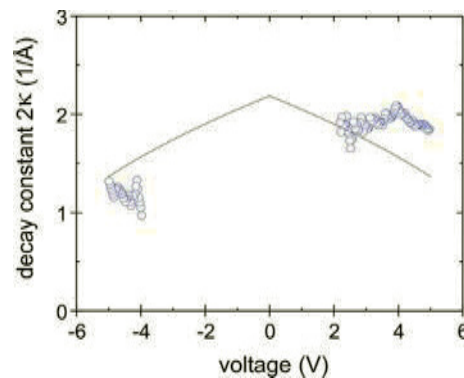
FIG. 3: Decay constant 2κ as a function of the voltage (open circles). The solid line shows the calculated trend for tunneling with zero parallel wave vector. These data reflect the dispersion of the surface states.

Finally, the filled DOS leading to I_{acc} is several orders of magnitude smaller than that of an accumulation zone in the conduction band. This is in good agreement with an origin of I_{acc} in pinning states, whose concentration is typically in the range of 10^{11} to 10^{13} cm^{-2}, i.e. much less than the DOS of the conduction band or of a dangling bond surface state. Thus, no intrinsic N and Ga derived dangling bond surface states are present in the fundamental band gap of GaN($1\bar{1}00$) surfaces and the observed Fermi level pinning cannot arise from the dangling bond surface states. Instead it can be attributed to the large step densities.

[1] L. Ivanova, S. Borisova, H. Eisele, M. Däne, A. Laubsch, and Ph. Ebert, Appl. Phys. Lett. **93**, 192110 (2008).

Strain in SrTiO$_3$ layers embedded in a scandate/titanate multilayer system

M. Luysberg[1,3], D. Ávila[1,3], M. Boese[1,3], T. Heeg[2], J. Schubert[2]

[1] IFF-8: Microstructure Research
[2] IBN-1: Semiconductor Nanoelectronics
[3] ER-C: Ernst Ruska-Centre for Microscopy and Spectroscopy with Electrons

162

Deposition of earth alkali titanate thin films on different substrates allows to tune the strain and, as consequence, their dielectric properties. In this sense, the large range of available lattice constants in rare earth scandates make them very useful candidates to serve as substrate materials for epitaxial growth. In this work we have employed aberration corrected high-resolution transmission electron microscopy (HRTEM) to quantify the strain in different scandate/titanate multilayers by using the geometrical phase analysis method [1]. Besides, we applied electron energy loss spectroscopy (EELS) and ab initio calculations to obtain information about the effect of the strain on the electronic structure of these materials.

The multilayers of DyScO$_3$/SrTiO$_3$ (DSO/STO) and GdScO$_3$/SrTiO$_3$ were grown by Pulsed Laser Deposition (PLD) using GdcSO$_3$ or DyScO$_3$ substrates [2, 3]. The HRTEM study was carried out in an image corrected CM200 microscope. EEL spectra were recorded in a probe corrected Titan microscope. Ab-initio calculations were performed with the Feff8.2 code based on the real space multiple scattering method.

Exit-plane wave reconstruction [4] was utilized for the analysis of DyScO$_3$/SrTiO$_3$ multilayers recording a focus series of 20 images with a focal increment of 1.7 nm. Figure 2 displays the result obtained by the geometric phase analysis. On the left hand side the phase image of the STO/DSO multilayer system is shown. Two components of the Fourier transform obtained from the phase image have been analyzed: the in plane component, which shows variations of the lattice parameter within the interface, and the out of plane component, which carries information about the lattice parameter in growth direction. According to the prefect epitaxial growth on the DSO substrate, a tetragonal distortion of the STO layers is expected. Indeed the in plane lattice (ip) parameter shows almost no variations across the multilayer system, whereas the out of plane (op) component reveals a larger lattice parameter within the DSO layers (right hand side Fig. 2). Here the evaluation was performed within the area marked by the red frame, which extends perpendicular to the multilayer system. The tetragonal distortion of the STO layers amounts to a maximum 2% of tensile strain, trans-
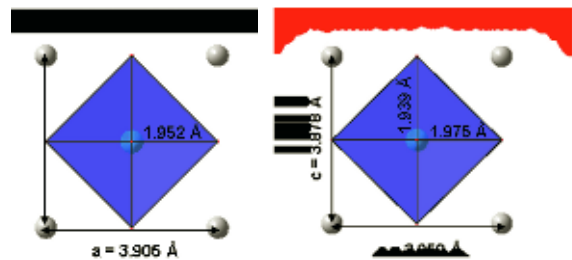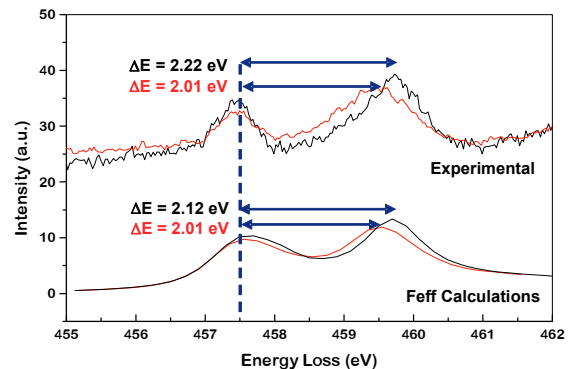
FIG. 1: *Experimental and calculated EEL spectra of the TiL$_3$ edge obtained for cubic SrTiO$_3$ (black curves) and tensilely strained SrTiO$_3$ (red curves). In the strained case, i.e. the in plane lattice parameter resumes the value of DyScO$_3$ the average Ti-O bond is by 0.01 Å larger, resulting in a smaller crystal field splitting.*

lating to an 8 pm smaller lattice parameter of SrTiO$_3$ compared with the in plane lattice parameter of 395 pm = a$_{DSO}$.

Electron energy loss spectra have been recorded for the strained STO layers within the multilayer system. The TiL$_{23}$ edge is formed by four well split peaks attributed to excitations of 2P$_{3/2}$ and 2P$_{1/2}$ subshells to unoccupied t2g and eg states. Figure 1 displays experimental (top) and calculated (bottom) spectra of the TiL$_3$ edge in STO. Compared to a reference spectrum obtained from a STO substrate, a significant smaller splitting of the L$_3$ edge is detected for the tetragonally distorted STO layer within the multilayer system. In cubic SrTiO$_3$ the Ti is surrounded by six O forming a regular octahedron with Ti-O distances of 0.195 nm. However, under tensile strain this octahedron is distorted yielding an average distance Ti-O of 0.196 nm. This enlargement of the dis-
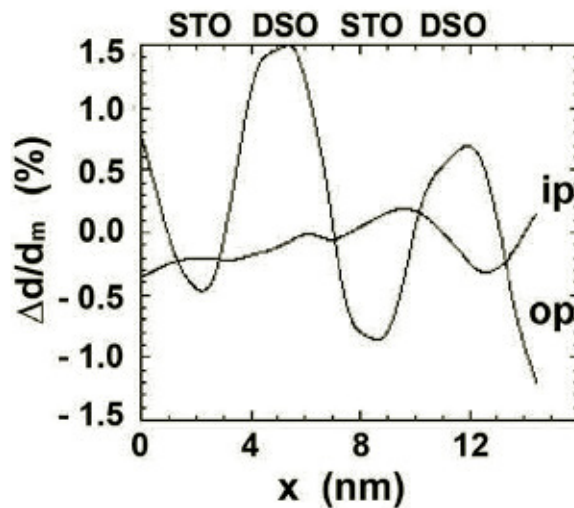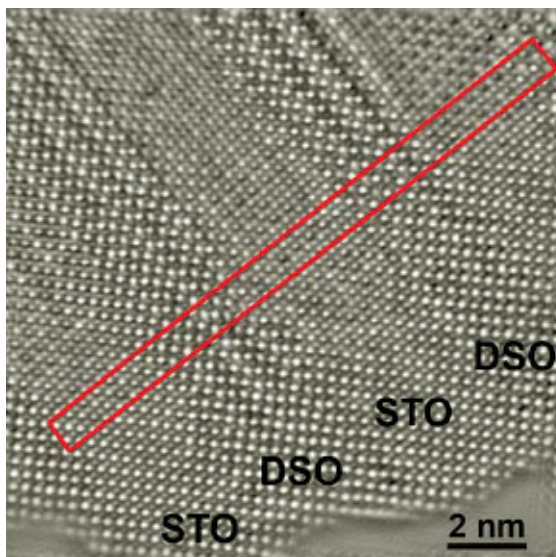
FIG. 2: Phase image obtained from a through focus series of SrTiO$_3$/DyScO$_3$ (STO/DSO) multilayers. The line scans on the right hand side show the variation of the in plane (ip) and out of plane (op) lattice parameters with the distance measured along the red frame within the phase images. The in plane lattice parameter shows only small variations, whereas the out of plane parameter varies by 2% across the layer system.
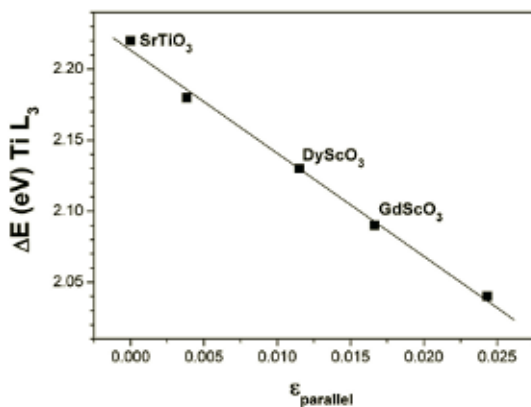
FIG. 3: The splitting of the TiL$_3$ edge of SrTiO$_3$ was calculated by the FEFF 8.2 code for different tensile strains. The labels indicate the strain for SrTiO$_3$ grown onto DyScO$_3$ and GdScO$_3$ substrates, respectively. The splitting decreases linearly with increasing in plane strain, $\varepsilon_{parallel}$.

tances produces a weaker crystal field, which results in a smaller splitting. The reduction of the crystal field splitting is reproduced by ab initio calculations of the TiL$_3$ edges using the Feff8.2 code (Fig. 1 bottom).

Calculations of the L$_3$ edge for different strain situations reveal, that the splitting of the L$_3$ linearly decreases with increasing biaxial strain. In Figure 3 the crystal field splitting of the TiL$_3$ edge is plotted as a function of the strain. The labels indicate the strain situation for relaxed SrTiO$_3$ and STO grown onto DyScO$_3$ and GdScO$_3$ substrates, respectively. This result indicates, that the splitting of the L$_3$ edge is well suited for measurements of local strain variations in SrTiO$_3$.

[1] M. J. Hytch, E. Snoeck, R. Kilaas, R. Ultramicroscopy 74 (1998)

[2] T. Heeg, M. Wagner, J. Schubert, Ch. Buchal, M. Boese, M. Luysberg, E. Cicerrella, J. L. Freeouf, Microelectronic Engineering **80**, (2005) 150

[3] M. Boese, T. Heeg, J. Schubert, M. Luysberg, J. Mat. Sci. **41**, (2006) 4434

[4] A. Thust, W. Coene, M. Op de Beeck, and D. Van Dyck, Ultramicroscopy **64** (1996), 211-230

163

Controlling the magnetization direction in molecules via their oxidation state

N. Atodiresei[1], P. H. Dederichs[3], Y. Mokrousov[1], L. Bergqvist[3], G. Bihlmayer[1], S. Blügel[1]

[1] IFF-1: Quantum Theory of Materials
[3] IFF-3: Theory of Structure Formation

By means of *ab initio* calculations we predict an oscillatory behavior of the easy axis of the magnetization as a function of the oxidation state of the molecule - a new effect, which could lead to revolutional technological applications. We demonstrate this novel effect on the $Eu_2(C_8H_8)_3$ molecule, in which the hybridisation of the outer π-rings states with the Eu $4f$-states causes a redistribution of the orbitals around the Fermi level leading to a strong ferromagnetism due to a hole-mediated exchange mechanism.

The miniaturization of the structures used in modern ultra-high-density magnetic recording aims at non-volatility, low-energy consumption and short access times for reading and writing. Very promising candidates as working units for spintronics are the organic molecular magnets. From the technological functionality point of view, besides a small size, they are required to have a strong ferromagnetic coupling of local spin moments and large values of magnetic anisotropy energy (MAE), a quantity crucial for practical applications.

However, an easy way to control the spin polarized electrons in downscaling devices has proved to be quite a challenge. In particular, the effective ways of dynamical control of the magnetization direction in small magnetic bits used for storage and transport applications are still to be established. Because of the reduced dimensions, for the high-temperature applications the magnetic bits have to exhibit huge values of magnetic anisotropy to resist the temperature fluctuations. Moreover, controlling the magnetization direction, electronic and transport properties of the bits have to be easily manageable and should avoid applying enormous external magnetic fields due to huge anisotropies.

In this letter we propose a simple way to control the magnetization direction in organic magnetic molecules via a basic mechanism, which is common for the biomolecular world: an oxidation-reduction reaction. Here we demonstrate that for a special class of ferromagnetic organic molecules the transfer of electrons in or out of the molecule results in drastic change in the magnetization direction, preserving the large spin due to a strong ferromagnetic coupling and sizable magnetic anisotropies.

Our calculations confirm that the structures of the
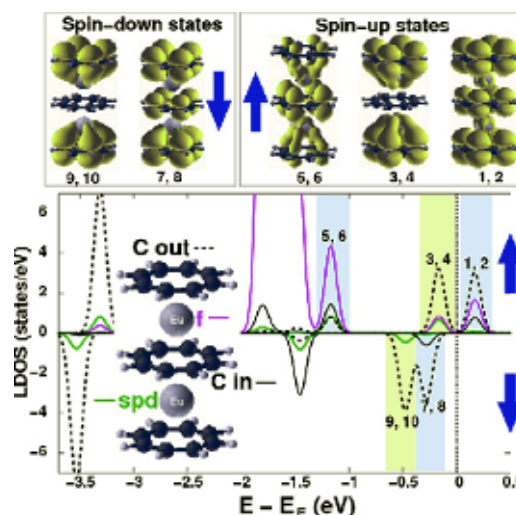
FIG. 1: *The ferromagnetic spin-resolved density of states of the neutral $Eu_2(C_8H_8)_3$ molecule ($U = 3.7$ eV) and the charge density plots of the states in the shaded areas. The $4f$ electrons of Eu atom are drastically shifted from the core region towards Fermi level due to the hybridization with the aromatic orbitals of C_8H_8 rings.*

$Eu_2(C_8H_8)_3$ molecule and its ionic species are sandwiches with the metal atom above the center of gravity of C_8H_8 ligand molecules. All the $Eu_2(C_8H_8)_3$ ionic species have a ferromagnetic ground state, with the total spin moment increasing linearly with the number of additional electrons: from $10\mu_B$ for $Eu_2(C_8H_8)_3^{+2}$ cation up to $14\mu_B$ for the $Eu_2(C_8H_8)_3^{-2}$ anion. The total energy difference between the ferromagnetic (FM) and antiferromagnetic (AFM) spin configuration lies in the range of $100 - 120$ meV for all ionic species, with the exception of the $Eu_2(C_8H_8)_3^{-2}$ anion for which the energy difference between FM and AFM magnetic states vanishes.

The ferromagnetic local density of states (LDOS) and plots of the molecular orbitals (see Fig. 1) provide an insight into the mechanism responsible for the bonding between the Eu and C_8H_8 ligand molecules. In a qualitative picture, based on frontier orbital interactions arguments, when the C_8H_8 molecules and Eu atom are brought together, the highest occupied and lowest unoccupied π-type conjugated orbitals of C_8H_8 interact with the Eu $4f$-orbitals of the same symmetry and hybridization occurs. Due to the
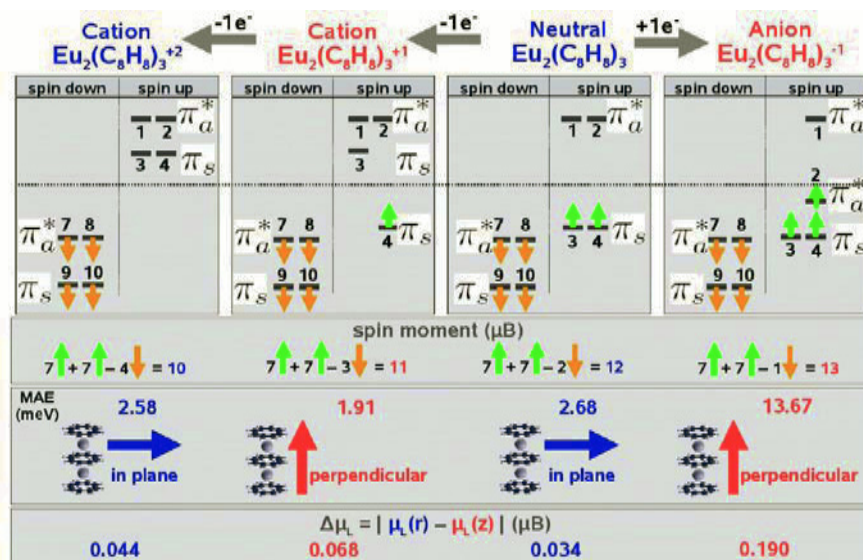
FIG. 2: Schematic view of the the highest occupied and the lowest unoccupied energy levels of $Eu_2(C_8H_8)_3$ ionic species. The anisotropy energy (MAE) favors the in-plane magnetization (r) for the $Eu_2(C_8H_8)_3$ and $Eu_2(C_8H_8)_3^{+2}$, while the perpendicular to plane magnetization (z) is favored for the $Eu_2(C_8H_8)_3^{+1}$ and $Eu_2(C_8H_8)_3^{-1}$. The orbital moment μ_L is always larger for the favored magnetization direction by a value $\Delta\mu_L$.
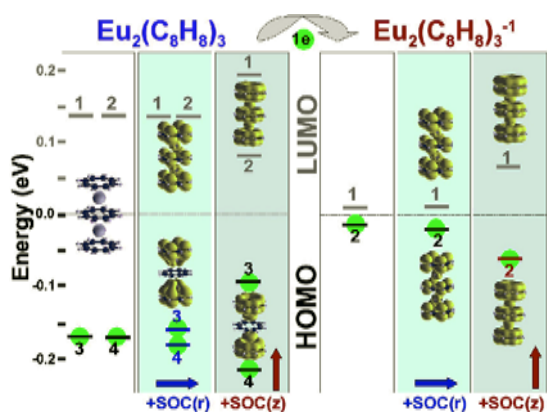
FIG. 3: The highest occupied and the lowest unoccupied molecular orbitals of $Eu_2(C_8H_8)_3$ and $Eu_2(C_8H_8)_3^{-1}$ without and with spin-orbit coupling (SOC) for two magnetization directions are presented. The energy levels for $Eu_2(C_8H_8)_3$ and $Eu_2(C_8H_8)_3^{-1}$ are shown as follow: left panel – without SOC, middle panel – SOC in r-direction, right panel – SOC in z-direction. The larger spin-orbit splitting value of the HOMO-LUMO gap corresponds to a stronger bonding in the molecule and depends on the magnetization direction, as well as oxidation state. The orbitals 2 and 4 are obtained by rotating orbitals 1 and 3, respectively, around the z-axis by $\pi/4$.

strong aromatic character of the π-orbitals located at the C_8H_8 rings the $4f$ electrons are drastically shifted in energy from the low part of the valence electrons towards the Fermi level (which is placed in the middle of the HOMO-LUMO gap). The new molecular orbitals accommodate the $6s$ as well as small fractions of $4f$ electrons of the Eu atoms.

Characteristic for all ionic species when the magnetization points in-plane (r) the 1, 2 orbitals ($^\uparrow\pi_a^*$) have mainly $f_{m_l=-2}$ orbital character while 3, 4 ($^\uparrow\pi_s$) orbitals have mainly $f_{m_l=+1}$, $f_{m_l=+3}$ contributions. The spin-orbit splitting is small and leaves the value of

the HOMO-LUMO gaps unaffected. Orienting the magnetization in the z-direction results in a lifting of the symmetry allowing the $f_{m_l=-2}$, $f_{m_l=+1}$ and $f_{m_l=+3}$ states on two Eu atoms to hybridize. The effect of the spin-orbit coupling is quite large, leading to an effective splitting between the states 1, 2 ($^\uparrow\pi_a^*$) and 3, 4 ($^\uparrow\pi_s$) and a significant change of the corresponding HOMO-LUMO gaps. The stabilization of a specific magnetization direction is a consequence of the electronic structure at the Fermi level: as compared to other magnetization directions a higher orbital moment μ_L is the result of a larger spin-orbit splitting of the energy levels (see Fig. 3) due to a stronger bonding in the molecule. For the $Eu_2(C_8H_8)_3$ and $Eu_2(C_8H_8)_3^{+2}$ the HOMO-LUMO gap and μ_L are larger for the r-magnetization (the anisotropy energy favors the in-plane magnetization by a value of 2.68 meV and 2.58 meV, respectively), while for $Eu_2(C_8H_8)_3^{+1}$ and $Eu_2(C_8H_8)_3^{-1}$ the HOMO-LUMO gap and μ_L are larger when the magnetization points in z-direction (the anisotropy energy favors the perpendicular to plane magnetization by a value of 1.91 meV and 13.67 meV, respectively).

This novel effect together with the ferromagnetic coupling could be used in many technological applications, for instance in data storage or in the single electron transistor using a single redox active organic molecule.

[1] N. Atodiresei, P. H. Dederichs, Y. Mokrousov, L. Bergqvist, G. Bihlmayer, and S. Blügel, Physical Review Letters 100, 117207 (2008)

Spin-transfer torque and anisotropy in Fe/Ag/Fe spin-torque oscillators

R. Lehndorff, D. E. Bürgler, A. Kákay, R. Hertel, C. M. Schneider

IFF-9: Electronic Properties

166

Current-driven magnetization dynamics in spin-torque oscillators (STOs) has strong potential for high-frequency (HF) applications. We investigate the influence of magnetocrystalline anisotropy on the current-driven magnetization dynamics in single-crystalline Fe/Ag/Fe(001) STOs. The four-fold in-plane anisotropy of the Fe(001) films stabilizes the 90°-state with perpendicular magnetizations in addition to parallel and antiparallel alignment. The current-driven dynamics in the 90°-state is governed by the interplay between spin-transfer torque and anisotropy and enables a steady-state precession of the free magnetization at low applied magnetic field. Thus, we demonstrate a new route to realize STNOs operating without applying an external field.

High current densities passing through magnetic nanostructures can induce magnetization switching or excite steady-state oscillations. These phenomena are due to spin angular momentum transfer from spin-polarized currents to the magnetization, where it acts as the so-called spin-transfer torque (STT). Generation of HF signals in STOs is promising for applications in communication technology. In standard STOs a strong externally applied magnetic field is required to prevent switching and to stabilize the steady-state precessional motion [1]. This external magnetic field, however, imposes problems for the application of STOs. Recently presented possibilities to circumvent the necessity of an external field rely on shaping the spin accumulation by suitable material combinations [2] or on exploiting the shape anisotropy of elliptically shaped free layers [3]. Here we present a third possibility [4] by employing a strong internal magnetic field instead of the external field. In our single-crystalline Fe/Ag/Fe(001) nanopillars the magnetocrystalline anisotropy of bcc-Fe results in an effective field with four-fold in-plane symmetry. The total torque –the sum of STT and effective field induced torque– that finally acts on the magnetization has a local minimum when the relative angle ϑ of the two magnetizations is 90°. In the vicinity of this minimum a zero-field precession is possible.

We fabricate our STOs by applying a combined optical and e-beam lithography process to 1 nm Fe (seed layer), 150 nm Ag (buffer layer), 20 nm Fe (fixed layer), 6 nm Ag (interlayer), 2 nm Fe (free layer), and 50 nm Au (capping layer) multilayers grown by molecular beam epitaxy [5]. The final nanopillar as sketched in Fig. 1(a) has a circular cross-section with a diameter of 70 nm [Fig. 1(b)].

Resistance *versus* DC current measurements [Fig. 1(c)] starting in a low resistive state show a two-step switching at positive currents to an intermediate and high resistive level. The magnetization of the free layer (red arrow) first switches from a parallel to a 90°-orientation relative to the fixed layer magnetization (green arrow). In a second step at a larger current it finally switches to an antiparallel alignment. A similar behavior is observed for the sweep to negative currents. Figure 2 shows HF spectra taken at a low field of 5 mT for applied DC currents corresponding to the intermediate resistive 90°-state [red marked current range in Fig. 1(c)]. Note that 5 mT are much weaker than the anisotropy field and, thus, the HF signals can also be observed at zero field. With currents increasing from 6.0 to 6.75 mA the frequency increases from 6.93 to 7.04 GHz yielding a mode agility of 150 MHz/mA.

We perform macrospin simulations by numerically solving the Gilbert equation. In order to describe the current-driven magnetization dynamics, we use the
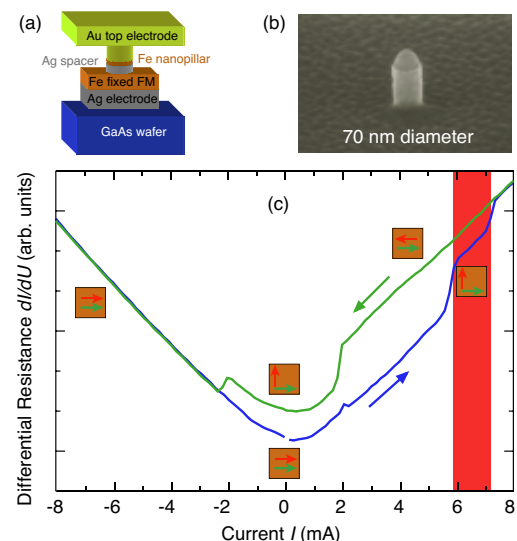

FIG. 1: (a) Sample structure. (b) SEM micrograph of the nanopillar after etching. (c) Resistance *versus* DC current measured at 5 K with a weak in-plane magnetic field of 7.9 mT along an easy axis of the Fe layers.
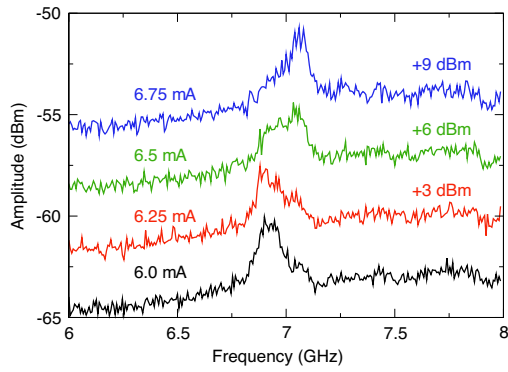
FIG. 2: *Microwave spectra recorded at 5 K and in a weak field of 5 mT. All curves are taken at DC currents corresponding to the 90° -state [red area in Fig. 1(c)].*

version expanded by the STT term as introduced by Slonczewski [6]:

$$\frac{d\vec{m}}{dt} = -\gamma \vec{m} \times \vec{H}_{\text{eff}} + \alpha \vec{m} \times \frac{d\vec{m}}{dt} + j \cdot g(\vartheta) \cdot \vec{m} \times (\vec{m} \times \vec{p}), \quad (1)$$

where $\vec{m}$ is the normalized magnetization vector, γ the gyromagnetic ratio, $\vec{H}_{\text{eff}}$ the effective field, α the Gilbert damping constant, j the current density, $\vec{p}$ the direction of the fixed layer magnetization, and $g(\vartheta)$ the STT efficiency with ϑ the angle between $\vec{m}$ and $\vec{p}$. We use $g(\vartheta)$ given in [7] based on more advanced calculations compared to the often used results from [6]:

$$g(\vartheta) = \frac{\hbar P \Lambda}{4e} \frac{1}{\Lambda \cos^2(\vartheta/2) + \Lambda^{-1} \sin^2(\vartheta/2)}, \quad (2)$$

where P is the spin polarization and Λ the asymmetry parameter as defined in Ref. [7]. For Fe/Ag/Fe(001) $\Lambda = 1.6 \ldots 3.4$ clearly deviates from unity [8]. Therefore, the maximum torque according to Eq. (2) occurs for $\vartheta > 90°$ [Fig. 3(a)]. Figure 3(b) shows simulations of the low-field precession enabled by the anisotropy. The magnetization of the free layer $\vec{m}$ is initially oriented along the $+y$-direction and, thus, perpendicular to the fixed layer magnetization. Red arrows indicate the direction and strength of the effective-field dependent damping torque and the blue arrows represent the STT. For $m_x < 0$ [right half of Fig. 3(b)] they point away from the precession axis and act as an excitation, where as for $m_x > 0$ [left half of Fig. 3(b)] the STT acts as a damping. The net action of the STT during one precessional cycle seems to vanish. However, the STT is asymmetric with respect to the direction of the precession axis (the $+y$-direction), *i.e.* the STT on the right side are stronger than on the left. Therefore, the net action of the STT does not vanish, which is essential for this dynamic mode. For increasing current density the net action of the STT dominates over damping and a steady-state precession can be sustained. The precession axis slightly shifts to $m_z > 0$. This results in a non-zero mean demagnetizing field contributing to $\vec{H}_{\text{eff}}$ and, therefore, increases the precession frequency for increasing current strength as observed in Fig. 2. Due to the partial cancelling of the STT the cone angle of the
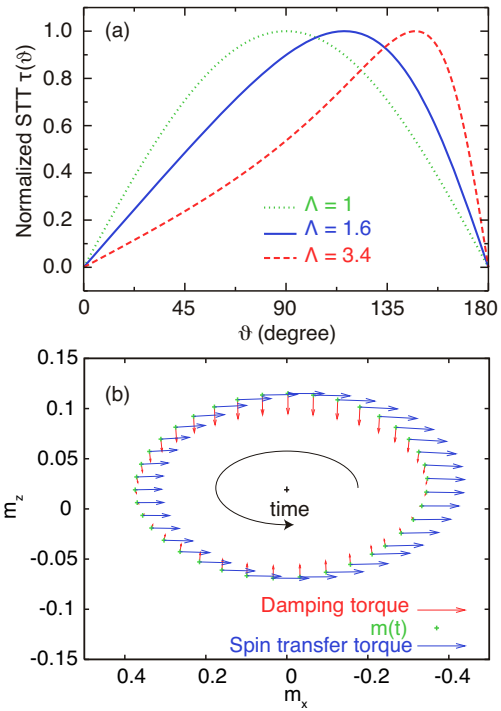
FIG. 3: *(a) Angular dependence of the STT amplitude $g(\vartheta) \sin(\vartheta)$ according to Eq. (2) for different Λ. (b) Representation of the STT (blue arrows) and damping torque (red arrows, enlarged by factor 5 relative to the STT) for the low-field precession in the 90° -state.*

precession is relatively small, but the low-field precession covers the region of the GMR(ϑ) curve with the steepest gradient and therefore results in measurable microwave signals (Fig. 2).

In conclusion, the low-field HF excitations found in the 90°-state demonstrate a new route to realize spin-transfer oscillators without the need for applying strong external magnetic fields.

[1] S. I. Kiselev, J. C. Sankey, I. N. Krivorotov, N. E. Emley, R. J. Schoelkopf, R. A. Buhrman, and D. C. Ralph, Nature **425**, 380 (2003).

[2] O. Boulle, V. Cros, J. Grollier, L. G. Pereira, C. Deranlot, F. Petroff, G. Faini, J. Barnas, and A. Fert, Nature Physics **3**, 492 (2007).

[3] T. Devolder, A. Meftah, K. Ito, J. A. Katine, P. Crozat, and C. Chappert, J. Appl. Phys. **101**, 063916 (2007).

[4] R. Lehndorff, D. E. Bürgler, A. Kakay, R. Hertel, and C. M. Schneider, IEEE Trans. Magn. **44**, 1951 (2008).

[5] H. Dassow, R. Lehndorff, D. E. Bürgler, M. Buchmeier, P. A. Grünberg, C. M. Schneider, and A. van der Hart, Appl. Phys. Lett. **89**, 222511 (2006).

[6] J. C. Slonczewski, J. Magn. Magn. Mater. **159**, L1 (1996).

[7] J. C. Slonczewski, J. Magn. Magn. Mater. **247**, 324 (2002).

[8] R. Lehndorff, D. E. Bürgler, A. Kakay, R. Hertel, and C. M. Schneider, Phys. Rev. B **76**, 214420 (2007).

167

Topologically protected surface states: Sb(111) vs. Bi(111)

G. Bihlmayer[1,2]

[1] IFF-1: Quantum Theory of Materials
[2] IAS: Institute for Advanced Simulation

Thin films of Sb(111) show surface state dispersions that are a signature of the topologically non-trivial band ordering in the bulk. Density functional theory calculations of films of Sb(111) and the (trivial) Bi(111) give insight into the nature of the electronic states of the topological insulator BiSb that show spin-textures that can support the quantum spin-Hall effect.

Electronic states at the boundary of a material can exhibit exotic properties: E.g. edge states on insulators in high magnetic fields can carry dissipationless currents due to the quantum-Hall effect. Without external magnetic fields, spin-orbit coupling effects can lead to spin-accumulation or spin separation (spin Hall effect) in a non-magnetic material. Recently, a new class of materials has been predicted that can support dissipationless spin-currents: the topological insulators. Two years ago first experimental evidence for this new state of matter has been found by conductivity measurements at interfaces of HgTe-based heterostructures [1]. In contrast to these structures, surfaces offer the possibility to gain a direct view on the electrons that show this so called quantum spin-Hall effect (QSHE). Therefore, the search for surface-states that have the properties required for the QSHE have attracted considerable interest.

Surface states can form in the projected bandgaps of the bulk material depending on the nature of the states the boundaries of that gap. In the semimetals Bi and Sb for all $k_\parallel$ points of the surface Brillouin zone there is a gap in the vicinity of the Fermi level and in this gap surface states have been observed for many surface orientations. The strong spin-orbit coupling (SOC) in Bi (and to a bit less extent also in Sb) acts as a kind of internal magnetic field that induces a spin-splitting of these states even on a non-magnetic surface. This spin-polarization was confirmed (also experimentally) not only on surfaces of bulk material, but also on thin bismuth films [2]. Therefore, it was rather natural to expect the existence of this effect also in the chemically similar antimony.

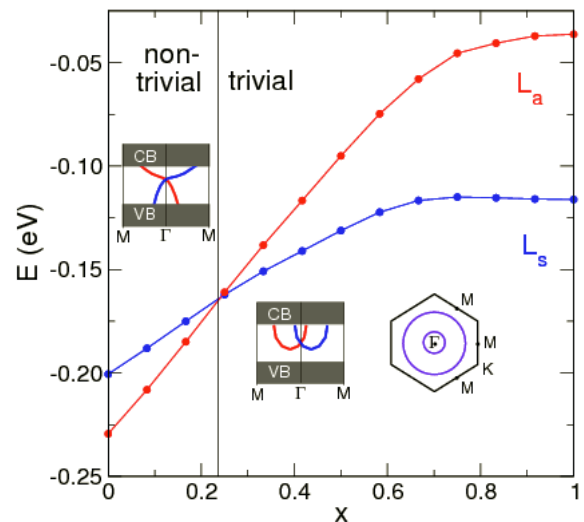Nevertheless, there is a subtle difference between the electronic states in Sb and Bi, which only becomes apparent when the symmetry of the wavefunctions is taken into account: At a certain point (L) in the bulk Brillouin zone, the symmetry of the states that form the upper and lower edge of the gap in Sb is

FIG. 1: *Energetic position of the symmetric (L_s) and antisymmetric (L_a) eigenfunction at the L point in Bi as a function of spin-orbit coupling strength. To simulate a Bi_xSb_{1-x} alloy, the SOC strength is continuously varied between the values for Sb ($x = 0$) and Bi ($x = 1$). Insets show schematically how the valence band (VB) and the conduction band (CB) are connected by a surface or edge state in the topologically non-trivial (left) and trivial (right) case and a sketch of the surface Brillouin zone with the Fermi contour (purple). Note, that in the trivial case the TRIMs ($\overline{\Gamma}$ and $\overline{M}$) are encircled two times, in the non-trivial case only once.*

reversed as compared to Bi. This exchange of bands is a consequence of the increased spin-orbit coupling in Bi, as can be seen from calculations, where the SOC strength is artificially decreased from the Bi to the Sb value (Figure 1). This little detail in the bandstructure turns out to have severe consequences for the surface states in both materials.

To see, how this happens, we have to look again at the nature of the above mentioned spin-splitting of the surface states: Similar to the Rashba-effect that occurs in semiconductor heterostructures, on a surface the electric field (potential gradient normal to the surface) is transformed in the rest-frame of the moving electron into a magnetic field (Lorentz transformation). For special electron momenta (at the so called time-reversal invariant midpoints, TRIMs) the electron is not moving and the splitting goes to zero, i.e. the spin-split bands have to cross. TRIMs

are at $\mathbf{k}_\parallel = 0$ ($\overline{\Gamma}$-point) or if $\mathbf{k}_\parallel$ is in the middle of two $\overline{\Gamma}$-points (e.g., for the (111) surface, the $\overline{M}$ point which is the projection of the L point from the bulk- to the surface-Brillouin zone). Now the symmetry of the bulk bands has the following effect: While in Bi (the so called topologically trivial case) the Fermi sur- face contours encircle the TRIMs an even number of times, in Sb an odd number of Fermi surface contours can be found to encircle these points (cf. Figure 1).

The consequences of the different Fermi-surface topologies can be best illustrated for a two- dimensional insulating material that shows these spin-split states at its edges. In the topolocially non- trivial case we see from the bandstructure that states with one spin (blue in the inset of Figure 1) can only move in $+\mathbf{k}_\parallel$ direction, while the particles with other spin (red) have to propagate in $-\mathbf{k}_\parallel$ direction. It follows that (i) there is a spin-current at the edge (no charges are moving, just spin) and (ii) a moving electron cannot be scattered by some impurity since there are no other states of the same spin available at this energy. Only by reverting the spin the elec- tron could change its momentum. In this sense, the spin-current is dissipationless. In the topolocially triv- ial case we see that two spin-currents circulate at the edges (in opposite directions) and scattering without spin-flip is possible. Therefore dissipation can occur and the spin-current is not "topologically protected".

From this, the analogy with the quantum-Hall ef- fect (QHE) should be visible: While in the QHE dis- sipationless charge currents arise in strong exter- nal magnetic fields, in topological insulators, as dis- cussed above, dissipationless spin currents are cre- ated by strong internal magnetic fields. Therefore, this phenomenon was termed quantum spin-Hall ef- fect (QSHE). In both cases the currents arise at the edges of the material and both states of matter can be mathematically classified by a so called topologi- cal number.

Let us come back to the case of Bi or Sb surfaces: As this materials are semimetals (i.e. there is a al- most vanishing density of states at the Fermi level, but no gap) the verification of the QSHE is not directly possible. Since the early seventies, it is known that alloying Sb with Bi produces a semimetal to semi- conductor transition and opens a bandgap of about 20 meV. While this value might seem small, for low temperature conductivity experiments it is sufficient. If alloying transforms the bandstructure of Sb from a semimetal to a semiconductor without producing any band crossings, the character of the parent com- pound is conserved and a topological insulator can be created.

Combining density functional theory calculations with spin- and angle-resolved photoemission experiments it was now possible to pin down the topological nature of the gaped BiSb alloy [3]. Our calculations confirm the non-trivial topological ordering of the bands in Sb and the surface states can also be clearly seen in the experiment (Figure 2). The spin texture of these bands has been analyzed experimentally and corre- sponds to the theoretical predictions. While the spin-
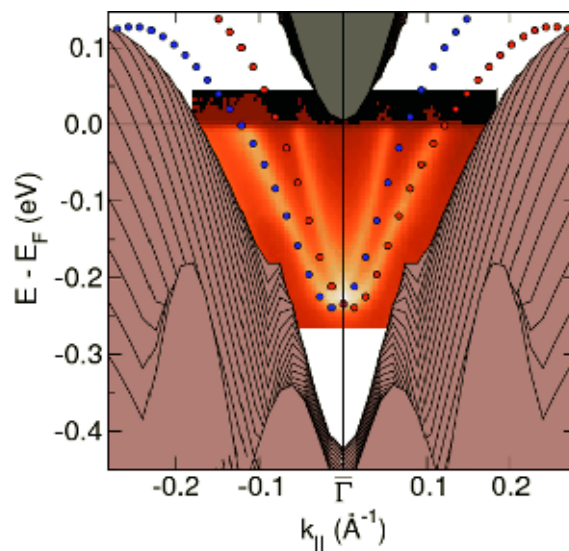
FIG. 2: *Experimentally measured dispersion of the Sb(111) surface state (orange) and the DFT calculation of the pro- jected bulk states (lines) and surface states (dots). The different spin-character of the surface state bands is indi- cated by red and blue. The valence and conduction band are shaded in brown and grey, respectively.*

orientation of the states near the $\overline{\Gamma}$ point are easy to measure, unfortunately the intensity decreases as $\mathbf{k}_\parallel$ approaches the $\overline{M}$ point and only for three states on the line $\overline{\Gamma M}$ the spin-orientation can be determined. Since the spin of the innermost state is opposite to the spin of the other two, these two states form a pocket that does not encircle any TRIM and can be neglected for our discussion. Our calculations show that the innermost state enters the conduction band in $\overline{\Gamma K}$ direction [2], both for Bi(111) and Sb(111), so the only TRIM that can be additionally enclosed by this state is the $\overline{M}$ point. Experimentally it is seen that the $\overline{M}$ point is encircled two times, so we count in total seven loops around the TRIMs (once around $\overline{\Gamma}$ and twice around the three $\overline{M}$ points). This con- firms that BiSb is a topological insulator.

Up to now experiments on topological insulators have confirmed quantum-Hall like transport properties [1] and the special spin-textures in these materials [3]. Combining these unusual properties, exploiting the QSHE, can allow to control both the flow and the ori- entation of spin at the boundaries of this new class of insulators.

[1] M. König, S. Wiedmann, C. Brüne, A. Roth, H. Buh- mann, L. W. Molenkamp, X.-L. Qi, S.-C. Zhang, Sci- ence **318**, 766 (2007)

[2] T. Hirahara, K. Miyamoto, A. Kimura, Y. Niinuma, G. Bihlmayer, E. V. Chulkov, T. Nagao, I. Matsuda, S. Qiao, K. Shimada, H. Namatame, M. Taniguchi, and S. Hasegawa, New J. Phys. **10**, 083038 (2008)

[3] D. Hsieh, Y. Xia, L. Wray, D. Qian, A. Pal, J. H. Dil, J. Osterwalder, F. Meier, G. Bihlmayer, C. L. Kane, Y. S. Hor, R. J. Cava and M. Z. Hasan, Science **323**, 919 (2009)

169

First-principles calculations on spin injection in Fe/Si(001)

Ph. Mavropoulos

IFF-1: Quantum Theory of Materials
IAS: Institute for Advanced Simulation

The possibility of spin injection from Fe into Si(001) through the Fe/Si Schottky barrier is shown by density-functional calculations for the electronic structure and a Landauer-Büttiker approach for the current. The current-carrying states are found to form five conductance hot spots on the (001) surface Brillouin zone (SBZ): one at the SBZ center and four symmetric satellites. A moderate strain along the [001] direction is found to be sufficient to lift the degeneracy, so that only states at the zone center can carry current, which under ideal conditions reaches almost 100% spin polarization.

Electrical spin injection in Si has been recently achieved by the groups of Appelbaum [1] and Jonker [2]. The great significance of these experiments lies in the extremely large spin coherence lengths of spins in Si, as well as in the use of Si in current semiconductor technology [3]. Motivated by these results, we performed density-functional calculations on the possibility of direct spin injection from Fe into Si through the Schottky barrier of the contact, as reported in Ref. [4]. Our focus was on idealized epitaxial, atomically flat Fe/Si(001) interfaces. The spin-dependent current was calculated using a Landauer-Büttiker type of approach.

For understanding and tuning the spin-dependent current, $I_\uparrow$ and $I_\downarrow$, and the current polarization, $P = (I_\uparrow - I_\downarrow)/(I_\uparrow + I_\downarrow)$, three factors are important, and the question on their influence must be investigated. (i) The position $\vec{k}_\parallel$ of the occupied electron states in the SBZ of the Si injection region at the Fermi level E_F; (ii) the complex band structure of the Si barrier, determining the decay parameter $\kappa(\vec{k}_\parallel; E_F)$; and (iii) the coupling of the spin-up and spin-down Fe states at E_F with the Si states at the interface.

Question (i) is readily answered by a simple examination of the Si conduction-band structure. This consists of six degenerate minima, also called *pockets*, close to the six equivalent X-points (i.e., in the $\langle 100 \rangle$ directions). For E_F just above the conduction-band edge E_c, these minima are occupied and carry current. Projected on the (001) SBZ, the minima form five conductance hot spots: one at the SBZ center ($\bar{\Gamma}$-point) and four, equivalent to each other, satellites close to the SBZ edges (we call these positions

$\vec{k}_\parallel^{\text{sat}}$).0
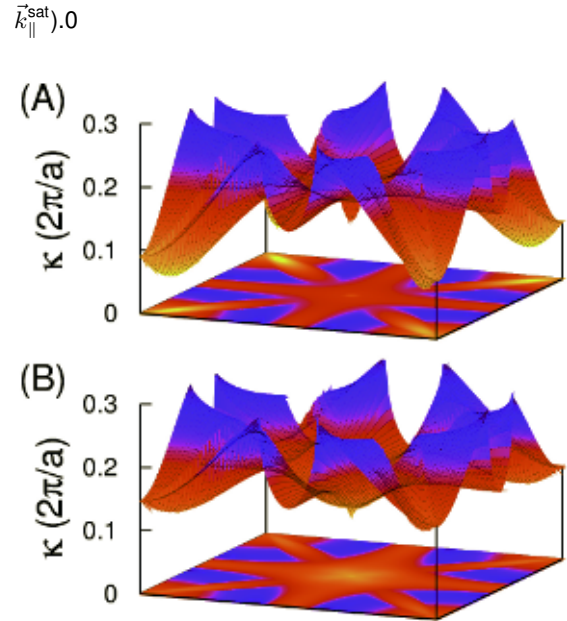
FIG. 1: *Decay parameter $\kappa(\vec{k}_\parallel; E_F)$ in the band gap of Si in the [001] direction for $E_F = E_v + 0.725$ eV (A) and at $E_F = E_v + 0.325$ eV (B). Brighter shaded regions correspond to lower κ and more efficient tunneling.*

We now turn to question (ii). The $\vec{k}_\parallel$-dependent current becomes smaller with the barrier thickness d as $\exp[-\kappa(\vec{k}_\parallel; E_F)\, d]$. Depending on the position of E_F with respect to E_c in the barrier region, the $\bar{\Gamma}$-point or the satellites' contribution can dominate. If E_F is high, close to E_c, then $\kappa(\vec{k}_\parallel^{\text{sat}}; E_F) \ll \kappa(\bar{\Gamma}; E_F)$, and the satellites have the dominant contribution. This is due to the ellipsoidal anisotropy of the Si conduction band pockets, from which an anisotropy of the complex bands is inherited: when the long axis of a pocket is along z (current direction), $\Delta E(\kappa)$ has low curvature and κ becomes large even if $\Delta E = |E_F - E_c|$ is small; this is the $\bar{\Gamma}$-case. If a short axis of the pocket is along z, $\Delta E(\kappa)$ has high curvature and κ remains small. So much is true close to E_c; however, close to the valence band edge E_v, the situation is reversed. As the E_v is located exclusively at Γ, $\kappa(\bar{\Gamma}; E_F)$ can become arbitrarily small as $|E_F - E_v|$ decreases, while $\kappa(\vec{k}_\parallel^{\text{sat}}; E_F)$ remains large. Then, the contribution of the SBZ center to the current dominates. To demonstrate this, we show in Fig. 1 the decay parameter $\kappa(\bar{\Gamma}; E_F)$ in the full SBZ

for two different cases: (A) E_F close to the conduction band edge and (B) E_F a little lower than the middle of the gap. In the former case the smallest decay is at the center of the SBZ, while in the latter case it is at the satellite positions.

In order to answer question (iii), the transmission probability has been calculated around each one of the hot spots for both spin directions. This was done for several band alignments of the barrier, representing different experimental doping situations. In all cases it was found that the current polarization of the satellites was of the order of 50-60%, while the current polarization at $\bar{\Gamma}$ varies between 50 and 100%. Before discussing this, we note that, when the barrier band alignment brings E_c close to E_F, the satellites contribution dominates [due to factor (ii)], and the polarization cannot approach the ideal 100%. If, however, E_v approaches E_F, the calculation of the current shows that the $\bar{\Gamma}$-point contribution dominates.

We now discuss the high spin polarization at $\bar{\Gamma}$. Under the assumption of a perfectly ordered interface, $\vec{k}_\parallel$ is conserved during transmission from Fe to Si. Examining the Fe and Si wavefunctions at $\bar{\Gamma}$, we find that there is symmetry matching between the Si and spin-up Fe states (both are of Δ_1 symmetry), while there is a symmetry mismatch between the Si and spin-down Fe states (the latter are not of Δ_1 symmetry). This is the origin of spin-selective transmission at $\bar{\Gamma}$ [5]. However, in the injection region also states close to, but not exactly at, $\vec{k}_\parallel = 0$ are populated: there is current for $k_\parallel < k_{max}$, with $E_F - E_c = \hbar^2 k_{max}^2 / 2m^*$. For $\vec{k}_\parallel \neq 0$ the symmetry selection rule does not apply, and the spin-down current rises. This is represented in Fig. ?? (top). There, we see that the spin-up current forms a peak at $\bar{\Gamma}$, while the spin-down current forms a double-peak structure with a pronounced minimum at $\bar{\Gamma}$.

It follows that two conditions must be satisfied to reach a high polarization. Firstly, the satellites, which are not subject to a symmetry mismatch rule, must be eliminated. As we saw, this can be done by appropriately aligning the bands in the tunneling region, so that the satellites decay fast. However, there is an alternative. By straining Si, with $c/a < 1$ (c is here the junction growth axis), the degeneracy of the conduction band edge is lifted such that the satellite positions rise in energy. Already a modest strain of 0.5%, which is experimentally feasible [6], raises the satellite pocket energy by ~ 30 meV (according to our calculations), which is enough to cut them off from transport.

Assuming that the satellites have been eliminated, it is interesting to see the polarization as a function of $\delta = E_c - E_F$ in the injection region. We call δ a gate voltage, assuming that it can be tuned by gating. When δ is large, the double-peak structure in spin-down conductance, shown in Fig. ?? (top), will reduce the injection efficiency. However, as δ is reduced, k_{max} becomes confined very close to the $\bar{\Gamma}$-point, and the spin-down conductance becomes negligible. This is demonstrated in Fig. ?? (bottom), where P is shown as a function of Schottky barrier
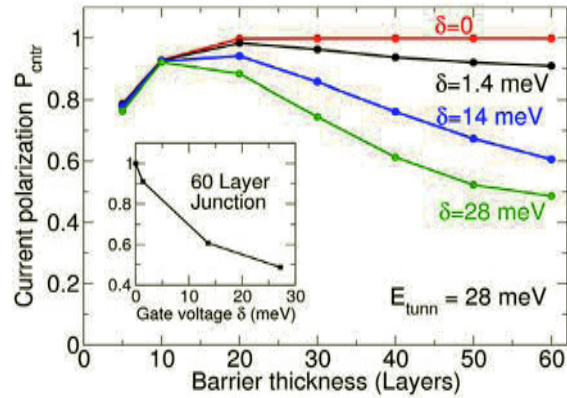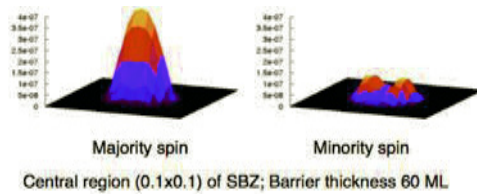
FIG. 2: Top: Calculated spin-up (majority-spin) and spin-down (minority-spin) conductance as function of $\vec{k}_\parallel$ close to the SBZ center. Bottom: Polarization around the $\bar{\Gamma}$ point for small values of gate voltage δ. Inset: Zero-gate "anomaly" of the polarization for a 60-layer barrier.

thickness and gate voltage. We see that $P > 90\%$ can be achieved for $\delta < 1.4$ meV. However, a drawback is that this effect can only be observed at low temperatures; taking into account that 1 meV corresponds to 11.6 K, high values of P require temperatures of only a few Kelvin. Otherwise, a current polarization of $\sim$50-60% is expected.

[1] I. Appelbaum, B. Huang, and D.J. Monsma, Nature **447**, 295 (2007).

[2] B.T. Jonker, G. Kioseoglou, A.T. Hanbicki, C.H. Li, and P.E. Thompson, Nature Physics **3**, 542 (2007).

[3] Igor Žutić, Jaroslav Fabian, and Steven C. Erwin, Phys. Rev. Lett. **97**, 026602 (2006).

[4] Phivos Mavropoulos, Phys. Rev. B **78**, 054446 (2008).

[5] The same effect has been discussed in the past in Fe/GaAs (001) junctions. See, e.g., O. Wunnicke, Ph. Mavropoulos, R. Zeller, P. H. Dederichs, and D. Grundler, Phys. Rev. B **65**, 241306 (R) (2002).

[6] D. Buca, B. Hollander, S. Feste, St. Lenk, H. Trinkaus, S. Mantl, R. Loo, and M. Caymax, Appl. Phys. Lett. **90**, 032108 (2007).

171

Predicting formation of long chains in break junctions

A. Thiess[1,2,3], Y. Mokrousov[1,2,3], S. Blügel[1,3], S. Heinze[2]

[1] IFF-1: Quantum Theory of Materials
[2] Institute for Applied Physics, University of Hamburg
[3] IAS: Institute for Advanced Simulation

We introduce a generic model of chain formation in break junctions by formulating criteria for the stability and producibility of suspended monatomic chains based on total energy arguments. Using *ab initio* calculations including spin-polarization and spin-orbit coupling, we apply our model to the formation of monatomic 4d and 5d transition metal (TM) chains. We explain the physical origin of the experimentally observed general trend of increasing probability for the creation of long chains for late 5d TMs and suppressed chain formation for 4d TMs.

Recent investigations show that transition metal (TM) chains exhibit large magnetic moments, giant and colossal magneto-crystalline anisotropy energies and reveal a number of intriguing ballistic spin-dependent transport-related phenomena [1]. A very promising experimental approach to study the quantum transport through such nanosystems are break junction (BJ) experiments [2]. In a typical BJ experiment, the leads, being initially in contact, are pulled apart and the conductance of the system is measured simultaneously. Upon pulling, atoms are extracted from the leads and may form a chain consisting of a few atoms. While for later TM elements and Au, chains with quite a large number of atoms can form, for earlier $5d$ and $4d$ metals long chain creation in BJs does not occur [2]. This observation raises the question of which material-specific physical quantities are responsible for successful chain formation in BJs.

Computationally, treating the process of chain formation in a BJ with the accuracy of *ab initio* methods is an extremely challenging task even for the fastest schemes, since the motion of hundreds of atoms has to be taken into account on a phonon time scale. Moreover, the exact structure of the leads is unknown, which leaves a great deal of uncertainty in the initial configuration of the system. This motivates the development of generic models able to provide an insight in terms of a chemical trend. Here, we present a model for chain formation in a BJ, which is based on total energy arguments leading to criteria for the stability and producibility of long suspended chains [3]. We attain a drastic decrease in computational time, dividing the system into two distinct subsystems, considered separately: the leads, and the suspended chain.
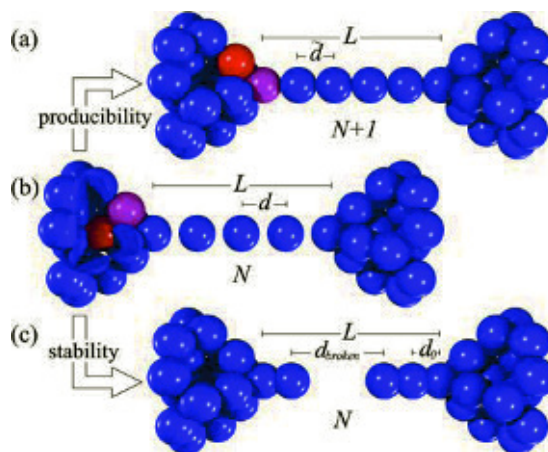
FIG. 1: *A suspended three-atoms chain (N=3) under tension (b) lowers its energy via pulling one more atom out of the leads (a) or by breaking (c). All configurations have fixed tip-to-tip distance L.*

In our model, which is based on the atomic configurations shown in FIG 1, chain formation succeeds if the *criterion for stability* and for productivity [3] are met. The *criterion for stability* quantifies the break of the suspended monowire (MW) based on the disruption of interatomic bonds between nearest neighbor chain atoms. The *criterion for producibility* is concerned with the chain elongation that is composed of two processes. At first one atom has to be extracted out of the lead into the chain. This rearrangement leads to a reduction of the coordination of this distinctive atom and consequently additional external energy is requested, which we account for by the difference $\Delta E_{lead} = E_{\mathrm{MW}} - E_{lead}$ of the energy of cohesion for lead E_{lead} and chain E_{MW}. Secondly, if an additional atom enters the chain all bonds relax to a smaller interatomic distance and relaxation energy is gained. These competing contributions to the total energy of the system determine whether it is energetically favorable to grow the chain by one atom or not. In order to apply both the *criteria for stability* and *producibility* only two physically transparent quantities have to be known: The potential energy of a MW atom as a function of interatomic distance and the cohesive energy difference ΔE_{lead}.

We performed first-principles calculations using the 1D-FLAPW method [4] as implemented in the FLEUR@juDFT code for linear infinite MWs of $4d$

and $5d$ TMs as well as Ag and Au varying the interatomic distance. We used the bulk version of the same code to calculate the cohesion energy differences as explained in Ref. [3]. In all cases we included spin-polarization and spin-orbit coupling. In order to operate with continuous quantities we fit the calculated binding energy potentials by the Morse-potential, which provides the analysis on the basis of three physical transparent parameters: The cohesive energy difference, ΔE_{lead}, the maximal slope of the potential energy, $F_0=F(\hat{d})$, and the position of the inflection point $\hat{d}$ relative to the equilibrium interatomic distance.
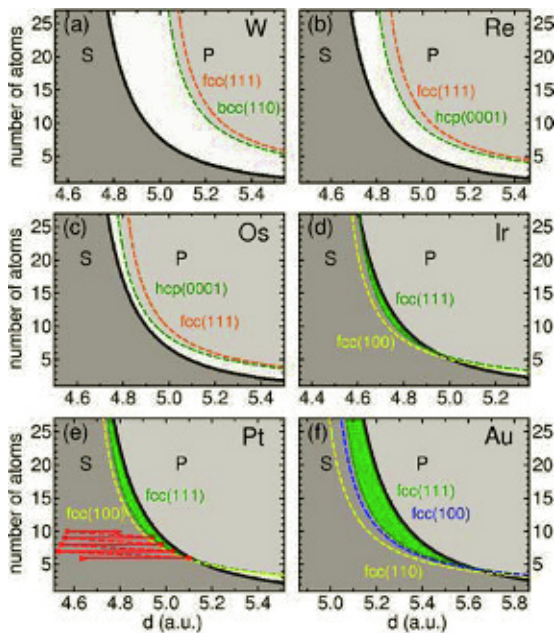
FIG. 2: (a)-(d): Regions of stability (S, medium grey) and producibility (P, light grey) for $5d$ TMs from W to Au. The boundary of the S-region is marked with a solid black line. The P-region depends on the crystal structure and surface orientation assumed for the leads. The area between S- and P- regions is shown in white (a),(b),(c). In (d)-(f) the SP-region exists for all surfaces, and the smallest of them is marked in green. The starting point along the x-axis is the equilibrium interatomic distance d_0. The trace of a chain formation process in (N,d) phase space is drawn for Pt (e). describing the chain formation process.

On the basis of these parameters we analyse the stability and producibility of suspended chains in terms of maps in (N,d)-space, where N is the number of atoms in the chain and d is their interatomic distance (FIG 2). Applying the criteria clear regions of stability (S) and producibility (P) can be determined in this space. For a successful chain formation the S- and P-regions have to overlap. As shown in FIG 2 such regions do not exist for the early $5d$ TMs Hf, Ta, W, Re and Os, while Ir, Pt and Au have a probability to form long chains for tips of different surface geometry. For the $4d$ elements we observe a suppressed tendency to chain formation only resulting in small overlapping S and P areas for Ru and Ag. These results agree one to one with the experimental findings, which proves the predictive power of our model.

Moreover, it facilitates the analysis of the physical origin of the observed trends.

For an optimal probability for chain formation both small cohesion energy differences ΔE_{lead} and a high stiffness of the chain described by F_0 is required. Throughout the $5d$'s we find a maximum for ΔE_{lead} for Ta and W reducing considerably to the end of the series, while F_0 peaks late in the series for Os and Ir. Combining the effect of both parameters the best conditions for successful chain formation is found at the end of the $5d$ series and Au. The lower chain elongation probability of $4d$ elements is of different nature: It turns out that ΔE_{lead} is equally large for $4d$ and $5d$ TMs, while comparing F_0 of the $4d$'s is strongly reduced by a factor of two relative to the $5d$'s due to relativistic effects.

Supplemental to the prediction whether chains form successfully or not, our model intrinsically contains detailed structural information of the chain formation process. As shown in FIG 2(e), traces of chain growth can be derived, including information on the critical interatomic distances where a chain pulls an additional atom out of the tip, where the remaining atoms relax to and where the wire breaks. This insight can be of utmost importance for the analysis of transport measurements or real-time TEM experiments.

Being computationally easily accessible, our model relies only on a few system specific quantities with transparent physical meaning giving detailed insight in the energetics of the complex chain formation process. Moreover, our model can be easily extended to wires containing impurities as e.g. AuO [3]. Thereby, it triggers the search for novel successfully forming chains of elements or compounds through the entire periodic table.

[1] Y. Mokrousov, G. Bihlmayer, S. Heinze, and S. Blügel, Phys. Rev. Lett. **96**, 147201 (2006).

[2] R. H. M. Smit, C. Untiedt, A. I. Yanson, and J. M. van Ruitenbeek, Phys. Rev. Lett. **87**, 266102 (2001).

[3] A. Thiess, Y. Mokrousov, S. Blügel, and S. Heinze, Nano Lett. **8**, 2144 (2008).

[4] Y. Mokrousov, G. Bihlmayer, and S. Blügel, Phys. Rev. B **72**, 045402 (2005).

173

Peapod synthesis on substrates

C. Meyer[1,2], C. Spudat[1,2], L. Houben[3,4], C. M. Schneider[1,2]

[1] IFF-9: Electronic Properties
[2] JARA Fundamentals of Future Information Technologies
[3] IFF-8: Microstructure Research
[4] ER-C: Ernst Ruska-Centre for Microscopy and Spectroscopy with Electrons

We present how carbon nanotubes can be grown and filled with fullerene molecules directly on a substrate. The resulting peapods are very clean and thus suitable for the fabrication of electronic devices. Since oxidation of the nanotubes is a crucial step during the peapod synthesis, we investigate the effects in more detail using high resolution transmission electron microscopy (HRTEM) and Raman spectroscopy. Two different oxidation methods, heating in air and acid treatment, are compared.

Carbon nanotubes (CNTs) filled with fullerene molecules, so-called "peapods", recently have generated a lot of interest as systems for electronic applications. The C_{60} fullerenes inside the tubes modulate the local density of states due to hybridization of the molecular orbitals with the conduction band and $Gd@C_{82}$ fullerenes inside a semiconducting tube can change the band gap. These effects allow one to build ambipolar CNT field effect transistors and to tune the gate-dependent conductance of single electron transistors. Filling with fullerenes can change mechanical properties of CNTs, e.g., softening the vibrational modes, which is interesting for the fabrication of nano-electro-mechanical devices.

For electronic applications it is desirable to use CNTs synthesized by chemical vapor deposition (CVD). This method yields CNTs which can be several micrometers long and grown on predefined sites on the substrate. Therefore, they do not cluster to ropes like CNTs dispersed on a substrate from solution. Carbon nanotubes grown with CVD have to be filled directly on the substrate in order to keep these advantages for the resulting peapods.

The carbon nanotubes grown by CVD are closed and have to be opened before they can be filled. This is usually done using oxidation either by heating in air or by acid treatment. For CNTs grown on substrate only the former method had been studied [1, 2]. We investigated the influence of both methods on the creation of defects [3]. By doing so, we gained information on how chemical reactions affect single tubes compared to powder samples.

The carbon nanotubes were grown with CVD directly on TEM substrates (DuraSiN™, Protochips Inc.). Oxidation by annealing in air was done at 450 °C for 20 min, oxidation by acid treatment was carried out in 5 molar HNO_3 at 100 °C for 3 h. The defects and filling of individual CNTs were studied with high-resolution transmission electron microscopy (HRTEM) using aberration correction.

After oxidation the tubes are filled with amorphous carbon (see Fig.1). Both methods damage the caps of the CNTs as well as the sidewalls. Annealing the tube in air seems to have the same effect for individual tubes as for "bulk" samples. The inner walls are opened along with the outer walls, as expected (Fig.1a). In contrast, the acid treatment has a stronger impact on single tubes than on tubes in powder samples. We could show that the tubes can be dissolved from inside (Fig.1b). Thus, the carbon residue inside the CNTs may consist of remnants from destroyed inner walls.
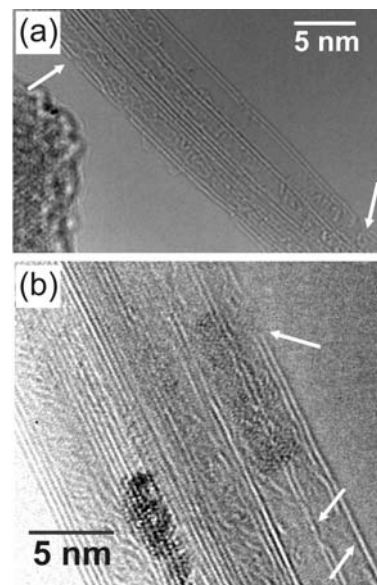
FIG. 1: Oxidation of CVD carbon nanotubes leads to amorphous carbon residue inside the tubes. Arrows indicate defects on the sidewalls. Atoms appear bright in this case due to the negative spherical aberration imaging used for optimized phase contrast. (a) Heating in air usually affects inner walls along with the outer walls. (b) Acid treatment can dissolve walls from inside-out (bottom arrows).

This residue inside the tube can be removed at least for CNTs oxidized by heating in air. High temperature annealing at 900 °C and with a pressure $p \leq 1 \cdot 10^{-6}$

mbar seems to remove the plug, since afterwards the nanotubes can be filled with fullerenes as shown in Fig.2. Filling was carried out under UHV conditions ($p \leq 1 \cdot 10^{-7}$ mbar). A thin film of C_{60} was evaporated onto the TEM substrate with the opened nanotubes. Afterwards the sample was held at $400°$C $\leq T \leq 450°$C for 24 h. During this step, the fullerenes are free to move along the nanotube walls until they can enter through a defect. Finally, the substrate was heated above $700°$C for 24 h in order to clean the sample from excess fullerenes. Indeed, we obtain very clean peapods after this procedure suitable for transport devices.

FIG. 2: *Peapods can be synthesized after an additional step for removing the plugs of amorphous carbon. Atoms appear dark in this case for the benefit of enhanced contrast.*

High resolution TEM imaging can cause defects on nanotubes as well as on fullerenes and even completely destroy them. Therefore it 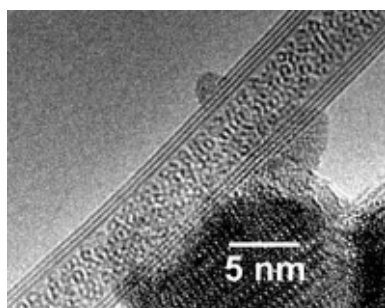is desirable to find a different method for characterization of the nanotube structure and chemical modifications, in particular the filling with fullerenes. Raman spectroscopy is a versatile tool to determine the effects of functionalization, for example creation of defects or changes in the electronic structure. In order to correlate the changes of Raman modes with particular defects, we use the complementary information about the atomic structure gained by HRTEM. As a first step towards detecting the degree of filling for a single CNT, we investigated the change of Raman modes during the oxidation process on "bulk" samples [4]. We focused on the shift of the D*-mode at a Raman shift of ~ 2600 cm^{-1}, which is an overtone of the defect mode D at ~ 1300 cm^{-1} and sensitive to changes of the electronic structure.

The D*-mode shows an up-shift for all methods investigated (Fig.3). However, we observed different behavior of the shift depending on the oxidation method. For heating in air, the shift of the D*-mode is strongest and about twice as large as the shift of the D-mode, as expected (Fig.3a). For the acid treated sample shown in Fig.3b, the D*-mode shows an up-shift of 5.3 cm^{-1} after 4 hours, while the D-mode shifts by 4.1 cm^{-1}. Thus, the shift of the D*-mode is smaller than expected from the shift of the D-mode and may be related to changes of the electronic structure. However, the origin remains unclear as treatment with HNO$_3$ causes p-doping of the CNTs, which should result in a shift to larger wave numbers [5]. During subsequent heating, the peaks shift further until they reach the limit $\Delta\omega^* \approx 2\Delta\omega$ (not shown here). This indicates that the effect of the acid treatment can be at least partially reversed.

Additional information was gained from the changes of the peak intensities. In case of thermal oxidation changes in the D/G ratio, usually used to characterize the purity of a sample, are rather caused by defects than by increase of amorphous carbon. In contrast, the increase of the D/G ratio could be traced back to the shielding effect, i.e. amorphous carbon around the tubes leads to a decrease in the intensity of the G-mode and the D*-mode.
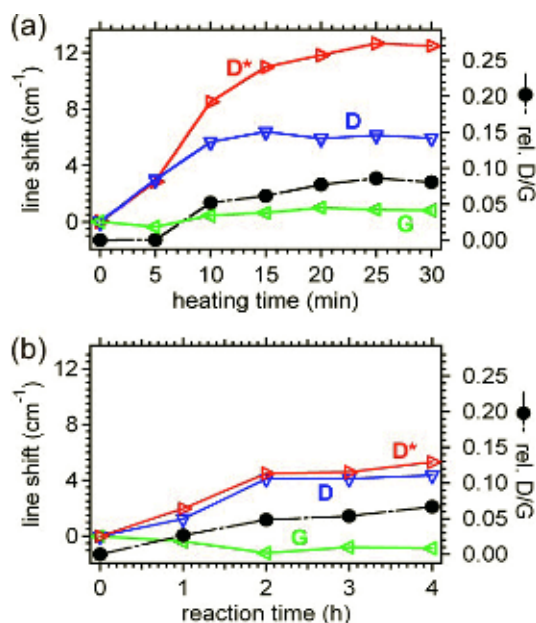
FIG. 3: *Relative shifts of the D-mode (blue), G mode (green), D* mode (red) and the D/G ratio (black) for heating in air (a) and for acid treatment (b).*

Our future plans are to investigate the influence of the other steps during the peapod synthesis on the Raman spectrum before comparing the results on bulk samples to confocal Raman measurements on individual carbon nanotubes.

[1] S. B. Chikkannanavar, D. E. Luzzi, S. Paulson, A. T. Johnson, Nano Lett. **5**, 151 (2005)

[2] Y. Ohno, Y. Kurokawa, S. Kishimoto, T. Mizutani et al., Appl. Phys. Lett. **86**, 023109 (2005)

[3] C Meyer, C Spudat, L. Houben, C. M. Schneider, Nanotechnology **20**, 065603 (2009)

[4] C. Spudat, C. Meyer, C. M. Schneider, Phys. Stat. Sol. b **245**, 2205 (2008)

[5] A. G. Souza Filho, A. Jorio, Ge. G. Samsonidze, G. Dresselhaus et al., Nanotechnol. **14**, 1130 (2003)

Liquid identification by Hilbert spectroscopy

Y. Divin, M. Lyatti, U. Poppe, K. Urban

IFF-8: Microstructure Research

Fast and reliable identification of liquids is of great importance in security, biology and beverage industry. An unambiguous identification of liquids could be made by electromagnetic measurements of their dielectric functions in the frequency range of their main dispersions, but this frequency range, from a few GHz to a few THz, were not covered by any conventional spectroscopy. We have developed a concept of liquid identification, based on our new Hilbert spectroscopy and high-T_c Josephson junctions, which can operate at the intermediate range from microwaves to terahertz frequencies. The first proof-of-principle measurements of reflection spectra from various bottled liquids in the range 10- 300 GHz have been demonstrated with total scanning time of 1 second.

After recent terrorist plots involving liquid explosives, it became clear that fast and reliable identification of bottled liquids is required. Among various discussed ways, the techniques using electromagnetic radiation are considered as having a great potential [1]. From the point of view of electromagnetic theory, the electric displacement-field response of any substance to a rapidly varying electrical field is defined by a complex dielectric permittivity function $\varepsilon(f)$, which is determined by the internal dynamics of the molecules [2]. Therefore, liquid can be identified by measuring its dielectric function $\varepsilon(f)$ over a wide spectral range, where the liquids of concern have specific dispersions, and comparing it with reference data. However, this frequency range, from a few GHz to a few THz, cannot be covered by any single conventional spectroscopy.

From the low-frequency side, the dielectric properties of liquids are studied by reflection, transmission and resonator microwave techniques at fixed frequencies [3]. However, due to non-monotonous behaviour of the permittivity of two-component liquid mixtures with increase of the concentration of one component, the measurement of the dielectric function at fixed frequency cannot distinguish unambiguously between some solutions and the liquids of concern. From the high-frequency side, the dielectric functions are studied using far-infrared Fourier and terahertz time-domain spectroscopies. But time-domain and more conventional Fourier spectroscopies involve extended measurement times, since a mechanically-driven variable optical time-delay or beam path lines 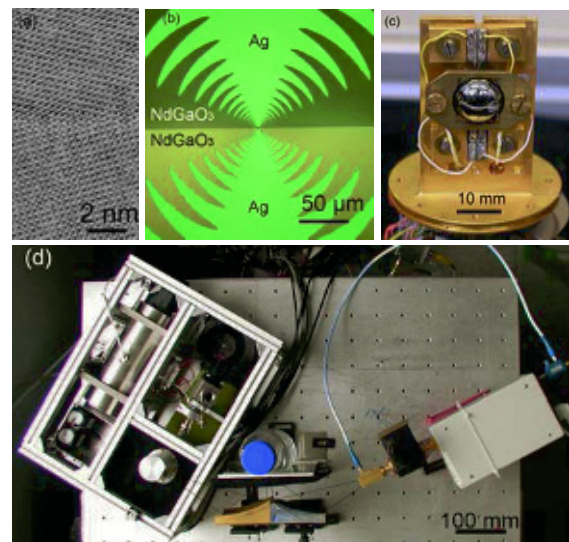are used in both techniques. Recently, we have attracted attention to a great potential of high-T_c Josephson technology in security applications and presented a concept of fast and liquid identification based on our broadband Hilbert spectroscopy [4, 5]. Here, we present first proof-of-principle experiments.

FIG. 1: HREM of a $YBa_2Cu_3O_{7-x}$ bicrystal Josephson junction (a), the junction with a logperiodic antenna (b), a junction holder with a Si lens (c), experimental set-up with a Hilbert spectrometer in a Stirling cryocooler (d).

Low-resistance [001]-tilt $YBaCu_3O_{7-x}$ bicrystal Josephson junctions were optimized for application in Hilbert spectroscopy [4]. A high-resolution microscopy (HREM) image of a plane-view of one of our junctions is shown in Fig. 1a. A light-microscope photo of the junction, developed for Hilbert spectroscopy, is presented in Fig. 1b. The Ag log-periodic antenna is integrated with a 2μm-wide $YBaCu_3O_{7-x}$ bridge crossing the $NdGaO_3$ bicrystal substrate boundary. A junction holder with an integrated focusing Si lens is shown in Fig. 1c. An experimental set-up is presented in Fig. 1d. The holder with the junction is mounted into a cryogen-free electrically-driven Stirling cooler, shown on the left side of Fig. 1d. Biasing and amplifying room-

temperature electronics for the Josephson junction is integrated in the same block with the Stirling cooler. The Hilbert spectrometer with the Josephson detector in the Stirling cooler at 80K was operated in a voltage bias mode.

A frequency multiplier can be found on the right side of Fig. 1d. The output of the multiplier, depending on the frequency f_0 of microwave pump, consists of radiation with a nominal frequency of $6f_0$ plus several high-order harmonics, unspecified by the manufacturer. It was possible starting from the pump frequencies in the range of 12.5-18 GHz to detect the harmonic content at the output of the multiplier up to 300 GHz with Hilbert spectroscopy [4, 5]. Additionally, low-intensity radiation with the pump frequency f_0 through a directional coupler was also fed into the output horn of the multiplier. The main frequency component at $6f_0$ was selectively suppressed to the power level of around 10^{-7} W by a polarization attenuator. The polychromatic radiation from the multiplier was focused by an elliptical mirror on the bottle with the liquid, and the radiation, reflected from the bottle, was focused on the Josephson detector inside Hilbert spectrometer with the help of a second elliptical mirror. The output of the microwave oscillator, pumping the multiplier, was modulated by a PIN switch with a modulation frequency of 50 kHz. The junction voltage V was scanned linearly in time with total scanning time of 1 second. The voltage dependences of the response $\Delta I(V)$ and current $I(V)$ were detected, amplified, shown on the oscilloscope, digitized by a PCMCIA acquisition card, stored and processed in a PC notebook according to the algorithm of Hilbert spectroscopy [4].

reflection spectra were modified in a way, which is specific for each liquid in the bottle. The PET plastic bottles are transparent in the frequency range below 0.5 THz, and their contribution to the reflection was small. The measured spectra in Fig. 2 are in a qualitative agreement with the dielectric functions of liquids under study. Water is known to possess a high value of static dielectric constant $\varepsilon_0 \cong 80$ and relaxation time τ=8.3 ps, i.e. the reflectance should be high in the frequency range under study, and it follows from Fig. 2 (blue curve). Ethanol has $\varepsilon_0 \cong 20$ and τ=163 ps and thus it has low values of reflectance at the spectral range above 10 GHz (green curve). The static value of $\varepsilon_0 \cong 20$ for acetone is close to that of ethanol but relaxation time τ=3.3 ps for acetone is even lower than that of for water. So, the reflection spectra of acetone should be between those of for water and ethanol, as one see from Fig. 2 (red curve).

The difference in the reflection coefficients for three liquids was demonstrated at several frequencies between 10 and 300 GHz. It is more reliable to identify liquids starting from multifrequency, spectral measurements rather than from a single low-frequency measurement. It is clear that more work should be done with radiation sources to increase their spectral range and the efficiency of radiation coupling to liquids.

In future we shall spread the frequency range of reflection measurements to the gigahertz range as low as 5 GHz and to the terahertz range as high as 1 THz to increase the accuracy of liquid identification. Also, the scanning time will be decreased to values around 100 milliseconds.

[1] Existing and Potential Standoff Explosives Detection Techniques, Nat. Academies Press, Washington, D.C., 2004.

[2] L.D. Landau, E.M. Lifshitz, Electrodynamics of continuos media, Oxford: Pergamon Press, 1963.

[3] U. Kaatze, Y. Feldman. "Broadband dielectric spectrometry of liquids and biosystems." Meas. Sci. Technol., vol. 17, pp. R17-R35 (2006)

[4] Y. Divin, U. Poppe, V. N. Gubankov, K. Urban, "High-T_c Josephson Square-Law Detectors and Hilbert Spectroscopy for Security Applications," IEEE Sensors J., vol. 8, pp.750-757, 2008 (invited).

[5] Y. Divin, U. Poppe, K. Urban. "Hilbert spectroscopy of liquids for security screening." in Detection of Liquid Explosives and Flammable Agents in Connection with Terrorist Actions (NATO Science for Peace and Security Series B: Ed. H. Schubert, A. Kuznetsov, Springer, 2008), pp.189-204.

FIG. 2: *Reflection spectra, measured by a Hilbert spectrometer, when a metal plate was installed at the place of a bottle (black), or a plastic bottle with water (blue), acetone (red) or ethanol (green) was placed in the set-up. A harmonic multiplier with a horn, operating at pump frequency of 15 GHz, was used as radiation source*

The calibration of the reflectance in the set-up was carried out with an Al plate, installed on the place of a bottle. The corresponding spectrum is shown in Fig. 2 (black curve). The spectrum of the multiplier in this case consisted of three main lines at 15, 90 and 150 GHz. When the metal plate was replaced by a bottle with ethanol, acetone or water, the measured

Epitaxial thick film SQUIDs with large voltage swing at 77 K

M. I. Faley[1], S. B. Mi[1], C. L. Jia[1], U. Poppe[1], K. Urban[1], R. L. Fagaly[2]

[1] IFF-8: Microstructure Research
[2] Quasar Federal Systems, San Diego, CA 92121 USA

Low-noise operation of superconducting quantum interference devices (SQUIDs) in magnetic fields and strong pinning of vortices in the superconducting electrodes and in the flux transformer were achieved by implementation of thick (>1μm) YBa$_2$Cu$_3$O$_{7-x}$ (YBCO) films on the SrTiO$_3$/BaZrO$_3$-bilayer buffered MgO substrates. Further improvement of the unshielded operation of SQUIDs was achieved by optimization of SQUID inductance. This has allowed fabricating the flip-chip dc-SQUID magnetometers with a voltage swing up to 100μV and a field resolution 30fT/$\sqrt{}$Hz limited by the Nyquist noise in the resonance-damping resistance of the 8mm flux transformer at 77K[1].

Magnetometers based on superconducting quantum interference devices (SQUIDs) are the most sensitive sensors for measurements of magnetic field components and they are used for many applications like, e.g., biomagnetic or geomagnetic measurements [2]. The lowest achieved white noise for the high-T$_c$ dc-SQUIDs operating at 77 K is 3.5 fT/$\sqrt{}$Hz [3]. The goal now is to perform the low noise measurements with the high-T$_c$ SQUIDs without magnetic shielding which could significantly reduce costs and broaden the field of SQUID applications. In the case of unshielded operation, the SQUIDs are exposed to the Earth's magnetic field, where the detected field component can change during SQUID movements from -50μT to +50μT, and line-frequency electromagnetic fields. The latter vary from $\approx$ 10 nT up to several μT in peak-to-peak swing under laboratory conditions at different locations in the building. Such conditions impose strong requirements on the dynamic range and the slew rate of the sensitive high-T$_c$ dc-SQUID systems. In addition to a perforated or slotted layout of the SQUID washer, the pinning of Abrikosov vortices in the superconducting films of the SQUID body should be improved to reduce low-frequency noise of the SQUIDs in magnetic fields. The SQUID voltage swing should be also enhanced for a larger slew rate and frequency bandwidth of the measurement system. In the present paper we describe high-T$_c$ flip-chip dc-SQUID magnetometers optimized for the sensitive measurements without magnetic shielding in the Earth's magnetic field.

Thick (>1μm) YBCO films on buffered MgO substrates [4] were used for the preparation SQUIDs with ramp-type or bicrystal Josephson junctions and multilayer flux transformers. A photograph and noise spectra of a dc SQUID with ramp-type Josephson junctions are shown in Fig. 1 (a) and (b), respectively. The low-frequency noise increased first at magnetic fields above 300 μT. In the case of the SQUIDs with standard 100 nm thick electrodes this takes place already at a magnetic field of $\approx$ 100 μT.

a)

b)
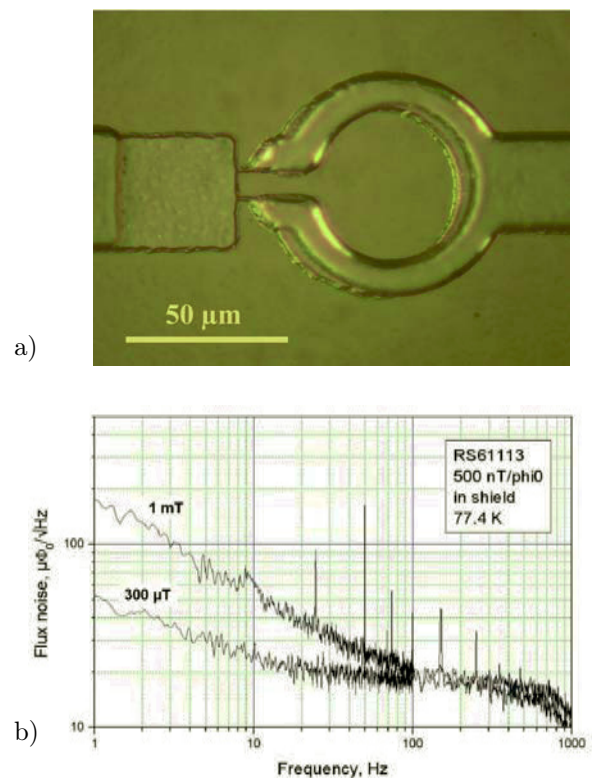
FIG. 1: (a) Photograph of the first 3 μm thick SQUID with ramp-type Josephson junctions. (b) Noise spectra in magnetic fields for the 3 μm thick SQUID with ramp-type Josephson junctions measured at 77 K.

Bicrystal grain boundary (GB) Josephson junctions with the required critical current have a fixed cross-section determined by the misorientation angle, but the wide electrodes of the junctions can be made much thicker (see Fig. 2). The thick superconducting electrodes should reduce the demagnetizing coefficient of the wider parts of the SQUID body and
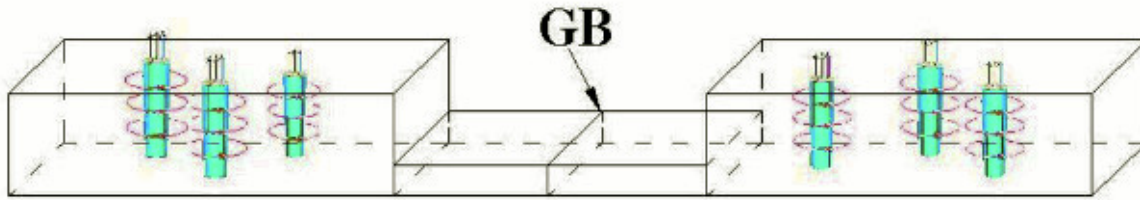
FIG. 2: A schematic of the grain boundary (GB) Josephson junction with the variable thickness thick film superconducting electrodes. The Abrikosov vortices (blue) can be effectively pinned in the thick electrodes.

provide a better pinning of the Abrikosov vortices to reduce the low-frequency noise of the SQUIDs in the magnetic field. We integrated such "variable thickness" GB junctions in the flip-chip dc-SQUID magnetometers and gradiometers with multilayer flux transformers. Thus the thick SQUID washer has much better withstood the changes of the magnetic field amplified by the flux transformer.

An additional optimization of the SQUID inductance has resulted in a doubling of the SQUID voltage swing with a simultaneous reduction of the flux noise. For the HTM-8 type magnetometers [5] an estimated SQUID inductance $L_S \approx 80$ pH, typical SQUID voltage swing $V_{pp} \approx 30$ μV, a spectral density of the flux noise, and a field sensitivity $B_N \approx 15$ fT/$\sqrt{}$Hz at 77 K were achieved. We have observed that a reduction of the SQUID inductance down to $L_s \approx 45$ pH for the new, so called, HTM-8x type magnetometers increased the voltage swing up to $V_{pp} \approx 100$ μV, reduced flux noise but increased the field noise up to $B_N \approx 30$ fT/$\sqrt{}$Hz at 77 K. The estimated SQUID inductance of the HTM-8x type magnetometers was $L_S \approx 50$ pH, consisting of ≈ 40 pH of geometrical inductance and ≈ 10pH kinetic inductance. The kinetic inductance was reduced down to ≈ 3 pH by the increased thickness of the YBCO film in the SQUID washer. This was observed by an increase of the voltage swing for the magnetometers with similar layouts but with different thickness of the YBCO film in the dc-SQUID washer. The energy sensitivity of the HTM-8x sensors is $\approx 3 \times 10^{-30}$ J/Hz at 77 K. The dc-SQUID sensors were operated in an unshielded environment without suppression of either the bias current or the SQUID voltage swing. The white noise of the sensors in unshielded environment was not changed either.

The frequency bandwidth and slew rate are important for the operation of unshielded SQUID systems. Both of them are inversely proportional to the system flux noise which, in turn, is proportional to the square of SQUID inductance:

$$S_\Phi \approx \left(\frac{4k_B T R_D^2}{R_n} \right) \left[1 + \frac{1}{2} \left(\frac{I_0}{I} \right)^2 \right] \left(\frac{R_n}{L_S} \right)^{-2} \propto \frac{L_S^2}{R_n}$$

A slew rate of ≈ 5 MΦ_0/s was demonstrated for the HTM-8 magnetometers with direct readout SQUID electronics. For the new HTM-8x type magnetometers with the SQUID inductance $L_s \approx 50$ pH the expected slew rate is ≈ 10 MΦ_0/s, which is a typical

slew rate of the systems with the low-T_c SQUID magnetometers that have a similar voltage swing.

The field resolution of the inductively coupled magnetometers should improve with reduction of L_s as long as there is no significant degradation of the coupling coefficient "k":

$$B_N = \frac{L_P + L_i}{kA\sqrt{L_i L_S}} S_\Phi^{1/2} \propto \frac{1}{k} \sqrt{\frac{L_S}{R_n}}$$

where for the HTM-8x-type flip-chip high-T_c dc-SQUID magnetometers the inductance of the pick-up loop $L_p \approx 40$ nH is equal to the inductance of the input coil L_i and the area of the pick-up loop $A \approx 64$ mm^2. It was observed that the Nyquist noise in the resonance-damping resistance of the multilayer flux transformer limits the field resolution of the sensors at 77 K.

Thanks to the epitaxial multilayer buffering technology [4] the resolution of the dc-SQUID sensors can be further improved by implementation of larger pick-up loops, prepared on, e.g., up to 10 cm x 10 cm large single crystal MgO substrates, which are available now.

[1] M.I.Faley, S.B.Mi, C.L.Jia, U.Poppe, K.Urban, and R.L.Fagaly, Journal of Physics: Conference Series, **97**, 012164 (2008)

[2] R.L.Fagaly, Rev. Sci. Instr., **77**, 101101 (2006).

[3] M.I.Faley, C.L.Jia, U.Poppe, L.Houben, and K.Urban Superc. Sci. Technol., **19**, S195 (2006)

[4] M.I.Faley, S.B.Mi, A.Petraru, Jia C L, Poppe U, and K.Urban, Appl. Phys. Lett., **89**, 082507 (2006)

[5] M.I.Faley, U.Poppe, K.Urban, D.N.Paulson, T.Starr and R.L.Fagaly, IEEE Trans. on Appl. Supercond., **11**, 1383-1386 (2001)

Separation of bulk and interface contributions to the electroforming of epitaxial Fe-doped SrTiO$_3$ thin films

T. Menke, P. Meuffels, R. Dittmann, K. Szot, R. Waser

IFF-6: Electronic Materials

By means of impedance spectroscopy we separate the bulk and interface contributions to the electroforming behavior of Pt/STO(Fe)/Nb:STO devices. It was possible to assign two distinctive features observed in the impedance spectra to the STO(Fe)-bulk and to the depletion layer of the Pt/STO(Fe) Schottky contact. We attribute the resistance change during the DC forming process to a local bypassing of the depletion layer caused by oxygen effusion to the environment.

Among the ternary transition metal oxides, SrTiO$_3$ plays a key role as a prototype material for further elucidation of the microscopic resistive switching mechanism [1]. To enable the resistive switching properties in this band-gap insulator, generally a forming procedure is needed. By applying either thermal or electrical stress, the conductivity can be drastically increased due to self-doping induced by the formation of oxygen vacancies. The location of the forming and the switching phenomena within metal/insulator/metal (MIM)-structures has been investigated by using lateral electrode configurations. To close the link between capacitive and lateral MIM-structures and get a deeper understanding of the forming mechanisms, we studied the electrical properties in capacitor-like structures of epitaxial grown Fe-doped SrTiO$_3$ (STO(Fe)) thin films by impedance spectroscopy.

The fabrication process of the Pt/STO(1at%Fe)/Nb:STO devices and the measurement equipment used for the electrical characterization can be extracted from [2].

The I-V curves of pristine samples showed rectifying characteristics which we could assign to the Schottky contact formed at the interface between the high work function metal Pt (ϕ: 5.65eV) and the STO(Fe) film which exhibits significant n-type conductivity.

We measured the impedance spectra of a 750nm thick STO(Fe) sample in the pristine, unformed state. The corresponding Cole-Cole plot and the equivalent circuit which is proposed to fit the data are shown in Fig. 1 and in inset i), respectively. The series inductance of the signal leads as well as the series resistance of the Nb:STO bottom electrode were taken into account for fitting the equivalent circuit. The impedance spectra of the STO(Fe) film can be perfectly described by two Voigt elements resulting from the bulk and the Schottky depletion layer properties.
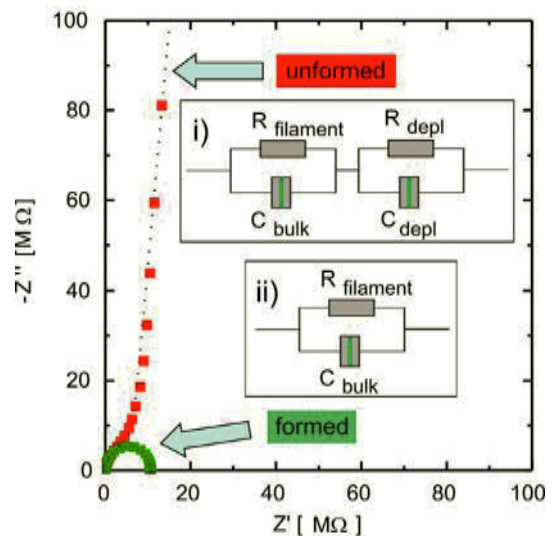
FIG. 1: *Impedance spectra of a Pt/STO(Fe)/Nb:STO MIM-structure before and after a DC-forming process. The equivalent circuits used for fitting are displayed in the inset for (i) the unformed case with $R_{filament}$=7.3MΩ, C_{bulk}=277pF, R_{depl}=17.9GΩ and C_{depl}=914pF and for (ii) the formed case with $R_{filament}$=10.7MΩ and C_{bulk}=273pF.*

By means of atomic force microscopy equipped with a conducting tip the filamentary conduction of our STO(Fe) thin films could be proved. Thus, the bulk related contribution to the impedance of the thick films has to be described by conducting filaments in a more or less insulating matrix (1/R = 1/R$_{matrix}$+ 1/R$_{filament}$ $\sim$ 1/R$_{filament}$).

To attribute the Voigt elements to their physical origin, DC-bias dependent impedance measurements were performed. It is well known that the bulk impedance should only be slightly influenced by an applied DC bias, whereas the depletion layer impedance should clearly vary with an applied DC bias. This was indeed found for our samples. Additionally, the film thickness dependence of both elements showed a scaling of the bulk capacitance and a thickness independence of the depletion layer capacitance so that the two Voigt elements could be clearly allocated. This analysis implies that the overall resistance is dominated by the depletion layer resulting from the Schottky contact at the Pt/STO(Fe) interface.

Unlike to samples with a low initial resistance which do not need any forming treatment the investigated devices with Pt electrodes require an electroforming step setting the sample to the low resistance state (LRS). For this purpose, a DC voltage of +10V was applied to the Pt electrode, corresponding to the forward direction of the Schottky contact. The resulting current-time (I-t) curve is shown in Fig.2. During the first 25s, the current remains in the sub-nA regime and increases only slightly and continuously with time. After this initial time period, spike-like current fluctuations appear. We contribute this resistance fluctuation to the competing reduction and re-oxidation of filament fragments within one or more filaments.
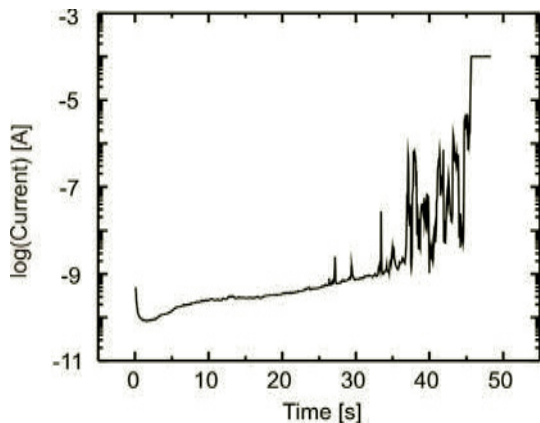

FIG. 2: I-t curve during electroforming recorded by applying +10V to the Pt top electrode.

After 45s, a steep increase of the current occurs and the current compliance, which was set to $100\mu A$ to prevent the sample from electrical breakdown, is attained. As soon as the current reached the compliance, we stopped the forming process because, according to our experience, at this stage bipolar switching can be observed. The result of the impedance measurements on the formed pad can be seen in Fig.1 and can be described using the equivalent circuit displayed in inset ii). The most significant change is that in the case of a formed sample only one Voigt element is needed to fit the data. As the values for the resistance and the capacitance are comparable to the values obtained for the bulk related Voigt element in the unformed state, we attribute the Voigt element in the formed state to bulk contribution.

In order to understand our experimental observations, we have to consider that electroforming removes oxygen ions from the STO lattice which becomes evident due to the appearance of gas bubbles under the anode [1]. By applying a positive bias to the top electrode oxygen ions migrate along extended defects towards the top interface and are released to the surrounding. In contrast to STO single crystals, where a virtual cathode moves towards the anode until a conductive path is established during the forming procedure, our as-deposited thin films already contain preformed conducting paths as a result of the reducing deposition conditions.
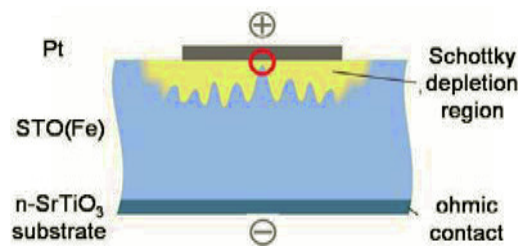
FIG. 3: Model of the electroforming process and the local bypassing of the Schottky depletion layer.

Since the overall resistance in the unformed case is dominated by the depletion layer, most of the applied voltage drops in the vicinity of the top interface. Taking into account that the movement of oxygen ions is a field-driven process, we conclude that the electroforming process most likely removes oxygen directly next to the top interface where the electrical field is strongly enhanced. Due to the donor character of oxygen vacancies a significant reduction of the effective Schottky barrier height and the depletion layer width at the Pt/STO(Fe) interface can be expected. This is in agreement with the voltage-induced elimination of the Schottky barrier observed at the interface between Pt and TiO_2 single crystals [3].

In order to clarify whether electroforming is a local or a homogenous effect, an additional experiment was performed. After a successful electroforming step at a certain MIM device, the electrode pad was divided into two parts and each part of the device was measured again. Whereas one part showed the reduced resistance which was measured before on the whole electroformed device, the other part was in the initial high-ohmic state. This experiment clearly points to the local nature of the electroforming process. This localized bypassing of the Schottky depletion layer explains the vanishing of the complete contribution of the depletion layer to the impedance and also that the bulk properties are not significantly changed during the forming procedure.

In conclusion, we presented that the impedance spectra of pristine Pt/STO(Fe)/Nb:STO structures exhibits a bulk and a depletion layer related contribution. A DC forming process removes oxygen along extended defects in the vicinity of the Pt/STO(Fe) interface thus bypassing the Schottky depletion layer.

[1] K. Szot et al., Nature Materials 5, 312-20 (2006)

[2] T. Menke et al., Journal of Applied Physics 105, 7 (2009)

[3] J. R. Jameson et al., Appl. Phys. Lett. 91,112101 (2007)

Liquid injection ALD of ferroelectric oxide and noble metal thin films

S. Hoffmann-Eifert[1], S. K. Kim[1], T. Watanabe[1,3], R. Waser[1,2]

[1] IFF-6: Electronic Materials
[2] Institute of Electronic Materials II, RWTH Aachen University
[3] left to Canon research laboratories, Tokyo, Japan

Atomic layer deposition (ALD) is the industrial state-of-the-art technique for conformal growth of extremely thin films ($<$ 10 nm) onto severe three dimensional structures like e.g. trench and stack cells or tube structures. Two different processes have been developed: 1) a multi component Liquid Injection (LI) ALD process for growth of complex ferroelectric $Pb(Ti_{1-x}Zr_x)O_3$ films and 2) a new LI-ALD process for deposition of metallic Ru films as electrodes.

As two-dimensional miniaturizations of microelectronic devices are now being pursued, the device structures have been stretched perpendicularly to the wafer surface to further shrink the footprint area. In addition, new materials like high-k oxides and metals are introduced into silicon-based devices to decrease their size and power consumption and to increase their performance. An interesting complex oxide is the ferroelectric PZT material which has been considered for non-volatile FeRAM applications due to its remnant polarization. Ru metal is an interesting electrode material because it has a high work function, a low resistivity, it is easily dry etched, and the corresponding oxide RuO_2 is also a conducting material. To achieve highest performance in the integrated MIM capacitor structures the thin films have to be homogeneous in thickness and in composition across the entire 3D structure. Hence, a film growth technique that can uniformly deposit a multi component material on a 3D structure with a width of less than 100 nm and a height of up to $\sim \mu$m must be adopted.
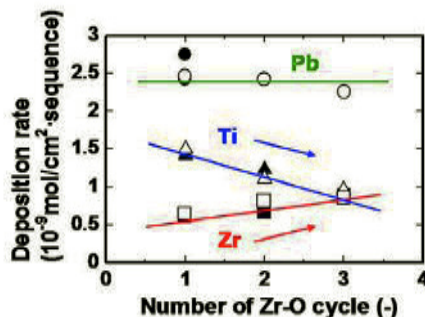
FIG. 1: Deposition rates as a function of the repetition numbers of the Zr-O cycle in one (Pb-O)-n(Zr-O)-(Ti-O) ALD sequence.
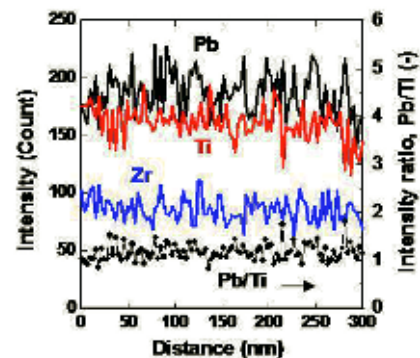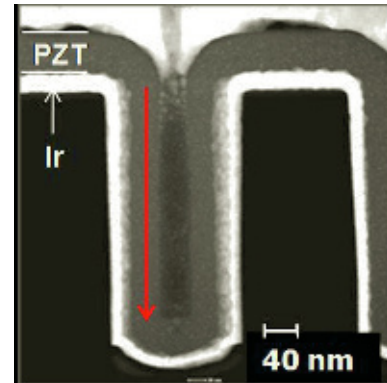
FIG. 2: LI-ALD $Pb(Zr,Ti)O_3$ thin film conformally grown on an Ir covered Si hole structure with a diameter of 180 nm. Homogeneity of films' thickness and composition is proofed by cross section TEM and EDS line scans.

We modified the standard ALD process for use of liquid precursor sources. Pulses of the liquid precursor are sprayed into a vaporizer and fed to the reactor. By this technique the thermal budget for the precursor is kept low and even chemicals with low vapor pressure can be used. LI-ALD of multicomponent PZT films was studied in a combination of three ALD processes of the binary oxides using $Pb(C_{11}H_{19}O_2)_2$, $Ti(OCH(CH_3)_2)_4$, and $Zr(C_9H_{15}O_2)_4$ dissolved in ethylcyclohexane (ECH), and water as oxidant. By control of the process the Zr/(Zr+Ti) ratio in the PZT films can be changed, while the Pb/(Zr+Ti) ratio conveniently remained at the stoichiometric value (Fig.1). This process window was attributed to the limited chemisorption sites on the growing Pb-O surface for the $Zr(DIBM)_4$ and

Ti(Oi-Pr)$_4$ molecules. After crystallization annealing, a clear hysteresis loop was observed for a 70 nm thick PZT film. PZT films were deposited on pinhole structures with a diameter of 0.18 μm and depth of 0.30 μm to assess the feasibility of ALD as a tool for covering 3D structures uniformly. In Fig. 2 it is shown that the as-deposited amorphous PZT films had conformal cation composition over the 3D structure. Even after crystallization annealing, the cation composition was still uniform over the structure. By this we could demonstrate why the multi-precursor ALD process is to be seen as a promising approach for uniformly coating 3D nanostructures with complex oxide materials.

Noble metal Ru thin films were deposited at growth temperatures of 330 and 380 ˚C by LI-ALD using Ru(C$_{11}$H$_{19}$O$_2$)$_3$ dissolved in ECH and oxygen as reactants. The film thickness clearly saturates with increasing injected volume of Ru solution. Very pure Ru thin films with an oxygen content < 1 at % were grown by LI-ALD [3] in contrast to films obtained from the standard bubbler-type ALD process which contained about 5.5 at% O [2].
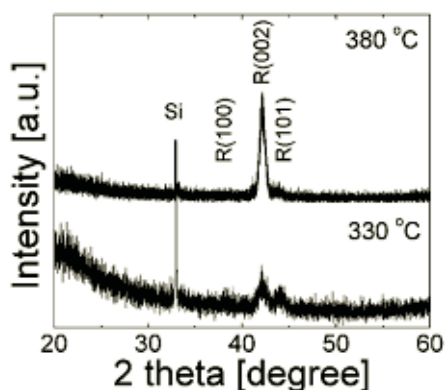
FIG. 3: θ-2θ XRD spectra of Ru films grown at 330 (12 nm) and 380 ˚C (7 nm) under a high O$_2$ flow rate (500 sccm) at an O$_2$ feeding time of 2 s. [3]

Figure 3 shows that a preferred (002) orientation is dominant for Ru films grown at 380 $^{\circ}$C.
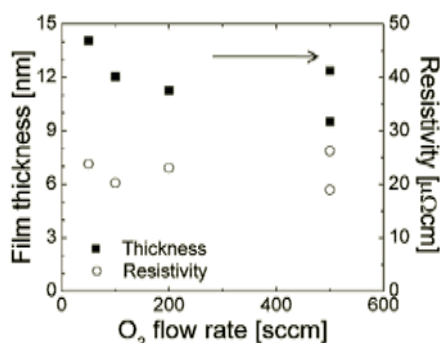
FIG. 4: Variations in thickness and resistivity of the films grown at 380 ˚C as a function of O$_2$ flow rate at an O$_2$ feeding time of 2 s.

LI-ALD noble metal Ru films with a thickness of about 10 nm showed a reasonable resistivity of ~ 20 $\mu\Omega$cm (Fig. 4). On contrary to standard ALD, the variation in the concentration of the Ru solution in this LI-ALD Ru process resulted in a different growth rate although the saturation behavior towards the number of injections of Ru solution was confirmed.
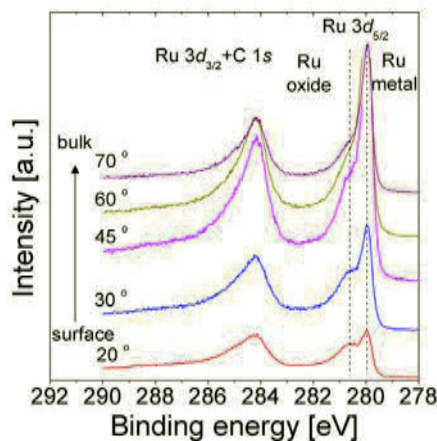
FIG. 5: Angle-resolved Ru 3d XPS spectra of LI-ALD grown Ru thin film sowing that RuO$_2$ is only existing in the top surface layer due to ex-situ oxidation in atmosphere.

This phenomenon which is unique for the LI-ALD Ru process is consistently explained by a reduction of adsorbed oxygen atoms by ECH during feeding of the Ru solution. The adsorbed oxygen atoms are removed from the subsurface because the equilibrium oxygen partial pressure for oxidation of noble metals such as Ru is relatively high (see Fig. 5). Therefore, LI-ALD is effective in reducing the content of the corresponding oxides in noble metal films irrespective of the type of precursor.

[1] T. Watanabe, S. Hoffmann-Eifert, C. S. Hwang, R. Waser, *J. Electrochem. Soc.* **155 (11)**,D715-722 (2008).

[2] T. Aaltonen, M. Ritala, K. Arstila, J. Keinonen, M. Leskelä, *Chem. Vap. Dep.,* **10**, 215 - 219 (2004).

[3] S. K. Kim, S. Hoffmann-Eifert, R. Waser, *J. Phys. Chem. C,* submitted.

183

Atomic-scale study of domain walls in ferroelectric $PbZr_{0.2}Ti_{0.8}O_3$ films

C. L. Jia[1,2], S. B. Mi[1,2], K. Urban[1,2], I. Vrejoiu[3], M. Alexe[3], D. Hesse[3]

[1] IFF-8: Microstructure Research
[2] ER-C: Ernst Ruska-Centre for Microscopy and Spectroscopy with Electrons
[3] Max Planck Institute of Microstructure Physics, Weinberg 2, D-06120 Halle, Germany

Using the negative spherical-aberration imaging technique in an aberration-corrected high-resolution transmission electron microscope we investigate the cation-oxygen dipoles near 180˚ domain walls in epitaxial $PbZr_{0.2}Ti_{0.8}O_3$ thin films on the atomic scale. The width and dipole distortion across a transversal wall and a longitudinal wall are measured, and on this basis the local polarization is calculated. For the first time, a large difference in atomic details between charged and uncharged domain walls is reported [1].

Ferroelectric thin films find potential applications in electronic and electro-optical devices including, e.g., non-volatile and high-density memories, thin-film capacitors, and piezoelectric and pyroelectric devices. The performance of such devices depends strongly on the magnitude and stability of the switchable ferroelectric polarization of the ferroelectric layer. Polarization switching is realized by nucleation and growth of polarization domains under an external electrical field. The properties of the domain walls, in particular their structure, width and mobility, are important parameters.

Recently it has been shown that atomic resolution including oxygen can be achieved by a novel technique called negative spherical-aberration (C_S) imaging (NCSI) in a C_S-corrected transmission electron microscope [2]. Using this technique we investigate the atomic details and dipole distortion on an atomic scale near 180° domain walls in thin epitactic films of $PbZr_{0.2}Ti_{0.8}O_3$ sandwiched between two $SrTiO_3$ layers and prepared by pulsed laser deposition [3].

Figure 1a shows a 10 nm thick $PbZr_{0.2}Ti_{0.8}O_3$ layer between the two $SrTiO_3$ layers. The viewing direction is along a crystallographic [-110] direction. The interfaces are marked by two horizontal arrows. The two insets show magnifications overlying the respective areas in the upper left, domain I, and the lower right side of the figure, domain II. As illustrated by the schematic in Figs. 1b and 1c, the atom arrangement exhibits shifts of the atoms with respect to the cubic perovskite structure. In domain I (left inset) the Zr/Ti atom columns are shifted upward (along the [001] direction) towards the upper PbO positions and away from the respective lower ones. The oxygen atoms are also shifted upward but more strongly and thus are no longer co-linear with the Zr/Ti atoms. The

atom arrangement leads to a separation of the centre of the anionic negative charge of oxygen from that of the cationic positive charge of the metal cations. The corresponding charge dipoles define the direction of the vector of spontaneous polarization $\boldsymbol{P}_S$ parallel to [00-1]. The atom shifts in domain II (right inset) are in the opposite direction compared to those in domain I. In fact, Fig. 1a contains two polarization domains where, upon changing from one domain to the other, the polarization vector changes by 180°. The position of the respective 180° domain wall is indicated by a dotted line.

The horizontal part of domain wall is a segment of longitudinal domain wall (LDW). Across the wall the polarisation vectors are meeting head-to-head. As a result, the electric fields do not cancel and the wall is charged. The oblique parts of the wall are made up of LDW segments and segments of transversal domain wall (TDW). The TDW is uncharged since the electric fields characterised by the polarisation vectors of the adjoining boundary segments just cancel each other. Since we have genuine atomic resolution we have access to each individual atomic position. This allows to make individual measurements of the atomic shifts. The atomic separations were measured fitting two-dimensional Gaussians to the atomic intensity maxima [4]. The Gaussian regression analysis indicates a precision of better than $\pm$ 5 pm (for a 95 % confidence level). According to our measurement the width of the TDW is found to be of the order of one unit cell. This is in excellent agreement with first-principles total energy calculations indicating an abrupt change of polarization direction across the wall.

Figure 2 shows for a longitudinal domain wall the measurement results. In Figure 2(a) blue squares denote measurements of the c-axis lattice parameter carried out on PbO atomic positions. Red squares denote measurements on Zr/Ti positions. The minimum value of c occurs in the domain wall centre with an accompanying increase of the a-axis lattice parameter. With increasing distance from the central area, c increases and results in a maximum tetragonality value of c/a = 1.059 in domain I and 1.072 in domain II. In the central area of 4 to 5 unit cells in width, the value of c/a is about 1.005.

Figure 2 (b) depicts the values of the vertical displacements $\delta_{Zr/Ti}$ and δ_O as a function of the ver-
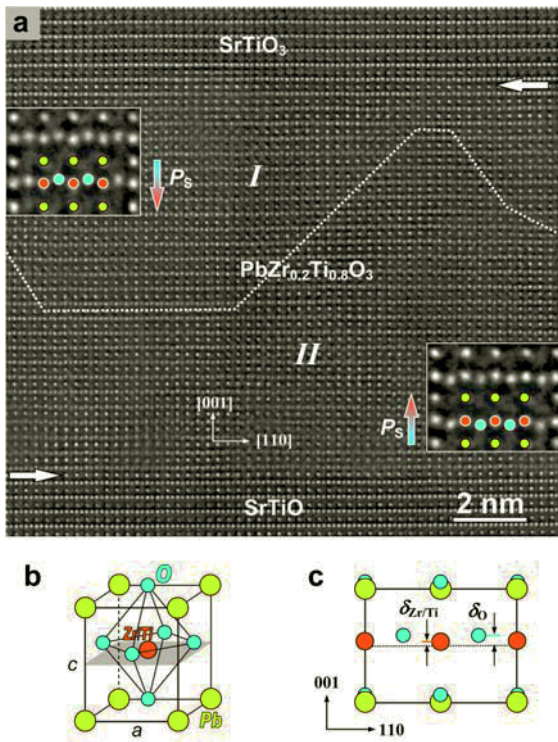
FIG. 1: (a) Image of a $SrTiO_3/PbZr_{0.2}Ti_{0.8}O_3/SrTiO_3$ thin-film heterostructure. The atom columns appear bright on a dark background. The dotted line traces the 180° domain wall. The arrows denoted by "P_S" show the directions of the polarization in the 180° domains. Insets display magnifications of the dipoles formed by the displacements of ions in the unit cells (yellow: PbO, red: Zr/Ti, blue: O). (b) Schematic perspective view of the unit cell. (c) Projection of the unit cell along the [-110] direction. $\delta_{Zr/Ti}$ and δ_O denote the shifts of the Zr/Ti atoms and the oxygen atoms, respectively, from the centrosymmetric positions.

in the wall should be too high to allow its formation.

FIG. 2: (a) c-axis lattice parameter. Blue squares and red squares show the values measured from Pb to Pb atom positions and from Zr/Ti to Zr/Ti, respectively. (b) The displacements of the Zr/Ti atoms ($\delta_{Zr/Ti}$) and the O atoms (δ_O) across the LDW. Positive values denote upward shifts and negative values downward shifts. (c) The spontaneous polarization P_S calculated on the basis of the c-lattice parameters and the atomic displacements shown in (a) and (b). The positive values represent upward polarization and the negative values downward polarization.

tical separation from the domain wall plane. These displacements show essentially the same behaviour as c with the exception of the central area of 4 to 5 unit cells where the increase of the displacements is not accompanied by an increase of the c-value. Considering the variation of c, we infer a width of the LDW of $3c$ (domain I) to $7c$ (domain II), considerably wider than the respective value for the TDW.

Figure 2 (c) shows the spontaneous polarization vs. distance from the central plane of the domain wall. The values of P_S are calculated on the basis of the c-axis lattice parameters and the atomic displacements shown in Figs. 2a and 2b and the effective charge values of the ions for $PbTiO_3$. The maximum value of the modulus of P_S is about 75 $\mu C/cm^2$ for domain I and about 80 $\mu C/cm^2$ for domain II. Inside the domain wall the polarization changes direction.

Previous experimental studies on the 180° domains were focused on the TDW since it is generally assumed that the formation of the LDW is hampered by the fact that any tilt of the wall habit plane away from that of the ideal TDW induces local charge due to the head-to-head or tail-to-tail configuration of the polarization across the wall. In the extreme case of the LDW, the energy due to the uncompensated charge

The fact that these walls have a width of the order of 10 unit cells can be understood in terms of their particular charge status. The system energy can be reduced by distributing the polarization charge over an extended thickness of the wall. This is supported by the strong reduction of the c-axis lattice parameter and therefore the tetragonality in the wall area. Indeed exploiting the potential of the new ultra-high resolution techniques we can determine local physical properties, for cases where these depend on structure and atomic displacements, directly from measurements of shifts of the individual atom positions. This fulfils an old dream in materials science to be able to obtain a direct link between atomic level information and macroscopic properties.

[1] C. L. Jia, et al. Nature Mater. **7**, 57 (2008)

[2] C. L. Jia, M. Lentzen and K. Urban, Science **299**, 870 (2003).

[3] I. Vrejoiu, et al. Adv. Mater.**18**, 1657 (2006).

[4] L. Houben, A. Thust and K. Urban, Ultramicroscopy **106**, 200 (2006).

185

A mechanism for bipolar resistive switching in a Pt/TiO$_2$/Pt cell

D. S. Jeong, H. Schroeder

IFF-6: Electronic Materials

A possible mechanism is suggested for bipolar switching in a Pt/TiO$_2$/Pt resistive switching cell in terms of electrochemical reactions involving oxygen ions/vacancies. The electrochemical reactions are considered to take place at an interface between Pt electrode and TiO$_{2-x}$ solid electrolyte and they modulate the Schottky barrier height at the interface. Calculation results using this proposed mechanism can explain a bipolar switching behaviour and semi-quantitatively describe experimental data.

Recently, bipolar switching in oxide materials such as TiO$_2$ [1], and SrTiO$_3$ [2] have been vigorously investigated for application to resistive random access memory (RRAM) devices. The possible application of the oxide materials has attracted increased interest in an enlarged data base as well as in a mechanism for the bipolar switching, which is hardly understood at present. For TiO$_2$, experiments reveal several, mostly indirect hints about possible mechanisms of electroforming and bipolar switching, but there has been no theoretical description of them. Because of the dependence of bipolar switching on the polarity of the electro-forming voltage or current [3], it is usually assumed that bipolar switching involves the migration of charged particles, most probably ions. Further-more, an evolution of gas bubbles at the anode of a Pt/TiO$_2$/Pt switching cell was observed during electroforming, possibly indicating the electro-chemical formation of oxygen gas [4].

In this contribution, we suggest a mechanism for bipolar switching in Pt/TiO$_2$/Pt in terms of the modulation of the Schottky barrier height (SBH) at one "activated" interface (determined by the asymmetric, i.e. polarity dependent forming step [3]) in a region of oxygen deficient TiO$_{2-x}$ due to the voltage-dependent variation of large space charge densities of mobile oxygen vacancies, V$_O$**, close to that interface. The assumed geometry of the cell is sketched in Fig. 1a. It includes also thin dipole ("Helmholtz") layers at the interfaces.

Electro-chemical reactions involving oxygen and oxygen vacancies are assumed at the Pt/TiO$_{2-x}$ interface to describe some oxygen exchange. The energy for this exchange reaction is plotted with respect to the reaction coordinate for two different voltages in Fig. 1b. The net flux at the interface is dependent
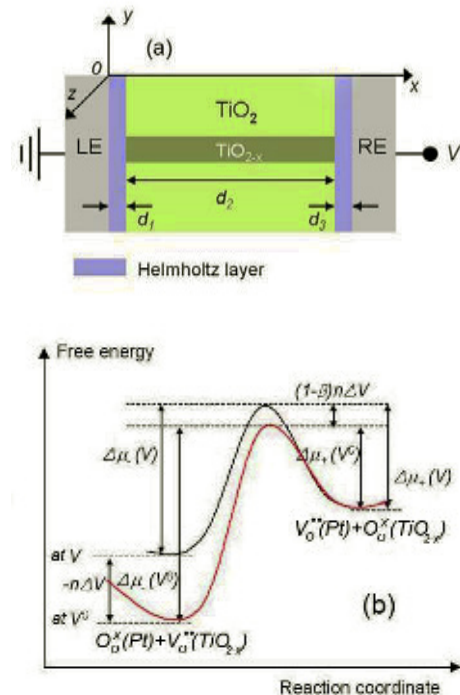
FIG. 1: (a) Configuration of a TiO$_2$ switching cell. (b) Free energy diagram of reaction equation with respect to a reaction coordinate. The red and black lines denote diagrams at applied voltages of V^0 (reference voltage) and V (= $V^0 + \Delta V$), respectively.

on the applied voltage and described by a form of a Butler-Vollmer equation [5, 6]. Therefore, this reaction varies the density of oxygen vacancies at the interface which is used as boundary condition for the drift-diffusion equation within the TiO$_{2-x}$. A similar condition is used for the electrons so that their injection current at the cathode equals their drift-diffusion current inside. Due to the large voltage drop in the Helmholtz layer and its transparency for electrons because of the very thin layer ($<$1 nm), we can describe the modulation of the SBH and thereby the thermionic injection of the electrons in terms of the variation of the internal electric field in the Helmholtz layer. The internal field was calculated by the Poisson equation.

As this set of differential equations can not be solved analytically a finite difference method was ap-
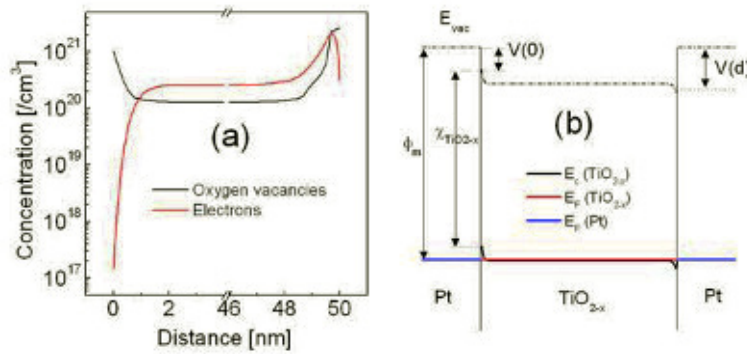
FIG. 2: (a) Initial distribution of oxygen vacancies and free electrons in TiO_{2-x} between LE and RE at V=0. (b) Calculated band diagram of a $Pt/TiO_{2-x}/Pt$ switching stack
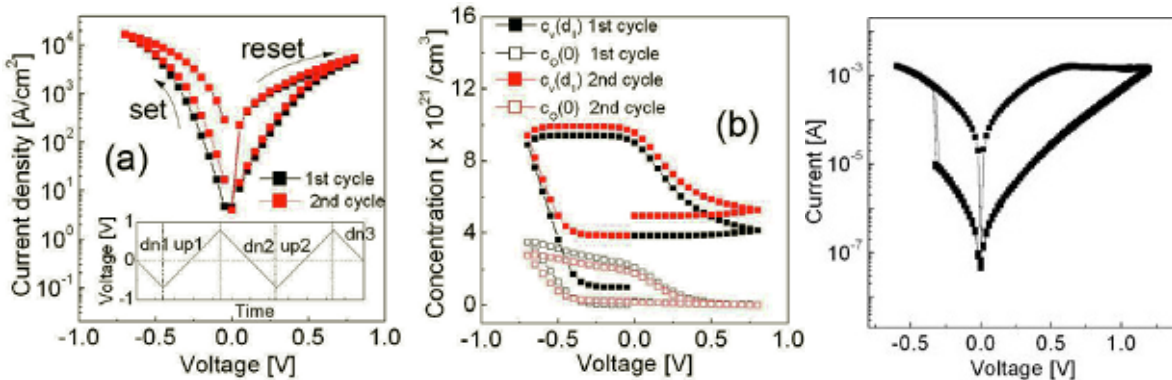
FIG. 3: : (a) Simulated J-V curves with the applied voltage cycles shown in the inset and a voltage delay time of 0.1 sec. (b) Variation of oxygen vacancy concentration, c_v, on the TiO_{2-x} side and oxygen ion concentration, c_O, on the LE side of the LE/TiO_{2-x} interface with respect to the applied voltage cycles. The mobility of oxygen vacancies was assumed to be 3.87×10^{-17} $cm^2/V \times s$ corresponding to a diffusivity of 10^{-18} cm^2/s. The voltage sweep rate was 0.5 V/s. (c) Bipolar switching curves measured on a $Pt(100\ nm)/TiO_2(100\ nm)/Pt(100\ nm)$ switching cell.

plied for simulation calculations for a 50 nm thick sample. The assumed initial densities of oxygen vacancies at the left and right boundaries of the Helmholtz layers (created by the forming procedure) were 1×10^{21} cm^{-3} and 2.66×10^{21} cm^{-3}, respectively. Their one-dimensional concentration profile and that of the electrons is plotted in Fig. 2a for $V_{appl} = 0$. In Fig. 2b the corresponding band diagram is shown. V(0) and V(d) are the voltage drops in the Helmholtz layers, respectively. These voltage drops are dependent on the applied voltage and therefore, the electron injection current is affected via a corresponding change of the SHB.

In Fig. 3 simulated J-V (leakage current) curves are shown for two cycles together with the corresponding concentrations of oxygen (c_O) and oxygen vacancies (c_v) at the Pt/TiO_{2-x} interface and compared with a measured switching cycle of a $Pt/TiO_2/Pt$ cell. The simulated J-V curves show a hysteretic behaviour with some more smooth transitions from high to low resistance state ("set") and vice versa ("reset") than measured. A change of a factor of two in the oxygen vacancy concentration induces an order of magnitude change in the current. A comparison of the absolute numbers of the currents in Figs. 3a and c reveals an active area of the TiO_{2-x} "filaments" of about 10 μm^2.

In conclusion, a mechanism for bipolar switching in a $Pt/TiO_2/Pt$ switching cell after asymmetric electroforming is suggested in terms of oxygen-related elec-

trochemical reactions, oxygen vacancy formation and annihilation reactions at one of the Pt/TiO_2 interfaces, which is activated by the polarity of the asymmetric electroforming process. By taking into account the Helmholtz layer at the active interface the reaction constants for the formation and the annihilation of oxygen vacancies are expressed as a function of the applied voltage, thus the concentration of oxygen vacancies is given with respect to the applied voltage. The variation of oxygen vacancy concentration at the active interface leads to a change in the SBH, consequently, giving rise to a transient resistive switching relying on the polarity of the applied voltage. The transient nature of this suggested switching mechanism may affect the retention which has to be investigated in more detail.

[1] D.S. Jeong, H. Schroeder, and R. Waser, Electrochem. & Solid-State Letters 10, G51 (2007).

[2] K. Szot, W. Speier, G. Bihlmayer, and R. Waser, Nature Materials 5, 312 (2006).

[3] D.S. Jeong, H. Schroeder, U. Breuer, and R. Wa-ser, J. Appl. Phys. 104, 123716 (2008).

[4] H. Schroeder and D.S. Jeong, Microel. Eng. 84, 1982 (2007).

[5] D.S. Jeong, Thesis, RWTH Aachen, 2008.

[6] D.S. Jeong, H. Schroeder, and R. Waser, submitted to Phys. Rev. B.

187

Resistive switching in Sr$_{1-0.05}$La$_{0.05}$TiO$_3$

K. Szot[1], M. Pilch[1,2], W. Speier[1]

[1] IFF-6: Electronic Materials
[2] University of Silesia, Katowice, Poland

The analysis of the electronic structure of La-doped SrTiO$_3$ single crystals, La$_x$Sr$_{1-x}$TiO$_3$ with x=5 at % (LSTO), shows that additional electrons in the host matrix are accommodated by a change of the valence of Ti ions from Ti^{+4} to Ti^{+3}. We found, however, no evidence of a metallic peak near the Fermi level by electron spectroscopy. Similarly, electrical characterisation of the material revealed only semiconducting behaviour. This stands in contrast to the general idea of a macroscopic insulator-to-metal transition in LSTO at a doping level of a few percent of La. By means of conducting AFM we found evidence of an inhomogeneity of the in-plane conductivity at the nano-scale and the possibility of locally manipulating the electric resistivity by means of an electrical stimuli, i.e. resistive switching. The observed inhomogeneity is attributed to a non-uniform distribution of La doping and a high density of extended defects in LSTO crystal.

The simple tunability of the electric properties of ABO$_3$ materials with perovskite structure, either by chemical doping, thermal post-treatment or electrical stimuli, is one of the fascinating aspects which has made this kind of material highly attractive for basic research and technological application. Of particular interest is the reversible insulator-to-metal transition (I/M-transition) as it holds great promise in the context of resistive switching and its potential application for Terabit memories. LSTO is widely recognized as model system for substitutional doping in perovskites: its electrical properties ranges from a band insulator, SrTiO$_3$, a metallic conductor for 0<x<1 to a Mott insulator, LaTiO$_3$. However, the material shows a lack of reproducibility in the conductivity data (see [1], and references therein). In fact, the critical concentration of La for the I/M-transition is not well determined and can vary between 0.001at% and 20at%, depending critically on the preparation conditions. At the same time, the ease with which this material can be driven from one electronic state to another [2] immediately raises the question concerning the stability of the different electronic phases, but also opens the pathway of easily manipulating the electronic properties of the material. This requires a detailed analysis of the different physical and chemical properties at the macro- and nano-scale induced in the perovskite matrix by doping or generated by, e.g., an electrical field.

Analysis of commercial single crystals La$_x$Sr$_{1-x}$TiO$_3$ with x=5% (CrysTec-Berlin), either by X-ray analysis or X-ray photoelectron spectroscopy (XPS, Al$_{K\alpha-mono}$ for cleaved surfaces in UHV), implies that the crystallographic structure, the electronic structure and the stoichiometry of LSTO are perfect: the measured lattice parameters reproduce the literature data for this level of doping (a=b=c= 3.907Å, Pm3m), the stoichiometry near the surface corresponds to the nominal chemical composition and the concentration of Ti with a valence of +3 ions is, as shown in Fig. 1a, approximately equal to the concentration of La ions (by analysis of La 3d core levels).
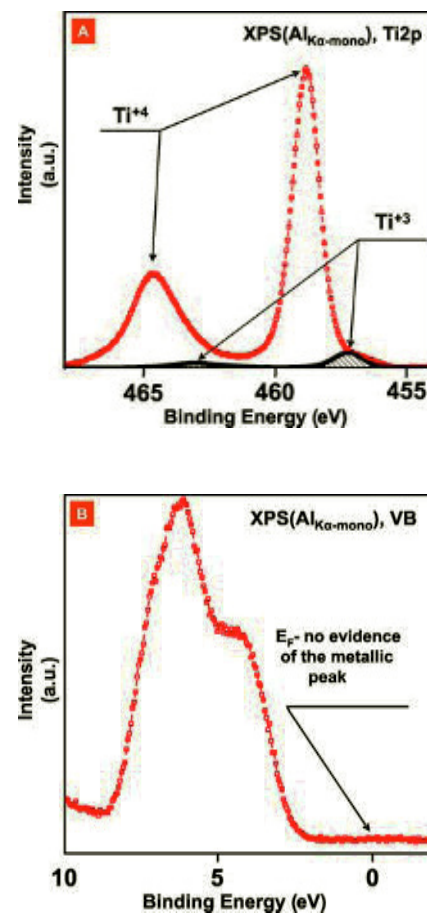
FIG. 1: Ti 2p core level with doublets Ti+4 and Ti+3 (a) and valence-band spectra without additional states near E$_F$.

However, the problem arises when analysing the valence band spectra for *in situ* fractured surfaces (Fig. 1b). One expects to observe the so called metallic peak near E_f (0eV), as predicted by band-structure calculations. Although we prepared several times fresh surfaces by scraping under UHV-conditions, we did not observe the typical metallic peak. Also, measurement of thermal dependency of the electrical conductivity shows that the conductivity is thermally activated, typical for semiconducting, i. e. not metallic, behaviour. But, this semiconducting character of conductivity is only observed, with either a two-point or four-point probe method, for small currents or at small voltages. Increasing the current density to values of μA to mA or polarisation voltages U>0.6V leads to a change in the electrical conductivity revealing a metallic character.

We used vacuum LC-AFM to analyse the electrical character of the crystals at the nano-scale and to check the possibility of electrically addressing different locations. The conductivity map of a cleaved LSTO (cleaved parallel to a 100- plane) shows a lateral inhomogeneity of the local conductivity for small voltages (U<0.5V). Different types of "electrical patterns" were found for the scanned regions (Fig. 2a and 2b). Fig. 2a shows a semi-regular pattern with preferential orientation of conducting clusters (phi∼30nm) along the [110]-direction, the dynamical range of electric conductivity between the conducting and less conducting regions being more than 4 orders of magnitude.
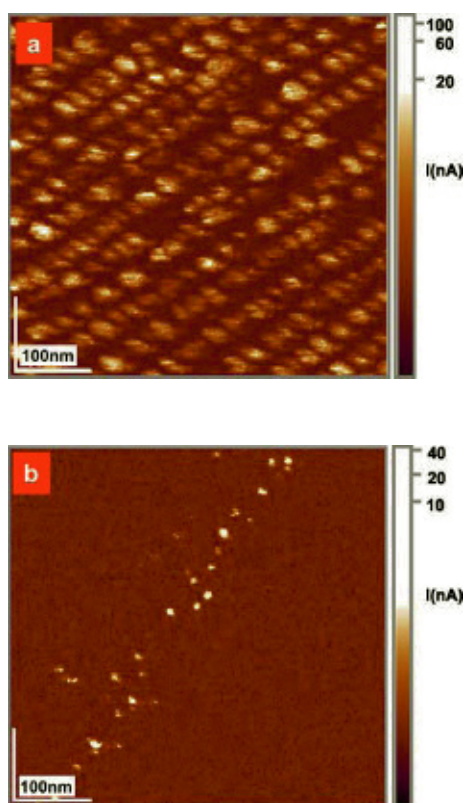
FIG. 2: *Change in the character of the distribution of conducting clusters (LC AFM measurement in- plane) for LSTO in two different positions (a,b) on the cleaved surface.*

The second example (Fig. 2b) is typical for a region with a dominating fraction of a non-conducting surface layer and only a small band of conducting clusters crossing the scanned region. We found that the clusters with enhanced conductivity can be reversibly switched as shown by the hysteretic I/V curve in Fig. 3.

Further studies demonstrated that the origin of the complicated pattern of electrical conductivity at the nano-scale is accompanied by a very high density of extended defects and a local variation of the concentration of La. TEM investigations of LSTO give evidence that the dominating types of extended defects are stacking faults and elemental analysis (combining EDX, EELS and TOF-SIMS) revealing that the distribution of La is modulated at the nano- as well as at the macro-scale.

Therefore, the understanding of the nature of the resistive switching phenomena in LSTO at room temperature should go beyond the standard models of the electric transport in this kind of material, which have been developed on the basis of a homogeneous material, and should instead focus on the local electronic structure, the effect of electro-migration and kinetic demixing at the nano-scale and take into consideration the percolative character of the transport at the macro-scale.
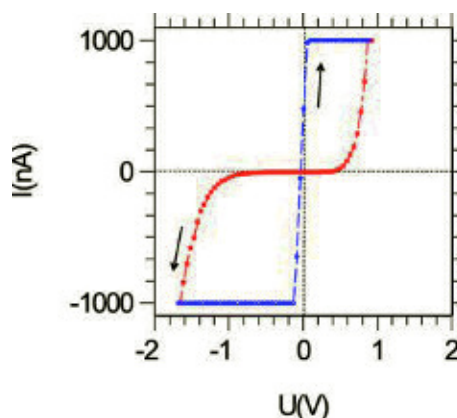
[1] S. Hashimoto et al., Journal of Alloys and Compounds **397**, 245 (2005)

[2] S. Hirose et al., Journal of Applied Physics **104**, 053712 (2008)

Field emission resonances at tip/ mercaptoalkylferrocene/Au interfaces

L. Müller-Meskamp[1], S. Karthäuser[1], H. J. W. Zandvliet[1,2], M. Homberger[3], U. Simon[3], R. Waser[1,4]

[1] IFF-6: Electronic Materials
[2] MESA+ Institute for Nanotechnology, University of Twente
[3] Institute of Inorganic Chemistry (IAC), RWTH Aachen University
[4] Institute of Electronic Materials II, RWTH Aachen University

The electrical properties of α,ω-mercaptoalkyl ferrocenes with different alkyl chain lengths, FcCn with n = 3, 5, 11, embedded in a self-assembled host matrix of alkanethiols on Au(111) are studied by scanning-tunneling microscopy (STM) and spectroscopy (STS). Based on current-distance spectroscopy (I-s), as well as on the evaluation of Fowler-Nordheim tunneling current oscillations, the apparent barrier height of ferrocene is determined independently by two methods. The electronic coupling of the ferrocene moiety to the Au(111)-substrate depends also on the length of the alkane spacer chain like shown in [1].

The ability to access and to use electronic properties of individual molecules together with the inherent capability of self-organization promises new possibilities for future nanoelectronic devices. Especially interesting are molecules with reliable redox behavior, which have the potential to be used as switches or storage elements. In this study the electrical properties of chemisorbed, standing-up α,ω-mercaptoalkyl-ferrocenes are studied by UHV-STS. To minimize the configurational freedom of the chemisorbed molecules the matrix isolation approach is chosen. The mercaptoalkyl-ferrocene molecules are embedded into self-assembled monolayers of alkanethiols, which serve as well defined host matrices with known electrical and structural properties.

Performing voltage-dependent imaging, shown in Figure 1, the step height between ordered surface domains of mercaptopropyl-ferrocene, FcC3, and the surrounding octanethiol, C8, monolayer is measured in constant-current mode for bias voltages ranging from -0.8 V to -1.8 V using UHV-STM. It is obvious from the selected images that the apparent height of the ferrocene derivatives depends strongly on the bias voltage. This behaviour has not been observed so far for other molecules inserted in an alkanethiol matrix. For lower bias voltages only slightly elevated features are visible, whereas for higher negative bias bright, well-defined features appear. It is concluded that the apparent step height changes of FcC3 with respect to C8 as a function of U_b are mainly electronic in origin [1].

The electrical transport through FcC11 molecules embedded in a C12 SAM matrix was characterized by current-distance spectroscopy, a well accepted method to characterize the chemical specificity of the sample surface and the local electronic charge. The spectra recorded on extended patches of FcC11 inserted into C12 are shown in Figure 2. I-s spectroscopy on mercaptoalkyl-ferrocenes in our measurement setup clearly proves that the decay constant is not constant over the entire length of the system, but depends strongly on the nature of the respective material. Three different parts of the I-s curve with different decay constants can be identified: the tunneling gap between the STM tip and the molecule (β_{vac}), the ferrocene moiety (β_{Fc}), and the alkane chain (β_{CH}). It was found [1] that in the case of mercaptopropyl-ferrocene a bias voltage of ± 1 V is high enough to be remarkably larger than the apparent barrier height, e.g. the tunneling barrier shape changes to a triangular barrier resulting in Fowler-Nordheim tunneling or field emission [2]. For this case the experimentally determined β_{Fc} = 2.8 nm^{-1} corresponds to an apparent tunneling barrier height of 0.62 eV for the ferrocene moiety.
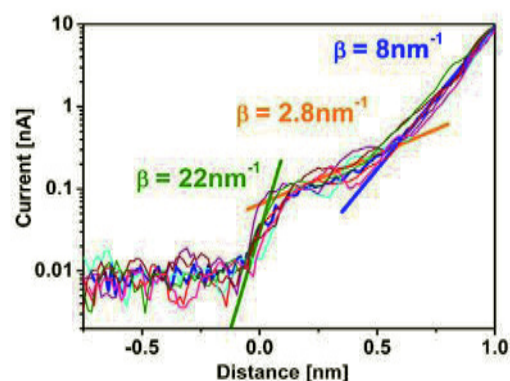
FIG. 2: Current-distance (I-s) spectroscopy on mercaptoundecyl-ferrocene. The slopes in the semi-logarithmic I-s plot reflect the decay-constants.

In addition I-U spectroscopy of mercaptoalkyl-ferrocenes with different chain length, FcCn with n = 3, 5, 11, inserted into the corresponding alkanethiol host matrices has been performed. Most interestingly a characteristic increase in current is observed, when the applied bias voltage exceeds the apparent
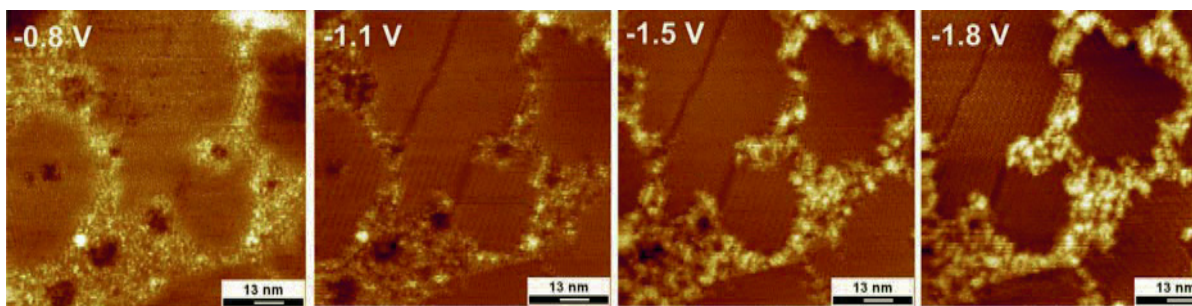
FIG. 1: Voltage-dependent imaging: the step height between ordered surface domains of FcC3 and the surrounding C8 monolayer is measured in constant-current mode for bias voltages ranging from -0.8 V to -1.8 V using UHV-STM.

tunneling barrier height of ferrocene due to the onset of Fowler-Nordheim tunneling (Fig 3). This conduction threshold is found at higher voltages for mercaptoalkyl ferrocenes with longer alkane chains [1].

In the regime of high bias voltages, according to Gundlach [3], the tunneling current exhibits additional oscillations resulting from electron standing waves in the vacuum gap between emitter (e.g. tip) and collector (e.g. ferrocene moiety). Thus the conductance versus U_b curve shows maxima at well-defined voltages, from which the apparent tunneling barrier height of ferrocene can be calculated. The thus obtained value of 0.60 eV is in excellent agreement with the value of 0.62 eV obtained by current-distance spectroscopy.

[1] L. Müller-Meskamp, S. Karthäuser, H. Zandvliet, M. Homberger, U. Simon, and R. Waser, Small **5**, 496-502 (2009).

[2] W. Wang, T. Lee, M. A. Reed, in Nano and Molecular Electronics Handbook, (Ed: S. E. Lyshevski), CRC Press, Boca Raton, 2007, Ch. 1.

[3] K. H. Gundlach, Solid-State Electron. **9**, 949 (1966).
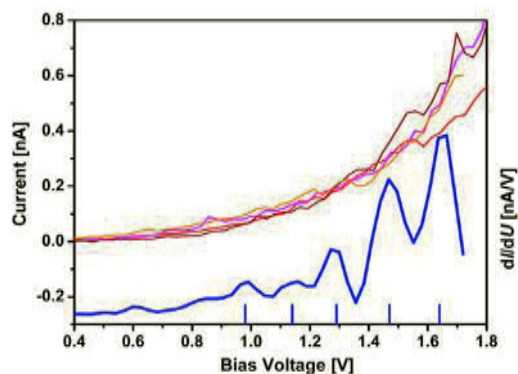
FIG. 3: Current-voltage curves of FcC3 (reddish) and differential conductance (bluish) showing Fowler-Nordheim tunnelling with superimposed Gundlach oscillations.

In conclusion two UHV-SPS methods, e.g. current-distance spectroscopy and current-voltage spectroscopy, were applied successfully on ordered domains of mercaptoalkyl-ferrocenes embedded into alkanethiols. The results are in excellent agreement and reveal that the main conduction mechanism of ferrocene is Fowler-Nordheim tunneling. Furthermore Gundlach-oscillations are clearly observed in the current-voltage spectra. The onset of the Fowler-Nordheim tunneling can be additionally modulated by the attached alkane spacer chains. Thus, ferrocene moieties are attractive candidates to tailor the electron transport properties in future nanoelectronic devices.

Neutrons show where atoms are and what atoms do: The Jülich Centre for Neutron Science (JCNS) at the IFF was founded in 2006 to operate state-of-the-art neutron scattering instruments at the most modern of highest flux sources in the world. Here: The Small Angle Neutron Scattering spectrometer KWS 1 at FRM II, Garching.

Large-scale facilities for research with photons, neutrons and ions

This research programme coordinates the activities taking place at the large scale facilities involved in the HGF research field Structure of Matter. These facilities offer unique research opportunities with photons, neutrons and ions for a multitude of science disciplines, ranging from physics, chemistry, biology and geology to material science, engineering science, and environmental research. A particular feature of this programme is the support of external user groups, which utilize the major part of the available access time. These user groups come mainly from universities, but also from non-university research institutions and industry.

With its excellence in neutron research – manifested in the Jülich Centre for Neutron Science (JCNS) – the IFF supplies a key contribution to this research programme. The strong reputation of the IFF in the German and international neutron landscape is closely related to:

• a powerful in-house research in the area of condensed matter focusing particularly on soft matter and magnetism,

• a large user operation in these research areas being extensively supported by IFF experts and facilities,

• a science-driven programme for the development of new methods and instruments, and

• exploitation of the novel neutron research opportunities provided by pulsed MW spallation sources.

The IFF neutron research is carried out to a large extent at the new state-of-the-art research reactor FRM II in Munich and at the ILL in Grenoble (France), with new opportunities being created at the SNS spallation source in Oak Ridge (USA). These activities are a cornerstone of the HGF programme "Condensed Matter Physics" and provide important contributions also to other HGF programmes, such as "Information Technology with Nano-electronic Systems".

193

The first year of operation of the backscattering spectrometer SPHERES

J. Wuttke[1], G. J. Schneider[1], L. C. Pardo Soto[1,2], M. Prager[†3], A. Budwig[4], M. Drochner[5], U. Giesen[4], A. Ioffe[1], H. Kämmerling[4], H. Kleines[5], B. Lindenau[4], V. Ossovyi[1], U. Pabst[4], H. Schneider[1], P. P. Stronciwilk[1], D. Richter[3]

[1] JCNS: Jülich Centre for Neutron Science
[2] Departament de Física i Enginyeria Nuclear, Universitat Politècnica de Catalunya, Barcelona
[3] IFF-5: Neutron Scattering
[4] ZAT: Central Technology Division
[5] ZEL: Central Institute for Electronics

Our backscattering spectrometer SPHERES has been successfully operated throughout 2008. Ten external experiments were performed. After refurbishing the chopper, the signal-to-noise ratio was increased from 330:1 to 600:1.

Background reduction: When routine operation started in fall 2007, the signal-to-noise ratio was about 300:1. It was found that almost half of the background came from fast neutrons produced in Li absorbers in the chopper wheel. Therefore in fall 2008 the graphite deflectors were transferred into a new wheel where B_4C is used instead of Li (Fig. 1). To prepare the in-situ balancing of the new wheel, we undertook a detailed vibration analysis of the entire chopper. As a result, the signal-to-noise ratio is now at least 600:1 (Fig. 2); this value has been confirmed and even surpassed in real experiments with user-provided samples.

FIG. 1: Vu Thanh Nguyen und Björn Poschen retrieve the graphite crystals from the old chopper wheel. Michael Prager watches closely.

Software development: Spectrometer components are controlled by a number of independent, elementary programs (in C for tracking the monochromator motion and for accumulating neutron histograms, in Ruby for controlling the shutter, the neutron velocity selector, the Doppler drive, the sample temperature controller, and other peripherals). Instrument scientists and technicians can intervene at all levels
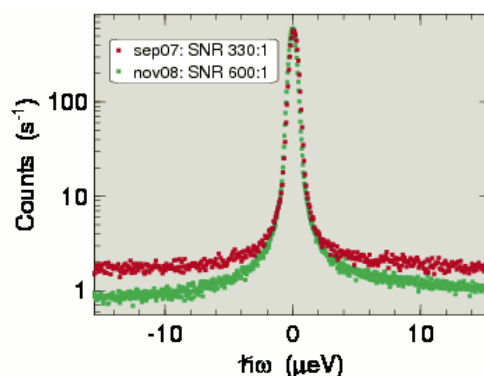
FIG. 2: Instrumental resolution, measured on a PET standard scatterer. Thanks to the refurbishment of the chopper wheel, the signal-to-noise ratio has become quite satisfactory; the resolution is now dominated by the wings characteristic of a crystal spectrometer.

through a command-line interface. Users can issue all commands they need through a graphical interface. At the same time, this interface gives a complete overview over the current status of the spectrometer and results from the current measurement. We are now working on extending this dual approach (command-line based, with graphical interface on top of it) towards data reduction procedures.

Confined water: In confined geometry, water can be supercooled far below its bulk freezing point 273 K. The monolayer of water absorbed to a protein surface can be supercooled to about 150K. This hydration shell is believed to have decisive influence upon the thermal fluctuations of the protein. Recently, it has been postulated that hydration water relaxation, as measured on the backscattering spectrometer HFBS at NIST, can be interpreted in terms of a fragile-to-strong crossover (Chen et al. 2006). Taking advantage of the better energy resolution of SPHERES, we are currently evaluating these claims (Busch, Doster et al., work in progress)

The kinetics of water in cement is particularly important for the retention of radioactive waste. SPHERES has been used to measure the diffusivity of water in different cements. Taking into account different curing conditions, contributions from pores and from cracks can be separated (Aldridge et al. [1]).

Polymer and protein dynamics: Quasielastic scattering can be used to investigate segmental dynamics of

polymers and proteins. To identify and separate different types of motion, it is necessary to scan broad energy, wavenumber, and temperature ranges.

In an extensive study of poly(ethyl methacrylate), methyl group rotation has been separated from backbone motion, The latter can be described by the Fourier transform of a stretched exponential (KWW function), extending observations made by dielectric specroscopy. The q dependence, however, significantly deviates from expectations, requiring further study (Fig. 3, Génix et al., report 1294).

FIG. 4: Inelastic and elastic scattering from $(NH_4)_2PdCl_6$ in the low-temperature limit. The inelastic lines have fwhm= 0.84 μeV (read off from Gaussian fits, solid curves). The central line has fwhm= 0.66 μeV (dashed curve), which is compatible with the known resolution of SPHERES.
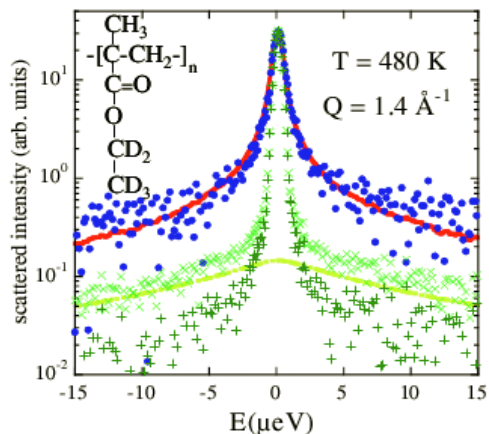
FIG. 3: Scattering function of poly(ethyl methacrylate) at $q = 1.4$ Å^{-1}, $T = 480$ K (blue). The fit (red) is a convolution of a KWW function (describing the overall segmental dynamics) with an effective convolution (green $\times$), which accounts for methyl group rotations (yellow) and the instrumental resolution (green $+$) [Génix et al.].

In the study of small proteins, a somewhat similar convolution approach is used to separate intramolecular motion from diffusion. Anomalies in the temperature dependence are used to detect miscellisation (Gaspar et al., report 667).

Molecular rotations: Backscattering spectroscopy is ideally suited for studying slow rotations of methyl groups or ammonium ions. With decreasing temperature, one sees a transition from classical jump rerotation to quantum-mechanical tunneling.

The ammonium ions in $(NH_4)_2PdCl_6$ are all located at equivalent lattice sites of cubic symmetry. Therefore, the ammonium ions are particularly simple tetrahedral rotors; the librational ground state is split into no more than three energetically different tunneling states. In the low-temperature limit, the E–T splitting is about 29 μeV, which fits perfectly into the dynamic range of SPHERES (–30.6...30.9 μeV). Fig. 4 shows the discrete lines measured at 3.7 K. The inelastic lines at ± 29 μeV are significantly broader than the instrumental resolution. From the temperature dependence, we can rule out thermally activated processes. As tunneling lines are very sensitive to slight variations in the potential barriers, the broadening is probably due to a spread of tunneling splittings caused by crystal imperfections (Prager et al., continued by Wuttke).

Combining backscattering and time-of-flight spectra, the dynamics of $(NH_4)_2S_2O_8$ was studied over more
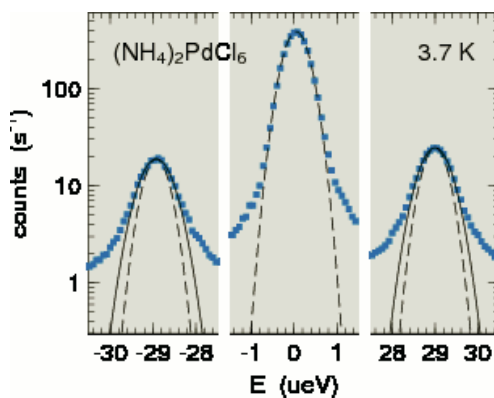
than five decades in energy. Due to the absence of symmetry at the ammonium site, the librational ground state is split into four bands, with transition energies differing by orders of magnitude. In consequence, in a good first approximation, the ammonium motion can be modelled as a one-dimensional rotational (Prager et al. [2]).

Nuclear spin excitations: Neutron backscattering can also be used for the study nuclear spin excitations. On SPHERES, hyperfine splitting of antiferromagnetic $NdMg_3$ and of ferroelectric $NdCo_2$ has been measured as function of temperature and energy (Fig. 5). Together with data on other Nd compounds, results allowed to establish a linear relationship between the nuclear excitation energy and the ordered magnetic moment of the Nd ion (Chatterji et al. [3]).
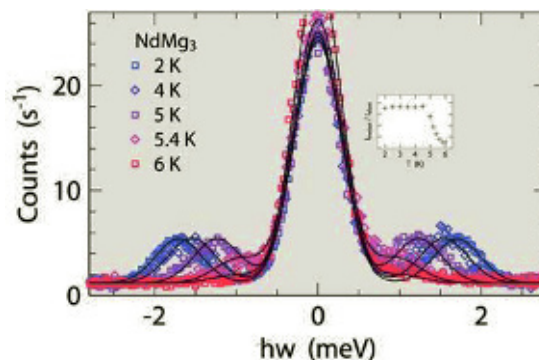
FIG. 5: Hyperfine spectrum of $NdMg_3$. On approaching the Néel temperature 6 K, the intensity of the inelastic line decreases rapidly (inset).

[1] L. P. Aldridge, H. N. Bordallo, K. Fernando, W. K. Bertram, J. Wuttke, L. C. Pardo, Cement Concrete Res. (submitted).

[2] M. Prager, H. Grimm, I. Natkaniec, D. Nowak, T. Unruh, J. Phys.: Condens. Matter 20, 125218 (2008).

[3] T. Chatterji, G. J. Schneider, and R. M. Galera, Phys. Rev. B 78, 012411 (2008).

195

DNS: diffuse neutron scattering with polarization analysis

Y. Su[1], W. Schweika[2], R. Mittal[1], P. Harbott[2], K. Bussmann[2], E. Küssel[2], H. Schneider[1], M. Skrobucha[3], A. Gussen[3], H. Kleines[4], F. Suxdorf[4], R. Möller[4], A. Ioffe[1], Th. Brückel[1,2]

[1] JCNS: Jülich Centre for Neutron Science
[2] IFF-4: Scattering Methods
[3] ZAT: Central Technology Division
[4] ZEL: Central Institute for Electronics

DNS is a versatile diffuse scattering spectrometer with polarization analysis at FRM II. With its compact design, DNS is optimized as a high intensity instrument with medium resolution for magnetism and strongly correlated electron systems. Since reaching a major milestone with the delivery of the first neutrons and intense polarized neutron beams in September of 2007, DNS has been in routine user operation for the investigations of complex magnetic correlations in a wide range of emergent materials.

DNS is a new cold neutron multi-detector time-of-flight spectrometer with both longitudinal and vector polarization analysis at FRM II. This allows the unambiguous separation of nuclear coherent, spin incoherent and magnetic scattering contributions simultaneously over a large range of scattering vector Q and energy transfer E, which attracts a broad user community from soft matter physics to magnetism. With its compact size DNS is optimized as a high intensity instrument with medium Q- and E- resolution. DNS is therefore ideal for the investigations of magnetic, lattice and polaronic correlations in frustrated magnets and highly correlated electron systems. With its unique combination of single-crystal time-of-flight spectroscopy and polarization analysis, DNS is also complimentary to many modern polarized cold neutron triple-axis spectrometers.

The DNS instrument has experienced a major reconstruction within the process of relocation from the Jülich reactor FRJ-2 to the FRM II at Garching. This process and the construction of the new DNS at FRM II have started in 2006. A new double focussing graphite monochromator has been built and set up at the neutron guide NL6. With its fine, almost transparent Mg-support structure, the transmitted beam can be used without significant losses at the down stream backscattering instrument SPHERES. The first neutrons and intense polarized neutron beam were delivered to DNS in September of 2007. Newly constructed polarizer and polarization analyzers, both using m = 3 Schärpf bender-type focusing supermirrors, perform extremely well. A polarized neutron flux as high as 5×10^6 n/s/cm^2 has been achieved at the neutron wavelength with 4.74 Å. The polariza-

tion rate of the incident neutron beams is nearly 96%. The expanded polarization detector bank has largely improved the measurement efficiency. Since early 2008, DNS has been in routine operation for both internal and external user groups using polarized neutrons and polarization analysis in diffraction mode. Attractive sample environment, such as He^3/He^4 dilution refrigerator for cooling down to 20 mK, has been provided to the users in routine operation. The implementation of the new chopper system for time-of-flight spectroscopy is scheduled for 2009 and will be accompanied with a further major upgrade by a new position sensitve detector system. In addition to the improved E- and Q-resolution this adds a new dimension, the vertical Q component. The DNS will greatly improve possibilities for single crystal TOF spectroscopy with efficient measurements in all 4 dimensions of S(Q,E).

FIG. 1: Current look of DNS at FRM-II.

Science at DNS:

The tradition of DNS has been characterized by studies of disorder in materials [1], contribution to the understanding of complex magnetism, such as the spin correlations in highly frustrated 2D Kagome systems [2], and structural properties of polymer glasses [3], or dynamic "rattling" disorder as seen in soft modes of thermoelectric materials [4]. Nowadays, with the increased flux and efficiency of the DNS at the FRM-II, the exploration of unusual magnetic properties has been extended to single crystals. Figs. 2,3 depict recent examples on complex and frustrated magnetic systems, involving hundreds of sample positions each measured for a few minutes. Here, polarization analysis allows to distinguish in detail the anisotropy of moments and correlations. Fig. 2 shows probably the most frustrated 3D spin system, a layered Kagome system with tetrahedral coordination, which despite of strong exchange coupling remains only short-range ordered even at a very low temperature of 40 mK.
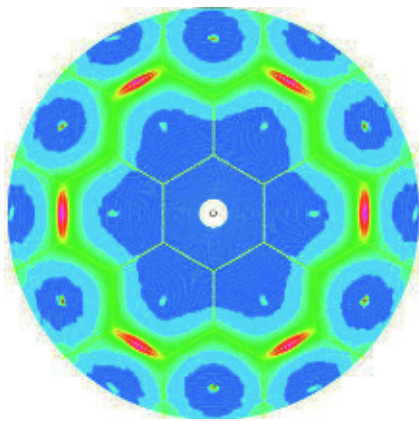
FIG. 2: Magnetic diffuse scattering in the hexagonal plane of a highly frustrated kagome spin system due to in-plane spin-components as determined by spin-flip scattering of initial P_z polarization.

The second result from a spin-ice compound, shown in Fig. 3, reveals a peculiar feature of pinch points, nodes at gamma points with highly anisotropic intensities arising from long-range dipolar interaction.

Recently, it has also been realized that polarized diffraction on DNS is complementary to standard neutron powder diffraction and may be extremely useful for magnetic structure refinements, particularly in case of small moments by improving the signal to background ratio. The research on the new pnictide superconductors has remarkably ruled the worldwide condensed matter physics in 2008. Here, in Fig. 4 we show the magnetic scattering of such a pnictide compound $CaFe_2As_2$, as obtained by polarization analysis.
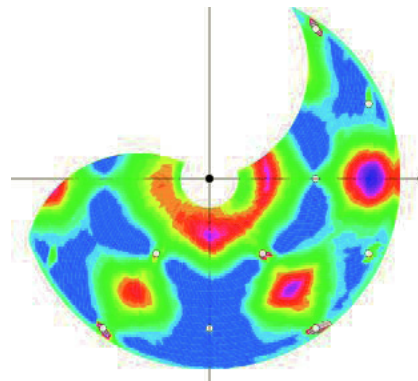
FIG. 3: The magnetic diffuse scattering due to correlations of in-plane spin components in the (hhl) reciprocal plane in spin-ice pyrochlore.
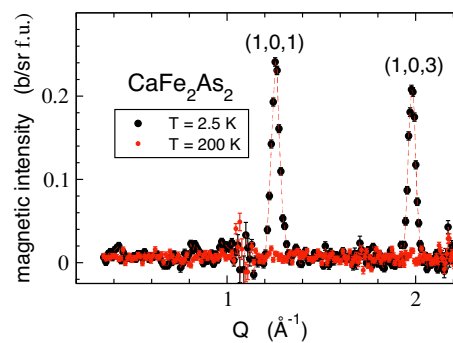
FIG. 4: Magnetic S(Q) of iron pnictides $CaFe_2As_2$ as obtained via neutron polarization analysis, indicating the presence of spin-density wave ordering at low temperatures and vanishingly small diffuse magnetic scattering above T_N.

[1] Schweika W., Easton S., Neumann K.-U., Neutron News **16** (2) (2005) 14.

[2] Schweika W., Valldor M., Lemmens P., Phys. Rev. Lett. **98** (2007) 067201.

[3] Narros A., Arbe A., Alvarez F., Colmenero J. , Zorn R., Schweika W., Richter D., Macromolecules **38** (2005) 9847.

[4] Hermann R. P., Jin R., Schweika W., Grandjean F., Mandrus D., Sales B. C., and Long G. J., Phys. Rev. Lett. **90** (2003) 135505, highlighted in Physical Review Focus, 3 April 2003.
Schweika W., Hermann R. P., Prager M., Perßon J., Keppens V., Phys. Rev. Lett. **99**, 125501 (2007).

197

Aspherical neutron lenses for the SANS diffractometers KWS-1 and KWS-2

H. Frielinghaus[1], V. Pipich[1], A. Radulescu[1], M. Heiderich[2], R. Hanslik[3], K. Dahlhoff[3], D. Schwahn[2]

[1] JCNS: Jülich Centre for Neutron Science
[2] IFF-5: Neutron Scattering
[3] ZAT: Central Technology Division

Parabolic neutron lenses have been introduced as new focussing elements to extend conventional SANS diffractometers without dramatic changes. Spherical lenses give rise with stronger aberrations and are thus limited to smaller illuminated areas, while the parabolic lenses overcome aberrations widely and thus allow for rather large illuminated areas. In test measurements the new lenses proved to work successfully. The improved resolution was characterized by the primary beam measurement and by a first sample measurement. The simulation of lenses agrees widely with the measurements. The sample measurement with the new lenses was corrected to complementary measurements.

Focussing techniques in combination with small angle neutron scattering were first realized with mirrors [1]. But also neutron lenses are considered as a useful tool for small angle neutron scattering cameras for several years [2]. Especially these focussing refractive objects can be used in transmission, which means that an already existing SANS diffractometer only needs minor changes in the setup. Neutron lenses can be used to increase the overall intensity at the same resolution or to increase the resolution without too large intensity losses. This development can be seen in parallel to photo cameras. While the pin hole camera took longer illumination times, the lens camera overcame this problem on the expense that the object of interest needed to be focussed. For SANS, the entrance aperture is imaged on the detector. The shape of the image corresponds to the resolution function at small scattering angles where the wavelength spread does not influence the resulting scattering angle Q [3]. Thus, the use of neutron lenses can be driven in the direction of high resolution or high intensity [4].

Historically, spherical lenses were easier to produce, but in the applications they showed spherical aberration effects. This means that rays with different distances from the optical axis are focussed at different distances from the lens. Already Gauss proposed parabolic lenses, which have much smaller aberration effects than the spherical counterpart. For small angle scattering they have been introduced by Lengeler [5] in the context of x-rays. An array of parabolic neutron lenses is shown in Fig. 1. The testing of the lenses took place at the SANS-J-II diffrac-
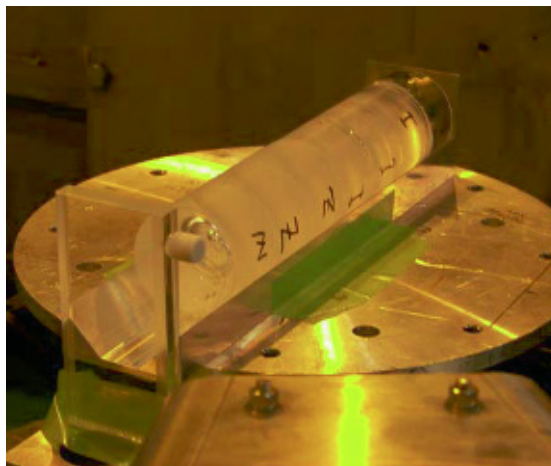
FIG. 1: Seven MgF_2 neutron lenses in a prism holder as used at SANS-J-II. The square cadmium entrance aperture defines the circularly illuminated area with a diameter of 5cm. The sample is placed behind the lenses as seen in the front of the picture.

tometer at the JAEA facility in Tokai, Japan. At this stage we had seven pieces placed in front of a scattering sample as discussed below. The lenses were produced by Zeiss, Jena and Ingeneric, Aachen. All lenses are made of MgF_2 which has a high transparency and low incoherent background scattering. Further phonon scattering can be overcome by cooling as discussed in a parallel publication [6]. The lenses have an active diameter of 5cm. The concave curvature is specified by a radius of 2cm in the centre of the lens. This testing configuration achieved a focal length of 5m with a neutron wavelength of 19.2Å.

A primary beam measurement in experiment and simulation is shown in Fig. 2. The full width at half maximum $\Gamma_{1/2}$ agrees well between these two methods. It lies in the range of $2 \times 10^{-4} Å^{-1}$. The typical background at the double value, i.e. $2\Gamma_{1/2}$, is found to be 3×10^{-3} for the simulation and 8×10^{-3} for the experiment. For ideal lenses the entrance aperture would be depicted with sharp boundaries on the detector. The wavelength spread $\Delta\lambda/\lambda$ of 10% in concert with the chromatic aberration causes a defocusing. This effect is already captured in the simulation and leads to the relatively soft decay of the primary beam. The even slower decay of the experiment must be connected to parasitic scattering of windows. Ex-

perimentally, the profile of the primary beam is important for the optimal resolution, i.e. the minimum Q reachable, and it describes the resolution function for small scattering angles. So $\Gamma_{1/2}$ is tightly connected to the minimum Q and the minimal measurable peak width of a sharp scattering signal.
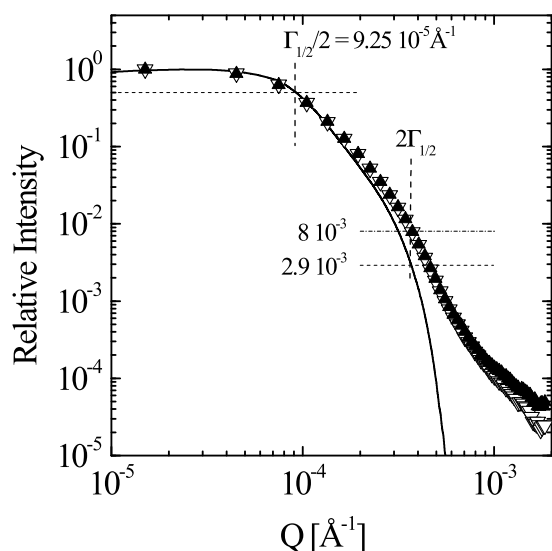
FIG. 2: *The primary beam profile as measured (open symbols) and simulated (line). The full width at half maximum $\Gamma_{1/2}$ agrees well, while the background at $2\Gamma_{1/2}$ deviates. The solid symbols were measured with the sample.*

The full symbols in Fig. 2 show the sample measurement which includes the primary beam and the sample scattering. The subtraction leads to the pure scattering which is shown in Fig. 3 (red symbols). The finally and practically obtained minimum Q was 10^{-4}Å.
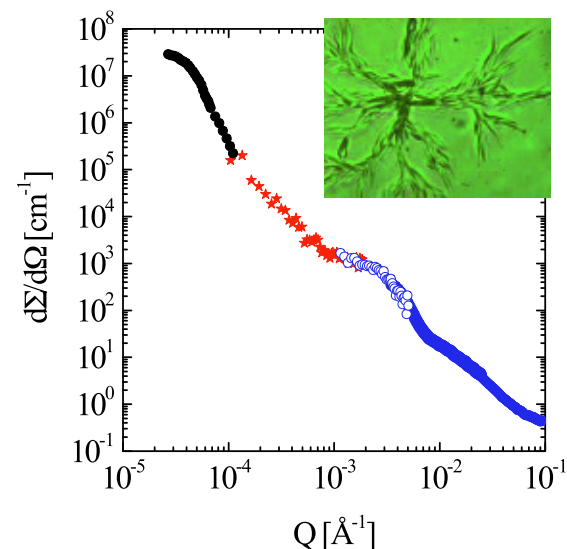
FIG. 3: *Complementary measurements with USANS (black), aspherical lenses (red), spherical lenses (open symbols) and conventional SANS (blue). All measurements performed at JAEA, Tokai, Japan.*

The overall scattering curve in Fig. 3 is completed by a Bonse-Hart type Double-Crystal-Diffractometer at low Q, by spherical neutron lenses at SANS-J-II in the medium Q, and conventional SANS at higher Q (also at SANS-J-II). The sample is a random copolymer dissolved in d-decane. It tends to form hierarchical structures with different length scales as also shown by microscopy. There are long nanoscale platelets which compose to long cylinders. These cylinders aggregate further and form blossom like structures as shown by microscopy. This polymer can be used in diesel fuel to inhibit wax crystallisation at low temperatures. The scientific background of this polymer is already discussed in [7] where similar measurements confirm the present findings of the current sample with a slightly different thermal history.

To summarize, we could prove that aspherical neutron lenses can be used successfully in classical SANS diffractometers with little changes. The primary beam profile was characterized to measure the resolution function and the minimum Q. The Q-range of such an extended instrument can safely be expanded to roughly 10^{-4}Å^{-1}. The current testing diffractometer allowed for a maximum detector distance of 10m, while standard SANS machines with 20m detector distance might even improve the minimum Q to 5×10^{-5}Å^{-1}. A first sample measurement shows that a continuous scattering curve is obtained in concert with USANS and classical SANS.

[1] Alefeld, B., Hayes, C., Mezei, F., Richter, D., Springer, T. Physica **B234-236**, 1052 (1997)

[2] Eskildsen, M.R., Gammel, P.L., Isaacs, E.D., Detlefs, C., Mortensen, K., Bishop, D.J., Nature **391**, 563 (1998)

[3] Glinka, C.J., Barker, J.G., Hammouda, B., Krueger, S., Moyer, J.J., Orts, W.J., J. Appl. Cryst. **31**, 430 (1998)

[4] Choi, S.M., Barker, J.G., Glinka, C.J., Cheng, Y.T. Gammel, P.L., J. Appl. Cryst. **33**, 793 (2000)

[5] Lengeler, B., Tümmler, J., Snigirev, A., Snigireva, I., Raven, C., J. Appl. Phys. **84**, 5855 (1998)

[6] Frielinghaus, H., Pipich, V., Radulescu, A., Heiderich, M., Hanslik, R., Dahlhoff, K., Iwase, H., Koizumi, S., Schwahn, D., J. Appl. Cryst. to be published.

[7] Radulescu, A., Fetters, L.J., Richter,D., Adv. Pol. Sci. **210**, 1 (2008)

199

Developments and status of the J-NSE in Munich

O. Holderer[1,2], M. Monkenbusch[1,2], N. Arend[1,2], N.R. De Souza[1,2], H. Kleines[3], F. Suxdorf[3], M. Wagener[3], M. Drochner[3], W. Westerhausen[4], C. Tiemann[4], B. Laatsch[4], R. Schätzler[1,2], D. Richter[1,2]

[1] IFF-5: Neutron Scattering
[2] JCNS: Jülich Centre for Neutron Science
[3] ZEL: Central Institute for Electronics
[4] ZAT: Central Technology Division

Neutron spin echo (NSE) spectroscopy is due to its high energy resolution an indispensable tool for studying slow dynamics on mesoscopic length scales in complex fluids like polymer melts, microemulsions or protein solutions or the dynamics of glass forming systems that become slow on all length scales close to the glass transition. Slow magnetic fluctuations are another realm of the NSE method. The Jülich NSE spectrometer J-NSE has been moved from the Jülich research reactor FRJ-2 to the new research reactor FRM II of the TU München. In the context of the transfer, parts of the spectrometer have been renewed and improved, leading to a significantly larger energy resolution and larger dynamic range.

200

The high energy resolution of NSE spectroscopy is obtained by encoding tiny velocity changes into changes of the spin direction of the neutrons. The normalized intermediate scattering function is measured in terms of polarization loss of the scattered neutrons. Since the high resolution, i.e. the polarization change, results from the difference of velocities of the same neutron before and after scattering, the instrument can accept a beam with a wide velocity distribution and correspondingly high intensity without compromising the resolution.

The new end position in the neutron guide hall of the FRM II provides a very intense neutron beam with a 15 fold gain of intensity at the sample position compared to the setup in Jülich at a wavelength of 8 Å. The accessible wavevector (q) range is 0.02 to 1.7 $Å^{-1}$, corresponding to distances of interest from 0.37 to 30 nm. Fourier times between 3 ps and 150 ns can be accessed at the moment by combining wavelength between $\lambda = 4.5 \cdots 17$ Å and field integral variation form $J = 3 \times 10^{-4} \cdots 0.3$ Tm. The Fourier time $\tau/\text{ns} \simeq 0.2 \times J/(\text{Tm}) \times (\lambda/\text{Å})^3$. Ongoing development will improve the correction coils, which will allow using field integrals up to the maximum of 0.5 Tm of the main solenoids, thereby increasing the dynamic range of the spectrometer by a factor of 2.

Besides its applications in studying slow processes in soft matter, neutron spin-echo spectroscopy can

FIG. 1: The sample position (on the right) and second precession coil (green) of the J-NSE spectrometer.

also serve to investigate the dynamics of paramagnetic scatterers, for example spin glasses. Additional coils ("y-coils") have been therefore installed at the sample position which allow to turn the spin in any direction at the sample position and separate paramagnetic from nuclear scattering for the normalization of the intermediate scattering function $S(q, \tau)$.

Science at J-NSE: During the first year where the instrument has been open to external users, experiments have been performed addressing questions from many different parts of soft matter physics but also the first paramagnetic experiments have been carried out, some examples are given below.

FIG. 2: Coherent dynamic structure factor of deuterated PEO at 391 K compared with MD simulations. At a wavelength of 5 Å, the smallest accessible Fourier time is 3 ps, the largest q vector 1.7 $Å^{-1}$

The dynamics of deuterated PEO above the melting temperature has been studied at high q values around the structure factor peak ($q < 1.7$ Å^{-1} and low Fourier times ($\tau > 3$ ps) (see Fig. 2). The collective dynamics of the PEO melt is probed in this way. The results have been compared with atomistic Monte Carlo (MC) simulations [3], showing an excellent agreement between the measured and simulated dynamic structure factor. Experimentally not accessible parameters could then be quantified by the MC simulations.

Different experiments have been performed on bicontinuous (sponge like) microemulsions, consisting of oil, water and a surfactant, where the dynamics of the surfactant interface layer is measured with NSE. The influence of temperature or co-surfactants on the bending rigidity can thus be studied. A new system in this context are microemulsions with supercritical CO_2 as oil at elevated pressure and temperature. First experiments on the dynamics of such "unconventional" microemulsions allowed to determine the bending rigidity of the surfactant layer therein. It has been observed that the bending rigidity is lowered by a factor of two, which can be explained by the lower average viscosity of the medium (oil, CO_2) surrounding the membrane. Additionally, the bending rigidity varies with pressure and surfactant concentration.
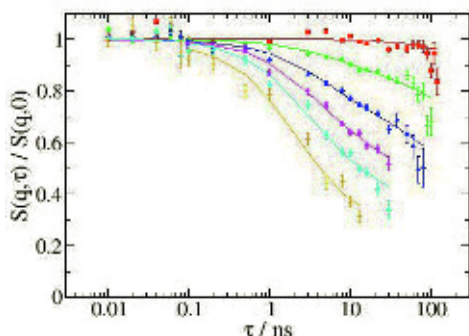
FIG. 3: *Coherent dynamic structure factor of PI in PDMS covering more then four decades of Fourier time from 10 ps to 120 ns.*

The dynamics of polymer chains confined in micellar systems of diblock copolymers, consisting of PI and PDMS, has been studied in different contrasts to highlight different parts of the system [4]. Structural investigations with SANS revealed a cylindrical structure of PI domains surrounded by PDMS. In "bulk" contrast, protonated PI and deuterated PDMS has been used to measure the dynamics of the PI-PDMS interface. The dynamic structure factor over four decades of Fourier times is shown in Figure 3. Evaluation of results is in progress and will shed light on surface undulations of the cylindrical PI domains.

Correction coil developments: Magnetic fields of the main solenoids have been corrected by six spiral aluminum coils (Fresnel coils), which can be shaped that not only quadratic corrections, but also higher terms

are taken into account. Nonetheless, the precision of different steps in the manufacturing process were the limiting factor for the quality of correction, especially at high magnetic fields. Development is going on to improve the correction elements. The existing coils will, where possible, be exchanged by so called "Pythagoras" coils [5], which consist of two rectangular parts, each part applying a quadratic correction to the magnetic field in x- and y-direction. The sum of the two coils leads then to a radial quadratic correction. A first prototype has been installed at the J-NSE and showed that this concept is very promising. Other correction coils will be replaced as soon as available. The largest correction coil is located at the end of the second main precession coil where the scattered beam has the largest cross section. It is the position with the highest requirements concerning the correction and higher terms than the quadratic one play a significant role. There, a coil with the "Pythagoras" design can only do a part of the correction. Different concepts are currently studied, either using modified spiral Fresnel coils or a combination of spiral and "Pythagoras" coils.
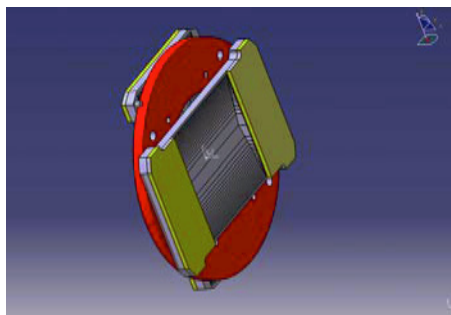
FIG. 4: *Drawing of a "Pythagoras" correction coil. The performance of the first coil which has been installed at the J-NSE spectrometer showed that this design corrects well the field inhomogeneities*

[1] Holderer, O., Monkenbusch, M., Borchert, G., Breunig, C., Zeitelhack, K., Nucl. Instrum. Methods Phys. Res. A **586** (2008) 90-94

[2] Holderer O., Monkenbusch M., Schätzler R., Kleines H., Westerhausen W., Richter D., Meas. Sci. Technol.**19** (2008) 034022

[3] Brodeck M., Alvarez F., Arbe A., Juranyi F., Unruh T., Holderer O., Colmenero J., Richter D., J. Chem. Phys. (2009), accepted

[4] Thanks to R. Lund, Donostia International Physics Center, San Sebastian, Spain and L. Willner (IFF-5: Neutron Scattering) for the permission of presenting the data.

[5] Based on a concept developed and also used at IN15, ILL by B. Farago and G. Kali.

201

MARIA: status of the new reflectometer of JCNS at the FRM II

S. Mattauch [1], U. Rücker [2], D. Korolkov [1], K. Bussmann [2], V. Fracassi [3], R. Schmitz [3], J. Daemen [3], A. Budwig [3], P. Kämmerling [4], F. Suxdorf [4], H. Kleines [4], M. Bednarek [5], E. Babcock [1], A. Ioffe [1], Th. Brückel [1,2]

[1] JCNS: Jülich Centre for Neutron Science
[2] IFF-4: Scattering Methods
[3] ZAT: Central Technology Division
[4] ZEL: Central Institute for Electronics
[5] G-TG: Technical Management, Process Technology/Switch Cabinet Construction

At the outstation of the Jülich Center for Neutron Science JCNS at FRM II, a new reflectometer MARIA is being build. This instrument is optimized for the study of magnetic nanostructures, serving the rapidly growing field of Spintronics or Magnetoelectronics, i.e. information storage, transport and processing using the spin of the electrons. The instrument will have unique features, such as polarisation analysis for large angular range, extreme focusing to small sample sizes, high flux, largely variable wavelength band selection, GISANS option, provision for kinematic studies down to the μs range, in-situ sample preparation etc. Its neutronic performance was optimised by Monte Carlo simulations and specially developed codes for various neutron optical devices.

The new neutron reflectometer MARIA (Magnetism Reflectometer with high Incident Angle) of the JCNS (Jülich Center of Neutron Science) is designed for investigations of thin magnetic layered structures down to the monolayer scale (optimised for layer thicknesses between 3-300Å) and lateral structures of nm to μm sizes. Consequently the instrument is optimised for small focused beam and sample sizes of 1cm^2 and has polarisation analysis as standard. Beside the reflectometer mode with good resolution in the horizontal scattering plane, MARIA will be able to measure in the GISANS mode with

Scattering plane	horizontal
Monochromator	velocity selector
Wavelength	4.5-10Å
Wavelength spread	1%, 3%, 10%
Expected pol. flux	7x10^7 n/(s*cm^2) (3mrad coll.)
Detector size	400 x 400 mm^2
Detector resolution	1-2mm
Sample detector dist.	2m
Max. detector angle	120°
Q$_z$-range	0.002 - 3.2Å^{-1}
Q$_x$-range	6·10^{-5} - 0.001Å^{-1}
α_f	-10 - 90°
Polarisation	double reflection polariser
Polarisation analysis	Radial solid state polariser / ^{3}He
Collim. (scat. plane)	4m long, Slits: 0 - 40 mm
Focussing	vertically focussing elliptic guide
GISANS option	4m long collimation
Q$_y$-range	0.002 -0.2 Å^{-1}

TABLE 1: Characteristic data of MARIA.

FIG. 1: Expected polarised flux of MARIA at the sample position

additional resolution in the vertical direction. The latter mode allows one to measure lateral structures down to the nm scale.

The neutronic performance of the complete instrument was optimised with the Monte Carlo simulation package VITESS and specially developed codes for various neutron optical devices like Fermi chopper and selector. The expected flux from the VITESS simulations for a polarised neutron beam with 3 mrad collimation is depicted in Fig. 1. Compared to the former HADAS reflectometer at the Jülich research reactor DIDO, we expect a gain in flux of at least two orders of magnitude.

The rising interest in thin magnetic layers with lateral structures in the nanometer scale started with the discovery of the Interlayer Coupling in 1986 and the GMR-Effect in 1989 by P. Grünberg (IFF) and A. Fert (Paris). These effects allow one to store, transport and process information related to the spin of the electron. In combination with lateral structures approaching the nanometer size in thin film materials, new effects are expected. For the investigation of effects like the behaviour of magnetic domains inside nanostructures buried under nonmagnetic layers, magnetic effects in the vicinity of interfaces of different materials or dipolar interactions of nanostructures, polarised neutrons are a powerful and unique tool. All these phenomena can be studied with a polarised neutron reflectometer designed to have a high signal to noise ratio (8-9 orders of magnitude) with standard polarisation analysis on an area detector.

The main task last year was to build and test all instrument components.

FIG. 2: Left: Last check of the selector shielding. Right: Selector shielding installed in the neutron guide hall at the FRM II.

FIG. 4: Drawing of the collimation, the absorber (inlet upper left corner) of the GISANS mode and both four segment slits.

Selector: The selector housing is already installed at the FRM II (see Fig. 2).

Fermi chopper: Although the Fermi chopper is not planned to be installed in the first stage of the instrument, the main parts are constructed and will be ordered soon. It will fit into the narrow chopper chamber and the rotor of the Fermi chopper will consist of an aluminium cylinder of 1mm wall thickness. This very lightweight rotor reduces the need of a massive shatter protection.

Polarisation chamber: In Fig. 3 the polarisation chamber and the lifting device is shown. The lifting device will operate in vacuum and move one of the three possible guides (polarised guide, non polarised guide and one option for the future) into the beam. It is therefore an essential part of the construction of MARIA. After extensive tests, simulating a live time of 5 years we can state that the lifting device runs smoothly inside and outside the vacuum and is ready to be shipped to the FRM II.

Collimation: The collimation (see Fig. 4) is the end of the guide and the most important part for the focusing of the vertically elliptic neutron guide. The construction of the absorber plates looks simple, but has to work quite accurately not to damage the expensive

super mirrors.

Sample table: It consists of a Hexapod which can support heavy loads such as magnets, cryostats, furnaces, etc. (see Fig. 5).

[3]He neutron spin-filter: As a polarisation analyser a [3]He neutron spin-filter with the SEOP (Spin Exchange Optical Pumping) method has been chosen. This will enable us to analyse the polarisation over large detector areas without any loss of resolution. At the same time we can use the polarisation analyser as a flipper. For more information please have a look to the report: [3]He neutron spin-filter program at JCNS.

The installation of MARIA at the FRM II in Munich will start soon, so that the instrument will see the first neutrons in the first half of 2009.

203

FIG. 3: Polarisation chamber (left) and lifting device (right).

FIG. 5: The Hexapod of the sample table. Below the Hexapod will be an additional turn table and a friction wheel driven detector arm.

BIODIFF: single crystal diffractometer for biological macromolecules

M. Monkenbusch[1], A. Ostermann[2], B. Laatsch[3], W. Petry[2], D. Richter[1]

[1] IFF-5: Neutron Scattering
[2] FRM II, Garching
[3] ZAT: Central Technology Division

In the space between the N-REX+ reflectometer and the entry of neutron guides into the FRM II guide hall west a single crystal diffractometry station for crystals with large units cells will be build using neutrons from the NL-1 guide. The project is a collaboration of the FZJ and the FRM II. Neutrons of a freely selectable wavelength between 2.4 and 5.6 Å will be reflected out of the lower part of the NL-1 by a graphite crystal. Higher order contamination will be removed by a mechanical velocity selector. The expected flux at the sample is 9×10^6 n/cm^{2}s for λ=2.4 Å with a divergence of 0.70°. The maximum allowed unit cell dimension will be up to 100Å. The unique wavelength variability enables one an optimization of the experiment for a given unit cell dimension. As main detector a cylindrical neutron image plate with online reading facility is foreseen. An auxiliary CCD based detector will facilitate adjustment and fast assessment of the crystal. Plan is that the instrument will be ready for operation in summer 2010.

Crystallography is a powerful tool to look into the molecular and even atomistic details of the structure of proteins as soon as single crystals are available. Whereas X-ray diffraction yields the bulk of related structural information questions pertaining the position and role of hydrogen atoms require neutron techniques. Hydrogen atoms, especially flexible ones, are barely visible in X-ray structure determinations of proteins but clearly visible in a neutron structure analysis even at moderate resolutions of $d_{min} <2.0$Å (compare fig. 1). Hydrogen atoms in polarized bonds play often critical roles in enzymatic catalysis. They are involved in the substrate binding process and are essential for example in proton transfer reactions during the catalysis. Therefore the knowledge about protonation states of amino acid residues in the active centre of proteins are crucial for the understanding of their reaction mechanisms. In addition neutrons allow to discriminate between hydrogen and deuterium. Therefore it is possible to use H/D exchange patterns of exchangeable hydrogen atoms to gain information about the flexibility and accessibility for water molecules of regions of interest in the protein matrix. Also the hydration shell of proteins which play an essential role for the protein dynamics can be investigated in great structural detail. Gene technology together with the development of techniques to grow bacteria in fully deuterated media meanwhile enable the production of fully deuterated proteins which are ideally suited for crystallographic studies.
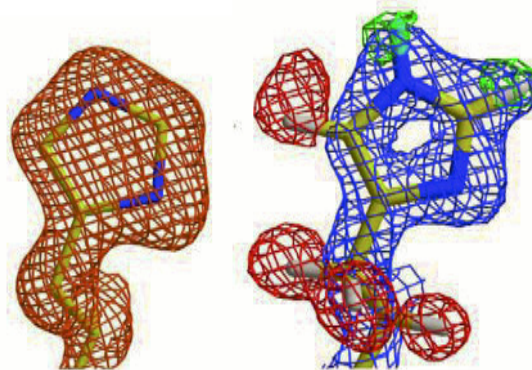
FIG. 1: X-ray (left) versus neutron (right) reconstruction (d_{min}=1.5 Å) of a detail (histidine 97) of the myoglobin structure. Model colour code: carbon (yellow), nitrogen (blue), hydrogen ^{1}H (white) and deuterium ^{2}H (turquoise). From: Ostermann A, Tanaka I, Engler N, Niimura N, Parak F (2002) Biophys. Chem. 95:183

The large number of atoms in the unit cell of a protein crystal requires that correspondingly many reflection intensities have to be collected to reconstruct the structure. The needed large solid angle coverage in combination with high spatial resolution, reasonable sensitivity, reliability and affordability currently is only given by an image plate detector which also is used in the other related reactor based macromolecular diffractometers LADI-III at ILL and BIX-3,4 at the Tokai reactor. The image plate detector covers a solid angle of 2π with a resolution of a few tenth of a mm (the expected spot size of a reflections is 1..3mm). Electronic detectors like gas multiwire chambers would give a better detection efficiency and discrimination against background γ-radiation, however, there are none with the same solid angle coverage and spatial resolution at the same time. The only viable alternative would be a highly sensitive CCD camera looking on a ZnS:Li scintillator which as a system can supply a similar sensitivity as the image plate, however, for the same solid angle coverage a larger number of modules (8..16) would be needed. For adjustment and assessment purposes the addition of one such module as auxiliary detector for BIODIFF is foreseen.

Since it is vital for an optimized instrument to be able to measure as many reflection intensities as possible in a given time, besides an efficient large area detector, a high neutron flux on the sample is essential. For this the neutron guide NL-1 offers an excellent start. Figure 2 shows the foreseen location in the guide hall and Figure 3 the neutron flux in the allocated guide.

FIG. 2: Location of the biodiffractometer (BIO) in the FRM II guide hall.
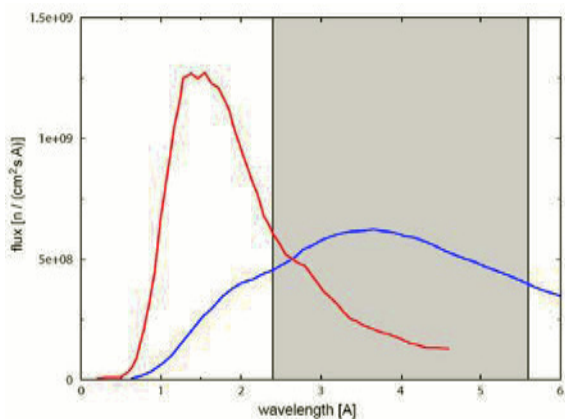
FIG. 3: Neutron flux as function of the wavelength for a thermal beam SR-5 (red) compared to the NL-1 flux (blue). In the BIODIFF range the NL-1 nearly everywhere offers higher flux.

Neutrons are reflected out of the lower part (height 25mm) of the neutron guide cross section by a pyrolytic graphite crystal. The wavelength can then be varied between 2.4 and 5.6Å thereby enabling optimization of the number of measurable reflections and the spatial resolution. Higher order wavelength contaminations are removed by a velocity selector. Figure 4 displays the arrangement of the main components on a tanzboden.

Monte-Carlo simulations (McStas) indicate that the expected flux at the sample position varies between 9×10^6 at 2.4 Å to 7.6×10^6 n/cm^{2}s at 4 Å with a wavelength spread $\Delta\lambda/\lambda$=2.9% and 2.5% respectively.

A simulation of the diffraction pattern from a $80 \times 80 \times 80$Å^3 unit cell (crystal size: 1.5x1.5x1.5 mm^3) is shown for 2.4Å and mean scattering angles of -74° and -106° is shown in Figure 5. One recognizes that the reflections are well separated and have a extension of 2-3mm on the detector plane as

a combined effect from the sample crystal size and the beam divergence.
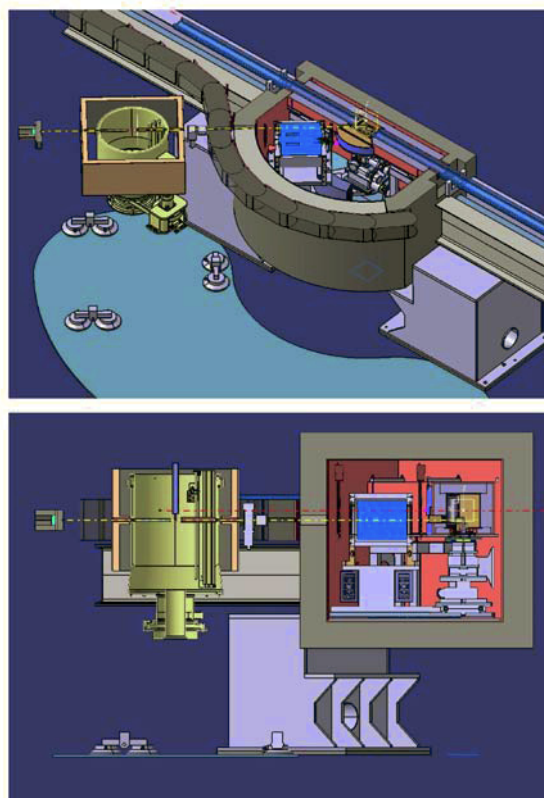
FIG. 4: Neutron guide monochromator shielding (gray) including velocity selector (blue) and outer detection unit (amber). The carrying structure connecting the detector unit with the air cushions are not shown. The sample position is in the center of the detection unit. Top: cut along the scattering plane, bottom: vertical cut.
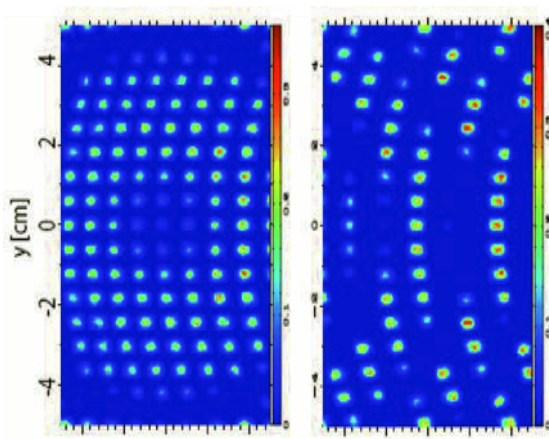
FIG. 5: Simulated intensity pattern on image plate sections.

Currently the granite tanzboden at the location of the diffractometer is being made. In autumn 2009 the monochromator gap in the neutron guide will be opened and the shielding will be installed. Operation of the instrument is anticipated to start summer 2010.

205

TOPAS: a new thermal time-of-flight spectrometer with polarization analysis

J. Voigt[1,2], M. Prager[†3], K. Bussmann[1], P. Harbott[1], H. Kämmerling[4], A. Heynen[4], Th. Brückel[1]

[1] IFF-4: Scattering Methods
[2] JCNS: Jülich Centre for Neutron Science
[3] IFF-5: Neutron Scattering
[4] ZAT: Central Technology Division

TOPAS is the future thermal time-of-flight spectrometer at the research reactor FRM II. The scientific scope of the instrument includes the determination of coherent and localized excitations in novel materials. Equipped with a position sensitive detector system, it will allow the mapping of 4D dispersion relations over an energy range from 20 to 150 meV. The high neutron flux over the wide energy range with a modest divergence is realized by the combination of a focusing neutron guide system and a high resolution energy selection, consisting of a set of Fermi choppers. The application of polarization analysis will make TOPAS a unique instrument for the investigation of the dynamics in magnetic and hydrogen containing materials.

Inelastic neutron scattering has proven to be one of the most powerful techniques for the study of dynamics in novel materials. Our understanding of phonons, magnetic excitations, hydrogen bonding in materials, and soft-modes at phase transitions has come primarily from the results of inelastic neutron scattering studies. In recent years, this technique has been used to examine an ever-widening range of subjects and phenomena such as the dynamics of polymers, the nature of disordered and amorphous materials, phase transitions in geological materials and subtle electron-lattice interactions. By the use of thermal neutrons, a large range in energy and momentum transfer can be probed. In the direct time-of-flight geometry, the measurement of the momentum transfer is decoupled from the measurement of the energy transfer. Time-of-flight spectroscopy from single crystals explores simultaneously the $(\vec{Q}, \omega)$ space and maps a variety of excitations by covering a large solid angle with detectors. Accordingly, TOPAS can be used for a wide range of applications, particularly for novel materials:

- The physics of correlated electrons is one of the most active and challenging fields today in hard condensed matter. High temperature superconductivity, colossal magneto resistance and many more phenomena have attracted interest because of their high relevance to both, the basic understanding of condensed matter and the potential for new technical applications. Electronic, spin, lattice and orbital degrees of freedom determine the ground state and dynamics by a subtle interplay. The dynamics of these degrees of freedom can be studied by inelastic neutron scattering, some of them exclusively. Frustration in such systems leads to a loss of long range order, but the dynamic correlations on a mesoscopic length scale, that will be visualized by TOPAS, reflect the atomic interactions. For the study of magnetic systems, the full information about the vector properties can be extracted by polarization analysis.

- The interaction potentials within a single molecule and between molecules determine the molecular and crystal structure and therewith for example the structure-activity relation of biological systems. The experimental vibrational phonon density of states is the benchmark to test new concepts in molecular dynamics and the corresponding software systems. A special case remains water with its 12 known phases. Polarization analysis will allow to suppress the incoherent scattering to study the dynamics also in non-deuterated samples.

- It is well known that the properties of a solid can change dramatically with the reduction of the size of crystallites. Since band formation may be suppressed a conducting microcrystal may transform into an isolating nanocrystal etc. The change of macroscopic properties is based on changes on the atomic level which can be characterized by the vibrational density of phonon states or a broadening of excitations due to the finite size of nanoparticles.

- A sufficiently fast proton dynamic is needed to use metal hydrides as hydrogen storage systems or batteries. The extreme sensitivity of neutrons for hydrogen makes inelastic incoherent neutron scattering an exceptionally suited tool to study the hydrogen potentials via the microscopic jump diffusion step.

Since novel materials can often be synthesized only in small amounts, high flux instruments are needed to study the dynamics in a wide range of external parameters like temperature, magnetic or electric field or pressure. TOPAS will provide the high flux by means of a focusing neutron guide system. The double-elliptical shape makes it possible to reduce
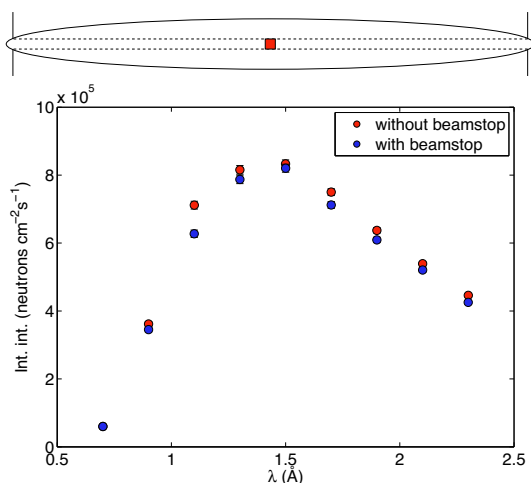
FIG. 1: Comparison of the monochromatic flux of an instrument with and without beamstop in the centre of the ellipse as sketched in the upper part of the figure.

FIG. 2: 3d model of the primary and secondary spectrometer. The neutron energy is selected by the phase between the Fermichoppers FC1 and FC2. The disc chopper suppresses neutron velocities that could also pass through the Fermi choppers

the the size of the neutron window at the reactor window. Optimizing the shape of the ellipse, we find that the size of the entrance window can be as small as 15x50 mm^2 while the optimum dimension of the exit window is 18x45 mm^2. The rather small window dimensions enable a new route to prevent the direct sight from the spectrometer onto the reactor core: One can place a 16.5x47.5 mm^2 beamstop at the centre of the double elliptic guide. The covered area amounts there to less than 8% of the cross section. The numerical simulations give an flux reduction of less than 5%, as shown in Fig. 1, since the flux is slightly higher closer to the walls inside the neutron guide. As a result we expect very low background conditions and also a facilitated shielding concept.

A set of Fermi choppers will select the neutrons with the chosen energy and create pulses of the length $\Delta t \approx 10\mu$s, see Fig. 2. The system can provide a wavelength resolution $\Delta \lambda < 2\%$, reaching rotation speeds up to 36000 revolutions per minute. However, the concept gives us a large flexibility to trade intensity and resolution by changing the chopper speed and timing as it is desired by the experimentalist.

The secondary spectrometer shown in Fig. 2 will be completely evacuated down to a pressure $p < 10^{-5}$ mbar to enable a window-free operation even at cryogenic sample temperatures (of course with thin radiation shielding). Therefore the position sensitive detector is mechanically decoupled from the vessel, which deforms on evacuation and venting. For the exchange of the sample environment the central part of the vessel can be separated from the main flight-path volume. The sample environment is mounted into a rotation stage, providing 360° rotations to access to the 4dimensional $S(\vec{Q}, \omega)$.

Polarization analysis for a thermal time-of-flight spectrometer poses the major challenge to the project. As outlined above, it will offer completely new possibilities to different scientific fields. Polarized ^{3}He is the method of choice to analyze the spin of thermal neutrons. Since the whole detector vessel
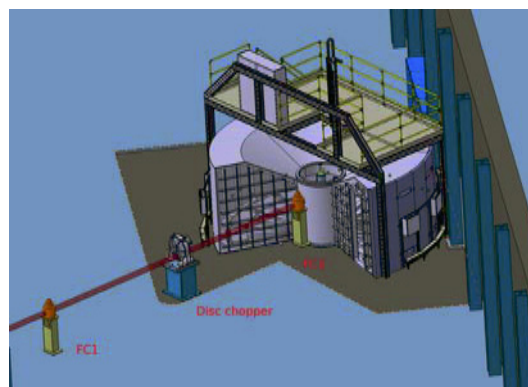
of TOPAS will be evacuated, we need to implement the polarizer/analyzer such, that it can be either re-filled remotely or pumped continuously. A wide angle analyzer will be employed to cover simultaneously a range of scattering angles. Presently, JCNS is developing a concept superceding former projects, as it foresees the application of modest magnetic fields in combination with polarization analysis.

In summary TOPAS will be a high flux time-of-flight spectrometer for a wide range of applications. It combines a good energy resolution with a modest angular resolution thanks to the combination of a Fermi chopper system and a double elliptical neutron guide. Polarization analysis will give a new insight into the dynamics of magnetic and hydrogen containing materials.

Michael Prager started the TOPAS project as a successor of the SV29 spectrometer in Jülich and had a strong impact on the present design. He past away unexpectedly last November. While his personality and experience cannot be replaced, we dedicate the realization of TOPAS to his commemoration.

POWTEX: the new high-intensity time-of-flight neutron diffractometer

A. Houben[1], W. Schweika[2], P. Harbott[2], J. Walter[3], R. Achten[4], B. T. Hansen[3], R. Dronskowski[1]
Th. Brückel[2]

[1] Institute of Inorganic Chemistry, Chair of Solid-State and Quantum Chemistry, RWTH Aachen University
[2] IFF-4: Scattering Methods
[3] Geoscience Centre Göttingen, University of Göttingen
[4] ZAT: Central Technology Division

POWTEX is the new high-intensity time-of-flight neutron diffractometer built by RWTH Aachen University, Forschungszentrum Jülich and Göttingen University. The instrument will be installed at the FRM II reactor in Munich as part of the JCNS instrumentation pool. POWTEX, whose name stands for POWder and TEXture, will be the first pulsed, time-of-flight neutron powder diffractometer at a continuous source. With its high flux and the huge solid angle of detector coverage, the instrument will provide a rapid and efficient data acquisition for structural and texture analysis serving for the needs of the large chemistry and physics as well as the geo- and materials science communities.

Conventional neutron diffractometers at research reactors are monochromatic instruments, whereas POWTEX in constrast is a pulsed instrument using a wide wavelength spectrum combined with time-of-flight analysis. In particular, the neutron beam optics is optimized with respect to equal horizontal and vertical collimation and resolution, which allows us to cover rigorously the solid angle around the sample for detection. Therefore, POWTEX will outperform conventional instruments with much higher efficiency by more than an order of magnitude. In comparison to diffractometers at pulsed spallation sources, to be competitive or complementary, the POWTEX design has to profit from the advantage that the pulse structure is not restricted to the low repetition rates of the new MegaWatt sources. The immediate consequence is the choice for high repetition rates and high intensity rather than high resolution, which is in concordance with the needs of the user community. A beneficial aspect is that it is much less expensive to cover a large solid angle under these demands than for high resolution instruments.

A detailed description of the initial instrument design has been published recently [1]. The basic features of the instrument are: the double elliptic beam compressor with horizontal and vertical focusing super-mirrors, the phase-coupled four-unit disk-chopper system, including the pulse double-chopper, the use of Position Sensitive Detectors (PSDs) to access the full Debye-Scherrer cones by a huge solid angle. The high neutron flux at the sample position will allow for short measurement times and thus a high sample throughput for applications like crystallographic and magnetic structure determination, the characterization of phase transitions or even the determination of whole phase diagrams by parametric scans of temperature, pressure or magnetic and electric fields. Furthermore, we will be able to in-situ investigate chemical reactions. Based on texture analyzes of whole series of natural geological samples, POWTEX will be used to study the kinematics of entire geological structures. Other geoscience applications will be in-situ deformation, recrystallization/annealing and simultaneous stress and texture analysis.

While the main concepts like the flight-path scheme are still valid, we constantly improved many details in comparison to the first design (see FIG. 1). A major improvement to the double-elliptic beam guide system was the change from a rectangular to a quadratic cross sections. By this, the guide will as nicely illuminate the whole sample position of 1×1 cm^2 as in [1] but with a more homogeneous divergence profile as well in horizontal *and* vertical direction. Furthermore, the entrance window dimensions and with this also the whole geometry of the two ellipses were optimized to yield the best compromise between the wavelength dependent divergence profile which is suited also to the detector resolution and the flux at the sample position. All optimizations were calculated with the VITESS Monte Carlo program running on the cluster of the Center for Computing and Communication of RWTH Aachen University.

A new idea is to use multi-slit chopper discs; by varying simply the phase relationship between the different chopper discs it is possible to realize also a pulsed overlap mode [2] as an additional measurement option increasing flux and efficiency by another order of magnitude. Especially for samples with a higher symmetry, this option will be suited for rapid kinetic studies.

The detector system using a cylindrical area equipped with horizontally aligned ^{3}He position-sensitive detectors has been redesigned reducing the radius from 175 cm to 125 cm without any compromise to resolution (see FIG. 2). As additional benefit the covered solid angle could be increased from 6.2 steradian to ≈ 10 steradian. Apart from the significant cost reduction, the new smaller sized concept facili-

FIG. 1: Flight-path scheme with new chopper positions on the right and elliptical beam guide system on the left. The focal points in the ellipsis system are indicate by blue dots. The beam cross section at the pulse chopper is as large as the sample size (1×1 cm^2). A third neutron guide is used to refocus the transmitted beam for the high pressure instrument.

tates the realization of an evacuated detector vessel, which is important for background reduction. The re-designed forward- and back-scattering detectors also offer a higher coverage of the solid angle by arranging those 1 m PSDs in a hexagonal like shape. In order to improve the resolution in forward scattering only 0.5" PSDs will be used. The access to the sample position will be possible by horizontally dividing the cylindrical detector in the top-most position and sliding both halves sideways. This will also allow for a crane access.
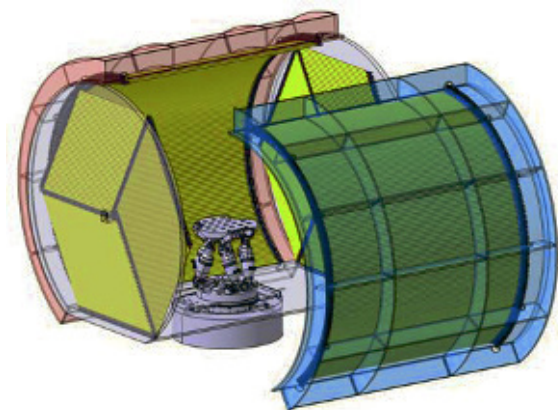
FIG. 2: The new detector design of POWTEX. A cylindrical part with a radius of 125 cm is equipped with 2 m, 1" ^{3}He position-sensitive detectors (Achten, ZAT). In the forward- and back-scattering area 1 m long PSDs with a width of 0.5" and 1.0" are arranged in a hexagonal like system.

We have simulated typical measurement results of powder samples produced by POWTEX taking into account the specific design parameters of POWTEX (see FIG. 3), in order to assure that POWTEX can fulfill the requirements of the different communities.

Finally, it is foreseen to locate a new experimental facility, the high pressure cell from Bayreuth University, immediately behind POWTEX. Thus the high pres-

sure instrument will profit also from the pulsed beam and can be operated in parallel. For this purpose the transmitted neutron beam of POWTEX will be refocused on the very small sample position in the sub-centimeter regime of this instrument.

While POWTEX is under construction at the very moment, we expect to conduct the first measurements in the year 2012.

The POWTEX project is funded by the BMBF.
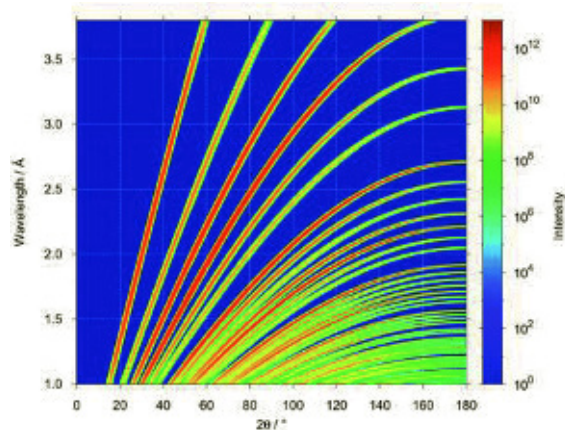
FIG. 3: Simulation of a powder pattern for the ternary nitride RhFe$_3$N ($Pm\overline{3}m$) with POWTEX instrumental parameters. Please note that the width of the wavelength band is limited to $\Delta\lambda = 1.4$ Å.

[1] H. Conrad, Th. Brückel, W. Schäfer, J. Voigt *J. Appl. Cryst.* **2008**, *41*, 836–845.

[2] U. Stuhr *Nucl. Instrum. Meth. A* **2005**, *545*, 319–329.

209

IN12: the cold neutron three-axis spectrometer at the ILL

K. Schmalzl[1], W. Schmidt[1], S. Raymond[2], R. Hermann[3], H. Feilbach[4], K. Bussmann[3], T. Brückel[1,3]

[1] JCNS at ILL, 38042 Grenoble, France
[2] CEA-Grenoble, INAC SPSMS MDN, 38054 Grenoble, France
[3] IFF-4: Scattering Methods
[4] IFF Technical Services and Administration

The cold neutron three-axis spectrometer IN12 is operated by JCNS in collaboration with the CEA Grenoble as a CRG-B instrument at the Institut Laue-Langevin (ILL) in Grenoble, France. IN12 is dedicated for high-resolution studies of low energy excitations. Recent experiments with JCNS contributions comprised studies of magnetic systems, like multiferroics or strongly correlated electron systems, magnetic studies on thin films as well as lattice dynamics in clathrates. The upgrade with a multi-analyser option and the upcoming move to a new position ensure also in future a powerful and unique instrument.

As a CRG-B instrument the scheduled beam time is shared amongst the collaborating partners: 30% of the beam time is made available for the ILL, whereas the remaining time is assigned to CEA and FZ Jülich with 35% share each. Two thirds of the available time for German users is distributed through the JCNS proposal process by an international review committee, while one third is reserved for in-house research.

Typical experiments on IN12 include mainly elastic and inelastic studies of low energy structural and magnetic excitations, like, e.g., excitations in low dimensions, spin waves in localised magnets, magnetic correlations in heavy-fermion systems and non-Fermi liquids, magnetic multilayers and thin films, low lying phonons as well as critical scattering and phase transition phenomena. IN12 also proofed to be well suited for studies on glasses and liquids at low momentum transfers. Recently also the dynamics of model membranes was investigated.

Some recent experiments with JCNS contribution on IN12 included, e.g., multiferroic materials like the recently discovered system MnWO4 (M. Braden et al.). It shows a strong coupling of ferroelectricity and magnetism what is thought to result in new collective excitations, hybridised spin-phonon excitations. Here for the first time spherical polarisation analysis (Cryopad) with simultaneous application of an electric field has been installed on IN12.

Continued interest exists also in the heavy-fermion compound $CeCu_2Si_2$ due to the appearing interplay between antiferromagnetic order and superconductivity (O. Stockert et al.). While conventional superconductivity is generally incompatible with magnetism, here in the superconducting state a spin excitation resonance was found demonstrating their relevance for the superconductivity.

Another project covered the lattice dynamics in thermoelectric materials and the measurement of the low energetic part of the phonon dispersion in the clathrate $Sr_8Ga_{16}Ge_{30}$ (R. Hermann et al.).

Besides single crystal experiments also neutron diffraction on thin films by polarised and unpolarised neutrons play a major role.

Upgrade IN12-UFO: Presently IN12 is being upgraded with a multi analyser option superior to existing RITA type instruments: UFO (Universal Focusing Option) [1, 2] is a new secondary spectrometer interchangeable with the present set-up: 15 analysers, which can be rotated and positioned individually, and a two-dimensional position sensitive detector will allow to program simultaneous scans in Q-ω-space.
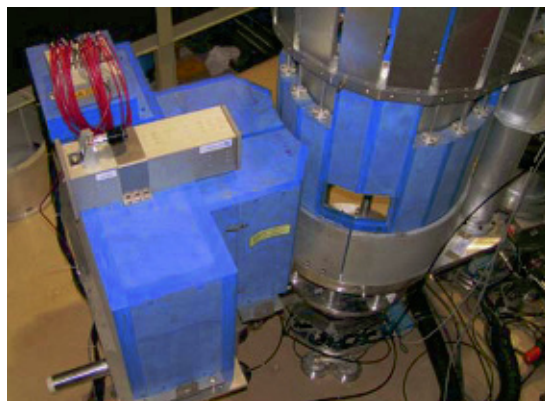
FIG. 1: The new analyser tower with large housing of the position sensitive detector (left) during tests on IN12.

Depending on the requirements the user will be able to define scans, e.g., with a constant energy transfer or scans that map a path along a certain Q-direction. The analysers will be positioned so as to avoid gaps or overlaps as seen from the sample (optimum coverage) while all reflected beams meet at one single focus point on their way to the detector. This focus point is controlled by a movable diaphragm being the only

opening between analyser and detector shielding. In that way a low background will be provided. The detector housing is coupled to the analyser housing via several intermediate pieces of different lengths to accommodate variable detector distances. The whole assembly is shown in Fig. 1.

The detector tubes have an active length of about 60 cm and are mounted horizontally in zig-zag configuration to effectively cover an effective height of about 33 cm, see Fig 2. Each tube is electronically read out as 256 channels while the real physical resolution is about 6 mm. The detector assembly together with its read out electronics has already been successfully tested with neutrons on IN12 using different test samples.
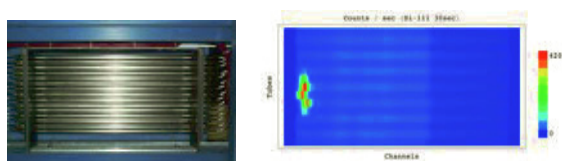
FIG. 2: The 15 position sensitive 3He-tubes of the new detector (left) and raw data from a corresponding shot of a Bragg reflection from a Si crystal (right).

The completion of the electronic control system and its programming is in progress at the ZEL institute. The commissioning of IN12-UFO is planned later in 2009. Then an interface to the standard instrument control program will be implemented as well as routines for scan control and data treatment.

IN12 relocation: Another major project concerns the move of the spectrometer to a new position. In the framework of the ILL Millennium Program IN12 will be relocated within the guide hall ILL7 and will get its own guide with an end position. This allows further improvements and the following key components will be implemented:

- A modern m=2 guide with an optimised ballistic shape and the virtual source concept together with a double focusing monochromator

will provide IN12 with an extended wavelength range of 1.5 - 6.3 Å (now 2.4 - 6 Å). This new design promises an increase of the overall count rate of about an order of magnitude

Additional components are planned to further improve the performance and efficiency of the spectrometer:

- a new monochromator shielding adapted to the requirements of the end position, the higher flux and the larger angular range of the extended wavelength band.

- a velocity selector will eliminate higher order contributions and guarantee a low background.

- a guide changer with cavities and a transmission polariser for an efficient and easy-to-use polarisation of the incident beam.

- a guide changer in front of the monochromator to permit also a collimated beam option (high and tunable Q-resolution) instead of the focusing (high divergence) option - a rare option on many spectrometers but indispensable for many experiments like high pressure studies or UFO (see above).

- optionally a perfectly bent silicon monochromator to focus the beam on small sample volumes.

Extended simulations have already been performed for the design and layout of the various components using different simulation packages (McStas, SimRes). One of the difficulties was to combine a ballistic guide shape with a continuous curvature of the guide, which cannot be avoided due to external restrictions. But with an asymmetric elliptical shape an excellent focusing without sacrifying a smooth divergence profile can be achieved. For the polariser, "v"-shaped polarising tilted plates will be placed into the guide as an interchangeable unit. The calculations taking into account multiple reflections between these plates and the guide walls show a polarisation of around 95%. For an tilt angle of about 0.30° a good transmission for a wide wavelength range can be achieved.

Altogether, with the calculated data for the guide and a matching monochromator a first estimate for the gain compared to the present flux is shown in Fig. 3.
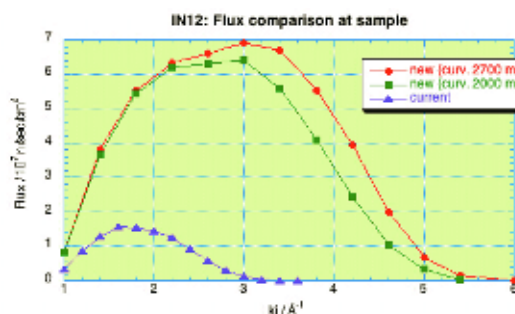
FIG. 3: Flux distribution at the sample position shown for the current set-up (violet) and the proposed new layout. The simulations (SimRes) are plotted for two different guide curvatures. The simulations for the current instrument layout match calibrated monitor measurements.

The new layout promises a huge gain of flux for a much wider range in wavelength as we have today. The planned relocation will therefore be a unique chance to really enhance an already outstanding instrument.

[1] W. Schmidt et al., Physica B **350**, e849 (2004)

[2] W. Schmidt et al., Physica B **385-386**, 1073 (2006)

NSE at SNS: installation approaches completion

M. Ohl[1], N. Arend[1], M. Monkenbusch[1], T. Kozielewski[1], D. Richter[1], M. Butzek[2], Ch. Tiemann[2], R. Achten[2], B. Laatsch[2], H. Soltner[2], U. Pabst[2], B. Lindenau[2], M. Leyendecker[2], H. Stelzer[2], H. Kleines[3], P. Kaemmerling[3], R. Moeller[3], M. Wagener[3], M. Drochner[3]

[1] IFF-5: Neutron Scattering
[2] ZAT: Central Technology Division
[3] ZEL: Central Institute for Electronics

In summer 2008 the bulk of spectrometer components for the NSE at the spallation neutron source (SNS) has been sent to Oak Ridge. The secondary radiation and magnetic shielding enclosure as well as the primary beam path shieldings were ready at that time to allow installation of the proper spectrometer parts. After finishing cabling and connecting to electrical power and other media the initial operation is prepared. Thus that end of 2009 the first genuine NSE experiments may be performed.

Neutron spin-echo spectroscopy (NSE) is the only inelastic neutron scattering technique that significantly overcomes the resolution limit of $\sim 1\mu$eV of the crystal (backscattering) or conventional time-of flight spectrometers. However, NSE is a Fourier method and yields the intermediate scattering function S(Q,t) instead of S(Q,ω), to which it is related by a Fourier transform. An energy transfer resolution of $\hbar\omega=0.7\mu$eV corresponds to a Fourier time of t=1ns, the new NSE spectrometer is designed to reach times of about 1μs i.e. corresponding to a resolution of 0.7neV. This is achieved by a combined utilization of high field integral, J ($>$1Tm) in the precession coils and long neutron wavelength λ; t/ns$\cong 0.2\times$J/(Tm)$\times(\lambda/$Å$)^3$. On the other hand use of short wavelengths in combination with short precession coils, times down to 1ps and will result in a dynamic range of 1:10^6, see Figure 1.
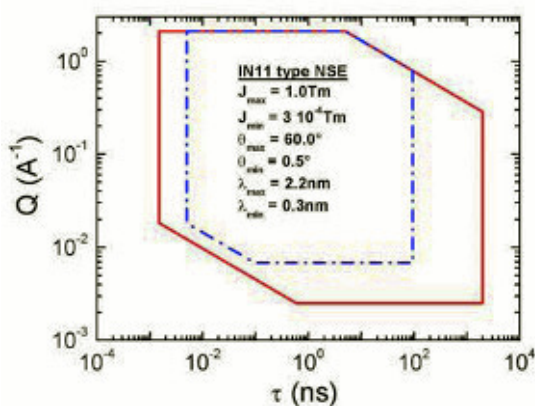
FIG. 1: Expected coverage of (Q,t) range (just for 60° scattering angle).

NSE spectroscopy is especially well suited to iden-tify and measure motions respectively mobility in the nanoscopic domain. That extends from polymer dynamics in the scale between single segments to macromolecules in solution or melts to the internal domain motions of proteins [1]. Neutrons as probe have the unique advantage that by isotopic replacement of H by D in selected substructures of the sample the behaviour of different subsystems can separately be highlighted. Advanced molecular dynamics facilities meanwhile allow for a detailed comparison with NSE experiments [2].

Beside these and further topics in the field of bio-soft matter [3, 4], slow diffusion in general and slow magnetic fluctuations are further fields where NSE spectroscopy is needed to yield a more complete coverage of dynamical processes. Examples from these fields are e.g. the 1D diffusion of alkanes in zeolithes [5] and spin relaxations in colossal magnetoresistive manganites [6].

The NSE instrument at the SNS is located at the beamline BL15 that looks at a cold coupled moderator. The spectrometer uses superconducting main solenoids in order to achieve a large magnetic field integral within the given length limits. The instrument itself is located inside a double wall magnetic mu-metal shield which decouples magnetic noise from the environment from the sensitive neutron flight path regions. An overall (transparent) view of the spectrometer installation is illustrated in Figure 2. The layout of the spectrometer comprises a system of 4 choppers and one of 3 polarizing solid state benders in a remotely controlled revolver to prepare the neutron beam and select the proper wavelength frame. After passing the 4th chopper and a section, where the spins are adiabatically turned from upright to longitudinal direction, the beam then enters a magnetically shielded enclosure that hosts the proper spectrometer. It consists mainly of the two stray field compensated superconducting precession coils and analyzer and a detector. The whole secondary spectrometer can be positioned at different moderator-detector distances between 18m and 27m. The former supplying the largest wavelength frame whereas the latter has the larges scattering angle range (up to 83°).

Figure 4 shows the layout with the spectrometer at the 27m position. Figure 3 shows a step of the chopper installation.

Except for the superconducting coils all major parts
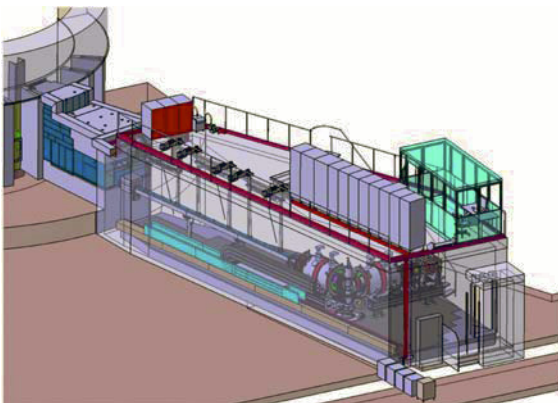
FIG. 2: Schematic view of the assembled spectrometer within its shielding.

are installed and in the final stage of cabling and connecting to the SNS systems. Electrical function tests of single components and subsystems are currently being conducted.

FIG. 3: Chopper installation.

Figure 4 shows the superconducting main solenoids waiting for the final acceptance test at the manufacturer (Babcock). The acceptance test is in february 2009. After delivery these will be installed on the carrier structures that already are installed in the magnetic and shielding enclosure and equipped with a large number of auxiliary coils, analyzer, detector, monitors etc., see Figures 5.
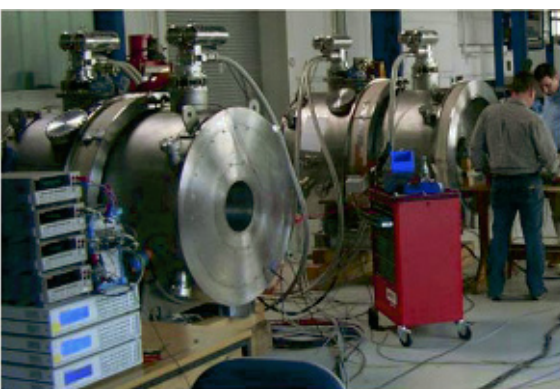
FIG. 4: Test setup of the superconducting coils at the factory.

The sophisticated cabling leading connections to

more than 40 current sources, water, air, signal cables from the top of the enclosure through the magnetic shield to their targets on the carriers such that a smooth moderator distance variation is enabled with connected cables. To remove neutron guide sections (3 times 3m) depending on the selected moderator distance, winches are installed that raise the unused guide sections close to the ceiling of the enclosure. So with the year 2008 the installation phase has started for this spectrometer and approaches completion with the instrument readiness review at the SNS. The considerable progress made until now is best expressed by Figure 5 showing the secondary spectrometer in the mu – metal housing and concentrated commissioning work is going on there.
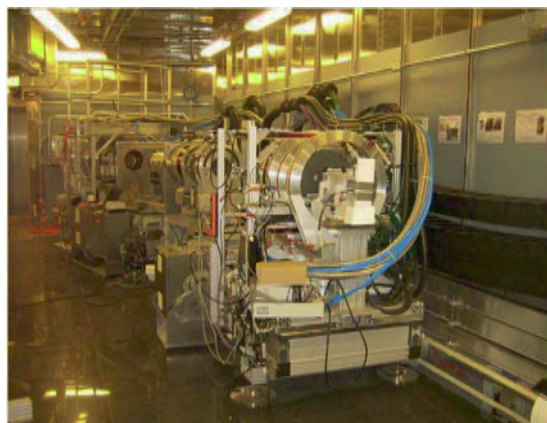
FIG. 5: Carriers and part of the solenoids installed on them during installation inside the magnetic and radiation shielding enclosure. Direction of view is from moderator side towards the person entrance into the chamber. The shiny surface in the upper part is uncovered mu-metal, at the floor the granite tanzboden is seen.

To complete the system integration such that all submodules communicate and work reliably and simultaneously under control of the main operation computer is a current challenge. In this context the instrument readiness review coming soon is an important step after which we will be enabled to start operation with neutrons. During summer the superconducting solenoids will be installed and set into operation.

[1] D. Richter, J. Appl. Cryst. 40, S28 (2007)

[2] W. Paul, GD. Smith, Reports On Progress In Physics 67, 1117 (2004)

[3] Z. Bu, R. Biehl, M. Monkenbusch et al., PNAS 102, 17646 (2005)

[4] R. Biehl, B. Hoffmann, M. Monkenbusch et al., PRL 101, 138102 (2008)

[5] H. Jobic, B. Farago, JCP 129, 171102 (2008)

[6] J. Gutierrez, JM. Barandiaran, J. Bermejo, et al., PRB 76, 184401 (2007)

213

Jülich neutron scattering instruments for the new Chinese research reactor

H. Conrad[1], Th. Brückel[1,2], K. Bussmann[1], S. Mattauch[2], B. Schmitz[1], Z. Wu[3], D. Chen[3]

[1] IFF-4: Scattering Methods
[2] JCNS: Jülich Centre for Neutron Science
[3] Laboratory for Neutron Scattering, China Institute of Atomic Energy, Beijing 102413

Jülich's reputation for developing and applying new techniques in neutron scattering instrumentation as well as the comprehensive instrument suite at the FRJ-2 reactor led to the inquiry of Chinese scientists for acquiring instruments from the reactor after its shut-down. Eventually, the triple axis spectrometer SV30 for magnetic and nuclear inelastic scattering - the last instrument to be built at the FRJ-2 and for which a new location could not be found at FRM II - and the twin-diffractometer SV28 for single-crystal structure analysis were selected. These instruments are just being installed at the recently finished high flux reactor CARR at the China Institute of Atomic Energy (CIAE) in Fang Shan near Beijing. With an expected perturbed thermal neutron flux density of ca. $1 \times 10^{15} \mathrm{cm}^{-2}\mathrm{s}^{-1}$ this reactor will be the second most intense neutron source in the world after the ILL reactor in Grenoble The scientific utilization of both instruments at their new location will be ruled by a cooperation agreement between Jülich, the CIAE and the Chinese Academy of Science (CAS).

The Chinese research reactor CARR [1] is a modern single fuel element high flux reactor. It comprises tangential beam tube thimbles with up to date twin beam ports built into rotary shutters for flexible lateral freedom for instrument positioning. The individual beam port cross sections can be adapted to the special instrument requirements. This is taken advantage of for the spectrometer SV30 [2] requiring a beam port cross section of $9 \times 10 \mathrm{~cm}^2$. The beam port for the diffractometer SV28 is constructed accordingly.

The electronic and mechanical components of the twin-diffractometer SV28 [3] were updated and refurbished, respectively. In particular, the entire electronics was replaced by new components and the physics software adapted to the latest version used at a similar instruments at the Munich reactor. The two Eulerian cradles were mechanically and electrically overhauled and tested.

Since the spectrometer SV30 was finished late in 2005 and operational for less than a year only, there was no need for any refurbishment. The entire electronics is based on SP7 industry standard from the Siemens company with easily available spare parts. Therefore a long service life of the spectrometer is warranted.

FIG. 1: Spectrometer SV30 during disassembling at the FRJ-2 reactor.

FIG. 2: Twin beam port plug for SV30 at the Chinese reactor CARR before insertion into the respective reactor shielding cavern.

214

FIG. 3: Lifting an 8 t monochromator shielding part into one of six 20-feet ocean containers inside the service hall of the FRJ-2 reactor.

In order to transfer the instruments to their new location in China, they had to be dismantled in a qualified manner, stored temporarily and then prepared for shipment. In particular for SV30, the latter had to be done very cautiously, since about 70 tons of less sensitive monochromator shielding components had to go in large ocean shipping containers together with extremely delicate high-tech components like the focusing single crystal monochromators, analyzers and detectors as well as the many electronic racks.
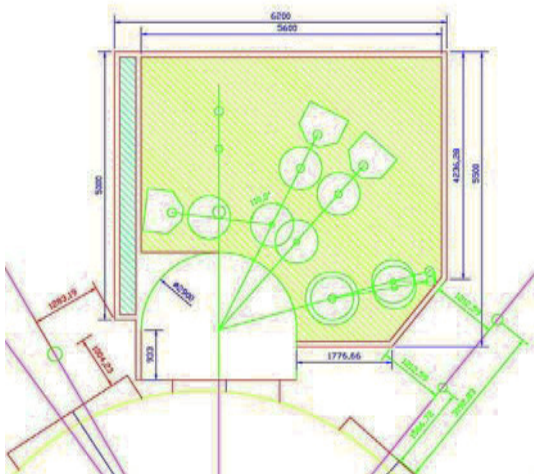
FIG. 4: Floor plan at the SV30 location inside the CARR reactor hall. The extension of the dance floor (hatched area) is 5.5 m by 5.6 m. The semi-circular area close to the polygonal reactor shielding outline corresponds to the SV30 monochromator shielding contour.

The SV30 instrument's most important parts, i.e. both the sample table and the analyzer/detector tower move during operation on air cushions across a high precision polished surface (the so-called dance floor) around the instrument's monochromator shielding (cf. Fig. 4). In order to be able to operate SV30 accordingly, the Chinese engineers had to provide an equally smooth and absolutely horizontal floor. Since there was no experience in China in accomplishing this task, it was necessary to check the quality of the floor during the course of manufacturing it. To this end, a mock-up device resembling the geometry and weight of the analyzer/detector tower (approx. 1.5 t) was built at CARR and successfully tested on the polished granite floor around the SV30 location (Fig. 5). The installation of the instruments is expected to be finished in the second half of 2009.

In order to strengthen the scientific relationship between China and Germany both SV28 and SV30 will be jointly used by CIAE and FZJ with a share of up to 30% each. CIAE will provide access to the instruments for staff members of FZJ and their partners. The rest of the total beam time will be provided free of charge to users through a proposal system. Moreover, both FZJ and CIAE as well as CAS have agreed to cooperate in future developing neutron scattering techniques.

FIG. 5: Dance floor (polished granite floor) around the monochromator shielding area at the SV30 location inside the reactor hall (cf. Fig. 4). The diameter of the mock-up device base plate is 1 m, the load of 1.5 t not shown. The mock-up device is moved on three air pads of exactly the same kind as used with the actual SV30 analyzer/detector tower.

[1] CARR: China Advanced Research Reactor
http://www.ciae.ac.cn

[2] H. Conrad, Th. Brückel, A. Budwig, K. Bussmann, J. Heinen, A. Ioffe, E. Küssel, B. Schmitz, F. Suxdorf and Th. Zeiske. A new thermal triple axis spectrometer at the research reactor FRJ-2. J. Neutron Res. Vol. 16, No. 1, 2008, 1-8.

[3] Neutron diffractometer SV28 in: Neutron scattering experiments at the research reactor in Jülich, Jülich 2003; http://www.fz-juelich.de/iff/wns_sv28

220 students and young scientists from 25 countries and five continents attended the 39th international IFF Spring School "Soft Matter - from Synthetic to Biological Materials". Leading scientists from research and industry gave them a comprehensive overview of the interdisciplinary research field "Soft Matter" at the interface between physics, chemistry, biology and the life sciences. The unique intensive course organized by the IFF took place fom 3 March to 14 March.

Appendix

217

Publications

Akola, J.; Jones, R. O.
Binary alloys of Ge and Te: order, voids, and the eutectic composition
Physical Review Letters, 100 (2008), 205502

Akola, J.; Jones, R. O.
Structural Patterns in Ge/Sb/Te Phase-change Materials
NIC Symposium 2008: proceedings/ed.: G. Münster, D. Wolf, M. Kremer. – Jülich, John von Neumann Institute for Computing, 2008. – (NIC Series; 39). – 978-3-9810842-5-1. – S. 179 – 186

Allgaier, J.
Polymer synthesis
Soft Matter: From Synthetic to Biological Materials: Lecture manuscripts of the 39th Spring School of the Institute of Solid State Research; this spring school was organized by the Institute of Solid State Research in the Forschungszentrum Jülich on March 3 – 14, 2008/ed.: J. K. G. Dhont, G. Gompper, G. Nägele, D. Richter, R. G. Winkler. – Jülich, Forschungszentrum, Zentralbibliothek, 2008.
(Schriften des Forschungszentrums Jülich. Reihe Schlüsseltechnologien/Key Technologies; 1). – 978-3-89336-517-3. – S. A5.1 – A5.12

Allgaier, J.; Frielinghaus, H.
Effects of polymers on the properties of micro emulsion
Microemulsions/ed.: C. Stubenrauch. – Oxford/UK, John Wiley & Sons, 2008. – 1-4051-6782-3. – S. 122 – 145

Andersson, M.; Feuerbacher, M.; Rapp, Ö.
Magnetoresistance and Hall Effect of the complex Metal alloy Mg_2Al_3
Physical Review B, 78 (2008), 024201

Angst, M.; Hermann, R. P.; Christianson, A. D.; Lumsden, M. D.; Lee, C.; Whangbo, M. H.; Kim, J. W.; Ryna, P. J.; Nagler, S. E.; Tian, W.; Jin, R.; Sales, B. C.; Mandrus, D.
Charge order in $LuFe_2O_4$: Ant ferroelectric ground state and coupling to magnetism
Physical Review Letters, 101 (2008), 227601-1-227601-4

Arbe, A.; Genix, A. C.; Colmenero, J.; Richter, D.
Anomalous Relaxation of Self Assembled Alkyl-Nanodomains in higher order Poly (n-Alkyl Metacrylates)
Soft Matter, 4 (2008) 9, 1792 – 1795

Arrott, A. S.; Hertel, R.
Formation and transformation of vortex structures in soft ferromagnetic ellipsoids
Journal of Applied Physics, 103 (2008), 07E739

Atodiresei, N.; Caciuc, V.; Blügel, S.; Hölscher, H.
Manipulation of benzene on Cu(110) by dynamic force microscopy: An ab-initio study
Physical Review B, 77 (2008), 153408

Atodiresei, N.; Caciuc, V.; Franke, J. H.; Blügel, S.
Role of the van der Waals interactions on the bonding mechanism of pyridine on Cu(110) and Ag(110) surfaces: A first-principles study
Physical Review B, 78 (2008), 045411

Atodiresei, N.; Caciuc, V.; Hölscher, H.; Blügel, S.
Ab initio modeling of noncontact atomic force microscopy imaging of benzene on Cu(110) surface
International Journal of Quantum Chemistry, 108 (2008) 15, 2803 – 2812

Atodiresei, N.; Dederichs, P. H.; Mokrousov, Y.; Bergqvist, L.; Bihlmayer, G.; Blügel, S.
Controlling the magnetization direction in molecules via their oxidation state
Physical Review Letters, 100 (2008), 117207

Auriemma, F.; De Rosa, C.; Ricciardi, R.; Lo Celso, F.; Triolo, R.; Pipich, V.
Time-Resolving Analysis of Cryotropic Gelation of Water/Poly(vinyl alcohol) Solutions via Small-Angle Neutron Scattering
Journal of Physical Chemistry B, 112 (2008) 3, 816 – 823

Auth, T.
Statistical Mechanics of Membranes
Soft Matter: From Synthetic to Biological Materials: Lecture manuscripts of the 39th Spring School of the Institute of Solid State Research; this spring school was organized by the Institute of Solid State Research in the Forschungszentrum Jülich on March 3 – 14, 2008/ed.: J. K. G. Dhont, G. Gompper, G. Nägele, D. Richter, R. G. Winkler. - Jülich, Forschungszentrum, Zentralbibliothek, 2008.
– (Schriften des Forschungszentrums Jülich. Reihe Schlüsseltechnologien/Key Technologies; 1). – 978-3-89336-517-3. – S. C5.1 – C5.34

Balanetskyy, S.; Meisterernst, G.; Heggen, M.; Feuerbacher, M.
Reinvestigation of the Al-Mn-Pd alloy system in the T-and R-phases
Intermetallics, 16 (2008), 71 – 87

Balanetskyy, S; Grushko, B.
A study of the high-Al part of the Al-Pd-Re phase diagram
J. Alloys Comp. 456, 105 – 112 (2008)

Balanetskyy, S; Grushko, B.
A study of the Al-rich part of the Al-Re alloy system
J. Alloys Comp. 457, 348-356 (2008)

Banchio, A. J.; McPhie, M. G.; Nägele, G.
Hydrodynamic and electrokinetic effects on the dynamics of charged colloids and macromolecules
Journal of Physics: Condensed Matter, 20 (2008), 404213-1 – 404213-14

Banchio, A. J.; Nägele, G.
Short-time transport properties in dense suspensions: From neutral to charge-stabilized colloidal spheres
Journal of Chemical Physics, 128 (2008), 104903

Bar-Sadan, M.; Houben, L.; Wolf, S. G.; Enyashin, A.; Seifert, G.; Tenne, R.; Urban, K.
Toward Atomic-Scale Bright-Field Electron Tomography for the Study of Fullerene-Like Nanostructures
Nano Letters, 8 (2008), 891 – 896

Barthel, J.; Thust, A.
Quantification of the Information Limit of Transmission Electron Microscopes
Physical Review Letters, Vol. 101, 200801 (2008)

Baumgaertner, A.
Biological Macromolecules
Soft Matter: From Synthetic to Biological Materials: Lecture manuscripts of the 39th Spring School of the Institute of Solid State Research; this spring school was organized by the Institute of Solid State Research in the Forschungszentrum Jülich on March 3-14, 2008/ed.: J. K. G. Dhont, G. Gompper, G. Nägele, D. Richter, R. G. Winkler. - Jülich, Forschungszentrum, Zentralbibliothek, 2008. – (Schriften des Forschungszentrums Jülich. Reihe Schlüsseltechnologien/Key Technologies; 1). – 978-3-89336-517-3. – S. C7.1 – C7-16

Baumgaertner, A.
Concepts in Bionanomachines: Translocators
Journal of Computational and Theoretical Nanoscience: for all Theoretical and Computational Aspects in Science, Engineering, and Biology, 5 (2008) 9, 1852 – 1890

Biehl, R.; Hoffmann, B.; Monkenbusch, M.; Falus, P.; Préost, S.; Merkel, R.; Richter, D.
Direct Observation of Correlated Interdomain Motion in Alcohol Dehydrogenase
Physical Review Letters, 101 (2008), 138102-1 – 138102-4

Birczynski, A.; Ylinen, E. E.; Punkkinen, M.; Prager, M.; Szymocha, A. M.; Lalowicz, Z. T.
Deuteron NMR relaxation, spectra, and evidence for the order-disorder phase transition in $(ND_4)_2PtCl_6$
Journal of Chemical Physics, 128 (2008), 184510

Blanco, P.; Polyakov, P.; Bou-Ali, M.; Wiegand, S.
Thermal diffusion values for some alkane mixtures: A comparison between thermo-gravitational column and thermal diffusion forced Rayleigh scattering
Thermal Nonequilibrium: Lecture Notes of the 8th International Meeting on Thermodiffusion/ed.: S. Wiegand, W. Köhler, J. K. G. Dhont. – Jülich, Forschungszentrum, Zentralbibliothek, 2008. – (Schriften des Forschungszentrums Jülich. Reihe Schlüsseltechnologien/Key Technologies; 3). – 978-3-89336-523-4. – S. 15 – 22

Blanco, P.; Polyakov, P.; Bou-Ali, M.; Wiegand, S.
Thermal diffusion and molecular diffusion values for some alkane mixtures: a comparison between thermogravitational column and thermal diffusion forced Rayleigh scattering
Journal of Physical Chemistry B, 112 (2008) 28, 8340 – 8345

Bodnarchuk, V. I.; Kraan, W. H.; Rekveldt, M. T.; Ioffe, A.
Neutron spin turners with a rotating magnetic field: first experiments
Measurement Science and Technology, 19 (2008), 034012

Bosak, A.; Schmalzl, K.; Krisch, M.; van Beek, W.; Kolobanov, V.
Lattice dynamics of beryllium oxide: Inelastic X-ray scattering and ab initio calculations
Physical Review B, 77 (2008), 224303-1 – 224303-7

Bóta, A.; Varga, Z.; Goerigk, G.
Structural description of the nickel part of a raney-type catalyst by using anomalous small-angle X-ray scattering
Journal of Physical Chemistry C, 112 (2008) 12, 4427 – 4429

Brener, E. A.; Temkin, D.
Steady-state migration of the liquid film along a grain boundary during melting of alloys
Acta Materialia, 56 (2008), 2290

Brückel, T.
A neutron primer: Elastic scattering and the properties of the neutron
Neutron Scattering: Lectures of the JCNS Laboratory Course held at Forschungszentrum Jülich and the research reactor FRM II of TU Munich; in cooperation with RWTH Aachen and University of Münster/ed.: T. Brückel, G. Heger, D. Richter, R. Zorn. – Jülich, Forschungszentrum, Zentralbibliothek, 2008. – (Schriften des Forschungszentrum Jülich. Reihe Schlüsseltechnologien/Key Technologies; 5). – 978-3-89336-532-6. – S. 2-1 – 2-31

Brückel, T.
Applications of neutron scattering
Neutron Scattering: Lectures of the JCNS Laboratory Course held at Forschungszentrum Jülich and the research reactor FRM II of TU Munich; in cooperation with RWTH Aachen and University of Münster/ed.: T. Brückel, G. Heger, D. Richter, R. Zorn. – Jülich, Forschungszentrum, Zentralbibliothek, 2008. – (Schriften des Forschungszentrum Jülich. Reihe Schlüsseltechnologien/Key Technologies; 5). – 978-3-89336-532-6. – S. 6-1 – 6-27

Brückel, T.
Correlated electrons in complex transition metal oxides
Neutron Scattering: Lectures of the JCNS Laboratory Course held at Forschungszentrum Jülich and the research reactor FRM II of TU Munich; in cooperation with RWTH Aachen and University of Münster/ed.: T. Brückel, G. Heger, D. Richter, R. Zorn. – Jülich, Forschungszentrum, Zentralbibliothek, 2008. - (Schriften des Forschungszentrum Jülich. Reihe Schlüsseltechnologien/Key Technologies; 5). – 978-3-89336-532-6. – S. 15-1 – 15-20

Brückel, T. (Hrsg.); Heger, G. (Hrsg.); Richter, D. (Hrsg.); Zorn, R. (Hrsg.)
Neutron Scattering: Lectures of the JCNS Laboratory Course held at Forschungszentrum Jülich and the research reactor FRM II of TU Munich; in cooperation with RWTH Aachen and University of Münster
Jülich, Forschungszentrum, Zentralbibliothek, 2008
Schriften des Forschungszentrums Jülich. Reihe Schlüsseltechnologien/Key Technologies; 5

Buchal, C.; Bürgler, D. E.
Peter Grünberg – Nobelpreis für Physik 2007
Köln, MIC GmbH, 2008

Buitenhuis, J.
Colloid Synthesis
Soft Matter: From Synthetic to Biological Materials: Lecture manuscripts of the 39th Spring School of the Institute of Solid State Research; this spring school was organized by the Institute of Solid State Research in the Forschungszentrum Jülich on March 3-14, 2008/ed.: J. K. G. Dhont, G. Gompper, G. Nägele, D. Richter, R. G. Winkler. - Jülich, Forschungszentrum, Zentralbibliothek, 2008. – (Schriften des Forschungszentrums Jülich. Reihe Schlüsseltechnologien/Key Technologies; 1). – 978-3-89336-517-3. – S. A6.1 – A6.16

Bulla, R.; Costi, T. A.; Pruschke, T.
Numerical renormalization group method for quantum impurity systems
Reviews of Modern Physics, 80 (2008), 395

Buscaglia, M. T.; Buscaglia, V.; Viviani, M.; Dondero, G.; Röhrig, S.; Rüdiger, A.; Nanni, P.
Ferroelectric hollow particles obtained by solid-state reaction
Nanotechnology, 19 (2008), 225602

Butz, B.; Störmer, H.; Gerthsen, D.; Bockmeyer, M.; Krüger, R.; Ivers-Tiffée, E.; Luysberg, M.
Microstructure of Nanocrystalline Yttria-Doped Zirconia thin films obtained by sol-gel processing
J. Am. Ceram. Soc, Vol. 91, No. 1-9, 2281-2289 (2008)

Camley, R.E.; McGrath, B. V.; Khivintsev, Y.; Celinski, Z.; Adam, R.; Schneider, C. M.; Grimsditch, M.
The effect of cell size in calculating frequencies of magnetic modes using micromagnetics: The special role of the uniform mode
Physical Review B, 78 (2008), 024425

Cannavacciuolo, L.; Winkler, R. G.; Gompper, G.
Mesoscale simulations of polymer dynamics in microchannel flows
Europhysics Letters, 83 (2008), 34007-1 - 34007-6

Chatterjee, S.; Barma, M.
Shock probes in a one dimensional Katz-Lebowitz-Spohn Model
Physical Review E, 77 (2008), 061124-1 – 061124-8

Chatterji, T.; Henry, P. F.; Mittal, R.; Chaplot, S. L.
Negative thermal expansion of ReO_3: Neutron diffraction experiments and dynamical lattice calculations
Physical Review B, 78 (2008), 134105-1 – 134105-6

Chatterji, T.; Schneider, G. J.; Galera, R. M.
Low-energy nuclear spin excitations in $NdMg_3$ and $NdCo_2$
Physical Review B, 78 (2008), 012411

Chen, H. Y.; Jia, C. L.; Schubert, J.
Microstructure of high-k dielectric $LaLuO_3$ films on (001) $SrTiO_3$ Substrates
Thin Solid Films, 517 (2008), 631 – 634

Chen, J.; Jung, P.; Hoffelner, W.; Ullmaier, H.
Dislocation loops and bubbles in oxide dispersion strengthened ferritic steel after helium implantation under stress
Acta Materialia, 56 (2008), 250 – 258

Chen, J.; Jung, P.; Pouchon, M. A.; Rebac, T.; Hoffelner, W.
Irradiation creep and precipitation in a ferritic ODS steel under helium implantation
Journal of Nuclear Materials, 373 (2008), 22 – 27

Cherstvy, A. G.
DNA Cholesteric Phases: The Role of DNA Molecular Chirality and DNA-DNA Electrostatic Interactions
Journal of Physical Chemistry B, 112 (2008), 12585 – 12595

Cherstvy, A.; Kolomeisky, A. B.; Kornyshev, A. A.
Protein - DNA interactions: Reaching and Recognizing the Targets
Journal of Physical Chemistry B, 112 (2008), 4741 – 4750

Clemens, S.; Dippel, A. C.; Schneller, T.; Waser, R.; Rüdiger, A.; Röhrig, S.
Direct electrical characterization of embedded ferroelectric lead titanate nanoislands
Journal of Applied Physics, 103 (2008), 034113

Conrad, H.; Brückel, T.; Schäfer, W.; Voigt, J.
POWTEX – the high-intensity time-of-flight diffractometer at FRM II for structure analysis of polycrystalline materials
Journal of Applied Crystallography, 41 (2008), 836 – 845

Dasgupta, A.; Huang, Y.; Houben, L.; Klein, S.; Finger, F.; Carius, R.; Luysberg, M.
Effect of filament and substrate temperatures on the structural and electrical properties of SiC thin films grown by the HWCVD technique
Thin Solid Films, Vol. 516, 622-625 (2008)

Dasgupta, A.; Klein, S.; Houben, R.; Carius, R.; Finger, F.; Luysberg, M.
Microstructure of highly cristallyne silicon carbide thin films grown by HWCVD technique
Thin Solid Films, Vol. 516, 618-621 (2008)

Datta, S.; Ning, H.; Sottmann, T.; Wiegand, S.
Soret effect of nonionic surfactants in water studied by different transient grating setups
Thermal Nonequilibrium: Lecture Notes of the 8th International Meeting on Thermodiffusion/ed.: S. Wiegand, W. Köhler, J. K. G. Dhont. - Jülich, Forschungszentrum, Zentralbibliothek, 2008. – (Schriften des Forschungszentrums Jülich. Reihe Schlüsseltechnologien/Key Technologies; 3). – 978-3-89336-523-4. – S. 147 – 152

Delcea, M.; Krastev, R.; Gutberlet, T.; Pum, D.; Sleytr, U. B.; Toca-Herrera, J. L.
Thermal stability, mechanical properties and water content of bacterial protein layers recrystallized on polyelectrolyte multi-layers
Soft Matter, 4 (2008), 1414 – 1421

Dhont, J. K. G.
Dynamics of Colloids
Soft Matter: From Synthetic to Biological Materials: Lecture manuscripts of the 39th Spring School of the Institute of Solid State Research; this spring school was organized by the Institute of Solid State Research in the Forschungszentrum Jülich on March 3 – 14, 2008/ed.: J. K. G. Dhont, G. Gompper, G. Nägele, D. Richter, R. G. Winkler. – Jülich, Forschungszentrum, Zentralbibliothek, 2008. – (Schriften des Forschungszentrums Jülich. Reihe Schlüsseltechnologien/Key Technologies; 1). – 978-3-89336-517-3. – S. B3.1 – B3.40

Dhont, J. K. G.; Briels, W. J.
Gradient and vorticity banding
Rheologica Acta, 47 (2008), 257 – 281

Dhont, J. K. G.; Briels, W. J.
Single-particle thermal diffusion of charged colloids: double-layer theory in a temperature gradient
Thermal Nonequilibrium: Lecture Notes of the 8th International Meeting on Thermodiffusion/ed.: S. Wiegand, W. Köhler, J. K. G. Dhont. – Jülich, Forschungszentrum, Zentralbibliothek, 2008. – (Schriften des Forschungszentrums Jülich. Reihe Schlüsseltech-nologien/Key Technologies; 3). – 978-3-89336-523-4. – S. 257 – 260

Dhont, J. K. G.; Briels, W. J.
Single-particle thermal diffusion of charged colloids: Double-layer theory in a temperature gradient
European Physical Journal E, 25 (2008), 61 – 76

220

Dhont, J. K. G.; Gompper, G.
Introduction: Soft Matter
Soft Matter: From Synthetic to Biological Materials: Lecture manuscripts of the 39th Spring School of the Institute of Solid State Research; this spring school was organized by the Institute of Solid State Research in the Forschungszentrum Jülich on March 3 – 14, 2008/ed.: J. K. G. Dhont, G. Gompper, G. Nägele, D. Richter, R. G. Winkler. – Jülich, Forschungszentrum, Zentralbibliothek, 2008. – (Schriften des Forschungszentrums Jülich. Reihe Schlüsseltechnologien/Key Technologies; 1). – 978-3-89336-517-3. – S. I.1 – I.18

Dhont, J. K. G. (Hrsg.); Gompper, G. (Hrsg.); Nägele, G. (Hrsg.); Richter, D. (Hrsg.); Winkler, R. G. (Hrsg.)
Soft Matter - From Synthetic to Biological Materials:
Lecture Notes of the 39th Spring School 2008; This Spring School was organized by the Institute of Solid State Research in the Research Centre Jülich on 3 – 14 March, 2008
Jülich, Forschungszentrum, Zentralbibliothek, 2008
Schriften des Forschungszentrums Jülich. Reihe Schlüsseltechnologien/Key Technologies; 1
9783893365173

Dietrich, C.; Hertel, R.; Huber, M.; Weiss, D.; Schäfer, R.; Zweck, J.
Influence of perpendicular magnetic fields on the domain structure of Permalloy microstructures grown on thin membranes
Physical Review B, 77 (2008), 174427

Dil, H.; Meier, F.; Lobo-Checa, J.; Patthey, L.; Bihlmayer, G.; Osterwalder, J.
Rashba-Type Spin-Orbit Splitting of Quantum Well States in Ultrathin Pb Films
Physical Review Letters, 101 (2008), 266802

Dippel, A. C.; Schneller, T.; Waser, R.
Thin films of undoped lead titanate: Morphology and electrical properties
Integrated Ferroelectrics, 98 (2008), 3 – 10

Disch, S.; Cheetham, A. K.; Ruschewitz, U.
Formation of unsaturated C_3 hydrocarbons by the protolysis of magnesium sesquicarbide with ammonium halides
Inorganic Chemistry, 47 (2008), 969 – 973

Divin, Y.; Poppe, U.; Gubankov, V.; Urban, K.
High-Tc Josephson Square-Law Detectores and Hilbert Spectroscopy for Security Applications
IEEE Sensors Journal, 8 (2008), 750 – 757

Divin, Y., Poppe, U., Gubankov, V., Urban, K.
Hilbert spectroscopy of liquids for security screening to be published in nato science series: Detection of liquid explosives and flammable agents in connection with terrorist actions
Ed. H. Schubert; A. Kuznetsov, Springer, (2008)

Divin, Y., Poppe, U., Kotelyanskii, I. M., Gubankov, V.N., Urban, K.
Terahertz spectroscopy based on Josephson high-temperature superconductor junctions
J. Comm. Techn. Electronics, Vol. 53, No. 10, 1137-1152 (2008)

Divin, Y.; Poppe, U.; Urban, K.
Hilbert Spectroscopy of Liquids for Security Screening Detection of Liquid Explosives and Flammable Agents in Connection with Terrorist Actions
Detection of Liquid Explosives and Flammable Agents in Connection with Terrorism/ed.: H. Schubert, A. Kuznetsov. – Springer, 2008. – (NATO Science for Peace and Security Series). – 978-1-4020-8465-2. – S. 189 – 204

Dolinsek, J.; Slavonek, J.; Jaglicic, Z.; Heggen, M.; Balanetskyy, S.; Feuerbacher, M.; Urban, K.
Broken ergodicity, memory effect and rejuvenation in Taylor-phase and decagonal Al_3Mn, Pd, Fe complex intermetallics
Physical Review B, 77 (2008), 064430

Dolfen, A.; Koch, E.
Realistic description of TTF-TCNQ – a strongly correlated organic metal
NIC Symposium 2008/ed.: G. Münster, D. Wolf, M. Kremer. – Jülich, NIC, 2008. – (NIC series; 39). – 978-3-9810843-5-1. – S. 237

Dolfen, A.; Luo, Y. L.; Koch, E.
Simulating materials with strong correlations on Blue Gene/L
Parallel Computing: Architectures, Algorithms and Applications/ed.: C. Bischof, M. Bücker, P. Gibbon, G. Joubert, T. Lippert, B. Mohr, F. Peters. – Amsterdam, IOS Press, 2008. – (Advances in Parallel Computing; 15). – 978-1-58603-796-3. – S. 601

Ehlers, G.; Mamontov, E.; Zamponi, M.; Faraone, A.; Qiu, Y.; Cornelius, A. L.; Booth, C. H.; Kam, K. C.; LeToquin, R.; Cheetham, A. K.; Gardner, J. S.
Frustrated spin correlations in diluted spin ice
$Ho_{2-x} La_x Ti_2 O_7$
Journal of Physics: Condensed Matter, 20 (2008), 235206

Elefant, D.; Schäfer, R.; Thomas, J.; Schneider, C. M.
Spin-flip and spin-flop magnetic configuration in NiFe/Cu multilayers and related changes in magnetoresistance, magnetization, and domain structures
Physical Review B, 77 (2008), 014426

Elefant, D.; Schäfer, R.; Thomas, J.; Vinzelberg, H.; Schneider, C. M.
Competition of spin-flip and spin-flop dominated processes in magnetic multilayers: Magnetization reversal, magnetotransport, and domain structure in the NiFe/Cu system
Physical Review B, 77 (2008), 014426

Elgeti, J.; Gompper, G.
Hydrodynamics of Active Mesoscopic Systems
NIC Symposium 2008/ed.: G. Münster, D. Wolf, M. Kremer. – Jülich, Forschungszentrum, John von Neumann Institut für Computing, 2008. – (NIC Series ; 39). – 978-3-9810843-5-1. – S. 53 – 62

Ellerkmann, U.; Schneller, T.; Nauenheim, C.; Böttger, U.; Waser, R.
Reduction of film thickness for chemical solution deposited $PbZr_{0.3}Ti_{0.7}O_3$ thin films revealing no size effects and maintaining high remanent polarization and low coercive field
Thin Solid Films, 516 (2008) 15, 4713 – 4719

Faley, M. I.; Mi, S. B.; Jia, C. L.; Poppe, U.; Urban, K.; Fagaly, R. L.
Epitaxial thick film high-Tc SQUIDs
Journal of Physics: Conference Series, 97 (2008), P. 012164

Ferriani, P.; von Bergmann, K.; Vedmedenko, E. Y.; Heinze, S.; Bode, M.; Heide, M.; Bihlmayer, G.; Blügel, S.; Wiesendanger, R.
Atomic-Scale Spin Spiral with a Unique Rotational Sense: Mn Monolayer on W(001)
Physical Review Letters, 101 (2008), 027201

Feuerbacher, M.; Balanetskyy, S.; Heggen, M.
Novel Metadislocation Variants in Orthorhombic Al-Pd-Fe
Acta Materialia, 56 (2008), 1849

221

Feuerbacher, M.; Thomas, C.; Roitsch, S.
Single-crystal growth of the complex metallic alloy phase $Mg_{32}(Al,Zn)_{49}$
Intermetallics, 16 (2008), 943 – 947

Finken, R.; Lamura, A.; Seifert, U.; Gompper, G.
Two-dimensional fluctuating vesicles in linear shear flow
European Physical Journal E, 25 (2008), 309 – 321

Fleer, G. J.; Tuinier, R.
Analytical phase diagrams for colloids and non-adsorbing polymer
Advances in Colloid and Interface Science, 143 (2008), 1 – 47

Fleer, G. J.; Tuinier, R.
Conditions for the existence of a stable colloidal liquid
Highlights in Colloid Science/ed.: D. Platikanov, D. Exerowa. – Weinheim, Wiley-VCH, 2008. – S. 119 – 134

Flocke, A.; Noll, T. G.; Kügeler, C.; Nauenheim, C.; Waser, R.
A fundamental analysis of nano-crossbars with non-linear switching materials and its impact on TiO_2 as a resistive layer
Proceedings of the 8th IEEE Conference on Nanotechnology. – 2008. – S. 319 – 322

Foster, L. J.; Schwahn, D.; Pipich, V.; Holden, P. J.; Richter, D.
SANS characterization of polyhydroxyalkanoates and their PEgylated hybrids in solution
Biomacromolecules, 9 (2008), 314 – 320

Frank, C.; Frielinghaus, H.; Allgaier, J.; Richter, D.
Hydrophilic Alcohol Ethoxylates as Efficiency booster for Microemulsions
Langmuir, 24 (2008), 6036

Frank, S.; Winkler, R. G.
Polyelectrolyte electrophoresis: Field effects and hydrodynamic interactions
Europhysics Letters, 83 (2008), 38004

Freimuth, F.; Mokrousov, Y.; Wortmann, D.; Heinze, S.; Blügel, S.
Maximally localized Wannier functions within the FLAPW formalism
Physical Review B, 78 (2008), 035120

Freysoldt, C.; Eggert, P.; Rinke, P.; Schindlmayr, A.; Scheffler, M.
Screening in two dimensions: GW calculations for surfaces and thin films using the repeated-slab approach
Physical Review B, 77 (2008), 235428

Frielinghaus, H.
Conformations of polymer chains
Soft Matter: From Synthetic to Biological Materials: Lecture manuscripts of the 39th Spring School of the Institute of Solid State Research; this spring school was organized by the Institute of Solid State Research in the Forschungszentrum Jülich on March 3-14, 2008/ed.: J. K. G. Dhont, G. Gompper, G. Nägele, D. Richter, R. G. Winkler. – Jülich, Forschungszentrum, Zentral-bibliothek, 2008. – (Schriften des Forschungszentrums Jülich. Reihe Schlüsseltechnologien/Key Technologies; 1). – 978-3-89336-517-3. – S. C1.1 – C1.23

Fu, Q. X.; Mi, S. B.; Wessel, E.; Tietz, F.
Microstructure and Electrical Conductivity of Yttrium-Substituted $SrTiO_3$: Influence of Starting Composition and Sintering Atmosphere
Journal of the European Ceramic Society, 28 (2008), 811 – 820

Galanakis, I.; Özdogan, K.; Sasioglu, E.
Ab initio electronic and magnetic properties of half-metallic NiCrSi and NiMnSi Heusler alloys: The role of defects and interfaces
Journal of Applied Physics, 104 (2008), 083916

Galanakis, I.; Özdogan, K.; Sasioglu, E.
Role of defects and disorder in the half-metallic full-Heusler compounds
Advances in Nanoscale Magnetism: Proceedings of the International Conference on Nanoscale Magnetism/ed.: B. Aktas, F. Mikailov. – Springer, 2008. – (Springer Proceedings in Physics; 122). – S. 1 – 19

Galanakis, I.; Özdogan, K.; Sasioglu, E.; Aktas, B.
Ferrimagnetism and antiferro-magnetism in half-metallic Heusler alloys
Physica Status Solidi A, 205 (2008), 1036 – 1039

Galanakis, I.; Sasioglu, E.; Özdogan, K.
Magnetic phase transition in half-metallic CoMnSb and NiMnSb semi-Heusler alloys upon Cu doping: First-principles calculations
Physical Review B, 77 (2008), 214417

Garbrecht, M.; Spieker, E.; Jäger, W.; Tillmann, K.
Aberration-corrected HRTEM study of incommensurate misfit layer compound interfaces
Instrumentation and Methods: Proceedings of the 14th European Microscopy Congress, held in Aachen, Germany, 1 – 5 September 2008; jointly organised by the European Microscopy Society (EMS), the German Society for Electron Microscopy (DGE) and the local microscopists from RWTH Aachen University and the Research Centre Jülich/ed.: M. Luysberg, K. Tillmann, P. Weirich. – Berlin, Springer, 2008. – (EMC 2008; 1). – 978-3-540-85154-7. – S. 113 – 114

Genix, A. C.; Arbe, A.; Arres-Igor, S.; Colmenero, J.; Richter, D.; Frick, B.; Deen, P.
Neutron scattering and dielectric investigation of a dilute blend of poly(ethyleneoxide) in polyethersulfone
Journal of Chemical Physics, 128 (2008), 184901

Gilles, S.; Meier, M.; Prömpers, M.; von Hart, A.; Kügeler, C.; Offenhäusser, A.; Mayer, D.
UV nanoimprint lithography with rigid polymer molds
Proceedings of the 34th International Conference on Micro & Nano Engineering, September 15 – 19, 2008, Athens, Greece. – 2008. – S. 417 – 418

Gliga, S.; Hertel, R.; Schneider, C. M.
Flipping magnetic vortex cores on the picosecond time scale
Physica B: Condensed Matter, 403 (2008) 2/3, 334 – 337

Gliga, S.; Hertel, R.; Schneider, C. M.
Switching a magnetic antivortex core with ultrafast field pulses
Journal of Applied Physics, 103 (2008), 07B115

Gliga, S.; Yan, M.; Hertel, R.; Schneider, C. M.
Ultrafast dynamics of a magnetic antivortex – Micromagnetic simulations
Physical Review B, 77 (2008), 060404(R)

Gögelein, C.; Nägele, G.; Tuinier, R.; Gibaud, T.; Stradner, A.; Schurtenberger, P.
A simple patchy colloid model for the phase behavior of lysozyme dispersions
Journal of Chemical Physics, 129 (2008), 085102

Gögelein, C.; Tuinier, R.
Phase behaviour of a dispersion of charge-stabilised colloidal spheres with added non-adsorbing interacting polymer chains
European Physical Journal E, 27 (2008), 171 – 184

222

Goerigk, G.
Decomposition kinetics in copper-cobalt alloys systems: Applications of small-angle X-ray scattering
Neutrons and Synchrotron Radiation in Engineering Materials Science/ed.: W. Reimers, A.-R. Pyzalla, A. Schreyer, H. Clemens.– Weinheim, Wiley-VCH, 2008. – S. 249 – 256

Goldman, A. I.; Argyriou, D. N.; Ouladdiaf, B.; Chatterji, T.; Kreyssig, A.; Nandi, S.; Ni, N.; Bud'ko, S. L.; Canfield, P. C.; McQueeney, R. J.
Lattice and magnetic instabilities in $CaFe_2As_2$: A single crystal neutron diffraction study
Physical Review B, 78 (2008), 100506(R)

Gompper, G.; Dhont, J. K. G.; Richter, D.
Editorial: A unified view of soft matter systems?
European Physical Journal E, 26 (2008), 1 – 2

Gompper, G.; Noguchi, H.
Blood Flow
Soft Matter: From Synthetic to Biological Materials: Lecture manuscripts of the 39th Spring School of the Institute of Solid State Research; this spring school was organized by the Institute of Solid State Research in the Forschungszentrum Jülich on March 3 – 14, 2008/ed.: J. K. G. Dhont, G. Gompper, G. Nägele, D. Richter, R. G. Winkler. - Jülich, Forschungszentrum, Zentralbibliothek, 2008. - (Schriften des Forschungszentrums Jülich. Reihe Schlüsseltechnologien/Key Technologies; 1). – 978-3-89336-517-3. – S. D7.1 – D7.23

Gordan, O. D.; Persson, B. N. J.; Cesa, C. M.; Mayer, D.; Hoffmann, B.; Dieluweit, S.; Merkel, R.
On Pattern Transfer in Replica Molding
Langmuir, 24 (2008), 6636 – 6639

Gossuin, Y.; Hocq, A.; Vuong, Q. L.; Disch, S.; Hermann, R. P.; Gillis, P.
Physico-chemical and NMR relaxometric characterization of gadolinium hydroxide and dysprosium oxide nanoparticles
Nanotechnology, 19 (2008), 475102-1 – 475102-8

Gray, D. L.; Long, G. J.; Grandjean, F.; Hermann, R. P.; Ibers, J. A.
Syntheses, Structure, and a Mössbauer and Magnetic Study of $Ba_4Fe_2I_5S_4$
Inorganic Chemistry, 47 (2008) 1, 94 – 100

Grelet, E.; Lettinga, M. P.; Bier, M.; van Roij, R.; van der Schoot, P.
Dynamical and structural insights into the smectic phase of rod-like particles
Journal of Physics: Condensed Matter, 20 (2008), 494213

Großkinsky, S.; Schütz, G. M.
Discontinuous Condensation Transition and Nonequivalence of Ensembles in a Zero-Range Process
Journal of Statistical Physics, 132 (2008), 77 – 108

Grosskinsky, S.; Chleboun, P.; Schütz, G. M.
Instability of condensation in the zero-range process with random interaction
Physical Review E, 78 (2008) 3, 030101

Grünberg, P.
It's the coupling that creates resistance: Spin electronics in layered magnetic structures
Annalen der Physik, 17 (2008) 1, 17

Grünberg, P.
Nobel Lecture: From spin waves to giant magnetoresistance and beyond
Reviews of Modern Physics, 80 (2008), 1531

Grushko, B.; Balanetskyy, S.
A study phase equilibria in the Al-rich part of the Al-Mn alloy system
Int. J. Mater. 99, 1319-1323 (2008)

Grushko, B.; Pavlyuchkov D.
X-ray powder diffraction data for Al-Cu-Ir Ω and C_2 phases of
Powder diffraction 23, 356-359 (2008)

Grushko, B.; Przepiórzyñski B.; Pavlyuchkov, D.
On the constitution of the high-Al region of the Al-Cr alloy system
J. Alloys Comp. 453, 191-196

Grushko, B.; Przepiórzyñski B.; Pavlychukov, D.
On the constitution of the high-Al region of the Al-Cr alloy system
J. Alloys Comp. 454, 214-220 (2008)

Grushko, B.; Kowalski, W.; Pavlyuchkov, D.; Przepiórzyñski B.; Surowiec, M.
A contribution to the Al-Ni-Cr phase diagram
J. Alloys Comp. 460, 299-304 (2008)

Grushko, B.; Kowalski, W.; Przepiórzyñski B.; Pavlyuchkov, D.
Constitution of the high-Al region of Al-Cu-Rh
J. Alloys Comp 464, 227-233 (2008)

Grushko, B.; Balanetskyy, S.
X-ray powder diffraction data for $Al_{73.5}Ni_{18.5}Re_8$ orthorhombic phase
Powder diffraction. 23, 251-254 (2008)

Gugenberger, C.; Spatschek, R.; Kassner, K.
Comparison of phase-field models for surface diffusion
Physical Review E, 78 (2008), 016703

Guo, X.
Nanostructured ionic and mixed conducting oxides
Annual Review of Nano Research/ed.: C. J. Brinker, G. Cao. – 3 (2008). – Singapore, World Scientific Publishing. – S. 495 – 543

Gupta, M.; Gupta, A.; Stahn, J.; Gutberlet, T.
Ordering and self-diffusion in FePt alloy film
New Journal of Physics, 10 (2008), 053031

Halder, S.; Schneller, T.; Waser, R.; Majumber, S. B.
Electrical and optical properties of chemical solution deposited barium hafnate titanate thin films
Thin Solid Films, 516 (2008) 15, 4970 – 4976

Harish, R.; Karevski, D.; Schütz, G. M.
Molecular traffic control for a cracking reaction
Journal of Catalysis, 253 (2008), 191 – 199

Heggen, M.; Engel, M.; Balanetskyy, S.; Trebin, H. R.; Feuerbacher, M.
Structural variations in Epsilon-type Al-Pd-(Mn, Fe) complex metallic alloy phases
Philosophical Magazine, 88 (2008), 507 – 521

Heggen, M.; Feuerbacher, M.
Quasicrystal plasticity in the framework of a constitutive model: Interaction of the microstructural parameters at high strain-rates
Philosophical Magazine, 88 (2008), 2325

Heggen, M.; Houben, L.; Feuerbacher, M.
Metadislocations in the orthorhombic structurally complex alloy $Al_{13}Co_4$
Philosophical Magazine, 88 (2008), 2333

223

Heide, M.; Bihlmayer, G.; Blügel, S.
Dzyaloshinskii-Moriya interaction accounting for the orientation of magnetic domains in ultrathin films: Fe/W(110)
Physical Review B, 78 (2008), 140403(R)

Helmes, R. W.; Costi, T. A.; Rosch, A.
Kondo Proximity Effect: How does a Metal penetrate into a Mott Insulator?
Physical Review Letters, 101 (2008), 066802

Helmes, R. W.; Costi, T. A.; Rosch, A.
Mott transition of fermionic atoms in a three-dimensional optical trap
Physical Review Letters, 100 (2008), 056403

Hermann, R.
Scattering of Neutrons & Photons
Soft Matter: From Synthetic to Biological Materials: Lecture manuscripts of the 39th Spring School of the Institute of Solid State Research; this spring school was organized by the Institute of Solid State Research in the Forschungszentrum Jülich on March 3 – 14, 2008/ed.: J. K. G. Dhont, G. Gompper, G. Nägele, D. Richter, R. G. Winkler. – Jülich,
Forschungszentrum, Zentralbibliothek, 2008. – (Schriften des Forschungszentrums Jülich. Reihe Schlüsseltechnologien/Key Technologies; 1). – 978-3-89336-517-3. – S. A1.1 – A1.30

Hirahara, T.; Komorida, T.; Sato, A.; Bihlmayer, G.; Chulkov, E. V.; He, K.; Matsuda, I.; Hasegawa, S.
Manipulating quantum-well states by surface alloying: Pb on ultrathin Ag films
Physical Review B, 78 (2008), 035408

Hirahara, T.; Miyamoto, K.; Kimura, A.; Niinuma, Y.; Bihlmayer, G.; Chulkov, E. V.; Nagao, T.; Matsuda, I.; Qiao, S.; Shimada, K.; Namatame, H.; Taniguchi, M.; Hasegawa, S.
Origin of the surface-state band-splitting in ultrathin Bi films: From a Rashba effect to a parity effect
New J. Phys. 10 083038 (2008)

Holderer, O.; Monkenbusch, M.; Borchert, G.; Breunig, C.; Zeitelhack, K.
Layout and performance of the polarizing guide system for the J-NSE spectrometer at the FRM II
Nuclear Instruments and Methods in Physics Research Section A, 586 (2008) 1, 90 – 94

Holderer, O.; Monkenbusch, M.; Schätzler, R.; Kleines, H.; Westerhausen, W.; Richter, D.
The JCNS neutron spin-echo spectrometer J-NSE at the FRM II
Measurement Science and Technology, 19 (2008), 034022

Holmqvist, P.; Kleshchanok, D.; Lang, P. R.
Interaction potential and near wall dynamics of spherical colloids in suspensions of rod-like fd-virus
European Physical Journal E, 26 (2008), 177 – 182

Homberger, M.; Karthäuser, S.; Simon, U.; Voigtländer, B.
Formation of Nanostructures by Self-Assembly
Information Technology I/ed.: R. Waser. – Wiley, 2008. – (Nanotechnology ; 3). – S. 305 – 347

Hu, R.; Thomas, K. J.; Lee, Y.; Vogt, T.; Choi, E. S.; Mitrovic, V. F.; Hermann, R. P.; Grandjean, F.; Canfield, P. C.; Kim, J. W.; Goldman, A. I.; Petrovic, C.
Colossal positive magnetoresistance in a doped nearly magnetic semiconductor
Physical Review B, 77 (2008), 085212-1 – 085212-5

Huang, C. C.
Kinetics and dynamics of wormlike micelles under shear
Europhysics Letters, 81 (2008), 58002

Hüller, A.; Prager, M.; Press, W.; Seydel, T.
Phase III of solid methane: The orientational potential and rotational tunneling
Journal of Chemical Physics, 128 (2008), 034503

Huotari, S.; Sternemann, C.; Schülke, W.; Sturm, K.; Lustfeld, H.; Sternemann, H.; Volmer, M.; Gusarov, A.; Müller, H.; Monaco, G.
Electron-density dependence of double-plasmon excitations in simple metals
Physical Review B, 77 (2008), 195125

Ioffe, A.
A new neutron spin-echo technique with time-gradient magnetic fields
Nuclear Instruments and Methods in Physics Research Section A, 586 (2008) 1, 31 – 35

Ioffe, A.; Bodnarchuk, V.; Bussmann, R.; Müller, R.; Georgii, R.
A new neutron spin-echo spectrometer with time-gradient magnetic fields: First experimental test
Nuclear Instruments and Methods in Physics Research Section A, 586 (2008) 1, 36 – 40

Ishida, H.; Liebsch, A.
Origin of metallicity of $LaTiO_3$/$SrTiO_3$ heterostructures
Physical Review B, 77 (2008), 115350

Ivanova, L, Borisova, S.; Eisele, H.; Dähne, M.; Laubsch, A.; Ebert, Ph.
Surface states and origin of the Fermi level pinning on nonpolar GaN(110) surfaces
Applied Physics Letters 93, 192110 (2008)

Jeong, D. S.; Schroeder, H.; Breuer, U.; Waser, R.
Characteristic electroforming behavior in Pt/TiO_2/Pt resistive switching cells depending on atmosphere
Journal of Applied Physics, 104 (2008), 123716

Jia, C. L.; Mi, S. B.; Urban, K.; Vrejoiu, I.; Alexe, M.; Hesse, D.
Atomic-scale study of electric dipoles near charged an uncharged domain walls in ferroelectric films
Nature Materials, 7 (2008), 57 – 61

Jones, R. O.
Materials Science
NIC Symposium 2008: proceedings/ed.: G. Münster, D. Wolf, M. Kremer. – Jülich, John von Neumann Institute for Computing, 2008. – NIC Series; 39). – 978-3-9810842-5-1. – S. 161 – 162

Jones, R. O.; Akola, J.
Density functional study of amorphous, liquid and crystalline $Ge_2Sb_2Te_5$: homopolar bonds and/or AB alternation?
Journal of Physics: Condensed Matter, 20 (2008), 465103

Jones, R. O.; Akola, J.
Density functional simulations of Te-based phase change materials
European Phase Change and Ovonics Symposium 2008/ed.: T. Wagner. – University of Pardubice, Czech Republic, 2008. – 978-80-7395-111-5. – S. 6 – 13

224

Kang, K.; Dhont, J. K. G.
Double-layer polarization induced transitions in suspensions of colloidal rods
EPL: a Letters Journal Exploring the Frontiers of Physics, 84 (2008), 14005

Kang, K.; Lettinga, M. P.; Dhont, J. K. G.
Is vorticity-banding due to an elastic instability?
Rheologica Acta, 47 (2008), 499 – 508

Kapnistos, M.; Lang, M.; Vlassopoulos, D.; Pyckhout-Hintzen, W.; Richter, D.; Cho, D.; Chang, T.; Rubinstein, M.
Unexpected power-law stress relaxation of entangled ring polymers
Nature Materials, 7 (2008), 997 – 1002

Karatas, Y.; Pyckhout-Hintzen, W.; Zorn, R.; Richter, D.; Wiemhöfer, H. D.
SANS Investigation and Conductivity of Pure and Salt-Containing Poly(bismethoxy-phosphazene)
Macromolecules, 41 (2008), 2212 – 2218

Katayama-Yoshida, H.; Sato, K.; Fukushima, T.; Toyoda, M.; Kizaki, H.; Dinh, V. A.; Dederichs, P. H.
Computational nano-materials design for II-VI compound semiconductor-based spintronics
Journal of the Korean Physical Society, 53 (2008), 1 – 12

Kentzinger, E.; Rücker, U.; Toperverg, B.; Ott, F.; Brückel, T.
Depth-resolved investigation of the lateral magnetic correlations in a gradient nanocrystalline multilayer
Physical Review B, 77 (2008), 104435-1 – 104435-19

Kimber, S. A. J.; Argyriou, D. N.; Yokaichiya, F.; Habicht, K.; Gerischer, S.; Hansen, T.; Chatterji, T.; Klingeler, R.; Hess, C.; Behr, G.; Kondrat, A.; Büchner, B.
Magnetic ordering and negative thermal expansion in PrFeAsO
Physical Review B, 78 (2008), 140503-1 – 140503-4(R)

Kishikawa, Y.; Kita, R.; Kriegs, H.; Wiegand, S.
Ludwig-Soret Effect for Aqueous and Non-aqueous Solutions of Polysaccharide
Thermal Nonequilibrium: Lecture Notes Thermal Nonequilibrium: Lecture Notes of the 8th International Meeting on Thermodiffusion/ed.: S. Wiegand, W. Köhler, J. K. G. Dhont. – Jülich, Forschungszentrum, Zentralbibliothek, 2008. – (Schriften des Forschungszentrums Jülich. Reihe Schlüsseltechnologien/Key Technologies; 3). – 978-3-89336-523-4. – S. 97 – 102

Kleshchanok, D.; Tuinier, R.; Lang, P. R.
Direct measurement of polymer-induced forces
Journal of Physics: Condensed Matter, 20 (2008), 073101

Koch, E.; Pavarini, E.
Multiple Scales in Solid State Physics
Multiscale Modeling and Simulation in Science/ed.: B. Engquist, P. Lötstedt, O. Runborg. – Berlin, Springer, 2008. – 978-3-540-88856-7. – S. 295

Koch, E.; Sangiovanni, G.; Gunnarsson, O.
Sum-rules and bath-parametrization for quantum cluster theories
Physical Review B, 78 (2008), 115102

Kohlstedt, H. H.; Petraru, A.; Szot, K.; Rüdiger, A.; Meuffels, P.; Haselier, H.; Waser, R.; Nagarajan, V.
Method to distinguish ferroelectric from nonferroelectric origin in case of resistive switching in ferroelectric capacitors
Applied Physics Letters, 92 (2008), 062907

Kolasinska, M.; Krastev, R.; Gutberlet, T.; Warszynski, P.
Swelling and Water Uptake of PAH/PSS Polyelectrolyte Multilayers
Progress in Colloid and Polymer Science, 134 (2008), 30 – 38

Koroteev, Yu. M.; Bihlmayer, G.; Chulkov, E. V.; Blügel, S.
First-principles investigation of structural and electronic properties of ultrathin Bi films
Physical Review B, 77 (2008), 045428

Kriegs, H.; Meier, G.; Gapinski, J.; Patkowski, A.
The effect of intramolecular relaxations on the damping of longitudinal and transverse phonons in polysiloxanes studied by Brillouin spectroscopy
Journal of Chemical Physics, 128 (2008), 014507

Kronast, F.; Ovsyannikov, R.; Kaiser, A.; Wiemann, C.; Yang, S. H.; Bürgler, D. E.; Schreiber, R.; Salmassi, F.; Fischer, P.; Dürr, H. A.; Schneider, C. M.; Eberhardt, W.; Fadley, C. S.
Depth-resolved soft X-ray photoelectron emission microscopy in nanostructures via standing-wave excited photoemission
Applied Physics Letters, 93 (2008), 243116

Krug, I. P.; Hillebrecht, F. U.; Gomonaj, H.; Haverkort, M.; Tanaka, A.; Tjeng, L. H.; Fraile-Rodriguez, A.; Nolting, F.; Schneider, C. M.
Impact of interface orientation on the magnetic coupling in highly ordered systems – A case study on Fe_3O_4/NiO
Physical Review B, 78 (2008), 064427

Krug, I. P.; Hillebrecht, F. U.; Haverkort, W.; Gomonay, H.; Tanaka, A.; Tjeng, L. H.; Schneider, C. M.
Magnetic coupling in highly-ordered NiO/Fe_3O_4(110): Ultrasharp magnetic interfaces vs. long-range magnetoelastic interactions
Europhysics Letters, 81 (2008), 17005

Kügeler, C.; Hennings, A.; Böttger, U.; Waser, R.
Design and realization of an integrated microwave switch based on piezoelectric PZT and PLHT thin films
Proceedings of the 19th MicroMechanics Workshop, September 28-30, Aachen. – 2008. – S. 21 – 24

Kügeler, C.; Hennings, A.; Böttger, U.; Waser, R.
An integrated microelectromechanial microwave switch based on piezoelectric acuation
Journal of Electroceramics, (2008)

Kügeler, C.; Rosezin, R.; Schneller, T.; Böttger, U.; Waser, R.
Large area piezoelectric actuators using metal foil substrates with $Pb(Zr_xTi_{1-x})O_3$ thin films
Integrated Ferroelectrics, 100 (2008), 254

225

Lang, P. R.
Particle Wall Interactions and Near-Wall Dynamics of Colloids
Soft Matter: From Synthetic to Biological Materials: Lecture manuscripts of the 39th Spring School of the Institute of Solid State Research; this spring school was organized by the Institute of Solid State Research in the Forschungszentrum Jülich on March 3 – 14, 2008/ed.: J. K. G. Dhont, G. Gompper, G. Nägele, D. Richter, R. G. Winkler. – Jülich, Forschungszentrum, Zentralbibliothek, 2008. – (Schriften des Forschungszentrums Jülich. Reihe Schlüsseltechnologien/Key Technologies; 1). – 978-3-89336-517-3. – S. C14.1 – C14.16

Lazo, C.; Caciuc, V.; Hölscher, H.; Heinze, S.
Role of tip size, orientation, and structural relaxations in first principles studies of magnetic exchange force microscopy and spin polarized scanning tunneling microscopy
Physical Review B, 78 (2008), 214416

Lebedev, D. V.; Filatov, M. V.; Kuklin, A. I.; Islamov, A. K.; Stellbrink, J.; Pantina, R. A.; Denisov, Y. Y.; Toperverg, B. P.; Isaev-Ivanov, V. V.
Structural hierarchy of chromatin in chicken erythrocyte nuclei based on small-angle neutron scattering: Fractal nature of the large-scale chromatin organization
Crystallography Reports, 53 (2008), 110 – 115

Lehndorff, R.; Bürgler, D. E.; Kakay, A.; Hertel, R.; Schneider, C. M.
Spin-Transfer Induced Dynamic Modes in Single-Crystalline Fe-Ag-Fe Nanopillars
IEEE Transactions on Magnetics, 44 (2008) 7, 1951 – 1956

Lentzen, M.
Contrast transfer and resolution limits for sub-angstrom high-resolution transmission electron microscopy
Microscopy and Microanalysis, 14 (1), 16-26 (2008)

Lettinga, M. P.
The Dynamics of Rods in Different Phases
Soft Matter: From Synthetic to Biological Materials: Lecture manuscripts of the 39th Spring School of the Institute of Solid State Research; this spring school was organized by the Institute of Solid State Research in the Forschungszentrum Jülich on March 3-14, 2008/ed.: J. K. G. Dhont, G. Gompper, G. Nägele, D. Richter, R. G. Winkler. – Jülich, Forschungszentrum, Zentralbibliothek, 2008. – (Schriften des Forschungszentrums Jülich. Reihe Schlüsseltechnologien/Key Technologies; 1). – 978-3-89336-517-3. – S. D4.1 – D4.34

Liebsch, A.
Doping-driven Mott transition in $La_{[1-x]}Sr_xTiO_3$ via simultaneous electron and hole doping of t2g subbands as predicted by LDA+DMFT calculations
Physical Review B, 77 (2008), 115115

Liebsch, A.; Ishida, H.
Coulomb correlations do not fill the e'_g hole pockets in $Na_{[0.3]}CoO_2$
European Physical Journal B, 61 (2008), 405

Liebsch, A.; Ishida, H.; Merino, J.
Multisite versus multiorbital Coulomb correlations studied within finite-temperature exact diagonalization dynamical mean-field theory
Physical Review B, 78 (2008), 165123

Lonetti, B.; Kohlbrecher, J.; Willner, L.; Dhont, J. K. G.; Lettinga, M. P.
Dynamic response of block copolymer wormlike micelles to shear flow
Journal of Physics: Condensed Matter, 20 (2008), 404207

Lott, D.; Fenske, J.; Schreyer, A.; Mani, P.; Mankey, G. J.; Klose, F.; Schmidt, W.; Schmalzl, K.; Tartakovskaya, E. V.
Antiferromagnetism in a $Fe_{50}Pt_{40}Rh_{10}$ thin film investigated using neutron diffraction
Physical Review B, 78 (2008), 174413-1 – 174413-10

Lounis, S.; Dederichs, P. H.; Blügel, S.
Magnetism of Nanowires Driven by Novel Even-Odd Effects
Physical Review Letters, 101 (2008), 107204

Lounis, S.; Reif, M.; Mavropoulos, P.; Glaser, L.; Dederichs, P. H.; Martins, M.; Bluegel, S.; Wurth, W.
Non-collinear magnetism of Cr nanostructures on $Fe_3ML/Cu(001)$: First principles and experimental investigations
Europhysics Letters, 81 (2008), 47004

Manoshin, S.; Ioffe, A.
New modules for the VITESS software package: Time-gradient magnetic fields and neutron refractive lenses
Nuclear Instruments and Methods in Physics Research Section A, 586 (2008) 1, 81 – 85

Mavropoulos, P.
Spin injection from Fe into Si(001): Ab initio calculations and role of the Si complex band structure
Physical Review B, 78 (2008), 054446

McGuire, M. A.; Christianson, A. D.; Sefat, A. S.; Sales, B. C.; Lumsden, M. D.; Jin, R.; Payzant, E. A.; Mandrus, D.; Luan, Y.; Keppens, V.; Varadarajan, V.; Brill, J. W.; Hermann, R. P.; Sougrati, M. T.; Grandjean, F.; Long, G.
Phase transitions in LaFeAsO: Structural, magnetic, elastic, and transport properties, heat capacity and Mössbauer spectra
Physical Review B, 78 (2008), 094517-1 – 094517-10

McPhie, M.; Nägele, G.
Nonmonotonic density dependence of the diffusion of DNA fragments in low-salt suspensions
Physical Review E, 78 (2008), 060401(R)

McWhirter, J. L.
Phase behavior of a simple dipolar fluid under shear flow in an electric field
Journal of Chemical Physics, 128 (2008), 034502

Meier, M.; Gilles, S.; Schindler, C.; Rosezin, R.; Mayer, D.; Rüdiger, A.; Kügeler, C.; Waser, R.
Resistively switching Pt/spin-on glass/Ag nanocells for non-volatile memories fabricated with UV nanoimprint lithography
Proceedings of the 34th International Conference on Micro & Nano Engineering, September 15-19, 2008, Athens, Greece. – 2008. – S. 108

Meier, G.; Kriegs, H.
A high pressure cell for dynamic light scattering up to 2 kbars with conservation of plane of polarization
Review of Scientific Instruments, 79 (2008), 013102

Meier, G.; Vavrin, R.; Kohlbrecher, J.; Buitenhuis, J.; Lettinga, M. P.; Ratajczyk, M.
SANS and dynamic light scattering to investigate the viscosity of toluene under high pressure up to 1800 bar
Measurement Science and Technology, 19 (2008), 034017

Meier, M.; Nauenheim, C.; Gilles, S.; Mayer, D.; Kügeler, C.; Waser, R.
Nanoimprint for future non-volatile memory and logic devices
Microelectronic Engineering, 85 (2008), 870 – 872

226

Mi, S. B.; Jia, C. L.; Vaithyanathan, V.; Houben, L.; Schubert, J.; Schlom, D. G.; Urban, K.
Atomic structure of the interface between SrTiO$_3$ thin films and Si(001) substrates
Applied Physics Letters, 93 (2008), 101913

Mittal, R.; Su, Y.; Chatterji, T.; Chaplot, S.L.; Schober, H.; Rotter, M.; Johrendt, D.; Brückel, T.
Inelastic neutron scattering and lattice-dynamical calculations of BaFe$_2$As$_2$
Physical Review B, 78 (2008), 104514

Mittal, R.; Su, Y.; Rols, S.; Tegel, M.; Chaplot, S. L.; Schober, H.; Chatterji, T.; Johrendt, D.; Brueckel, Th.
Phonon dynamics in Sr$_{0.6}$K$_{0.4}$Fe$_2$As$_2$ and Ca$_{0.6}$Na$_{0.4}$Fe$_2$As$_2$ from neutron scattering and lattice-dynamical calculations
Physical Review B, 78 (2008) 22, 224518-1 – 224518-5

Mofidi, M.; Prakash, B.; Persson, B. N. J.; Albohr, O.
Rubber friction on (apparently) smooth lubricated surfaces
Journal of Physics: Condensed Matter, 20 (2008) 8, 085223

Molak, A.; Szot, K.; Kania, A.
Insulator-metal transition in Mn-doped NaNbO$_3$ induced by chemical and thermal treatment
Phase Transitions, 81 (2008), 977 – 986

Monkenbusch, M.
Time-of-flight spectrometers including NSE
Neutron Scattering: Lectures of the JCNS Laboratory Course held at Forschungszentrum Jülich and the research reactor FRM II of TU Munich; In cooperation with RWTH Aachen and University of Münster/ed.: T. Brückel, G. Heger, D. Richter, R. Zorn. – Jülich, Forschungszentrum, Zentralbibliothek, 2008. – (Schriften des Forschungszentrum Jülich. Reihe Schlüsseltechnologien/ Key Technologies; 5). – 978-3-89336-532-6. – S. 10.1 – 10.34

Müller-Meskamp, L.; Karthäuser, S.; Waser, R.; Homberger, M.; Simon, U.
Striped Phase of Mercaptoalkylferrocenes on Au(111) with a Potential for Nanoscale Surface Patterning
Langmuir, 24 (2008), 4577

Münstermann, R.; Dittmann, R.; Szot, K.; Mi, S.; Jia, C. L.; Meuffels, P.; Waser, R.
Realization of regular arrays of nanoscale resistive switching blocks in thin films by Nb-doped STO
Applied Physics Letters, 93 (2008), 023110

Nägele, G.
Theories of Fluid Microstructures
Soft Matter: From Synthetic to Biological Materials: Lecture manuscripts of the 39th Spring School of the Institute of Solid State Research; this spring school was organized by the Institute of Solid State Research in the Forschungszentrum Jülich on March 3 – 14, 2008/ed.: J. K. G. Dhont, G. Gompper, G. Nägele, D. Richter, R. G. Winkler. – Jülich, Forschungszentrum, Zentralbibliothek, 2008. – (Schriften des Forschungszentrums Jülich. Reihe Schlüsseltechnologien/Key Technologies; 1). – 978-3-89336-517-3. – S. B2.1 – B2.47

Narros, A.; Arbe, A.; Alvarez, F.; Colmenero, J.; Richter, D.
Atomic motions in the alpha-beta merging regime of 1-4 polybutadiene: A molecular dynamics simulation study
Journal of Chemical Physics, 128 (2008), 224905

Nauenheim, C.; Kügeler, C.; Rüdiger, A.; Waser, R.; Flocke, A.; Noll, T. G.
Nano-crossbar arrays for nonvolatile resistive RAM (RRAM) applications
Proceedings of the 8th IEEE Conference on Nanotechnology. – 2008. – S. 464 – 467

Niedzwiedz, K.; Wischnewski, A.; Pyckhout-Hintzen, W.; Allgaier, J.; Richter, D.; Faraone, A.
Chain Dynamics and Viscoelastic Properties of Poly(ethyleneoxide)
Macromolecules, 41 (2008), 4866

Ning, H.; Datta, S.; Sottmann, T.; Wiegand, S.
Soret effect of nonionic surfactants in water studied by different transient grating setups
Journal of Physical Chemistry B, 112 (2008), 10927 – 10934

Ning, H.; Dhont, J. K. G.; Wiegand, S.
Thermal-Diffusive Behavior of a Dilute Solution of Charged Colloids
Langmuir, 24 (2008), 2426 - 2432

Noguchi, H.; Gompper, G.
Transport coefficients of off-lattice mesoscale-hydrodynamics simulation techniques
Physical Review E, 78 (2008), 016706-1 – 016706-12

Nygard, K.; Satapathy, D. K.; Bunk, O.; Diaz, A.; Perret, E.; Buitenhuis, J.; Pfeiffer, F.; David, C.; van der Veen, J. F.
Structure of confined fluids by X-ray interferometry using diffraction gratings
Optics Express, 16 (2008) 25, 20522 – 20529

Oh, I.; Mattauch, S.; Heger, G.; Lee, C. E.
Neutron Diffraction Study of a Rb$_{0.5}$T$_{10.5}$H$_2$PO$_4$ Single Crystal
Journal of the Physical Society of Japan, Vol.77, No 9 (2008), 094602-1- 94602-4

Ott, R. T.; Heggen, M.; Feuerbacher, M.; Park, E. S.; Kim, D. H.; Kramer, M. J.; Besser, M. F.; Sordelet, D. J.
Anelastic strain and anisotropy in homogeneoesly deformed Cu$_{64.5}$Zr$_{35.5}$ metallic glass
Acta Materialia, 56 (2008), 5575 – 5583

Özdogan, K.; Galanakis, I.; Sasioglu, E.; Aktas, B.
Role of the presence of transition-metal atoms at the antisites in CrAs, CrSe and VAs zinc-blende compounds
Journal of Magnetism and Magnetic Materials, 320 (2008), 197 – 203

Özdogan, K.; Sasioglu, E.; Galanakis, I.
Engineering the electronic, magnetic, and gap-related properties of the quinternary half-metallic Heusler alloys
Journal of Applied Physics, 103 (2008), 023503

Papagiannopoulos, A.; Fernyhough, C. M.; Waigh, T. A.; Radulescu, A.
Scattering Study of the Structure of Polystyrene Sulfonate Comb Polyelectrolytes in Solution
Macromolecular Chemistry and Physics, 209 (2008), 2475 – 2486

Patkowski, A.; Gapinski, J.; Fluerasu, A.; Holmqvist, P; Meier, G.; Lettinga, M. P; Nägele, G.
Structure and dynamics of colloidal suspensions studied by means of XPCS
Acta Physica Polonica A, 114 (2008) 2, 339 – 350

227

Paul, A.; Buchmeier, M.; Bürgler, D. E.; Rücker, U.; Schneider, C. M.
Twisted magnetization state at the interface of an antiferromagnetically coupled Fe/Si multilayer as probed by specular and off-specular polarized neutron scattering
Physical Review B, 77 (2008), 184409-1 – 184409-16

Pavarini, E.; Tarantino, S. C.; Boffa Ballaran, T.; Zema, M.; Ghigna, P.; Carretta, P.
Effect of high pressure on competing exchange couplings in Li_2VOSiO_4
Physical Review B, 77 (2008), 014425

Pavlyuchkov, D.; Grushko, B.; Velikanova, T. Ya.
An investigation of the Al-Pd-Ir phase diagram between 50 and 100 at.%Al
J. Alloys Comp. 453, 191-196 (2008)

Pavlyuchkov, D.; Grushko, B.; Velikanova, T. Ya.
A contribution to the Al-Ir phase diagram
Intermetallics. 16, 801-806 (2008)

Pavlyuchkov, D.; Grushko, B.; Velikanova, T. Ya.
An investigation of the high-Al part of the Al-Pd-Ru phase diagram at 1000 and 1100°C
Chem. Met. Alloys. 1, 84-87 (2008)

Pavlyuchkov, D.; Grushko, B.; Velikanova, T. Ya.
Al-rich region of Al-Pd-Ru at 1000 to 1100°C
J. Alloys Comp. 464, 101-106 (2008)

Persson, B. N. J.
Capillary adhesion between elastic solids with randomly rough surfaces
Journal of Physics: Condensed Matter, 20 (2008) 31, 315007

Persson, B. N. J.
Influence of frozen capillary waves on contact mechanics
Wear, 264 (2008) 9/10, 746 – 749

Persson, B. N. J.
On the elastic energy and stress correlation in the contact between elastic solids with randomly rough surfaces
Journal of Physics: Condensed Matter, 20 (2008) 31, 312001

Persson, B. N. J.; Sivebaek, I. M.; Samoilov, V. N.; Zhao, K.; Volokitin, A. I.; Zhang, Z.
On the origin of Amonton's friction law
Journal of Physics: Condensed Matter, 20 (2008) 39, 395006

Persson, B. N. J.; Yang, C.
Theory of the leak-rate of seals
Journal of Physics: Condensed Matter, 20 (2008) 31, 315011

Pertsev, N. A.; Petraru, A.; Kohlstedt, H.
Dynamics of ferroelectric nanodomains in $BaTiO_3$ epitaxial thin films via piezoresponse force microscopy
Nanotechnology, 19 (2008), 375703

Petraru, A.; Kohlstedt, H.; Poppe, U.; Waser, R.; Solbach, A.; Klemradt, U.; Schubert, J.; Zander, W.; Pertsev, N. A.
Wedgelike ultrathin epitaxial $BaTiO_3$ films for studies of scaling effects in ferroelectrics
Applied Physics Letters, 93 (2008), 072902

Pfeiffer, J.; Kemmler, M.; Koelle, D.; Kleiner, R.; Goldobin, E.; Weides, M.; Feofanov, K.; Lisenfeld, J.; Ustinov, A. V.
Static and dynamic properties of 0, pi, and 0-pi ferromagnetic tunnel Josephson junctions
Physical Review B, 77 (2008), 214506

Picozzi, S.; Lezaic, M.
Ab-initio study of exchange constants and electronic structure in diluted magnetic group-IV Semiconductors
New Journal of Physics, 10 (2008), 055017

Pilipenko, D.; Brener, E. A.; Hüter, C.
Theory of dendritic growth in the presence of lattice strain
Physical Review E, 78 (2008), 060603

Pipich, V.; Balz, M.; Wolf, S. E.; Tremel, W.; Schwahn, D.
Nucleation and Growth of $CaCO_3$ Mediated by the Egg-White Protein Ovalbumin: A Time-Resolved in-situ Study Using Small-Angle Neutron Scattering
Journal of the American Chemical Society, 130 (2008) 21, 6879 – 6892

Plucinski, L.; Sell, B. C.; Minar, J.; Braun, J.; Ebert, H.; Schneider, C. M.; Fadley, C. S.
Band mapping in higher-energy X-ray photoemission: Phonon effects and comparison to one-step theory
Physical Review B, 78 (2008), 035108

Polyakov, P.; Müller-Plathe, F.; Wiegand, S.
Reverse nonequilibrium molecular dynamics calculation of the soret coefficient in liquid heptane/benzene mixtures
Journal of Physical Chemistry B, 112 (2008) 47, 14999 – 15004

Polyakov, P.; Wiegand, S.
Systematic study of the thermal diffusion in associated mixtures
Journal of Chemical Physics, 128 (2008), 034505

Polyakov, P.; Wiegand, S.
Study of the thermal diffusion behavior of simple and associated mixtures
Thermal Nonequilibrium: Lecture Notes Thermal Nonequilibrium: Lecture Notes of the 8th International Meeting on Thermodiffusion/ed.: S. Wiegand, W. Köhler, J. K. G. Dhont. – Jülich, Forschungszentrum, Zentralbibliothek, 2008. – (Schriften des Forschungszentrums Jülich. Reihe Schlüsseltechnologien/Key Technologies; 3). – 978-3-89336-523-4. – S. 57 – 61

Popkov, V.; Salerno, M.; Schütz, G. M.
Asymmetric simple exclusion process with periodic boundary driving
Physical Review E, 78 (2008) 1, 011122

Prager, M.; Desmedt, A.; Unruh, T.; Allgaier, J.
Dynamics and adsorption sites of guest molecules in methyl chloride hydrate
Journal of Physics: Condensed Matter, 20 (2008), 125219

Prager, M.; Grimm, H.; Natkaniec, I.; Nowak, D.; Unruh, T.
The dimensionality of ammonium reorientation in $(NH_4)_2S_2O_8$: the view from neutron spectroscopy
Journal of Physics: Condensed Matter, 20 (2008), 125218

Priezzhev, V. B.; Schütz, G. M.
Exact solution of the Bernoulli matching model of sequence alignment
Journal of Statistical Mechanics: Theory and Experiment, (2008), P09007

Radulescu, A.; Fetters, L. J.; Richter, D.
Polymer driven wax crystal control using partially crystalline polymeric materials
Advances in Polymer Science, 210 (2008), 1 – 100

228

Radulescu, A.; Ioffe, A.
Neutron guide system for small-angle neutron scattering instruments of the Jülich Centre for Neutron Science at the FRM II
Nuclear Instruments and Methods in Physics Research Section A, 586 (2008) 1, 55 – 58

Ramzi, A.; Rijcken, C.; Veldhuis, T.; Schwahn, D.; Hennink, W.; van Nostrun, C.
Core-Shell Structure of Degradable, Thermosensitive Polymeric Micelles studied by Small-Angle Neutron Scattering
Journal of Physical Chemistry B, 112 (2008) 3, 784 – 792

Reckermann, F.; Leijnse, M.; Wegewijs, M. R.; Schoeller, H.
Transport signature of pseudo Jahn-Teller dynamics in a single-molecule transistor
Europhysics Letters, 83 (2008), 58001

Richter, D.
Basic assumptions of quantum mechanics and the born approximation – a brief tutorial
Neutron Scattering: Lectures of the JCNS Laboratory Course held at Forschungszentrum Jülich and the research reactor FRM II of TU Munich; in cooperation with RWTH Aachen and University of Münster/ed.: T. Brückel, G. Heger, D. Richter, R. Zorn. – Jülich, Forschungszentrum, Zentralbibliothek, 2008. – (Schriften des Forschungszentrum Jülich. Reihe Schlüsseltechnologien/Key Technologies; 5). – 978-3-89336-532-6. – S. II-1 – II-32

Richter, D.
Dynamics of macromolecules
Soft Matter: From Synthetic to Biological Materials: Lecture manuscripts of the 39th Spring School of the Institute of Solid State Research; this spring school was organized by the Institute of Solid State Research in the Forschungszentrum Jülich on March 3-14, 2008/ed.: J. K. G. Dhont, G. Gompper, G. Nägele, D. Richter, R. G. Winkler. – Jülich, Forschungszentrum, Zentralbibliothek, 2008. - (Schriften des Forschungszentrums Jülich. Reihe Schlüsseltechnologien/Key Technologies; 1). – 978-3-89336-517-3. – S. D1.1 – D1.33

Richter, D.
Dynamics of macromolecules
Neutron Scattering: Lectures of the JCNS Laboratory Course held at Forschungszentrum Jülich and the research reactor FRM II of TU Munich; In cooperation with RWTH Aachen and University of Münster/ed.: T. Brückel, G. Heger, D. Richter, R. Zorn. – Jülich, Forschungszentrum, Zentralbibliothek, 2008. – (Schriften des Forschungszentrum Jülich. Reihe Schlüsseltechnologien/Key Technologies; 5). – 978-3-89336-532-6. – S. 14.1 – 14.33

Ripoll, M.
Mesoscale Hydrodynamics
Soft Matter: From Synthetic to Biological Materials: Lecture manuscripts of the 39th Spring School of the Institute of Solid State Research; this spring school was organized by the Institute of Solid State Research in the Forschungszentrum Jülich on March 3 – 14, 2008 ed.: J. K. G. Dhont, G. Gompper, G. Nägele, D. Richter, R. G. Winkler. – Jülich, Forschungszentrum, Zentralbibliothek, 2008.-(Schriften des Forschungszentrums Jülich. Reihe Schlüsseltechnologien/Key Technologies; 1). – 978-3-89336-517-3. – S. B4.1 – B4.18

Ripoll, M.; Holmqvist, P.; Winkler, R. G.; Gompper, G.; Dhont, J. K. G.; Lettinga, M. P.
Attractive Colloidal Rods in Shear Flow
Physical Review Letters, 101 (2008), 168302-1 – 168302-4

Ripoll, M.; Winkler, R. G.; Mussawisade, K.; Gompper, G.
Mesoscale hydrodynamics simulations of attractive rod-like colloids in shear flow
Journal of Physics: Condensed Matter, 20 (2008), 404209

Roosen, D.; Wegewijs, M. R.; Hofstetter, W.
Nonequilibrium Dynamics of Anisotropic Large Spins in the Kondo Regime: Time-Dependent Numerical Renormalization Group Analysis
Physical Review Letters, 100 (2008), 087201

Rosenbaum, R.; Balanetskyy, S.; Grushko B.; Przepiórzyñsky B.
Very low temperature electronic transport in Al-Pd-Re quasicrytalline alloys
J. Low-temperature Phys. 150, 82-100 (2008)

Rüdiger, A.; Waser, R.
Size effects in ferroelectric nanostructures
Journal of Alloys and Compounds, 449 (2008) 1/2, 2 – 6

Rusek, K.; Kruczek, J.; Szot, K.
Non-linear properties of $BaTiO_3$ above Tc
Ferroelectrics, 375 (2008), 165

Rzhevsky, A. A.; Krichevtsov, B. B.; Bürgler, D. E.; Schneider, C. M.
Interface and bulk magnetization dynamics in biaxial Fe/Cr structures induced by ultrashort optical pulses
Journal of Applied Physics, 104 (2008), 083918

Rzhevsky, A. A.; Krichevtsov, B. B.; Bürgler, D. E.; Schneider, C. M.
Domain structure in biaxial Fe/Cr films induced by lateral fluctuations of the magnetic anisotropy
Physical Review B, 77 (2008), 174432

Sacharow, L.; Wiesendanger, R.; Bihlmayer, G.; Blügel, S.; Morgenstern, M.
Anisotropic superexchange in one-dimensional Fe-chains on InAs(110)
Surface Science, 602 (2008), 3297 – 3302

Saptsov, R. B.
On the instability of a homogeneous state of a weakly interacting Bose gas under external cooling
JETP Letters, 86 (2008), 687 - 691

Sasioglu, E.; Sandratskii, L. M.; Bruno, P.
Role of conduction electrons in mediating exchange interactions in Mn-based Heusler alloys
Physical Review B, 77 (2008), 064417

Schindler, C.; Szot, K.; Karthäuser, S.; Waser, R.
Controlled local filament growth and dissolution in Ag-Ge-Se
Physica Status Solidi - Rapid Research Letters, 2 (2008) 3, 129 – 131

Schindler, C.; Weides, M.; Kozicki, M. K.; Waser, R.
Low current resistive switching in $Cu-SiO_2$ cells
Applied Physics Letters, 92 (2008), 122910

229

Schmalzl, K.; Strauch, D.; Hiess, A.; Berger, H.
Temperature dependent phonon dispersion in 2H-NbSe$_2$ investigated using inelastic neutron scattering
Journal of Physics: Condensed Matter, 20 (2008), 104240-1 – 104240-3

Schmidt, H.; Gupta, M.; Gutberlet, T.; Stahn, J.; Bruns, M.
How to measure atomic diffusion processes in the sub-nanometer range
Acta Materialia, 56 (2008), 464 – 470

Schneider, G. J.; Kerscher, M.; Göritz, D.
Messung der Volumenänderung von Elastomeren bei hohen Dehnraten = Measurement of Volume Changes of Elestomeres at High Strain Rates
Kautschuk Gummi Kunststoffe, 6 (2008) , 317 – 321

Schneider, U.; Hackermueller, L.; Will, S.; Best, Th.; Bloch, I.; Costi, T. A.; Helmes, R. W.; Rasch, D.; Rosch, A.
Metallic and Insulating Phases of Repulsively Interacting Fermions in a 3D Optical Lattice
Science, 322 (2008), 1520

Schneller, T.; Kohlstedt, H.; Petraru, A.
Investigation of the amorphous to crystalline phase transition of chemical solution deposited Pb(Zr$_{0.3}$Ti$_{0.7}$)O$_3$ thin films by soft X-ray absorption and soft X-ray emission spectroscopy
Journal of Sol-Gel Science and Technology, 48 (2008), 239 – 252

Schober, H.; Farhi, E.; Mezei, F.; Allenspach, P.; Andersen, K.; Bentley, P. M.; Christiansen, P.; Cubitt, B.; Heenan, R. K.; Kulda, J.; Langan, P.; Lefmann, K.; Lieutenant, K.; Monkenbusch, M.; Willendrup, P.; Saroun, J.; Tindesmans, P.; Zsigmond, G.
Tailored instrumentation for long-pulse neutron spallation sources
Nuclear Instruments and Methods in Physics Research Section A, 589 (2008) 1, 34 – 46

Schubert, J.; Trithaveesak, O.; Zander, W.; Roeckerath, M.; Heeg, T.; Chen, H. Y.; Jia, C. L.; Meuffels, P.; Jia, Y.; Schlom, D. G.
Characterization of epitaxial lanthanum lutetium oxide thin films prepared by pulsed-laser deposition as an alternative gate dielectric
Applied Physics A, 90 (2008), 577 – 579

Schütz, G. M.; Brandaut, M.; Trimper, S.
Exact solution of a stochastic susceptible-infectious-recovered model
Physical Review E, 78 (2008), 061132

Schwahn, D.
Polymer phase transitions
Soft Matter: From Synthetic to Biological Materials: Lecture manuscripts of the 39th Spring School of the Institute of Solid State Research; this spring school was organized by the Institute of Solid State Research in the Forschungszentrum Jülich on March 3-14, 2008/ed.: J. K. G. Dhont, G. Gompper, G. Nägele, D. Richter, R. G. Winkler. - Jülich, Forschungszentrum, Zentral-bibliothek, 2008. – (Schriften des Forschungszentrums Jülich. Reihe Schlüsseltechnologien/Key Technologies; 1). - 978-3-89336-517-3. – S. C2.1 – C2.17

Schweika, W.
Polarized neutron scattering
Neutron Scattering: Lectures of the JCNS Laboratory Course held at Forschungszentrum Jülich and the research reactor FRM II of TU Munich; in cooperation with RWTH Aachen and University of Münster/ed.: T. Brückel, G. Heger, D. Richter, R. Zorn. – Jülich, Forschungszentrum, Zentralbibliothek, 2008. – (Schriften des Forschungszentrum Jülich. Reihe Schlüsseltechnologien/Key Technologies; 5). – 978-3-89336-532-6. – S. 3-1 – 3-23

Scudino, S.; Sperling, S.; Sakaliyshka, M.; Thomas, C.; Feuerbacher, M.; Kim, K. B.; Ehrenberg, H.; Eckert, J.
Phase transitions in mechanically milled and annealed Beta-Al$_3$Mg$_2$
Acta Materialia, 56 (2008), 1136

Seeck, O. H.; Kentzinger, E.
Grazing incidence neutron scattering
Neutron Scattering: Lectures of the JCNS Laboratory Course held at Forschungszentrum Jülich and the research reactor FRM II of TU Munich; in cooperation with RWTH Aachen and University of Münster/ed.: T. Brückel, G. Heger, D. Richter, R. Zorn. – Jülich, Forschungszentrum, Zentralbibliothek, 2008. – (Schriften des Forschungszentrum Jülich. Reihe Schlüsseltechnologien/Key Technologies; 5). – 978-3-89336-532-6. – S. 5-1 – 5-26

Shen, W.; Dittmann, R.; Breuer, U.; Waser, R.
Improved endurance behavior of resistive switching in (Ba, Sr)TiO$_3$ thin films with W top electrode
Applied Physics Letters, 93 (2008) 22, 222102-1

Shibuya, K.; Mi, S.; Jia, C. L.; Meuffels, P.; Dittmann, R.
Sr$_2$TiO$_4$ layered perovskite thin films grown by pulsed laser deposition
Applied Physics Letters, 92 (2008), 241918

Shiratori, Y.; Magrez, A.; Kato, M.; Kasezawa, K.; Pithan, C.; Waser, R.
Pressure-induced phase transitions in micro-, submicro-, and nanocrystalline NaNbO$_3$
Journal of Physical Chemistry C, 112 (2008), 9610 – 9616

Sinko, K.; Huesing, N.; Goerigk, G.; Peterlik, H.
Nanostructure of gel-derived aluminosilicate materials
Langmuir, 24 (2008) 3, 949 – 956

Sivebaek, I. M.; Samoilov, V. N.; Persson, B. N. J.
Frictional properties of confined polymers
European Physical Journal E, 27 (2008), 37 – 46

Smilijanic, S.; Smontara, A.; Bilusic, A.; Barisic, N.; Stanic, D.; Lukatela, J.; Dolinsek, J.; Feuerbacher, M.; Grushko, B.
Thermal and electrical conductivities in Al-based complex metallic alloys
Philosophical Magazine, 88 (2008), 2155

Smontara, A.; Smiljaniæ, I.; ABilušiæ, A.; Grushko, B.; Balanetskyy, S.; Jaglièiæ, Z.; Vrtnik, S.; Dolinšek, J.
Complex ∊-phases in the Al-Pd-transition-metal systems: towards a combination of an electrical conductor with a thermal insulator
J. Alloys Comp. 450, 92-102 (2008)

230

Soni, R.; Meier, M.; Rüdiger, A.; Holländer, B.; Kügeler, C.; Waser, R.
Integration of "Ge$_x$Se$_{1-x}$" in crossbar arrays for non-volatile memory application
Proceedings of the 34th International Conference on Micro & Nano Engineering, Athen – 2008. – S. 269
Athen: 15.09.2008 - 19.09.2008

Soni, R.; Schindler, C.; Weides, M.; Rüdiger, A.; Kügeler, C.; Waser, R.
A novel dual-layered electrolyt resistance memory with enhanced retention
Proceedings of the 8th IEEE Conference on Nanotechnology. – 2008. – S. 764 – 766

Sougrati, M. T.; Hermann, R. P.; Grandjean, F.; Long, G. J.; Brück, E.; Tegus, O.; Trung, N. T.; Buschow, K. H. J.
A structural, magnetic, and Mössbauer spectral study of the magnetocaloric Mn$_{1.1}$Fe$_{0.9}$P$_{1-x}$Ge$_x$ compounds
Journal of Physics: Condensed Matter, 20 (2008), 475206-1 – 475206-9

Spatschek, R.; Brener, E. A.; Pilipenko, D.
Crack Growth by Surface Diffusion in Viscoelastic Media
Physical Review Letters, 101 (2008), 205501

Sprakel, J.; Spruijt, E.; Cohen Stuart, M. A.; Besseling, N. A. M.; Lettinga, M. P.; van der Gucht, J.
Shear banding and rheochaos in associative polymer networks
Soft Matter, 4 (2008) 8, 1696 – 1705

Spudat, C.; Meyer, C.; Schneider, C. M.
Oxidation induced shifts of Raman modes of carbon nanotubes
Physica Status Solidi B, 245 (2008), 2205 – 2208

Stellbrink, J.; Lonetti, B.; Rother, G.; Willner, L.; Richter, D.
Shear induced structures of soft colloids: Rheo-SANS experiments on kinetically frozen PEP-PEO diblock copolymer micelles
Journal of Physics: Condensed Matter, 20 (2008), 404206

Stelzer, H.; Weissbacher, C.; Soltner, H.; Janssen, F.; Butzek, M.; Kozielewski, T.; Lindenau, B.; Monkenbusch, M.; Ohl, M.
Investigation of the temperature rise due to eddy currents in large chopper disks operated at polarized neutron beamlines
Nuclear Instruments and Methods in Physics Research Section A, 594 (2008) 2, 228 – 231

Strempfer, J.; Hupfeld, D.; Voigt, J.; Bihlmayer, G.; Goldman, A. I.; Brückel, Th.
Resonant magnetic x-ray scattering from terbium
Journal of Physics: Condensed Matter, 20 (2008), 445208-1 – 445208-7

Tao, Y. G.; Götze, I. O.; Gompper, G.
Multiparticle collision dynamics modeling of viscoelastic fluids
Journal of Chemical Physics, 128 (2008), 144902-1 – 144902-12

Teixeira, S. C. M.; Zaccai, G.; Ankner, J.; Bellissent-Funel, M. C.; Bewley, R.; Blakeley, M. P.; Callow, P.; Coates, L.; Dahint, R.; Dalgliesh, R.; Dencher, N. A.; Forsyth, V. T.; Fragneto, G.; Frick, G.; Gilles, R.; Gutberlet, T.; Haertlein, M.; Hauß, T.; Häußler, W.; Heller, W. T.; Herwig, K.; Holderer, O.; Juranyi, F.; Kampmann, R.; Knott, R.; Krueger, S.; Langan, P.; Lechner, R. E.; Lynn, G.; Majkrzak, C.; May, R. P.; Meilleur, F.; Mo, Y.; Mortensen, K.; Myles, D. A. A.; Natali, F; Neylon, C.; Niimura, N.; Ollivier, J.; Ostermann, A.; Peters, J.; Pieper, J.; Rühm, A.; Schwahn, D.; Shibata, K.; Soper, A. K.; Strässle, Th.; Suzuki, J.; Tanaka, I.; Tehei, M.; Timmins, P.; Torikai, N.; Unruh, T.; Urban, V.; Vavrin, R.; Weiss, K.
New Sources and Instrumentation for Neutrons in Biology
Chemical Physics, 345 (2008), 133 – 155

Theis-Bröhl, K.; Westphalen, A.; Zabel, H.; Rücker, U.; McCord, J.; Höink, V.; Schmalhorst, J.; Reiss, G.; Weis, T.; Engel, D.; Ehresmann, A.; Toperverg, B. P.
Hyper-domains in exchange bias micro-stripe pattern
New Journal of Physics, 10 (2008), 093021-1 – 093021-21

Thiess, A.; Mokrousov, Y.; Blügel, S.; Heinze, S.
Theory and Application of Chain Formation in Break Junctions
Nano Letters, 8 (2008), 2144 – 2149

Tong, L. N.; Matthes, F.; Müller, M.; Lee, C. G.; Schneider, C. M.
Influence of MgO overlayers on the electronic states of Fe(001) thin films grown on GaAs(001)
Physical Review B, 77 (2008), 064421

Tuinier, R.
Depletion
Soft Matter: From Synthetic to Biological Materials: Lecture manuscripts of the 39th Spring School of the Institute of Solid State Research; this spring school was organized by the Institute of Solid State Research in the Forschungszentrum Jülich on March 3 – 14, 2008/ed.: J. K. G. Dhont, G. Gompper, G. Nägele, D. Richter, R. G. Winkler. – Jülich, Forschungszentrum, Zentralbibliothek, 2008. – (Schriften des Forschungszentrums Jülich. Reihe Schlüsseltechnologien/Key Technologies; 1). – 978-3-89336-517-3. – S. C13.1 – C13.15

Tuinier, R.; Dhont, J. K. G.; Taniguchi, T.; Fan, T. H.
Nanoparticle Retardation in Semidilute Polymer Solutions
Complex Systems: 5th International Workshop on Complex Systems; Sendai, Japan, 25-28 September 2007/ed.: M. Tokuyama, I. Oppenheim, H. Nishiyama. – American Institute of Physics, 2008. – (AIP Conference Proceedings . Mathematical and Statistical Phsyics; 982). – 978-0-7354-0501-1. – S. 326 – 330

Tuinier, R.; Fan, T. H.
Scaling of nanoparticle retardation in semi-dilute polymer solutions
Soft Matter, 4 (2008), 254 – 257

Tuinier, R.; Smith, A.; Poon, W. C. K.; Egelhaaf, S. U.; Aarts, D. G. A. L.; Lekkerkerker, H. N. W.; Fleer, G. J.
Phase diagram for a mixture of colloids and polymers with equalsize
EPL: a Letters Journal Exploring the Frontiers of Physics, 82 (2008), 68002

Ueba, H.; Hayashi, M.; Paulsson, M.; Persson, B. N. J.
Adsorbate hopping via vibrational-mode coupling induced by femtosecond laser pulses
Physical Review B, 78 (2008) 11, 113408

231

Ueba, H.; Persson, B. N. J.
Heat transfer between adsorbate and laser-heated hot electrons
Journal of Physics: Condensed Matter, 20 (2008) 22, 224016

Ueba, H.; Persson, B. N. J.
Heating of adsorbate by vibrational-mode coupling
Physical Review B, 77 (2008) 3, 035413

Urban, K.
Studying atomic structures by aberration-corrected transmission electron microscopy
Science 321, 506-510 (2008)

Urban, K.; Houben, L.; Jia, C. L.; Lentzen, M.; Mi, S. B.; Thust, A.; Tillmann, K.
Atomic-Resolution Aberration-Corrected Transmission Electron Microscopy in: Advances in Imaging and Electron Physics,
edited by Peter Hawkes, published by Elsevier Inc. (London, Amsterdam and New York) Vol. 153, Chapter 11, 439-480 (2008)

Varga, Z.; Bóta, A.; Goerigk, G.
Unbinding Transition in Lipid Multibilayers Induced by Copper (II) Ions
Journal of Physical Chemistry B, 112 (2008) 29, 8430 – 8433

Vasenko, A. S.; Golubov, A. A.; Kupriyanov, M. Yu.; Weides, M.
Properties of tunnel Josephson junctions with a ferromagnetic interlayer
Physical Review B, 77 (2008), 134507

Verberck, B.; Heresanu, V.; Rouziere, S.; Cambedouzou, J.; Launois, P.; Kovats, E.; Pekker, S.; Vliegenthart, G.; Michel, K. H.; Gompper, G.
Fullerene-cubane: X-ray Scattering Experiments and Monte Carlo Simulations
Fullerenes Nanotubes and Carbon Nanostructures, 16 (2008), 293 – 300

Vliegenhart, G. A.
Introduction to Computer Simulations
Soft Matter: From Synthetic to Biological Materials: Lecture manuscripts of the 39th Spring School of the Institute of Solid State Research; this spring school was organized by the Institute of Solid State Research in the Forschungszentrum Jülich on March 3-14, 2008/ed.: J. K. G. Dhont, G. Gompper, G. Nägele, D. Richter, R. G. Winkler. – Jülich, Forschungszentrum, Zentralbibliothek, 2008. – (Schriften des Forschungszentrums Jülich. Reihe Schlüsseltechnologien/Key Technologies; 1). – 978-3-89336-517-3. – S. B1.1 – B1.33

Vliegenthart, G.; Gompper, G.
Mechanical properties of icosahedral virus capsids
Journal of Computer-Aided Materials Design, 14 (2007), 111 – 119

Volokitin, A.; Persson, B. N. J.
Theory of the interaction forces and the radiative heat transfer between moving bodies
Physical Review B, 78 (2008), 155437

Walter, M.; Akola, J.; Lopez-Acevedo, O.; Jadzinsky, P. D.; Calero, G.; Ackerson, C. J.; Whetten, R. L.; Grönbeck, H.; Häkkinen, H.
A unified view of ligand-protected gold clusters as superatom complexes
Proceedings of the National Academy of Sciences of the United States of America, 105 (2008), 9157 – 9162

Waser, R.
Information Technology I
1. Auflage; Weinheim, Wiley-VCH, 2008; Nanotechnology; 3; 9783527317387

Waser, R. (Hrsg.)
Information Technology II
Weinheim, Wiley-VCH, 2008; Nanotechnology; 4; 9783527317370

Watanabe, T.; Hoffmann-Eifert, S.; Hwang, C. S.; Waser, R.
Growth behavior of atomic-layer-deposited $Pb(Zr,Ti)O_x$ thin films on planar substrate and three-dimensional hole structures
Journal of the Electrochemical Society, 155 (2008), D715

Weides, M.
Magnetic anisotropy in ferromagnetic Josephson junctions
Applied Physics Letters, 93 (2008), 052502

Weides, M.; Goldobin, E.
Quantum computation – Principles and solid-state concepts
Information Technology II/ed.: R. Waser. – Weinheim, Wiley-VCH, 2008. – (Nanotechnology ; 4). – Chapter 13, S. 363

Widmer, R.; Maeder, R.; Heggen, M.; Feuerbacher, M.; Groening, O.
X-Ray Photoelectron Diffraction on the 6-fold $(001)\mu$-Al_4Mn Approximant Surface
Philosophical Magazine, 88 (2008), 2095

Wiegand, S.; Köhler, W.
Determination of molecular weights and their distributions
Comprehensive analytical chemistry/ed.: J. M. Chalmers, R. Meier. – Elsevier, Amsterdam, 2008. – (Molecular Characterization and Analysis of Polymers; 53). – Chapter 6, S. 205 – 251

Wiegand, S (Hrsg.); Köhler, W. (Hrsg.); Dhont, J. K. G. (Hrsg.)
Thermal Nonequilibrium:
Lecture Notes of the 8th International Meeting on Thermodiffusion; This Thermodiffusion Meeting has been organized by the Institute of Solid State Research and the University of Bayreuth in Bonn ... 9 – 13 June 2008 Jülich, Forschungszentrum, Zentralbibliothek, 2008 Schriften des Forschungszentrums Jülich . Reihe Schlüsseltechnologien/Key Technologies; 3
9783893365234

Winkler, R. G.
Microfluidics
Soft Matter: From Synthetic to Biological Materials: Lecture manuscripts of the 39th Spring School of the Institute of Solid State Research; this spring school was organized by the Institute of Solid State Research in the Forschungszentrum Jülich on March 3 – 14, 2008/ed.: J. K. G. Dhont, G. Gompper, G. Nägele, D. Richter, R. G. Winkler. – Jülich, Forschungszentrum, Zentralbibliothek, 2008. – (Schriften des Forschungszentrums Jülich. Reihe Schlüsseltechnologien/Key Technologies; 1). – 978-3-89336-517-3. – S. D8.1 – D8.35

Xu, X. S.; Angst, M.; Brinzari, T. V.; Hermann, R. P.; Musfeldt, J. L.; Christianson, A. D.; Mandrus, D.; Sales, B. C.; McGill, S.; Kim, J.-W.; Islam, Z.
Charge order, dynamics, and magneto-structural transition in multiferroic $LuFe_2O_4$
Physical Review Letters, 101 (2008), 227602-1 227602-4

Yaginuma, S.; Nagaoka, K.; Nagao, T.; Bihlmayer, G.; Koroteev, Y. M.; Chulkov, E. V.; Nakayama, T.
Electronic Structure of Ultrathin Bismuth Films with A7 and Black-Phosphorus-like Structures
Journal of the Physical Society of Japan, 77 (2008), 014701

232

Yamauchi, K.; Freimuth, F.; Blügel, S.; Picozzi, S.
Magnetically induced ferroelectricity in orthorhombic manganites: Microscopic Origin and chemical trends
Physical Review B, 78 (2008), 014403

Yan, H.; Frielinghaus, H.; Nykanen, A.; Ruokolainen, J.; Saiani, A.; Miller, A. F.
Thermoreversible lysozyme hydrogels: properties and an insight into the gelation pathway
Soft Matter, 4 (2008) 6, 1313

Yang, C.; Persson, B. N. J.
Contact mechanics: contact area and interfacial separation from small contact to full contact
Journal of Physics: Condensed Matter, 20 (2008) 21, 215214
Yang, C.; Tartaglino, U.; Persson, B. N. J.
Nanodroplets on rough hydrophilic and hydrophobic surfaces
European Physical Journal E, 25 (2008) 2, 139 – 152

Yang, Y.; Elgeti, J.; Gompper, G.
Cooperation of Sperm in Two Dimensions: Synchronization, Attraction and Aggregation through Hydrodynamic Interactions
Physical Review E, 78 (2008), 061903

Xia, J. H.; Jiang, X.; Jia, C. L.; Dong, C.
Hexahedral nanocementites catalizing the growth of carbon nanohelices
Appl. Phys. Lett., Vol. 92, 063121 (2008)

Yu, W.; Houben, L.; Tillmann, K.; Mader, W.
Atomic-resolution studies of $In_2O_3.ZnO$ compounds on aberration-corrected electron microscopes
Proceedings of the 14th European Microscopy Congress, Aachen (Germany)/ed. J. Mayer ... – 2 (2008). – S. 169 – 170

Zamponi, M.; Wischnewski, A.; Monkenbusch, M.; Willner, L.; Richter, D.; Falus, P.; Farago, B.; Guenza, M.G.
Cooperative dynamics in homopolymer melts: a comparision of theoretical predictions with neutron spin echo experiments
Journal of Physical Chemistry B, 112 (2008), 16220 – 16229

Zelenak, V.; Badanicova, M.; Halamova, D.; Cejka, J.; Zukal, A.; Murafa, N.; Goerigk, G.
Amine-modified ordered mesoporous silica: Effect of pore size on carbon dioxide capture
Chemical Engineering Journal, 144 (2008) 2, 336 – 342

Zeller, R.
Improving the charge density normalization in Korringa-Kohn-Rostoker Green-function calculations
Journal of Physics: Condensed Matter, 20 (2008), 035220

Zeller, R.
Linear-scaling total-energy with the tight-binding Korringa-Kohn-Rostoker Green function method
Philosophical Magazine, 88 (2008), 2807

Zeller, R.
Towards a linear-scaling algorithm for electronic structure calculations with the tight-binding Korringa-Kohn-Rostoker Green function method
Journal of Physics: Condensed Matter, 20 (2008), 294215

Zhou, P. H.; Moras, P.; Ferrari, L.; Bihlmayer, G.; Blügel, S.; Carbone, C.
One-Dimensional 3d Electronic Bands of Monatomic Cu Chains
Physical Review Letters, 101 (2008), 036807

Ziebinska, A.; Rytz, D.; Szot, K.
Birefringence above T_c in single crystals of barium titanate
Journal of Physics: Condensed Matter, 20 (2008), 142202

Zorn, R.
Fourier transform
Neutron Scattering: Lectures of the JCNS Laboratory Course held at Forschungszentrum Jülich and the research reactor FRM II of TU Munich; In cooperation with RWTH Aachen and University of Münster/ed.: T. Brückel, G. Heger, D. Richter, R. Zorn. – Jülich, Forschungszentrum, Zentralbibliothek, 2008. – (Schriften des Forschungszentrum Jülich. Reihe Schlüsseltechnologien/Key Technologies; 5). – 978-3-89336-532-6. – S. I-1 – I-29

Zorn, R.
Polyelectrolytes
Soft Matter: From Synthetic to Biological Materials: Lecture manuscripts of the 39th Spring School of the Institute of Solid State Research; this spring school was organized by the Institute of Solid State Research in the Forschungszentrum Jülich on March 3 – 14, 2008/ed.: J. K. G. Dhont, G. Gompper, G. Nägele, D. Richter, R. G. Winkler. – Jülich, Forschungszentrum, Zentralbibliothek, 2008. – (Schriften des Forschungszentrums Jülich. Reihe Schlüsseltechnologien/Key Technologies; 1). – 978-3-89336-517-3. – S. C3.1 – C3.23

Zorn, R.; Mayorova, M.; Richter, D.; Frick, B.
Inelastic neutron scattering study of a glass-forming liquid in soft confinement
Soft Matter, 4 (2008), 522 – 533

Zorn, R.; Mayorova, M.; Richter, D.; Schönhals, A.; Hartmann, L.; Kremer, F.; Frick, B.
Effect of nanoscopic confinement on the microscopic dynamics of glass-forming liquids and polymers studied by inelastic neutron scattering
AIP Conf. Proc. *982* 79 84 (2008)

Zorn, D.; Richter, D.
Correlation functions measured by scattering experiments
Neutron Scattering: Lectures of the JCNS Laboratory Course held at Forschungszentrum Jülich and the research reactor FRM II of TU Munich; in cooperation with RWTH Aachen and University of Münster/ed.: T. Brückel, G. Heger, D. Richter, R. Zorn. – Jülich, Forschungszentrum, Zentralbibliothek, 2008. – (Schriften des Forschungszentrum Jülich. Reihe Schlüsseltechnologien/Key Technologies; 5). – 978-3-89336-532-6. – S. 4.1 – 4.24

233

Ph.D. theses

Autin, A.; Sager, W. (Copromoter)

Precipitation of barium carbonate nanoparticles within water-in-oil microemulsion systems.

Relations between particle growth and surfactant environment

Nijmegen, Universiteit Nijmegen, 2008

Nijmegen, Univ., Diss., 2008

Barthel, J.

Ultra-Precise Measurement of Optical Aberrations for Sub-Angström Transmission Electron Microscopy

Jülich, Forschungszentrum, Zentralbibliothek, 2008

Berichte des Forschungszentrums Jülich; 4274

Aachen, RWTH, Diss., 2008

Frank, S.

Polyelectrolyte electrophoresis and sedimentation of polymers: A mesoscale simulation study

Jülich, Forschungszentrum Jülich, Institut für Festkörperforschung, 2008

Aachen, RWTH, Diss., 2008

Gögelein, C.

Phase behaviour of proteins and colloid-polymer mixtures

Forschungszentrum Jülich GmbH, Zentralbibliothek , 2008

Schriften des Forschungszentrums Jülich. Reihe Schlüsseltechnologien/Key Technologies; 9

9783893365555

Düsseldorf, Univ., Diss., 2008

Jeong, D. S.

Resistive Switching in Pt/Tio2/Pt

Jülich, Forschungszentrum Jülich, Institut für Festkörperforschung, 2008

Aachen, RWTH, Diss., 2008

Korolkov, D.

Structural analysis of diblock copolymer nanotemplates using grazing incidence scattering

Jülich, Forschungszentrum, Zentralbibliothek, 2008

Schriften des Forschungszentrums Jülich. Reihe Schlüsseltechnologien/Key Technologies; 2

9783893365227

Aachen, RWTH, Diss., 2008

Krug, I. P.

Magnetic Proximity Effects in Highly-ordered Transition Metal Oxide Heterosystems – A Study by Soft-X-Ray Photoemission Microscopy

Jülich, Forschungszentrum, Zentralbibliothek, 2008

Schriften des Forschungszentrums Jülich . Reihe Information / Information; 2

9783893365210

Duisburg, Univ., Diss., 2008

Li, H.

Synthesis of CMR manganites and ordering phenomena in complex transition metal oxides

Jülich, Forschungszentrum, Zentralbibliothek, 2008

Schriften des Forschungszentrums Jülich. Reihe Schlüsseltechnologien/Key Technologies; 4

9783893365272

Aachen, RWTH, Diss., 2008

Meßlinger, S.

Hydrodynamics of Rod-like Colloids and Vesicles

Jülich, Forschungszentrum Jülich, Institut für Festkörperforschung, 2008

Köln, Univ., Diss., 2008

Müller-Meskamp, L.

Ferrocenes as Potential Building Blocks for Molecular Electronics Self-Assembly and Tunneling Spectroscopy

Jülich, Forschungszentrum, Zentralbibliothek, 2008

Schriften des Forschungszentrums Jülich. Reihe Information / Information; 1

9783893365098

Aachen, RWTH, Diss., 2008

Nandy, B.

Theoretical Studies of the Chemotaxis of Biological Cells

Jülich, Forschungszentrum Jülich,

Institut für Festkörperforschung, 2008

Duisburg-Essen, Diss., 2008

Plonka, R.

Impact of the interface on the paraelectric-to-ferroelectric phase transition in epitaxial $BaSrTiO_3$ thin film capacitors

Jülich, Forschungszentrum, Zentralbibliothek, 2008

Berichte des Forschungszentrums Jülich; 4266

Aachen, RWTH, Diss., 2007

234

Polyakov, P.
Study of the thermal diffusion behavior of simple binary mixtures
Jülich, Forschungszentrum Jülich, Institut für Festkörper-forschung, 2008
9789036527545
Twente, Univ., Diss., 2008

Ratajczyk, M.; Lettinga, P. (Copromoter)
Behaviour of colloidal dispersions under high pressure
Posen, Mieckiewicz University, 2008
Posen, Univ., Diss., 2008

Tabatabei, F.
Hydrodynamics of colloids in a narrow channel: An analytical and a simulation study Institution
Mathematisch-naturwissenschaftliche Fakultät der Rheinischen Friedrich-Wilhelms-Universität Bonn, Univ., Diss., 2008

Woodford, S.
Ultrafast Magnetization Dynamics
Jülich, Forschungszentrum, Zentralbibliothek, 2008
Schriften des Forschungszentrums Jülich. Reihe Schlüsseltech-nologien / Key Technologies ; 6
9783893365364
Aachen, RWTH, Diss., 2008

Yang, C.
Role of Surface Roughness in Tribology: From Atomic to Macroscopic Scale
Jülich, Forschungszentrum, Zentralbibliothek, 2008
Schriften des Forschungszentrums Jülich Reihe Schlüsseltech-nologien / Key Technologies; 7
9783893365371
Berlin, TU, Diss., 2008

235

Diploma theses

Albiez, S.

Herstellung heteroepitaktischer Ferroelektrika und Charakterisierung mittels elektromechanischer Rastersondenmikroskopie

Jülich, Forschungszentrum Jülich,

Institut für Festkörperforschung, 2008

Aachen, RWTH, 2008

de Groot, J.

Strukturelle und magnetische Ordnung von multiferroischen TbMnO$_3$ Untersuchungen in Einkristallen und in Dünnschichten

Jülich, Forschungszentrum Jülich,

Institut für Festkörperforschung, 2008

Aachen, RWTH, 2008

Glavic, A.

Interferenzlithografie zur Erzeugung magnetischer Nanostrukturen: Von der lateralen Strukturierung bis zur Untersuchung der magnetischen Eigenschaften

Jülich, Forschungszentrum Jülich,

Institut für Festkörperforschung, 2008

Aachen, RWTH, 2008

Möchel, A.

Magnetische Struktur und Anregungen von SEMnO$_3$ Multiferroika (SE = Gd, Tb)

Jülich, Forschungszentrum Jülich,

Institut für Festkörperforschung, 2008

Bonn, Univ., 2008

Rosezin, R.

Herstellung und Charakterisierung von Elektrodensystemen für Nanocrossbar-Architekturen

Jülich, Forschungszentrum Jülich,

Institut für Festkörperforschung, 2008

Aachen, RWTH, 2008

Schumacher, D.

2-Dimensionaler Magnetismus von Eisen-Monolagen in Palladium

Jülich, Forschungszentrum Jülich,

Institut für Festkörperforschung, 2008

Aachen, RWTH, 2008

236

Conferences and schools

January 10 – 12   International Workshop on Computational Physics and Materials Science
Progress in Computational Electronic Structure Theory
Gustav-Stresemann-Institut Bonn, Germany

March 3 – 14   39th IFF Spring School
Soft Matter – From Synthetic to Biological Materials
Forschungszentrum Jülich, Germany

May 13 – 16   Nanoelectronics Days
RWTH Aachen University, Germany

June 9 – 13   8th International Meeting on Thermodiffusion
Gustav-Stresemann – Institut Bonn, Germany

August 31 – September 5
Gordon Research Conference Magnetic Nanostructures
Centre Paul Langevin Aussois, France

September 1 – 12   12th Neutron Scattering Labcourse
Forschungszentrum Jülich, Germany

September 24 – 26   Neutron Scattering Workshop on
Biomolecular Dynamics and Protein-Water Interactions
Bildungszentrum Feldafing, Germany

October 9 – 10   NanoFerronics-2008 – International workshop on Nanoferronics
Novel multifunctional metal-oxide tunnel-junctions relevant for future devices
Technologiezentrum Jülich, Germany

October 15 – 17   JCNS Workshop 2008
Modern Trends in Neutron Scattering Instrumentation
Hotel Seeblick, Bernried, Germany

November 12 – 14   Jülich Soft Matter Days 2008
Gustav-Stresemann – Institut Bonn, Germany

237

Kolloquia

February 1   John E. Inglesfield
University Cardiff, Great Britain
Time-dependent embedding

April 18   Gerald Kneller
Université d'Orléans, France
The Dynamics of Proteins and Liquids – From Brownian to Fractional Brownian Dynamics

April 25   Raffaele Resta
University of Trieste, Italy
Orbital magnetization in condensed matter

May 16   Matthias Fuchs
Universität Konstanz, Germany
Micro- and Macro-Rheology in dense colloidal dispersions

May 30   Marisol Ripoll
IFF, Forschungszentrum Jülich, Germany
Mesoscopic hydrodynamic simulations of soft matter systems in external fields

June 20   Jaroslav Fabian
Universität Regensburg, Germany
Semiconductor spintronics: from spin coherence to spin transistors

June 27   Jean-Marc Triscone
University of Geneva; Switzerland
New Phenomena at Interfaces between Insulating Oxides

July 4   Berend De Groot
Max Planck Institute for Biophysical Chemistry, Göttingen, Germany
Water and ion permeation through natural and synthetic membrane channels

July 11   Martin Aeschlimann
Universität Kaiserslautern, Germany
Time- and angle-resolved photoemission spectroscopy using a femto-second high-harmonic light-source

September 12   Gerald Manning
Rutgers University, USA
Topics in macromolecular electrostatics: effective charges, free energies, and conformational transitions

October 31   Bogdan Botar
IFF, Forschungszentrum Jülich, Germany
Chemical challenges in solar energy utilization

November 28   Maxim Mostovoy
University Groningen, The Netherlands
Magnetoelectric coupling in frustrated magnets

Institute of Solid State Research (IFF)

Institute of Solid State Research

Managing Director 2008
Prof. Dr. C. M. Schneider

Permanent Deputy Managing Director
D. Schlotmann

Divisions

IFF-1	Quantum Theory of Materials
	Prof. Dr. S. Blügel

IFF-2	Theoretical Soft-Matter and Biophysics
	Prof. Dr. G. Gompper

IFF-3	Theory of Structure Formation
	Prof. Dr. H. Müller-Krumbhaar

IFF-4	Scattering Methods
	Prof. Dr. T. Brückel

IFF-5	Neutron Scattering
	Prof. Dr. D. Richter

IFF-6	Electronic Materials
	Prof. Dr. R. Waser

IFF-7	Soft Condensed Matter
	Prof. Dr. J. K. G Dhont

IFF-8	Microstructure Research
	Prof. Dr. K. Urban

IFF-9	Electronic Properties
	Prof. Dr. C. M. Schneider

Technical Services and Administration

Administration
D. Schlotmann

Engineering & Design
H. Feilbach

Workshop
K. Hirtz

Accelerator Group
R. Hölzle

Networks & Numerics
D. Schlotmann

(1 October, 2008)

239

Personnel

Staff members (centrally financial)

- Scientific Staff   186
  Including those funded externally   *46*

- Technical Staff   66
  Including those funded externally   *3*

Staff members of service-groups   40

Administrations including Secretaries   18

Graduate students   68
Including those funded externally   *14*

Diploma students   31
Including those funded externally   *7*

Trainees   27

Guests Scientists staying for two weeks or longer   186

Invited lectures   127

240

Scientists on leave   51

Scientific Advisory Board

Joint Scientific Council
The joint Scientific Council of the IFF and IBN advises the Institute and the committees of Research Centre Jülich and functions as a supervisory board. The members of the council are leading scientists from research and industry. They are appointed for five years.

Prof. Dr. Georg Bednorz
IBM Research GmbH, Rüschlikon (CH)

Prof. Dr. Wim J. Briels
University Twente, AE Enschede (NL)

Dr. Kurt Clausen
Paul Scherrer Institut, Villingen (CH)

Dr. Manfred Horstmann
AMD Saxony LLC & Co. KG, Dresden (D)

Prof. Dr. Klaus Kern
Max-Planck-Institut, Stuttgart (D)

Prof. Dr. Jürgen Kirschner
Max-Planck-Institut, Halle (D)

Prof. Dr. Beate Klösgen
University of Southern Denmark, Odense (DK)

Prof. Dr. Hilbert von Löhneysen
Forschungszentrum Karlsruhe (D)

Prof. Dr. Werner Press (Chairman)
Christian Alberts-Universität Kiel (D)

Prof. Dr. Friederike Schmid
Universität Bielefeld (D)

Prof. Dr. Herbert Schöller
RWTH Aachen (D)

Prof. Dr. Clivia M. Sotomayor-Torres
University College Cork (IRE)

Prof. Dr. Hans-Rainer Trebin
Universität Stuttgart (D)

Prof. Dr. Gero Vogl
Universität Wien (A)

241

Scientists

Adam, Roman
Electronic Properties

Allgaier, Jürgen
Neutron Scattering

Angst, Niklaus Manuel
Scattering Methods

Appavou, Marie-Sousai Deveramban
Jülich Centre for Neutron Science

Arend, Nikolas
Jülich Centre for Neutron Science

Atodiresei, Nicolae
Quantum Theory of Materials

Auth, Thorsten
Theoretical Soft-Matter and Biophysics

Babcock, Earl
Jülich Centre for Neutron Science

Balanetskyy, Sergiy
Microstructure Research

Barthel, Juri
Microstructure Research

Baumgarten, Lutz
Electronic Properties

Baumgärtner, Artur
Theoretical Soft-Matter and Biophysics

Bechthold, Paul-Siegfried
Electronic Properties

Belhadji, Brahim
Theory of Structure Formation

Belushkin, Maxim
Theoretical Soft-Matter and Biophysics

Biehl, Ralf
Neutron Scattering

Bihlmayer, Gustav
Quantum Theory of Materials

Blügel, Stefan
Quantum Theory of Materials

Botar, Bogdan
Electronic Properties

Brener, Efim
Theory of Structure Formation

Brückel, Thomas
Scattering Methods

Buitenhuis, Johan
Soft Condensed Matter

Bürgler, Daniel-Emil
Electronic Properties

Busch, Peter
Jülich Centre for Neutron Science

Caciuc, Vasile
Quantum Theory of Materials

Carsughi, Flavio
Neutron Scattering

Chatterjee, Sakuntala
Theoretical Soft-Matter and Biophysics

Chatterjii, Apratim
Theoretical Soft-Matter and Biophysics

Chelakkot Govindalayam, Raghunath
Theoretical Soft-Matter and Biophysics

Chelaru, Liviu Ionut
Electronic Properties

Cherstvy, Andrey
Theoretical Soft-Matter and Biophysics

Claver-Cabrero, Ana
Neutron Scattering

Conrad, Harald
Scattering Methods

Costi, Theodoulos
Theory of Structure Formation

Cramm, Stefan
Electronic Properties

Dahbi, Louisa
Neutron Scattering

de Souza, Nicolas Raphäel Louis
Jülich Centre for Neutron Science

Dhont, Jan-Karel
Soft Condensed Matter

Dittmann, Regina
Electronic Materials

Divin, Yuri
Microstructure Research

Ebert, Philipp-Georg
Microstructure Research

Elgeti, Jens
Theoretical Soft-Matter and Biophysics

Faley, Mikhail
Microstructure Research

Feuerbacher, Michael
Microstructure Research

Frank, Sandra
Theoretical Soft-Matter and Biophysics

Frielinghaus, Henrich
Jülich Centre for Neutron Science

Frielinghaus, Xiuli
Neutron Scattering

Goerigk, Günter
Jülich Centre for Neutron Science

Gögelein, Christoph
Soft Condensed Matter

Gompper, Gerhard
Theoretical Soft-Matter and Biophysics

Gorelov, Evgeny
Theory of Structure Formation

Götze, Ingo Oliver
Theoretical Soft-Matter and Biophysics

Gourdon, Olivier
Jülich Centre for Neutron Science

Grushko, Benjamin
Microstructure Research

Guo, Xin
Electronic Materials

Gutberlet, Thomas Werner
Jülich Centre for Neutron Science

Head, David Andrew
Theoretical Soft-Matter and Biophysics

Heggen, Marc
Microstructure Research

Heide, Marcus
Quantum Theory of Materials

Heilmann, David Bernhard
Theory of Structure Formation

Heiß, Alexander
Neutron Scattering

Hermann, Raphael
Scattering Methods

Hertel, Riccardo
Electronic Properties

Hoffmann-Eifert, Susanne
Electronic Materials

Holderer, Olaf
Jülich Centre for Neutron Science

Holmqvist, Jan Peter
Soft Condensed Matter

Houben, Lothar
Microstructure Research

Huang, Chien-Cheng
Theoretical Soft-Matter and Biophysics

Hübner, Eike Gerhard
Neutron Scattering

Inoue, Rintaro
Neutron Scattering

Ioffe, Alexander
Jülich Centre for Neutron Science

Jeong, Doo Seok
Electronic Materials

Ji, Shichen
Theoretical Soft-Matter and Biophysics

Jia, Chunlin
Microstructure Research

Jiang, Run
Theoretical Soft-Matter and Biophysics

Kakay, Attila
Electronic Properties

Kang, Kyong Ok
Soft Condensed Matter

Karthäuser, Silvia
Electronic Materials

Kentzinger, Emmanuel
Scattering Methods

Kleshchanok, Dzina
Soft Condensed Matter

Koch, Erik Eduard
Quantum Theory of Materials

Kohlstedt, Herbert Hermann
Electronic Materials

Korolkov, Denis
Jülich Centre for Neutron Science

Kriegs, Hartmut Oskar Kurt
Soft Condensed Matter

Krug, Ingo Peter
Electronic Properties

Krutyeva, Margarita
Neutron Scattering

243

Kügeler, Carsten
Electronic Materials

Kusmin, André
Neutron Scattering

Landrock, Sebastian
Microstructure Research

Lang, Peter Robert
Soft Condensed Matter

Lazic, Predrag
Quantum Theory of Materials

Lehndorff, Ronald
Electronic Properties

Lentzen, Markus
Microstructure Research

Lettinga, Minne Paul
Soft Condensed Matter

Lezaic, Marjana
Quantum Theory of Materials

Liebsch, Ansgar
Quantum Theory of Materials

Lo Celso, Fabrizio
Neutron Scattering

Lonetti, Barbara
Neutron Scattering

Lounis, Samir
Quantum Theory of Materials

Lustfeld, Hans
Quantum Theory of Materials

Luysberg, Martina
Microstructure Research

Lyatti, Matvey
Microstructure Research

Mattauch, Stefan Hans Josef
Jülich Centre for Neutron Science

Matthes, Frank
Electronic Properties

Mayorova, Maria
Neutron Scattering

McPhie, Mathieu Gordon
Soft Condensed Matter

McWhirter, James Liam Yates
Theoretical Soft-Matter and Biophysics

Meier, Gerhard
Soft Condensed Matter

Meßlinger, Reginhard Sebastian
Theoretical Soft-Matter and Biophysics

Meuffels, Paul
Electronic Materials

Meyer, Carola
Electronic Properties

Mi, Shaobo
Microstructure Research

Miao, Jun
Electronic Materials

Mittal, Ranjan
Jülich Centre for Neutron Science

Monkenbusch, Michael
Neutron Scattering

Müller, Martina
Electronic Properties

Müller-Krumbhaar, Heiner
Theory of Structure Formation

Nägele, Gerhard
Soft Condensed Matter

Niesert, Manfred
Quantum Theory of Materials

Ning, Hui
Soft Condensed Matter

Niu-Ebert, Aizhen
Neutron Scattering

Noguchi, Hiroshi
Theoretical Soft-Matter and Biophysics

Nünighoff, Kay Uwe
Scattering Methods

Ohl, Michael
Jülich Centre for Neutron Science

Pandian, Ramanathaswamy
Electronic Materials

Pardo Soto, Luis Carlos
Jülich Centre for Neutron Science

Pavarini, Eva
Theory of Structure Formation

Persson, Bo
Quantum Theory of Materials

Perßon, Jörg
Scattering Methods

Petraru, Adrian Ion
Electronic Materials

Pipich, Vitaliy
Jülich Centre for Neutron Science

Pithan, Christian
Electronic Materials

Plucinski, Lukasz
Electronic Properties

Polyakov, Pavel
Soft Condensed Matter

Poppe, Ulrich
Microstructure Research

Prager, Michael
Neutron Scattering

Pyckhout-Hintzen, Wim
Neutron Scattering

Qureshi, Mohammad
Electronic Properties

Radulescu, Aurel
Jülich Centre for Neutron Science

Richter, Dieter
Neutron Scattering

Ripoll Hernando, Maria Soledad
Theoretical Soft-Matter and Biophysics

Rücker, Ulrich
Scattering Methods

Rüdiger, Andreas
Electronic Materials

Rushchanskii, Konstantin
Quantum Theory of Materials

Sager, Wiebke
Soft Condensed Matter

Saha, Debasish
Neutron Scattering

Saptsov, Roman
Theory of Structure Formation

Schindlmayr, Arno
Quantum Theory of Materials

Schmalzl, Karin Elisabeth
Jülich Centre for Neutron Science

Schmidt, Wolfgang
Jülich Centre for Neutron Science

Schneider, Claus Michael
Electronic Properties

Schneider, Gerald-Johannes
Jülich Centre for Neutron Science

Schroeder, Herbert
Electronic Materials

Schütz, Gunter-Markus
Theoretical Soft-Matter and Biophysics

Schwahn, Dietmar
Neutron Scattering

Schweika, Werner
Scattering Methods

Shibuya, Keisuke
Electronic Materials

Singh, Sunil
Theoretical Soft-Matter and Biophysics

Spatschek, Robert Philipp Maximilian
Theory of Structure Formation

Staikov, Georgi Tzvetanov
Electronic Materials

Stellbrink, Jörg
Neutron Scattering

Stiakakis, Emmanuel Ioannis
Soft Condensed Matter

Su, Yixi
Jülich Centre for Neutron Science

Swiatek, Piotr
Electronic Properties

Szot, Krzysztof
Electronic Materials

Tabatabaei, Panah
Theoretical Soft-Matter and Biophysics

Thust, Andreas
Microstructure Research

Tillmann, Karsten
Microstructure Research

Tsukamoto, Shigeru
Quantum Theory of Materials

Tuinier, Remco
Soft Condensed Matter

Upadhyay, Chandan
Soft Condensed Matter

Urban, Knut
Microstructure Research

Vliegenthart, Gerard Adriaan
Theoretical Soft-Matter and Biophysics

Voigt, Jörg Jakob
Jülich Centre for Neutron Science

Waser, Rainer
Electronic Materials

Wegewijs, Maarten Rolf
Theory of Structure Formation

Weides, Martin Peter
Electronic Materials

Weng, Robert
Electronic Materials

245

Wiegand, Simone
Soft Condensed Matter

Wiemann, Carsten
Electronic Properties

Willner, Lutz
Neutron Scattering

Winkler, Roland
Theoretical Soft-Matter and Biophysics

Wischnewski, Andreas
Neutron Scattering

Woodford, Simon Richard
Quantum Theory of Materials

Wortmann, Daniel
Quantum Theory of Materials

Wuttke, Joachim
Jülich Centre for Neutron Science

Xiao, Yinguo
Scattering Methods

Yan, Ming
Electronic Properties

Yang, Chunyan
Quantum Theory of Materials

Yoon, Songhak
Electronic Materials

Zagonel, Luiz Fernando
Electronic Properties

Zamponi, Michaela
Jülich Centre for Neutron Science

Zeller, Rudolf
Theory of Structure Formation

Zhang, Jing
Soft Condensed Matter

Zorn, Reiner
Neutron Scattering

Graduate students

Al-Zubi, Ali
Quantum Theory of Materials

Arlt, Bastian
Soft Condensed Matter

Baumeister, Paul Ferdinand
Quantum Theory of Materials

Betzinger, Markus
Quantum Theory of Materials

Brodeck, Martin
Neutron Scattering

Chogondahalli Muniraju, Naveen Kumar
Scattering Methods

Claudio Weber, Tania
Scattering Methods

de Groot, Joost
Scattering Methods

Disch, Sabrina
Scattering Methods

Dolfen, Andreas
Quantum Theory of Materials

Fleck, Michael
Theory of Structure Formation

Frank, Sandra
Theoretical Soft-Matter and Biophysics

Freimuth, Frank
Quantum Theory of Materials

Fu, Zhendong
Scattering Methods

Gerstl, Christine Ilona
Neutron Scattering

Gierlich, Andreas Gottfried
Quantum Theory of Materials

Glavic, Artur Gregor
Scattering Methods

Gliga, Sebastian
Electronic Properties

Gögelein, Christoph
Soft Condensed Matter

Goß, Karin
Electronic Properties

Gugenberger, Clemens Matthias
Theory of Structure Formation

Heers, Swantje
Quantum Theory of Materials

Heidelmann, Markus
Microstructure Research

Heinen, Marco
Soft Condensed Matter

Hüter, Claas
Theory of Structure Formation

July, Christoph
Soft Condensed Matter

Kerscher, Michael
Neutron Scattering

Kowalzik, Peter
Electronic Materials

Lehndorff, Ronald
Electronic Properties

Lennartz, Maria Christina
Electronic Materials

Lipinska-Chwalek, Marta Agata
Microstructure Research

Lorenz, Boris
Quantum Theory of Materials

Lüsebrink, Daniel Alexander
Theoretical Soft-Matter and Biophysics

Manheller, Marcel
Electronic Materials

Marx, Kristian
Theoretical Soft-Matter and Biophysics

Meier, Matthias
Electronic Materials

247

Menke, Tobias
Electronic Materials

Mennig, Martin Julius
Electronic Properties

Meßlinger, Reginhard Sebastian
Theoretical Soft-Matter and Biophysics

Möchel, Anne
Scattering Methods

Münstermann, Ruth
Electronic Materials

Nauenheim, Christian
Electronic Materials

Nusser, Klaus Lothar Josef
Neutron Scattering

Pavlyuchkov, Dmytro
Microstructure Research

Polyakov, Pavel
Soft Condensed Matter

Rahmanizadeh, Kourosh
Theory of Structure Formation

Reckermann, Felix David
Theory of Structure Formation

Röhrig, Sergre
Electronic Materials

Rosezin, Roland Daniel
Electronic Materials

Schindler, Christina
Electronic Materials

Schlipf, Martin Ulrich
Quantum Theory of Materials

Schumacher, Daniel
Scattering Methods

Schützendorf, Patrick Rene
Electronic Materials

Shanmugavadivelu, Gopinath
Soft Condensed Matter

Shen, Wan
Electronic Materials

Sluka, Volker
Electronic Properties

Soni, Rohit
Electronic Materials

Spudat, Christian
Electronic Properties

Steffens, Lars
Electronic Materials

Thieß, Alexander Reinhold
Quantum Theory of Materials

Tomczyk, Karolina Renata
Soft Condensed Matter

Tranca, Ionut Claudiu
Theory of Structure Formation

Tsigkri, Angeliki
Soft Condensed Matter

Woodford, Simon
Quantum Theory of Materials

Yang, Lin
Electronic Materials

Yang, Chunyan
Quantum Theory of Materials

Yang, Yingzi
Theoretical Soft-Matter and Biophysics

Technical staff

Bergs, Wolfgang
Scattering Methods

Bickmann, Konrad
Electronic Properties

Bierfeld, Hermann-Josef
Electronic Materials

Bläsen, Franz
Networks and Numerical Methods

Bongartz, Dieter
Networks and Numerical Methods

Borowski, René Michael
Electronic Materials

Both, Sabrina-Aloisia
Networks and Numerical Methods

Braun, Waldemar
Design/Workshop

Bremen, Arnd
Design/Workshop

Bünten, Ulrich
Neutron Scattering

Bussmann, Klaus Max
Scattering Methods

de Waal, Sylvia-Maria
Soft Condensed Matter

Doghmi, Jaouad
Networks and Numerical Methods

Emmerich, Hans-Matthias
Design/Workshop

Enns, Andreas
Design/Workshop

Erven, Andreas
Jülich Centre for Neutron Science

Esser, Heinz-Peter
Design/Workshop

Feilbach, Herbert
Design/Workshop

Friedrich, Jochen
Electronic Materials

Früh, Stefanie Maria
Design/Workshop

Funk-Kath, Ursula
Networks and Numerical Methods

Gebauer, Manfred
Electronic Materials

Gehlhaar, Reimund Werner
Design/Workshop

Gerst, Marcel
Electronic Materials

Gödel, Marco
Jülich Centre for Neutron Science

Gossen, Frank
Jülich Centre for Neutron Science

Graf, Karl-Heinz
Microstructure Research

Gülak, Fatma
Networks and Numerical Methods

Gurzi, Dennis
Jülich Centre for Neutron Science

Hahn, Christoph
Networks and Numerical Methods

Harbott, Peter
Scattering Methods

Haselier, Johann
Electronic Materials

Heiderich, Manfred
Neutron Scattering

Heinen, Josef
Networks and Numerical Methods

Henkel, Dorothea
Networks and Numerical Methods

Hiller, Peter
Scattering Methods

249

Hintzen, Maria Elisabeth
Neutron Scattering

Hirtz, Kurt
Design/Workshop

Hoffmann, Hans-Jürgen
Soft Condensed Matter

Hölzle, Micha Marc Gerhard
Jülich Centre for Neutron Science

Horriar-Esser, Christel
Scattering Methods

Jansen, Thomas
Electronic Properties

John, Holger
Electronic Materials

Johnen, Karl-Heinz
Design/Workshop

Jungbluth, Heinrich
Scattering Methods

Kinzel, Gernot
Networks and Numerical Methods

Klein, Horst
Scattering Methods

Kluck, Günther
Neutron Scattering

Köhne, Franz-Josef
Electronic Properties

Kohnke, Thomas
Jülich Centre for Neutron Science

Kozielewski, Tadeusz
Jülich Centre for Neutron Science

Küpper, Bernhard
Electronic Properties

Kusche, Harald
Jülich Centre for Neutron Science

Küssel, Eckhard
Scattering Methods

Lauer, Jürgen
Electronic Properties

Leuchtenberg, Anton
Design/Workshop

Lingenbach, Peter Josef
Design/Workshop

Lumma, Nils Friedemann
Design/Workshop

Macht, Kay
Jülich Centre for Neutron Science

Makovicka, Cerstin Renate
Electronic Materials

Makselon, Joanna Maria
Electronic Properties

Matulewski, Anton
Design/Workshop

Meertens, Doris
Microstructure Research

Nebel, Andreas Fabian
Jülich Centre for Neutron Science

Nguyen, Vu-Thanh
Neutron Scattering

Olefs, Bodo-August
Networks and Numerical Methods

Ossovyi, Vladimir
Jülich Centre for Neutron Science

Peters, Alexander
Networks and Numerical Methods

Pfeifer, Heinz
Electronic Properties

Pickartz, Georg
Electronic Materials

Pieper, Werner
Microstructure Research

Pohl, Maria
Design/Workshop

Radermacher, Bert Hubert
Design/Workshop

Rehfisch, Jessica
Design/Workshop

Reisen, Christian
Neutron Scattering

Sachsenhausen, Hans-Rudolf
Design/Workshop

Sausen-Malka, Ulrike
Neutron Scattering

Schätzler, Liane
Networks and Numerical Methods

Schätzler, Reinhardt
Neutron Scattering

Schmidt, Marita
Microstructure Research

Schmitz, Michael
Neutron Scattering

Schmitz, Berthold-Klaus
Scattering Methods

Schneider, Harald Michael
Jülich Centre for Neutron Science

Schnitzler, Helmut-Hubert
Design/Workshop

Schnitzler, Jens-Willi
Design/Workshop

Schnitzler, Norbert
Electronic Properties

Schramm, Franz-Josef
Design/Workshop

Schreiber, Reinert
Electronic Properties

Schumacher, Miriam Helga
Networks and Numerical Methods

Sellinghoff, Karin
Soft Condensed Matter

Speen, Hans-Rolf
Microstructure Research

Starc, Thomas
Neutron Scattering

Stefelmanns, Hans-Peter
Design/Workshop

Stollenwerk, Robert
Neutron Scattering

Stronciwilk, Peter
Jülich Centre for Neutron Science

Sybertz, Wilma
Microstructure Research

Telschow, Roger
Networks and Numerical Methods

Thomas, Carsten
Microstructure Research

Thomas, Rita
Networks and Numerical Methods

Triefenbach, Dieter
Soft Condensed Matter

Vehres, Guido
Neutron Scattering

Wassenhoven, Gabriele-Marie
Microstructure Research

Werges, Fred
Scattering Methods

Westphal, Elmar
Networks and Numerical Methods

Wingerath, Kurt
Networks and Numerical Methods

Würtz, Eva Maria
Microstructure Research

251

Administrative staff and secretaries

Borges, Martina
Neutron Scattering

Garcia y Gonzales, Maria
Electronic Materials

Göcking, Marie-Luise
Soft condensed matter

Gollnick, Jutta
Electronic Properties

Griesen, Johann Engelbert
Administration

Hölzle, Rainer
Accelerator Group

Köppchen, Barbara-Dorothea
Scattering Methods

Michel, Franziska
Jülich Centre for Neutron Science

Mirea, Elena
Administration

Ockenfels, Silke
Administration

Oubenkhir, Saida
Neutron Scattering

Paffen, Helga
Theoretical Soft-Matter and Biophysics

Rische-Radloff, Ingrid
Mictrostructure Research

Schlotmann, Dirk
Administration

Schnitzler, Anna Christine
Neutron Scattering

Sittardt, Hanne
Administration

Snyders, Luise
Theory of Structure Formation

Wassenhoven, Gertrud
Administration

Wenzik, Angela
Administration

Winkler, Ute
Quantum Theory of Materials

Scientists on leave

Appavou, Marie-Sousai Deveram
Jülich Centre for Neutron Science, München, Germany

Arend, Nikolas
Spallation Neutron Source , Oak Ridge, USA

Atodiresei, Nicolae
Osaka University, Japan

Betzinger, Markus
University Erlangen, Germany

Brodeck, Martin
Donostia International Physical Center, San Sebastian, Spain

Busch, Peter
Jülich Centre for Neutron Science, München, Germany

Chatterji, Tapan
Insitut Laue Langevin, Grenoble, France

Deac-Renner, Alina Maria
Spallation Neutron Source , Oak Ridge, USA

Elgeti, Jens
Institute Curie, Paris, France

Erven, Andreas
Jülich Centre for Neutron Science, München, Germany

Frielinghaus, Henrich
Jülich Centre for Neutron Science, München, Germany

Frielinghaus, Xiuli
Jülich Centre for Neutron Science, München, Germany

Gierlich, Andreas-Gottfried
Chiba University, Chiba, Japan

Goerigk, Günter
Jülich Centre for Neutron Science, München, Germany

Gossen, Frank
Jülich Centre for Neutron Science, München, Germany

Gutberlet, Thomas Werner
Jülich Centre for Neutron Science, München, Germany

Heggen, Marc
Harvard University, Cambridge, USA

Hölzle, Micha Marc Gerhard
Jülich Centre for Neutron Science, München, Germany

Holderer, Olaf
Jülich Centre for Neutron Science, München, Germany

Ioffe, Alexander
Jülich Centre for Neutron Science, München, Germany

Korolkov, Denis
Jülich Centre for Neutron Science, München, Germany

Kozielewski, Tadeusz
Spallation Neutron Source , Oak Ridge, USA

Krug, Ingo-Peter
CEA, Saclay, France

Lässer, Rainer
EFDA CSU, München-Garching, Germany

Lehndorff, Ronald
University of Colorado, Colorado Springs, USA

Lezaic, Marjana
University of California, Santa Barbara, USA

Macht, Kay
Jülich Centre for Neutron Science, München, Germany

Mattauch, Stefan Hans Josef
Jülich Centre for Neutron Science, München, Germany

Mittal, Ranjan
Jülich Centre for Neutron Science, München, Germany

253

Müller, Martina
Francis Bitter Magnet Laboratory,
Massachusetts, USA

Münstermann, Ruth Christine
Hewlett-Packard Quantum Research Laboratory,
Palo Alto, USA

Nebel, Andreas Fabian
Jülich Centre for Neutron Science, München,
Germany

Nusser, Klaus Lothar Josef
Jülich Centre for Neutron Science, München,
Germany

Ohl, Michael
Spallation Neutron Source, Oak Ridge, USA

Ossovyi, Vladimir
Jülich Centre for Neutron Science, München,
Germany

Pipich, Vitaliy
Jülich Centre for Neutron Science, München,
Germany

Radulescu, Aurel
Jülich Centre for Neutron Science, München,
Germany

Rüdiger, Andreas
Institute National de la Recherche Scientifique,
Québec, Canada

Schindlmayr, Arno
University of Paderborn, Germany

Schmalzl, Karin Elisabeth
Institut Laue Langevin, Grenoble, France

Schmidt, Wolfgang
Institut Laue Langevin, Grenoble, France

Schneider, Gerald-Johannes
Jülich Centre for Neutron Science, München,
Germany

Schneider, Harald Michael
Jülich Centre for Neutron Science, München,
Germany

Spatschek, Robert Phillip Maximilian
University of California,
Davis, USA

Ströbl, Michael
Jülich Centre for Neutron Science, München,
Germany

Stronciwilk, Peter
Jülich Centre for Neutron Science, München,
Germany

Su, Yixi
Jülich Centre for Neutron Science, München,
Germany

Swiatec, Piotr
ESF/COST-Büro,
Brüssel, Belgium

Voigt, Jörg Jakob
Jülich Centre for Neutron Science, München,
Germany

Wischnewski, Andreas
Bundesministerium für Bildung
und Forschung,
Bonn, Germany

Wuttke, Joachim
Jülich Centre for Neutron Science, München,
Germany

Zamponi, Michaela
Spallation Neutron Source , Oak Ridge, USA

254

Guest scientists

Argentina

di Napoli, Dr., Solange
Quantum Theory of Materials
University of Buenos Aires

Manuel, Dr., Luis O.
Quantum Theory of Materials
Nationel University of Rosario

Australia

Foster, Dr., Leslie John Ray
Neutron Scattering
University of New South Wales, Sydney

Hambe, Michael
Electronic Materials
University of New South Wales, Sydney

Belgium

Pilipenko, Dr., Denis
Theory of Structure Formation
Universite Libre de Bruxelles

Reddy, Naveen Krishna
Soft Condensed Matter
Katholieke Universiteit Leuven

Verberck, Dr., Bart
Theoretical Soft-Matter and Biophysics
Universität Antwerpen

Vermant, Prof. Dr., Jan
Soft Condensed Matter
K. V. Leuven

Canada

Arrott, Prof. Dr., Anthony S.
Electronic Properties
Simon-Fraser-Universität, Vancouver

Marceau, Vincent
Theoretical Soft-Matter and Biophysics
Laval University

Chile

Florez Uribe, Juan Manuel
Quantum Theory of Materials
Universidad Federico Santa Maria

Vargas, Prof., Patricio
Quantum Theory of Materials
Universidad Santa Maria

China

Han, Xiujun
Theory of Structure Formation
Northwestern Polytechnical University, Xian

Jiang, Ying
Microstructure Research
Chinese Academy of Sciences Peking

Li, Dr., Peigang
Electronic Materials
Zhejiang sci-tech University

Li, Yang
Electronic Materials
University of Technology

Na, Lei
Electronic Properties
Fudan University Shanghai

Xia, Junhai
Microstructure Research
Dalian University of Technology,
Liaoning Province

Zhou, Zhiyay
Electronic Materials
Chinese Academy of Sciences Shanghai

Zhou, Zhiyong
Electronic Materials
Chinese Academy of Sciences Shanghai

Colombia

Gross, Katherine
Scattering Methods
Universidad del Valle

Croatia

Lazic, Dr., Predag
Quantum Theory of Materials
Ruder Boskovic Institute

Denmark

Sivebak, Dr., Ion
Quantum Theory of Materials
Technical University of Denmark

France

Bécu, Dr., Lydiane
Soft Condensed Matter
Polymeres, Colloides, Interfaces (CNRS), Le Mans

Pouget, Dr., Emilie
Soft Condensed Matter
Centre de Research Paul Pascal

Slipukhina, Ivetta
Quantum Theory of Materials
CEA Grenoble

Zaccai, Joseph
Neutron Scattering
Institut de Biologie Structurale, Grenoble

Zhang, Zhenkun
Soft Condensed Matter
C.R.P.P Avenue Albert Schweitzer, Pessac

Germany

Al-Hada, Dr., Mohamed
Electronic Properties
Technische Universität Berlin

Arunthavarajah, Abiramy
Soft Condensed Matter
Fachhochschule Jülich

Beigmohamadi, Dr., Maryam
Microstructure Research
RWTH Aachen

Böttger, Dr., Ulrich
Electronic Materials
RWTH Aachen

Boussinot, Dr., Guillaume
Theory of Structure Formation
RWTH Aachen

Bräuhaus, Dennis
Electronic Materials
RWTH Aachen

Bückins, Dr., Matthias
Microstructure Research
RWTH Aachen

Burkert, Andreas
Electronic Materials
RWTH Aachen

Clemens, Sven
Electronic Materials
RWTH Aachen

Darlinski, Grzegorz
Electronic Materials
RWTH Aachen

Dehoff, Carsten
Electronic Materials
RWTH Aachen

Dippel, Ann-Christin
Electronic Materials
RWTH Aachen

Egelhaaf, Prof. Dr., Stafan Ulrich
Neutron Scattering
Heinrich-Heine Universität, Düsseldorf

Evertz, Udo
Electronic Materials
RWTH Aachen

Friedrich, Dr., Christoph
Quantum Theory of Materials
Universität Paderborn

Ghadimi, Dr. rer. nat., Reza
Microstructure Research
RWTH Aachen

Gorelov, Dr., Evgeny
Quantum Theory of Materials
Universität Hamburg

Grychtol, Patrick
Electronic Properties
Universität Karlsruhe

Hanes, Richard
Soft Condensed Matter
Universität Düsseldorf

Heins, Martina
Electronic Materials
RWTH Aachen

Heinze, Dr., Stefan
Quantum Theory of Materials
Universtät Hamburg

Hennings, Dr. rer. nat., Detlef
Electronic Materials
Philips Forschungslabor Aachen

256

Hergesell, Hans-Günther
JCNS Garching
Correct Power Inst. Ltd.

Hermes, Dr., Helen
Neutron Scattering
Universität Düsseldorf

Herzog, Stefan
Theory of Structure Formation
RWTH Aachen

Hönig, Andreas
Quantum Theory of Materials
Stiftung Caesar Bonn

Houben, Andreas
Scattering Methods
RWTH Aachen

Hüwel, Albert
JCNS Garching
Correct Power Inst. Ltd.

Jahan, Sangida
Soft Condensed Matter
Fachhochschule Aachen

Jenkins, Dr., Matthew
Soft Condensed Matter
Universität Düsseldorf

Jungblut, Swetlana
Soft Condensed Matter
Johannes-Gutenberg-Universität Mainz

Kaiser, Alexander
Electronic Properties
Universität Duisburg-Essen

Karakatsanis, Ioannis
Electronic Materials
RWTH Aachen

Kever, Thorsten
Electronic Materials
RWTH Aachen

Klopstra, Bart
Electronic Materials
RWTH Aachen

Kögerler, Paul
Electronic Properties
RWTH Aachen

Kollamana, Jobynson
Electronic Properties
RWTH Aachen

Konstantinidis, Nikolaos
Theory of Structure Formation
RWTH Aachen

Linn, Eike
Electronic Materials
RWTH Aachen

Lorenz, Boris
Quantum Theory of Materials
RWTH Aachen

Mayer, Prof. Dr., Joachim
Microstructure Research
RWTH Aachen

Menzel, Stephan
Electronic Materials
RWTH Aachen

Mokrousov, Dr., YuriyQuantum
Theory of Materials
Universität Hamburg

Morgenstern, Prof., Markus
Electronic Materials
RWTH Aachen

Nickel, Florian
Electronic Properties
Universität Dortmund

Oligschleger, Prof. Dr., Christina
Theory of Structure Formation
Fachhochschule Rheinbach

Pohl, Darius
Microstructure Research
Leibniz-Institut für Festkörper- und Werkstoffforschung

Reichenberg, Bernd
Electronic Materials
RWTH Aachen

Reinholt, Dr., Alexander
Microstructure Research
RWTH Aachen

Roitsch, Dr., Stefan
Microstructure Research
RWTH Aachen

Röscher, Mark
Electronic Materials
RWTH Aachen

Sasioglu, Ersoy
Quantum Theory of Materials
Max-Planck-Institut Halle

Schindlmayr, Prof. Dr., Arno
Quantum Theory of Materials
Universität Paderborn

Schmelzer, Sebastian
Electronic Materials
RWTH Aachen

Schmitz, Thorsten
Electronic Materials
aisACCT Systems GmbH, Aachen

Schneller, Theodor
Electronic Materials
RWTH Aachen

Simon, Prof., Ulrich
Electronic Materials
RWTH Aachen

Solbach, Axel
Electronic Materials
RWTH Aachen

Sologubenko, Alla
Microstructure Research
RWTH Aachen

Sottmann, Dr. rer. nat., Thomas
Neutron Scattering
Universität zu Köln

Spatschek, Dr., Robert
Theory of Structure Formation
Universität Bochum

Sprungmann, Dirk
Electronic Materials
Ruhr-Universität Bochum

Steinkühler,
JCNS Garching
Correct Power Inst. Ltd.

Straube, Prof., Ekkehard
Neutron Scattering
Martin-Luther-Univeristät Halle Wittenburg

Strey, Prof. Dr., Reinhard
Soft Condensed Matter
Universität zu Köln

Tiedke, Stephan
Electronic Materials
RWTH Aachen

Walter, Dr., Jens Martin
Scattering Methods
Universität Göttingen

Weirich, Thomas
Microstructure Research
RWTH Aachen

Weng, Robert
Electronic Materials
RWTH Aachen

Greece

Iatrou, Dr., Ermolaos
Neutron Scattering
University of Athens

Loppinet, Dr., Benoit
Soft Condensed Matter
FORTH Heraklion

Michailidou, Dr., Vassiliki
Soft Condensed Matter
FORTH Institute of Electronic Structure Heraklion

Petekidis, Dr., George
Soft Condensed Matter
FORTH Heraklion

Renou, Dr., Frederic
Neutron Scattering
FORTH Heraklion

Vlassopoulos, Prof. Dr., Dimitris
Soft Condensed Matter
FORTH Heraklion

Voudouris, Panayiotis
Soft Condensed Matter
FORTH Institute of Electronic Structure Heraklion

Hungary

Vass, Dr., Szabolcs
Soft Condensed Matter
KFKI Atomic Energy Res. Institute, Budapest

India

Gupta, Sudipta
Neutron Scattering
Indian Institute of Technology

Joshi, Rohit
Neutron Scattering
IIT Guwahati, Assam

Kamra, Akashdeep
Electronic Properties
Indian Institute of Technology Kanpur

Murthy, Dr., K.P.N.
Theoretical Soft-Matter and Biophysics
University of Hyderabad

Nandy, Bidisha
Theoretical Soft-Matter and Biophysics
Indian Institute of Technology, Kharagpur

258

Saha, Dabasish
Neutron Scattering
IIT Madras

Yadav, Ajay Kumar
Electronic Materials
Indian Institute of Technology Kanpur

Iran

Alaei, Mojtaba
Quantum Theory of Materials
Isfahan University of Technology

Bamdad, Kourosh
Theoretical Soft-Matter and Biophysics
Tarbiat Modarres University, Tehran

Israel

Bar Sadan, Maya
Microstructure Research
Weizmann Institute Rehovot

Italy

Botti, Dr., Alberto
Neutron Scattering
Universita di Roma Tre, Roma

Carbone, Dr., Guiseppe
Quantum Theory of Materials
Politecnico di Bari, Bai

Lamura, Antonio
Theoretical Soft-Matter and Biophysics
Instituto Applicazioni Calcolo, CNR, Bari

Perroni, Dr., Antonio Carmine
Quantum Theory of Materials
Physics Department Napoli

Picozzi, Dr., Silvia
Quantum Theory of Materials
Universita di L'Aquila

Popkov, Vladislav
Theoretical Soft-Matter and Biophysics
Universität Salerno

Scaraggi, Michele
Quantum Theory of Materials
Politecnico di Bari

Tartaglino, Dr., Ugo
Quantum Theory of Materials
INFM Democtritos National Simulation Center, Trieste

Japan

Ishida, Hiroshi
Quantum Theory of Materials
Nihon University, Tokyo

Ishii, Prof., Fumiyuki
Quantum Theory of Materials
Kanazawa University

Katsu, Hayato
Electronic Materials
Murata Manufacturing Co. LtD

Komura, Dr., Shigeyuki
Theoretical Soft-Matter and Biophysics
Metropolitan University Tokio

Noguchi, Dr., Hiroshi
Theoretical Soft-Matter and Biophysics
University of Tokyo, Kashiwa

Ogura, Dr., Masako
Theory of Structure Formation
Osaka University, Osaka

Sato, Kazunori
Theory of Structure Formation
Department of condensed matter physics, Osaka

Shibuya, Kesiuke
Electronic Materials
University of Tokyo, Kashiwa

Shishidou, Dr., Tatsuya
Quantum Theory of Materials
Hiroshima Science University

Suga, Prof. Dr., S.
Electronic Properties
Osaka University, Osaka

Yamauchi, Kunihiko
Quantum Theory of Materials
Universität Osaka

Yanagisawa, Susumu
Quantum Theory of Materials
Universität Osaka

Korea

Jeong, Doo Seok
Electronic Materials
Seoul National Univeristy Shillim-dong, Gwanak-gu

Seong, Dr., Kim
Electronic Materials
Seoul National University

259

Yoon, Songhak
Electronic Materials
Department of Materials Sci. & Eng., Pohang

Netherlands

Briels, Wim
Soft Condensed Matter
Universität Twente

Ramanathaswamy, Dr.
Electronic Materials
Universität Groningen

Zandvliet, Prof. Dr., Harold
Electronic Materials
University of Twente

Poland

Busiakiewicz, Dr., Adam
Electronic Materials
University of Lodz

Cichocki, Prof. Dr., Bogdan
Soft Condensed Matter
Universität Warschau

Ekiel-Jezewska, Dr., Maria
Soft Condensed Matter
Polish Academy of Sciences

Gapinski, Dr., Jacek
Soft Condensed Matter
A Mickiewicz University, Poznan

Kaczkowski, Jakub
Quantum Theory of Materials
Polish Academy of Sciences

Klamecka, Camila
Soft Condensed Matter
A Mickiewicz University, Poznan

Kowalski, Wojciech
Microstructure Research
University of Silesia, Kaowice

Krok, Dr., Franciszek
Electronic Materials
Jagiellonian University

Lipinska-Chwalek, Maria
Microstructure Research
AGH University of Science

Molak, Dr., Andrzej
Electronic Materials
University of Silesia, Kattowice

Oles, Tomasz
Neutron Scattering
Universität Warschau

Patkowski, Prof., Adam
Soft Condensed Matter
A. Mieckiewicz University, Poznan

Pilch, Michal
Electronic Materials
Schlesische Universität Kattowice

Ratajczyk, Dr., Monika
Soft Condensed Matter
A. Mieckiewicz University, Poznan

Rogala, Maciej
Electronic Materials
Lodz Universität

Siemiatkowska, Anna
Soft Condensed Matter
A Mickiewicz University, Poznan

Romania

Botar, Dr., Alexandru
Electronic Properties
JIALEX SRL, Cluj-Napoca

Russia

Marchenko, Vladimir
Theory of Structure Formation
Russische Akademie der Wissenschaften, Chernogolovka

Pertsev, Dr., Nikolay
Electronic Materials
A.F. Ioffe Physico-Techn. Inst.

Rzhevsky, Alexey
Electronic Properties
Ioffe Physical Technical Institute of the Russian, St. Petersburg

Samoilov, Prof. Dr., Vladimir
Quantum Theory of Materials
Moscow State University

Volokitin, Prof., Alexander
Quantum Theory of Materials
Department of Physics, Samara

Serbia und Montenegro

Ilic, Dr., Marjia
Neutron Scattering
Universität Belgrad

Spain

Arbe, Dr., Maria Aranzazu
Neutron Scattering
Universität San Sebastian

Avila, Dr., David
Microstructure Research
Universidad Complutense de Madrid

Banchio, Prof. Dr., Adolfo
Soft Condensed Matter
Universidad Nacional de Cordoba

Colmenero, Prof. Dr., Juan
Neutron Scattering
Universität Pais Vasco, San Sebastian

Lund, Dr., Reidar
Neutron Scattering
Universität San Sebastian

Pardo, Dr., Soto
JCNS Garching
Ministerio de Education y Ciencia CMECI

Sweden

Bergqvist, Lars, Tore
Theory of Structure Formation
Universität Uppsala

Switzerland

Kohlbrecher, Dr., Joachim
Soft Condensed Matter
PSI Villigen

Vavrin, Ronny
Soft Condensed Matter
ETHZ & PSI, Villigen

Taiwan

Lin, Jung-Hsing
Quantum Theory of Materials
Research Center for Applied Science, Taipei

UK

Dammone, Oliver
Soft Condensed Matter
University of Oxford

Reissig, Louisa
Neutron Scattering
University of Edinburgh

Ukraine

Kapush, Denys
Microstructure Research
Frantsevich Institute for Problems of Materials Science

Velikanova, Tamara
Microstructure Research
National Academy of Sciences of Ukraine, Kiev

USA

Burkhardt, Theodore
Theoretical Soft-Matter and Biophysics
Temple University, Philadelphia

Fadley, Prof. Dr., Charles
Electronic Properties
ALS Berkeley

Fetters, Dr., Lewis J.
Neutron Scattering
Cornell University

Kapadia, Rehan
Electronic Materials
University of Texas at Austin

Luettmer-Strathmann, Jutta
Soft Condensed Matter
University of Akron

McWhirter, Dr., James Liam Yates
Theoretical Soft-Matter and Biophysics
University of Thessaly

Zhao, Ke
Quantum Theory of Materials
Oak Ridge National Laboratory, Tennessee

Zheng, Nan
Quantum Theory of Materials
Oak Ridge National Laboratory, Tennessee

261

IFF scientists teaching at universities

PD Dr. Artur Baumgärtner
Duisburg

Prof. Dr. Paul-Siegfried Bechthold
Köln

Prof. Dr. Stefan Blügel
Aachen

Prof. Dr. Thomas Brückel
Aachen

PD Dr. Daniel-Emil Bürgler
Köln

Prof. Dr. Jan-Karel Dhont
Düsseldorf

PD Dr. Philipp-Georg Ebert
Aachen

Prof. Dr. Gerhard Gompper
Köln

PD Dr. Raphael Hermann
Liège, Belgium

PD Dr. Riccardo Hertel
Duisburg-Essen

PD Dr. Erik E. Koch
Aachen

PD Dr. Herbert H. Kohlstedt
Köln

PD Dr. Peter R. Lang
Düsseldorf

PD Dr. Hans Lustfeld
Duisburg

Prof. Dr. Heiner Müller-Krumbhaar
Aachen

Prof. Dr. Gerhard Nägele
Düsseldorf

Prof. Dr. Eva Pavarini
Aachen

Prof. Dr. Dieter Richter
Münster

Prof. Dr. Claus M. Schneider
Duisburg-Essen

Prof. Dr. Herbert Schroeder
Aachen

Prof. Dr. Gunter-Markus Schütz
Bonn

PD Dr. Werner Schweika
Aachen

Prof. Dr. Krzysztof Szot
Katowice

Prof. Dr. Knut Urban
Aachen

Prof. Dr. Rainer Waser
Aachen

PD Dr. Simone Wiegand
Köln

Prof. Dr. Roland Winkler
Ulm

PD Dr. Reiner Zorn
Münster

Imprint

263